

Optical Resonators – Science and Engineering

Edited by

Ram Kossowsky, Miroslav Jelinek
and Josef Novak

NATO ASI Series

Optical Resonators – Science and Engineering

NATO ASI Series

Advanced Science Institutes Series

A Series presenting the results of activities sponsored by the NATO Science Committee, which aims at the dissemination of advanced scientific and technological knowledge, with a view to strengthening links between scientific communities.

The Series is published by an international board of publishers in conjunction with the NATO Scientific Affairs Division

A Life Sciences	Plenum Publishing Corporation
B Physics	London and New York
C Mathematical and Physical Sciences	Kluwer Academic Publishers
D Behavioural and Social Sciences	Dordrecht, Boston and London
E Applied Sciences	
F Computer and Systems Sciences	Springer-Verlag
G Ecological Sciences	Berlin, Heidelberg, New York, London,
H Cell Biology	Paris and Tokyo
I Global Environmental Change	

PARTNERSHIP SUB-SERIES

1. Disarmament Technologies	Kluwer Academic Publishers
2. Environment	Springer-Verlag / Kluwer Academic Publishers
3. High Technology	Kluwer Academic Publishers
4. Science and Technology Policy	Kluwer Academic Publishers
5. Computer Networking	Kluwer Academic Publishers

The Partnership Sub-Series incorporates activities undertaken in collaboration with NATO's Cooperation Partners, the countries of the CIS and Central and Eastern Europe, in Priority Areas of concern to those countries.

NATO-PCO-DATA BASE

The electronic index to the NATO ASI Series provides full bibliographical references (with keywords and/or abstracts) to more than 50000 contributions from international scientists published in all sections of the NATO ASI Series.

Access to the NATO-PCO-DATA BASE is possible in two ways:

- via online FILE 128 (NATO-PCO-DATA BASE) hosted by ESRIN, Via Galileo Galilei, I-00044 Frascati, Italy.
- via CD-ROM "NATO-PCO-DATA BASE" with user-friendly retrieval software in English, French and German (© WTV GmbH and DATAWARE Technologies Inc. 1989).

The CD-ROM can be ordered through any member of the Board of Publishers or through NATO-PCO, Overijse, Belgium.



Optical Resonators – Science and Engineering

edited by

Ram Kossowsky

Emerging Technologies, Inc.,
Pittsburgh, Pennsylvania, U.S.A.

Miroslav Jelinek

Institute of Physics,
Czech Academy of Science,
Prague, Czech Republic

and

Josef Novak

Institute of Electrical Engineering,
Slovak Academy of Science,
Bratislava, Slovak Republic

SPC 97-1056

F6170897-W-~~84~~
0131



Kluwer Academic Publishers

Dordrecht / Boston / London

Published in cooperation with NATO Scientific Affairs Division

Proceedings of the NATO Advanced Research Workshop on
Optical Resonators – Theory and Design
Smolenice Castle, Slovak Republic
July 1–5, 1997

Library of Congress Cataloging-in-Publication Data

Optical resonators : science and engineering / edited by Ram
Kossowsky, Miroslav Jelínek, Josef Novák.
p. cm. -- (NATO ASI series. Partnership sub-series 3, High
technology; v. 45)
Includes index.
ISBN 0-7923-4962-8 (alk. paper)
1. Lasers--Resonators. 2. Optical resonance. 3. Laser beams.
I. Kossowsky, Ram. II. Jelínek, Miroslav. III. Novák, Josef, Ing.
IV. Series: NATO ASI series. Partnership sub-series 3, High
technology ; vol. 45.
TA1677.O79 1998
621.36'6--dc21

97-51920

ISBN 0-7923-4962-8

Published by Kluwer Academic Publishers,
P.O. Box 17, 3300 AA Dordrecht, The Netherlands.

Sold and distributed in the U.S.A. and Canada
by Kluwer Academic Publishers,
101 Philip Drive, Norwell, MA 02061, U.S.A.

In all other countries, sold and distributed
by Kluwer Academic Publishers,
P.O. Box 322, 3300 AH Dordrecht, The Netherlands.

Printed on acid-free paper

All Rights Reserved

© 1998 Kluwer Academic Publishers

No part of the material protected by this copyright notice may be reproduced or
utilized in any form or by any means, electronic or mechanical, including photo-
copying, recording or by any information storage and retrieval system, without written
permission from the copyright owner.

Printed in the Netherlands

List of Sponsors

North Atlantic Treaty Organization
Scientific Affairs Division

European Office of Aerospace Research and Development of US Air Force, London, UK
Institute of Electrical Engineering, SR
Slovak Academy of Sciences

TABLE OF CONTENTS

LIST OF SPONSORS	v
PREFACE	xi
PART I: PHYSICS AND THEORY	1
Yu. A. Anan'ev*	
Theory of Laser Resonators and of the Beam Divergence	3
S. G. Anikichev*	
Laser Resonator Theory	13
A. E. Siegman*	
Nonorthogonal Optical Modes and Resonators	29
I. B. Orlova**	
Influence of Intra-Cavity Distortions on Output of Unstable Resonators	55
K. A. Prokhorov and D. G. Afonin	
Optical Resonators with Dielectric Body	79
Manjusha Mehendale and W. Andreas Schroeder	
Thermal Lensing in Kerr-Lens Modelocked Solid-State Lasers	87
PART II: PHASE CONJUGATION	101
H. J. Eichler*, A. Haase, B. Liu and O. Mehl	
Phase Conjugation Techniques	103
V. E. Sherstobitov*	
Phase Conjugation of CO ₂ Laser Radiation And Its applications	119
A. F. Kornev, V. P. Pokrovsky, L. N. Soms, V. K. Stupnikov, and V. Yu. Venediktov	
Conjugated Cavity With the Wide Field of Vision	153
PART III: OPTICS	161

* Key Lecturer ** Invited Speaker
Norman Hodgson*

Beam Quality and Efficiency of Annular Gain Lasers	163
Gregory C. Dente** and Michael L. Tilton Unstable Resonators for Semiconductor Lasers	185
Richard C. Wade** Chemical Lasers with Annular Gain Media	211
A. F. Shkapa, Yu. V. Golgopolov, A. M. Dudov, V. A. Khustalev, G. A. Kirillov, G. G. Kochemasov, S. M. Kulikov, V. M. Murugov, A. V. Ryadov, A. B. Smirnov, S. A. Sukharev and L. I. Zykov Beam Quality Control of an Iodine Laser With SBS	225
S. -A Amarande Flattened Gaussian Beams With Rectangular Symmetry	243
R. M. Hofstra, F. A. Van Goor and W. J. Witteman Beam Divergency Studies on a Long Pulse XeCl Excimer Laser	253
E. F. Plinski, K. M. Abramski and J. S. Witkovski Optical Resonators For a Slab-Waveguide Lasers	267
D. G. Afonin, A. V. Kazakov and A. K. Malyshkin Investigations of Open Resonators With Diffraction Coupling	281
M. J. Galushkin, V. S. Golubev, Yu. N. Zavalova, And V. Ya Panchenko Enhancement of Small-Scale Optical Nonuniformities In Active Medium of High-Power CW FAF CO ₂ laser	289
V. N. Shekhtman Synthesis of Interferograms by Lateral Shear To Measure Wave Front from a Light Beam	301
PART IV: OPTIMIZATION OF DESIGN	309
S. A. Dimakov* Resonators For Lasers Used in Precision Technological Operations	311
W. A. Clarkson* and D. C. Hanna Resonator Design Considerations For Efficient	327

Operation of Solid-State Lasers End-Pumped
By High-Power Diod-Bars

- P. Y. Baskaev, A. V. Lavrov and V. V. Lobachev
Heterogeneity Structure of Active Medium Refraction
For Three-Dimensional Pre-Mixing and Mixing Nozzle
Banks of Gasdynamic Laser 363
- T. Dascalu, N. Pavel and M. Poterasu
Optimized Resonators for High Energy Long-Pulse
Nd:YAG Laser 373
- V. Magni* and M. Zavelani-Rossi
High Power Diffraction Limited Solid-State Lasers
With Stable Resonators 381
- A. Lucianeti**, N. G. Muller, R. Weber, A. Papashvili
A. V. Konyushkin and T. T. Basiev
Highly Efficient High-Average Power Nd:YAG
Laser With a Passive Q-Switch 407
- M. Jelinek**, R. W. Eason, A. A. Anderson, C. Grivas
D. S. Gill, J. Šonský, J. Lancok, L. M. B. Hickney,
N. A. Vianos and P. Hribek
Planar waveguide Lasers of Ti:Sapphire and Nd:YAG
(YAP) Grown by LPD 419
- A. S. Bashkin**, B. I. Katargin and N. A. Pirogov
Problems of CW Chemical Lasers Scaling 427
- J. Lancok**, M. Jelinek, J. Bulir, and P. Machac
Creation of Channels Into Ti:Sapphire
Waveguiding Layers 435
- A. A. Kuznetsov and M. Z. Novgorodov
Properties of the Cavities for Compact Slab
Gas Lasers 441
- A. Mocofanescu and V. Babin
Nd:YAG Laser Resonators Using External
Stimulated Brillouin Scattering Q-Switching Mirror 453
- *Key Lecturer ** Invited Speaker
- V. E. Zharov, S. N. Markova and V. A. Krainov
The Construction of Laser Gyroscope 463

x

PART V: LATE SUBMISSION	477
L. Zykov, S.Buyko, and Yu.Dolgoplov SBS Properties of High-Pressure Xenon at a Density of 0.3-1 g/cm ³	479
D.L. Glebov, V.A. Stepanov, B.I. Vasiliev and A.B. Yastrebkov New Optical Scheme of Complicated Resonator in a Two-Frequency NH ₃ -CO ₂ Lidar	489
Index	495
List of Participants	499

PREFACE

This book contains most, but regrettably not all, the papers that were presented at The Advanced Research Workshop, held July 1-5, 1997, at Smolenice Castle, Slovak Republic.

The problem of angular divergence is of great importance in quantum electronics: low divergence is required not only in most of practical laser applications, but also for achieving high efficiency of parametric laser frequency conversion, and harmonic generation. The large volume of available studies aimed at improving the pump systems and the spectroscopic properties of lasing media, brought about no more than 2-3 fold increases in laser efficiency, while concurrent studies of angular divergence and the implementation of the findings, resulted in several order of magnitude of increases in radiance.

The spatial beam structure that is formed in the laser cavity together with the active element constitute the most critical laser elements. The engineering devices, such as excitation systems, lasing gas circulation systems, etc., are usually at the top of the agenda of scientific meetings and of gatherings of engineering experts. The divergence problem has never been discussed by a broad community of experts in this field.

The conversion of scientific and technological experiences accumulated during the developments of high power military lasers, where efficiency was not necessarily a major driving force, into commercially viable industrial lasers, will require that a focused attention be paid to the general problems of beam divergence. The ARW was structured to initiate, probably for the first time, a dialogue among specialists in resonator and cavity design from NATO and CP countries.

The format used in the ARW was that proven to be successful in the previous conferences; namely, the major portion of the time was devoted to presentations by the Key Lecturers and the Invited Speakers, with ample time allocated for discussions. Submitted papers were assigned to poster sessions. A balance among theory, experimental studies and applications was maintained. We have also included special panel discussions which were designed to explore and summarize major questions following a group of structured lectures.

We thank all the contributors and participants for their effort. Thanks are also due to the personnel of the Scientific Affairs Division of NATO. Our daily routines were greatly facilitated by the management and personnel of the Smolenice Castle, which is owned and operated by the Slovak Academy of Sciences. The financial support of the US Army Research Office in London is sincerely appreciated. Thanks are due to Dr. Hanita Kossowsky who assisted from the inception of the project to its successful conclusion.

Dr. Ram Kossowsky
Prof. Miroslav Jelinek
Prof. Josef Novak

November 1997

PART I: PHYSICS AND THEORY

THEORY OF LASER RESONATORS AND OF THE BEAM DIVERGENCE

A Review

Yu.A. ANAN'EV

St. Petersburg State Technical University

193251, Politekhnicheskaya 29, St. Petersburg, Russia

My intimate acquaintance with lasers dates as far back as 35 years: indeed, in 1962 I succeeded in achieving generation in the first Russian lasers with cryogenic cooling. During the subsequent years, laser technology has made amazing progress; in particular, radiation brightness increased several orders of magnitude, current-day lasing spectra are immeasurably more narrow than those of the first lasers, and the beam divergence problem has gone a considerable way toward its solution. And while one should not certainly underestimate the importance of the laborious work on making gain media and their excitation systems more efficient, nevertheless improvement of the laser resonators has contributed to a very large extent to this progress.

The resonator is known to be a major component of the laser. It is here that the lasing radiation whose specific properties distinguish the laser from among the other sources of light is formed. And it is on the resonator problem, and on the problem of the laser beam divergence which is closely related to it, that I am going to dwell in my communication.

We shall start with a bit of history. The cornerstone of the resonator theory in its present form was laid by the brilliant work of Fox and Li [1]. This work demonstrated for the first time the existence of modes in open resonators and revealed the main properties of these modes for a few simplest cases. The introduction of the concept of diffraction losses has proved to be essential; it has turned out to be much more useful as applied to laser resonators than their quality factor and has almost completely superseded it.

Reading the work of Fox and Li today still rouses admiration; its impact on the subsequent developments in this area has been so profound that even the small errors overlooked by the authors (see p. 81 in my book [2]) is still present in many textbooks on quantum electronics.

This work was followed by papers of Boyd, Gordon, and Kogelnik [3, 4], who made a more general analysis of open resonators consisting of two spherical mirrors with arbitrary radii of curvature, and proposed a classification of such resonators according to the corresponding diffraction losses.

The works of Collins and of Kogelnik and Li published in the mid-60s [5-7] were the next major step forward. They developed general methods to analyze devices made up of an arbitrary number of simple optical components arranged on a common straight line. These methods provided the possibility of reducing such systems to equivalent two-mirror arrangements.

One of the most essential works which made a significant impact on subsequent progress in quantum electronics was a paper [8] published at about the same time by Professor Siegman who has honored this workshop by his presence. It attracted general interest to the so-called unstable resonators, which until that time seemed to be useless. As a result of the subsequent theoretical works of Siegman and of an extensive series of our theoretical and experimental studies (see [2], sections 3.5 and 5.1.4), it is the resonators of this class that have become employed on an increasingly broader scale in high-power lasers with a small beam divergence. We have proposed, studied, and implemented specific arrangements based on these resonators, which are capable of providing presently an answer to a variety of problems in quantum electronics. I have in mind multipass amplifiers with gigantic gain in one stage, field rotation resonators with compact output aperture, resonators with super-high stability of emission direction etc ([2], sections 5.3, 5.4).

Thousands of works dealing with resonators for diverse applications and designed to operate in various conditions have appeared hence. An analysis of the properties of even empty resonators turns out sometimes to be very cumbersome. The task becomes progressively more complex when a resonator contains a gain medium, and one has to take into account the various nonlinear processes involved. Note also that the geometry of radiation interaction with the excited medium is in many cases far from simple. For all these reasons, making now even a cursory review of all these studies would be a problem of daunting complexity indeed, and therefore we shall restrict ourselves only to a broad-brush account of the aspects we believe most interesting.

In nearly all the above mentioned works, the various methods of analysis were supported by the results of numerical calculations, or were based totally on such results. The explosive growth in popularity of personal computers makes numerical calculations increasingly more important in all walks of our life, including resonator design. Let us therefore devote a few words to the methods used in such calculations.

Until now the most popular method is the one used for the first time in that very famous paper of Fox and Li [1]. It is based on considering the evolution of a monochromatic light beam in its multiple transits around the resonator.

This procedure is essentially an iterative technique to find the eigenfunctions of the corresponding integral equation. For over more than one decade, this iterative procedure has been subjected to only insignificant improvements. In particular, one has succeeded in increasing somewhat the number of the lowest modes amenable to calculation by this method; it has been found that the iterative approach permits one to include a nonlinear gain medium into the analysis. At the same time using in each iteration step the cumbersome calculational process based on the Huygens-Fresnel principle resulted quite frequently in unjustifiably long computing times.

A large step forward was made only in the mid-70s, when Professor Siegman together with Sziklas proposed the so-called fast Fourier transform [9, 10]. This method permitted one in many important cases to cut down dramatically on the volume of numerical calculations and, thus, to broaden the range of the resonator parameters which can be calculated numerically.

A highly original approach was proposed by L. A. Vainshtein and described in his monograph [11]. This approach permitted Vainshtein to explain some of the processes which occur in resonators but did not at the time obtain satisfactory interpretation, and to obtain relatively simple expressions for a number of important cases which did not yield to analysis by other methods until then.

The approach of Vainshtein, which is based on taking into account diffractive reflection from resonator edge, was quite popular in the 60s - 70s. It was found subsequently that the part played by this process is mostly not large, and this method is employed presently only in certain particular cases.

The analysis of the evolution of coherent light beams based on using the concept of point eikonal, which is essentially the optical path, has enjoyed a different fate. This method is popular in classical optics and, when applied to the theory of resonators, was extended considerably and is presently used both in studies of an analytical character and in numerical calculations.

This approach was initiated by the paper of Collins [5] published in 1964, which has already been mentioned by us. In this very first work, Collins succeeded in establishing fairly general properties of resonators with simple astigmatism (such optical systems are called frequently orthogonal).

The work of Collins did not, however, contain useful recommendations for calculation of the eikonal, and therefore subsequent studies proceeded primarily in the direction delineated by the classical works of Kogelnik and Li [6, 7], likewise mentioned already. The ray matrix formalism proposed by them yielded an extremely simple expression, called sometimes the ABCD relation, which describes the behavior of Gaussian and similar beams, generated primarily by lasers.

Sometime between the 60s and the 70s it was found that matrix formalism permits one not only to use the ABCD relation but to calculate the eikonal itself (see, for example, [12]); thus these two methods have become intimately connected. Their synthesis leads to universal integral relations, which make possible finding the field distribution at the output of multi-component optical systems from the given distribution at their input.

During the many subsequent years this method could be applied, however, only to a comparatively narrow class of optical systems possessing two mutually perpendicular planes of symmetry. Only in the late 80s, I together with Bekshaev have succeeded in extending this method to systems with arbitrary astigmatism and misalignments, which contain, besides optical components which are comparatively easy to take into account, inclined ellipsoidal interfaces, diffraction gratings, and sections of a medium with a refractive index whose dependence on transverse coordinates is described by a complex second-order polynomial [13, 14]. The results obtained in these studies are summed up in Appendix to my book [2]. We are presently completing, in cooperation

with scientists from Aachen, development of computer programs based on these methods.

Besides the above mentioned methods or in combination with them, there are many others adopted from quantum mechanics, automatic control theory etc. We are not going to dwell on them; it should now be clear that the theory of laser resonators has long become an independent branch of quantum electronics. People specializing in this area, just as in any other, possess a large volume of specific knowledge and have accumulated immense practical experience in resonator design. This specifically relates to those of them who participated in development of lasers of various types. Among them are my former students delivering a number of review lectures at this workshop, namely representing Russia Sherstobitov, Orlova, Dimakov and presently Canadian Anikichev. I should mention that the knowledge of the technical solutions proposed in diverse situations permits one to master virtually all techniques used to improve laser optics. This provides a considerable edge over other designers of laser technology who quite frequently have dealt only with one laser type and may not be aware of the useful solutions reached for lasers of another kind.

Nevertheless, one frequently meets in practice with an underestimation of the importance of this experience and knowledge. Therefore I am going to explain now what is the use of people specializing in optical resonators and, on a broader scale, in methods of solving the problem of the quality of laser radiation, a problem of paramount importance indeed.

I immediately point out the expediency of their participation in the very early stages of a new laser project. This is sometimes neglected for one of the two following reasons: specialists in methods of excitation of gain media either believe that their own knowledge in resonators is more than sufficient or are of the opinion that one has first to make a laser, and the beam divergence problem can be shelved until a later time. It is not hard to guess what such an approach can lead to. I know of more than one case where time-consuming work on development of a laser of a new type proceeded for a long time without invoking the help of resonator specialists in a direction which, from the standpoint of spatial characteristics of radiation, was totally a blind alley. And after the laser has been built, and it turns out that its operation is unsatisfactory, the people in charge come to a sudden realization that something is wrong, but the train has already departed, as we say.

As an illustration, I could tell here about some very expensive projects on development of high-power liquid-medium lasers started in our country. At the same time it would not have been difficult for resonator specialists, acquainted at least superficially with thermo-optical properties of liquids, to draw a conclusion on total fruitlessness of such ventures.

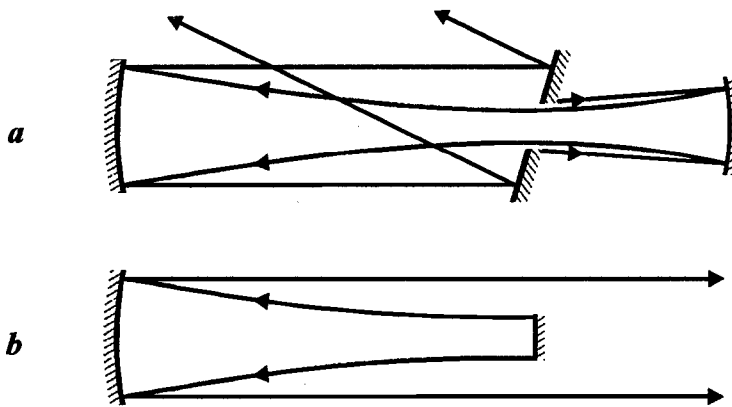
After the general direction of work on the project has already been chosen, one starts with developing the optical arrangement of the corresponding laser, which sometimes requires searching for novel solutions; we shall see at this workshop that the process of generation of these new solutions has not come to an end. As a rule, such novel solutions will require experimental verification, and professional experience and expertise in resonator development permits one sometimes to carry out this verification

by straightforward and cheap means. For instance, we managed once in avoiding truly colossal expenses by simulating resonators for giant chemical lasers using the simplest neodymium-glass laser.

Although at first glance the laser resonator appears to be a simple device of which everybody knows everything, it is by far not every laser-technology designer that is acquainted with its subtle features. This relates especially to the arrangements that have appeared quite recently. I shall permit myself a few fairly recent examples.

In the early 80s, Italian researchers proposed the so-called unstable resonator with spatial filtration of radiation (SFUR) (see its schematic in Fig. 1,a). In contrast to conventional unstable arrangements, the output distribution of this laser is close to Gaussian. True, at the center there is an area unfilled by radiation, but if the medium provides a high gain this area is small, and it does not affect strongly the far-zone distribution.

Figure 1



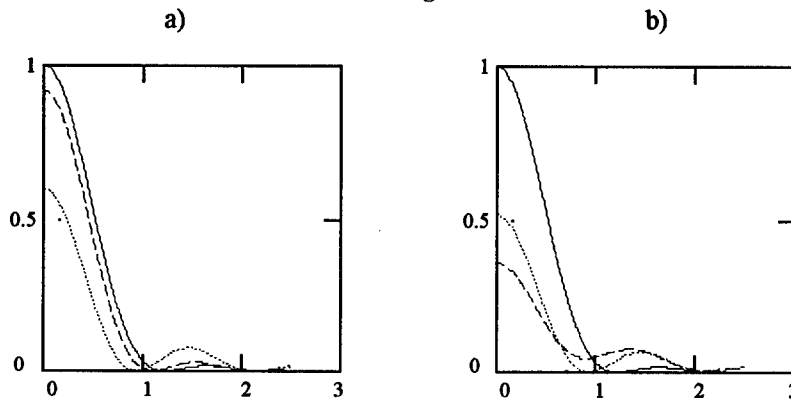
Many researchers are acquainted with this arrangement and sometime use it, but much less known is the following: our analysis [15] showed that the right-hand part of this resonator can be replaced by one plane mirror (Fig. 1,b). The new resonator, while providing the same lasing parameters, is not only simpler in design but at the same time is more convenient in that the radiation is led out here along the optical axis rather than off it.

A few years ago a group of Japanese researchers started to employ unstable resonators with a semitransparent output mirror. The idea behind this arrangement is that adding to an annular cross-section beam at least a weak beam with an appropriate phase from the central zone could increase substantially the fraction of the energy confined within the central spot in the angular distribution.

This approach is illustrated by Fig. 2, a. The upper (solid) curve shows the angular distribution of radiation for an ideal plane-wavefront emitter with uniform distribution over a circular output aperture, the lower (dot) one relates to a conventional unstable resonator with 60%-losses, and the third (dash), to unstable resonators which have output mirrors with a finite transmission coefficient $T=0.3$ but the same losses (for

which purpose one has to reduce the coefficient of magnification M). We readily see that in this idealized case of no intracavity aberrations this approach can turn out quite useful.

Figure 2



This example gives us grounds to voice the following consideration. The authors proposing a new arrangement try usually to stress all its merits, however small, while passing over in silence its drawbacks. But the specialist using various designs in practice must know these shortcomings. In this particular case, this arrangement has a serious drawback which our analysis has immediately revealed, namely, it is highly sensitive to intracavity aberrations. This is readily seen from Fig. 2, b, where the upper curve is the same as on Fig 2, a, and two others relating to the same resonator designs as Fig. 2, a, but in the presence of spherical wave aberrations of only $\lambda/8$ in single transit though an active medium. In these conditions resonators with partially transmitting mirrors turn out to be not better but worse than the conventional designs. Rather than multiplying examples of such kind, we shall devote a few words to the beam divergence problem, which is intimately connected with the resonators.

The factors on which the angular divergence depends are well known, as is well known also the large variety of means by which one can try to approach its diffraction-limited value. While introducing unstable resonators permitted one to make considerable progress on this way, there still exist the limitations associated with inhomogeneities of the gain media. Attempts at overcoming these limitations by means of the so-called wavefront conjugation have been made with varying success for over a quarter of a century. The history of this method goes as far back as the mid-60s, when Kogelnik proposed it to improve observation systems; in 1971, I proposed a similar technique to correct the wavefront of high-power laser emitters [16] (here one has in mind the very popular scheme of two-transit laser amplifier with intermediate wavefront conjugation).

An analysis of all these problems on this workshop being impossible, I shall talk only about what one should strive for. I have in mind the radiation field distributions which are most favorable from the applications standpoint, an aspect which is connected

intimately with the criteria to be used in comparing various emitters of the same power from view-point of their angular distribution.

In our country the angular divergence of laser radiation was most frequently characterized by one of two parameters, namely, the divergence at 0.5 intensity level and that at 0.5 (sometimes 80%) energy level. The first of them is actually the width of the central maximum in the angular distribution which is measured at the level corresponding to one half the maximum intensity, and the second, the angular width of the cone confining one half (or 80%) of the total radiation flux.

Any systematic analysis of the shape of the angular distribution radiated by various coherent sources showed, however, that attempts at comparing the practical significance of sources in the value of only one of these two parameters can easily lead to an erroneous conclusion. Take, for instance, the angular distributions produced in diffraction of a plane wave from a round hole and from rings with the same outer diameter (the latter shape is characteristic of conventional unstable resonators). Calculations yield the following results: the angular divergence of the radiation emitted by round hole measured at the 0.5 intensity level or at the 0.5 energy level is nearly the same; but when we proceed to annular emitters, the first value decreases and the second quickly increases. For instance, if inner diameter of ring is equal to 80% of outer diameter, these two parameters differ more than 6 times.

The general conclusion that any attempt at characterizing the divergence in any situation with only one parameter seemed to me fairly obvious (see, for example, my books). Nevertheless, in the late 80s Western specialists in laser technology accepted the so-called "beam quality" M^2 as such a universal parameter.

This parameter is based on calculation of second-order moments of near- and far-field intensity distributions. The theory of beam moment evolution in the course of propagation is in itself quite elegant, and Professor Siegman played a prominent part in developing and spreading this method. A certain contribution to this area is due to me with Bekshaev [17]; indeed, whereas before our paper the moment evolution laws were known only for beams of comparatively simple shape propagating through orthogonal optical systems, we solved the problem for arbitrary beams and for systems of a much broader class.

The definition itself of the beam quality in terms of second-order moments implies that the significance of the distribution tails, for which the weighting factor equal to the squared distance from the axis is too large, is here clearly overevaluated. A more careful analysis shows indeed that the beam quality, as a criterion for comparing various sources of coherent radiation in their usefulness, has an inherent deficiency, which do not have the parameters mentioned before. Indeed, the beam divergence of any radiation source of practical significance, measured at any intensity or energy level, has always a definite and finite value. At the same time the beam quality has a finite reasonable value only if fairly rigid conditions imposed on the field distribution shape are satisfied. For many realistic coherent-radiation sources these conditions are formally not met.

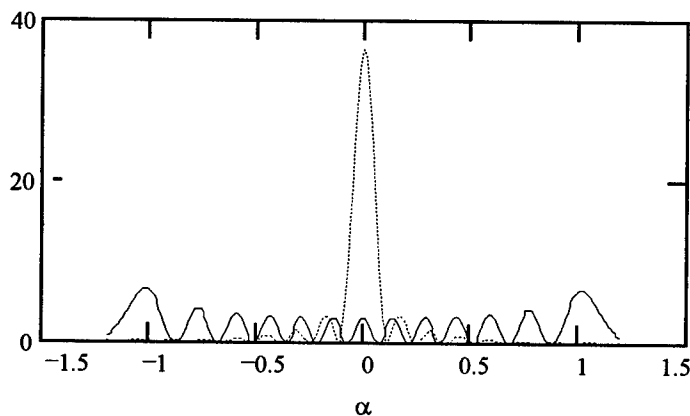
Indeed, it can be easily shown that if the dependence of intensity on transverse coordinates has breaks, the second moments of the angular distribution and, hence, the

beam quality become infinitely large. Note that such breaks inevitably occur in the case of diffraction from rigid diaphragms, which are always used in optical systems.

While in principle this difficulty can be sidestepped by introducing an apodization factor in a theoretical consideration, or by limiting properly the aperture in far-field distribution measurements, the result will now become dependent on the width and shape of the corresponding transmission function.

Because of that, the comparison of the potential of different sources by the magnitude of M^2 can lead to absurd results. The well-known paper of Siegman [18] may serve as a convincing illustration of this fact. I shall permit myself giving here one more revealing illustration; just as in the paper of Siegman, it relates to the case of phase correction for beams with alternating amplitude distribution. Solid curve in Fig. 3 displays the angular distribution of radiation for a high-order mode of a stable resonator (it is for such beams that this method of correction was originally proposed); after the correction, the angular distribution assumes the shape of the dot curve.

Figure 3



It is certainly obvious that the phase correction has dramatically improved the angular distribution; indeed, the central lobe, which originally contained 4% of the total power, now confines 70%. At the same time the quantity M^2 retained its original value of 25 after the correction only because a negligible fraction of the radiation is scattered through large angles.

I think the most universal parameter characterizing an angular distribution in the cases where the output laser aperture does indeed limit the beam cross section and, thus, determines the diffraction-limited divergence, is the aberration factor introduced in my book [19]. It is equal to the ratio of the axial luminous intensity (i.e. intensity at the center of the angular distribution or of the focusing zone) to its maximum possible value at the given output power and cross section of output aperture. It is interesting that above-mentioned maximum possible value of the axial luminous intensity is

reached in the case where the wavefront is plane, and the radiation density fills uniformly the aperture rather than has the Gaussian distribution.

For problems associated with illumination of distant objects the adequacy of this criterion is obvious. Besides this case there is a number of other important applications where Gaussian beams are far from optimal.

In connection with all this I do not understand why the manufacturers of industrial lasers show such inclination toward Gaussian beams; indeed, despite the fact that the people with whom I presently work have great experience in the use of lasers in cutting, welding etc., we have not been able to find any weighty arguments in favor of application of pure Gaussian beams in any process.

All this provides support for my opinion, expressed more than once, that it is impossible to characterize the beam quality with an only parameter appropriate for any conceivable case. Beams with different intensity distributions can be found suitable for different applications, and, thus, one will inevitably have to use different beam quality criteria.

In conclusion, I shall permit myself a short and possibly somewhat disagreeable digression. At any conference dealing with a broad scope of problems bearing on resonators and the angular divergence of radiation one invariably hears too many ideas and learns about so many studies which had been reported and discussed in Russian-language literature long ago.

This workshop has not been, alas, an exclusion to the rule. Rather than presenting numerous examples in support of this statement, I shall restrict myself to only one of them. I have in mind the report of Prof. Siegman, whom I hold in a high esteem and to whom, by the way, I am greatly indebted. The concept developed in this report was proposed by me and Anikichev as far back as 1986 [20].

It will not be an overstatement to say that during the recent two decades I have come across ideas and considerations new to me only on a few occasions. There are two reasons for this.

One of them consists in that in the late 60s Russian researchers have found themselves in a particularly favorable situation. At that time, our country was spending huge amounts of money on military purposes; this provided us with a unique possibility to bring together a large group of good specialists, which now already for 30 years have been working exclusively on problems connected with resonators and the angular divergence. This group has been taking part for a long time in practically all large Soviet laser projects and has accumulated a truly enormous experience. We studied comprehensively all problems arising in building resonators for high-power lasers. All results of scientific significance were published in literature; it should be added that rather than limiting ourselves to listing the various methods of solution for the corresponding problem, we expressed our opinion concerning the potential of these solutions. And we can see now that in the vast majority of cases these opinions have turned out to be correct.

The second reason, and not a less significant one, is that nobody in the West appears to read our papers and books, although our magazines and books are published in an English edition as well. One has to admit that the quality of translation is quite often

unsatisfactory. This does not, however, relate to my recent book [2] which summed up numerous Russian studies. Translated by my good friend G. P. Skrebtsov, it was published also in the West; and although all reviewers estimated the translation as excellent, and a preface to the book was written by Prof. Siegman himself, nobody reads it either, as this has become obvious at this Workshop!

At the same time if no efforts were spent to understand anew what was already learned before, and no mistakes which were made by other researchers were repeated time and again, our progress would be much faster and much more rational.

References

1. Fox A.G. and Li T. (1961) Resonant modes in a maser interferometer, *Bell Syst. Tech.* **40**, 453-488
2. Anan'ev Yu. (1992) *Laser Resonators and The Beam Divergence Problem*, Adam Hilger, Bristol, Philadelphia and New York
3. Boyd G.D. and Gordon I.P. (1961) Confocal multimode resonator for millimeter through optical wavelength masers, *Bell Syst. Techn. J* **40**, 489-508
4. Boyd G.D. and Kogelnik H. (1962) Generalized confocal resonator theory, *Bell Syst. Techn. J.* **41**, 1347-1369
5. Collins S.A. (1964) Analysis of optical resonators involving focusing elements, *Appl. Optics* **3**, 1263-1274
6. Kogelnik H. (1965) Imaging of optical modes - resonators with internal lenses, *Bell Syst. Techn. J.* **44**, 455-494
7. Kogelnik H. and Li T. (1966) Laser beams and resonators, *Appl. Optics* **5**, 1550-1567
8. Siegman A.E. (1965) Unstable optical resonators for laser application, *Proc. IEEE* **53**, 277-287
9. Siegman A.E. and Sziklas E. (1974) Diffraction calculations using fast Fourier transform methods, *Proc. IEEE* **62**, 410
10. Sziklas E. and Siegman A.E. (1975) Mode calculations in unstable resonator with flowing saturable gain. II. Fast Fourier transform method, *Appl. Optics* **14**, 1874-1889
11. Weinstein L.A. (1966) *Open Resonators and Open Waveguides*, Sovetskoye Radio, Moscow
12. Amaud J.A. (1970) Nonorthogonal optical waveguides and resonators, *Bell Syst. Techn. J.* **49**, 2311-2348
13. Anan'ev Yu.A. and Bekshaev A.Ya. (1989) Matrix method for analysis of misaligned optical systems with astigmatic elements, *Optika i spektroskopiya* **66**, 910-913
14. Anan'ev Yu.A. and Bekshaev A.Ya. (1989) Local elements in matrix method of analysis of misaligned optical systems, *Optika i spektroskopiya* **66**, 702-708
15. Anan'ev Yu.A., Anikichev S.G. and Soloviev V.D. (1990) Half-confocal resonator with diffraction output, *Optika i spektroskopiya* **68**, 1213-1215
16. Anan'ev Yu.A. (1971) Method of low-divergence radiation formation, Inventors Certificate № 414935 of 12.10.1971, *Byull. Izobr.*, 1974, № 3, 171
17. Anan'ev Yu.A. and Bekshaev A.Ya. (1994) Theory of intensity moments of arbitrary light beams, *Optika i spektroskopiya* **76**, 624-635
18. A.E. Siegman (1993) Binary phase plates cannot improve laser beam quality, *Optics letters* **8**, 675-677
19. Anan'ev Yu.A. (1990) *Optical resonators and problem of laser radiation*, "Nauka", Moscow
20. Anan'ev Yu.A. and Anikichev S.G. (1986) About decomposition on set of eigenfunction of open resonator equations, *Optika i spektroskopiya* **61**, 856-860

LASER RESONATOR THEORY

S. G. ANIKITCHEV

SGA

44 Painted Rock, Richmond Hill,
Ontario, Canada L4S 1R6

This paper is about how to apply the knowledge of formal resonator theory to real laser situations.

1. Properties of hollow resonator eigen modes and expansions in eigenfunction series

We shall start from some well known properties of integral open cavity operators G^1 . Their eigen modes u_m and eigen values α_m are the solutions of the integral equation

$$\alpha_m u_m = G(u_m), \quad (1)$$

where $|\alpha_m| < 1$ due to diffraction loss.

Our goal now is to understand how one can use the set of eigen functions (modes) to describe a laser.

The kernels of resonator operators are complex symmetrical (or may be made symmetrical), which means that for an arbitrary pair of functions f and g the following relation is valid:

$$\int_S f G(g) dS = \int_S g G(f) dS, \quad (2)$$

where S is the surface on which functions are prescribed (in our case it is the surface of the mirrors). From (2) it follows that

$$\langle u_m, u_n \rangle = \int_S u_m u_n dS = 0, \quad (3)$$

if $\alpha_m \neq \alpha_n$. From (3) it follows that nondegenerated eigenfunctions of G are linearly independent. Let $\alpha u_\alpha = G(u_\alpha) \neq 0$, $\beta u_\beta = G(u_\beta)$, and $\gamma u_\gamma = G(u_\gamma)$ with $\alpha \neq \beta$, $\alpha \neq \gamma$, and $\beta \neq \gamma$. Let us also assume that one can find b and c such that $u_\alpha = b u_\beta + c u_\gamma$.

With the use of (3) we obtain $0 = \langle u_\alpha, u_\beta \rangle = b \langle u_\beta, u_\beta \rangle + c \langle u_\gamma, u_\beta \rangle = b; \dots c=0$ and, finally

$u_\alpha = 0$, which proves the statement. It should be noted that properties (2), (3) and linear independence are true only on the surface of mirrors of linear cavities.

There is some artificial analogy between properties (2) and (3) and properties of Hermitian operators K :

$$\int_S g K(f) dS = \int_S f (K(g))^* ds, \text{ and} \quad (4)$$

$$(\varphi_m, \varphi_n) = \int_S \varphi_m \varphi_n^* dS = 0, \quad (5)$$

where φ_m, φ_n are nondegenerated eigenfunctions of the operator, and the star denotes complex conjugation. The existence of (4) implies Hermitian orthogonality and completeness of the set $\{\varphi_n\}_{n=0}^\infty$ in the space H of functions with finite energy.

From the operator theory, in general, it does not follow that integral operators with complex symmetrical kernel G with properties (2), (3) possess a complete set of eigenfunctions. Despite this fact, formal similarity of Eqs (2), (3) and (4), (5) suggested to the authors of² and³ the possibility of representing the arbitrary functions prescribed on S in the form of series

$$f = \sum c_n u_n, \quad (6)$$

where c_n are calculated in a "natural" way, $c_n = \langle f u_n \rangle / \langle u_n u_n \rangle$. The question is how to use these expansions. By virtue of linear independence, the set of eigen modes u_n forms the basis of some subspace of $V \subset H$ and can be useful if we know, at least approximately, what we are losing.

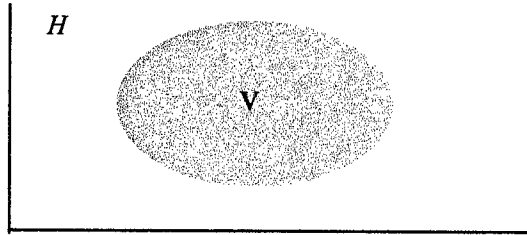


Fig. 1

For this reason it will be interesting to give an example which provides us with some rough idea about the case when an approach using eigen mode expansions is incorrect.

Let us consider a two-dimensional cavity of plane or spherical mirrors with a Gaussian distribution of reflection coefficient as the simplest model of an open cavity that permits analytical solutions. It is easy to verify¹ that in case of an unstable resonator an attempt to expand a converging wave $f_0 = (u_0)^*$ (Fig. 2) into a series (Eq. (6)) using eigenfunctions (modes) leads us to a diverging series.

The converging wave f_0 can be produced by the light-scattering sources inside the cavity⁴. Almost complete absence of loss over several passes is a typical feature of converging waves.

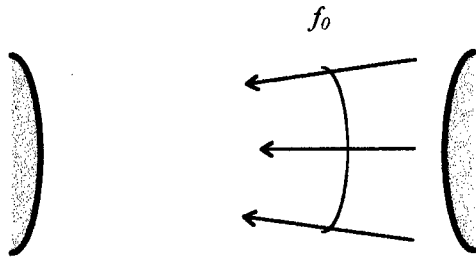


Fig. 2

We can also excite waves similar in properties in stable resonators with Gaussian mirrors by injecting them from an external source (or they can be produced by spontaneous radiation of the active medium). Under certain conditions such waves can not be represented as series (Eq. (6)), either. We, thus, can interpret divergence of the series for f_0 as impossibility to represent according to rule (6) a wave, which at a certain stage of evolution has energy loss per pass less than any cavity mode.

This assumption is substantiated by the following argument. As we can see, almost in all cavities we can find waves of " f_0 type", to which belong, for instance, the waves introduced in⁵. There are only two exceptions: ideal stable cavities with totally reflecting infinite mirrors, and confocal resonators. Their modes are real and, therefore orthogonal in Hermitian sense (in this case Eq. (6) becomes the Fourier series using complete orthogonal systems of functions). It is significant that in this case waves do not exist, and energy loss per pass is less than loss of the fundamental mode.

This statement is obvious for stable resonators with infinite mirrors and is proven in Ref. ⁱ and Ref. ⁱⁱ using different techniques. From considerations in Ref. ⁱ it also follows that any phase perturbation in a confocal cavity (which leads, for example, to slight change of configuration), lowers its Q : a perturbed cavity has a set of modes that does not match that of the confocal resonator and its zero-order mode does not possess the above property. Therefore, the only cavity with finite mirrors which has a complete and orthogonal set of eigenmodes is the confocal one.

The arguments given on the application of type (6) expansions do not provide us with answers to all possible questions and they are not mathematically rigorous. However, they can serve as a warning for those who use the eigenmode expansions.

2. Excitation of resonators

One of the conclusions that may be drawn from the previous is that the set of eigenmodes can not be used for representation of spontaneous radiation when considering the details of the onset problem. The point is that the amplitude distribution w of spontaneous emission is expressible in general case as

$$w = v + u, \text{ where } v \in V, u \in H \setminus V.$$

In other words, v can be represented as a linear combination of eigenmodes, and at the same time u belongs to the set of functions for which series (6) are diverging. It may be unimportant for empty cavities (converging waves after a full cycle of evolution become diverging and leave the resonator) but is of importance in case of a laser, because of gain saturation.

After this remark let us briefly consider the standard excitation problem:

$$f = G(f) + g, \quad (7)$$

where f is the solution sought, G is the cavity operator, and g is the prescribed function (the external source of radiation). In an empty resonator, G does not depend on f and g and is simply a linear compact operator. The formal solution of (7) is given by Neumann series

$$f = \sum_{n=0}^{\infty} [G(g)]^n \quad (8)$$

which is converging if norm $\|G\| < 1$; this statement is always valid for empty resonators because of energy loss. Eq. 8 provides us with an easy method for numerical calculations.

If the cavity contains saturable active medium, operator G depends on the intensity inside the resonator and problem (7) becomes much more complicated. However, it may be shown that because of saturation and diffraction loss operator G does possess the required properties and solution of the excitation problem with an external source is again given by (8).

The simplest and the most popular method of mode calculations in empty cavities is the method of iterations, where the solutions of (1) are given by the following equations:

$$\begin{aligned} u_{0,1} &= \lim_{n \rightarrow \infty} (v^n) \equiv \lim_{n \rightarrow \infty} (G(G(\dots G(v^0) \dots))), \\ \alpha_{0,1} &= \lim_{n \rightarrow \infty} (v^n / v^{n-1}). \end{aligned} \quad (9)$$

Here v^0 is a zero approximation; each distribution v^n (field after n passes over the cavity) is normalized in order to avoid the loss of accuracy. By picking symmetrical v^0 one can derive fundamental eigen mode and corresponding eigen value. In case of asymmetrical v^0 one can obtain the lowest asymmetrical mode. Usually these calculations are performed using Fox - Li or FFT methods.

To calculate high order modes, for example u_2 , we have to consider operator G as an operator defined in the space $H_{S,0}$ of symmetrical functions which are orthogonal to u_0 (they are automatically orthogonal to u_1). For calculation of u_4 we shall consider G in a space of $H_{S,0,2}$ and so on. Numerical procedure becomes bulky for it should include calculations of all low-order modes and Hermit orthogonalization at each iterative loop.

The numerical procedure gives us some information about the onset process in the resonator. With the use of this procedure one can roughly estimate the time which is necessary to select the fundamental mode from spontaneous emission. The time obtained from calculations depends not only on the parameters of the resonator but also on the type of initial distribution. This means that for proper simulation of the onset one has to have a reliable model of spontaneous emission, see Fig 3.

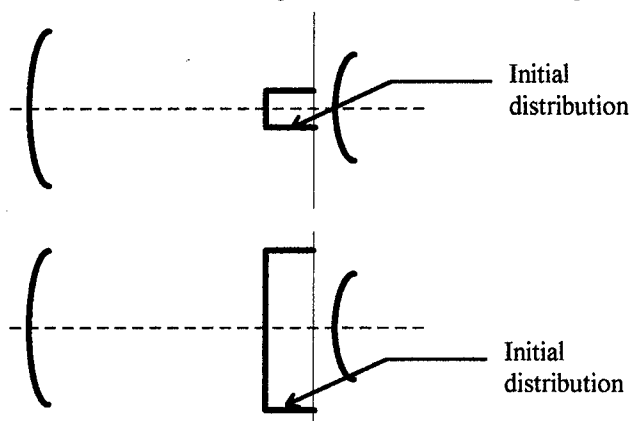


Fig. 3

As it follows from earlier sections, this approach works separately in the sets of functions with different types of symmetry: in order to calculate the lowest asymmetrical mode (and get information about the onset) one should start from purely asymmetrical initial distribution.

Very often introducing the saturable active medium in the model changes the onset process dramatically, for example when considering metal vapor and excimer lasers ^{6,7}.

In some cases, however, estimations of the time which is necessary for the selection of the fundamental mode, obtained from the Fox-Li calculations of empty cavities, may be useful. It happens if the onset occurs during linear or under threshold stage of oscillation in a condition when gain distribution is uniform and the final state of the laser is single-

mode oscillation. It primarily takes place in resonators with high diffraction loss, such as unstable and Fabri - Perot resonators with small apertures.

3. Resonators with saturable active medium

It should be mentioned in the beginning that there is no correct way of compiling the integral equation of the type (1) for resonators filled with saturable active medium. For this reason the numerical model of an active resonator introduced by Fox and Li⁸ is in common use (see Fig. 4).

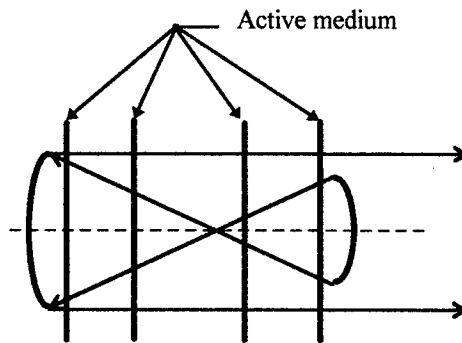


Fig. 4

Using this model, they replaced the operator G of the open resonator with a computer program which can take into account not only effects of diffraction but also uneven distribution of gain and its saturation by concentrating active medium into infinitely thin layers inside the cavity.

As it can be readily seen, the results of calculations using this modification of Fox-Li method (no matter which particular numerical approach is applied) depend not only on the parameters of the resonator and the active medium but also on the type of initial distribution.

Low gain and symmetrical initial distribution will result in a fundamental mode solution. In a situation when gain is higher, the problem may have more than one solution depending on the zero approximation.

It is possible to find a combination of parameters of the active medium and the resonator when Fox-Li approach will give three different results. Let us assume that we have symmetrical initial distribution of gain and the resonator is symmetrical with respect to the optical axis. The first solution will be TEM_0 (symmetrical initial approximation), the

second one will be TEM_1 , and the third one will be a combination of TEM_0 and TEM_1 for initial distribution which is a mixture of symmetrical and asymmetrical distributions of the field's amplitude, Fig. 5.

The first two solutions are unstable; the third solution is not converging within the frameworks of Fox-Li method because of the beating between the two modes. What this means is that iterative numerical calculations are not suitable for analysis of multiple mode lasing; any single mode solution should be checked for stability.

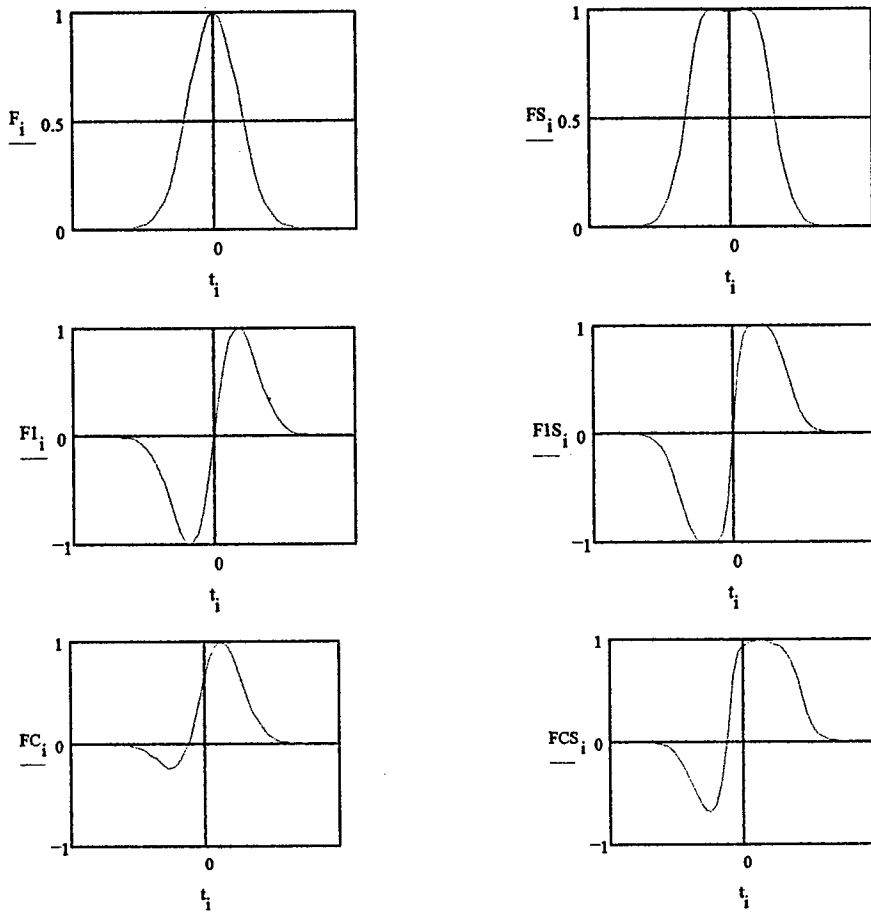


Fig. 5

4. Single-mode and multiple-mode operation

As it follows from the foregoing text, resonators filled with saturable active medium are hard to analyze. However, there are some important situations that can be described quite neatly.

Before proceeding any further, we should mention the fact that most lasers with unstable resonators are single-mode. Therefore, they can be worked on with the use of conventional Fox-Li method. Diffraction loss in such resonators is so high that at almost any gain we end up with one stable solution of the nonlinear Fox-Li problem. In this case the problem is quite simple for calculations, if we put aside the special case of lasers with high level of spontaneous emission and large gain, such as metal-vapor and excimer lasers^{vi}, ^{vii}. Hence, the analysis of mode structure is important only for stable and waveguide resonators. Laser developers are most often interested in finding out the parameters which ensure single-mode lasing. We shall consider here (using Fox-Li method as an illustration), step by step, a very simple method which is convenient when doing numerical simulations or analytical estimations.

1. We assume that parameters of the resonator and the active medium are such that the laser works on the lowest mode, TEM_0 . To find the distribution of its amplitude we should take symmetrical initial approximation. After finding the fundamental mode as a solution we should check if this solution is stable.
2. If the solution is not stable (we observe beating - periodical change of distribution at reference plane), we have got the answer: beating indicates that some symmetrical high-order modes are above the threshold and steady lasing at TEM_0 is impossible.
3. If we have a stable solution, it does not yet mean that the resonator ensures single-mode operation, for we lost all asymmetrical modes in the numerical calculations. To answer the question one should inject any asymmetrical function (better TEM_1 calculated for the empty cavity) into the resonator with the distribution of gain which corresponds to the gain saturated by TEM_0 (step #1). If TEM_1 is above the threshold, we have multiple-mode operation, otherwise - single mode lasing, Fig. 6.

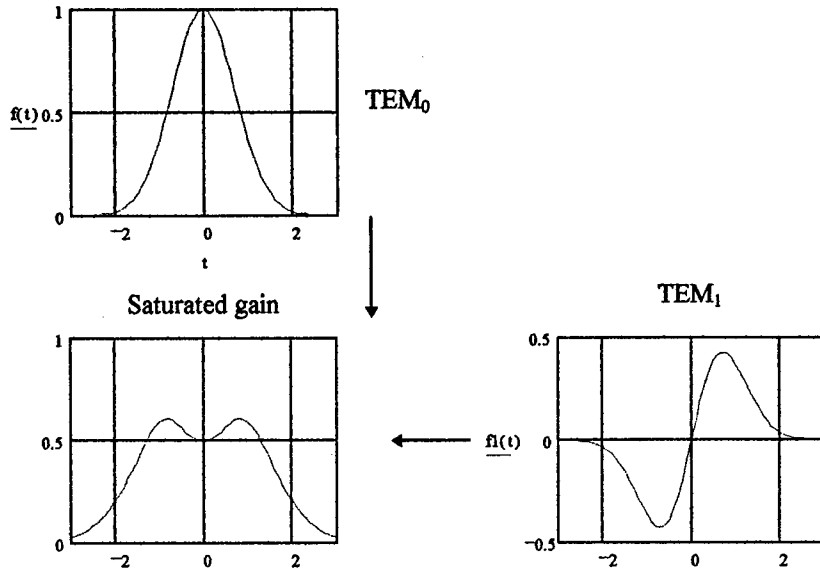


Fig. 6

In the situation of two-mirror linear stable resonators this logical pattern can be considerably improved and, in addition, some analytical results can be obtained⁹. The point is that to get reliable results one should take into account the 3-D nature of the active medium. It means that we have to reject the model in which the active medium is concentrated in thin layers adjacent to the mirrors and try to make all calculations analytically.

Without going into details, we shall just report that the result of consideration is the analytical criterion of single mode lasing in stable resonators. This criterion takes into account bulkiness of the active medium, the case of uneven distribution of small signal gain, and large excess above the threshold.

The most important fact, following from the criterion, is that permissible excess of threshold is defined by the difference of losses for hollow cavity modes TEM_{00} and TEM_{01} .

The analysis of multiple-mode lasing is relatively difficult¹⁰, and is not of interest for developers of lasers with low divergence.

5. Some examples

In this section one can find examples of how knowledge of elementary resonator theory can save time and help to develop resonators for lasers of new types.

5.1 WAVE-GUIDE SLAB RESONATORS

A major problem in resonator design for CO₂ slab-wave-guide lasers is to ensure low divergence in lateral direction for which Fresnel Number $N_{fr} \approx 1000$. For this reason, employment of an unstable resonator is an obvious idea. At the same time, positive-branch unstable resonators of low magnification exhibit very high sensitivity to misalignments of mirrors. The knowledge of this fact opens an opportunity to overcome this disadvantage by employment of a negative branch unstable resonator, making the idea commercial.

Another question that may arise is the beam quality in transverse (wave-guide) direction. Usually, the size of the gap between electrodes is about 1 - 2 mm, and lasing is automatically single-mode in transverse direction. However, there may be a necessity to analyze mode properties in wave-guide direction when considering optimal conditions of launching the radiation into the gap (distances between wave-guide and mirrors, curvatures of external mirrors, and so on).

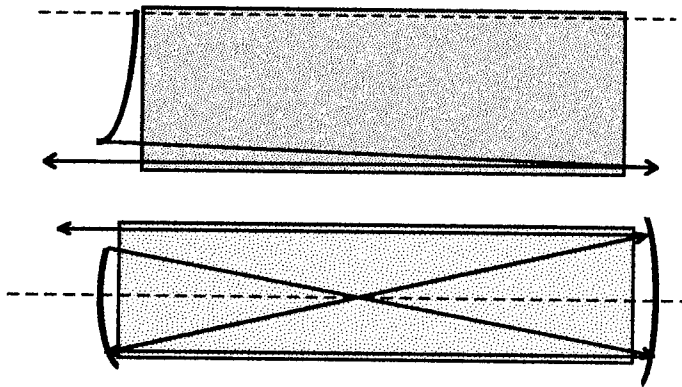


Fig. 7

The usual way to analyze this problem is to use the multiple-mode (about 10 modes) matrix calculations¹¹, based on a set of hollow wave-guide modes. At the same time, however, in a typical CO₂ laser there is a distributed negative lens inside the gap caused by the temperature difference between the central region of discharge and the wave-guide walls. This may significantly change the properties of wave-guide modes, taking away the validity of such "hollow-wave-guide" multiple-mode analysis.

5.2 RESONATOR FOR A WAVE-GUIDE LASER WITH AN ANNULAR CROSS SECTION

We shall briefly discuss now a resonator arrangement has which never been employed and, probably, will never be employed in a real laser, but provides us with an example of how ideas can be transferred from one case to another.

Let us consider a wave-guide (for a CO₂ laser) which is a coaxial wave-guide with a gap width of about 1-2 mm, diameter of about 20 cm and length of about 100 cm.

The idea of so-called Talbot resonators is well known for the set of rectangular wave guides or for the slab ones. It can be shown that properties of plane waves existing in lateral direction of slab wave-guides are very similar to that of helical waves in tangential direction in coaxial wave-guides. The understanding of this fact makes it possible to calculate the parameters of possible Talbot resonator design for the lasers with coaxial wave-guides¹². It also allows to save time and money on the experimental stage of the work, for one can wait for the first successful implementation of the idea in the case of a slab wave-guide laser.

5.3 RESONATORS WITH A LARGE EFFECTIVE LENGTH

The understanding of the fact that mode competition is determined by differences of losses for different modes, allowed Prof. Anan'ev¹³ with his coworkers to suggest a very effective resonator to ensure low beam divergence, Fig. 8 from¹.

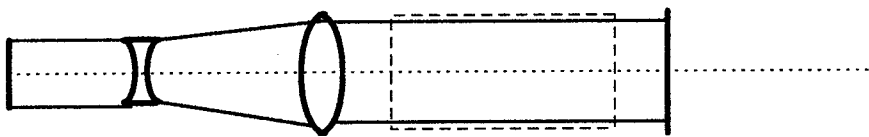


Fig. 8

Low Fresnel Number of this resonator is determined by the existence of a narrow part after the telescope.

5.4 RESONATOR WITH A LARGE EFFECTIVE LENGTH FOR LASERS WITH ANNULAR CROSS SECTION

Let us see how the same idea can be applied in a completely different situation. We shall now consider resonators with an annular cross section.

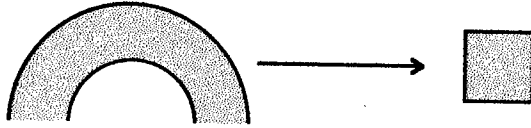


Fig. 9

First, we want to transform the annular cross section into a continuous one to have the region where we can place the optical axis, Fig. 9.

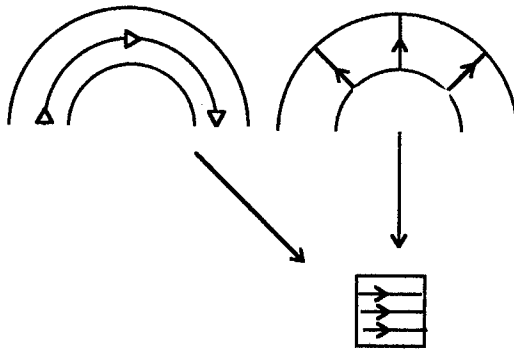
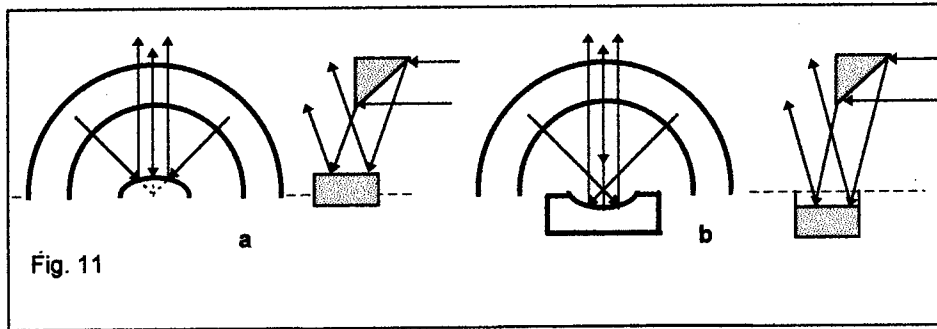
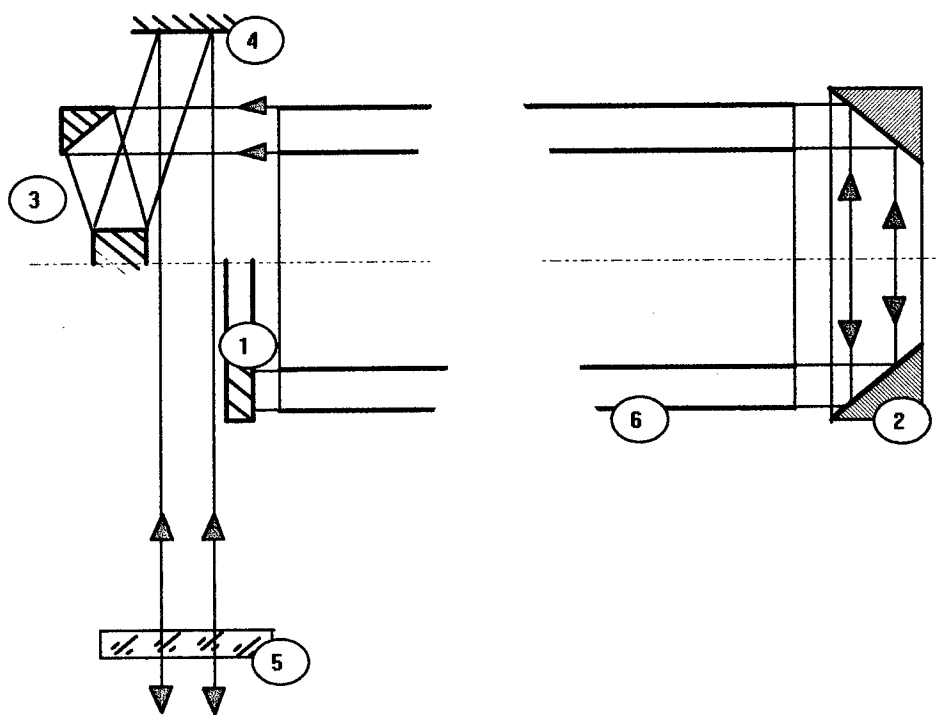


Fig. 10

At the same time we intend to transform the type of polarization which is suitable for an annular region (tangential or radial) to polarization which can exist in a single-mode laser, i.e. to the linear one. Arrangement that can solve both tasks (and can work as a telescope in a resonator with a large effective length) is depicted in Fig. 11. This is a telescope formed by conical and parabolic reflectors which convert half of the annular cross section into the rectangular one with the simultaneous transformation of polarization type.



After all of this it is easy to suggest a resonator with a large effective length for annular lasers¹⁴, Fig. 12.



5.5 A SIMPLE ANALOGUE OF A RESONATOR WITH SPATIAL FILTERING

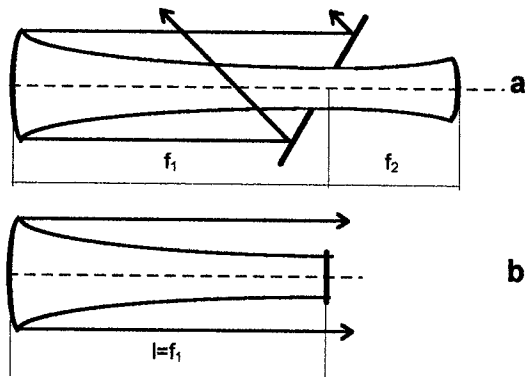


Fig. 13

The well known resonator with spatial filtering^{15, 16} is depicted in Fig. 13, a. Very simple considerations allowed Prof. Anan'ev and Dr. Solov'ev to find a more convenient analogue of such resonator¹⁷. The idea is that if we place a flat mirror in a focal plane of the spherical one, the beam incident on the flat mirror is the Fourier transform of the beam reflected from it. This means that for a fairly small flat mirror we shall have a wide and smooth distribution of the complex amplitude for the incident wave. In such a manner, we can get the property of spatial filtering in a very simple Half-Confocal Resonator shown in Fig. 13, b.

5.6 UNSTABLE RESONATOR WITH OPTICAL REPEATERS

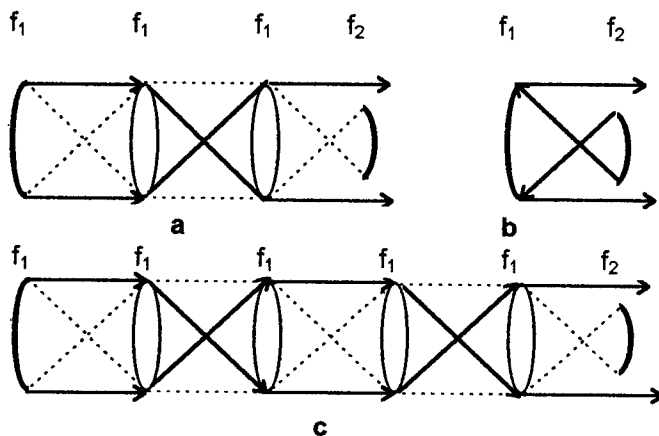


Fig. 14

This resonator was designed for multiple-pass industrial lasers with moderate Fresnel Numbers and gain. Positive-branch unstable resonators are usually employed in such lasers. Because of a relatively low gain, the optimal value of magnification here is about 1.1-1.2. Under these conditions, positive-branch unstable resonators are highly sensitive to misalignments. It is well known that negative-branch unstable resonators are much less sensitive to this kind of aberrations. However, one of the two beams inside a cavity has a long waist, resulting in high radiation loads at some intermediate mirrors. Because of this, negative-branch resonators are never used in multiple-pass arrangements.

To overcome this disadvantage, a resonator with optical repeaters, Fig. 14, was designed^{18, 19}. This arrangement is not only less sensitive to misalignments than a usual negative branch resonator, but also has a bigger Fresnel Number, reducing useless loss of energy due to diffraction wings typical for unstable resonators with low Fresnel numbers.

6. Conclusions

As I was trying to illustrate in this paper, knowledge of the resonator theory does not give immediate tools to design, analyze or simulate laser resonators. However, it is necessary for efficient work at every one of those.

This knowledge provides us with an ability

- to choose the right methods of analysis,
- to define frameworks of their practicality in order to avoid investigating the mathematical model instead of the real device,
- to verify results of any complicated calculations by means of simple estimations.

In addition, the conversance with literature gives us an opportunity to transfer technical solutions from well known situations into new ones.

References

1. Yu. A. Anan'ev and S. G. Anikichev, *Opt. Spectrosc. (USSR)*, **61** (4), October 1986, pp. 537 - 539.
2. L. A. Vainstein, *Open Cavities and open Wave-guides* (Moscow, 1966)
3. D. Gloge in *Quasioptics* (Moscow, 1966), pp. 266-279
4. Yu. Anan'ev, *Laser resonators and the beam divergence problem* (Adam Hilger, Bristol, Philadelphia and New York, 1992)
5. N. F. Balashov and V. A. Berenberg, *Sov. J. Quantum Electron.* **5**, 159 (1975).
6. Yu. A. Anan'ev and S. G. Anikichev, *Sov. Phys. Tech. Phys.*, v. 28, # 10, pp. 1205-1208.
7. Yu. A. Anan'ev, S. G. Anikichev, A. F. Bokhonov et al, *Sov. Phys. Tech. Phys.*, v. 34, # 7, pp. 772-774.
8. G. Fox and T. Li, *IEEE J. Quant Electron.*, vol. QE-2, pp. 774-783, 1966.
9. Yu. A. Anan'ev, S. G. Anikichev, *Sov. J. Optics and Spectroscopy*, v. 64, # 2, pp. 390 -396, 1988.

10. Yu. A. Anan'ev and S. G. Anikichev, *Opt. Spectrosc. (USSR)*, v. 67, #3, pp. 408-410, September 1989.
11. Banerji, A. R. Davies, C. A. Hill et al. *Appl. Optics*, Vol. 34, No 16/ p.p. 3000-3008.
12. Anikichev, V. Solov'ev, Yu. Anan'ev, V. Lopota, K. Schanz, "Koaxialer Wellenleiterlaser" (Coaxial wave-guide Talbot resonator), *Patent DE 43 25 063*, 1997.
13. Yu. A. Anan'ev, I. M. Belousova, O. B. Danilov, *Kvantovaya Elektronika*, 1974, V.1, p. 296.
14. Anikichev, V. Solov'ev, Yu. Anan'ev, V. Lopota, K. Schanz, *Pat. Appl.* of Rofin-Sinar Laser GmbH P 4421 600.9, filed June 21, 1994 (Germany)
15. Gobbi, S. Morosi, G.C. Reali, and A.S. Zarkasi, *Appl. Opt.*, v.26, p.26, 1985
16. Gobbi and G.C. Reali, *Opt. Commun.*, v.57, p.355, 1986
17. Yu. A. Anan'ev, S. G. Anikichev, and V. D. Solov'ev, *Opt. Spectrosc. (USSR)*, v. 73, #1, pp. 101-105, July 1992
18. Yu. A. Anan'ev and S. G. Anikichev, *Inventor's Certificate* No. 5014295, filed December 4, 1991 (USSR)
19. Yu. A. Anan'ev and S. G. Anikichev, *Opt. Spectrosc. (USSR)*, v. 74, #1, pp. 116-118, January 1993.

NONORTHOGONAL OPTICAL MODES AND RESONATORS

A. E. SIEGMAN

*E. L. Ginzton Laboratory
Stanford University
Stanford, California USA 94305
siegman@ee.stanford.edu*

1. Introduction

One of the basic tenets of quantum mechanics is that physical observables are represented mathematically by hermitian operators [1]. The eigenfunctions of these operators can then be used as a complete set of “normal modes” in terms of which the classical or quantum dynamics of such systems can be fully described [2]. Expanding the state of a system in terms of its eigenmodes is perhaps the most common analytical technique used in physics, and laser researchers make extensive use of its basic properties and consequences.

It has been understood for many years, however, that the operators which describe open-sided optical resonators and waveguides are *not* in general hermitian or self-adjoint [3–8], and that as a consequence the eigenmodes of laser cavities are in general not orthogonal to each other in the usual sense [9,10]. The familiar hermite-gaussian modes of stable optical resonators and the confined modes in metallic waveguides and in index-guided fibers are in general nearly orthogonal and behave in the fashion usually associated with normal modes in standard laser theory. The confined or guided modes associated with unstable optical resonators and with loss- or gain-guided optical systems such as gain-guided semiconductor diode lasers are, on the other hand, highly nonorthogonal in character. These systems still have clearcut propagation eigenmodes, but because the governing operators are not hermitian these eigenmodes are no longer power-orthogonal to each other in the usual sense.

The eigenmodes of these laser resonators are therefore not “normal modes” in the usual sense of this term. It may not be widely realized, however, just how abnormal these laser cavity modes can in fact be for certain widely used optical resonators and waveguides. The loss of conventional orthogonality in fact leads to a variety of unexpected and unusual physical and mathematical properties in such resonators. These unexpected properties include:

1. The familiar Rayleigh-Ritz variational procedure for estimating eigenvalues can no longer be relied upon in such systems.
2. The nonorthogonality of the modes complicates if not eliminates the conventional approach of second quantization for laser cavity modes and thus muddies the entire concept of photons in nonorthogonal laser cavities.
3. As described later in this paper, it turns out that one can achieve an excess coupling of input energy into individual eigenmodes, putting more energy in one given mode than into the resonator as a whole, through so-called adjoint coupling.
4. Quantum noise analyses predict that there will be a sizable excess quantum noise or excess spontaneous emission from laser atoms into the oscillating modes of these nonorthogonal systems. One consequence of this excess emission is a sizable increase in the Schawlow-Townes linewidths of laser oscillators employing biorthogonal modes, a prediction that has only recently been experimentally verified.
5. Finally, the loss of orthogonality also leads to a significant modification in the way minimum-error eigenmode expansions must be carried out in such nonhermitian systems, as we will discuss in some detail in this paper.

In the remainder of this paper we will review the basic theory of optical resonator modes including their nonhermitian or nonorthogonal properties, and then describe in more detail several of the unusual mode properties that arise in nonhermitian or nonorthogonal unstable resonators and gain-guided systems.

2. Optical Resonator Analysis

As a starting point, let us briefly review the theory of optical resonator modes [11,12]. In virtually all practical cases one can determine the transverse modes of an optical resonator either by following an optical wave through one round trip inside the laser cavity, starting from and returning to an arbitrary reference plane, or by following the same wave as it propagates through one period of a periodically iterated lensguide having the same optical elements in each period. The transverse modes of the resonator or of the equivalent lensguide are the same, but it can often be easier to envision the behavior of the lensguide.

Figure 1 shows, for example, one period of the lensguide corresponding to a typical ring-type unstable optical resonator. The solid and dashed lines in this figure show schematically the outer boundaries of the forward and reverse propagating eigenwaves along this lensguide; these eigenwaves correspond to the cavity modes propagating in the forward or reverse direction around the corresponding ring resonator. Note that these modes occupy substantially different volumes within the lensguide, although the resonator or lensguide will still have exactly the same losses and phase shift in either direction. Note also that the resonator

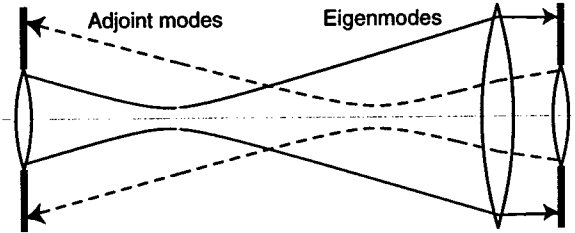


Figure 1. Schematic illustration of the forward or right-propagating eigenmodes and the reverse or left-propagating adjoint (or transpose) eigenmodes in a typical unstable resonator.

in this case is essentially confocal in the forward direction, but not in the reverse direction.

Propagation of a quasi monochromatic optical wave through one round trip in a resonator or one period of the equivalent lensguide can in general be carried out using a propagation operator \mathcal{L} . For most resonators this operator will involve primarily the use of Huygens integral to carry the wave through the free-space or paraxial sections of the lensguide, combined with the effects of any apertures or other nonparaxial elements within the cavity. This operator will then have a set of eigenfunctions $u_n(x)$ and eigenvalues γ_n which satisfy the eigenequation

$$\mathcal{L} u_n(x) = \gamma_n u_n(x) \quad (1)$$

including the boundary conditions of the resonator. For simplicity we write only a single transverse coordinate x and mode index n ; real resonators will of course generally have two transverse coordinates and two transverse indices and must be written as $u_{nm}(x, y)$.

In physical terms Eq. (1) means that each of the eigenfunctions u_n will reproduce itself exactly in form after one round trip but in the absence of laser gain will be attenuated by a power attenuation factor $|\gamma_n|^2 < 1$. If the resonator contains an amplifying laser medium whose saturated gain just balances this attenuation, however, the laser cavity can potentially oscillate in steady-state fashion in any of the eigenmodes u_n . These eigenmodes are thus the natural or physical oscillation modes of the resonator when used as a laser oscillator. As a practical matter gain competition effects will often mean that only the lowest-loss eigenmode u_0 actually oscillates, although steady-state oscillation in higher-order eigenmodes can also be obtained by various tricks. The laser cavity will automatically select its oscillation frequencies so as to compensate for the phase angle of the eigenvalue γ_n by oscillating in one or more axial-transverse mode frequencies ω_{qn} such that the total round-trip phase shift is an integer multiple of 2π , i.e.,

$$\frac{\omega_{qn} p}{c} + \arg[\gamma_n] = q \times 2\pi \quad (2)$$

where p is the round-trip optical path length and q is the (typically very large) axial mode integer.

The classic procedure for finding the lowest-loss eigenmode of Eq. (1) is the iterative numerical method pioneered by Fox and Li [13]. To implement the Fox and Li method one simply applies the propagation operator \mathcal{L} repeatedly to an arbitrary input function $u(x)$, raising the mode amplitude back up to some arbitrary value after each round trip, until the higher-loss modes are stripped out and only the lowest-loss mode u_0 remains. Other methods for finding the lowest and higher-order eigenmodes either analytically or numerically include matrix diagonalization [14], the Prony method [15], analytical approximations [16], and various more sophisticated analytical approaches [8,11,12].

The crucial point for this discussion is that for most open-sided resonators or lensguides such as are commonly employed in practical lasers, the operator \mathcal{L} is not in fact a hermitian operator and cannot easily be made so, if indeed this can be done at all. That is, the operators \mathcal{L} that describe nearly all real laser cavities will not satisfy the hermitian requirement that $\mathcal{L} = \mathcal{L}^\dagger \equiv (\mathcal{L}^*)^T$ where \mathcal{L}^\dagger indicates the hermitian conjugate or hermitian adjoint operator, \mathcal{L}^T indicates transposition of variables, and \mathcal{L}^* indicates ordinary complex conjugation. This lack of hermitian conjugation can be observed most directly by noting that the kernel of the Huygens integral for free-space propagation has the general form $\exp[-j(\pi/z\lambda)(x_2 - x_1)^2]$ which is complex symmetric but not hermitian.

Given that the Huygens integral used in these calculations is an exact solution to the paraxial wave equation, and the paraxial wave equation in turn is thoroughly hermitian, one may wonder how the resonator operators become nonhermitian. The answer is that the more strongly nonhermitian resonators such as the unstable optical resonator shown in Figure 1 have significant amounts of energy passing out the sides or past the end mirrors of the resonator and continuing on out to infinity. As a result, although the wave equation is fully hermitian the boundary conditions on the problem are not, with the consequence that the Huygens integral operator \mathcal{L} for the problem becomes nonhermitian. As another consequence, there does not seem to be any easy way to apply the familiar concepts of periodic boundary conditions or box normalization in three-dimensional space to these nonorthogonal or unstable resonator problems.

An immediate and worrisome consequence of nonhermiticity is the loss of any formal or rigorous guarantee that the set of eigenmodes envisioned in Eq. (1) may even exist for certain resonators. In fact, formal proofs of the existence of a general set of eigenmodes for Eq. (1) have only been given for a small subset of the general class of laser resonators. As a practical matter, however, numerical calculations based on Eq. (1) always seem to converge to reasonable and repeatable sets of eigenmodes for practical resonators of all sorts, and real lasers appear to have no trouble in finding stationary sets of eigenmodes in which to oscillate.

Perhaps the most important physical consequence of nonhermiticity, however, is the fact that the eigenmodes of Eq. (1), even if they exist, will in general not

be power-orthogonal in the usual sense. For example if we define an orthogonality matrix \mathbf{M} having coefficients M_{nm} given by

$$M_{nm} \equiv \int_{-\infty}^{\infty} u_n^*(x) u_m(x) dx \quad (3)$$

we can always scale or normalize the eigenmodes so that the diagonal elements of this matrix are unity, i.e. $M_{nn} = 1$. The diagonal elements of this matrix will in general not be zero, however, so that $M_{nm} \neq \delta_{nm}$. This is of course in sharp contradiction to the "normal mode" character of more familiar eigensystems.

The mode amplitudes in laser cavities thus represent clearly measurable physical observables which are *not* described by or equivalent to any hermitian operator. The properties of physical systems governed by nonhermitian operators are not widely discussed in the physics literature or in most classrooms. It can be shown however [1,17,18] that if the operator \mathcal{L} has a set of eigenmodes as in (1), then the hermitian adjoint \mathcal{L}^\dagger will have a set of adjoint eigenmodes v_n such that

$$\mathcal{L}^\dagger v_n(x) = \gamma_n^* v_n(x) \quad (4)$$

or alternatively the transposed operator \mathcal{L}^T will have a set of transpose eigenmodes $\phi_n(x)$ such that

$$\mathcal{L}^T \phi_n(x) = \gamma_n \phi_n(x) \quad (5)$$

where the eigenvalues γ_n in both cases are exactly the same as in Eq. (1). These two sets of eigenmodes are of course identical except for complex conjugation, so that either the adjoint or transposed eigenmodes $v_n(x)$ or $\phi_n(x)$ can be used in the following discussion. There is some merit to using the transposed eigenmodes $\phi_n(x)$ in optical resonator discussions because it can be shown that these modes directly represent the reverse or backward-propagating eigenmodes in a ring resonator or lensguide, as illustrated for example by the dashed boundary lines in Figure 1. It can then be shown [9,10] that the eigenmodes $u_n(x)$ and the adjoint or transposed eigenmodes $v_n(x)$ or $\phi_n(x)$ of such a system will be *biorthogonal* to each other in the sense that

$$\int_{-\infty}^{\infty} v_n^*(x) u_m(x) dx \equiv \int_{-\infty}^{\infty} \phi_n(x) u_m(x) dx \equiv \delta_{nm} . \quad (6)$$

It can also be useful to define an orthogonality matrix \mathbf{K} for the transpose or adjoint modes with coefficients K_{nm} given by

$$K_{nm} \equiv \int_{-\infty}^{\infty} v_n^*(x) v_m(x) dx \equiv \int_{-\infty}^{\infty} \phi_n(x) \phi_m^*(x) dx . \quad (7)$$

For properly normalized eigensystems with $M_{nn} = 1$, it can be shown from Eqs. (3) and (6) that the diagonal elements of the \mathbf{K} matrix will all be greater than unity,

or $K_{nn} > 1$ for all n . In physical terms these diagonal elements K_{nn} represent excess coupling factors or excess noise factors for the eigenmodes u_n [19]. The off-diagonal terms, which in general also obey $K_{nm} \neq 0$, represent cross-correlations between the thermal or quantum noise emitted into different eigenmodes [20,21].

3. Energies per Mode, and Photons

One of the most significant consequences of mode nonorthogonality is a considerable muddying of the concepts of the energy or power in a single cavity mode and, indirectly, of the whole basic concept of photons. Suppose the oscillating electric field in a laser cavity consists of the superposition of some finite number of cavity eigenmodes, so that

$$E(x) = \sum_{n=0}^N c_n u_n(x) . \quad (8)$$

If the eigenmodes themselves are normalized as discussed above and the E field is expressed in suitably normalized units, the total energy in the laser resonator (or alternatively the power flow along a lensguide) can be written as

$$\text{Cavity energy} = \int_{-\infty}^{\infty} |E(x)|^2 dx = \sum_{n=0}^N |c_n|^2 + \sum_{n \neq m} c_n^* c_m M_{nm} . \quad (9)$$

The first summation in the final part of this equation can be understood as a sum over the energies per mode in the cavity, assuming that each mode is normalized so that $\int |u_n(x)|^2 dx$ represents unit energy. The additional terms for $n \neq m$ are however no longer zero in the nonorthogonal case; they represent non-zero “cross-powers” or “cross energies” between different modes. More detailed examination then shows that the energies in individual modes in such a cavity can be greater than the total energy in the cavity, with the difference being made up by negative values of the cross-power terms.

The standard technique for quantizing the electromagnetic fields in a laser cavity is the method of second quantization [22] in which the mode coefficients c_n and c_n^* are replaced by quantum creation and annihilation operators a_n and a_n^\dagger and the energy expression of Eq. (9) is converted to a hamiltonian of the form

$$\mathcal{H} = \sum_{n=0}^N a_n^\dagger a_n \hbar \omega_{qn} + \sum_{n \neq m} a_n^\dagger a_m M_{nm} \hbar \sqrt{\omega_{qn} \omega_{qm}} . \quad (10)$$

If the modes are orthogonal, only the first summation remains, and this hamiltonian can then be interpreted as the superposition of a set of independent simple harmonic oscillators, one for each cavity mode. The number of photons in a given

cavity mode can then be interpreted as the number of quanta of excitation of the associated simple harmonic oscillator [23], and the photon statistics and other quantum properties of the cavity fields can be worked out using well-known simple harmonic oscillator and second-quantization methods. With nonorthogonal modes, however, it appears that this simple technique of second quantization is no longer feasible, and the idea of a photon as representing a single quantum of excitation in a given cavity mode is no longer obvious. Indeed, in some sense it might be argued that we now have “lasers without photons” [24] or at the least there is no simple or obvious way to handle the quantization of the fields in such lasers.

4. Matched Coupling and Adjoint Coupling

Considerable insight into the unusual properties of strongly nonorthogonal optical systems such as unstable resonators or gain-guided ducts can be obtained by considering the difference between matched coupling and adjoint coupling into such systems, as we will now do.

It is convenient to use as a model for examining these concepts an unstable lensguide consisting of periodically iterated divergent lenses combined with variable-transmission apertures as shown in the upper sketches of Figures 2 and 3. The apertures shown in Figures 2 and 3 can be hard-edged openings in which case the periodic lensguide will correspond to a conventional hard-edged unstable resonator and will have the complicated diverging eigenmode profiles characteristic of such resonators, or they can be smooth gaussian variable-transmission apertures in which case the modes at any plane within the periodic system will be complex-valued hermite-gaussian modes with the same basic properties as the hermite-gaussian modes of continuously loss- or gain-guided systems [25–27]. The basic physics is the same in either case.

The upper sketch in Figure 2 illustrates conventional “matched coupling” in which the amplitude and phase profile of the input wave is adjusted to match exactly the lowest-order (or, potentially, some higher-order) eigenmode of the lens-guiding system at the input plane. The lower plot shows how the intensity of this injected wave will decrease with distance, depending upon whether the injected wave is shaped to put all of its energy into the lowest-order $n = 0$ mode or into some higher-order and higher-loss eigenmode. The straight lines on the log plot represent of course exponential decay with distance for different eigenmodes in such a system.

Figure 3 illustrates the contrasting case of “adjoint coupling” into the same lensguide. In this case the input wave is matched in amplitude and phase to the adjoint of the lowest-order eigenmode of the system at the input plane. From a physical viewpoint, the important feature is that the input wave is injected such that it is initially converging inward toward the lower-loss (or alternatively the higher-gain) region on the axis of the system. The injected wave thus travels through the first few periods of the system with substantially smaller attenuation

matched input coupling

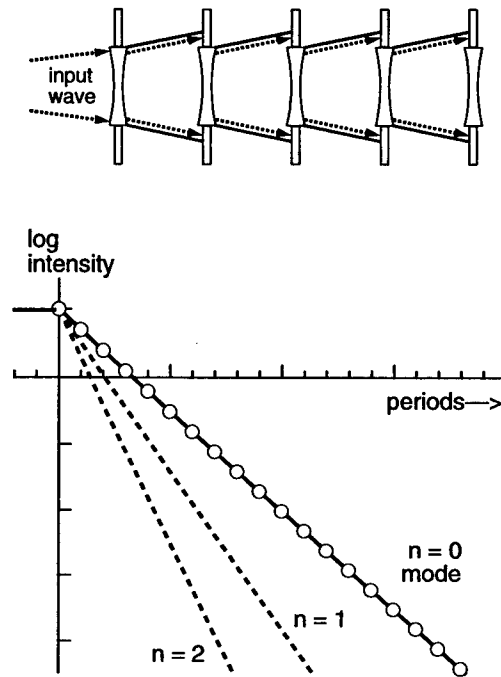


Figure 2. Upper sketch: Matched coupling into the lowest-order (or perhaps some higher-order) mode of a geometrically unstable lensguide. Lower sketch: Total power in the wave (on a log scale) as a function of distance if the input wave is matched into one or another of the three lowest-loss eigenmodes.

than the loss rates for any of the propagating eigenmodes of the system, including the lowest loss mode. The demagnifying properties of the geometrically unstable lensguide insure that the wave continues to demagnify by a fixed ratio in each successive period.

As the converging wave travels down the system, however, it eventually becomes small enough that diffraction spreading becomes important and the wave begins to diverge back outward. As it spreads, it begins to suffer increasing loss from the periodic apertures and eventually is shaped into the lowest-loss eigenmode of the system. In modal terms the adjoint-coupled input wave at the input plane must excite a mixture of the lowest-order and higher-order eigenmodes of the system. As these modes propagate along the system, the higher-order and thus higher-loss eigenmodes are gradually stripped away, leaving only the lowest-order eigenmode at a sufficiently large distance along the system.

The lower portion of Figure 3 illustrates graphically how the lowest-order eigenmode at large distances can be extrapolated back to an initial value which actually carries more power or energy than is in the input wave at this same point.

adjoint input coupling

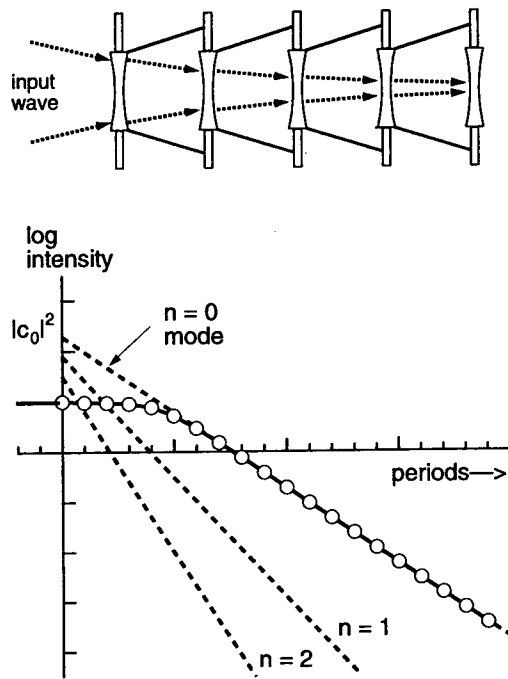


Figure 3. Upper sketch: Adjoint coupling into the lowest-order mode of a geometrically unstable lensguide. Lower sketch: Total power in the wave as a function of distance. The lower sketch illustrates the greater than unity excitation of the lowest-loss eigenmode that results from adjoint coupling.

In modal terms, this is a linear propagation system in which the adjoint coupling excites the $n = 0$ eigenmode at the input plane with more power than is in the input function $f(x)$. At the same time the input function also excites other higher-order eigenmodes with amplitudes that are also $\neq 0$ for $n > 0$. The apparent paradox that more initial power or energy goes into the u_0 mode than is contained in the initial input wave f , not to mention the additional energy going into higher-order modes, is compensated for by the negative "cross-power" terms between the modes that result from the nonorthogonality of the eigenmodes. This concept of adjoint coupling is of substantial practical importance for the optimum injection locking or injection seeding of unstable optical resonators with an external signal [28—30].

5. Gain-Guided Ducts and Complex-Valued Hermite-Gaussian Modes

Let us now consider a specific non-hermitian system for which the nonorthogonal eigenmodes can be written out analytically. The propagating modes in loss-guided

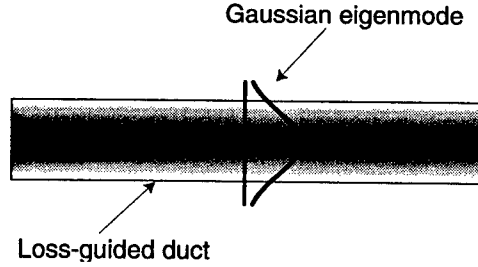


Figure 4. Schematic illustration of a loss- or gain-guided duct and the lowest-order gaussian mode that can propagate along it.

optical waveguides or ducts provide a physically simple and analytically solvable example of such a non-self-adjoint optical system. We consider a two-dimensional waveguide having transverse variations for both the refractive index $n(x)$ and the gain or loss coefficient $g(x)$ across the waveguide in the form

$$n(x) = n_0 - \frac{n_2 x^2}{2} \quad \text{and} \quad g(x) = g_0 - \frac{g_2 x^2}{2} \quad (11)$$

as illustrated schematically in Figure 4. Note that $g_0 > 0$ will correspond to on-axis amplification and $g_0 < 0$ to on-axis attenuation, but that $g_2 > 0$ corresponds to transverse loss or gain guiding in either case.

The eigenmodes for such a waveguide are then given within reasonable paraxial approximations by the complex-valued hermite-gaussian functions [25–27]

$$u_n(x) = u_{n0} H_n(\tilde{a}x) \exp[-\tilde{a}^2 x^2 / 2] \quad (12)$$

where H_n is the Hermite polynomial of order n and the “gaussian scale factor” \tilde{a} appearing in these solutions is a generally complex-valued parameter given by

$$\tilde{a} = \left(\frac{2\pi}{\lambda_0} \right)^{1/2} \left(n_0 n_2 + j \frac{\lambda_0}{2\pi} g_2 \right)^{1/4} \quad (13)$$

The normalization coefficient u_{n0} in Eq. (12) can be chosen to be purely real and to make the diagonal elements of the \mathbf{M} matrix unity.

A system of this type having pure index guiding, or $n_2 > 0$ and $g_2 = 0$, will lead to a purely real value of \tilde{a} and to the purely real hermite-gaussian index-guided modes which are familiar in graded-index optical fibers and some index-guided diode laser stripes. These purely real hermite-gaussian eigenmodes are well known to provide a complete and power-orthogonal set of functions which are widely used in optics, quantum theory, and other branches of physics.

Examination shows, however, that positive values for the loss-guiding coefficient or $g_2 > 0$, in combination with either positive or negative values for the

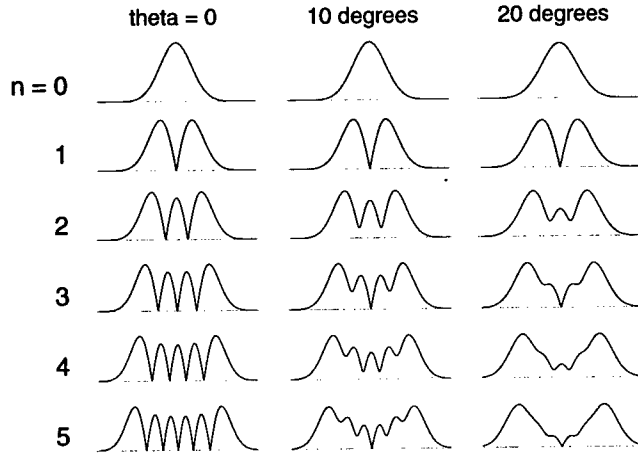


Figure 5. Transverse amplitude profiles of the 6 lowest-order complex-valued hermite-gaussian functions $u_n(x)$ for the purely real case $\theta = 0$ and the complex-valued cases $\theta = 10$ and 20 degrees.

index-guiding coefficient n_2 , will also produce confined or finite-energy propagating modes in loss-guided or gain-guided optical systems [27,31]. If the \tilde{a} parameter is separated into real and imaginary parts $\tilde{a} \equiv a_r + ja_i$, the allowed values of \tilde{a} such that the eigenfunctions will die out to zero as x becomes large are limited to the first octant in the complex $[a_r, a_i]$ plane, and thus the upper half plane in the $[n_2, g_2]$ plane, omitting the negative n_2 axis. In physical terms these complex hermite-gaussian modes remain confined for systems in which the loss guiding due to $g_2 > 0$ is accompanied by arbitrary amounts of either positive index guiding ($n_2 > 0$) or negative index anti-guiding ($n_2 < 0$). The magnitude of the \tilde{a} parameter moreover amounts simply to a transverse scaling of the x coordinate. It is then convenient for numerical calculations to set this scaling factor equal to unity and write the \tilde{a} parameter as simply

$$\tilde{a} \equiv \exp[j\theta] \quad (14)$$

where $0 \leq \theta < \pi/4$ for confined and perturbation-stable modes.

To give some insight into the behavior of the hermite-gaussian modes as \tilde{a} becomes complex, Figure 5 plots the amplitude profiles of the 6 lowest-order complex-valued hermite-gaussian functions for values of $\theta = 0, 10$ and 20 degrees. In comparison to the purely real hermite-gaussians, the complex-valued hermite-gaussians for $\theta > 0$ no longer have exact nulls along the real axis, and the outermost lobes of the higher-order eigenfunctions become more strongly emphasized as the angle θ increases. The complex scale factor in the Hermite polynomials also means that the phase fronts of these functions are no longer exactly quadratic for modes with $n \geq 2$, as will be illustrated later on.

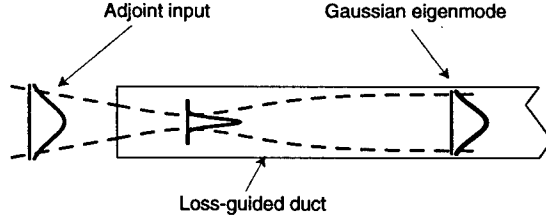


Figure 6. Schematic illustration of adjoint coupling of the lowest-order gaussian adjoint function into a loss- or gain-guided wave-propagating system.

The transition to complex values of the scale factor \tilde{a} means that the complex-valued hermite-gaussian eigenmodes are no longer orthogonal and thus require the introduction of an adjoint set of functions. In the hermite-gaussian case these adjoint functions $v_n(x)$ are in essence just the complex conjugates of the eigenfunctions $u_n(x)$, or

$$v_n(x) \equiv v_{n0} H_n(\tilde{a}^* x) \exp[-\tilde{a}^{*2} x^2 / 2] . \quad (15)$$

In the optical waveguide example these adjoint functions correspond physically to the complex conjugates of the eigenmodes propagating in the reverse direction along the same optical system. Normalization of the eigenmodes u_n as discussed in connection with Eq. (3), combined with biorthogonality between the u_n and v_n as in Eq. (6) requires, however, that the adjoint functions have different (and generally larger) normalization coefficients v_{n0} than do the eigenmodes u_n . Analytic formulas for the normalization coefficients u_{n0} and v_{n0} and the matrix elements of the \mathbf{M} and \mathbf{K} matrices for these complex-valued hermite-gaussian functions can be obtained in terms of Legendre and associated Legendre functions [31].

6. Adjoint Coupling to a Gain-Guided Duct

We will explore in the remainder of this paper the numerical results that we obtained in exploring adjoint coupling into a loss-guided duct using these complex-valued hermite-gaussian eigenmodes. A case of particular physical interest is adjoint coupling from the lowest-order adjoint mode into the lowest and higher-order eigenmodes of a loss-guided system as shown schematically in Figure 6. This example was also briefly considered some years ago by Anan'ev and Anikitchev [32]. In this example one injects the lowest-order normalized adjoint mode $f(x) = \text{const} \times v_0(x)$ into the system and attempts to expand this input in terms of the eigenmodes $u_n(x)$ of the system. This particular input is recognized in the theory of adjoint coupling as the input function which will excite the lowest eigenmode of the system with the maximum possible amplitude for a given input power or energy. In physical terms this means injecting a gaussian mode with a spherically converging or concave wavefront in the manner of Figure 3 into a waveguide

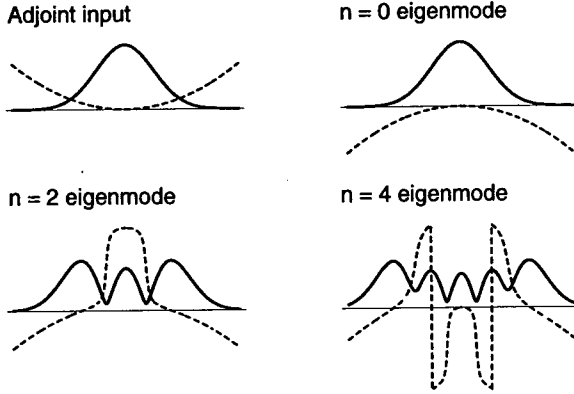


Figure 7. Adjoint coupling into the gain-guided duct of Figure 6 means that the concave-gaussian input function in the upper left plot is to be expanded in convex-valued hermite-gaussian eigenmodes like those in the remaining three plots, shown here for the case of $\theta = 6$ degrees.

or duct whose lowest-order eigenmode is a gaussian mode having an intensity profile of the same width but with a spherically diverging or convex wavefront of equal but opposite radius of curvature.

The mathematical problem is then to expand the input wave $f(x)$ in the form

$$f(x) = \sum_{n=0}^{\infty} c_n u_n(x) \quad (16)$$

using the eigenfunctions $u_n(x)$ from Eq. (12). In mathematical terms one is attempting to expand a gaussian input profile $f(x)$ with a concave wavefront as shown in the upper left-hand plot in Figure 7 in terms of a set of lowest and higher-order hermite-gaussian functions having the same gaussian spot size but oppositely curved or convex wavefronts, as shown for the first three even-order eigenmodes in the remainder of Figure 7. We will henceforth refer to these eigenmodes as “convex” rather than “diverging” functions, since the eigenmodes do not actually diverge in size as they propagate, although they do have convex wavefronts and do shed some energy transversely outward as the wave propagates. Note also that the higher-order eigenmodes, no longer have exactly spherical wavefronts because of the complex argument in the Hermite polynomials.

If this were a hermitian system one could simply multiply both sides of (16) by the orthonormal eigenfunctions $u_n^*(x)$ and integrate to obtain the expansion coefficients in the form

$$c_n[\text{Hermitian}] = \int_{-\infty}^{\infty} u_n^*(x) f_n(x) dx . \quad (17)$$

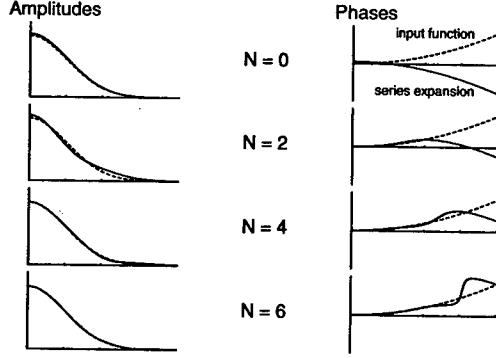


Figure 8. Amplitude and phase profiles for an adjoint-coupled duct given by finite quadrature expansions using increasing numbers of terms up to $n = N$ (solid lines), compared to the amplitude profile of the adjoint input function $f(x)$ (dashed lines), for the case $\theta = 10$ degrees.

For the nonhermitian case, the analogous procedure would seem to be to multiply both sides of Eq. (16) by the adjoint functions $v_n^*(x)$ and use the biorthogonality relation of Eq. (6) to obtain the expansion coefficients in the form

$$c_n^{[\infty]} = \int_{-\infty}^{\infty} v_n^*(x) f(x) dx . \quad (18)$$

We will refer to these coefficients as the *quadrature coefficients* for the biorthogonal case, and use the notation $c_n^{[\infty]}$ to refer to them. The overlap integrals needed to evaluate Eq. (18) for the loss or gain-guided waveguide example can be obtained in closed form in terms of Legendre functions [31].

These quadrature coefficients $c_n = c_n^{[\infty]}$ were used to carry out numerical evaluations of the eigenfunction expansion of Eq. (16) with increasing numbers of terms up to truncation indices $n = N$ for the adjoint-coupled example of Figures 6 and 7 using different values of the complex scale factor angle θ , with the following instructive results [31]. The calculations were performed using the *Mathematica* program on various Macintosh computers. Figure 8 shows, for example, how these quadrature expansions fit the input amplitude and phase profiles for the case of $\theta = 10$ degrees and for truncation indices up to $N = 6$. For this value of θ the input intensity profile is already fairly accurately fit by just the $n = 0$ term, but higher-order terms are needed to obtain successively better fits to the reversed phase profile of the input function. For this particular value of θ , as well as other values of $\theta < 15$ degrees, the quadrature expansion continues to converge reasonable well with increasing numbers of terms.

As a second example, Figure 9 shows how similar quadrature expansions compare to the amplitude profile of the input function $f(x)$ for an increasing number of terms using the quadrature coefficients with $\theta = 16.36$ degrees and truncation indices up to $N = 20$. It is apparent that the quadrature expansion converges

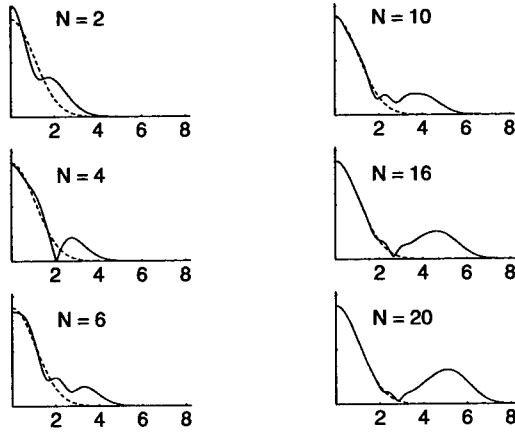


Figure 9. Amplitude profiles given by finite quadrature expansions using increasing numbers of terms up to $N = 20$ (solid lines) compared to the amplitude profile of the adjoint input function $f(x)$ (dashed lines) for the case of $\theta = 16.36$ degrees.

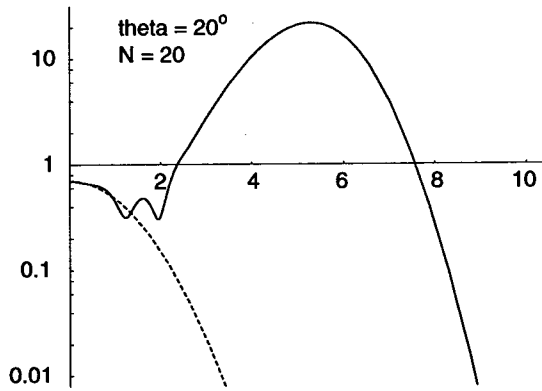


Figure 10. Amplitude profile given by the quadrature expansion truncated at $N = 20$ (solid line) compared to the gaussian input function (dashed line), both shown on a log scale, for the case of $\theta = 20$ degrees.

quite well in the central portion of $f(x)$, but that these expansions also develop pronounced outer peaks or “ears” on both sides of the central lobe with increasing numbers of terms. Further numerical exploration shows that these “ears” take on increasingly larger amplitudes as well as moving slowly outward in the transverse coordinate x as the number of terms in the adjoint expansion is increased. These outer lobes also become dramatically larger in systems having larger values of θ , as shown in Figure 10 for the case of $\theta = 20$ degrees and a truncation point $N = 20$. The series expansions using the quadrature coefficients evidently do not converge properly, at least for the larger values of θ .

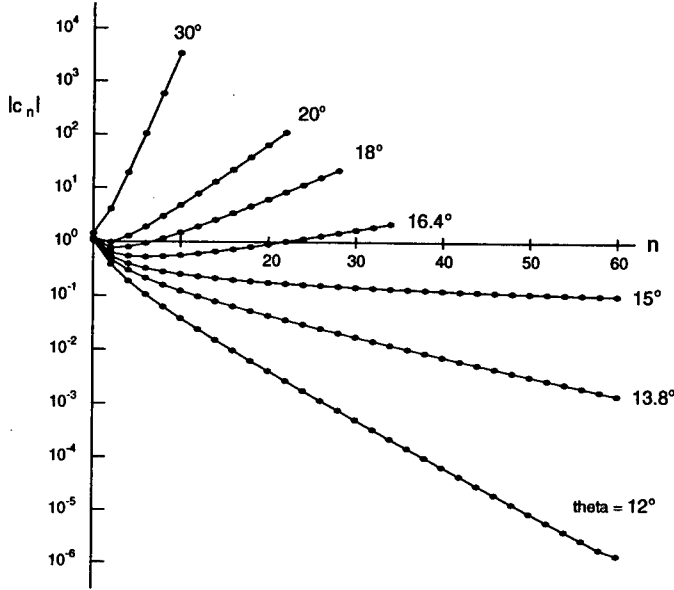


Figure 11. The quadrature expansion coefficient magnitudes $|c_n^{[\infty]}|$ obtained using the biorthogonality relation versus mode index n for increasing values of the parameter θ . The coefficients appear to diverge for values of $\theta > 15$ degrees.

To gain further insight into this behavior, Figure 11 plots the magnitudes of the quadrature expansion coefficient magnitudes $c_n^{[\infty]}$ versus the coefficient index n for various values of the angle θ . This figure indicates that there is a critical value of $\theta = 15$ degrees, below which the quadrature coefficients $c_n^{[\infty]}$ for the particular problem we are considering decrease in magnitude with increasing index n , but above which the quadrature expansion coefficients actually increase indefinitely with increasing n . This same failure of convergence for certain ranges of parameters was also noted by Anan'ev and Anikitchiev [32], who attributed it to lack of completeness of the complex hermite-gaussian eigenfunctions. We now believe, however, that this lack of convergence indicates rather that the simple quadrature integral approach is not the proper procedure for finding the minimum-error expansion coefficients c_n in a nonorthogonal system of this type, as discussed in the following section.

7. Minimum-Error Eigenmode Expansions

To understand better the deficiencies of the naive quadrature-integral approach outlined above, and to obtain a much improved series expansion approach, we derive in this section an improved minimum-error expansion procedure for general biorthogonal systems [31]. To obtain a minimum-error eigenfunction expansion in

the form of Eq. (16) for the general biorthogonal case, one can write the mean-square error ϵ_N for a finite series expansion truncated at index $n = N$ in the form

$$\begin{aligned}\epsilon_N &= \int_{-\infty}^{\infty} \left| f(x) - \sum_{n=0}^N c_n u_n(x) \right|^2 dx \\ &= 1 - \sum_{n=0}^N c_n^* f_n - \sum_{n=0}^N c_n f_n^* + \sum_{n=0}^N \sum_{m=0}^N c_n^* c_m M_{nm}\end{aligned}\quad (19)$$

where we have assumed in the second line that $f(x)$ is normalized to unit power. The coefficients f_n defined by

$$f_n \equiv \int_{-\infty}^{\infty} u_n^*(x) f(x) dx \quad (20)$$

are then just the hermitian series expansion coefficients from Eq. (17) that would be the appropriate series expansion coefficients c_n if the $u_n(x)$ were orthonormal in the conventional sense, and the matrix elements M_{nm} are the matrix elements of the orthogonality matrix defined earlier. If we introduce the column vector notations

$$\mathbf{C}_N \equiv \begin{bmatrix} c_0 \\ c_1 \\ \vdots \\ c_N \end{bmatrix} \quad \text{and} \quad \mathbf{F}_N \equiv \begin{bmatrix} f_0 \\ f_1 \\ \vdots \\ f_N \end{bmatrix} \quad (21)$$

the mean-square error ϵ_N can then be written in the matrix-product form

$$\epsilon_N = 1 - \mathbf{C}_N^\dagger \mathbf{F}_N - \mathbf{F}_N^\dagger \mathbf{C}_N + \mathbf{C}_N^\dagger \mathbf{M}_N \mathbf{C}_N. \quad (22)$$

The variation of the error ϵ_N with small variations in the coefficient vector \mathbf{C}_N can then be evaluated as

$$\delta \epsilon_N = [\mathbf{M}_N \mathbf{C}_N - \mathbf{F}_N]^\dagger \delta \mathbf{C}_N + \delta \mathbf{C}_N^\dagger [\mathbf{M}_N \mathbf{C}_N - \mathbf{F}_N] \quad (23)$$

where we have used the fact that the matrix \mathbf{M} is obviously hermitian. The vector array of coefficients c_n which will minimize the error ϵ_N is then evidently given by $\mathbf{M}_N \mathbf{C}_N = \mathbf{F}_N$ or

$$\mathbf{C}_N[\text{minimum error}] = \mathbf{M}_N^{-1} \mathbf{F}_N \quad (24)$$

where \mathbf{M}_N^{-1} denotes the inverse of \mathbf{M}_N . The mean-square error using these coefficients is then given by

$$\epsilon_N[\text{minimum error}] = 1 - \mathbf{F}_N^\dagger \mathbf{M}_N^{-1} \mathbf{F}_N. \quad (25)$$

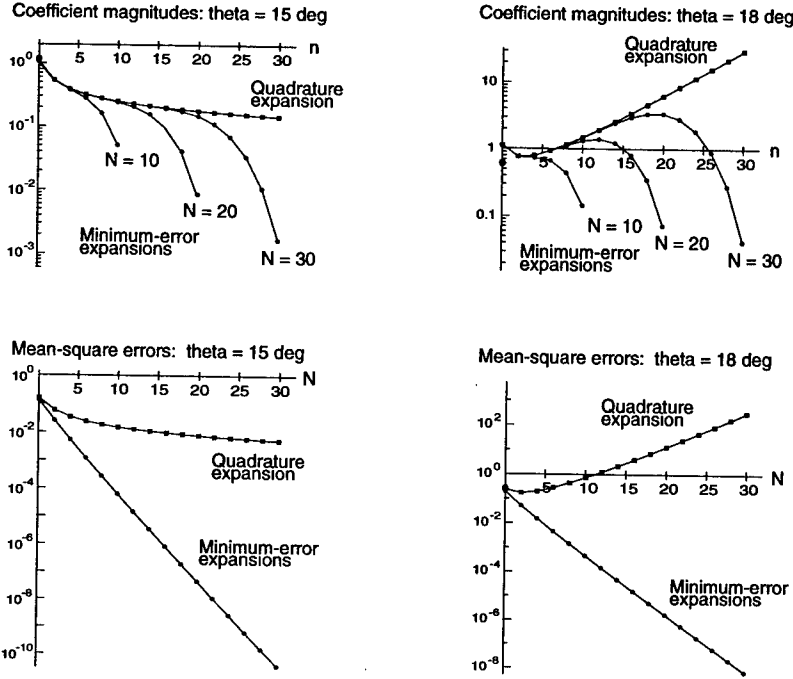


Figure 12. Upper plots: Magnitudes of the quadrature coefficients $c_n^{[\infty]}$ and of the minimum-error coefficients $c_n^{[N]}$ versus n for the cases of $\theta = 12, 15$ and 18 degrees and for three different minimum-error expansions with increasing truncation points $N = 10, 20$ and 30 . Lower plots: The mean-square errors ϵ_N for expansions using the quadrature coefficients versus number of coefficients N , and for minimum-error expansions using increasing truncation points from $N = 2$ to $N = 40$, for the same values of θ .

We will denote the minimum-error coefficients obtained from Eq. (24) by $c_n^{[N]}$ to indicate that one obtains a different set of such coefficients for each choice of the truncation index N . It can be rigorously shown, although we will not do so here, that the minimum-error coefficients $c_n^{[N]}$ for any given index value n will approach the quadrature coefficient value $c_n^{[\infty]}$ in the limit of large enough truncation index N .

We have carried out a large number of numerical experiments to explore how eigenfunction expansions using these minimum-error coefficients $c_n^{[N]}$ behave in comparison with expansions using the quadrature-integral coefficients $c_n^{[\infty]}$ for our particular problem of complex-valued hermite-gaussian eigenfunctions and lowest-order adjoint coupling [31]. The general result of these calculations is that the minimum-error coefficients $c_n^{[N]}$ produce finite series expansions which appear to be very well-behaved and always convergent, having mean-square errors ϵ_N which

decrease rapidly with increasing N , whereas the quadrature coefficients $c_n^{[\infty]}$ produce expansions which in some cases behave exactly the opposite. Typical results from these numerical experiments are summarized in Figure 12. The left and right-hand columns in Figure 12 show both quadrature-integral and minimum-error results for the two cases of $\theta = 15$ degrees (just at the divergence point for the quadrature case) and $\theta = 18$ degrees (well above the divergence point) for expansions extending up to large values of the truncation index N .

The upper plots in each column show the quadrature and minimum-error coefficient amplitudes versus coefficient index n , with the minimum-error coefficients evaluated for three different truncation points N in each case. Obviously the minimum-error coefficients roll over to decreasing values somewhere around $n \approx N/2$ in each case, while the quadrature coefficients continue to diverge with increasing n for $\theta = 18$ degrees. One can also see how the minimum-error coefficients for large enough N values at first follow the quadrature expansion coefficients, increasing in amplitude with increasing n , but then dropping to small values as n approaches the truncation value N chosen for each particular minimum-error expansion.

The lower plots in Figure 12 show the mean-square errors ϵ_N versus the number of terms for both the quadrature-integral expansions and the minimum-error expansions with increasing numbers of terms N . Note that each minimum-error point in the bottom plots represents a separate minimum-error calculation with the appropriate value of N . We observe from other plots of this type that for values of $\theta < 15$ degrees the errors in both the quadrature and minimum-error expansions continue to decrease with increasing N , although the minimum-error expansions always have significantly smaller errors for the same number of expansion terms. For the case of $\theta = 15$ degrees the left-hand column in Figure 12 shows that both the coefficient magnitudes and the mean-square errors appear to be trending toward constant values for increasing number of terms in the quadrature expansions, while the error values for the minimum-error expansions continue to decrease monotonically with increasing N , going to very small values for large enough numbers of terms. When one goes to $\theta = 18$ degrees as in the right-hand column, the quadrature expansions clearly become strongly divergent, with a rapidly increasing error, while the minimum-error expansions continue to behave very well.

Finally, just to demonstrate that the minimum-error expansion procedure continues to work properly even for still larger values of θ , Figure 13 shows the minimum-error expansions compared to the input function $f(x)$ for increasing truncation values from $N = 0$ (one term only) up to $N = 16$ (nine terms) for the particular case of $\theta = 30$ degrees. The minimum-error expansion in this case appears to remain clearly convergent with increasing numbers of terms, in agreement with the error calculations of Figure 12, although the convergence occurs somewhat more slowly than at lower values of θ . The quadrature expansion in this case is so wildly divergent as to be not worth plotting.

It would seem that the general approach to nonhermitian eigenfunction expansions developed in this section ought to be well known in the literature, but

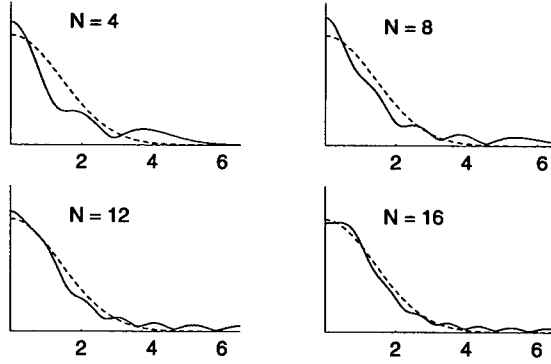


Figure 13. Minimum-error expansions for increasing numbers of terms (solid lines) compared to the exact input function $f(x)$ (dashed lines) for $\theta = 30$ degrees.

we are unable to point to any clearcut textbook or journal article citation for this approach (and, we have found a number of recent journal articles and texts which cite the apparently erroneous quadrature-integral approach given by Eq. (18)). Applying this general approach to our loss-guided waveguide example does, however, seem to yield excellent convergence for the physical case we have examined over all values of the angle θ that we examined

8. Excess Quantum Noise Measurements

As mentioned in the Introduction, another significant consequence of operator nonhermiticity or mode nonorthogonality in laser devices is an excess spontaneous emission factor that can, among other things, greatly increase the Schawlow-Townes or quantum-noise linewidth of a laser oscillator. If an unstable resonator laser oscillates in its lowest-order eigenmode u_0 in fact, the prediction [19–21,33] is that the equivalent spontaneous-emission noise source driving the oscillation will correspond not to the usual one additional noise photon per cavity mode as given in all standard quantum noise analyses, but to K_p excess noise photons per mode, where the Petermann excess noise factor K_p is the K_{00} matrix element of the \mathbf{K} matrix introduced earlier.

This prediction has now been definitively confirmed in a series of experiments carried out in the author's research group [34] as well as in continuing experiments on several types of lasers in Leiden [35]. Figure 14 illustrates one set of results from this work. These results seem to represent a rather dramatic confirmation that the loss of hermitian or orthogonal character leads to significant physical and even quantum mechanical consequences, not to mention mathematical differences, for laser resonator modes.

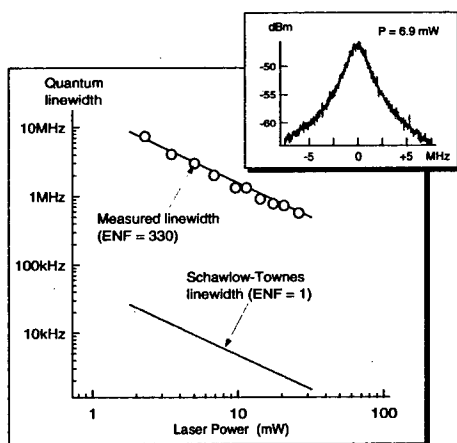


Figure 14. Example of excess noise measurements carried out on a miniature diode-pumped vanadate laser using a hard-edged unstable resonator. The measurements indicate a Petermann excess noise factor on the order of $K_p \approx 330$, in reasonable agreement with theoretical calculations [34].

9. Discussion

Finally, it may be helpful to bring out the connections between this paper and the lecture on Laser Resonator Theory by S. G. Anikitchev in this same volume. Rather than considering the eigenmodes $u_n(x)$ and adjoint modes $v_n(x)$ or $\phi_n(x)$ at any transverse plane along the resonator as in this paper, Anikitchev, following the path laid out in earlier work by himself and others under the guidance of Anan'ev [12,32], considers the eigenmodes $u_n(x)$ only on the resonator mirror surfaces, pointing out that these mirror-surface eigenmodes obey the general (non-power) orthogonality relation $\int u_n u_m = \delta_{nm}$. How does this approach connect to the eigenmode-adjoint mode approach used in this paper? We can make a few comments on this:

1) It seems clear that the physical and mathematical content of these two approaches are essentially identical. It is known that in stable resonators the phase profiles of the eigenmodes very nearly match the mirror profiles, i.e. the modes u_n are (very nearly) uniphase on the mirror surfaces, so that $u_n^* \approx u_n$. Anan'ev and Anikitchev's approach therefore has the useful feature of bringing out that $\int u_n u_m \approx \int u_n^* u_m \approx \delta_{nm}$ (for stable resonators only!). This approach thus makes it clear that the eigenmodes of stable cavities are indeed orthogonal (and the eigenmodes of unstable resonators are not).

2) On the other hand the approach in this paper, which considers both the eigenmodes u_n and the adjoint or transpose eigenmodes v_n or ϕ_n at any transverse surface in the resonator, may be more useful and more instructive in practice, as well as making direct contact with the mathematical literature on non-self-adjoint operators. One can of course always propagate Anikitchev's mirror-surface eigenmodes forward or backward from the mirror surfaces to find the fields on any other

plane. The adjoint approach, however, emphasizes that the transpose eigenmodes ϕ_n are in fact just the eigenmodes traveling in the reverse direction around a ring resonator or in the opposite direction along a periodic lensguide. Examining both the eigenmodes u_n and the transpose modes ϕ_n at various locations within a resonator can then bring out that the functions u_n and ϕ_n can be very different (i.e., have very different transverse phase and amplitude profiles) at non-mirror planes, especially in unstable resonators as illustrated in Figure 1.

3) The adjoint-mode approach also has the useful feature that one can define the eigenmode orthogonality matrix $M_{mn} \equiv \int u_n^* u_m$ with the u_n scaled so that $M_{nn} = 1$, and then employ the biorthogonality relation $\int \phi_n u_m = \delta_{nm}$ to prove immediately that in the adjoint orthogonality matrix \mathbf{K} the diagonal terms must obey $K_{nn} \geq 1$. Further one can use the adjoint functions to do gain and noise analyses which show that the diagonal K_{nn} terms are in fact exactly the Petermann excess noise factors for the eigenmodes u_n in a resonator, while the off-diagonal terms K_{nm} , $n \neq m$, give the correlations between the Langevin noise terms for spontaneous emission into different eigenmodes u_n and u_m [21,24]. The adjoint-mode approach, although not essential for the purpose, also helps to bring out the interesting physical properties of “adjoint coupling” as discussed in this paper and earlier [24,36].

4) Let us now turn to the subject of completeness. Anan’ev and Anikitchev in 1986 also attempted the same complex hermite-gaussian expansion as in this paper [32] and although they presented no numerical results, they were able to determine analytically that their (quadrature-integral-based) expansion did not converge, in agreement with the results in the present paper. (I believe the case they considered would correspond to $\theta \geq 22.5^\circ$ in the notation of the present paper.) They interpreted this failure to converge as representing a lack of completeness in the set of eigenfunctions u_n . The present paper demonstrates, however, that this failure to converge occurs because the quadrature coefficients obtained from the quadrature integral are not appropriate or correct for finite (truncated) series expansions. For finite expansions truncated at $n = N$ the quadrature coefficients $c_n^{[\infty]}$ must be replaced by the “minimum error” coefficients $c_n^{[N]}$ evaluated using the formulation in this paper (although for larger truncation values $N \gg 1$ the lower-order coefficients have the property that $c_n^{[N]} \approx c_n^{[\infty]}$ for all n except $n \simeq N$). If this is done, the hermite-gaussian series expansion in the eigenmodes $u_n(x)$ appears to converge very well for all cases we have considered.

The general question of the completeness of the complex-valued hermite-gaussian functions, or indeed of more general hard-edged unstable-resonator eigenmodes, thus seems to remain unresolved, and may remain so until attacked by a sufficiently skilled mathematician. With respect to the set of complex hermite-gaussian functions $H_n(\tilde{a}x) \exp[-\tilde{a}^2 x^2/2]$, however, since the n -th order Hermite polynomial only contains powers of x up to x^n , and vice versa, it would seem that any expansion in terms of complex valued Hermite polynomials H_n should be convertible to terms in x^n and from there into real Hermite polynomials. Since the real Hermite polynomials are known to be complete, it would seem that the

complex-valued ones probably should be also. With respect to the more complicated eigenfunctions $u_n(x)$ for any hard-edged unstable resonator, whether these are mathematically complete or not, the author's guess is that they are probably more than complete enough to represent any kind of propagating wave that can realistically exist and propagate for any distance within that unstable resonator, and hence are complete enough to be used for carrying out multimode expansions in high-output-coupling or unstable-resonator cavities using the approach outlined in [36]. It is interesting to note, for example, that Bowers has successfully carried out a number of expansions in hard-edged unstable resonators using the real resonator modes as a basis set, with no serious numerical or convergence problems observed [37].

In summary, the author believes that the approach followed in this and earlier publications, focusing on both the eigenmodes and the adjoint or transpose modes of these resonators, provides the best, the clearest, and the most instructive approach for understanding the unusual and interesting mathematical, physical and quantum properties of these resonators.

10. Acknowledgments

The author appreciates numerous contributions to these results from Yuh-Jen Cheng, Jean-luc Doumont, Geoff Fanning, Paul Mussche and Yan Sun of the Edward L. Ginzton Laboratory, and especially from Adnah Kostenbauder, as well as discussions with Professor Joseph Keller of Stanford University and with numerous participants in the Rochester Conference on Coherence and Quantum Optics CQO7 in June 1995. We also appreciate the continuing support of the Air Force Office of Scientific Research for this work.

11. References

1. Albert Messiah, *Quantum Mechanics*, Vol. 1, North-Holland Publishing Company, Amsterdam (1961); p. 188.
2. P. M. Morse and H. Feshbach, *Methods of Theoretical Physics*, McGraw-Hill Book Company, Inc., New York (1953); p. 885.
3. S. P. Morgan, On the integral equations of laser theory, *IEEE. Trans. MTT-11*, 191-193 (May 1963).
4. D. J. Newman and S. P. Morgan, Existence of eigenvalues of a class of integral equations arising in laser theory, *Bell Sys. Tech. J.* **43**, 113-126 (January 1964).
5. W. Streifer and H. Gamo, On the Schmidt expansion for optical resonator modes, in *Quasi Optics*, Polytechnic Press, Polytechnic Institute of Brooklyn (1964); pp. 351-365.
6. J. A. Cochran, The existence of eigenvalues for the integral equations of laser theory, *Bell Sys. Tech. J.* **44**, 77-88 (January 1965).

7. H. Hochstadt, On the eigenvalues of a class of integral equations arising in laser theory, *SIAM Rev.* **8**, 62 (January 1966).
8. L. A. Weinstein, *Open Resonators and Waveguides*, Golem Press, Boulder, Colorado (1969).
9. J. A. Arnaud, Nonorthogonal optical waveguides and resonators, *Bell Sys. Tech. J.* **49**, 2311–2348 (November 1970).
10. A. E. Siegman, Orthogonality properties of optical resonator eigenmodes, *Opt. Commun.* **31**, 369–373 (December 1979).
11. A. E. Siegman, *LASERS*, University Science Books, Mill Valley, California (1986), esp. Chapters 20 to 22.
12. Y. A. Anan'ev, *Laser Resonators and the Beam Divergence Problem*, Institute of Physics Publishing (formerly Adam Hilger) (1992).
13. A. G. Fox and T. Li, Resonant modes in a maser interferometer, *Bell. Sys. Tech. J.* **40**, 453–458 (March 1961); Modes in a maser interferometer with curved mirrors, *Quantum Electronics III*, Columbia University Press, New York (1964); pp. 1263–1270.
14. R. L. Sanderson and W. Streifer, Comparison of laser mode calculations, *Appl. Opt.* **8**, 131–136 (January 1969); Unstable laser resonator modes, *Appl. Opt.* **8**, 2129–2136 (October 1969).
15. A. E. Siegman and H. Y. Miller, Unstable optical resonator loss calculations using the Prony method, *Appl. Opt.* **9**, 2729–2763 (December 1970).
16. H. Kogelnik and T. Li, Laser beams and resonators, *Appl. Opt.* **5**, 1550–1566 (October 1966).
17. E. A. Coddington and N. Levinson, *Theory of Ordinary Differential Equations*, McGraw-Hill Book Company, Inc., New York (1955); p. 311.
18. M. A. Naimark, *Linear Differential Operators, Part I* (in translation), Frederick Ungar Publishing Company, New York (1967); pp. 89 and 129.
19. K. Petermann, Calculated spontaneous emission factor for double-heterostructure injection lasers with gain-induced waveguiding, *IEEE J. Quantum Electron.* **QE-15**, 566–570 (July 1979).
20. H. A. Haus and S. Kawakami, On the excess spontaneous emission factor in gain-guided laser amplifiers, *IEEE J. Quantum Electron.* **QE-21**, 63–69 (January 1985).
21. A. E. Siegman, Excess spontaneous emission in non-hermitian optical systems. I. Laser amplifiers, *Phys. Rev. A* **39**, 1253–1263 (1 February 1989); Excess spontaneous emission in non-hermitian optical systems. II. Laser oscillators, *Phys. Rev. A* **39**, 1264–1268 (1 February 1989).
22. P. A. M. Dirac, *The Principles of Quantum Mechanics*, Fourth Edition, Oxford University Press, 1958; pp. 230, 251.
23. M. Sargent, III, M. O. Scully and W. E. Lamb, Jr., *Laser Physics*, Addison-Wesley Publishing Company (1972); pp. 227, 288.
24. A. E. Siegman, Lasers without photons—or should it be lasers with too many photons, *Appl. Phys. B* **60**, 247–257 (February/March 1995); or Lasers Without Photons in *Coherence and Quantum Optics VII*, edited by J. H. Eberly, L. Mandel and Emil Wolf, Plenum Press (1995); pp. 229–238.

25. S. P. Morgan, Hermite-gaussian functions of complex argument as optical beam eigenfunctions, *IEEE Trans. on Microwave Theory and Techniques* **MTT-11**, 191–193 (1963).
26. A. E. Siegman, Hermite-gaussian functions of complex argument as optical beam eigenfunctions, *J. Opt. Soc. Am.* **63**, 1093–1095 (September 1973).
27. L. W. Casperson, Mode stability of lasers and periodic optical systems, *IEEE J. Quantum Electron.* **QE-10**, 629–634 (September 1974).
28. P. B. Corkum and H. A. Baldis, Extra-cavity feedback into unstable resonators, *Appl. Opt.* **18**, 1346–1349 (1979).
29. J. A. Benda, W. J. Fader and G. E. Palma, Influence of coupled resonator configuration for supermode discrimination, in *Modeling and Simulation of Optoelectronic Systems: Proc. SPIE* **1045**, 42–50 (1986).
30. D. L. Bullock and J. S. Yun, Fundamental beam quality considerations for modes of adjoint-coupled lasers, in *Modeling and Simulation of Laser Systems: Proc. SPIE* **1045**, 129–138 (1989).
31. A. Kostenbauder, Y. Sun and A. E. Siegman, Eigenmode expansions using biorthogonal eigenfunctions: complex-valued Hermite gaussians, *J. Opt. Soc. Amer. A* **14**, 1780–1790 (August 1997).
32. Y. A. Anan'ev and S. G. Anikichev, Eigenfunction series expansions of open cavity resonators, *Opt. Spectros. (USSR)* **61**, 537–539 (October 1986).
33. G. H. C. New, The origin of excess noise, *J. Mod. Opt.* **42**, 799–810 (April 1995).
34. Y.-J. Cheng, P. L. Mussche and A. E. Siegman, Measurement of laser quantum frequency fluctuations using a Pound-Drever stabilization system, *IEEE J. Quantum Electron.* **QE-30**, 1498–1504 (June 1994); Y.-J. Cheng, G. Fanning and A. E. Siegman, Experimental observation of a large excess quantum noise factor in the linewidth of a laser oscillator using nonorthogonal modes, *Phys. Rev. Lett.* **77**, 627–630 (22 July 1996).
35. W. A. Hamel and J. P. Woerdman, Observation of enhanced fundamental linewidth of a laser due to nonorthogonality of its longitudinal eigenmodes, *Phys. Rev. Lett.* **64**, 1506–1509 (26 March 1990); M. A. van Eijkelenborg, A. M. Lindberg, M. S. Thijssen and J. P. Woerdman, Resonance of quantum noise in an unstable cavity laser, *Phys. Rev. Lett.* **77**, 4314–4317 (18 November 1996); M. A. Van Eijkelenborg, A. M. Lindberg, M. S. Thijssen and J. P. Woerdman, Influence of transverse resonator symmetry on excess noise, *Opt. Commun.* **137**, 303–307 (1 May 1997); M. A. Van Eijkelenborg, A. M. Lindberg, M. S. Thijssen and J. P. Woerdman, Unstable-resonator diffraction losses and the excess-noise factor, *Phys. Rev. A* **55**, 4556–4562 (June 1997).
36. A. E. Siegman, Exact cavity equations for lasers with large output coupling, *Appl. Phys. Lett.* **36**, 412–414 (15 March 1980).
37. M. S. Bowers, Eigenmodes of misaligned unstable optical resonators with circular mirrors, *Appl. Opt.* **31**, 1185–1198 (20 March 1992); Diffractive analysis of unstable optical resonators with super-Gaussian mirrors, *Opt. Lett.* **17**, 1319–1321 (1 October 1992).

INFLUENCE OF INTRA-CAVITY DISTORTIONS ON OUTPUT OF UNSTABLE RESONATORS

I.B. ORLOVA

*Research Institute for Laser Physics
12 Birzhevaya line, St.Petersburg,
199034, Russia*

1. Introduction

In early time of unstable resonator (UR) history it was rejected as possessed very large diffraction losses. Soon after however, due to research works of A.Siegman in USA

[1-4] and the group of Russian scientists headed by Yu. Anan'ev [5,6,7], UR has attracted attention of laser researcher and designer community for its high energy extraction ability, high mode selectivity and lower, as compared to stable and flat-mirror resonators, sensitivity to intracavity distortions. Then it has been accepted as a very promising resonator for middle and high power lasers. With good optical quality of optical elements and active medium, this type resonator enables one to obtain extremely high on-axis brightness of laser radiation. However, in the presence of intra-cavity optical distortions inherent in the resonator of a real laser, to obtain optimal radiation parameters at the UR output becomes to be a great problem. These distortions can be caused by several different reasons associated with deformation of optical elements under radiation and also with inhomogeneities in the active media.

This lecture does not connect consideration of optical distortions in UR to a concrete laser design. It concerns only typical optical distortions which can occur in the resonator of a real device during the lasing process.

Although there is a lot of research works both of calculation and experimental nature devoted to study of optical distortions (or inhomogeneities) in lasers of different types with UR (see, for example [8, 9]), in this lecture we put more emphasis on techniques of obtaining the analytical estimates of intracavity distortion effects on output beam characteristics.

We are basing here primarily on works having been carried out in the Vavilov State Optical Institute where adequate approaches for solution the problem have been developed, which seem to be worthy of notice of everybody dealing with laser unstable resonators.

So far as angular selection, and thus, possibility of reduction of intracavity distortion effect on the laser radiation, is determined by the resonator mode

structure, it should be expedient to consider briefly the transverse modes of an unstable resonator.

Without loss of generality this consideration will be done for a symmetrical resonator version shaped by two similar convex mirrors (see Fig. 1a).

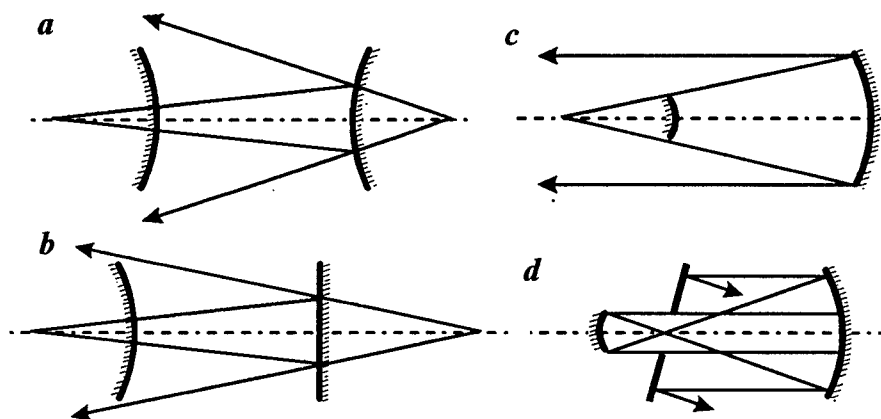


Figure 1. Unstable resonator versions: a) symmetrical; b) semi-symmetrical; c) confocal, positive branch ($M > 0$); d) confocal, negative branch ($M < 0$).

2. Modes of ideal empty UR

Speaking about the unstable resonator's transverse modes, one usually confines oneself, to consideration of the diverging spherical (cylindrical for 2-D resonator version) wave with homogeneous intensity and phase profile across the beam, in accordance with geometrical approximation. Though this model is quite adequate in a number of cases, however, to make predictions of output beam's parameters for a laser with medium possessing phase inhomogeneities requires more complete and exact knowledge of resonator's modes.

Most fruitful for description and understanding of UR mode features proved to be the waveguide-based approach, which was offered by L. Vainshtein (Russia) in early 60 - th [10] for flat-mirror resonators. It was further developed by the group of Russian scientists headed by Lubimov [11-17] for other laser resonator types. With this approach, a laser resonator is considered as a section of the waveguide, shaped by the surfaces of the two resonator's mirrors.

As is known from the waveguide theory, special wave forms exist which can propagate with low losses in a waveguide. At a waveguide open end, radiation goes partly out and partly (due to diffraction) back inward. But the returned into the resonator fraction of radiation can propagate in it only as eigen waves inherent in this kind of the waveguide. Thus, the scattered from the mirror edge radiation is again structuring into the waveguide eigen waves which can then oscillate in a resonance - like manner. They give a rise to resonator's transverse modes, which appear as stable multi-component resonant wave structures.

The typical waves inherent in an UR are shown in Fig. 2. They are of three types. There is the spherical diverging wave closely resembling one of geometrical

approximation, which being reflected from the mirror's edge transforms into converging wave which reduces its cross section until reaches its diffraction limit (see Fig.2a). After this, it again transforms into the diverging wave, and the circle repeats itself. The waves of another type being scattered by smaller angles from the mirror edges pass over a smaller distances in the resonator until reach their caustics (see Fig.2b). And finally, the third type comprises waves, scattered by larger angles at the waveguide ends, which can propagate across the whole resonator from one mirror edge to the other (see Fig.2c). These three wave types are in general involved in the mode, acting as players of an unified team. They oscillate at the same frequency and lose (due to diffraction) the same energy fraction per a round-trip along the resonator.

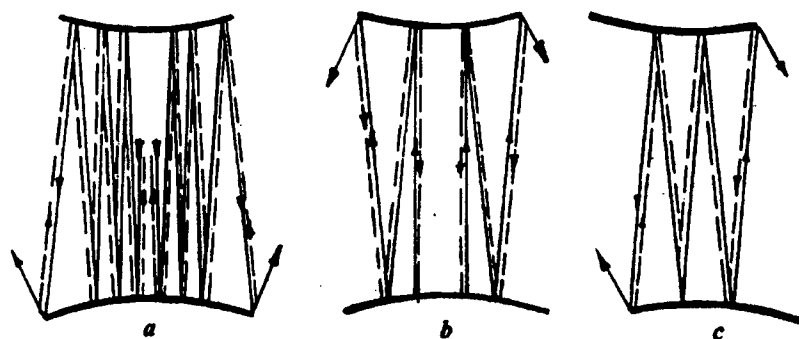


Figure 2. Type waves inherent in UR (symmetrical version).

The wave components relative weights in the mode structure are determined by the boundary conditions at the mirror edges and caustics, and thus depend on the resonator parameters. For instance, in the lowest loss resonator's mode its dominant component mostly comprises diverging and converging waves of geometrical approximation. In other cases, as it will be clear from the further consideration, the mode structure can be determined by several dominant wave components with approximately equal relative weights.

In terms of mathematics, the UR's modes are given as function

$$f(\varphi, \xi) = \cos(m\varphi)U(\xi) \quad (1)$$

being solutions of Helmholtz integral equation with Fresnel kernel. In the case of axial symmetry of the resonator geometry, the mode radial components $U(\xi)$ are determined by the equation

$$\gamma U(\xi) = \int_0^{\sqrt{2\pi V}} K(\xi\xi') U(\xi') d\xi', \quad (2)$$

where

$$K(\xi, \xi') = J_m(\xi\xi') \xi' \exp\{i\pi(m+1)/2\} \exp\{i(M^2+1)(\xi^2+\xi'^2)/4M\}, \quad (3)$$

$J_m(x)$ is the Bessel function of the first type of order m ,

$$\xi = r \sqrt{2\pi / \lambda L}, \quad (4)$$

$$N = a^2 / \lambda L, \quad (5)$$

$$N_{eq} = N \frac{(M^2 - 1)}{2M}, \quad (6)$$

is the equivalent Fresnel number, and the UR's magnification M is given as

$$M = 1 + \frac{L}{R} + 0.5 \sqrt{\frac{2L}{R} + \frac{L^2}{R^2}}, \quad (7)$$

L , R and a are the resonator length, and radii of the mirror curvature and aperture, respectively.

The solutions of the Eq. (2) is built basing on its eigen functions at the infinite integral upper term ($N \rightarrow \infty$). They are Whittaker functions of complex index and argument [18] (for the case of 2-D resonator, the basis functions are Veber- Hermitt functions of complex index and argument [19]).

The series of these functions being the solution of the Eq.(2) in the finite terms is determined by the boundary conditions. Analytical solution of the task may be obtained in asymptotic approximation of the Whittaker functions which represent compositions of diverging and converging waves (like ones exhibited in Fig.2) in the area

$$\xi^2 (M^2 - 1) / 4M \gg 1 \quad (8)$$

So, the function $U(\xi)$ can be written as

$$U(\xi) = \sum_j U_j(\xi) = \sum_j C_j (A_j w_{1j} + B_j w_{2j}), \quad (9)$$

where

$$w_{1,2}(\xi) = \xi^{-1} \left(\xi^2 \cdot \frac{M^2 - 1}{2M} \right)^{\pm 0.5(v_j + 0.5)} e^{\pm i \xi^2 \frac{(M^2 - 1)}{4M}}, \quad (10)$$

signs \pm corresponding with indices 1, 2, respectively, and indices v_j given as [14]

$$v_j = v + i2\pi j / \ln M, \quad j = 0, \pm 1, 2, 3 \quad (11)$$

and C_j are relative weights of the wave components in the composition (9).

Depending on indices v_j the waves may have caustics in the UR or freely propagate across the resonator from one mirror edge to the other.

The expression (10) describes the spherical wave front by the term $\exp\{\pm i \xi^2 (M^2 - 1) / 4M\}$ and differences of the wave functions from each other due to the complex index v_j . The $\text{Re} v_j$ is the same for all the waves in a mode and characterizes their equal diffraction losses per a round trip. Due to difference in their $\text{Im} v_j$, these waves differ from the spherical wave of geometrical

approximation and, thus, are responsible for the beam far-field intensity distribution side lobes.

Determination of the discrete values of index v characteristic of UR's modes as well as unknown coefficients C_j in (9) is performed by substitution (9) in the Eq.2 and integration of it after multiplication of its both sides by functions $U_l(\xi)$ ($l=0, \pm 1, 2, 3 \dots$) [20]. Then the obtained system of the algebraic equations, being truncated, is solved approximately.

Without mathematical details which can be found in [14] we discuss now some important results having been obtained on the basis of this approach.

Most sophisticated for understanding behavior of mode eigen functions as well as the beam intensity profile across the resonator, depending on its parameters, have been perfectly cleared in the frame of the above approach.

The results obtained analytically, with more extent of understanding, proved to be in excellent agreement with numerical calculations of other authors. Thus, periodical function of N_{eq} of the lowest-order-mode loss in UR, well known from a number of numerical investigations [1-6], has been deduced basing on the mode description as a single dominant standing-like wave shaped by waves resembling ones of geometrical approximation [1].

The estimation made in the frame of this description of the intensity modulation spatial period given as the ratio of coordinates of the intensity maxima (or minima)

$$x_{p+1}/x_p = \sqrt{\frac{p+1}{p}}, \quad p=1, 2, 3 \dots \quad (12)$$

also shows a very good agreement with the result of numerical calculation.

The positions of the beam intensity maxima (minima) on the mirror surface for the symmetrical UR with $N_{eq}=7.9$ and $M=1.3$ are shown by vertical lines in Fig.3. Numerical calculations have shown [3] that eigen values for UR's modes are limited in magnitude not only from above where they correspond to minimum diffraction losses, and, as is was already mentioned, are determined by the dominant diverging and converging waves of geometrical approximation, but also from below. The analysis of the wave structure of UR's modes has shown that to describe both the case of minimum $|\gamma|$ and of $|\gamma|$ corresponding to the highest order mode in the even mode group, one must take into account in (9) the wave components with indices $j=\pm 1$ along with the waves of geometrical approximation. With this, minimum $|\gamma|$ is achieved at $Jmv=\pm\pi/\ln M$.

This approach allowed us to deduce the analytical estimate [14] given as

$$n = \frac{\ln(N_{eq} \ln M + 2.4)}{\ln M} \quad (13)$$

of the number of modes involved in the low order group of the even symmetry modes. Accuracy of this expression increases with M and N_{eq} . However, the agreement with numerical results shown in Fig.4 are rather good at mean values M and N_{eq} as well.

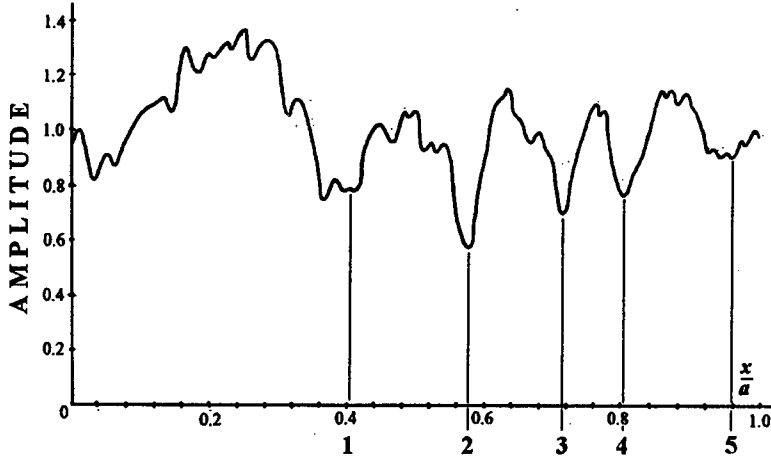


Figure 3. Amplitude profile (on the mirror surface) of the lowest order mode of symmetrical UR, $N_{eq} = 7.9$, $M = 1.3$. Vertical lines correspond to analytical estimate in Eq. (12)

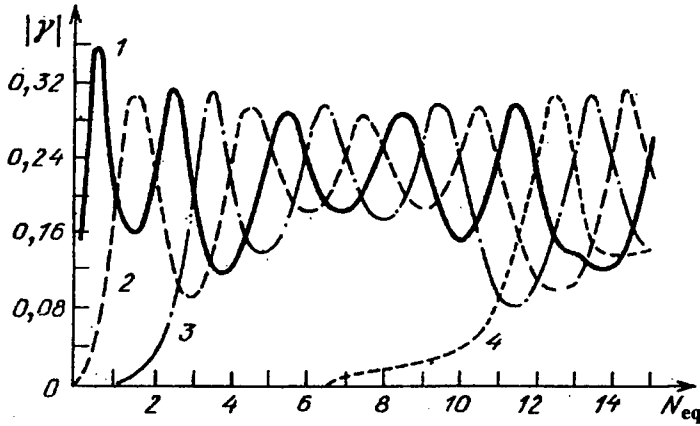


Figure 4. Eigen values of the group of even low order modes versus N_{eq} for symmetrical UR, $M = 5$ [3].

The waveguide approach allows one also to clear the way of improving mode selectivity of UR by tapering mirror edges [14, 16]. For an UR with sufficiently large N_{eq} a very narrow area of mirror edge tapering given as [21, 22]

$$\Delta a = \frac{a}{2N_{eq}} \quad (14)$$

makes the lowest order resonator mode approximate to the diverging wave of geometrical approximation.

For 2-D resonator version (resonator formed by cylindrical mirrors), it has been shown analytically [14] that the lowest loss mode separates from the mode group at a proper combination of UR parameters, and the analytical estimation of these parameters has been obtained given as

$$\frac{1.5(\ln(Q+1.3))}{\sqrt{Q}} \approx \ln M, \quad (15)$$

where

$$Q = 2\pi N_{eq}. \quad (16)$$

This estimate is in a rather good agreement with the numerical results exhibited in Fig.5 [23].

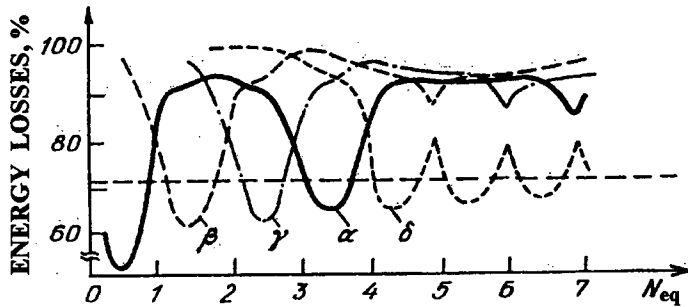


Figure 5. Diffraction losses of the group of even low order modes versus N_{eq} [23] of symmetrical 2-D UR, $M = 3.3$.

Table 1 summarizes the UR's key parameters important for determination of transverse modes features.

TABLE 1. The key parameters determinative for low-loss mode features in UR

Parameter	Analytical expression
Radius of the first equivalent Fresnel zone	$a_1 = \frac{a}{\sqrt{N_{eq}}}$
Maximum radius of caustic waist for the dominant waves in the mode group	$a_G = \frac{a_1}{\sqrt{\ln M}}$
Radii of caustic waists for the high order wave components in the mode	$a_j = a_1 \sqrt{\frac{2j}{\ln M}}$
The width of the one equivalent Fresnel zone area close to the UR mirror edge	$a_{ed} = \frac{a}{2\sqrt{N_{eq}}}$

Here, a_1 is radius of the first equivalent Fresnel zone that characterizes the caustic waist of the dominant wave components of the lowest order mode.

Distortion of the resonator within this area is expected to lead to reduction of the dominant wave component in the lowest loss mode structure that can be eventually completely suppressed. Radius a_c characterizes the caustic waist of the dominant wave components of the highest order mode in the group of low loss modes of even symmetry. Serious deformation of the resonator within this area may be expected to result in suppression of the low loss mode group as a whole. This will lead to dramatic deterioration of beam quality if lasing is really possible at all.

Radii a_j of intracavity caustics of j -wave components of the fundamental mode in UR are the characteristic parameters which allow one to estimate the number of wave components bounded by caustics in the resonator. The width a_{ed} of an equivalent Fresnel zone at the mirror edge determines the size of the area needed for efficient tapering of the mirror edge which enables one to separate effectively the lowest order mode that becomes closely resembling the wave of geometrical approximation. This tapering may be performed by different techniques [16, 24].

The estimates presented, as it will be clear in the further consideration, are very helpful to predict the mode behavior in the presence of distortions in an UR.

3. Optical distortions

Optical distortions in a resonator may be classified in their scales, types and positions across the resonator as is shown schematically in Fig.6.

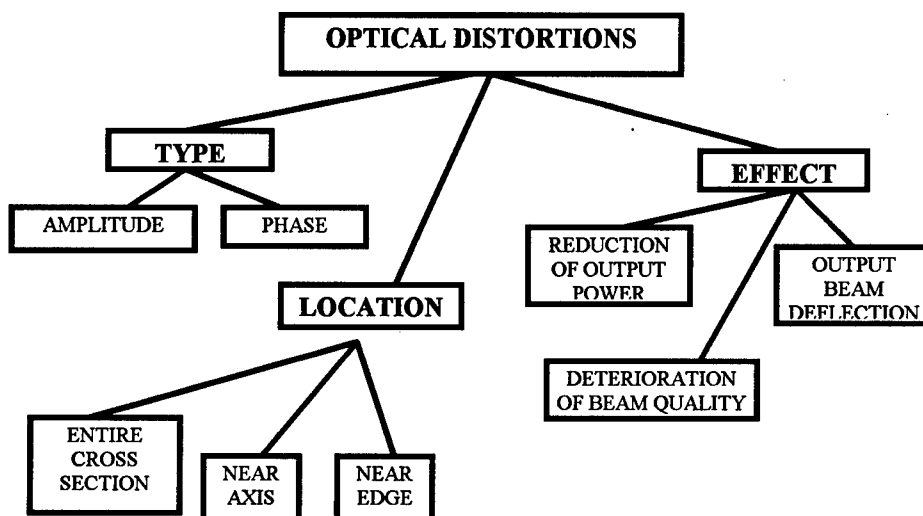


Figure 6. Schematic of classification of optical distortions in laser resonators.

3.1. AMPLITUDE DISTORTIONS

Amplitude distortions can be caused, for instance, by gain nonuniformity across the active volume.

From the above consideration it follows that the central area of the UR cross section is the most critical one for the lowest order resonator mode. Therefore it is expedient to observe first of all distortions in this region. Fig. 7 illustrates the case of unsaturated gain (g_0) dropping toward the resonator axis. Here are presented results of numerical calculations of the beam intensity at the plane of output mirror and its far-field distribution of the positive branch telescopic UR with the amplitude distortions, different in dimension.

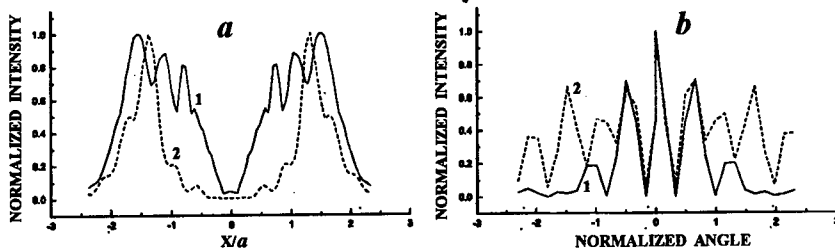


Figure 7. Normalized intensity of the lowest order mode at amplitude distortions caused by decrease of gain towards the mirror center. Confocal UR, $N_{eq} = 5$, $M = 2$, $2a = 2$ cm; (1) $g_0 = 2$, $l = 0.3$ cm; (2) $g_0 = 3$, $l = 1.2$ cm; 1 - spatial scale of distortion.

As is seen in the plot, radiation intensity is decreasing towards the mirror center, its angular distribution having the side lobes which are the larger in magnitude, the wider the zero gain area is. This tendency is clear from the point of the mode wave structure considered above. Gain reduction in the central area causes decrease of energy weight of the zeroth order wave component in the mode, resulting in growth of the weights of the higher order wave components bounded by caustics from the center. As for the waves of the other type, propagating across the resonator, they are reduced together with the zeroth order wave. It should be noted, however, that for the resonator of the given parameters (see Fig. 7), only waves of one type ($j=-1$) having intracavity caustic can exist in the UR. If these waves are being suppressed due to an amplitude distortion, the side lobes in the intensity angular distribution become extremely high (as is seen in Fig. 7, curve 2). This is the case the mode is formed by cross propagating waves of the types shown in Fig. 2 c.

Fig. 8 shows the step-wise variation of the unsaturated gain g_0 near the mirror edges. Effect of such a distortion is not so much pronounced as that of considered above distortions around the UR axis. The distortion in this case mainly affects the intensity across the beam due to some energy redistribution among the wave components in the mode composition. In the case of gain drop towards the mirror edge, amplitudes of the reflected from the edge waves are reduced. This leads to reduction of the intensity modulation magnitude across the resonator, the lowest order mode becoming more similar the wave of geometrical approximation. Curve 1 in Fig. 8a illustrates this situation for the gain in the near edge area being

half ($p=0.5$) as large as it is over the residual of the UR cross section. On the contrary, gain growth towards the mirror edges is followed by slight increase of the higher order wave components and the corresponding increase of the side lobes in the intensity angular distribution. Curves 2 in Fig.8 a,b illustrate this for g_0 being near the mirror edge of 1.5 its value in the residual area.

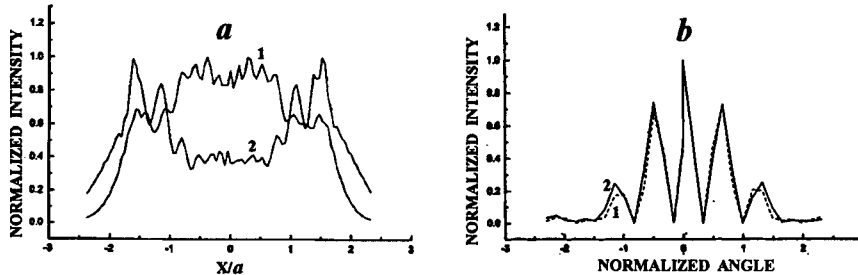


Figure 8. Normalized intensity of the lowest order mode at amplitude distortions caused by step-wise change of gain near the coupling mirror's edge
Confocal UR, $N_{eq} = 5$, $M = 2$, $2a = 2$ cm, $g_0 = 2$, (1) $p = 0.5$; (2) $p = 1.5$.

The far-field energy distributions for the considered amplitude distortions are exhibited in Fig.9. As is seen in the plot, the output beam quality does not depend very much on gain variations across the UR excepting the case of suppression of the lowest order mode in the central area which is followed by pronounced degradation of the output beam parameters.

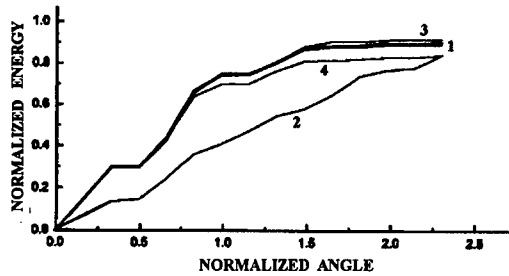


Figure 9. Normalized energy angular distribution at amplitude distortions shown in Fig. 7,8.
Curves 1,2 correspond with those in Fig. 7, curves 3,4 - with curves 1,2 in Fig. 8 respectively.

3.2. PHASE DISTORTIONS

3.2.1. Large scale distortions

First of all, we shall consider effects of some typical large scale distortions with dimensions as large as mirror diameter. One of the most commonly encountered type of phase distortions is misalignment of resonator optical elements. Generally, such a distortion may be considered as an optical wedge (of angle α). Its main effect in a resonator is that the resonator optical axis becomes to be fractured and displaced from the axis of the undistorted resonator. Fig.10 shows the optical axis views in several types of wedge-distorted UR. Extremely undesired effects of a wedge on the output radiation parameters are uncontrolled in general variation of the propagation direction (angle β) of the output beam and its displacement (H) in

the active volume. The last may result in that the beam may be cut away by the discharge chamber walls. This leads to growth of magnitude of intensity modulation across the resonator. Along with it, poor filling of the active volume causes reduction of the laser beam output energy. Table 2 exhibits relative values of the beam deflection angle (β/α) at the UR output and also of its intracavity displacement ($H/\alpha L$) from the axis of the undistorted resonator. Fig. 11 illustrates effect on beam parameters of an optical wedge in dependence on its location along the UR of different geometries. As is seen in the plot the symmetrical UR is less sensitive to wedge-wise distortions. The sensitivity of resonators of all the types is decreasing with the growth of M .

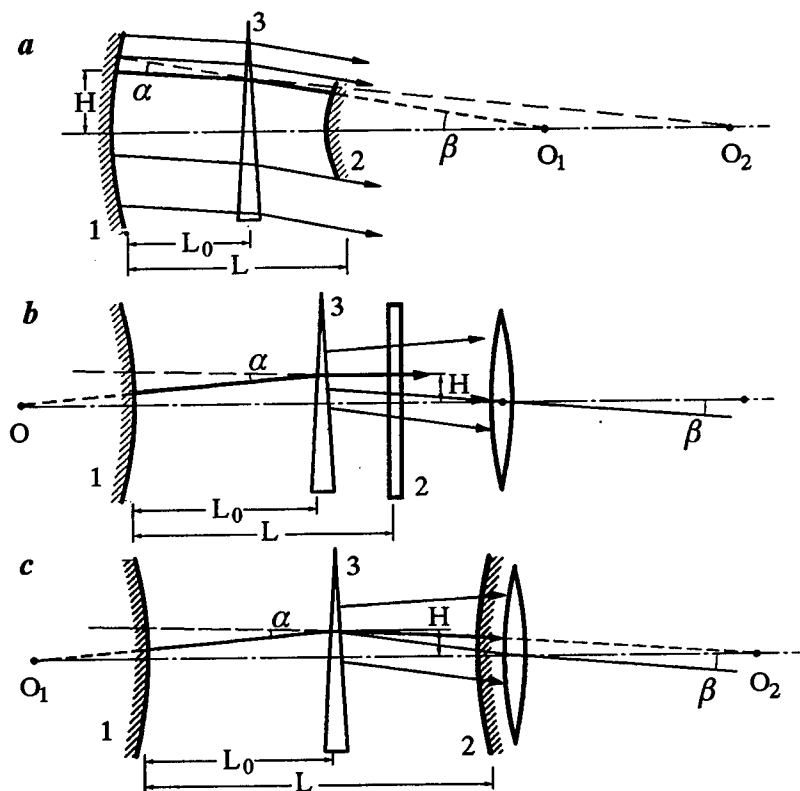


Figure 10. Ray traces in the presence of an optical wedge in UR.

a) Confocal UR (positive branch); b) Semi-symmetrical UR; c) Symmetrical UR.
1,2 - mirrors, 3 - optical wedge, 4 - lens for compensation for beam curvature.

TABLE 2. Relative angle of the output beam deflection and intracavity beam displacement from the axis of the undistorted UR

Resonator	β/α	$H/\alpha L$
Confocal UR (positive branch)	$\frac{2M}{M-1} - \frac{L_o}{L}$	$\frac{2M}{M-1} \cdot \left(\frac{M-1}{M+1} - \frac{L_o}{L} \right)$
Semi- symmetric UR	$\frac{4M}{M^2-1} + \frac{L_o}{L} \cdot \frac{M-1}{M+1}$	$\frac{4M}{(M-1)^2} + \frac{L_o}{L}$
Symmetric UR	$\frac{2M}{M^2-1} + \frac{L_o}{L} \cdot \frac{M-1}{M+1}$	$\left(\frac{2M}{(M-1)^2} + \frac{L_o}{L} \right) \left(\frac{M^2+1}{(M-1)^2} - \frac{L_o}{L} \right) \cdot \frac{(M-1)^2}{(M+1)^2}$

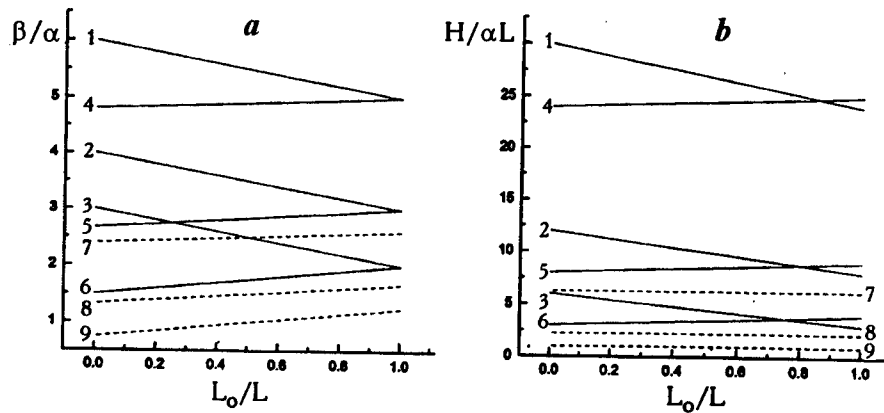


Figure 11. a) Relative deflection (β/α) of output beam from the axis of undistorted UR against the wedge location (L_o/L) in resonator; b) Relative displacement ($H/\alpha L$) of the UR optical axis (H) from the axis of the undistorted resonator against the wedge location (L_o/L); curves 1,2,3 - belong to confocal UR (Fig. 10 a), curves 4,5,6 - to semisymmetrical UR (Fig. 10 b), curves 7,8,9 - to symmetrical UR (Fig. 10 c). $M=1.5$ (curves 1,4,7), $M=2$ (curves 2,5,8), $M=3$ (curves 3,6,9).

Another very popular type of large scale distortions in laser resonators, especially for lasers of high power, is a lens-wise distortion. As a rule, these distortions are caused by thermal effects during the lasing process. Since distortions of such kind are virtually not quite lens but characterized by more complicated phase profile, we shall restrict this consideration by general estimates, made by Anan'ev in geometrical approximation in [25] for the case of confocal UR with smooth distortions of an arbitrary shape. In this approach refraction index $n(r)$ is exhibited as a power series of radial coordinates

$$n(r) = n_0 + n_1 r + n_2 r^2 + \dots \quad (17)$$

The phase variation of the output beam may be expressed as a total phase distortion on several round-trips along the resonator given as

$$\varphi_{out}=k\{\delta L(r)+\delta L(r/M)+\delta L(r/M^2)+.....\}, \quad (18)$$

where

$$\delta L(r)=L(n(r)-n_0) \quad (19)$$

denotes the optical path difference between the ray coming in the point with the r -coordinate and that one propagating along the resonator axis on a single round-trip through the UR. Substitution of (17) in (18) with the use of (19) gives

$$\varphi_{out}=kL \sum_j a_j(M) n_j r^j \quad (20)$$

where

$$a_j(M) = \left[1 + \frac{1}{j+1} \cdot \frac{M^{j+1}-1}{(M-1)M^j} \right] \frac{1}{1-M^{-j}}. \quad (21)$$

The coefficient a_j characterizes the value of a given component relative to its value in the original expression of the refraction index (17). Fig.12 presents M dependence of coefficients a_j for the telescopic UR (of positive and negative branches). These data show that output beam phase deformation (multi-pass distortion) approximates at sufficiently large M to the distortion the beam obtains on a single pass. At $M < 2$ effect of a distortion may be significantly larger. As is seen in the plot, the resulted beam phase deformation in the presence in the UR a lens-like distortion at $M=2$ is approximately twice as large as that on a single pass of the beam through the distortion. Here is also well seen that effect of odd deformations in UR of negative branch are less as compared to the resonator of positive branch. Most compensation for such deformations are achieved at $M < 3$. As for larger M , the output beam phase distortion of such kind proves to be virtually the same in both UR geometries.

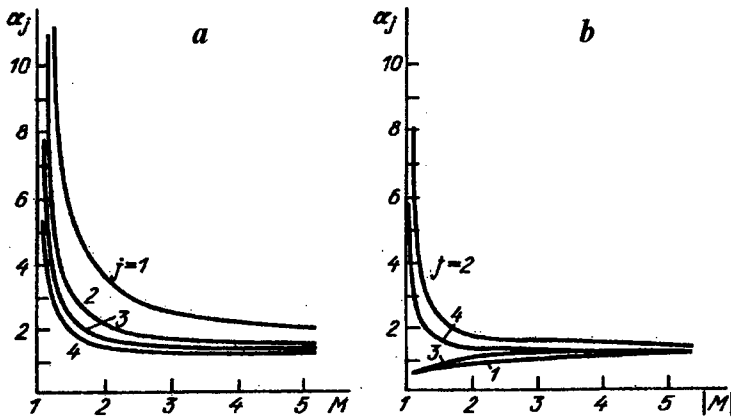


Figure 12. Dependence coefficients a_j on UR magnification M [25] a) confocal UR (positive branch) b) asymmetric UR shaped by confocal concave mirrors (negative branch).

3.2.2. Middle and small scale phase inhomogeneities

As middle and small scale distortions we mean those which spatial dimensions are more than 2 times less than the resonator mirror diameter. We will consider a single unit of area (local) distortions as well as distortions occupied the entier resonator cross section. In model simulations, all distortions, the beam takes on its pass through the active volume, will be assigned to the resonator mirrors. The characteristic parameters of distortions are shown in Fig.13. Since the most critical area for the mode structure in UR is their on-axis area, it is interesting to consider effect of distortions located here.

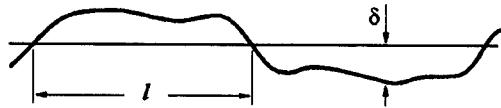


Figure 13. Characteristic parameters of middle and small scale phase distortions, l - spatial dimension, δ - phase variation.

The most effectively manifested are concave-type distortions of the mirror surface which can shape a local stable resonator around the UR optical axis. Fig.14 exhibits the result of the local resonator formation in confocal positive branch UR. As is seen, it is accompanied by concentration of the radiation intensity on the UR axis. Excitation here of the lowest order stable mode leads to suppression of the lowest order UR's mode. However, since the stable mode is limited in space, the UR can at sufficient gain support its eigen waves of higher orders, bounded by caustics from the central area. This results in degradation of output beam quality and reduction of output energy. Obviously, these effects depend on the ratio of volumes occupied by modes of the both resonators.

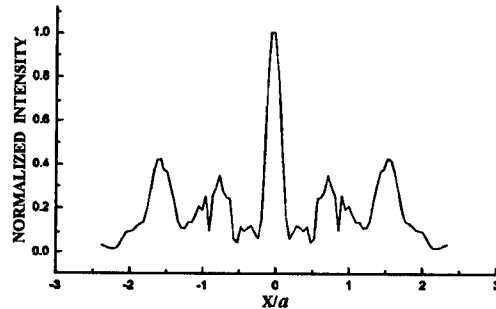


Figure 14. Normalized intensity of the lowest order mode of confocal 2-D UR with a concave type distortion at the mirror center resulting in shaping a local stable resonator.

$N_{eq} = 5$, $M = 2$, $2a = 2$ cm, $g_0 = 2$, $\delta = 0.15 \lambda$, $l = 0.3 a$.

The conditions of arrangement of a local stable resonator around the axis of the UR are given by the inequality

$$\frac{1}{M+1} < \frac{\rho}{2L} < \frac{M+1}{(M-1)^2} \quad (22)$$

where ρ denotes the curvature radius of the phase profile of the local concave-type distortion.

Table 3 exhibits data concerning parameters of distortion resulting in formation of a single-mode local on-axis stable resonator and parameters of its fundamental mode. Here ρ_{av} is the average curvature radius of distortion within the range determined by inequality (22) for $L=1$ m. The values w and δ_w/λ are the waist radius of the lowest order mode on the stable resonator mirror and the maximum phase variation produced by distortion of curvature radius ρ_{av} within the area of radius w , respectively. As it might be expected, growth of UR magnification M leads to the pronounced growth of the UR mirror distortion required for local resonator arrangement. Along with this, the first equivalent Fresnel zone significantly decreases in diameter. Therefore, the transverse dimension of the local stable resonator which is, at small M ($M \leq 1.5$ in the Table), smaller than the Fresnel zone, approximates to and then exceeds its diameter, with magnification increase. It is clear that the local resonator occupying a very small area within the Fresnel zone will weakly affect the dominant wave of the UR lowest loss mode and thereby the output beam parameters. The worse case is that the local stable resonator is close in dimension to the volume bordered by the first equivalent Fresnel diameter circle in the UR. Then the UR's lowest order mode might be suppressed completely, output beam quality degrading. In addition, at mean values of M the volume of the local stable resonator and the residual of the UR are close in dimension. This will result in the pronounced decrease of energy at the UR output. At large M the spatial dimension of the stable resonator mode is close to or exceeds the first equivalent Fresnel zone diameter. However, rather large magnitude of distortion is needed to shape the local stable resonator, the range of the required curvatures for the stable resonator formation being very small as compared to the case of small M ($M < 2$). So probability of the stable resonator advent in a distorted UR is not great at large M .

TABLE 3. Parameters of mirror distortions for arrangement of a local stable resonator and of its lowest order mode

M	N_{eq}	a_1/a	ρ_{av} (m)	w (cm)	δ_w/λ	min δ_w/λ
1.5	2.5	0.63	10	0.37	0.07	0.009
2.	5.	0.45	3.3	0.28	0.12	0.02
3.	10.	0.32	1.3	0.23	0.21	0.01
5.	20.	0.22	0.5	0.20	0.38	0.07
10.	45.	0.15	0.23	0.19	0.78	0.16
30.	145.	0.08	0.07	0.18	2.39	0.59

Now, let us consider on-axis resonator distortions of a convex-type curvature. As it is in the case of the local stable resonator, such a distortion affects primarily the lowest order UR's mode. The difference from the above case is here that the central area throws light energy about which leads to decrease of light intensity nearby the resonator axis (see Fig.15). This can lead, especially at large magnitude distortions, to suppression of the lowest loss mode of the initial UR. Along with this, radiation scattered from the central area, propagating across the residual of the UR, additionally reduces its output energy. The case, when the disturbed and undisturbed parts of the UR possess approximately equal diffraction losses so that the modes of the both resonator sections may be exited simultaneously, results in dramatic degradation of output radiation parameters. All the aforesaid about the tendency associated with the growth of M are quite right in this case too. The both considered types of distortions of small magnitude are similar in effect (see Fig.16). They weakly disturb the dominant wave of the UR fundamental mode, the weight of transformed waves slightly increasing. It results in some variation of intensity across the beam and negligible variations in far field patterns.

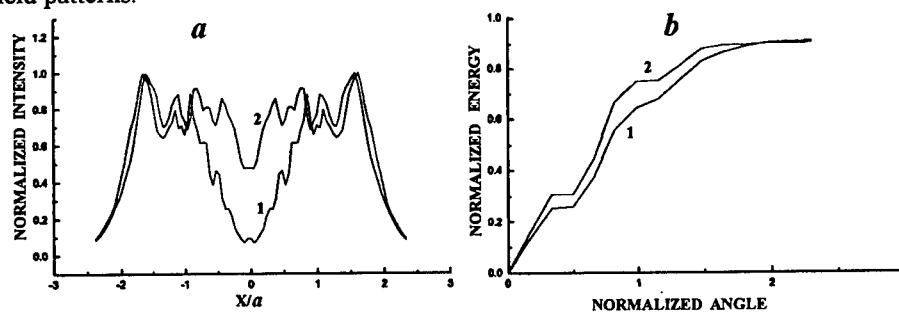


Figure 15. Normalized intensity and normalized energy angular distribution (far field) of the lowest order mode of confocal 2-D UR with a convex type distortion at the mirror center.
 $N_{eq} = 5$, $M = 2$, $2a = 2$ cm, $g_0 = 2$, $\delta = 0.15 \lambda$ (1), 0.03λ (2), $l = 0.3 a$

The similar effect on output beam characteristics is observed with small magnitude distortions occupied the entire resonator volume. This effect does not differ if the distortion occupies either the entire resonator or only its part. As an example we take a cos-wise distortion in a 2-D resonator version which was investigated in [26]. With a proper spatial period and amplitude such a distortion can lead to formation of a local on-axis stable resonator. Fig.17 illustrates this situation. As is seen in the plot the large amplitude distortions affect the output beam parameters fairly strongly (see Fig.17, solid curve).

3.2.3. Light scattering

Light scattering in UR may be caused by intracavity phase inhomogeneities characterized by a very small both phase variation and spatial dimension which are considered as random values. Therefore the total effect of distortions of such kind are estimated basing on their root-mean values. As the scattering radiation involves a lot of angular components, it is expedient to consider the continuous angular spectrum of

output radiation rather than phase relations of the separate components. Thus, characteristic parameters of the scattered beam on one pass through the scattering layer are the cone of directions given as

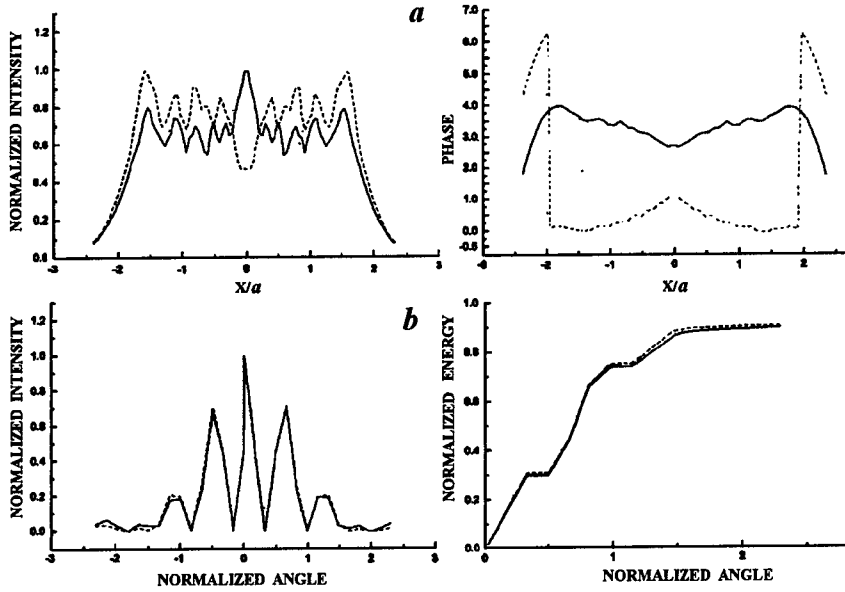


Figure 16. Normalized intensity and phase profile of the lowest order mode at the resonator output (near field) (a), and normalized intensity and energy angular distribution (b) of the confocal 2-D UR with concave (solid line) and convex (dashed line) distortion at the mirror center.
 $N_{eq} = 5$, $M = 2$, $2a = 2$ cm, $g_0 = 2$, $\delta = 0.03 \lambda$, $l = 0.3a$.

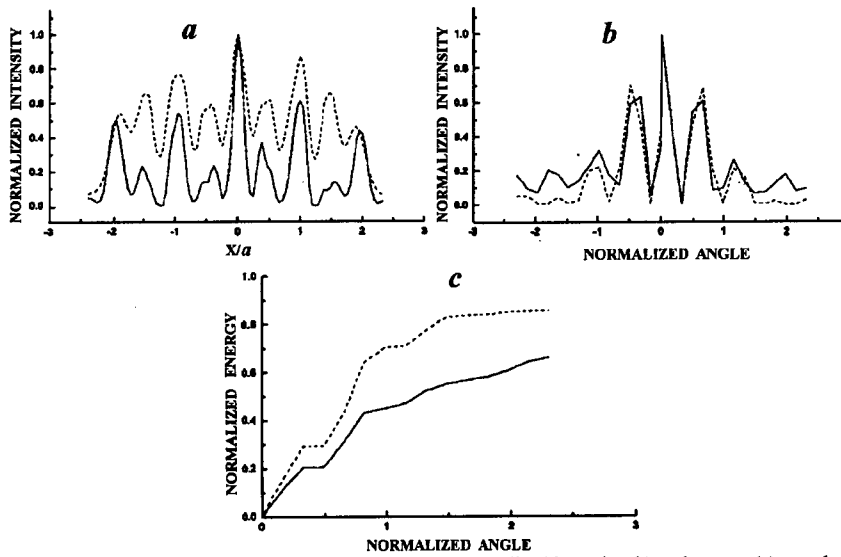


Figure 17. Normalized output beam intensity (a), and normalized intensity (b) and energy (c) angular distribution for the lowest order mode of the confocal 2-D UR with a spatial periodic phase distortion on the mirror surface. $N_{eq} = 5$, $M = 2$, $2a = 2$ cm, $\delta = 0.1 \lambda$ (solid line), 0.03λ (dashed line).

$$\theta \sim \lambda/l, \quad (23)$$

and the mean root magnitude of phase variations

$$\sigma = \sqrt{\langle \delta^2 \rangle}. \quad (24)$$

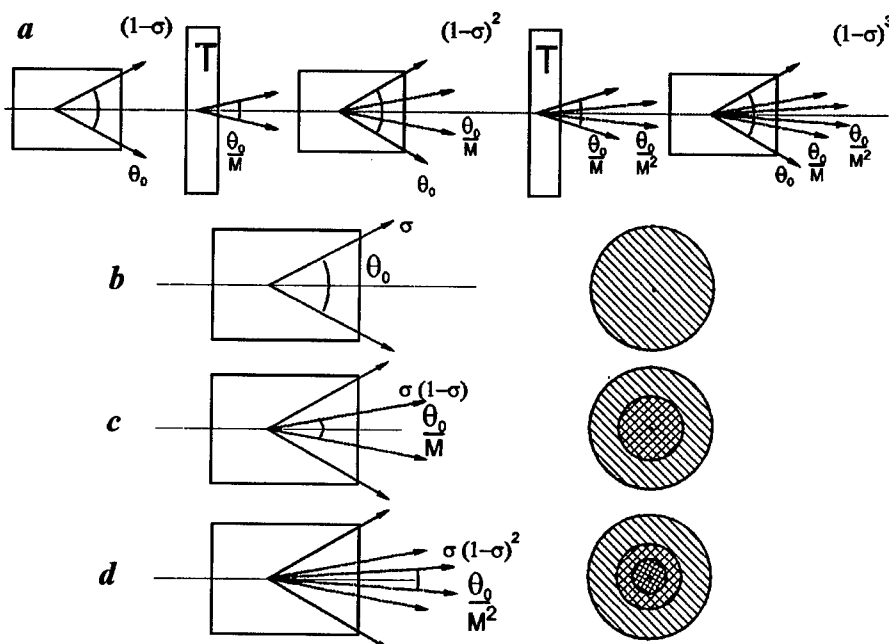


Figure 18. Sketch of light scattering stages on several passes of the ideal wave in the UR (a); radiation angular distribution after one (b) and two (c) round-trips of the ideal wave in the resonator (geometrical approximation); the final angular distribution after several round-trips (diffraction approximation) (d).

We follow here the consideration in [25]. Fig.18 illustrates transformation of the beam angular spectrum on several passes through a telescopic UR filled with a scattering medium. On each pass through the scattering layer the axial beam component losses the fraction of the radiation flow, equal to $1-\sigma$, via light energy transference to scattered components. Along with this, the UR, as a telescopic system, reduces the angle of directions by factor of M on each round trip, the angular width approximating the diffraction limit θ_d . So, formation of the far-field

distribution of radiation is completed after the number of passes of a beam through the resonator given as

$$m = \ln(\theta/\theta_d) / \ln M. \quad (25)$$

The resulting output beam axial intensity for a UR with a scattered medium is then expressed by

$$I_0 \cong (1 - \sigma)^m \cong \exp\{-\sigma \ln(\theta/\theta_d) / \ln M\}. \quad (26)$$

4. Light induced distortions

Light induced distortions are of specific UR nature. They manifest themselves mostly pronounced in lasers in cw and pulse-repetition operation. This is the well known LIMP effect discovered by Dr. Roper with colleagues [27] in UK in 1978 in CO₂ active medium.

LIMP effect arises here due to dependence of vibration-translation relaxation of exited molecule of CO₂ on local radiation intensity. When a laser beam passes through the amplifying CO₂ medium (see Fig 19 a) the exited molecule relax both via stimulated emission and transference of accumulated energy to heat (Fig.19 b). The relaxation time amounts 1mcs in the presence of radiation and about 15 to 18 mcs in the absence of it (Fig.19 b). This results in that temperature gradients arise at the light-shadow boarder which lead to local changes of gas density up to 1 percent and consequently to variations of refraction index about $\Delta n \sim (1-3)10^{-6}$. Here the beam phase distortions can reach 0.3λ within a distance of 1m. LIMP effect is favoured by beam inhomogeneities, both phase and amplitude, of different origin. An interference pattern in CO₂ laser medium taken from [29] shown in Fig.20 clearly illustrates this situation. One of the most important sources of beam inhomogeneities in UR appears diffraction effects at mirror edges. The progress in LIMP effect during lasing leads, as was found in [29], to dramatic mode degradation. Evolution of near- and far-field intensity distributions observed by Dimakov with colleagues are exhibited in Fig.20 b, which is confirmed by numerical calculations of the time dependence of lowest mode intensity carried out in [30] (see Fig.21). Arising bright spots can also destroy resonator mirrors and laser windows.

To reduce LIMP effect three approaches proved to be successful. These are: to shorten the pumping pulse duration to 3-5 mcs, keeping the constant input energy [28], to optimize gas mixture [31], and to taper the UR's mirror aperture [32]. Usage of the first of these techniques helps one to prevent from LIMP for lack of time needed for progress of this effect (see Fig.22). Investigations carried out in [31] have shown that LIMP effect may be more weakly pronounced with CO₂ active media selected in a proper way. The most favourable have been found so called «light» mixtures with more percentage of He. Fig.23 shows energetic features of output radiation of the laser in near- and far-field for two gas mixtures. The plot confirms that CO₂:N₂:He = 1:1:6 mixture is preferable. Usage of tapered aperture mirrors in UR is well known [16, 21, 24, 25] as a way of selection of the lowest order mode of geometrical approximation which is followed by much more

homogeneous beam intensity across the UR. Investigations carried out in [32] with tapered aperture mirrors in a UR have shown efficient reduction of the LIMP effect on the output energy characteristics of the laser radiation (see Fig.24). There are some techniques of smoothing the apertures edges. Along with this the important thing is to eliminate back scattering of all available surfaces on the beam way which was especially emphasized in [25]. The special measures are also needed to be taken against beam incidence on the side walls of the discharge chamber.

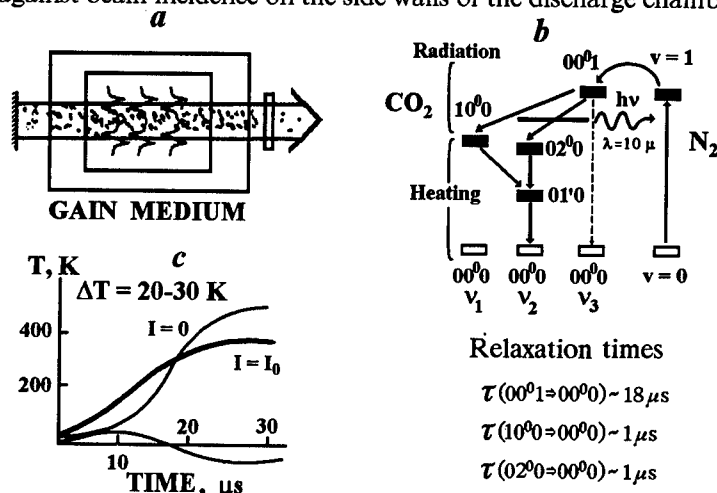


Figure 19. Radiation induced medium perturbation (LIMP) [28] a) laser beam passing a gain medium; b) system of energetic levels and energy transference in CO₂; c) time function of temperature growth under radiation.

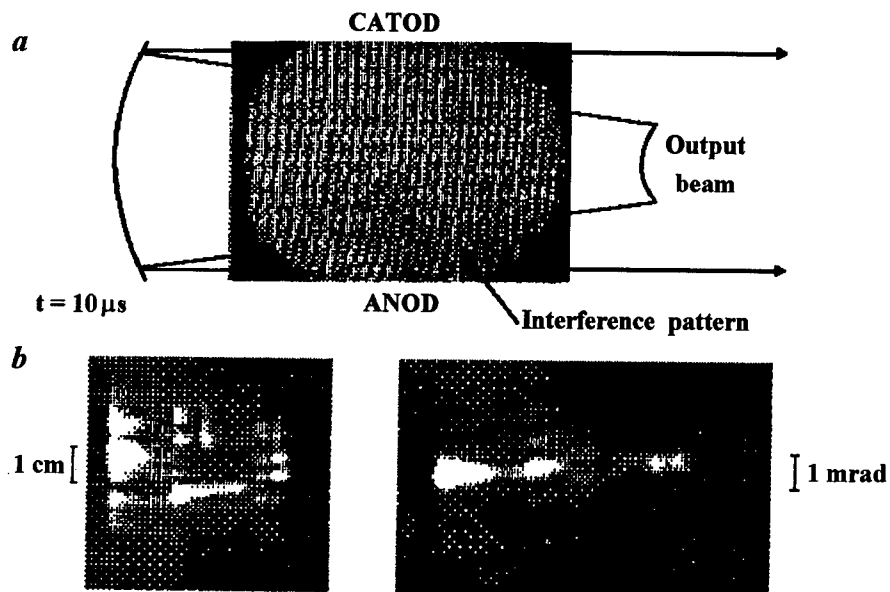


Figure 20. CO₂ active medium interference pattern in UR (a) and evolution of near (b) and far-field (c) intensity distributions [29].

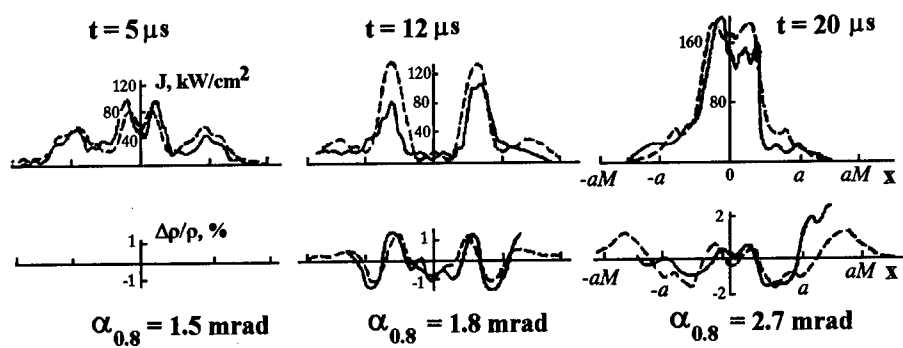


Figure 21. Numerical simulation of mode evolution in UR during the lasing process [30].

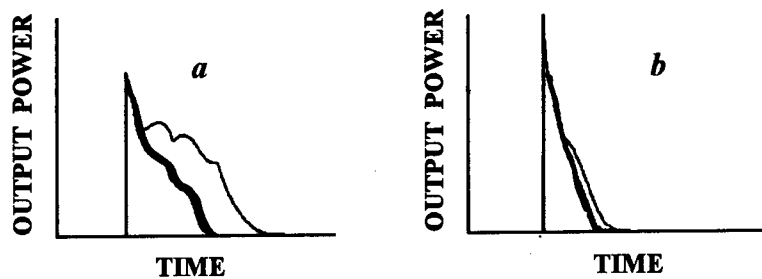


Figure 22. Minimization of LIMP-effect by shortening the pumping pulse with the maintaining the input energy.

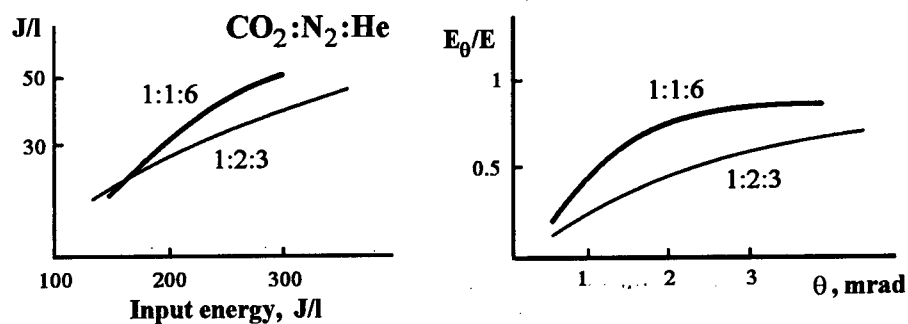


Figure 23. Minimization of LIMP-effect by proper selection of gas mixture.

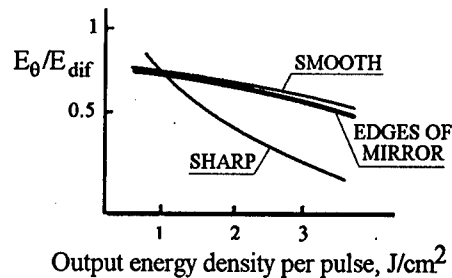


Figure 24. Reduction of diffraction based perturbations in active medium by smoothing mirror aperture in UR.

5. Conclusion

Concluding this consideration of optical distortions encountered in UR, it should be said that now, having got an adequate concept of the resonator's modes, we can predict with much of understanding how different intracavity distortions affect the output beam parameters. The ideas discussed have been verified in a great number of experimental works. However, the time has come when the resonator study is transferring from the theoretical field to the field of applications which is really unlimited. So, understanding of wave processes in UR is rather good basis for development of new resonator versions which enable one to improve laser beam characteristics. Now just as an illustration of this idea we consider two novel versions of UR, manifesting one of the new tendencies in laser design. Each of the resonators has an intra-cavity image optical system.

The version shown in Fig.25 is the UR with a «cat-eye» (CE) reflector. Here, the image optical system consists of lens 2 and the concave mirror 3. Peculiarity of this system is that it represents an equivalent convex mirror at the plane of coupler 2. The UR with required output beam parameters is formed by this mirror together with the mirror 1. It allows one to compensate partly for an optical wedge in an active medium employed and misalignment of mirror 1. In addition, the output beam aperture is related the aperture of the coupling mirror. As an example of advantages of the resonator may be presented the following data: the minimum beam deflection at the resonator output at $M=2$ is more than two times smaller as compared to the above conventional confocal UR with equivalent geometrical parameters. The minimum beam displacement in the active volume in this resonator is smaller about 7 times.

Another UR version shown in Fig. 26, having the similar, may be useful for application in lasers of tube geometry of the active volume. In both resonators thermal lenses in active elements may be employed as optical elements of the images systems. More of information about this and other versions of resonator designs is contained in the lecture of S.Dimakov [33].

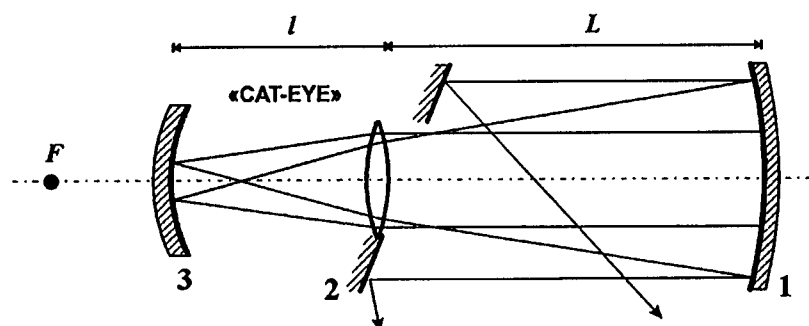


Figure 25. Schematic of UR with the "cat-eye" reflector.

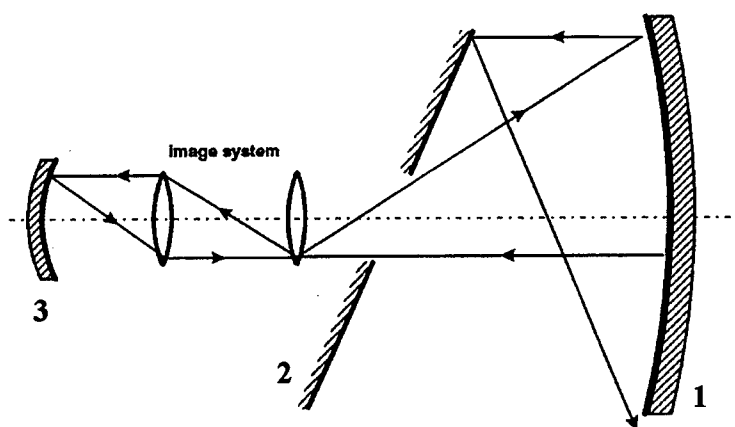


Figure 26. Schematic of UR with an intracavity optical image system.

6. References

1. Siegman, A.E. (1965) Unstable optical resonators for laser applications, *Proc. IEEE* **53**, 277-287.
2. Siegman, A.E., Arrathoon, R.W. (1967) Modes in unstable optical resonators and waveguides, *IEEE J. Quant. Electr.* **QE-3**, 156-163.
3. Siegman, A.E., Miller, H.Y. (1970) Unstable optical resonator loss calculations using the Prony method, *Appl. Opt.* **9**, 2729-2736.
4. Siegman, A.E. (1974) Unstable optical resonators, *Appl. Opt.* **13**, 353-367.
5. Anan'ev, Yu.A., Svetsitskaya, N.A., Sherstobitov, V.E. (1968) Properties of a laser with an unstable resonator, *Zhurnal Experim. i Teor. Fiz.* **55**, 130-140 (in Russian); (1969) *Sov. Phys. JETP* **28**, 69-74.
6. Anan'ev, Yu.A., Vinokurov, G.N., Koval'chuk, L.V., Svetsitskaya, N.A., Sherstobitov, V.E. (1970) Telescopic resonator laser, *Sov. Phys. JETP* **31**, 420-424.
7. Anan'ev, Yu.A. (1971) Unstable resonators and their applications, *Kvant. Elektron.* **6**, 3-34 (in Russian).
8. Sherstobitov, V.E. (1982) Angular divergence of radiation of gas-flow lasers (review), *Izvestiya Acad. Nauk SSSR* **46**, 1905-1914 (in Russian).
9. Zavgorodnaya, S.I., Koval'chuk, L.V., Semenov, V.E., Sherstobitov, V.E. (1984) Calculation of spatial characteristics of radiation of UR laser with random small-scale phase inhomogeneities, *Kvant. Elektron.* **11**, 324-330 (in Russian).

10. Vainshtein, L.A. (1966) *Open resonators and open wave-guides*, Sov. Radio, Mosc. (in Russian).
11. Lubimov, V.V., Orlova, I.B. (1970) Approximate calculations of modes in resonators with concave mirrors, *Optika i Spektroskopiya* **29**, 581-586 (in Russian).
12. Lubimov, V.V., Orlova, I.B., (1969) Estimation of effect of resonator misaligned mirrors on the loss and angular distribution of laser radiation, *Zhurnal Techn. Fiz.* **39**, 2183-2187 (in Russian).
13. Lubimov, V.V., Orlova, I.B., (1971) Modes of a resonator with tilted mirrors, *Optika i Spektroskopiya* **30**, 758-762 (in Russian).
14. Vinokurov, G.N., Lubimov, V.V., Orlova, I.B. (1973) Investigation of selective properties of open unstable resonators, *Optika i Spektroskopiya* **34**, 741-750 (in Russian).
15. Lubimov, V.V., Petrov, V.F., Pevgenen, N.N. (1973) Asymmetric unstable resonators, *Optika i Spektroskopiya* **35**, 1132-1136 (in Russian).
16. Lubimov, V.V., Orlova, I.B. (1976), Influence of the mirror edge shape on selective properties of unstable resonators, *Optika i Spektroskopiya* **41**, 288-291 (in Russian).
17. Lubimov, V.V. (1987), Divergence of laser radiation in the presence of intra-cavity inhomogeneities, *Izvestiya Acad. Nauk SSSR, ser. Fiz.* **51**, 1327-1330 (in Russian).
18. Whittaker, E.T., Watson, G.N. (1927), *A course of modern analysis (part 2)*, Cambridge, at the University Press.
19. Bateman, H., Erdelyi, A. (1953), *Higher transcendental functions (part 2)*, N.Y., Toronto, London Mc Graw Hill Book Company, INC.
20. Hildebrand (1965) *Methods of Applied Mathematics*, Prentice Hall, Englewood Cliffs, N.Y.
21. Anan'ev, Yu.A., Sherstobitov, V.E. (1971) Influence of the edge effects on the properties of unstable resonators, *Kvant. Elektron.* No 3, 82-89 (in Russian).
22. Sherstobitov, V.E., Vinokurov, G.N. (1972) Properties of an unstable resonator with a large Fresnel number, *Kvant. Elektron.* No 3, 36-44 (in Russian).
23. Sanderson, R.L., Streifer, W. (1969) Unstable laser resonator modes, *Appl. Opt.* **8**, 2129-2136.
24. Mc Allister, G., Steier, W.H., Lacina, W.B. (1974) Improved mode properties of unstable resonators with tapered reflectivity mirrors and shaped apertures, *IEEE J. Quant. Electr.* **QE-10**, 346-355.
25. Anan'ev, Yu.A. (1992) *Laser resonators and the beam divergence problem*, Adam Hilger, Bristol, Philadelphia and New York.
26. Sherstobitov, V.E., Koval'chuk, L.V. (1977) Influence of small-scale inhomogeneities on properties of unstable resonators, *Kvant. Elektron.* **4**, 2166-2172 (in Russian).
27. Roper, V.G., Lamberton, H.M., Parcell, E.W., and Manley, A.W.J. (1978) Laser induced medium perturbation in a pulsed CO₂ laser, *Opt. Commun.* **25**, 235-240.
28. Dimakov, S.A., Sherstobitov, V.E., et al. (1983), A study into optical homogeneity of the active medium of an atmospheric-pressure electroionization CO₂ laser upon stimulation emission of radiation, *Kvant. Elektron.* **10**, 397-402 (in Russian).
29. Dimakov, S.A., Pel'menev, A.G., Petrov, V.F., Sherstobitov, V.E., Yashukov, V.P. (1985) On an influence of the self-action effect on the structure of the field of an unstable-resonator electroionization CO₂ laser, *Kvant. Elektron.* **12**, 1285-1289 (in Russian).
30. Dimakov, S.A., Koval'chuk, L.V., Pel'menev, A.G., Petrov, V.F., Rodionov, A.Yu., Trusov, V.P., Sherstobitov, V.E., Yashukov, V.P. (1987) An effect of thermal nonlinearity on dynamics of the radiation from an unstable resonator electroionization CO₂ laser, *Kvant. Elektron.* **14**, 466-476 (in Russian).
31. Glukhikh, I.V., Yachnev, I.L., Yur'ev, M.S. et al. (1991) Stimulated scattering in active media of a pulse CO₂ laser and laser radiation divergence, *Izvestiya AN SSSR, Ser. Fiz.* **55**, 389-393 (in Russian).
32. Dimakov, S.A., Zavgorodnaya, S.I., Koval'chuk, L.V., Rodionov, A.Y., Sherstobitov, V.E., Yashukov, V.P. (1990), A study of spatial characteristics of the radiation from a CO₂ EIL with intra-cavity apodization, *Kvant. Elektron.* **17**, 291-295 (in Russian).
33. Dimakov S.A. Resonators for lasers used in precision technological operations (see the paper in this book).

OPTICAL RESONATOR WITH DIELECTRIC BODY

K.A. PROKHOROV¹ and D.G. AFONIN²

¹*General Physics Institute, Russian Academy of Sciences
Vavilova str., 38, Moscow 117942, Russia*

²*Physics Department of Moscow State University, Vorob'evy
Gory, Moscow 119899, Russia*

1. Introduction

Rigorous analysis of an optical resonator with dielectric inclusions is rather complex mathematical problem [1]. In this study we solve the problem for two simple resonator's geometries: (i) open resonator (OPR) consisting with two plane mirrors and a dielectric cylindrical element in the cavity; (ii) spherical resonator (SPR) or ball cavity with a small spherical dielectric body in the center.

2. Open resonator with two plane mirrors

Let us consider OPR with a thin dielectric cylinder attached to one of the mirrors and oriented along the axis of the system as shown in Figure 1. We assume that this resonant system is pumped through a coupling hole in the left-hand mirror. The following notations are introduced: $2a$ is the aperture diameter of the mirrors, $2d$ is the diameter of dielectric cylinder, l is the cylinder length, and L is the distance between mirrors.

We shall assume that the cylinder is thin, $d < a$, and the distance between the end of the cylinder and the right-hand mirror is small, $L - l \ll l$. Furthermore, we will calculate the characteristics of such OPR in suggestion that only E_{01} wave is excited in the dielectric cylinder.

It is reasonable to consider the cavity as consisting of four areas (1 to 4) as it appears on the Figure 1. Because of the gap $L-l$ is small and because of limited divergence of a wave that emerges from area 1, we can suggest that in the area 4 the field is vanished.

A standard formula for cavity's Q -factor could be introduced as

$$Q = \omega W / P,$$

where $W = W_1 + W_2 + W_3$ is the total of accumulated energies in the first, second and third cavity areas; P is the power lost on mirrors and inside the cavity, and ω is the excitation frequency of the resonant system.

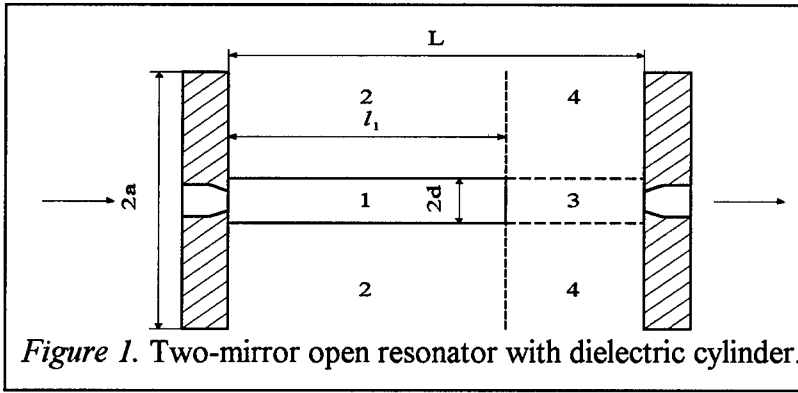


Figure 1. Two-mirror open resonator with dielectric cylinder.

Calculating the integrals of the above formula and simplifying the expressions, we can derive the following formula for the Q -factor of an open resonator with plane mirrors and a dielectric cylinder:

$$Q = \omega^2 \left[\mu_m \varepsilon_m^2 k_1 B^2 T_1 e^{-2\beta_1} + \mu_0 \varepsilon_0^2 k_2 T_2 A^2 e^{-2\gamma_1} + \mu \varepsilon_0^2 C^3 k_3 (e^{-2\kappa L} - e^{-2\kappa d}) T_3 \right] \quad (1)$$

$$\left(\omega \varepsilon_0^2 \sqrt{\frac{\omega \mu_m}{\sigma_1}} (e^{-\gamma_1} k_2 A^2 T_2 + k_3 C^2 T_3 e^{-L\kappa}) + \tan \delta \left\{ \varepsilon_m e^{-2\beta_1} B^2 \left[T_4 (\omega^2 \varepsilon_m^2 - \beta^2) \right. \right. \right.$$

$$\left. \left. + T_1 k_1 \beta^2 \right] + \varepsilon_0 C^2 (e^{-2\kappa L} - e^{-2\kappa d}) \left[\kappa^2 k_3 T_3 + T_5 (\omega^2 \varepsilon_0 - \kappa^2) \right] \right\} \right)^{-1},$$

where σ_1 is the conductivity of material of the mirrors, $\tan \delta$ is a tangent of the angle of losses for the dielectric cylinder, and

$$T_1 = \left[J_1^2(k_1 d) + J_0^2(k_1 d) - \frac{2}{k_1^2 d^2} J_0(k_1 d) J_1(k_1 d) \right] \frac{d^2 k_1}{2},$$

$$T_2 = \frac{a^2 k_2^2}{2} \left\{ \left[H_0^{(1)}(k_2 a) \right]^2 + \left[H_1^{(1)}(k_2 a) \right]^2 - \frac{2}{k_2^2 a^2} H_0^{(1)}(k_2 a) H_1^{(1)}(k_2 a) \right\}$$

$$- \frac{d^2 k_2^2}{2} \left\{ \left[H_0^{(1)}(k_2 d) \right]^2 + \left[H_1^{(1)}(k_2 d) \right]^2 - \frac{2}{k_2^2 d^2} H_0^{(1)}(k_2 d) H_1^{(1)}(k_2 d) \right\},$$

$$T_3 = \frac{k_3^2 d^2}{2} \left[J_1^2(k_3 d) + J_0^2(k_3 d) - \frac{2}{k_3^2 d^2} J_0(k_3 d) J_1(k_3 d) \right], \quad (2)$$

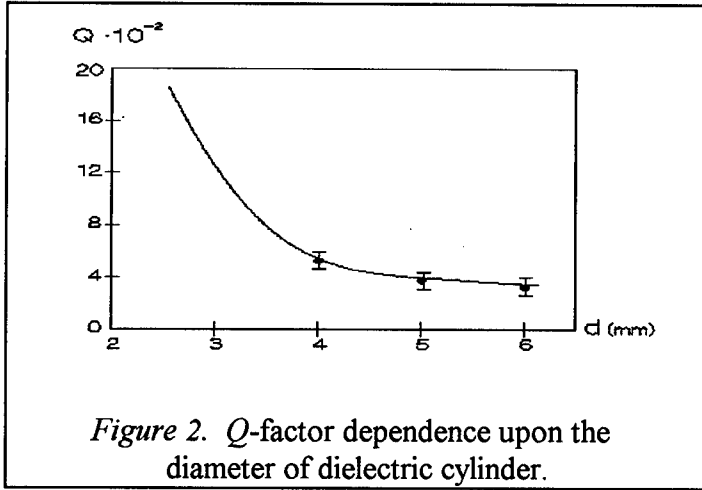
$$T_4 = \frac{k_1 d^2}{2} \left[J_0^2(k_1 d) + J_1^2(k_1 d) \right], \quad T_5 = \frac{k_3 d^2}{2} \left[J_0^2(k_3 d) + J_1^2(k_3 d) \right],$$

where $J_0(kr)$ and $J_1(kr)$ are the zero-order and first-order Bessel functions, $H_0^{(1)}(kr)$ and $H_1^{(1)}(kr)$ are the corresponding Hankel functions, k_1 , k_2 , k_3 , β , γ , and k are the longitudinal and transverse components of the wave vector K in the working areas of resonator.

3. Experiment with OPR in microwave region

We studied OPR system consisted of two metallic mirrors and a dielectric cylinder oriented along the axis of the resonator. The left-hand mirror, which was fixed with respect to the optical bench, had a coupling hole for pumping the system from an external oscillator in the millimeter wave range. We could move the right-hand mirror along the optical bench using a step motor. The signal was coupled out the resonator through a hole in the right-hand mirror. The output signal was registered by a detector and processed by electronics with PC. Using the method of a trail body we could investigate the distribution of the field for oscillation modes excited in the system.

Measurements allowed us to record the OPR spectrum and to determine the Q -factor. Figure 2 displays the Q -factor as a function of the diameter of the dielectric cylinder as calculated according to formulas (1) and (2) - solid line, and also measured in the experiment - bars. The experimental results were obtained for OPR with Teflon rods 100 mm long and 8, 10, 12 mm in diameter. It can be clearly seen that the theoretical calculations are consistent with the experimental results. The displayed dependence demonstrates that the Q -factor of the system decreases with the increasing of the diameter of the dielectric body. In the range of our analysis the upper limit of the cylinder's diameter is associated with the condition $d < a$, whereas the lower limit is set by the minimum diameter of the rod for which E_{01} wave can be excited.



4. Spherical resonator

Spherical resonator (SPR) with a small dielectric body in the center was also studied theoretically. The solution of the wave equation which determines the components of the field in a SPR with an ideally conducting smooth spherical surface and a small sphere in the center of the cavity can be obtained in the following form:

$$U(r, \varphi, \theta) = A_1 \sqrt{r} [J_{n+1/2}(kr) + N_{n+1/2}(kr)] P_n^{(m)}(\cos \theta) \begin{cases} \cos m\varphi \\ \sin m\varphi \end{cases} \quad (3)$$

where A_1 is a constant, r , φ and θ are spherical coordinates; $k = \omega \sqrt{\epsilon_0 \epsilon \mu_0 \mu}$, ϵ_0 and μ_0 are the dielectric constant and the magnetic permeability of a sphere placed in the center of SPR, ω is the eigenfrequency of SPR. $J_{n+1/2}(kr)$ and $N_{n+1/2}(kr)$ are respectively the Bessel and Neumann functions of half-integer orders, whereas $P_n^m(\cos \theta)$ are the Legendre polynomials.

The eigenfrequencies of electric and magnetic components could be found by using the corresponding boundary conditions. For the simplest case of an *empty spherical resonator*, the boundary conditions for electric and magnetic components correspondingly are

$$k_0 a_1 J_{n-1/2}(k_0 a_1) = n J_{n+1/2}(k_0 a_1) \quad (4)$$

$$J_{n+1/2}(k_0 a_1) = 0. \quad (5)$$

Here a_1 is the radius of the SPR and $k_0 = \omega \sqrt{\epsilon_0 \mu_0}$.

If we consider now *the spherical resonator with a spherical body* made with an ideal dielectric and placed in the center of SPR, then the eigen-frequencies of electric and magnetic oscillations could be determined from the following conditions:

$$\begin{aligned} & \epsilon J_{n+1/2}(k_\epsilon b) [k_0 a_1 J_{n-1/2}(k_0 a_1) - n J_{n+1/2}(k_0 a_1)] [k_0 b N_{n-1/2}(k_0 b) - n N_{n+1/2}(k_0 b)] \\ & + J_{n+1/2}(k_0 b) [k_\epsilon b J_{n-1/2}(k_\epsilon b) - n J_{n+1/2}(k_\epsilon b)] [k_0 a_1 N_{n-1/2}(k_0 a_1) - n N_{n+1/2}(k_0 a_1)] \\ & - \epsilon J_{n+1/2}(k_\epsilon b) [k_0 b J_{n-1/2}(k_0 b) - n J_{n+1/2}(k_0 b)] [k_0 a_1 J_{n-1/2}(k_0 a_1) - n J_{n+1/2}(k_0 a_1)] \\ & - N_{n+1/2}(k_0 b) [k_0 a_1 J_{n-1/2}(k_0 a_1) - n J_{n+1/2}(k_0 a_1)] [k_\epsilon b J_{n-1/2}(k_\epsilon b) - n J_{n+1/2}(k_\epsilon b)] = 0 \end{aligned} \quad (6)$$

$$\begin{aligned} & J_{n+1/2}(k_0 a_1) N_{n+1/2}(k_0 b) [k_\epsilon b J_{n-1/2}(k_\epsilon b) - n J_{n+1/2}(k_\epsilon b)] \\ & + J_{n+1/2}(k_\epsilon b) N_{n+1/2}(k_0 b) [k_0 b J_{n-1/2}(k_0 b) - n J_{n+1/2}(k_0 b)] \\ & - J_{n+1/2}(k_0 a_1) J_{n+1/2}(k_\epsilon b) [k_0 b N_{n-1/2}(k_0 b) - n J_{n+1/2}(k_0 b)] \\ & - J_{n+1/2}(k_0 b) N_{n+1/2}(k_0 a_1) [k_\epsilon b N_{n-1/2}(k_\epsilon b) - n J_{n+1/2}(k_\epsilon b)] = 0 \end{aligned} \quad (7)$$

where $k_\epsilon = k_0 \sqrt{\epsilon}$ and b is the radius of the dielectric body in the resonator.

The spectrum of *the spherical resonator with a lossier dielectric* could be calculated if ϵ in the above system of equations should be considered as a complex dielectric constant. However, the spectrum of SPR with a body having small losses ($\text{tg} \delta \ll 1$) practically coincides with the spectrum given by the system of equations (6) and (7) where ϵ is a real quantity.

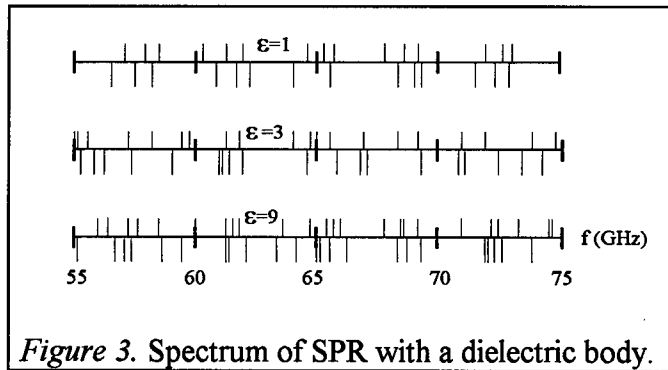


Figure 3. Spectrum of SPR with a dielectric body.

Figure 3 displays theoretically calculated spectra of SPR with a small dielectric spherical body for three different values of the body's dielectric constant. The spectrum of this system becomes thicker as ε grows, as well as when ε is fixed and the radius of the dielectric sphere increases. This is due to decreasing of the wavelength in the dielectric body.

5. Experiment with spherical resonator

For the experimental modeling a cavity in the form of a ball was made with a metal and a small spherical body was placed in its center as depicted in the Figure 4.

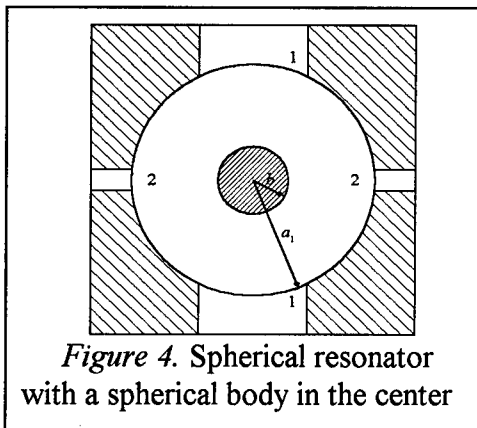


Figure 4. Spherical resonator with a spherical body in the center

Cavity had two symmetrical cut round segments denoted as (1-1) in the Figure 4. Two symmetrical small coupling holes (2-2) were made at the axis perpendicular to the axis of the segments. As in a barrel cavities, a greater part of the resonator volume in the ball cavity is bounded by a conducting surface and only an insignificant part of the volume is coupled with a free space by small apertures.

The SPR was excited by an external oscillator in the frequency range 55-75 GHz through a delivery waveguide and the holes. Two ways of excitation were used in the experiments: through one of the small coupling holes, and through the open segment. The SPR spectra, the distributions of the modes and Q -factor were studied by analyzing the shape and other parameters of the resonance curves observed on the oscilloscope display.

A series of spherical resonators which were made in laboratory typically had the following parameters: curvature radius in the range of 10-20.5 mm, diameter of the open segment from 4.5 to 20 mm, and diameter of the coupling holes from 1.5 to 2 mm.

Figure 5 represents the experimental spectrum recorded for one of the empty SPR, excited through its open segment.

Background comb of the vertical bars in this figure represents the spectrum calculated in accordance with (4) and (5). The discrepancy between some frequencies is associated chiefly with the difference

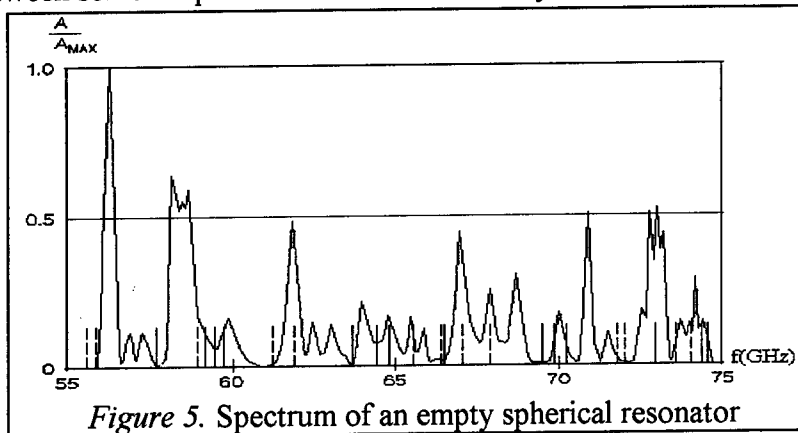


Figure 5. Spectrum of an empty spherical resonator

between theoretical model and experimentally studied SPR having the open segments.

Experimental analysis of the field distribution proved that both spatially distributed oscillations and oscillations of the whispering-gallery type, whose field is localized in a limited space near the cavity surface, could be excited in the SPR. The Q -factor of the studied resonators varied between 10^2 and 10^3 .

References

1. Raevski, S.B. (1970) *Sobstvennye kolebania otkritogo resonatora* (in Russian), *Izv. Vyssh. Uchebn. Zaved., Radiotekhnika*. **13**, 987-992.
2. Afonin, D.G., Dubrovskii, V.V., and Malyshev, A.K. (1993) *Avtomatizirovannaya ustanovka dlia issledovaniia elektrodinamicheskikh sistem* (in Russian), *Pribory i Tekhnika Eksperimenta* No 5, 75-78.

THERMAL LENSING IN KERR-LENS MODELOCKED SOLID-STATE LASERS

MANJUSHA MEHENDELE and W. ANDREAS SCHROEDER
*University of Illinois at Chicago, Department of Physics (M/C 273),
845 W. Taylor Street, Chicago IL 60607-7059, USA*

Abstract

Laser cavity simulations, based on a numerical beam propagation analysis, are used to demonstrate that thermal lensing shifts and distorts the resonator stability regions of and perturbs the modelocking mechanism in hard-apertured, Kerr-lens modelocked, laser-pumped solid-state lasers. The effect of positive and negative thermal lensing on the modelocking mechanism in both canonical asymmetric and symmetric resonators are compared and contrasted using Ti:sapphire and Cr:LiSrAlF₆ gain media respectively.

1. Introduction

In recent years, analysis of the Kerr-lens modelocking (KLM) mechanism in laser-pumped femtosecond solid-state lasers like Ti:sapphire [1-8] and Cr³⁺-doped LiSrAlF₆ (Cr:LiSAF) [9] has received considerable attention. In particular, the effects of cavity alignment [1-5,9], gain guiding [6], diffraction [7], and dispersive pulse broadening [8] have been treated. In contrast, the effect that the pump-induced thermal lens has on the operation of these femtosecond lasers has received relatively little attention [10,11]. This is somewhat surprising since the power of the thermal lens in a 1-2cm gain medium can be shown to be comparable to the nonlinear Kerr-lens in typical modelocked Ti:sapphire resonators producing 50-100fs pulse durations [12]. Consequently, due of its effect on the propagation of the intracavity laser mode through the solid-state gain medium, the thermal lens (i) shifts and distorts the stability regions of the laser resonator and (ii) affects the strength of the KLM mechanism since this irradiance-dependent effect is strongly influenced by the intracavity mode size in the gain medium.

In this paper, we extend our previous numerical analysis [12] of the influence of the pump-laser-induced thermal lensing on the operation of a hard-apertured KLM Ti:sapphire laser to include symmetric cavity arrangements which have been shown to result in improved KLM conditions [5]. In addition, the differing effects of positive and negative pump-induced thermal lensing on the KLM mechanism are investigated using Ti:sapphire and Cr:LiSAF gain media respectively.

2. Numerical Procedure

The numerical resonator simulations use a rigorous radial Gaussian beam propagation analysis to treat the canonical hard-apertured KLM laser resonator shown in Fig. 1 [12]. The propagation of both the intracavity laser beam and the pump laser beam (in the laser gain medium) are treated using the ABCD matrix formalism in the paraxial Gaussian beam approximation. The gain medium is divided into 1000 elements and a radially symmetric graded-index (GRIN) lens approximation is used to treat both the thermal and nonlinear Kerr lensing effects in each element. Following Refs. 13 and 14, the radial refractive index changes Δn associated with Kerr lensing effect in each element of the gain medium are approximated using a parabolic function of the form

$$\Delta n(r) = \frac{2n_2 P}{\pi w_L^2} \left(B_K - A_K \frac{2r^2}{w_L^2} \right), \quad (1)$$

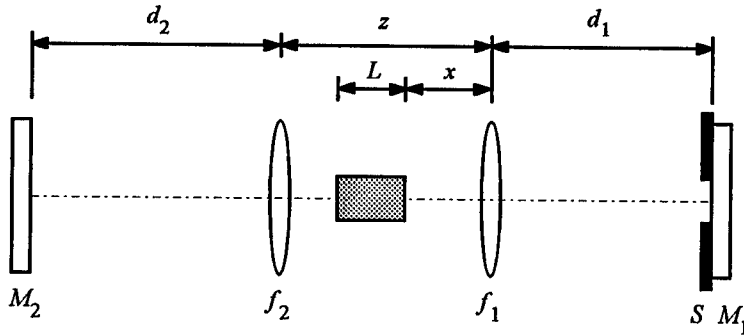


Figure 1. Schematic of the canonical hard-apertured solid-state laser resonator with arm lengths d_1 and d_2 used in the numerical simulations. The gain section mirrors, which are separated by z , are represented by the lenses f_1 and f_2 . The position of the gain medium of length L is defined with respect to f_1 . Both the output coupler M_1 and high reflector M_2 are plane mirrors and the slit aperture S is assumed to be next to the output coupler.

where w_L is the spot size of the laser beam, P is the intracavity laser power, and n_2 is the coefficient of nonlinear refraction. The parameters A_K and B_K , with values of 0.5 and 0.75 respectively, result from a weighted least squares fit of the parabolic refractive index variation to the Kerr lens associated with the Gaussian spatial laser mode [13,14].

The numerical simulation of the intracavity oscillation begins by selecting a plane-wave spot size w_2 at the high reflector M_2 and propagating the Gaussian mode through the resonator to the output coupler M_1 for a particular value of the rod position x in the *absence* of Kerr lensing (see Fig. 1). The two possible values for the gain section mirror separation z , corresponding to the two stability regions, are then found for which the laser mode is also a plane-wave at the output coupler M_1 . For each fixed pair of values (x, z) and in the *presence* of the Kerr lens, the procedure is now repeated iteratively for different spot sizes at the high reflector M_2 to find the new stable cavity mode [12]. To assess the ability of the resonator to sustain hard-apertured KLM operation, the spot sizes at the output coupler M_1 in the absence (w_{CW}) and presence (w_K) of the Kerr lens are compared. If $w_K < w_{CW}$, then the slit aperture S in front of M_1 (Fig. 1) can be used to favor modelocked operation by introducing higher losses for the CW oscillation. In accordance with previous work [2,5], we characterize this discrimination in terms of a "Kerr lens sensitivity" parameter δ which is defined by

$$\delta = \frac{P_c}{P} \left(\frac{w_K}{w_{CW}} - 1 \right), \quad (2)$$

where P_c is the critical power for self focusing. The linear variation of w_K with the laser power assumed in Eq. (2) has been shown to be valid for $P \leq 0.3P_c$ [13]. Repetition of the numerical procedure for different initial spot sizes at the high reflector allows both cavity stability regions to be completely investigated for potential hard-apertured KLM operation which requires $\delta < 0$.

To determine the influence of the pump-induced thermal lens on both the resonator stability and the KLM mechanism, we first investigated the operational characteristics of canonical solid-state resonators (with $f_1 = f_2 = 50\text{mm}$) in the *absence* of thermal lensing. The results are shown in Fig. 2 in the form of a contour plot of δ as a function of x and z for both symmetric ($d_1 = d_2 = 90\text{cm}$) and asymmetric ($d_1 = 80\text{cm}$, $d_2 = 100\text{cm}$) resonators. For clarity only the contours for $\delta < 0$ are shown since hard-apertured KLM requires $w_K < w_{CW}$. In these and subsequent simulations, an intracavity laser power of $0.25P_c$ was used. For a 100fs pulse, this corresponds to intracavity modelocked pulse energies of $\sim 50\text{nJ}$ and $\sim 180\text{nJ}$ for Ti:sapphire and Cr:LiSAF lasers respectively. Identical plots are obtained for both Ti:sapphire and

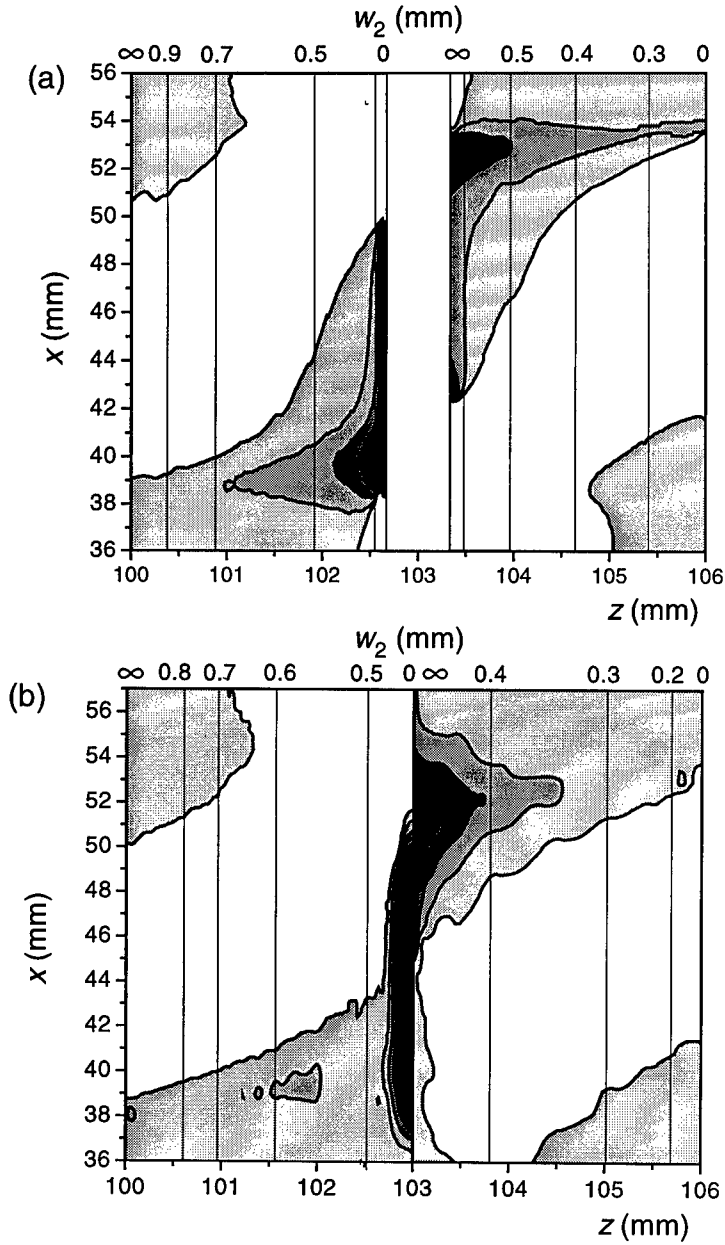


Figure 2. Contour plot of the Kerr-lens sensitivity parameter δ as a function of x and z for (a) an asymmetric cavity ($d_1 = 80$ cm and $d_2 = 100$ cm) and (b) a symmetric cavity ($d_1 = d_2 = 90$ cm). The gray scaling is from $\delta > 0$ (white) in steps of 0.4 to $\delta < -1.6$ (black). The fine vertical lines represent the CW stability conditions for a constant initial spot size w_2 at the high reflector M_2 .

Cr:LiSAF laser resonators provided that the divergence of the laser beam in the gain medium is the same in both cases, i.e. that the length of the gain medium L scales with its refractive index n . For the data in Fig. 2, a value for L/n of 11.4mm was used, giving $L = 20\text{mm}$ for Ti:sapphire and $L = 16\text{mm}$ for Cr:LiSAF. Other parameters used in the model are presented in Table 1.

The results indicate that for both the asymmetric (Fig. 2(a)) and symmetric (Fig. 2(b)) resonators, KLM operation is most strongly favored near the internal edge between the two stability regions, especially for $x \approx 39\text{mm}$ in region I ($z < 103\text{mm}$) and for $x \approx 52\text{mm}$ in region II ($z > 103\text{mm}$). It is also noticeable that discrimination between continuous wave (CW) and modelocked (ML) operation for these values of x and z is more pronounced for the symmetric cavity. These results are consistent with those obtained by other authors under similar conditions using a *single* ABCD matrix approximation for the Kerr lensing [2,5,9].

TABLE 1. Parameters used in the numerical simulations of the hard-apertured KLM Ti:sapphire and Cr:LiSAF laser resonators.

Parameter	Ti:sapphire	Cr:LiSAF
L (mm)	20	16
n	1.76	1.4
α (cm ⁻¹)	1.0	1.25
n_2 (m ² /W)	3×10^{-20}	1.1×10^{-20}
P_c (MW)	2.2	6.0
λ_{laser} (nm)	800	800
λ_{pump} (nm)	500 (Ar ⁺ laser)	650 (Kr ⁺ laser)
P_o (W)	6.0	1.0
k (Wm ⁻¹ K ⁻¹)	42	1.68
dn/dT (K ⁻¹)	12.6×10^{-6}	-4×10^{-6}

3. Pump-Induced Thermal Lensing

In laser-pumped solid-state lasers like Ti:sapphire, Cr:LiSAF, etc., part of the pump laser power is dissipated as heat which is removed by external cooling of gain medium. The resulting temperature gradient is responsible for the thermal effects in solid-state gain media [15]. The dominant thermal effect in nearly all solid-state laser crystals is the thermo-optic effect, i.e. the refractive index change with temperature. In

Ti:sapphire, this results in a positive pump-induced lensing mechanism since the variation of the refractive index with temperature dn/dT is positive [15] whereas for Cr:LiSAF it is negative [16].

The strength of the pump-induced thermal lensing in solid-state gain media can be determined by evaluating the temperature distribution $T(r)$ generated by the absorption of the pump radiation with a Gaussian heat source term of the form $\exp(-2r^2/w_p^2)$, where w_p is the spot size of the pump beam. The temperature distribution can be obtained from a series solution to the steady state radial thermal diffusion equation

$$k \left(\frac{\partial^2 T}{\partial r^2} + \frac{1}{r} \frac{\partial T}{\partial r} \right) + Q \exp\left(-\frac{2r^2}{w_p^2}\right) = 0, \quad (3a)$$

with

$$Q = \frac{2\alpha S P_o \exp(-\alpha\xi)}{\pi w_p^2}, \quad (3b)$$

where Q is the absorbed power per unit volume for each element in our GRIN lens approximation, P_o is the incident pump power, α is the linear optical absorption coefficient at the pump wavelength, ξ is the coordinate describing the propagation direction of the pump beam in the gain medium, and k is the thermal conductivity. The parameter S represents the fraction of the absorbed pump power that is converted to heat. For an Ar^+ -pumped ($\lambda_{\text{pump}} \approx 500$ nm) Ti:sapphire laser emitting at 800nm, this fraction is ≈ 0.38 , whereas in Cr:LiSAF laser emitting at 800 nm and pumped by a Kr^+ ion laser ($\lambda_{\text{pump}} \approx 650$ nm) it is ≈ 0.2 . The full series solution to Eq. (3) can be expressed as

$$T(r) = T_o + \frac{Q w_p^2}{8k} \sum_{m=1}^{\infty} \frac{(-1)^m}{m!m} \left(\frac{2r^2}{w_p^2} \right)^m, \quad (4)$$

where T_o is the peak on axis temperature at $r = 0$. In obtaining this solution, we have neglected thermal diffusion in the direction parallel to the propagation of the pump beam which is a good approximation since generally $\alpha^{-1} \gg w_p$.

To incorporate the thermal lensing into the GRIN lens resonator analysis, the function $\Delta T(r) = T(r) - T_o$ is approximated to a parabolic dependence of the form

$$\Delta T(r) = \frac{Qw_p^2}{4k} \left(B_T - A_T \frac{2r^2}{w_p^2} \right), \quad (5)$$

where A_T and B_T are the fitting parameters using a weighted least squares fit with an arbitrary Gaussian irradiance profile of the form $\exp(-2r^2/w^2)$. The resulting fit parameter A_T for arbitrary spot size ratios w/w_p is accurately described by the function [12]

$$A_T(w/w_p) = 0.334 + 0.681 \times \exp[-1.21(w/w_p + 0.0624)^2] \\ \approx \frac{1}{3} + \frac{2}{3} \exp[-(8w/7w_p)^2]. \quad (6)$$

Using this formulation, the effect of the pump-induced thermal lensing on both the pump beam itself ($w = w_p$) and the intracavity laser beam ($w = w_L$) are included in each GRIN lens element of the resonator analysis in a similar manner to the nonlinear Kerr lensing (Eq. 1) using the values of dn/dT for Ti:sapphire and Cr:LiSAF (Table 1).

We emphasize that in both cases, the incident pump laser Gaussian beam parameters were chosen to ensure the optimum spatial overlap with the oscillating intracavity mode in the gain medium for the majority of the values of x and z in both stability regions [12] - the low threshold operation condition. However, thermal expansion of the ends of the laser gain medium and refractive index changes due to thermally-induced stress in the bulk of the gain medium have not been included in the analysis. Thermal expansion can be shown to have a negligible effect on the intracavity mode parameters for gain media with $L > 1\text{cm}$ [12,15], while the inclusion of thermal stresses would require the use of a radially anisotropic analysis.

4. Asymmetric Laser Resonators

The effect that the pump-induced thermal lens has on the operational characteristics of KLM Ti:sapphire and Cr:LiSAF lasers are shown in the contour plots of Fig. 3 for the case of an asymmetric resonator ($d_1 = 80\text{cm}$, $d_2 = 100\text{cm}$) and the conditions listed in Table 1. The pump laser powers are typical of Ar^+ -pumped Ti:sapphire [4,5] and Kr^+ -pumped [17] (or laser-pumped [9]) Cr:LiSAF resonators producing 50-100fs pulses. It is important to note that although the temperature change $\Delta T(r)$ is about three times larger in Cr:LiSAF than in Ti:sapphire under these conditions (due to the much higher thermal conductivity of sapphire), the magnitudes of the pump-induced thermal lenses are very comparable since $\alpha SP_o(dn/dT)/k \sim 0.5$ in both cases. Thus, any differences in

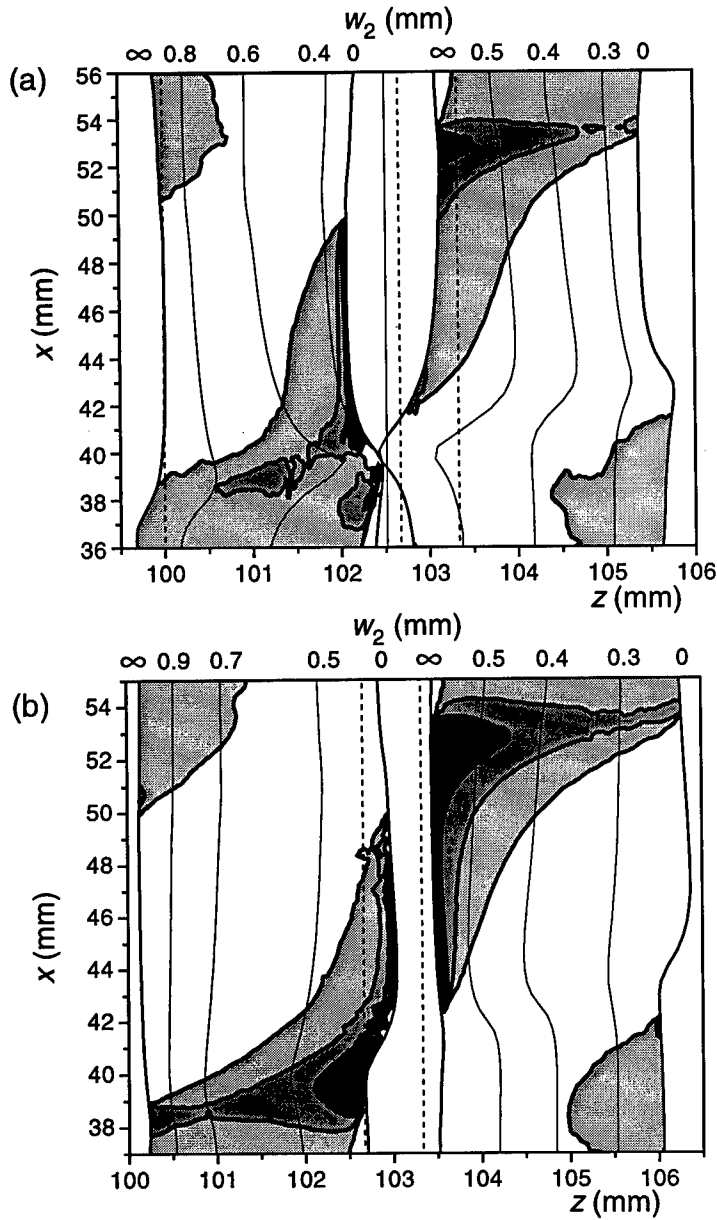


Figure 3. Contour plot of the Kerr-lens sensitivity parameter δ as a function of x and z for an asymmetric cavity ($d_1 = 80\text{cm}$ and $d_2 = 100\text{cm}$) with the pump-induced thermal lensing included for (a) Ti:sapphire and (b) Cr:LiSAF gain media. The dashed lines indicate the resonator stability edges in the *absence* of thermal lensing. The gray scaling is identical to that in Fig. 2 and the fine lines represent the CW stability conditions for a constant initial spot size w_2 at the high reflector M_2 .

the operational characteristics of KLM Ti:sapphire and Cr:LiSAF lasers caused by the thermal lens will be due to its sign rather than its strength.

The most noticeable feature of the results presented in Fig. 3 is the shift and distortion of the cavity stability regions with respect to the stability regions in the absence of thermal lensing (Fig. 2(a)) whose edges are displayed by the dashed lines. An indication of the distortion within the stability regions is given by the lines of constant w_2 (the initial CW spot size at the high reflector M_2) which are independent of x (the position of the gain medium between the gain section mirrors f_1 and f_2 (Fig. 1)) in the absence of thermal lensing effects (Fig. 2(a)). However, both the shift and distortion are dependent upon the *sign* of the thermal lens. The stability regions shift to lower z values for the positive thermal lens in Ti:sapphire (Fig. 3(a)) and to larger z for the negative thermal lens of Cr:LiSAF (Fig. 3(b)). This behavior is to be expected from a simple geometrical optics analysis of a cavity with three lenses - f_1 , f_2 , and the gain medium. The distortion of the resonator stability limits is much more pronounced for the positive thermal lens of Ti:sapphire than for the case of negative thermal lensing in Cr:LiSAF. Specifically, at $(z, x) \approx (102.4\text{mm}, 40.0\text{mm})$ in the Ti:sapphire resonator (Fig. 3(a)), the thermal lensing causes the two inner stability edges to just come in contact with each other. In fact, the two stability regions overlap if the thermal lens becomes stronger (due to an increased pump power, lower thermal conductivity, etc.) and/or if the resonator is more symmetric ($d_1 \approx d_2$) as shown in Section 5 below.

The numerical analysis also shows a distinct difference in the effect that positive and negative pump-induced thermal lensing has on hard-apertured KLM operation. This can be seen in a comparison between Fig. 2(a) and Figs. 3(a) and (b) of the size and shape of the regions in which KLM operation is most preferred, e.g. where $\delta < -0.8$. For Cr:LiSAF (Fig. 3(b)), the ability of the asymmetric resonator to sustain hard-apertured modelocking is enhanced near the inner stability edges of both stability regions relative to that in the absence of thermal lensing (Fig. 2(a)). This reduction in δ occurs because negative thermal lensing creates a larger oscillating Gaussian mode size in the gain medium. The resulting mode has a reduced divergence and, thus, is more susceptible to perturbation by the positive nonlinear Kerr lens. In contrast, the positive thermal lensing in Ti:sapphire (Fig. 3(a)) causes a reduction in the hard-apertured KLM efficiency, i.e. an increased δ . This effect is most pronounced at $(z, x) \approx (102\text{mm}, 39.0\text{mm})$ in stability region I where the positive pump-induced thermal lens has clearly strongly perturbed the favorable KLM operation observed in the absence of the thermo-optic effect (Fig. 2(a)). Thus, for a typical thermally-loaded asymmetric Ti:sapphire resonator, hard-apertured modelocked operation is most favored near $(z, x) \approx (103.2\text{mm}, 53.0\text{mm})$ in stability region II.

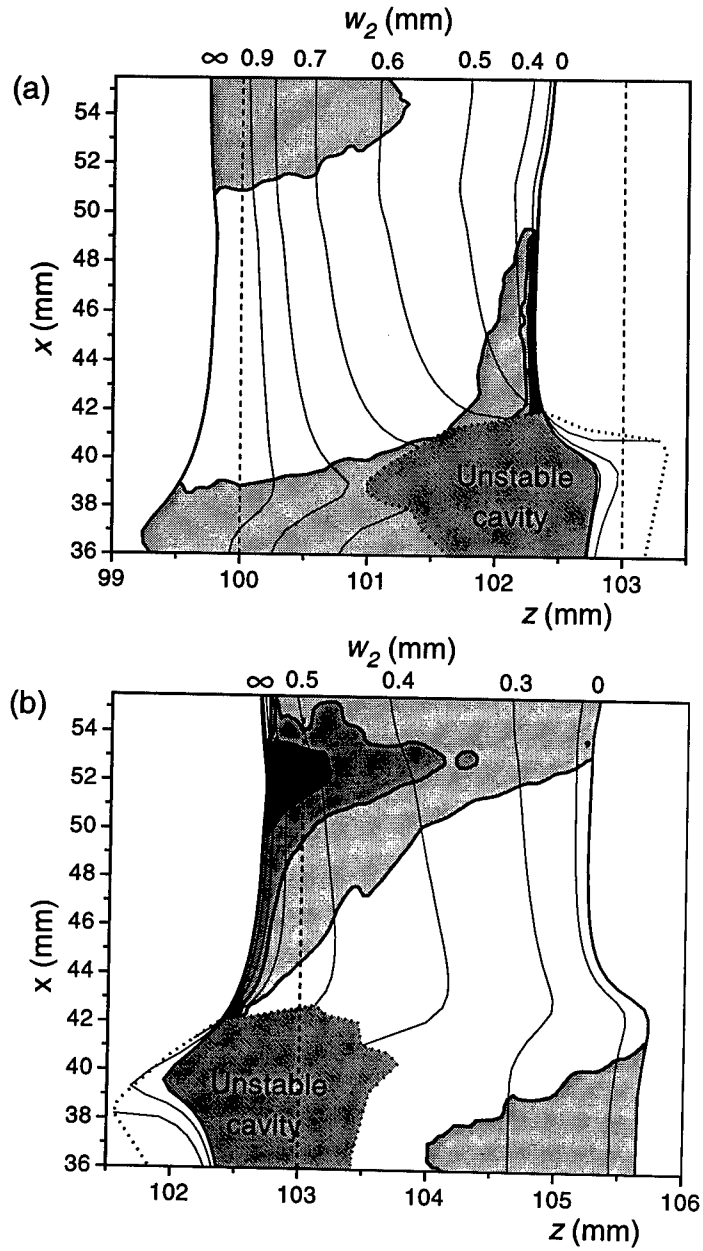


Figure 4. Contour plot of the Kerr-lens sensitivity parameter δ as a function of x and z for stability regions (a) I and (b) II of a symmetric Ti:sapphire cavity ($d_1 = d_2 = 90\text{cm}$) with pump-induced thermal lensing. The dashed lines indicate the resonator stability edges in the *absence* of thermal lensing. The gray scaling is identical to that in Fig. 2 and the fine lines again represent the CW stability conditions for a constant initial spot size w_2 at the high reflector M_2 .

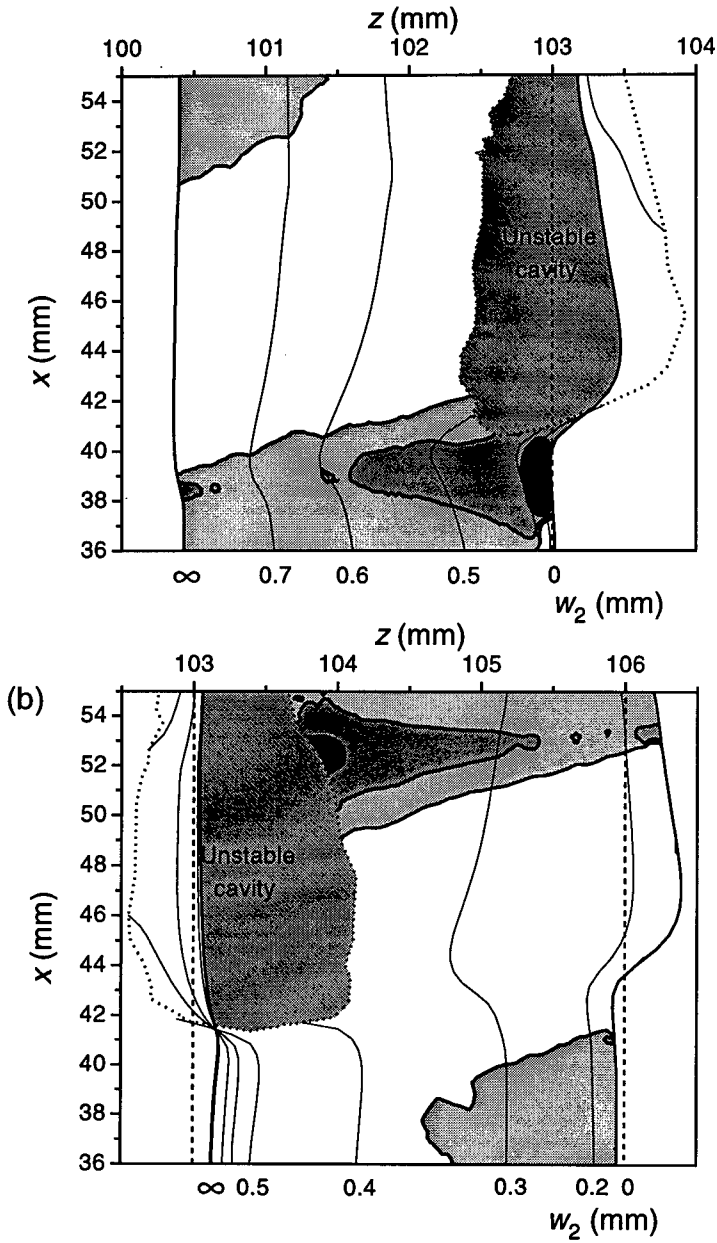


Figure 5. Contour plot of the Kerr-lens sensitivity parameter δ as a function of x and z for stability regions (a) I and (b) II of a symmetric Cr:LiSAF cavity ($d_1 = d_2 = 90\text{cm}$) with pump-induced thermal lensing. The dashed lines indicate the resonator stability edges in the *absence* of thermal lensing. The gray scaling is identical to that in Fig. 2 and the fine lines again represent the CW stability conditions for a constant initial spot size w_2 at the high reflector M_2 .

5. Symmetric Laser Resonators

The pump-induced thermal lens has a greater effect on hard-apertured KLM operation in symmetric resonators ($d_1 = d_2 = 90\text{cm}$) for both Ti:sapphire and Cr:LiSAF gain media as shown in Figs. 4 and 5 respectively. Most noticeable are the areas between the two stability regions ($z \approx 103\text{mm}$) where the resonators are unstable (grey shading), i.e. where there are no stable CW cavity modes due to the perturbation of the thermal lens. As a result, the lines of constant w_2 (the initial CW spot size at the high reflector M_2) are either discontinuous or terminate at the edge of the unstable regions. The different signs of the thermal lens in Ti:sapphire and Cr:LiSAF cause these unstable regions to appear at different values of (z, x) . For the Ti:sapphire resonator (Fig. 4), the unstable region occurs for $x < 42\text{mm}$ and extends from about $z > 101.5\text{mm}$ to $z < 103.5\text{mm}$ so that the area favored for KLM operation in stability region I in the absence of thermal lensing (Fig. 2(b)) is excluded. In contrast, the favored area around $(z, x) \approx (102.7\text{mm}, 52.0\text{mm})$ in stability region II is not strongly perturbed by the pump-induced thermal lensing. Similarly, for $x > 41\text{mm}$ and z between about 102.5 and 104mm, hard-apertured modelocked operation is not possible for the symmetric Cr:LiSAF resonator (Fig. 5). In this case, however, efficient hard-apertured KLM operation ($\delta < -0.8$) is adversely affected by the thermal lens in both stability regions.

6. Conclusions

We have demonstrated using a radial GRIN lens Gaussian beam propagation code that the pump-induced distributed thermal lens has a significant impact on the operational characteristics of hard-apertured KLM solid-state lasers with 1-2cm gain media. Furthermore, the effects of the thermal lens are strongly dependent upon its sign. The positive thermal lens in Ti:sapphire generally reduces the ability of the resonator to sustain hard-apertured KLM operation, whereas the negative thermal lens in Cr:LiSAF has the opposite effect. However, for a symmetric resonator, the perturbations introduced by the thermal lens to the cavity stability criteria are much more severe if its sign is negative. As a result, asymmetric resonators are preferred for hard-apertured KLM operation of a femtosecond Cr:LiSAF laser. In contrast, hard-apertured KLM operation with Ti:sapphire is favored for a symmetric cavity arrangement provided the resonator is modelocked in stability region II.

The results of these numerical simulations may affect and optimize the design of future hard-apertured KLM lasers such as those employing cerium doped LiSrAlF_6 or LiCaAlF_6 gain media for ultraviolet femtosecond pulse generation [18]. However, a deeper understanding of the role of pump-induced thermal lensing effects will require a simulation which includes Brewster-cut gain media with the required astigmatism

compensation [19], gain guiding effects [6] since the pump laser beam is also subject to the thermal lensing, and thermal stress dependent anisotropic refractive index changes [15].

7. References

1. Brabec, T., Spielmann, Ch., Curley, F.P., and Krausz, F. (1992) Kerr lens mode locking, *Optics Letters* **17**, 1292-1294.
2. Magni, V., Cerullo, G., and De Silvestri, S. (1993) Closed form gaussian beam analysis of resonators containing a Kerr medium for femtosecond lasers, *Optics Communications* **101**, 365-370.
3. Brabec, T., Curley, F.P., Spielmann, Ch., Wintner, E., and Schmidt, A.J. (1993) Hard aperture Kerr-lens mode locking, *Journal of the Optical Society of America B* **10**, 1029-1034.
4. Piché, M. and Salin, F. (1993) Self mode-locking of solidstate lasers without apertures, *Optics Letters* **18**, 1041-1043.
5. Cerullo, G., De Silvestri, S., and Magni, V. (1994) Self-starting Kerr-lens mode locking of a Ti:sapphire laser, *Optics Letters* **19**, 1040-1042.
6. Gatz, G. and Hermann, J. (1995) Astigmatism and gain guiding in Kerr-lens mode-locked lasers, *Optics Letters* **20**, 825-827.
7. Haderka, O. (1995) Influence of diffraction on hard-aperture Kerr-lens mode locking, *Optics Letters* **20**, 240-242.
8. Christov, I.P., Kapteyn, H.C., Murnane, M.M., Huang Chung-Po, and Zhou, J. (1995) Space-time focusing of femtosecond pulses in Ti:sapphire laser, *Optics Letters* **20**, 309-311.
9. Dymott, M.J.P. and Ferguson, A.I. (1994) Self-mode-locked diode-pumped Cr:LiSAF laser, *Optics Letters* **19**, 1988-1990.
10. Georgiev, D., Hermann, J., and Stamm, U. (1992) Cavity design for optimum nonlinear absorption in Kerr-lens mode-locked solid-state lasers, *Optics Communications* **92**, 368-375.
11. Wei, Z., Lee, W., Wong, S., Yu, Z., and Huang, X. (1995) Investigation of self-starting for self-mode-locked Ti:sapphire laser, *Chinese Journal of Lasers* **B4**, 1-8.
12. Mehendale, M., Nelson, T.R., Omenetto, F.G., and Schroeder, W.A. (1997) Thermal effects in laser pumped Kerr-lens modelocked Ti:sapphire lasers, *Optics Communications* **136**, 150-159.
13. Magni, V., Cerullo, G., and De Silvestri, S. (1993) ABCD matrix analysis of propagation of gaussian beams through Kerr media, *Optics Communications* **96**, 348-355.
14. Bridges, R.E., Boyd, R.W., and Agrawal, G.P. (1993) Effect of beam ellipticity on self-mode locking in lasers, *Optics Letters* **18**, 2026-2028.
15. Koechner, W. (1992) *Solid-State Laser Engineering*, Springer Series in Optical Sciences no. 1, 3rd edition, Springer Verlag, New York.
16. Perry, M.D., Payne, S.A., Ditmire, T., Beach, R., Quarles, G.J., Ignatuk, W., Olson, R., and Weston, J. (1993) Better materials trigger Cr:LiSAF laser development, *Laser Focus World* **29**, no. 9, 85-92.
17. Miller, A., LiKamWa, P., Chai, B.H.T., and Van Stryland, W. (1992) Generation of 150-fs tunable pulses in Cr:LiSAF, *Optics Letters* **17**, 195-197.
18. Marshall, C.D., Speth, J.A., Payne, S.A., Krupke, W.F., Quarles, G.J., Castillo, V., and Chai, B.H.T. (1994) Ultraviolet laser emission properties of Ce^{3+} -doped $LiSrAlF_6$ and $LiCaAlF_6$, *Journal of the Optical Society of America B* **11**, 2054-2064.
19. Magni, V., Cerullo, G., De Silvestri, S., and Monguzzi, A. (1995) Astigmatism in Gaussian-beam self-focusing and in resonators for Kerr-lens mode locking, *Journal of Optical Society of America B* **12**, 476-485.

PART II: PHASE CONJUGATIONS

PHASE CONJUGATION TECHNIQUES

H.J. EICHLER, A. HAASE, B. LIU, O. MEHL
Technische Universität Berlin, Optisches Institut/Sekr. P11,
Straße des 17. Juni 135, D-10623 Berlin, Germany

Abstract

Lasers with high average output power suffer from thermal lensing, stress birefringence and other phase distortions, which reduce the beam quality significantly. Self-pumped phase conjugating mirrors based on stimulated Brillouin scattering (SBS) were applied in different oscillators and master oscillator power amplifier systems (MOPA) to realize high beam qualities at average output powers up to 500 Watt. SBS-mirrors were applied from the mid-infrared down to the ultraviolet range. As an alternative to widely used SBS-materials like liquids and gases we developed a new kind of self-pumped SBS-mirror based on multimode quartz fibers.

1. Introduction

For laser applications in industry, science and medicine the brightness is an important parameter. The brightness depends on the square of the beam quality, whereas the power has a linear influence. Therefore, an increased beam quality leads to new fields of laser applications.

In this paper the interest will be focused on three important wavelengths: 1 μm Nd-doped solid state lasers, 3 μm Er-doped lasers for medical applications and 308 nm excimer lasers.

In case of solid state lasers the beam quality decreases rapidly with the average output power due to phase distortions introduced by strongly pumped laser crystals. Slab laser arrangements can be used to reduce the influence of phase distortions like stress birefringence and thermal lensing [1]. Diode pumping instead of flashlamp pumping can be used to reduce the thermal loading of the crystals and therefore the phase distortions [2]. This results in higher beam qualities at the same average output power. To achieve high

beam qualities for an average output power in the kW-range, however, the remaining phase distortions have to be compensated using phase conjugation.

In case of excimer lasers the beam quality suffers from the spatially incoherent emission structure of the beam resulting in large divergence and low beam quality although the transversal profile can be very smooth. Also here, phase conjugation can be used to realize higher beam qualities.

2. Self-pumped SBS-mirrors

SBS is the major process used for the realization of self-pumped phase conjugating devices for high average power laser systems. Liquid and gaseous media of high purity as well as solid materials like glass fibers can be used with high efficiency.

The SBS-mirror consists of a simple cell into which the laser beam is focused as shown in Figure 1a. The cell is filled with a liquid like carbon disulfide or a gas like SF_6 . Focal lengths and scattering media have to be chosen carefully to achieve a high SBS reflectivity and a good reproduction of the wavefront. Unwanted side-effects in the material like absorption, optical breakdown or other scattering processes have to be avoided.

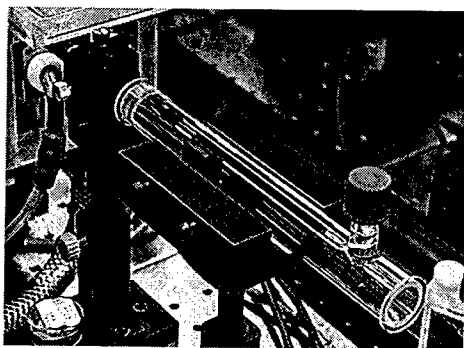


Figure 1a. Photograph of a Brillouin-cell filled with carbon disulfide.

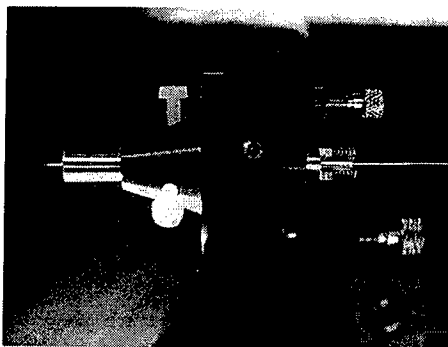


Figure 1b. Photograph of a fiber phase conjugator.

To reduce the power threshold of SBS waveguide geometries can be used [3]. The beam intensity inside the waveguide is high for a long interaction length resulting in a low power threshold. To avoid toxic liquids and gases under high pressure multimode quartz fibers can be used (see Figure 1b). The lower Brillouin gain of quartz glass compared to suitable SBS gases and liquids can be overcome using fibers with lengths of several meters.

Energy reflectivity, fidelity and SBS threshold were measured for fibers with different core diameters. Figure 2 shows the dependence of the SBS-reflectivity on the input power for a fiber with a core diameter of $200\text{ }\mu\text{m}$ and a length of 4.1 m . All values for the reflectivity and the power threshold are related to the full energy incident on the fiber and not corrected with respect to the energy coupled into the fiber.

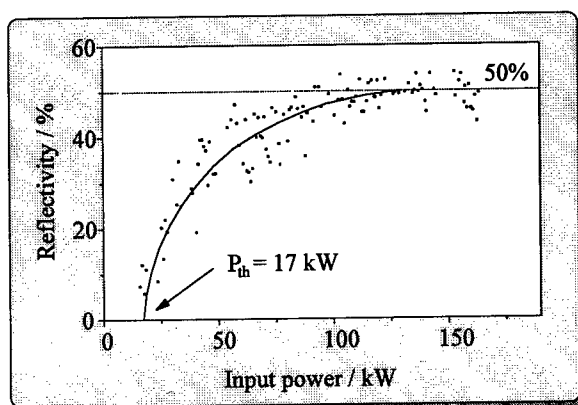


Figure 2. Reflectivity vs. input power for a fiber phase conjugator with $200\text{ }\mu\text{m}$ core diameter.

The stable behavior of the SBS process for an energy exceeding the threshold up to ten times is confirmed by the high fidelity. The fidelity is 93 % and the fidelity fluctuations of less than 2 % are in the same order of magnitude as the fluctuations of our pyroelectric energy meters.

The damage threshold of the fiber entrance surface is about 500 MW/cm^2 , if a homogeneous illumination with a beam diameter equal to the core diameter of $200\text{ }\mu\text{m}$ is assumed. Values up to 1.5 GW/cm^2 were observed for some fibers with a polished end surface.

TABLE 1. SBS-threshold for different core diameters of the fiber (* coherence length 6 m, otherwise 0.5 m)

Fiber core diameter / μm	SBS threshold / kW
400	29
200	17
100	6.4
50	0.5*
25	0.2*

We compared the performance of the fiber phase conjugator with a Brillouin cell filled with carbon disulfide. The pump beam was focused into the cell with a lens of 100 mm focal length. CS_2 is one of the SBS materials with the lowest SBS threshold, but has the disadvantage of toxicity. Table 2 gives a summary of the results obtained in case of a nearly diffraction-limited input beam and a distorted input beam. For a fiber with a core diameter of 200 μm and an input beam with a coherence length of about 50 cm the SBS thresholds P_{th} in both cases are nearly the same. But the fidelity F of the fiber is much higher with lower fluctuations.

TABLE 2. SBS threshold P_{th} , maximum reflectivity R and fidelity F for two different types of phase conjugators

200 μm fiber	Brillouin cell with CS_2
$P_{\text{th}} = 17 \text{ kW}$	$P_{\text{th}} = 13 \text{ kW}$
$R = 50\%$	$R = 70\%$
$F = (93 \pm 2)\%$	$F = (75 \pm 13)\%$

In case of highly distorted beams the Brillouin cell and the fiber phase conjugator show significantly different behaviors.

TABLE 3. SBS threshold P_{th} , maximum reflectivity R and fidelity F for two different types of phase conjugators using a highly distorted beam ($M^2 = 10$)

200 μm fiber	Brillouin cell with CS_2
$P_{\text{th}} = 17 \text{ kW}$	$P_{\text{th}} = 57 \text{ kW}$
$R = 50\%$	$R = 10\%$
$F = 78\%$	$F = 70\%$

The power threshold increases to 57 kW for the Brillouin cell and thus the reflectivity decreases rapidly. Therefore, in case of a strongly distorted input beam, the fiber phase conjugator shows better properties. This can be explained, that in case of a Brillouin cell the SBS properties depend strongly on the far field distribution of the incoming beam. Phase distortions in a beam with bad quality result in high amplitude fluctuations in the far field. Due to the SBS threshold the beam cannot be reproduced perfectly in the focal region of the Brillouin cell lens. Therefore the reflectivity and fidelity decrease. In case of a fiber the amplitude distribution of the light is nearly homogeneous due to the mode conversion. Therefore the threshold does not depend on the incoming beam quality.

3. Phase Conjugation for Nd-Lasers

For high average power Nd-doped solid state lasers SBS is favorable for phase conjugating elements due to the absence of absorption inside the SBS-medium. Different oscillators and MOPA-systems (Master oscillator power amplifier) were realized.

3.1. OSCILLATORS WITH SBS-MIRRORS

Laser oscillators with SBS phase conjugating mirrors have perspective to generate diffraction-limited beam quality up to several 10 Watt average output power in a simple way [4]. The highly reflecting mirror in a linear resonator can be substituted by an SBS-mirror to increase the beam quality and to compensate thermal lensing of the pumped laser rod. The SBS-process leads to a simple Q-switch generating short and intensive pulses.

The intensity needed to build up the SBS-mirror has to be provided during the initial stages of the laser process. Therefore, to reach the SBS-threshold an auxiliary resonator can be used [5,6]. The auxiliary mirror and a lens to focus the beam into the SBS-medium can be integrated in one SBS-cell. Figure 3 shows an oscillator with such an SBS-mirror.

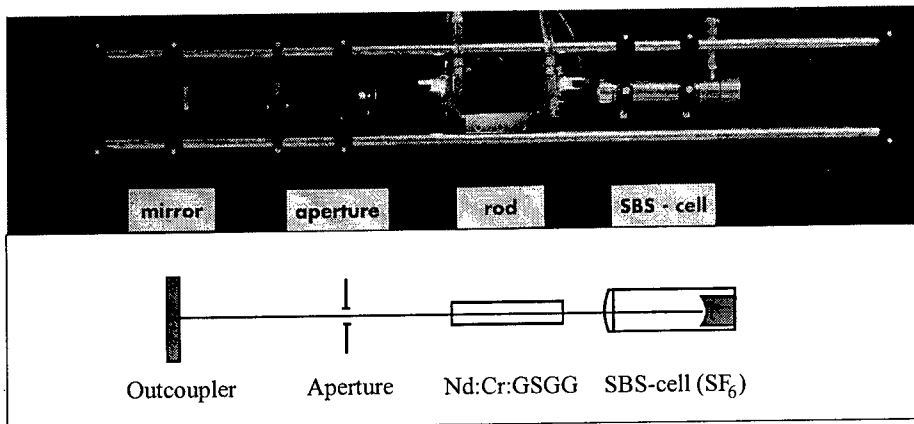


Figure 3. Setup and photograph of a Nd-oscillator with SBS-mirror.

A system with a single Nd:YAG rod and an average output power up to 17 Watt has been realized with a nearly diffraction-limited beam quality [7].

New developments in this field lead to an oscillator with a fiber phase conjugator. Figure 4 shows a photograph and the setup. The repetition rate can be tuned from 1 Hz up to 25 Hz. Due to the low SBS-threshold a train of Q-switched pulses per flashlamp shot can be observed (see Figure 5).

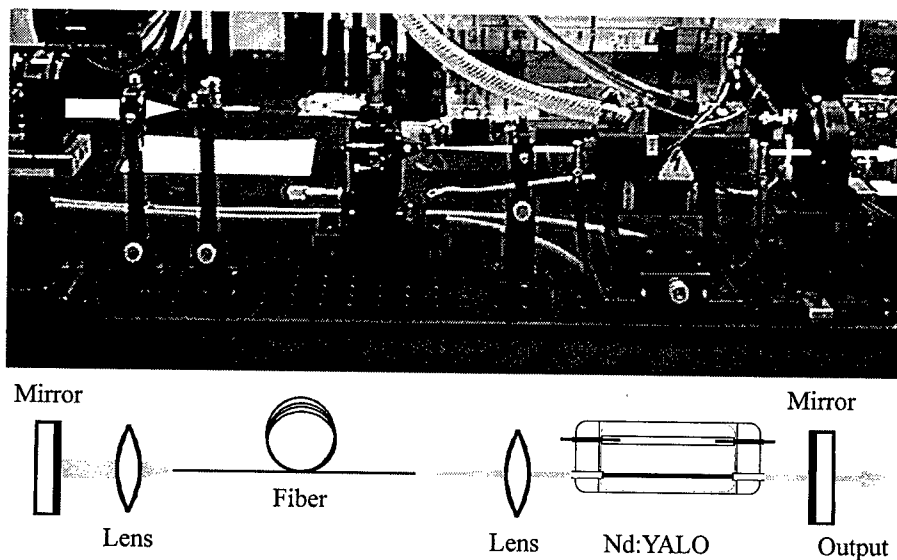


Figure 4. Setup and photograph of an oscillator with fiber Q-switch.

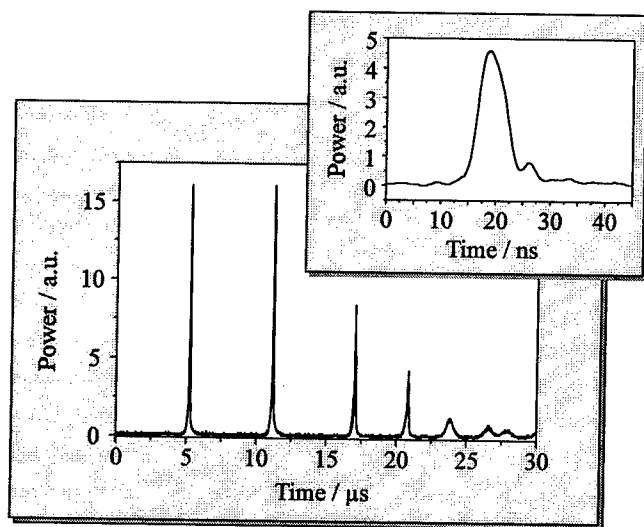


Figure 5. Temporal structure of the oscillator per flashlamp shot.

3.2. PULSED 500 WATT MOPA-SYSTEM

To achieve high average output powers up to the kW-level we realized a multi-amplifier system. Figure 6 shows the setup and Figure 7 a photograph of the system.

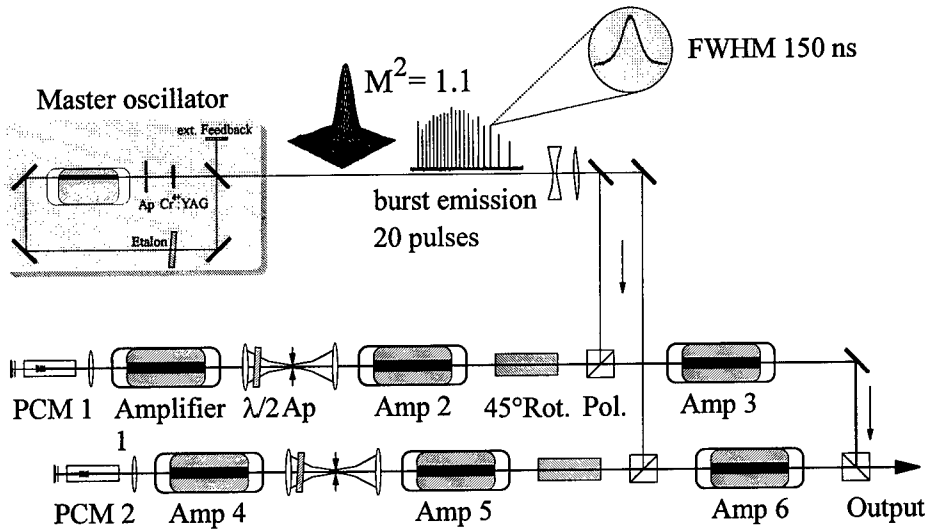


Figure 6. Setup of the 500 W multi-amplifier system with phase conjugation.

The laser is flashlamp pumped and pulsed at a typical repetition rate of 100 Hz. The master oscillator consists of a ring resonator and an additional etalon to increase the coherence length up to 23 cm. This guarantees a high reflectivity and fidelity from the phase conjugating mirrors. To reach the SBS-threshold of about 20 kW a chromium doped YAG-crystal is used as passive Q-switch. Thus the oscillator emits per shot a train of 20 Q-switched pulses, each with a width of 150 ns. The beam is diffraction limited at an average output power of 3.5 Watt.

The beam is then divided in two parts and each of them is coupled into a serial arrangement of two amplifier rods. A phase conjugating mirror (PCM) after the first amplifier pass compensates the phase distortions of the pumped amplifier rods. Therefore after the second amplification pass the beam profile of the oscillator can be reproduced at the polarizer (Pol). To avoid depolarization of the beam during the amplification we use the polarization preserving medium Nd:YALO. Due to the anisotropic gain of YALO the optical isolation consists of a 45° Faraday rotator and the polarizer.

Both beams are coupled out by the polarizer and amplified in a single path in amplifier 3 and 6. Using a thin film polarizer both beams can be combined resulting in one beam with statistical polarization direction.

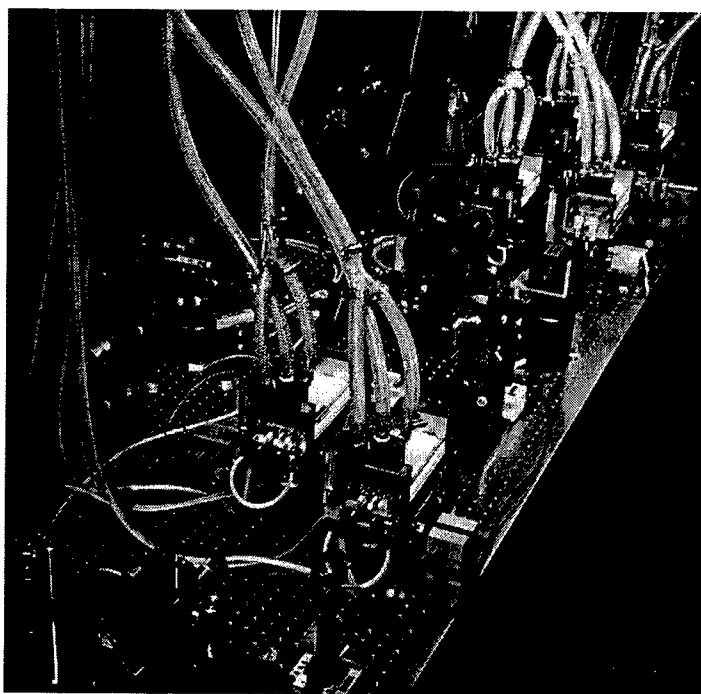


Figure 7. Photograph of the 500 W multi amplifier system with phase conjugation.

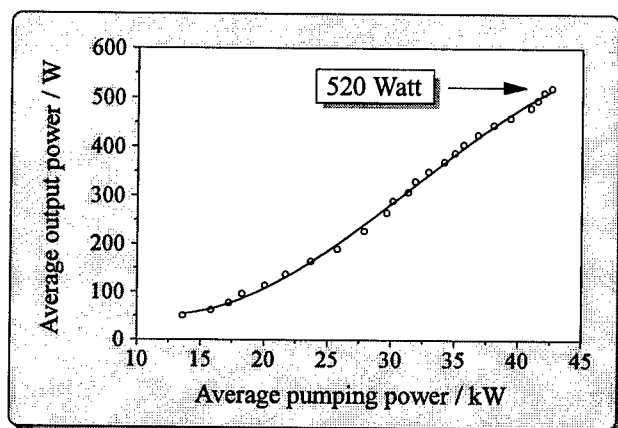


Figure 8. Measured average output power vs. total average pumping power.

Due to an optical system between the amplifier rods [8,9] and the PCM the average output power can be varied over a wide range without changes of the beam parameters. Figure 8 shows the measured average power of the system in dependence of the total average pumping power. The total stored power in the amplifier rods is 1200 Watt. Therefore 43% of the stored power can be extracted with high beam quality.

3.3. CONTINUOUSLY PUMPED MOPA-SYSTEM

Continuously pumped laser systems are preferable due to their compactness and moderate price. To increase the peak power for drilling or cutting and other applications in materials processing, such lasers are Q-switched with repetition rates in the range of several kHz. An improvement of the beam quality of these systems leads to better processing results.

In case of cw-pumped lasers, the SBS threshold of a Brillouin-cell filled with a gas or a liquid is too high for such systems. The threshold has to be reduced down to one kW. Different methods were investigated [see for example 10], but they fail in case of strong thermal lensing or high average power. Using a multimode glass fiber the interaction length inside the fiber is high and, therefore, the SBS threshold can be reduced significantly.

With such fibers we have realized a continuously pumped Q-switched MOPA-system. Figure 9 shows the setup including a photograph of the laser. To achieve a peak power in the kW-range the oscillator is actively Q-switched with an acousto-optical modulator. The high frequency signal is modulated to achieve self-seeding in order to obtain a high coherence length. The pulse width is about 220 ns at a pulse rate up to 20 kHz.

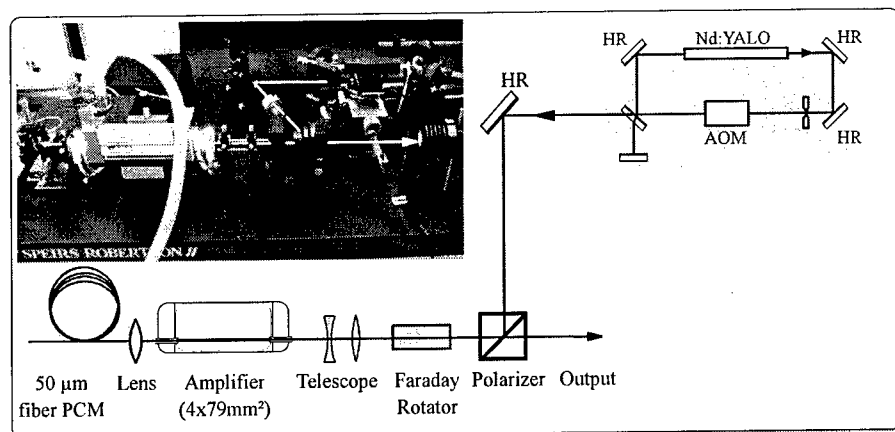


Figure 9. Photograph and setup of the continuously pumped MOPA system.

The beam from the oscillator is then reduced in diameter to achieve a relatively high gain in the first amplification pass.

A crucial point is to choose an appropriate diameter and length of the used multimode glass fibers. The power threshold P_{thr} for a fiber phase conjugator can be estimated using the following formula:

$$P_{thr} = \frac{17 \cdot D^2}{L_{int} g} \quad (1)$$

where D is the core diameter, L the interaction length and g the Brillouin gain. The interaction length is given by the coherence length of the incident beam. By decreasing the core diameter the threshold power can be reduced significantly. On the other hand only radiation with a beam quality K better than a limit, given as follows, can be coupled into the fiber:

$$K \geq \frac{2\lambda}{\pi D \cdot NA} \quad (2)$$

where λ is the wavelength and NA the numerical aperture of the fiber. With a core diameter of $50 \mu m$ for standard fibers a 17 times diffraction limited beam can be phase conjugated. This is a theoretical limit and valid only in case of perfect adjustment of the fiber. For lower core diameters the adjustment of the fiber becomes difficult. Therefore, we use core diameters between 25 and $200 \mu m$.

Figure 10 shows the SBS-reflectivity versus the repetition rate of the system for two different core diameters of the fiber phase conjugator.

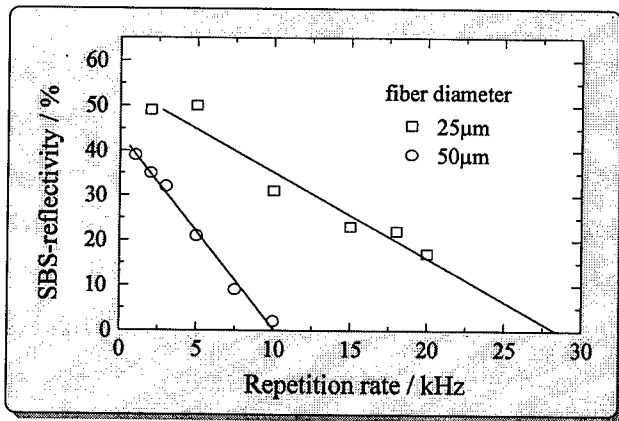


Figure 10. SBS-reflectivity versus repetition rate.

4. Phase Conjugation for Er-Lasers

Laser radiation at $3\ \mu\text{m}$ is of great interest in medical treatments, because the absorption maximum of water is in this optical range. Many difficulties exist to scale the output power of $3\ \mu\text{m}$ erbium lasers. One of them comes from thermal lensing in the active medium itself. Due to λ^2 -dependence of the SBS threshold in liquids [11], SBS phase conjugation has not been successfully applied to $3\ \mu\text{m}$ erbium lasers before.

We have realized an Er:Cr:YSGG laser in a MOPA-arrangement incorporating an SBS-cell as phase conjugating mirror as shown in Figure 11 to compensate phase distortions introduced by the amplifier rod.

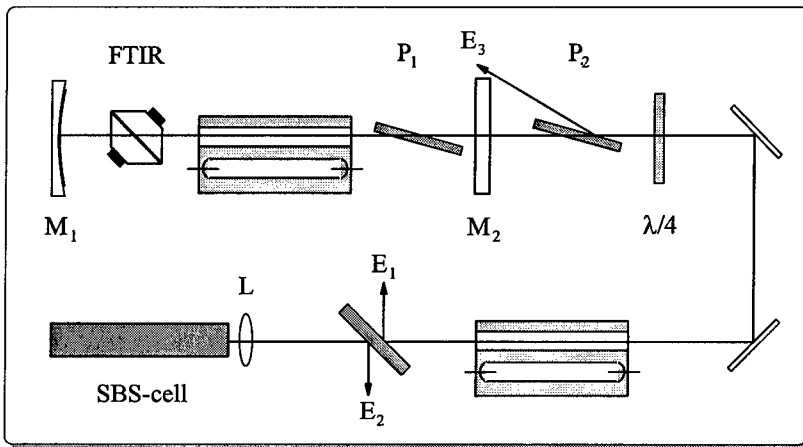


Figure 11. Setup of the Er-MOPA system with SBS phase conjugation.

The laser oscillator consists of a dielectric end mirror M_1 and a sapphire etalon plate as output coupler M_2 to reduce the damage risk of the resonator mirrors at $3\ \mu\text{m}$ [12]. The laser rod is 4 mm in diameter and 90 mm in length without AR-coatings. An FTIR-shutter is used as Q-switch to generate 35 ns pulses [13]. A silicon plate P_1 in the Brewster angle polarizes the laser beam [14]. The output energy is limited to about 30 mJ. One additional silicon plate P_2 in the Brewster angle in combination with a quarter-wave plate consisting of a simple LiNbO_3 crystal enables an optical isolation and output coupling of the SBS reflected beam. The laser rod for the amplifier is 4 mm in diameter and 90 mm in length with AR-coatings. The output energy from the amplifier can be varied between 20 mJ and 60 mJ. The SBS-cell is 25 mm in diameter and 200 mm in length and the window material is CaF_2 without AR-coating. Carbon disulfide (CS_2) was used as the SBS medium due to its relatively low

SBS-threshold. A CaF_2 plate positioned between the focusing lens L and the SBS-cell couples out a small portion of the input and reflected beams for monitoring purpose. Two energy detectors at positions "E₁" and "E₂" in Figure 11 measure the energy ratio of the input beam and the SBS-reflected beam to determine the SBS reflectivity.

The demonstration of phase conjugation at $2.8\text{ }\mu\text{m}$ through stimulated Brillouin scattering in the CS_2 -cell and the resulted healing of phase distortions induced in the power amplifier has been done by comparing the transverse patterns of the input oscillator beam and the amplified beams after the first and second pass. It was found that the good beam quality from the oscillator is distorted after single pass through the highly pumped power amplifier. However, the good beam quality from the oscillator can be restored again in the phase conjugated beam after double pass through the amplifier.

An SBS-threshold of 285 kW and a reflectivity of 25% are obtained as shown in Figure. 12. The pulse width was 30 ns.

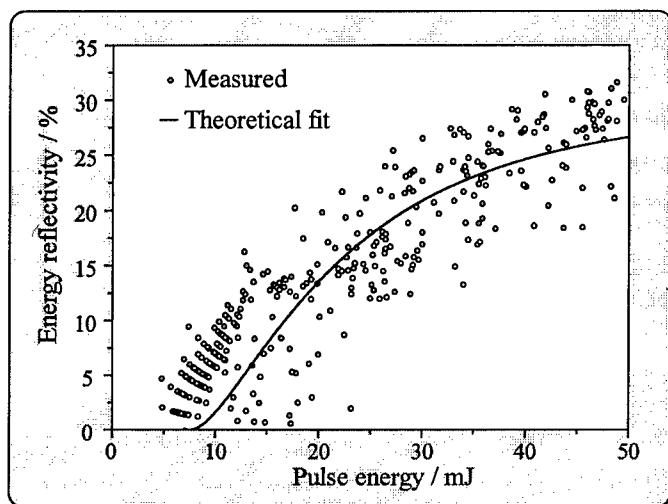


Figure 12. Energy reflectivity versus pulse energy for the SBS-cell at a wavelength of $2.8\text{ }\mu\text{m}$.

5. Phase Conjugation for Excimer Lasers

For standard excimer lasers with a conventional mirror cavity the short effective gain duration leads just to few amplified resonator round trips. The output is spatially and temporally incoherent as well as divergent resulting in relatively large laser spots.

A single-stage XeCl oscillator (Lambda-Physik LPX 200) was equipped with an SBS-mirror. Due to the high gain an auxiliary resonator to start the SBS-reflectivity is not necessary. Figure 13 shows the setup.

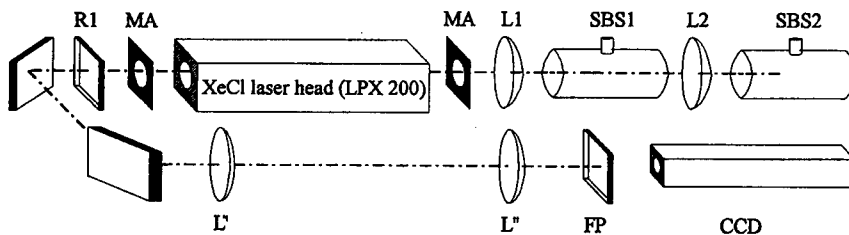


Figure 13. Setup of the self-starting XeCl oscillator with SBS-cells.

The self-starting SBS resonator consists of a conventional output mirror, R1, and a phase conjugating mirror. The phase conjugating mirror is realized using one or two liquid SBS-cells leading to higher SBS-reflectivity. The used liquids are 2,2-dimethylbutane/n-pentane (DBP) and n-octane. Figure 14 shows the measured transversal beam profiles with and without phase conjugation.

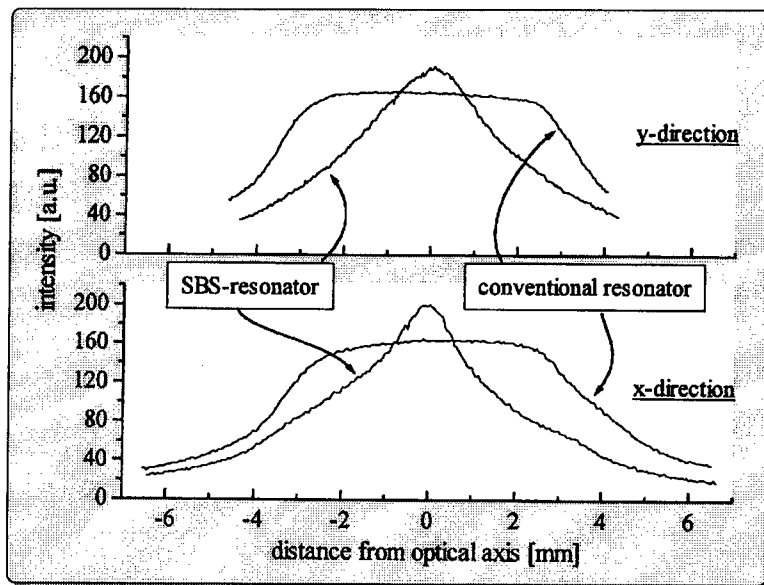


Figure 14. Measured transversal beam profiles with and without phase conjugation.

The SBS-cells lead to a beam quality improvement of 60% resulting in 50% higher brightness (see Figure 15). The brightness is here defined by

$$B = \frac{P}{\lambda^2 M_x^2 M_y^2} \quad (3)$$

where P is the peak power, λ the wavelength and M^2 the diffraction limited factor.

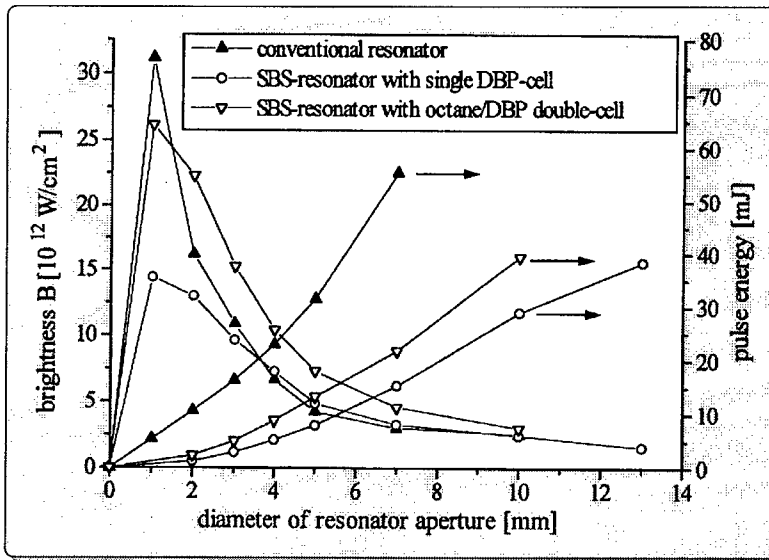


Figure 15. Brightness and pulse energy versus the diameter of the resonator aperture.

6. Summary

We developed different pulsed and continuously pumped laser systems from the mid-infrared down to the ultraviolet range with SBS phase conjugation. In case of high average power solid state lasers 500 Watt with high beam quality could be obtained. As an alternative to often used SBS-cells filled with toxic liquids or high pressure gases we developed a new SBS-device based on multimode glass fibers. For a wavelength of 2.8 μm SBS phase conjugation could be realized for the first time.

7. Acknowledgments

The authors wish to thank the following co-workers for experimental help and stimulating discussions: J. Kunde, O. Sperlich, J. Schwartz and S. Heinrich. Financial support from the Bundesministerium für Forschung und Bildung (BMBF) and the Verein Deutscher Ingenieure (VDI) is gratefully acknowledged.

8. References

1. TRW Space Group, R. Moyer et al., „Kilowatt Diode-pumped Nd:YAG Lasers for Precision Laser Machining“, CLEO '96, Post deadline paper.
2. D. Golla, S. Knoke, W. Schöne, M. Bode, A. Tünnermann, „Diode-pumped Nd:YAG lasers operating at output powers of several 100 Watt“, CLEO '96 Technical Digest, Vol. 9, 304-305, invited talk CWH3.
3. H.-J. Eichler, J. Kunde, B. Liu, A. Haase, „Fiber phase conjugators with high fidelity and reflectivity, and low power threshold“, German patent pending, 1996.
4. M. Ostermayer, A. Heuer, V. Watermann, R. Menzel, „Single-rod Nd:laser with phase conjugating SBS-mirror and large transversal mode for average output powers above 20 Watts“, CLEO '96 Technical Digest, Vol. 9, 447-448, talk CThN3.
5. H.J. Eichler, Chen Jun, A. Kummrow, R. Menzel, D. Schumann, (1993), „Nd-YAG-Laser with SBS-Q-switching mirror and repetition rate up to 50 Hz, Int. J. of Nonl. Opt. Phys. 2 , 187-204.
6. H.J. Eichler, H. Meng, R. Menzel, D. Schumann, „Laser with frequency adapted sound wave mirror“, German patent DE 41 02 409.
7. H.J. Eichler, A. Haase, B. Liu, J. Schwartz, „Phase conjugation for realizing lasers with diffraction-limited beam quality and high average power, SPIE Vol. 2771, 13-21.
8. H.-J. Eichler, A. Haase, O. Mehl, „Serial amplifier arrangement with optical system for compensation of strong thermal lens variation“, German patent pending, 1996.
9. H.J. Eichler, A. Haase, B. Liu, O. Mehl, „Design and construction of high power solid-state laser amplifiers with phase conjugating mirror“, SPIE Vol. 2889, 8-19.
10. I.D. Carr, D.C. Hanna, Appl. Phys. B 36, 83-92 (1985).
11. H.J. Eichler, R. Menzel, R. Sander, M. Schulzke, J. Schwartz, „SBS at different wavelengths between 308 and 725 nm“, Opt. Comm. 121, 49-54 (1995).
12. H.J. Eichler, B. Liu, O. Sperlich, „IR-B Lasers with plates from infrared materials as reflector“, German patent pending (1995).
13. H.J. Eichler, B. Liu, M. Kayser, S.I. Khomenko, „Er:YAG-laser at 2.94 μm Q-switched by a FTIR-shutter with silicon output coupler and polarizer“, Optical Materials 5, 259-265 (1996).
14. H.J. Eichler, B. Liu, M. Kayser, „Lasers with silicon- and germanium-plates as reflector or polarizer“, German patent pending (1995)

PHASE CONJUGATION OF CO₂ LASER RADIATION AND ITS APPLICATIONS

V.E. SHERSTOBITOV
Research Institute for Laser Physics
12 Birzhevaya line, St.Petersburg,
199034, Russia

1. Introduction

During the last decades passed since the pioneer experimental work by Ragul'skiy and his colleagues [1] phase conjugation (PC) of laser radiation has proved to be a very powerful technique for compensation for wavefront distortions acquired by a laser beam propagating through an aberrated medium or a poor-quality optical system.

The approach has been discussed in detail in literature (see the reviews [2,3]) and is based on two-pass propagation of a high-quality initial laser beam through the aberrated medium (or optical system) with a procedure of phase conjugation after the first pass (see Fig. 1). If nonlinear effects are absent in the propagation path and information about the wavefront distortions is not lost after the first pass (e.g. due to a finite aperture of the phase conjugate mirror (PCM)), the phase conjugate beam propagating in backward direction through the same optical path should restore its initial perfect wavefront.

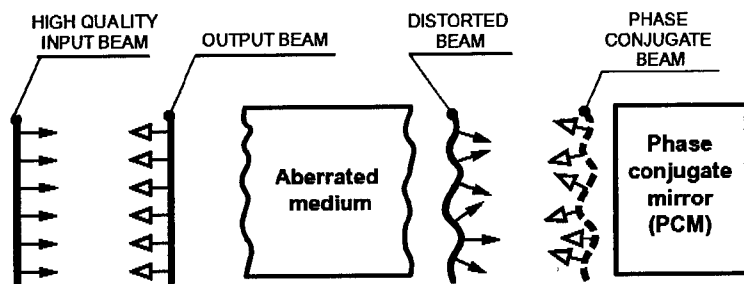


Figure 1. Two-pass concept of aberration correction via phase conjugation.

In [4,5] it was proposed to use this two-pass concept for compensating beam distortions in the gain medium of a laser amplifier. It was possible because in most cases the spatial scale of inhomogeneities in the amplifier is not very small and the nonlinear propagation effects can be neglected.

Since that time a lot of demonstration experiments has been performed with PC correction of aberrations in lasers operating in the visible and near infrared. This was due to development after [1] of simple and efficient PCMs using focusing the beam into a nonlinear medium and excitation of the stimulated Brillouin scattering (SBS).

By a number of physical reasons it is very difficult if not impossible to realize PC of CO₂ laser radiation via SBS. The wavelength dependence of SBS build-up time [6] results in this case in a very high SBS-threshold for realistic pulse durations and the radiation spectral width. This threshold turns to be higher than that for optical breakdown of components and put stringent limitations on implementation of PCMs in 10 μm range of spectrum. So the only nonlinear optical technique of phase conjugation for CO₂ laser radiation that has been developed up to the present is based on four-wave mixing (FWM) of radiation in a nonlinear medium demonstrated for the first time in [7,8].

The FWM involves interference of two sets of counter-propagating waves within the nonlinear medium whose polarization (usually both the refraction and absorption) depends on the intensity of the combined fields (Fig.2). Two counter-propagating waves E_1 and E_2 are called the pump waves, E_3 denotes the probe wave whose phase conjugate replica is sought and E_4 is the return wave arising in the nonlinear medium as a result of interaction. Under certain conditions this wave can be a phase conjugate replica of the incident wave E_3 .

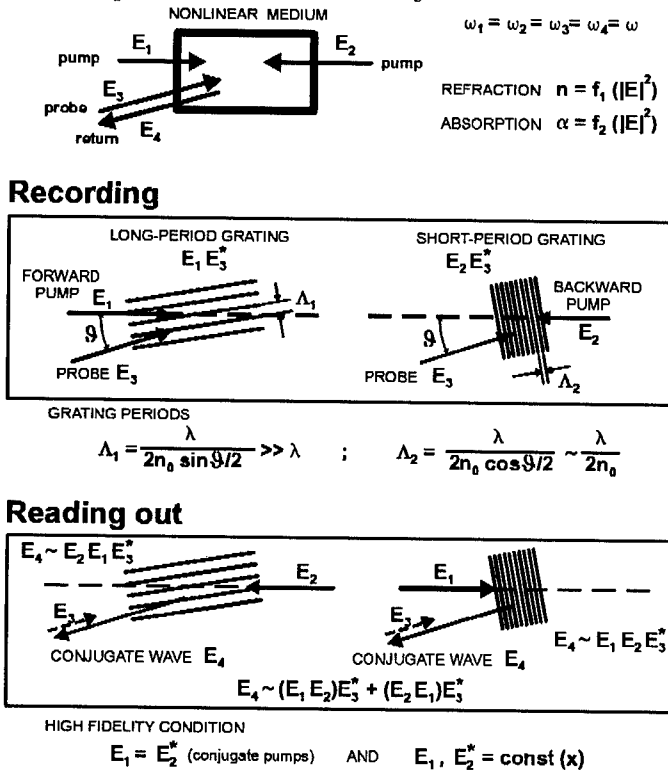


Figure 2. Degenerate four-wave mixing geometry.

In experiments on phase conjugation with CO₂ lasers one usually deals with a degenerate four-wave mixing, where the frequencies of all waves are equal to each other $\omega_1=\omega_2=\omega_3=\omega_4=\omega$. In this case FWM process has very much in common with conventional static holography [9,10] and the phase conjugate replica of the incident wave in the FWM process is analogous to the wave creating a pseudoscopic image in conventional holography.

Suppose the nonlinear medium is characterized by an intensity-dependent complex refractive index. Then forward pump wave E_1 and probe wave E_3 record a long-period grating corresponding to the interference term $E_1 E_3^*$ (the angle θ is usually small so the period is much large than the wavelength). The return wave $E_4 \approx E_2 E_1 E_3^*$ is produced by the Bragg diffraction of the second pump wave E_2 at this grating. At the same time probe wave E_3 and backward pump wave E_2 record the short period grating $E_2 E_3^*$. Diffraction of pump wave E_1 at this grating gives another component $E_4 \sim E_1 E_2 E_3^*$ of the same return wave. The total radiated field is a coherent superposition of the both components of E_4 and the relative role of these components depends on the experimental geometry and parameters of the nonlinear medium.

By analogy from holography, where the conjugate wave is used to obtain the pseudoscopic image, wave E_4 should be the sought phase conjugate replica of E_3 if E_1 and E_2 are phase conjugate, $E_2 = E_1^*$. However as is seen from the expression for E_4 to obtain high fidelity of phase conjugation it is necessary besides to have $|E_1| = |E_2| = \text{const}$ because only in this case $E_4 \sim \text{const} E_3^*$ will be a precise conjugate replica of E_3 . Thus to realize high-quality phase conjugation one should use as the pump beams two precisely counter-propagating beams with plane wavefronts and flat-top intensity distribution in the cross-section.

From a straightforward geometrical analysis of the holograms written in the nonlinear medium it is obvious that a small relative tilt or spherical deformation of pump wavefronts results in additional tilt and spherical deformation of the conjugate beam. To provide high quality of phase conjugation it is necessary to meet the conditions $\psi \ll \frac{\lambda}{d}$ and $\frac{2d}{\rho} \ll \frac{\lambda}{d}$, where ψ – relative tilt of the pump waves, λ –

wavelength, d – beams diameter, ρ – curvature of the pump beams wavefront. These are very stringent requirements but as will be shown below they can be met in practice. In some cases the dependence of the conjugate wave on the phase profiles of pumping waves can be used to control within the certain limits the direction and wavefront curvature of the conjugate beam (e.g. to provide a lead angle).

The important parameter of the FWM PC-mirror (PCM) is its "reflectivity" defined by the ratio $R = |E_4|^2 / |E_3|^2$. It is obvious that R can exceed 100% if the energy of pumping waves is high enough to provide high diffraction efficiency of the gratings.

This paper presents a brief review of experimental works on phase conjugation of CO₂ laser radiation and its applications which have been performed at S. I. Vavilov Optical Institute whose part was transformed into the Institute for Laser Physics about three years ago.

2. Development of FWM PCM

After the pioneer works on FWM PC of CO₂ laser radiation performed at Hughes Research Laboratories [11,12] respectively with germanium and sulfur hexafluoride SF₆ as a nonlinear medium a large number of investigations has been carried out. Various media with different types of nonlinearity were tested in FWM experiments such as semiconductors, resonantly absorbing gases, organic liquids with thermal-type nonlinearity, gain medium of pulse CO₂ lasers (see references in [13-15]).

In the main part of this review we confine ourselves to the results of experiments on phase conjugation with resonantly-absorbing gas SF₆. This medium turned out to be a very promising one for obtaining efficient phase conjugation of CO₂ laser radiation of pulse high energy CO₂ lasers and repetitively pulsed CO₂ lasers with high average power.

The first experiments with SF₆ performed with a TEA CO₂ laser and described in [12] demonstrated reflectivity up to 38% for P8 line of the 10.4 μ m transition of CO₂ molecule at a millijoule level of energy. Later Basov, Kovalev et al. [16] carried out experiments showing possibility of obtaining high fidelity PC with SF₆ as a nonlinear medium, but again at a millijoule level of energy. Optimizing parameters of the experiment our group [17,18] demonstrated for the first time that using SF₆ as the nonlinear medium it is possible to achieve the reflectivity exceeding 100% on the P10 line for the return pulse energy up to 300 millijoules. At the same time the reflectivity of the PCM on the P20 line which is optimum from the viewpoint of maximization the energy extraction from a CO₂ amplifier did not exceed 15-20% [18].

To provide application of such PCMs in high energy CO₂ lasers it was necessary to increase the pulse energy of the phase conjugate beam on the P20 line at least by an order of magnitude (up to several Joules), because the highest possible gain of a reasonably saturated two-pass CO₂ amplifier which seemed to be realistic was about 10³ one way [19].

The next step in scaling up the energy level and reflectivity of FWM PCM using SF₆ has been done in subsequent experiments of our group [20-22], performed with pump wave oscillator using an unstable cavity and SF₆ with isotope ³⁴S instead of ³²S as the nonlinear medium. Application of the unstable cavity enabled obtaining high-quality pump beams of rectangular cross-section 4×4 cm with a close to uniform energy distribution. Each of pump beams had a pulse energy of 15 J for pulse duration about 1 μ s. The idea of the replacement of ³²S for its isotopes was to place the P20 line of CO₂ laser radiation onto the "wing" of absorption spectrum of isotopically modified SF₆ to provide practically the same high nonlinearity that had been demonstrated in conventional SF₆ for the lines P8-P10. The use of sulfur hexafluoride with ³⁴S allowed us to increase several times the reflectivity R of the PCM on the P20 line and achieve R≈120% for the return beam energy of 2.5 J.

Fig. 3 illustrates the wavelength shift of absorption spectrum of SF₆ due to replacement of ³²S by its isotopes ³³S and ³⁴S with respect to maximum gain position corresponding to the P20 line. As seen from experimental curves given in the bottom

of Fig. 3 [33] the isotopes ^{33}S and ^{34}S gave practically the same reflectivity on the P20 line. The isotope ^{34}S is much cheaper than ^{33}S so in most subsequent experiments we used sulfur hexafluoride with the isotope ^{34}S as the nonlinear medium.

In Fig. 4 the results of phase conjugation test are presented for the P20 line [22,15] with compensation for distortions of a specially manufactured small-scale aberrator. A fragment of its interferogram is shown in Fig. 4a. The far-field pattern of the initial probe beam was close to the diffraction limited one (Fig. 4b). As the beam passed through the aberrator and reflected strictly in backward direction from a traditional plane mirror installed in front of the PCM the far-field pattern had a multiple-spot structure shown in Fig. 4c and characteristic for the aberrator. Removing this mirror resulted in restoration of the initial far-field pattern (Fig. 4d) which was the evidence of the aberration correction by the PCM. The more detail study showed [22] that selffocusing in SF_6 arising due to the same nonlinearity that was used for writing the gratings resulted in appearance of residual "wings" in the far field pattern of the of the return beam. However, the gain in energy-in-the-bucket obtained via phase conjugation was very significant for the angles close to the diffraction limit [22].

It is necessary to note that all the experiments described above were performed with TEA CO_2 lasers, that is with short pulses of about 1 μs and a high peak power of radiation. In some further experiments of our group it has been shown that similar results can be obtained using electron-beam sustained CO_2 lasers with much longer pulses (15-20 μs) [23] (see also [24],[15]). Though the radiation intensity is much lower in these cases the additional input of thermal nonlinearity of SF_6 allowed us to achieve practically the same 100%-level of reflectivity as had been obtained for 1 μs -pulses.

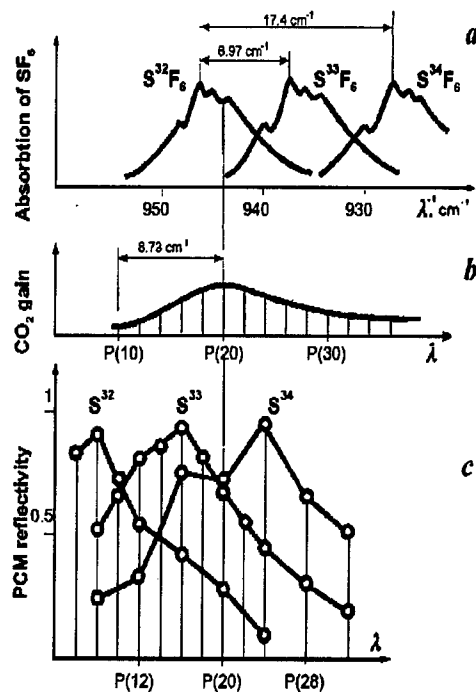


Figure 3. SF_6 as the nonlinear medium for FWM of CO_2 laser radiation.
a) Absorption spectrum of SF_6 for different isotopes of sulfur
b) Gain distribution for different lines of the 10.4 μm transition of CO_2 molecule
c) Experimental PCM-reflectivity for different isotopic modifications of SF_6 [33].

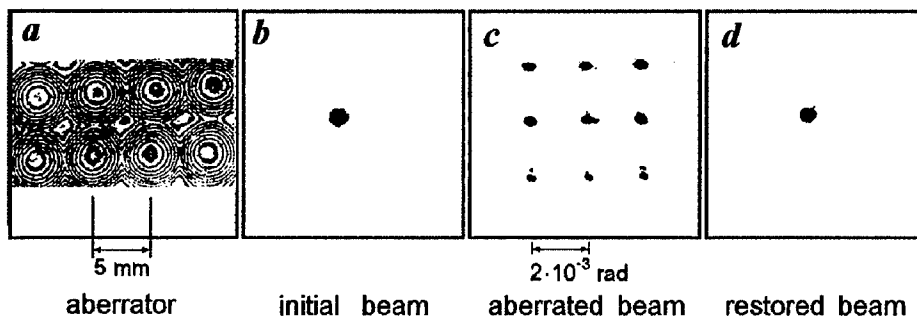


Figure 4. Compensation for aberrations via FWM phase conjugation (see text) [15]

Some results [24,15] demonstrating compensation of large-scale dynamical aberrations brought in by a deformable mirror into the probe beam of a repetitively pulsed electron-beam sustained CO_2 laser with pulse duration $\sim 20 \mu\text{s}$ is shown in Fig. 5. To provide heat removal from the FWM-cell at the repetition rate of 50 pps the nonlinear medium (SF_6 with ^{34}S isotope) was blown through the cell. As is seen from the Figure the probe beam observed through the cell was distorted by the mirror and deviated in time from its initial position. At the same time the phase conjugate beam reflected again from the deformable mirror retained practically the same direction and far-field pattern in spite of aberrations. The average power of the return conjugate beam was about 50 W.

In some situations it can be more convenient to use a gain medium of CO_2 lasers as the nonlinear medium for FWM PC. For pulse durations exceeding significantly $1 \mu\text{s}$ (e.g. in typical electron-beam-sustained CO_2 lasers) it is possible [25] to use the so-called LIMP-effect [26,25] for recording efficient dynamic gratings in the gain medium. The mechanism of this nonlinearity is based on the radiation intensity dependence of the V-T relaxation rate of excited molecules of CO_2 . The theory of this mechanism as applied to the four-wave mixing was developed by Galushkin, Onoshko, Sviridov and Rubanov and published in [27] along with the first results of experiments carried out by our group. It followed from the results of that work that due to this mechanism of nonlinearity a significant value of the refractive index variation equal to $(1\div 3) \cdot 10^{-6}$ can be achieved for rather moderate radiation intensity of about $50\text{--}100 \text{ KW/cm}^2$. In these experiments the reflectivity of 20% was demonstrated in a $15 \mu\text{s}$ -pulse for the beams interaction length $\sim 30 \text{ cm}$ and reflected energy $\sim 150 \text{ mJ}$. The pulse shape difference between the incident and reflected beams showed that the reflection was not connected with any parasitic effects. The phase conjugate nature of

the reflection was also confirmed by measuring the reflected energy angular distribution obtained when a severe aberrator (a lens with the focal length of 2 m) was placed into the incident beam path. Practically all the energy of the reflected beam was contained in the angle of 2 mrad that was only twice as large as the diffraction limited angle of the incident beam. Later on a scaled version of such a PCM was used in experiments on aberration correction in beam-forming telescopes (see Section 8).

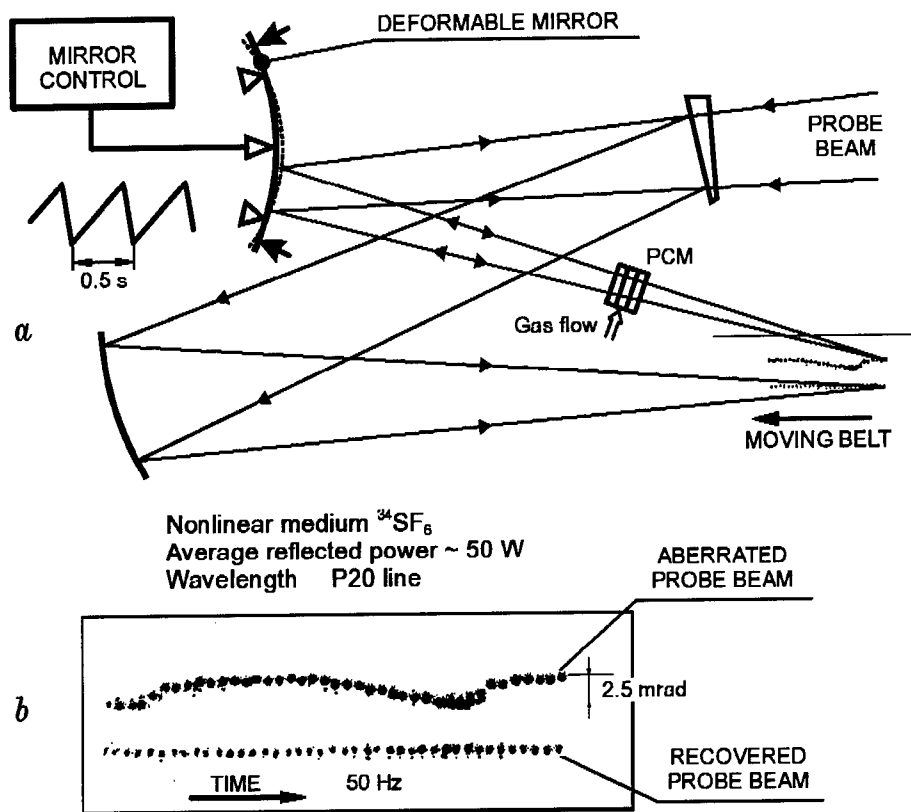


Figure 5. Demonstration phase conjugation experiment with gas-flow electron-beam sustained CO₂ laser. a) experimental setup b) far-field patterns of the incident (upper trace) and conjugate (lower trace) beams.

The principal drawback of all phase conjugation schematics discussed above is the necessity to use high quality pump beams of sufficient energy or average power. As a master oscillator is scaled up to provide such beams it becomes more and more difficult to ensure high optical quality of the pumps. So the main goal of the further experiments was to demonstrate that using the discussed above techniques and schematics of the FWM PC in combination with a high-energy CO₂ amplifier having a high gain per pass it is possible to compensate for distortions in the amplifier optical path and to achieve a near to the diffraction limit beam divergence of radiation at high levels of output pulse energy and average power. Such experiments described in the next Section have been performed by our group at a large-scale CO₂ laser facility

described in [28,29]. The work has been done in close cooperation with the group of research workers and technicians who provided operation of the laser facility and participated in experiments.

3. Compensation for aberrations in a high power CO₂ laser amplifier via FWM PC [30]

There is a number of factors deteriorating the beam quality and beam divergence of gas-flow high-energy repetitively pulsed CO₂ lasers operating at high average power. The first group of factors is connected with thermal loading of optical elements and comprises thermal deformation of laser mirrors and thermally induced aberrations in transmitting optical components (windows, beamsplitters etc.). The second group includes aberrations caused by inhomogeneities of the laser medium. In electron-beam-sustained CO₂ lasers that will be discussed in this Section these inhomogeneities are mainly connected with turbulence of the heated nonuniformly gas flow and acoustic effects caused by periodical energy load deposited into the medium. For lasers of interest with a pulse duration exceeding 3–5 μ s the laser-induced medium perturbations (LIMP-effect) became important [26,25,32]. And finally the third group of factors includes mechanical vibrations and misfigure aberrations of optical elements in the laser optical train. When the output pulse energy and average power of radiation is scaled up all these factors can result in the beam divergence that far exceeds the diffraction limit necessary in most applications. So the use of phase conjugation techniques to compensate simultaneously for most of this distortions can be the ultimate solution to the beam quality problem in such lasers.

Our experiments [30] have been performed with an electron-beam-sustained gas-flow CO₂ laser module (see [28,29]) of 20×40 cm² cross-section comprising two connected in series gain media with a total length of 4.5 m operating at repetition rate up to 100 pps with input pulse duration of (15–30) μ s.

According to the basic concept of PC aberration correction (see Fig. 1) we used in experiments [30] a well-known MOPA-PCM configuration shown in a simplified form in Fig. 6. It comprised a master oscillator (MO), a two-pass amplifier (PA) and a FWM phase-conjugate mirror (PCM).

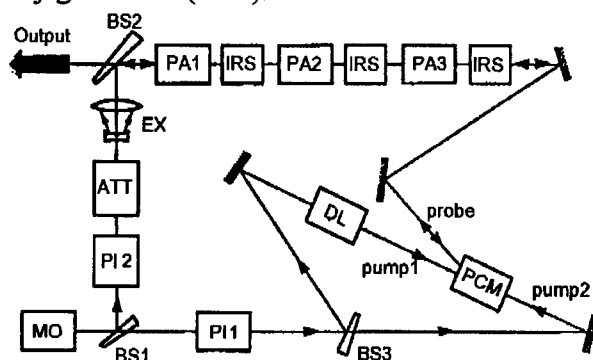


Figure 6. MOPA-PCM configuration.

MO output was split into two beams by beamsplitter BS1. The main fraction of the beam was used for creation of two counter-propagating beams pumping the PCM. The remaining part of the beam reflected by BS1 was attenuated additionally, expanded by a telescope and after reflection from beamsplitter BS2 was directed to the amplifier as a millijoule-level probe beam of 200 mm in diameter and then passed to PCM cell. Optical delay line DL in the forward going pump beam provided temporal coherence of this beam with respect to the probe beam passing to the cell through the amplifier. Polarization isolators PI1 and PI2 prevented the pump beams and the conjugate beam from coming back to the amplifier. According to the results obtained with the use of analytical procedure [19] for evaluation of energy extraction efficiency in a two-pass CO₂ amplifier with PCM the two-pass power amplifier PA comprised three passes of different cross-section (PA1, PA2, PA3) through the 4.5-meter-module to provide amplification of the 1-mJ input pulse up to 1 J at PCM and amplification of the reflected beam to a 1 KJ-level at the amplifier output.

As was already mentioned above it is important not to lose information about spatial characteristics of the aberrated probe beam as it passes through the amplifier to PCM. To provide a large field of view through the amplifier and reduce such losses we used special image relay systems (IRS) in the optical train of the amplifier. Special measures have been also taken to damp parasitic oscillations in the amplifier.

According to the results discussed in the previous Section to achieve the reflectivity of PCM about 100% for the reflected pulse energy of several Joules the master oscillator should provide two diffraction limited pump beams (each at least about 20 J) in a single line P20 with the linear polarization of radiation. With allowance made for inevitable losses in the pump beam delivery optical system the total output of MO should be as high as 100 J. To obtain a reliable operation of MO with such parameters of the beam at repetition rate up to 100 pps we used the MO designed as a low-energy driver oscillator (DO) and an intermediate amplifier (IA). Both were arranged within a small area of the same gain medium as the main power amplifier. The driver oscillator was based on a novel-type resonator [30,34] with the so called "cat-eye" reflector and produced 5-10 J in the diffraction limited beam on the P20 line of 10.4 μm transition exhibiting a very high spatial stability of the beam for the average power up to 500W. In Fig. 7 some examples of the near-field patterns of its output beam for the single-line (P20) (Fig. 7a) and two-line (P20 and P18) (Fig. 7b) operation of DO are shown along with far-field patterns obtained at a repetition rate of 100 pps (Fig. 7c) and demonstrating a subdiffraction limited beam position stability in time.

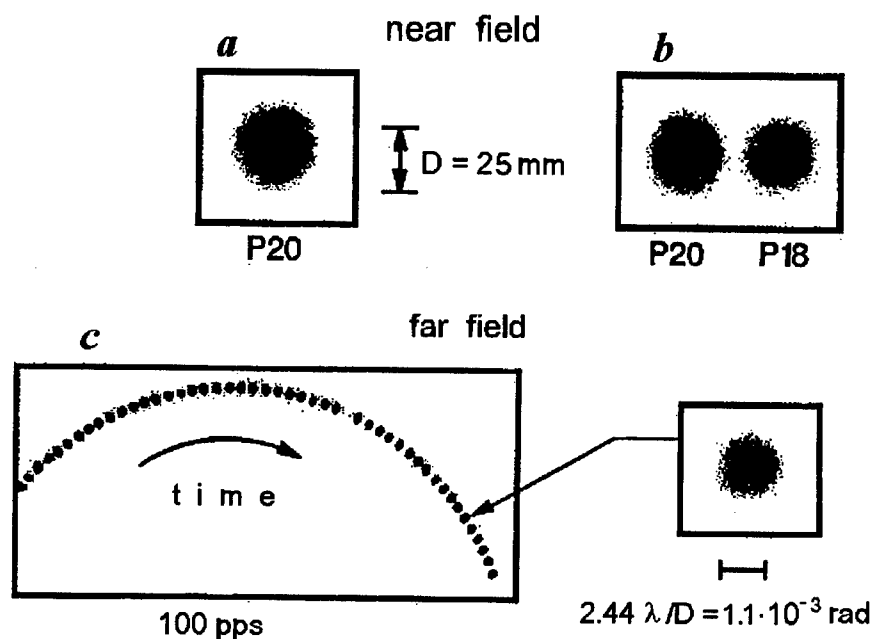


Figure 7. Output beam characteristics of the driver oscillator [30]:
pulse duration 12-15 μs ; pulse energy 5-10 J; average power up to 500 W.

To obtain the pulse energy about 100 J the driver oscillator output beam was expanded up to 90 mm in diameter and directed through the 4.5 m-long gain medium of the intermediate amplifier. The output beam with pulse energy from 100 to 140 J had a homogeneous intensity distribution in the cross-section (Fig. 8a) and as in the case of DO practically the diffraction limited beam divergence $\sim 3 \times 10^{-4}$ rad (see Fig. 8 b,d) and a rather high beam position stability (Fig. 8c). Some noticeable angular deviations of the beam at repetition rate of 100 pps (rms value $\sim 0.2 \times \text{DL}$) were connected with small mechanical vibrations of optical elements. The maximum average power of the beam was limited by some technical reasons and amounted to ~ 5 KW. This beam was used for creation of two pump beams with pulse energy ~ 30 J in each beam for single pulse operation (or ~ 15 J at repetition rate of 100 pps).

The phase conjugate mirror was designed as a closed-cycle device with circulation of $^{34}\text{SF}_6$ through the $10 \times 10 \text{ cm}^2$ FWM-cell to remove energy absorbed in the nonlinear medium by a heat exchanger. The gas pressure in the cell was kept about 100 torr. The forward-going pump beam and the aberrated probe beam that passed through the power amplifier intersected in the cell at an angle about 30 mrad and recorded a grating in the medium. The second pump beam produced a phase-conjugate beam as a result of diffracting.

The main task of the power amplifier design was rather contradictory because it was necessary to ensure the maximum gain for the beam propagating to and reflected off the PCM and to achieve at the same time the maximum extraction efficiency in the amplifier. As was shown analytically in [19] these requirements are contrary to each other in CO_2 two-pass amplifier with PCM. Besides it was necessary to suppress

parasitic oscillation in the amplifier. The power amplifier design was complicated additionally by the fact that about a quarter of its cross-section ($20 \times 40 \text{ cm}^2$) had been already used for creation of the driver oscillator and intermediate amplifier.

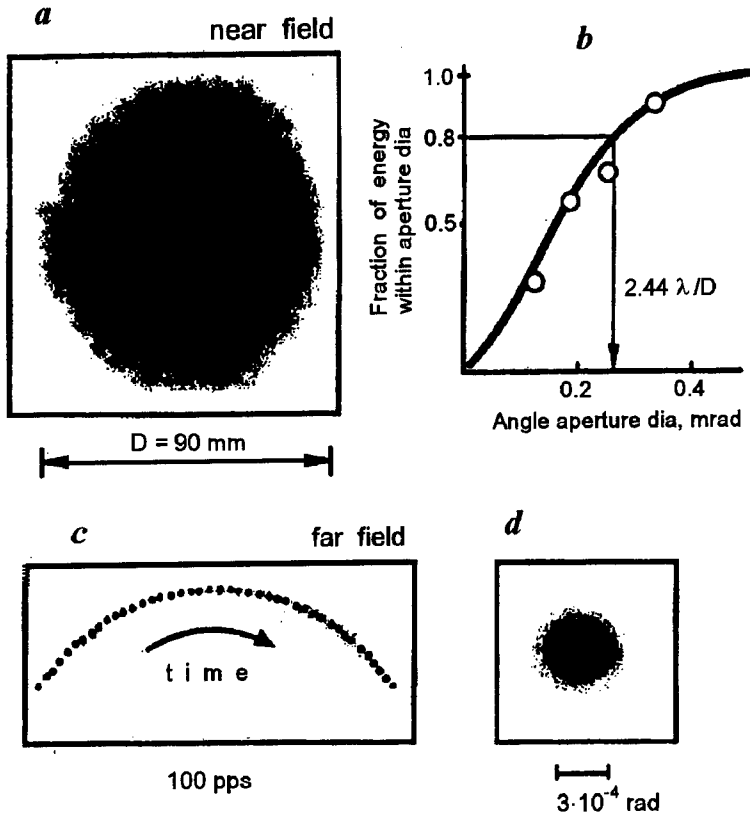


Figure 8. Output characteristics of the intermediate amplifier [30].

As followed from preliminary experiments with the amplifier the total amplification that could be achieved at output energy density from 1.5 to 2 J/cm^2 was about 10 per 4.5-m-long pass through the gain medium. Thus to obtain amplification about 10^3 it was necessary to use at least three passes through the gain module with the total length of gain medium about 13.5 m. It was just this version of the amplifier optical schematic that has been used in experiments with PCM and besides a special geometry [30] of the arrangement has been chosen to suppress parasitic oscillations.

Experimental investigations of the MOPA-PCM described above were performed both in a single pulse and repetition rate mode of operation. The typical near- and far-field patterns of the amplifier output obtained in a single pulse mode are shown in Fig. 9 a - 9d. A somewhat asymmetrical intensity distribution in the output beam cross-section of 200 mm in diameter (Fig. 9a) was connected with the gain nonuniformity in the discharge volume. The maximum pulse energy of the phase conjugate beam at the output of the amplifier was about 1.2 KJ. The beam divergence measured by a calorimeter with the use of standard beam sampling techniques was about 0.24 mrad for 0.7 KJ output as taken at 0.8-level of full energy (see Fig. 9b). That makes about twice the diffraction limit for the beam of 200 mm in diameter. With

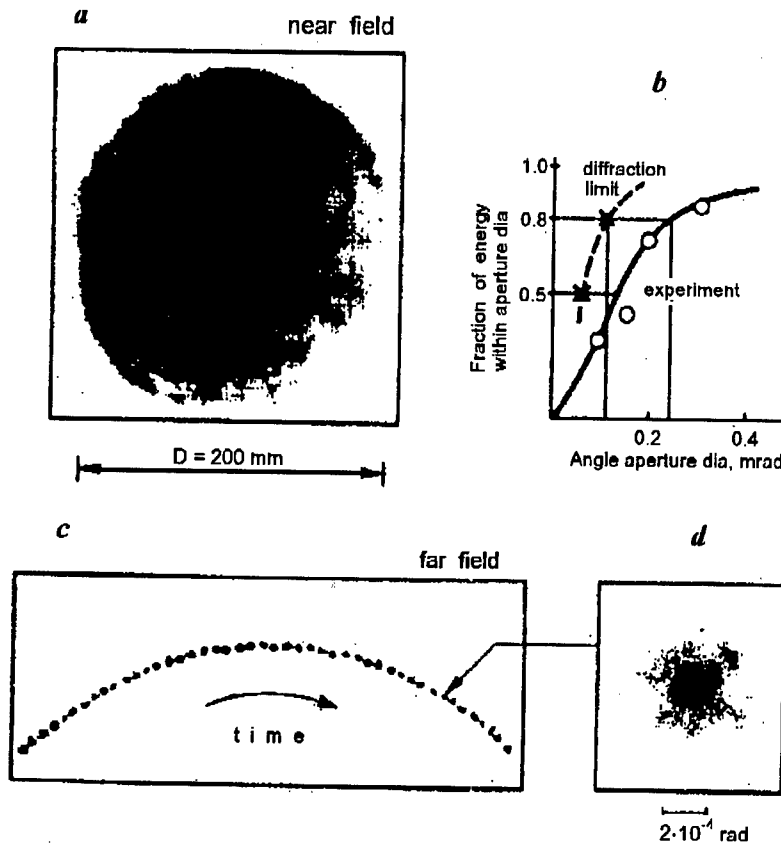


Figure 9. Output characteristics of power amplifier with the phase conjugate mirror [30].

allowance made for the above-mentioned nonuniform intensity distribution this result is indicative of rather high quality of PC correction for wavefront distortions in the optical train of the amplifier that comprised more than fifteen optical elements.

In experiments carried out at repetition rate of 100 pps the beam divergence of the amplifier output was a little larger than in a single pulse and amounted to 0.3 mrad (instead of 0.24) being averaged over the series of about 100 pulses. As is seen from

Fig. 9c where a fragment of a 100 pps-series of the far-field spots is shown (obtained with a rotating thermosensitive disk) this might be connected mainly with the output beam wandering in certain of the pulses. However, the rms value of this wandering was less than 2×10^{-5} rad (about 0.15 DL). By some technical reasons [30] the maximum averaged power achieved at the MOPA-PCM output was 40 KW.

Thus the results obtained in [30] have confirmed the capability of FWM phase-conjugate mirrors to compensate for beam distortions in the high-energy (up to 1.2 KJ) and high-power (up to 40 KW) electron beam sustained gas-flow CO₂ laser amplifier. This was the first to our knowledge experimental demonstration of MOPA-PCM arrangement as applied to CO₂ lasers operating at such a high level of pulse energies and average power.

4. Compensation for aberrations in the output beamsplitters of MOPA-PCM systems

One of the problems in implementation of high-average-power MOPA-PCM arrangements similar to that presented in Fig. 6 is connected with vibrations or thermal deformations of a beamsplitter which is installed at the exit of the two-pass amplifier and usually has a large size (e.g. BS2 in Fig. 6).

It is easily seen (Fig. 10a) that the distortions acquired by the beam when it reflects from the tilted beamsplitter on its way to PCM do not coincide with the distortions suffered by the conjugate beam as it propagates through the beamsplitter. As a result the output beam will deviate at 2α as the beamsplitter is tilted at angle α . Similar situation takes place with thermal deformations of the beamsplitter (Fig. 10b) where the solid lines show the rays path for a perfect beamsplitter and the dashed ones correspond to its thermal deformation. Thus PCM does not compensate for distortions of the beamsplitter, so the residual error can be very significant in vibration environment and grows as the size of the beamsplitter and the output average power are scaled up.

This problem can be solved if we use as the beamsplitter in the MOPA-PCM system a diffraction grating with a rather small number of grooves per millimeter

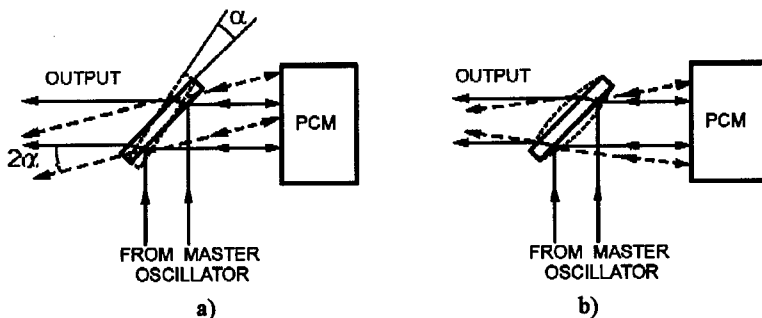


Figure 10. The influence of the beamsplitter tilts and deformation on the output beam.

(see Fig. 11). Similar diffraction beamsplitters are often used for sampling the beams in high-power CO₂ lasers [31] for measuring parameters of CO₂ laser radiation.

The idea of this approach is based on the fact that at some conditions (see below) small tilts of a mirror with a diffraction grating on its surface disturb practically in the same way, at one hand, the probe beam diffracted in the first order and propagating to PCM and, at the other, the phase conjugate beam propagating back and reflecting from the mirror in the zeroth order to yield the output beam. As a result the distortions can be cancelled by the phase-conjugation mirror.

To estimate the degree of compensation or the residual error let us consider the diffraction of a plane wave \vec{K}_1 on the grating with a period d applied at the surface of a mirror (see Fig. 11). Let γ is the angle of incidence of \vec{K}_1 at the mirror surface and 2θ – the angle between \vec{K}_1 and additional hypothetical plane wave \vec{K}_2 whose interference with \vec{K}_1 would give the interference pattern coinciding at the mirror surface with the grating. In terms of γ and θ the period d is expressed as follows:

$$d = \lambda [2 \sin \theta \cos(\gamma - \theta)]^{-1}, \quad (1)$$

where λ – the wavelength.

It is evident that the wave vector of the wave diffracted in the first order will coincide with \vec{K}_2 which is just vector \vec{K}_2 reflected from the mirror. As a result of phase conjugation \vec{K}_2 will be replaced by $(-\vec{K}_2)$ which yields after specular reflection from the mirror vector $(-\vec{K}_2)$ inclined to the normal at the angle $(\gamma - 2\theta)$. Thus in accordance with the principles of holography the output plane wave \vec{K}_{out} will be just a “reversed” plane wave \vec{K}_2 used for “writing” the grating.

Let us consider now a situation in which the direction of the incident wave \vec{K}_1 remains the same but the mirror is tilted at a small angle α (see Fig. 11b) in the plane orthogonal to the grooves. In a coordinate system of the tilted mirror the angle φ

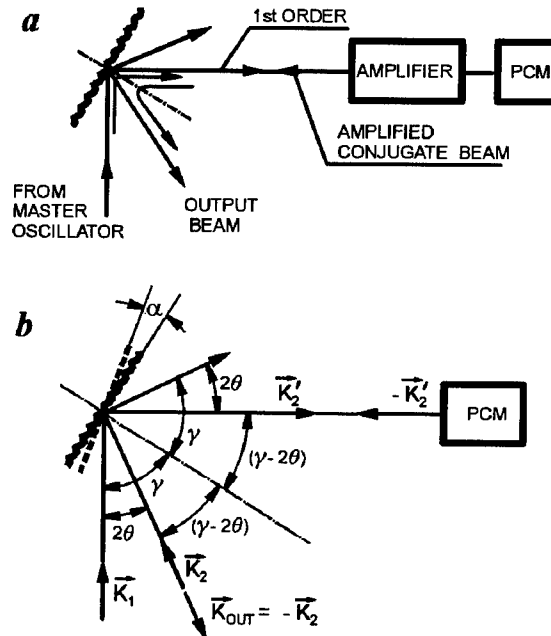


Figure 11. Diffraction grating as a beamsplitter in a MOPA-PCM arrangement
a) general concept
b) beam interaction geometry.

between the normal and the first diffraction order is given by a well-known equation:

$$d \sin(\gamma + \alpha) - d \sin \varphi = \lambda, \quad (2)$$

which together with (1) yields

$$\sin(\gamma + \alpha) - \sin \varphi = 2 \sin \vartheta \cos(\gamma - \vartheta). \quad (3)$$

As seen from (3), at $\alpha = 0$ we obtain $\varphi = \gamma - 2\vartheta$ in accordance with said above.

At $\alpha \neq 0$ there will be some deviation of the diffracted beam from its initial direction and consequently the same deviation of the phase conjugate and output beams. A straightforward analysis with realistic assumption that $|\alpha| \ll |\gamma - 2\vartheta|$ shows that deviation Δ of the output beam from its initial direction is given by expression

$$\Delta \approx \alpha \left[1 - \frac{\cos \gamma}{\cos(\gamma - 2\vartheta)} \right] \quad (4)$$

As is seen from (4) this deviation can be much less than the mirror tilt α if the angles of incidence and diffraction meet the requirement

$$\left| 1 - \frac{\cos \gamma}{\cos(\gamma - 2\vartheta)} \right| \ll 1. \quad (5)$$

There are two areas of parameters where this condition can be met. The first corresponds to the case of small angles of incidence and diffraction so as $|\gamma| \ll 1$, $|\gamma - 2\vartheta| \ll 1$, where both cosine-functions are close to 1. The second area is in the vicinity of the angles of incidence equal to a half of the diffraction angle $\gamma = \vartheta$ (both these angles are allowed not to be small). As this condition is met exactly the beam diffracted in the first diffraction order propagates in the direction exactly opposite to the direction of the incident beam \vec{K}_1 (autocollimation mode) which creates some inconveniences. However in the vicinity of the condition $\gamma = \vartheta$ this geometry can be used with equal success though in distinction to the case of small angles the period of the diffraction grating is much smaller at large angles of incidence which results in some additional technological difficulties.

Estimations show that both geometries can provide a dramatic reduction in sensitivity of the output beam direction to misalignments and vibrations of the beam-splitter as well as to its deformation. The ratio $\left| \frac{\alpha}{\Delta} \right|$ which is a measure of this reduction can exceed 10^3 in realistic situations.

5. PCM-correction for dynamic aberrations in beam-forming output telescopes with DOE on the primary mirror

The optical schematics we are going to consider in this Section have been investigated analytically and experimentally by our group in the mid-80s and were the result of a natural development of the approach discussed in the previous Section. The problem

that was necessary to solve concerned the correction for aberrations in beam-director telescopes expanding the output laser beam in systems based on MOPA-PCM configuration. The conventional configuration of such a system is shown in a simplified form in Fig. 12a. It is evident from the Figure that aberrations of the telescope (misfigure aberrations of the primary, vibrations, thermal deformations etc.) are not compensated for by PCM. As a result the angular divergence of the beam when it leaves the telescope can far exceed the diffraction limit even if a thorough beam clean-up has been performed in the laser. To solve this problem we attempted to include the output telescope into a phase conjugation loop by applying a specially designed diffraction optical element (DOE) onto the surface of the primary mirror (Fig. 12b). We found later that the same optical schematic had been put forward before by O'Meara [35] at Hughes Research Laboratory but have never seen any evidence of its experimental verification.

The optical schematic shown in Fig. 12b operates as follows. A weak high quality reference beam illuminates the primary mirror from the point located in some plane near the secondary mirror. A small portion of the beam is diffracted by DOE into the first order and acquires the distortions brought in by an aberrated amplifier train on its way to PCM. After phase conjugation and the further amplification the return beam again reflects from the primary mirror (this time in the zeroth order). As in the case of diffraction gratings discussed in the previous Section, the distortions brought in by the primary mirror into the beams, diffracted in the first and zeroth orders, are almost equal to each other (see below). As a result the distortions suffered by the beam in the

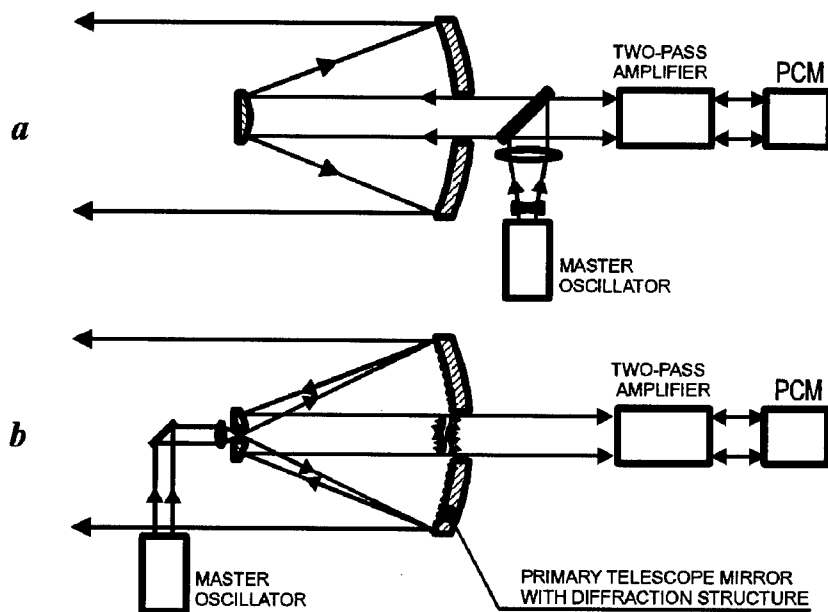


Figure 12. Beam-forming telescopes with PCM-compensation for aberrations in MOPA-PCM systems

- a) Conventional configuration of MOPA-PCM system with a telescope
- b) A concept based on the telescope with DOE on the primary mirror.

first pass through the telescope and the amplifier to PCM are cancelled in the return pass. In full accordance with the principles of holographic correction of aberrations should be perfect if the arrangement of "grooves" in the diffraction structure on the mirror corresponds exactly to the interference pattern that would be observed if we illuminate the primary mirror by the point-like source (as is shown in Fig 12b) and by the wave conjugated to the wave required at the telescope output (in our case by the plane wave coming along the axis from the infinity). It is necessary to note that any static aberrations of the primary including the most pronounced spherical aberration will be fully compensated if the beam diffracted in the first order is entirely intercepted by the PCM.

As the primary mirror with the DOE applied on its surface is deformed or tilted dynamically the degree of compensation should decrease because the conditions of reading out the "hologram" do not coincide now with those for "writing" the DOE. However as will be shown below it can be very high for realistic conditions.

To evaluate the efficiency of aberration correction at various geometries of the telescope let us consider a beam-forming telescope with a spherical primary mirror of diameter D and radius of curvature R . Let the reference point-like source is located in point O located near the plane of the secondary mirror (see Fig. 13). Without loss of generality we consider the case where it is required to obtain a plane wave at the output of the telescope. In this case DOE has a form of concentric "grooves" similar to the Fresnel zone plate. Transversal coordinate x of the angular "groove" with a number $N(x)$ (where $N(x) = 0, 1, 2, \dots$) is found from the evident condition for positions of interference rings

$$N(x) \lambda = \rho(x) - z(x), \quad (6)$$

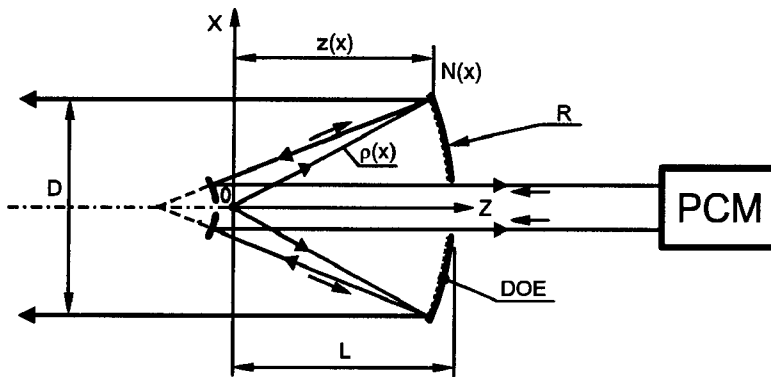


Figure 13. Beam-forming telescope with DOE on the primary mirror.

$$\text{where } \rho(x) = \{x^2 + z^2\}^{1/2} \quad (7)$$

$$\text{and } z(x) = (R^2 - x^2)^{1/2} - R + L \quad (8)$$

are the distances from the point x to the point O and the plane OX (see Fig. 13) respectively. The total amount N_{\max} of rings at the mirror aperture and the minimum distance between the rings t_{\min} are given by expressions:

$$N_{\max} \approx \frac{D^2}{8L\lambda}; t_{\min} \approx \frac{2L\lambda}{D} \quad (9)$$

As the reference beam is reflected from the primary mirror which is deformed, tilted or moved in some direction its phase on the surface in terms of x has the form

$$\varphi_0(x) = (2\pi/\lambda) \tilde{\rho}(x), \quad (10)$$

$$\text{where } \tilde{\rho}(x) = \{x^2 + \tilde{z}^2\}^{1/2} \quad (11)$$

is the distance from the point with coordinate x at the surface to the point source O , and $\tilde{z}(x)$ – the distance from the same point to the plane OX . In a general case both values $\tilde{\rho}(x)$ and $\tilde{z}(x)$ differ from $\rho(x)$ and $z(x)$ respectively due to some changes of the mirror surface position.

It is well-known that the phase profile $\varphi_1(x)$ of the beam diffracted in the first order of a grating differs from that in the zeroth order in such a way that the phase difference changes monotonously by 2π at each next "groove". So if $N(x)$ is the interference ring number for the ring located at x the first-order beam profile $\varphi_1(x)$ in terms of x at the mirror surface can be expressed as follows

$$\varphi_1(x) = \varphi_0(x) - 2\pi N(x) \quad (12)$$

After propagation of this beam to the PCM and back a wavefront deformation arising along the path will be cancelled. So the phase profile $\varphi_2(x)$ in the beam incident again at the mirror will be equal to $(-\varphi_1(x))$.

And now to obtain the phase distribution which the beam will have at the telescope output it is necessary to add $(2\pi/\lambda) \tilde{z}(x)$ to $\varphi_2(x)$. (See Fig. 13).

So the final expression for $\varphi_{\text{out}}(x)$ which can be considered as a residual error of aberration correction has the form

$$\varphi_{\text{out}}(x) = (2\pi/\lambda) [\rho(x) - \tilde{\rho}(x) - z(x) + \tilde{z}(x)] \quad (13)$$

where $\rho(x)$ and $z(x)$ are defined by (7) and (8). As follows from (13) if the mirror is not deformed at its position relative to the point-source not changed, $\rho(x) = \tilde{\rho}(x)$ and $z(x) = \tilde{z}(x)$, so $\varphi_{\text{out}}(x) = 0$. Thus we obtain a full compensation for spherical aberration as was noted above.

Let us consider now dynamic variations of the mirror surface profile and estimate a degree of their correction by the PCM.

Let the mirror with the DOE on its surface is tilted at a small angle α so that the position of the point where the surface is crossed by the axis is remained unchanged. At small angles $\alpha \ll (2L/\lambda)^{1/2}$ which are really of interest we can assume that the transverse coordinates of grooves do not change and besides $\tilde{z} \approx [R^2 - (x-h)^2]^{1/2} - R + L$ where $\alpha \approx h/R$.

Using (13) we obtain for this case:

$$\varphi_{\text{out}}(x) \approx \frac{2\pi}{\lambda} \alpha \frac{x^3}{2L^2} \quad (14)$$

Thus in the linear (in terms of x/L) approximation the primary tilt α is fully cancelled and the beam axis position remains exactly the same. According to (14) the output beam wavefront has some residual third-order wave aberration achieving its maximum at $|x| = D/2$. Assuming the maximum angle of the wavefront local tilt be equal to λ/D we obtain the maximum tolerable tilt of the primary mirror

$$\alpha_{\text{max}} \leq \frac{8L^2}{3D^2} \cdot \frac{\lambda}{D}. \quad (15)$$

It is seen from (15), that using the telescope with DOE on the primary mirror it is possible to obtain at large $L/D \gg 1$ the orders of magnitude gain in the tolerable error of the primary mirror alignment procedure. Note that α_{max} does not depend within the assumption made on R , i.e. on the telescope magnification.

Let us consider now the case of small variations in the primary mirror curvature

$$\Delta\rho = \frac{1}{R} - \frac{1}{\tilde{R}}, \quad (16)$$

that can arise for example as a result of thermal deformations.

Following the same procedure of calculations for $\varphi_{\text{out}}(x)$ defined by (13) and in view of $\tilde{z}(x)$ written now as $\tilde{z}(x) = [(\tilde{R}^2 - x^2)^{1/2} - \tilde{R} + L]$ we obtain for the residual error

$$\varphi_{\text{out}}(x) \approx \frac{2\pi}{\lambda} \Delta\rho \frac{x^4}{4L^2} \quad (17)$$

It follows from (17) that quadratic in terms of x distortions are fully cancelled and the residual error is determined by a forth-order term. Assuming again that maximum tolerable local tilt of the output beam wavefront at the edge $|x|=D/2$ is equal to λ/D we obtain for the tolerable sag S_{max} of the mirror surface

$$S_{\text{max}} \leq \lambda \frac{L^2}{D^2} \quad (18)$$

This condition is again the orders of magnitude less stringent than that used for primary mirrors in traditional beam-forming telescopes.

Let us estimate the residual error arising due to thermal expansion of the primary when a transverse coordinate x is increased due to temperature growth ΔT approximately by $\Delta x = \kappa x \Delta T$, where κ – thermal expansion coefficient. As follows from (13) for this case

$$\varphi_{\text{out}}(x) \approx \frac{2\pi}{\lambda} \frac{\kappa T x^2}{L}. \quad (19)$$

Thus, to provide the local tilt at the beam edge not to exceed λ/D we must meet the following requirement

$$\Delta D = \kappa \Delta T \cdot D \leq \frac{L\lambda}{D} = \frac{t_{\min}}{2}, \quad (20)$$

meaning that the beam diameter growth ΔD due to expansion should not exceed the half of the grooves period at the mirror edge. This requirement can be met in practice by a proper design of the mirror.

Some limitations are imposed on the system performance by the spectral width $\Delta\lambda$ of the point-source radiation due to dispersion of the DOE, because in the return pass the beam is reflected in a specular way, i.e. at equal angles for each spectral components. A straight-forward analysis shows that the coherence length of the radiation $l_{\text{coh}} = \lambda^2/\Delta\lambda$ should exceed $D^2/2L$. This requirement can be easily met for CO₂ lasers.

The first to our knowledge experimental verification of this approach to correction of varying in time aberrations of a beam-forming telescope primary has been performed by our group and described in [36] (see also [24]). Experimental setup is shown in Fig. 14. A TEA CO₂ laser operating in the fundamental mode at pulse repetition rate up to 40 pps with pulse energy ~ 3 J in the P20 line produced two beams for pumping a FWM PCM with SF₆ as the nonlinear medium and a reference point-source beam. Experiments were carried out with a model telescope ($D = 120$ mm,

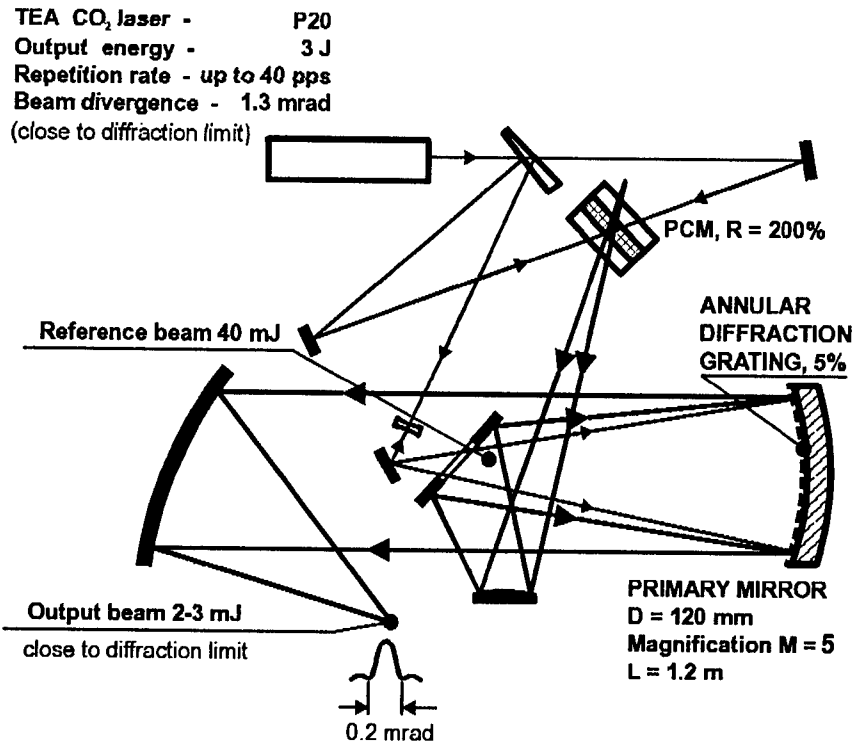


Figure 14. Optical schematic for demonstration of dynamic aberration correction via phase conjugation in the beam-forming telescope with DOE on the primary mirror

$L = 1.2$ m, magnification $M = 5$) having a DOE with a diffraction efficiency of 5% applied on the primary mirror surface (minimum period $t_{\min} = 0.21$ mm). About 40 mJ beam was injected into the telescope as the reference beam, so about 2 mJ-beam was diffracted by DOE in the first order and directed to the PCM. For such a small signal the reflectivity of the PCM was about 200%. The conjugate beam from the PCM propagated back to the primary mirror and after the specular reflection from the mirror was registered in the far-field.

To verify capability of the optical schematic to compensate for dynamic aberrations the primary mirror was tilted at an angle α that was increased gradually in time. Theoretical estimate (see [15]) for the angle α that can be compensated gives $\alpha_{\max} = \pm 266 \lambda/D$ for the telescope geometry used. In experiments the output beam was observed up to angles $\alpha \approx \pm 120 \lambda/D$. In full accordance with theoretical estimates the outgoing beam direction remained the same in all the range of the tilt variation with accuracy equal to small parts of the diffraction angle. The drop of output beam energy as a function of α to 0.5 of the maximum value at $\alpha \approx \pm 65 \lambda/D$ and to zero at $\alpha \approx \pm 120 \lambda/D$ was connected with vignetting the beam caused by the primary mirror tilt. The role of vignetting can be reduced significantly by increasing D/L and by the proper choice of the telescope geometry.

Estimations show that using the approach discussed above it is possible to create a high numerical aperture beam director telescope with $D = 1$ m, $L = 2$ m and magnification $M = 10$. The minimum period of DOE grooves t_{\min} in this telescope will be about 20 μm (for operation with a CO_2 laser as the reference) which is well within the capability of technology. Such a telescope geometry should provide compensation for the primary mirror dynamic tilts up to $\pm 11 \lambda/D$, dynamic spherical deformation of the primary up to $\sim 4\lambda$ and allow temperature variations $\Delta T \leq 4^\circ$ (for expansion coefficient $\sim 10^{-5}$). Note again that in this approach static aberrations of the primary (spherical aberration and manufacturing errors) are also compensated as well as aberrations of the secondary mirror and of the amplifier optical train.

6. PC beam control in a telescope with DOE on the primary mirror

In many applications it is necessary to control dynamically the direction of the beam at the output of the beam-forming telescope and the curvature of its wavefront. Using a telescope with DOE on the primary one can do it in a natural way by control of corresponding parameters of a weak reference beam illuminating DOE with subsequent phase conjugation and amplification of the diffracted beam.

Let us analyze the wavefront profile of the beam leaving the telescope output (See Fig. 13) when the point-source changes its distance to the primary mirror or transversal position.

Let the distance between the primary mirror and the point-source is decreased by a small amount δ and equal to $\tilde{L} = L - \delta$ (here $\delta \ll L$). In this case $\tilde{z}(x)$ and $\tilde{\rho}(x)$ in (13) take the form

$$\tilde{z}(x) \approx [R^2 - x^2]^{1/2} - R + L - \delta; \quad \tilde{\rho}(x) = [x^2 + \tilde{z}^2(x)]^{1/2} \quad (21)$$

Substituting these expressions into (13) and keeping the lowest order terms comprising x and δ yields the profile of the output beam wavefront

$$\varphi_{\text{out}} \approx -\frac{2\pi}{\lambda} \cdot \frac{x^2}{2L} \cdot \frac{\delta}{L} + \frac{2\pi}{\lambda} \frac{x^4 \delta}{8R^2 L^4} (R-L)(3R-L) \quad (22)$$

Thus in the first approximation we have at the telescope output a converging wave focusing at a distance

$$f = L^2/\delta. \quad (23)$$

Note that in distinction to conventional optical systems, decreasing the distance from the point-source to the concave primary mirror results in a converging wave instead of a divergent one. The residual aberration described by the second term in (22) limits the maximum tolerable value of δ and the minimum distance of focusing f_{min} .

Assuming as before the minimum acceptable tilt of the wavefront at $|x| = D/2$ to be equal to λ/D we obtain for magnification $M \gg 1$

$$\delta_{\text{max}} \leq \frac{16L^4}{D^4} \lambda \cdot \frac{R^2}{(R-L)(3R-L)} \quad (24)$$

So the minimum distance f_{min} at which the focusing will not result in a significant degradation of the beam will be given by expression

$$f_{\text{min}} \geq \frac{L^2}{\delta_{\text{max}}} \quad (25)$$

In the example of the telescope considered in the previous Section ($D=1$ m; $L=2$ m; $M=10$) f_{min} will be about 2 km and will be realized at $\delta_{\text{max}} \approx 1.9$ mm if the point source is located in the plane of the secondary mirror.

Using (23) it is possible to determine the range of the system "insensitivity" to longitudinal displacements of the point-source

$$|\delta| \leq \delta_{\text{min}} \approx \frac{L^2}{D^2} \lambda \quad (26)$$

Let us consider now a possibility of the output beam direction control using the beam-forming telescope of Fig. 13. Let the point-source illuminating the primary is displaced in a transversal direction at a small distance $H \ll D < L$. Using (13) and the calculation procedure similar to those used above we can show that the output wavefront in this case will be as follows:

$$\varphi_{\text{out}}(x) \approx \frac{2\pi}{\lambda} \left(\frac{Hx}{L} + \frac{Hx^3}{2RL^2} \right) \quad (27)$$

(We kept here only the lowest components of the series in terms of H/L and x/L).

As seen from (27) the output beam is deviated as a whole at angle H/L . Note again that the deviation takes place in the direction of the point-source displacement and not vice versa as in traditional optical systems without phase conjugation. Making the wavefront local tilt arising at the beam edge due to the second term in (27) be equal

to λ/D we obtain a maximum deviation angle $\vartheta_{\max} \approx \pm \frac{H_{\max}}{L}$ for which the beam steering does not result in a significant degradation of the beam quality:

$$|\vartheta_{\max}| \leq \frac{8RL}{3D^2} \cdot \frac{\lambda}{D} \quad (28)$$

It follows from (28) that at $M \gg 1$ ϑ_{\max} weakly depends on M and always exceeds $16L^2\lambda/(3D^3)$. In the example given above this amount is close to $21\lambda/D$. Experimental demonstration of beam-steering using PCM in a telescope with DOE on the primary mirror was carried out with the same setup (Fig. 14) [36,24] that was used before for verification of aberration correction.

It was shown in the experiments that the direction of the output beam is determined as was expected by the transverse position of the reference point-source and depends on its displacement H in a full accordance with (27). The beam divergence remained in all the experiments close to the diffraction limit. However, similarly to experiments on compensation for primary mirror tilts described in the previous Section the maximum angle ϑ_{\max} achieved in experiments on beam-steering was limited by technical features of optical components used and did not exceed $\pm 44\lambda/D$.

At such angles the output beam energy decreased two times due to vignetting by optical elements. Nevertheless these experiments have verified feasibility of PC beam-steering in telescopes with DOE on the primary and showed the potential advantages of this approach.

7. PCM-correction for a segmented mirror via dynamic HOE on its surface [37]

As follows from the previous Sections applying DOE on the primary mirror of the telescope provides a powerful approach to phase conjugation correction for aberrations in a telescope forming the laser beam at the output of a MOPA system with a phase conjugate mirror.

However, substantial restriction on application of this concept is imposed by the technological complexity of producing the DOE on a mirror surface of more than 50-100 cm across. The use of segmented primary mirror with separate fragments of the DOE is not a remedy in this case because the distortions caused by transverse displacements of the segments during their initial installation are not compensated since the procedure of transverse matching of the grooves on the adjacent segments is very difficult and practically impossible when the telescope numerical aperture is large (the grooves period at the mirror edge being comparable with the laser wavelength).

A possible solution of this problem was proposed and verified experimentally by our group in [37]. The idea of this solution is illustrated in Fig. 15 and is based on the use of a dynamically recorded holographic optical element (HOE) instead of the static DOE on the primary mirror. The dynamic HOE is written by two auxiliary laser beams in a layer of a nonlinear medium specially applied on the mirror surface (see Fig. 15). This dynamic HOE can be rewritten just before each pulse of the MOPA-PCM system, so the precise initial matching of "grooves" at the separate segments of the primary

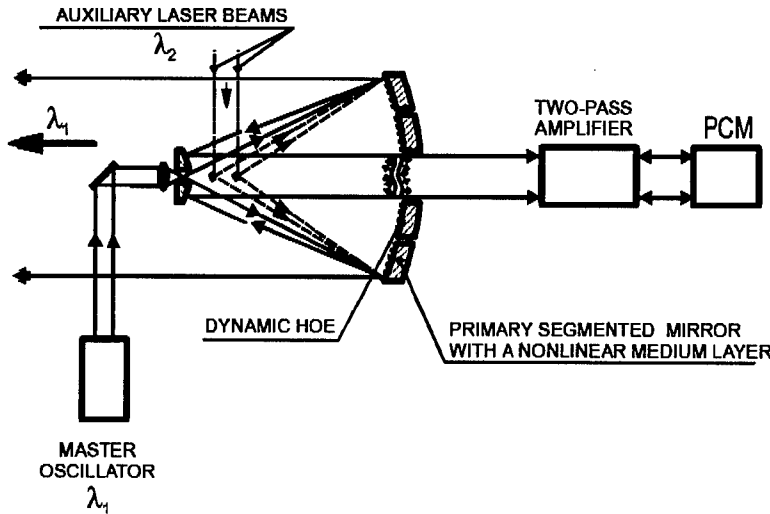


Figure 15. Concept of segmented mirror PCM-compensation using the dynamic HOE on the primary mirror. [37]

mirror is not required and is provided automatically. Thus all the aberrations of the primary including tilts and piston shifts of the segments should be cancelled by phase conjugation just in the same way as it had been demonstrated before for the solid primary mirror with the static DOE on its surface. It is evident that the efficiency of aberration correction using the dynamic HOE should be in general higher than that in case of the static DOE even for the solid primary, because for all deformations and displacements of the primary only HOE provides exact positioning of "grooves" on their proper places corresponding to the deformed profile of the primary mirror surface. The difference between DOE and dynamic HOE in terms of compensation efficiency is most pronounced in the sensitivity of the telescope to variations in the distance between the point-source reference and the primary mirror. In distinction to the case of DOE (see expression (26)) where these variations resulted in converging or diverging wave (depending on the variation sign) the telescope with dynamic HOE on the primary should be practically insensitive to longitudinal relative displacements of the reference source and the primary.

To carry out the experiments on the aberration correction using the dynamic HOE on the mirror we manufactured a two-segment mirror with a germanium layer on its surface as the nonlinear medium [37]. The optical schematic of the experiment is shown in Fig. 16. A small active volume TEA CO₂ laser with the wavelength control and an amplifier were used to produce a high-quality laser beam on the P24 line of the 10.4 μm transition with 2.3 J-pulse energy and pulse duration about 1 μs. Two pump beams with total energy of 0.45 J were formed by reflection of the beam from different faces of beamsplitter BS1 and pumped a FWM-cell with ³⁴SF₆ at the pressure of 150 torr.

The beam of the CO₂ amplifier that passed through the beamsplitter (with pulse energy about 0.8 J) was directed onto the two-segment mirror as a probe beam. This

beam simulated the reference beam illuminating the segmented primary mirror as was shown in Fig. 15.

The dynamic HOE was written in the surface Ge-layer of the two-segmented mirror by two interfering beams of a Nd^{3+} :YAG laser generating free carriers in Ge at interference maximums. Their total energy was about 0.2 J for pulse duration of about $0.5 \mu\text{s}$ (see Fig. 16). The energy density of each writing beam was close to 50 mJ/cm^2 . In such conditions the diffraction efficiency was about 1% for CO_2 laser radiation so the beam diffracted in a first diffraction order and carrying information about aberrations of the two-segment mirror had about 4 mJ energy being delivered to the PCM. After the phase-conjugate reflection with a reflectivity exceeding 100% the beam propagated back, reflected specularly from the two-segment mirror in the zeroth order and entered the recording system (see Fig. 16) for evaluation the correction degree for aberrations brought in by the mirror.

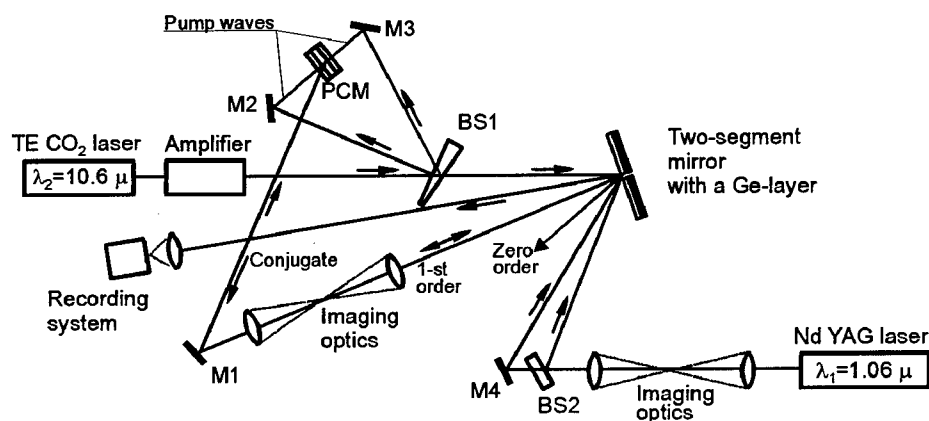


Figure 16. Basic optical schematic of the experiment on aberration correction with HOE on the mirror [37].

In the course of the experiments two segments of the Ge-coated mirror with the dynamic HOE were inclined and shifted relative to one another. The largest tilt angles $\theta_{\max} \sim 6\lambda_2/d_2$ (where $\lambda_2 = 10.6 \mu\text{m}$ and $d_2 = 15 \text{ mm}$ is the CO_2 laser beam diameter on the diffraction structure) were limited by the angle of view of the PCM that was equal to about 10 mrad. The piston shifts varied from zero to 2 mm.

Besides the far-field spot of the phase-conjugate beam reflected from the two-segment mirror it was possible to observe simultaneously during the experiment the CO_2 laser beam diffracted in the second diffraction order by the HOE written on the mirror surface. This beam was not intercepted by the PCM and was "reflected" from the mirror only once. So its far-field spot should be distorted by the mirror and can be used for comparison to demonstrate the degree and quality of the aberration correction.

The photographs of CO_2 laser beams obtained in the experiments [37] on a conventional photographic film using a subsequent exposition by a flash of the visible light are shown in Fig. 17. The upper patterns in the Figure represent the far-field radiation distributions obtained in the second diffraction order, the bottom ones show the far-field prints of the phase conjugate beam being reflected the second time by the

two-segment mirror. Fig. 17 a,b,c correspond to different tilts of the segments (from zero in Fig. 17a to 2.5 mrad in Fig. 17b and 4.5 mrad $\approx 6\lambda_2/d_2$ in Fig. 17c). As seen from the Figure, in spite of a severe tilt of the segments, which is evident from the growing angular distance δ (see upper patterns in Fig. 17 b,c) between the two beams reflected by the segments, phase conjugate beams (the bottom spots) retain their initial beam quality. The same quality was observed when a severe piston shift was brought between segments (up to 2 mm) (see Fig. 17d).

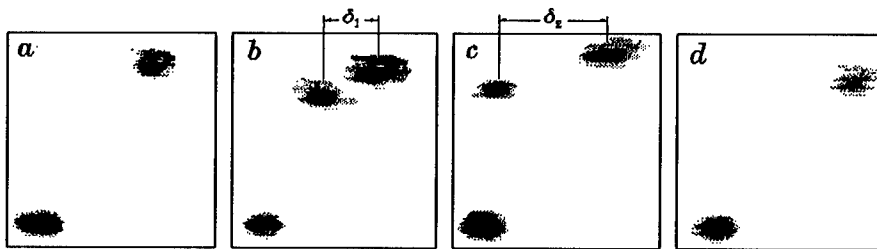


Figure 17. Far-field patterns of radiation reflected by the two-segment mirror with the dynamic HOE on the surface [37]:

- upper spots - the beams reflected in the second diffraction order
- bottom spots - the beams obtained with PC correction of aberrations
- a) segments are aligned accurately
- b) one of the segments is tilted at 2.5 mrad
- c) one of the segments is tilted at 4.5 mrad
- d) segments are aligned, piston shift is equal to 2 mm.

Thus for the first time to our knowledge, we demonstrated in experiments with a CO₂ laser the feasibility to correct for aberrations of a segmented mirror using phase conjugation in the optical schematic comprising the dynamic HOE recorded by an auxiliary laser source in a thin layer of a nonlinear material on the mirror surface. In our case the temporal behavior of the hologram was determined by the charge carriers generation and recombination time in Ge and the response time was of the order of 10^{-7} s so potentially this schematic was capable of compensating for dynamic aberrations of the segmented mirror with frequencies up to several megahertz. The practical significance of this technique substantially depends on the progress in development of novel nonlinear media, however even at present this approach to aberration correction seems to be promising in some applications.

8. Aperture scaling of laser beam-forming telescopes using phase conjugation

In some applications, for instance, when constructing a very long-distance space communication system based on CO₂ lasers, it can be required to have a spaceborn transmitting telescope of tens meters in diameter. The only approach to creation of such a beam-director telescope is based on the use of a multi-segment primary mirror with phase conjugation compensation for the beam distortions arising due to misfigure aberrations of each segment and to their mutual misalignments and piston shifts. However application of PC correction techniques described in the previous Sections is not realistic in this case because of very large sizes of the segments.

The problem can be solved using the optical schematic proposed and developed at our Institute by Leshchev and his colleagues several years ago [38]. In Russian literature this optical schematic is referred to as "TENOCOM" (Telescope with Nonlinear-Optical Compensation).

In the basis of the approach is a very ingenious combination of two different phase conjugation techniques of aberration correction in optical systems. One of them is the technique described in Section 6 and based on application of DOE on the mirror of the optical system to be corrected by a PCM. The other is the so called "by-pass" technique of phase conjugation correction for aberrations in optical systems [39]. The "by-pass" technique uses a standard two-pass concept of phase conjugation correction for distortions in a poor-quality optical element but in distinction to the traditional approach comprises some auxiliary low-dimension and high-quality optical elements. Being brought into the system so as to affect the return beam only (usually it is achieved by application of a polarization-type beamsplitter directing the beam through a by-pass channel) these elements to image the distorted element (e.g. the primary mirror) onto itself after the round trip from the distorted mirror to the PCM and back. As a result the distortions of the mirror turn to be compensated due to phase conjugation though the wavefronts of the input and output beams are not phase-conjugate replicas of each other in this case.

The optical schematic of TENOCOM is shown in Fig. 18. It operates as follows. A reference point-source beam illuminates segmented primary mirror 1 from the point close to the primary's centre of curvature. The reflected beam bearing information about the primary's distortions is intercepted by small concave mirror 2 (see Fig. 18) and is directed through lens 3 to additional convex mirror 4 and then to secondary mirror 5 of the telescope. On its surface there is a specially applied DOE equivalent to a concave mirror. Then the radiation diffracted in the (-1) diffraction order is reflected with phase reversal by the phase conjugate mirror (PCM) and directed again to secondary mirror 5. The parameters of all the elements are chosen in such a way that

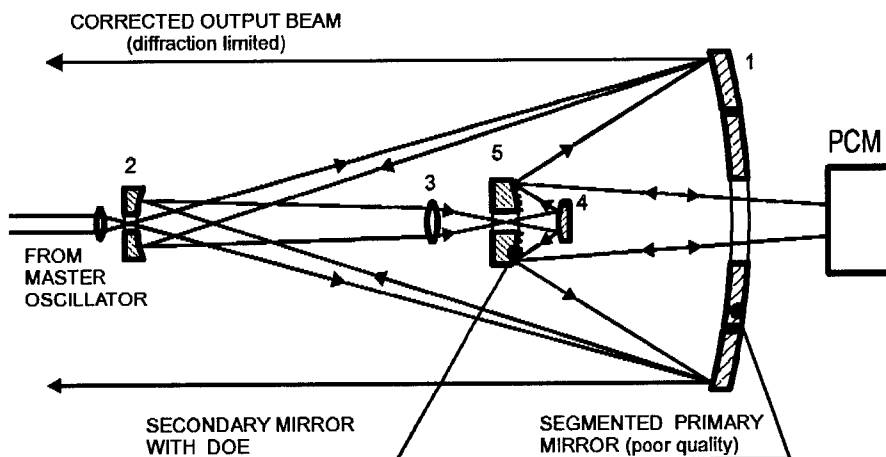


Figure 18. Large-scale laser beam-director telescope with nonlinear-optical compensation for aberrations (TENOCOM). [38]

after reflection from the secondary mirror each ray hits just the same point at the primary which it started from on the first pass. (It means that the primary is imaged onto itself after the round trip of the radiation through the system.) As a result the distortions of the primary mirror should be cancelled in the output beam (see Fig. 18) due to phase conjugation. It is easily seen that distortions brought in by the secondary mirror as well as by any optical elements placed between this mirror and PCM should be also cancelled by phase conjugation in accordance with the correction technique described in Section 6.

The first experiments on aberration correction in TENOCOM have been briefly described in [38]. They were carried out with a low energy (~ 1 J output) TEA CO_2 laser and a FWM phase conjugate mirror with $^{34}\text{SF}_6$ as the nonlinear medium. The telescope primary of 400 mm in diameter and the focal length of 2 m comprised 6 elements. The magnification of the telescope was equal to 6.5. The DOE was applied on the secondary mirror of 60 mm in diameter by the photolithographic technique. Some results of the experiment are shown in Fig. 19. Here the photographs of the far-field patterns are presented for the reference beam, reflected only once by the primary mirror with deliberately misaligned segments (Fig. 19a) and for the beam at the output of TENOCOM (Fig. 19b). Comparison of these patterns shows a dramatic improvement of the beam quality due to phase conjugation and demonstrates practically diffraction limited performance of the system in spite of severe misalignments of the segments and their misfigure aberrations.

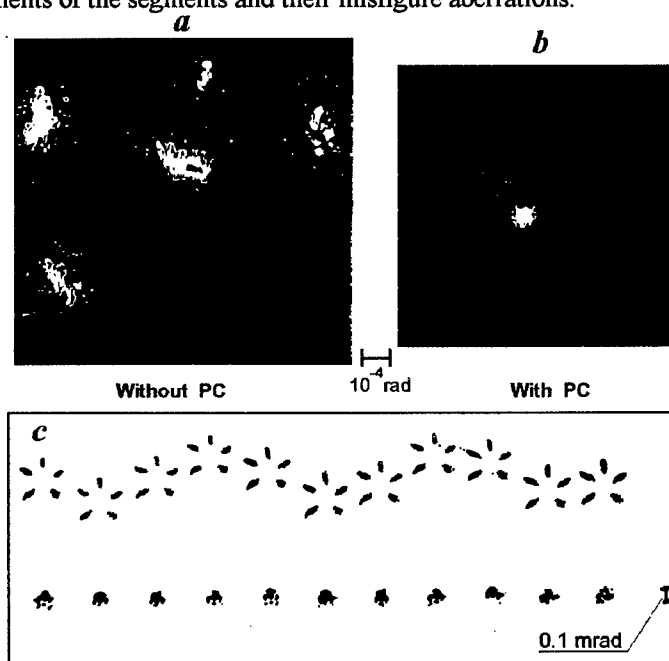


Figure 19. Experimental results on aberration correction using TENOCOM
a) far-field pattern of the beam reflected by the segmented primary mirror with the misaligned segments [38]
b) far-field pattern of the beam at the TENOCOM output [38]
c) far-field patterns obtained with TENOCOM in a pulse repetition mode; upper trace – without PC correction; lower trace – with PC correction [40].

The maximum tilt of segments that was compensated for in the experiments was up to $28 \lambda/D$ and was limited due to vignetting the beam by some elements of the optical schematic. The maximum piston shift amounted to 150λ . In all these cases the diffraction limited performance was obtained which is absolutely impossible to achieve using conventional optics with such aberrations.

Later on similar experiments were carried out by our group with the same six-segment telescope TENOCOM on the base of a repetitively pulsed e-beam sustained CO_2 laser [40]. The laser operated with the repetition rate of 50 pps. As the nonlinear medium of the FWM PCM a small part of the gain medium of the reference laser was used with the LIMP effect as the mechanism for writing the gratings [27]. Similarly to the experiments described above the segments of the primary mirror were misaligned in radial direction at approximately equal angles so that the far-field pattern of the beam distorted by the primary looked like a "star" shown in Fig. 19c (the sixth spot is not seen because of vignetting the beam by a mount of one of optical elements). The primary mirror as a whole was brought into oscillation by a special mechanical driver with a frequency about 12 Hz, so the beam reflected from the primary mirror moved periodically in vertical direction (see Fig. 19c, the upper trace). In spite of all these aberrations the output of the TENOCOM system retained its initial direction from pulse to pulse and its divergence was close to the diffraction limited (see Fig. 19c, the bottom trace). Thus the results of the experiments have confirmed feasibility of phase conjugation correction for aberrations in a beam-forming telescope using TENOCOM concept and demonstrated high compensation capabilities of this optical schematic.

9. Further progress and problems to be solved

Thus we have seen that phase conjugation can be a powerful technique for solving the problems of CO_2 laser beam divergence and beam-forming using large-aperture output telescopes.

Application of four-wave mixing phase-conjugate mirrors enables realizing the diffraction limited performance of CO_2 laser systems with parameters that in principle can not be achieved by traditional techniques. However not everything is so simple about application of phase conjugation in CO_2 laser systems as it probably seemed to be at a glance. The most serious of them is connected with necessity to have a separate and rather powerful laser oscillator to provide high-quality pumping beams. Usually one needs to have two 10 J-pump beams to obtain a phase conjugate beam with pulse energy from 1 to 2 Joules. When the master oscillator is scaled up in average power it becomes difficult to provide high optical quality of the pumps. So application of FWM PCM turns to be reasonable only in combination with a long and high-gain laser amplifier whose output is at least an order of magnitude higher than that of the master oscillator.

On the other hand as the two-pass amplifier with a PCM is scaled up in length the two additional problems can arise. If the master oscillator is placed in the vicinity of the PCM it becomes necessary to have a long delay line in the pumping beam path to equalize the optical paths of the beams interfering in the FWM cell. This can be a

problem in vibration environment. The second problem concerns the amplifier angle of view. It should be large to pass the probe beam distorted by aberrations (e.g. severe aberrations of a segmented mirror telescope) without losses. One of the ways to enlarge it is based on the use of image relay systems within the amplifier (see Section 3). However at high output pulse energy it can require application of vacuum chambers to eliminate optical breakdown of air. The other way is to increase m times the sizes of the cross-section of the amplifier discharge chamber for the given length of the amplifier. That requires however the m^2 times-increase in the energy input into the discharge chamber. The analysis of limitations mentioned above along with limitations [19] connected with a trade off between the requirements of high-gain and high extraction efficiency of the two-pass CO₂ amplifier with a FWM PCM shows that PCMs with external pumps can be efficiently used only in unique large-scale high-average-power CO₂ laser systems.

The further progress in development of PCMs that could be more suitable for applications in middle-power CO₂ lasers will be probably connected with development of loop-type self-pumped FWM PCMs put forward by Bel'dyugin, Galushkin and Zemskov [41]. In these PCMs, sometimes referred to as FWM PCMs with a feedback, the high-beam-quality pumping oscillators are not required and the phase conjugate wave should be generated within a ring cavity comprising a laser amplifier and a FWM cell as the coupling mirror. Such PCMs have been implemented for the first time by Betin and his colleagues [42] in TEA CO₂ lasers (see also [14,43]) and later investigated also by our group [44]. In its simplest form such a loop-type PCM operates as follows (Fig. 20 [42]). Incident wave E_1 and wave E_3 (the latter, as shown in the Figure, is the same wave E_1 but propagated along the ring) record a long-period grating (thick hologram) $E_1 E_3^*$ in a cell with a nonlinear medium. This grating is similar to a conventional mirror with a reflection $\rho = \eta |E_1 E_3^*|^2$, where η - the diffraction efficiency of the grating as measured at the exit of the diffracted beam out of the cell. As the incident wave E_1 is sufficient to yield the reflectivity $\rho = G^{-1}$, where G - the small-signal gain of the amplifier within the loop, oscillation builds up in the ring cavity. According to the theory [41] one of the counterpropagating oscillating waves (E_2 in Fig. 20) should be a sought phase-conjugate replica of the incident wave E_1 .

Application of such loop-type PCMs could eliminate the necessity to have a very long high-gain amplifier, because the reflectivity of these PCMs can exceed 100% by the order of magnitude (see [14]). It was shown by the experiments [42,14,44] that the loop type PCM can actually compensate for severe aberrations brought in by optical elements within the loop and can produce at their output the beam whose direction is practically opposite to the direction of the input diffraction limited beam. That was the evidence of a phase conjugate nature of the PCM "reflection". At the same time the fidelity of phase conjugation was somewhat lower than that obtained in FWM PCMs with external pumps. It can be explained by the fact that the phase conjugate wave oscillating within the loop is only one of the transverse modes of the ring cavity comprising the holographic mirror [41] and higher-order modes can also take part in oscillation if mode selection is not sufficient. The latter depends on the correct choice of the cavity geometry, the "thickness" of the dynamic hologram written

in the FWM-cell and parameters of a small-scale phase plate inserted usually into the loop [41,42].

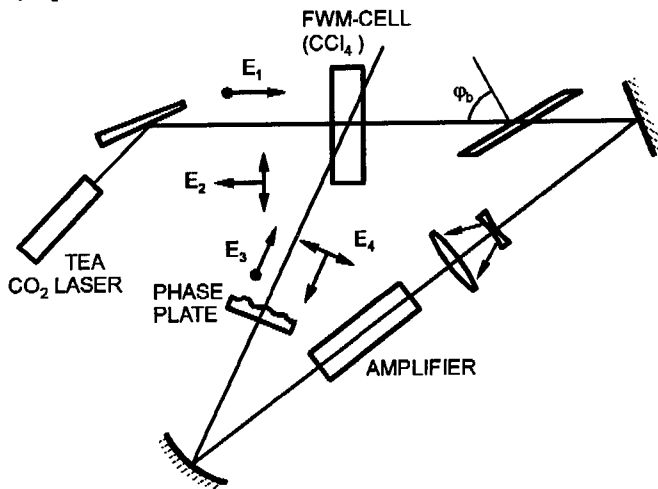


Figure 20. First experimental realization of a self-pumped phase conjugate mirror for TEA CO₂ laser radiation [42]

The largest experiment with the loop-type PCM is described in [45]. In this paper it was reported about obtaining a 1.6 KJ – beam with divergence of 0.2 mrad for the 200 mm-dia output in the loop configuration comprising a 8 m-long electron-beam sustained CO₂ amplifier and a cell with CCl₄ as the nonlinear medium. This output beam was obtained in a 20 μ s-pulse with the master oscillator input pulse having the duration ~ 1 μ s and energy about 0.25 J. Thus the “reflectivity” of the PCM defined as the ratio of output to input was about 6000 [45].

It is necessary to note however that in all the experiments carried out to date with loop-type PCMs the input beam was always rather close to the diffraction limited one. As we have seen from the previous Sections in applications one often needs a PCM that can operate with the beams whose beam divergence far exceeds the diffraction limit. A feasibility of the loop-type PCM performance with highly aberrated beams is not investigated well at present experimentally in CO₂ lasers. One of the reasons for that is that such investigation requires a loop providing a large field of view. This requirement is rather difficult to meet in CO₂ lasers as the “reflectivity” of the holographic mirror is usually very small (about several per cent) and to overcome the oscillation threshold in the ring cavity one needs a high-gain and rather long (typically 5-7 meters) amplifier. In the middle-power CO₂ lasers the cross-section of the gain medium is usually rather small (several centimeters) so with such a length it is difficult to provide a large field of view in the loop without special image relay systems. The question of transverse mode selection in high Fresnel number loop-type cavities is also not studied well for highly aberrated input beams, especially in the case of small-scale phase distortions of the input beam wavefront. Probably some novel geometries of loops should be elaborated and studied to cope with these problems.

In our review we have not touched upon the problem of phase conjugation in cw CO₂ lasers. The solution of this problem is much more difficult, because of orders of

magnitude decrease of the radiation intensities as compared to pulsed CO₂ lasers with results in a corresponding dramatic decrease in diffraction efficiency of dynamic holograms in the process of FWM.

The first experiments on phase conjugation of cw CO₂ laser radiation were performed by Antipov, Betin et al. [46] who used as the nonlinear medium for FWM a thin layer of organic solvents applied on the surface of a metal mirror exhibiting high thermoconductivity and achieved the PCM reflectivity of 20%. In the paper of our group [47] developing the same approach optimization of parameters enabled obtaining the reflectivity about 70-75% for the reflected beam power about 3 W. The further scaling up in reflected radiation power was limited by a strong lensing in the front window of the FWM cell. Unfortunately all the problems discussed above concerning pulsed CO₂ amplifiers with PCM remain the same or even more serious because the small signal gain in cw CO₂ lasers is typically lower than that realized in a pulse mode of operation. At the same time in some aspects, e.g. in the absence of the air breakdown in fast-optics image relay systems, cw CO₂ lasers are more suitable for implementation of large-field-of-view amplifiers than the pulsed ones.

In conclusion I would say that the potential benefit due to application of phase conjugation in CO₂ lasers and laser systems seems to be very significant even at the today's level of PCM development. So I hope that most of the problems mentioned above will be solved in the nearest future and we will be the witnesses of implementation of various types of efficient CO₂ laser systems with correction for aberrations via phase conjugation.

Acknowledgments

The author is grateful to all his colleagues and co-authors who participated in obtaining the results used in the review. The technical assistance of M. Pol'skaya, A. Kokushkin, L. Martyukhina and S. Sherstobitov is also acknowledged.

10. References

1. Zel'dovich, B.Ya., Popovichev, V.I., Ragul'skiy, V.V. and Faizullov, F.S. (1972) On the relation between the wavefronts of the reflected and exciting light on stimulated Brillouin scattering, *Pis'ma v JETP* **15**, 160-164. (In Russian).
2. Zel'dovich, B.Ya., Pilipetskiy, N.F. and Shkunov, V.V. (1982) Wavefront reversal via stimulated scattering, *Uspekhi Fiz. Nauk* **138**, 249-288. (In Russian).
3. Pepper, D.M. (1982) Nonlinear optical phase conjugation, *Opt. Engineering* **21**, 156-181.
4. Anan'ev, Yu.A. (1974) Method of low divergence radiation formation. Inventors certificate No 414935 of 12.10.1971, *Bull. izobr.* No 3, 171. (In Russian).
5. Nosach, O.Yu., Popovichev, V.I., Ragul'skiy, V.V. and Faizullov, F.S. (1972) Compensation for phase distortions in a gain medium via "Brillouin mirror", *Pis'ma v JETP* **16**, 617-621. (In Russian).
6. Zel'dovich, B.Ya., Pilipetskiy, N.F. and Shkunov, V.V. (1985) *Wavefront reversal*, Nauka, Moscow. (In Russian).
7. Woerdman, J.P. (1970) Formation of a transient free carrier hologram in Si, *Opt. Commun.* **2**, 212-214.
8. Stepanov, B.I., Ivakin, E.I. and Rubanov, A.S. (1971) On recording thin and volume dynamic holograms in "bleachable" media, *Doklady Akad. Nauk SSSR* **196**, 567-569. (In Russian).

9. Denisjuk, Yu.N. (1963) On mapping of the object optical features in the wave field of scattered radiation, *Optika y Spektroskopiya* **15**, 522-532. (In Russian).
10. Kogelnic, H. (1965) Holographic image projection through inhomogeneous media, *Bell Syst. Techn. J.* **44**, 2451-2455.
11. Bergman, E.E., Bigio, I.J., Feldman, B.J. and Fisher, R.A. (1978) High efficiency 10.6 μm phase-conjugation of pulsed CO₂ laser radiation via four-wave mixing in SF₆, *Opt.Lett.* **3**, 82-84.
12. Lind, R.C., Steel, D.G., Klein, M.B., Abrams, R.L., Giuliano, C.R. and Jain, R.K. (1979) Phase conjugation at 10.6 μm by resonantly enhanced degenerate four-wave mixing, *Appl.Phys.Lett.* **34**, 457-459.
13. Kovalev, V.I. (1995) Phase conjugation for middle-infrared laser radiation: the influence of frequency dispersion and decay time of the third-order nonlinear susceptibility, in V.E. Sherstobitov (ed.), *Laser Optics '95: Phase Conjugation and Adaptive Optics, Proc. SPIE* **2771**, 95-103.
14. Bespalov, V.I., Betin, A.A., Mitropol'skiy, O.V. et al (1989) Phase conjugation of CO₂ laser radiation in a medium with thermal nonlinearity, *IEEE J. of Quant.Electron.* **QE-25**, 360-367.
15. Sherstobitov, V.E. (1993) Phase conjugation of CO₂ laser radiation, *Inter. J. of Nonlinear Optical Physics* **2**, 465-482.
16. Basov, N.G., Kovalev, V.I., Lesiv, A.R. (1982) Investigation of wave-front phase conjugation of pulsed CO₂ laser radiation via four-wave mixing in SF₆, *Sov. Journ. Tech. Phys. Lett.* **8**, 451-455. (In Russian).
17. Goryachkin, D.A., Irtuganov, V.M., Kalinin, V.I., Mazurenko, Yu.T. and Rubinov, Yu.A. (1980) Atmospheric and above atmospheric pressure CO₂ lasers with a selfmaintained discharge, *Bull Acad. Sci. USSR, ser.phys.* **46**, 1877-1885. (In Russian).
18. Goryachkin, D.A., Kalinin, V.P., Komin, I.A., Petrova, I.M. and Romanov, N.A. (1983) Effective degenerate four-wave mixing in SF₆, *Optika I Spektroskopiya* **55**, 1089-1091. (In Russian).
19. Betin, A.A. and Sherstobitov, V.E. (1983) The problems of radiation forming in a double-pass CO₂ amplifier with a phase-conjugate mirror, *Izv. Akad. Nauk SSSR, ser. phys.* **47**, 2397-2407. (In Russian).
20. Goryachkin, D.A., Kalinin, V.P., Kozlovskaya, I.M. and Sherstobitov, V.E. (1987) A phase-conjugate mirror for CO₂ laser radiation using ³⁴SF₆, in *Proc. of the Fifth Conf. "Laser Optics", Leningrad, S.I.Vavilov Optical Institute*, p.344. (in Russian).
21. Goryachkin, D.A., Kalinin, V.P., Kozlovskaya, I.M. and Sherstobitov, V.E. (1989) The influence of selffocusing effects on phase conjugation fidelity of CO₂ laser radiation in SF₆, *Optika I Spektroskopiya* **67**, 200-205. (In Russian).
22. Goryachkin, D.A., Kalinin, V.P. and Kozlovskaya, I.M. (1990) On compensation for small-scale distortions in the process of degenerate four-wave interaction accompanied by selffocusing, *Optika I Spektroskopiya* **69**, 167-169. (In Russian).
23. Betin, A.A., Zinchenko, V.I., Kalinin, V.P., Komin, I.A., Sokolov, V.N., Chirkov, V.N., Sherstobitov, V.E. and Yachnev, I.L. (1987) Investigation of a phase conjugate mirror via degenerate four-wave mixing for CO₂ laser with pulse duration of 20 μs , in A.S.Rubanov (ed.), *Phase Conjugation in Nonlinear Media*, Phys. Inst. Acad. Sci. BSSR, Minsk, pp.22-28. (In Russian).
24. Sherstobitov, V.E., Kalinin, V.P., Goryachkin, D.A., Romanov, N.A., Dimakov, S.A. and Kuprenyuk, V.I. (1991) CO₂ lasers and phase conjugation, in A. D. Schnurr (ed.), *Modelling and Simulation of Laser Systems II*, L.-A., CA, *Proc. of SPIE*, **1415**, 79-89.
25. Dimakov, S.A., Malakhov, L.N., Sherstobitov, V.E. and Yashukov, V.P. (1983) A study into optical homogeneity of the active medium of an atmospheric pressure electroionization CO₂ laser upon stimulated emission of radiation, *Kvantovaya elektronika* **10**, 397-402. (In Russian).
26. Roper, V.G., Lamberton, H.M., Parcell, E.W. and Manley, A.W.Y. (1978) Laser induced medium perturbation in a pulsed CO₂ laser, *Opt. Commun.* **25**, 235-240.
27. Galushkin, M.G., Dimakov, S.A., Onoshko, R.N., Robachevskaya, M.A., Rubanov, A.S., Sviridov, K.A. and Sherstobitov, V.E. (1990) Phase conjugation via four-wave mixing in gain media *Izv. Akad. Nauk SSSR, ser. phys.* **54**, 1042-1052. (In Russian).
28. Babaev, I.K., Bardakovskiy, S.V., Blinov, N.A., Bulaev, V.D., Krasovskiy, V.M. et al. (1991) Obtaining the emission with the radiant intensity at the level of several TeraWatt/steradian in a repetitively pulsed electroionization CO₂ system composed of a master oscillator and an amplifier, *Kvantovaya elektronika* **18**, 6-7. (In Russian).
29. Babaev, I.K., Bardakovskiy, S.V., Blinov, N.A., Bulaev, V.D., Golyshkov, A.N. et al. (1991) Divergence of the radiation from an atmospheric pressure EI CO₂ amplifier with the pulse duration of 20 μs , *Kvantovaya elektronika* **18**, 12-14. (In Russian).
30. Sherstobitov, V.E., Ageichik, A.A., Bulaev, V.D., Dimakov, S.A., Gerke, M.N., Goryachkin, D.A., Kalinin, V.P., Koval', I., Paryshev, E.N., Režumkov, Yu.A., Romanov, N.A., Rodionov, A.Yu., Stepanov, V.V. and Zemlyanykh, V.V. (1991) Phase conjugation in a high-power E-beam-sustained CO₂ laser, *Proc. of SPIE, Nonlinear Optical Processes in Solids* **1841**, 135-143.

31. Belousova, I.M., Grigor'ev, V.A., Danilov, O.B., Kiselev, V.M., Leonov, S.N., Novoselov, N.A., Semenov, V.E., Smirnov, V.A., Utkin, A.B. (1995) On the effective transportation of laser radiation through the atmosphere, *Proc. of SPIE* 2771, 252-262.
32. Dimakov, S.A., Koval'chuk, L.V., Pel'menev, A.G., Petrov, V.F., Rodionov, A.Yu., Trusov, V.P., Sherstobitov, V.E. and Yashukov, V.P. (1987) An effect of thermal nonlinearity on dynamics of the radiation from an unstable resonator electroionization CO₂ laser, *Kvantovaya elektronika* 14, 466-476. (In Russian).
33. Goryachkin, D.A., Kozlovskaya, I.M., Kalinin, V.P. and Sherstobitov, V.E. (1992) Comparative characteristics of PC-mirrors based on degenerate four-wave mixing in SF₆, ³³SF₆ and ³⁴SF₆, *Optica I Spektroskopia* 73, 934-939. (In Russian).
34. Dimakov, S.A., Kliment'ev, S.I., Kuprenyuk, V.I., Orlova, I.B., Sergeev, V.V. and Sherstobitov, V.E. (1994) Low-sensitive to misalignments resonator, *Proc. of SPIE* 2257, 187-192.
35. O'Meara, T.R. (1982) Compensation of laser amplifier trains with nonlinear conjugation techniques, *Optical Engineering* 21, 243-251.
36. Andreev, R.B., Volosov, V.D., Irtuganov, V.M., Kalinin, V.P., Kononov, V.V. and Sherstobitov, V.E. (1991) On PC correction for distortions in a forming telescope with a diffractive optical element, *Kvantovaya elektronika* 18, 762-765. (In Russian).
37. Bogdanov, M.P., Dimakov, S.A., Gorlanov, A.V., Goryachkin, D.A., Grigor'ev, A.M., Irtuganov, V.M., Kalinin, V.P., Kliment'ev, S.I., Kozlovskaya, I.M., Orlova, I.B., Sherstobitov, V.E. and Venediktov, V.Yu. (1996) Correction of segmented mirror aberrations by phase conjugation and dynamic holography, *Opt. Commun.* 129, 405-413.
38. Vasil'ev, M.V., Venediktov, V.Yu., Leshchev, A.A. and Semenov, P.M. (1993) Laser beam forming telescopic system with output tract compensation via phase conjugation, *Kvantovaya elektronika* 20, 317-318. (In Russian).
39. Vasil'ev, M.V., Venediktov, V.Yu., Leshchev, A.A., Pasmanik, G.A. and Sidorovich, V.G. (1991) Compensation for distortions in imaging systems via phase conjugation, *Izv. Akad. Nauk SSSR, ser. phys.* 55, 260-266. (In Russian).
40. Ageichik, A.A., Kotyaev, O.G., Leshchev, A.A., Reznikov, Yu.A., Safronov, A.L., Stepanov, V.V., Vasil'ev, M.V. and Venediktov, V.Yu. (1996) Experimental study on phase conjugation correction of distortions imposed by the telescope elements, in V.E. Sherstobitov (ed.), *Laser Optics'95: Phase Conjugation and Adaptive Optics, Proc. SPIE* 2771, 136-139.
41. Bel'dyugin, I.M., Galushkin, M.G., Zemskov, E.M. (1984) Phase conjugation of laser radiation with the use of four-wave mixing with a feedback, *Kvantovaya elektronika* 11, 887-893. (In Russian).
42. Betin, A.A., Mitropol'skiy, O.V. (1987) Laser oscillation at 10 μm via four-wave mixing with a feedback, *Kvantovaya elektronika* 14, 1002-1009. (In Russian).
43. Bepalov, V.I., Betin, A.A., Ergakov, K.V., Zhukov, E.A., Mitropol'skiy, O.V., Osipov, D.V., Turgenev, S.G. (1991) Self-phase-conjugation of middle infrared radiation by four-wave mixing and stimulated scattering, *Proc. SPIE* 1841, 124-134.
44. Goryachkin, D.A., Kalinin, V.P., Kozlovskaya, I.M. and Sherstobitov, V.E. (1990) An experimental study of phase self-conjugation of the CO₂ laser radiation, *Kvantovaya elektronika* 17, 1349-1355. (In Russian).
45. Babaev, I.K., Cheburkin, N.V., Krasnov, N.Yu., Mitin, K.V., Seryogin, A.M., Bulaev, V.D., Paryshev, E.N., Betin, A.A., Ergakov, K.N., Mitropol'skiy, O.V. (1994) High power amplifier with WFR-mirror, in *Proc. of the Int. Conf. on Lasers '93, Lake Tahoe, NV, USA, December 6-9, 1993*, STS Press, pp.748-750.
46. Antipov, O.L., Betin, A.A. et al. (1989) Four-wave mixing of the mid-IR radiation in media with thermal nonlinearity, *Kvantovaya elektronika* 19, 387-401. (In Russian).
47. Kliment'ev, S.I., Kononov, V.V., Kuprenyuk, V.I. (1989) Optimization of conditions for the four-wave mixing of cw radiation in an absorbing medium, *Kvantovaya elektronika* 19, 1465-1468. (In Russian).

CONJUGATED CAVITY WITH THE WIDE FIELD OF VISION

A.F.KORNEV, V.P.POKROVSKY, L.N.SOMS,
V.K.STUPNIKOV, V.YU.VENEDIKTOV
*Research Institute for Laser Physics, SC "Vavilov State
Optical Institute", 199034, Birjevaya, 12, St.-Petersburg,
Russia*

1. Introduction

Lasers with the conjugated cavities (the cavities of zero effective length) [1,2] are widely used for various applications, needing fast tilt (scanning) of laser beam, generation of pulses in various, arbitrary controlled direction or simultaneous generation of complicated pattern (some image). This paper is one of the cycle of papers, devoted to the realization of the laser with the controlled addressing of the beam across the extended field of vision.

One of the problems, which was to be solved with the purpose to realize the wide field of vision laser was its optical design, including correction for the intracavity lenses aberrations. There exist various kinds of such cavities. In the Fig.1 one can see the optical scheme of one variant. This scheme consists of two plain mirrors, one of which is

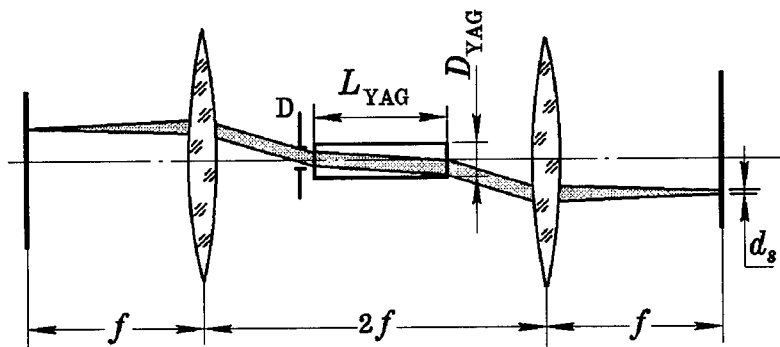


Fig. 1. Optical scheme of the conjugated cavity.

combined with the spatial light modulator [3] (and thus this scheme provides the possibility to use the standard spatial light modulator, deposited onto the plain substratum), two identical lenses and the small-size active element; generation wavelength $\lambda=1.06 \mu\text{m}$. The symmetrical scheme with two identical lenses was chosen first of all due to the cheaper cost of its production. In such a scheme the distances from the lenses to the diaphragm and neighboring cavity mirrors are to be equal to these lenses focal length. In the geometry optics approximation the elementary mode of such a cavity between the lenses and inside the active element looks like the plain wave, tilted to this or that angle with respect to the system axis. The lenses are focusing this "beam" onto the surfaces of plain mirrors.

In such a cavity, which is also called the cavity with the degenerated modes, it is possible to realize generation of a lot of such "TEM₀₀" modes, all propagating at the cavity output parallel to the cavity axis, but displaced in this or that distance in transverse direction. Such a generation can be realized in turn within the randomly controlled sequence or in time, providing thus generation of the image.

The goal of this work was to realize the cavity with the number of such "pixels" approaching the TV standards. The number of resolution element across the cavity diameter was chosen to be at least 240, while the transverse size of the modulator cell was supposed to be equal $d=0.25 \text{ mm}$. Each such cell corresponds to single pixel in beam scanning and thus to single mode of laser generation. So the diameter of the output mirror and of lenses was to be equal 60 mm.

2. Conjugated Cavity

The diameter of the active element, mounted in the central zone of the cavity, is to be chosen with the account to two parameters, important from the point of view of laser generation: (1) energy efficiency and (2) energy losses from the elementary mode of the cavity due to optical distortions and vignetting at the active element aperture.

(1) The optical damage threshold under the loading by the free run oscillation inside such a cavity for the LC SLM cell of such a size can be done as high as $\sim 1 \text{ mJ}$ and more. Simple evaluations show that in the case

of laser pumped active element the sufficient energy efficiency of generation (work with the energy nearby the saturation energy) can be realized for the active element with the diameter of $\sim 1\text{mm}$.

(2) The diameter of the active element aperture in such a cavity is a very important parameter. Each cell of the modulator has to correspond to the elementary mode of the cavity, i.e. its diameter is to be equal to $d = 2.44 \lambda D/F$; here D is the diameter of the active element clear aperture and F is the focal length of the lens. The reduce of D will result in reduce of F and thus in the increase of the numerical aperture of the lenses. For the said number of resolution elements and size of active element this numerical aperture should be rather high - somewhat about 1:2. Obviously, in such a scheme we could not neglect the optical aberrations, first of all the astigmatism of the "thin" (elementary) beam and had thus to carry out the routine of the aberration correction. These aberrations reveal themselves in several different kinds. First, one can see that the elementary beams, corresponding to the tilted modes, are "sliding" across the surface of the lens. From the point of view of the traditional optics such a scheme is similar to the optical system, formed by the humane eye with its small size pupil and spectacles. Two elementary aberrations of Zeidel kind are most important in this case. The first is the astigmatism of the narrow beam, caused by the difference of the sagittal and meridional curvatures of the refracting surface. The second is the curvature of the field of vision, resulting in some error of beam focusing onto the plain mirror. One more source of energy losses from the elementary mode is caused by the violation of telecentricity of the elementary mode beam(also due to aberrations), resulting in inclination of this beam on its propagation between the mirror and the lens with respect to the cavity axis and thus in the transverse shift of the active element aperture image with respect to this very aperture after double pass around the cavity.



Fig.2. Designed conjugated cavity (in scale). 1 - position of active element, working as the aperture (diaphragm), 2 - coupling plain mirror with the modulator, 3 - plain backward mirror, 4 - intracavity lenses.

We have carried out the numerical simulation of several cavities with the single component lenses, following the same procedure which is discussed further and have found out that these distortions begin reveal themselves for the numerical aperture of the lenses of $\sim 1:5 - 1:4$.

Then we have tried the lenses with the single aspherical components and with two spherical components. The latter approach has revealed the better possibilities of correction for distortions; it is, at the same time, simpler from the point of view of the technology. So final choice was to use the dual component lenses. Then a series of numerical design attempts with different value of D were done, following the procedure, described further. We have tried to obtain as small D as possible and succeeded to realize the system with the required parameters for the diameter of the generation zone of the active element equal $D = 1.2$ mm. (Fig.2).

Now let us discuss the special features of such a cavity design. The generation beams are to have plain wave fronts in the AE, and are to fill into the modulator cells when focused by lenses to the modulator. Hence, the paraxial focal length of lenses was chosen to be equal $F=120$ mm, so that in the case of the diffraction limited performance of these lenses the size of the main lobe of the generation beam diffraction pattern corresponded to the cell diameter: $d \approx 2.44 \lambda F/D$.

Usually in design of laser cavities there is used the approach, based on direct evaluation of generation properties, which is, in turn, based on simulation of multiply beam tracing via such a cavity. Such tracing simulation is usually carried out using the fast Fourier transform procedure. However, in our case of the very wide field of cavity vision such an approach to its simulation and, especially, to intracavity optics optimization, required too large amount of calculations.

That is why we have chosen another approach to the cavity optimization. Instead of multiply beam tracing we have simulated and optimized the special effective optical scheme. This scheme consisted of the object/image plane (coupling mirror with modulator), four lenses (two intracavity lenses on the direct and backward passes), retroreflecting mirror and two apertures. This optical scheme had to image the points of the object plane (cells of the modulator) onto themselves.

Simulation and optimization of this scheme was carried out using the DEMOS software, elaborated in Vavilov State Optical Institute and widely used here for solution of optical design problems [4]. The

fulfillment of three requirements was to be preserved in course of scheme optimization:

1. minimization of the wave aberrations while imaging points across the coupling mirror onto themselves;

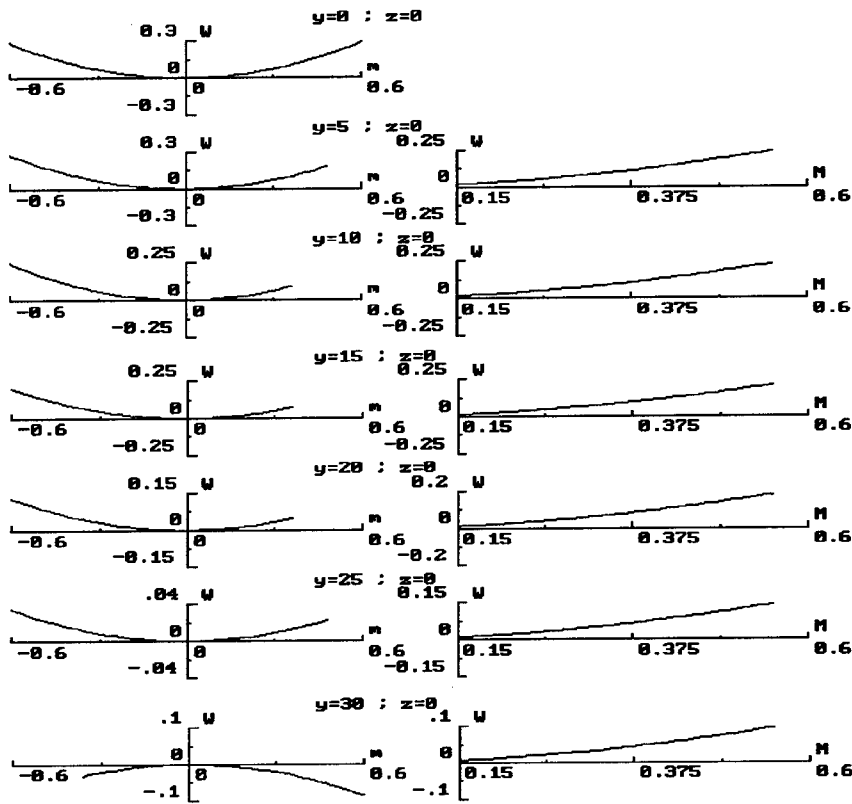


Fig.3. Meridional (left) and sagittal (right) sections of wave aberration of elementary beams, measured in terms of wavelength W . Pupil coordinate M is given in terms of radius across the beam at active element, coordinate y corresponds to point of beam cross with coupling mirror

2. minimization of transverse shift of these points images with respect to their position;

3. minimization of vignetting of the beam by the aperture (diaphragm on AE) on its backward pass via the cavity.

Table 1. Sources of energy loss of elementary beams

Radius at the coupling mirror, mm	Magnitude of toroidal distortion, λ	Magnitude of defocusing error, λ	Transverse shift of the beam, mm
0	0	0.29	0
5	0	0.29	0.1
10	0.01	0.27	0.18
15	0.02	0.23	0.22
20	0.04	0.18	0.20
25	0.065	0.115	0.10
30	0.095	0.025	0.11

3. Optimization Studies

According to the results of optimization, the best performance revealed the scheme with two component lenses with the following parameters. Both components are made of the standard optical crown glass; thickness of both lenses equals 15 mm and that of the air gap between them - 5 mm. The external component is double convex and the internal component has the menisci shape. The distances from the corresponding external surfaces of lenses to the coupling or backward mirror and to the central diaphragm equaled 120 mm.

In the Fig.2 are shown the calculated curves of wave aberration (measured in terms of radiation wavelength λ) across the elementary beams, corresponding to the points with the radii 0, 5..., 30 mm at the coupling mirror. Left curves correspond to the meridional section of beams and right - to the sagittal. Lacking parts of these curves correspond to beam screening by the aperture.

Earlier [1, 2] there was analyzed the influence of various distortions of the elementary beams on its generation. According to our calculations (see the Table) the magnitude of the most dangerous from that point of view astigmatic (toroidal) distortion of all beams did not exceed 0.1λ , while its defocusing (spherical aberration of first order) - 0.3λ . At the same time, the transverse shift of the beam, resulting in its screening did not exceed 0.2 of its diameter.

One can see also, that two main sources of energy losses - astigmatism and screening (both rather small), are of complementary character, thus additionally equalizing generation properties of various beams. So the conclusion can be drawn, which is confirmed by the experiment, that energy losses, caused by intracavity optics in the designed cavity would not be too large (some 20-30% per round pass along the cavity) and would be more or less uniform across the overall field of cavity vision.

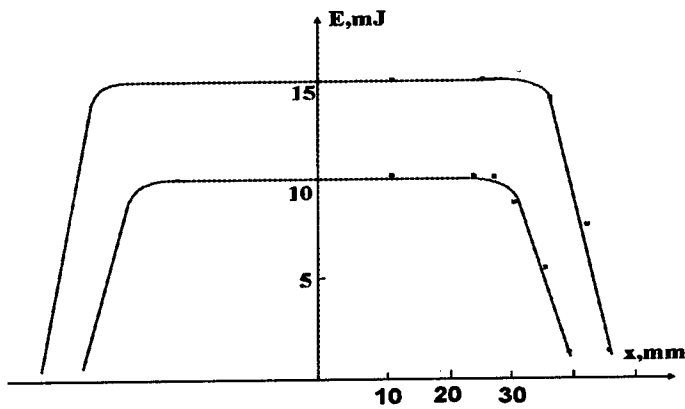


Fig.4. Experimental dependence of laser energy output vs. position of pinhole across the coupling mirror aperture.

Practical realization of the designed cavity had to take into account technology requirements.

1. Much cheaper variant of any optical system is the one using not the best from the point of view of numerical design curvatures of optical surfaces, but the closest to them values from standard sequence. Numerical simulation of the system, in which the above said figures were replaced by standard values did not result in significant (not more than 10%) aggravation of the above said parameters. 2. Simulation of such production errors as longitudinal and transverse dispositions of optical surfaces, has revealed that the designed system falls into the range of optical systems, permitting the use of the most rude optical standard, when all the dispositions of all surfaces (i.e. improper thickness of components and gaps, centering of component and mutual centering of its surfaces) can be as high as 0.2 mm. In this case one can use the cheapest production technology and the simplest design of two component lens.

This cavity was realized in the experiment. Small size Nd:YAG active element, pumped by the alexandrine laser radiation, was mounted in the central zone of the cavity. The pinhole, simulating the opened cell of SLM, was moved across the coupling mirror aperture. In the Fig.3 for two levels of pumping is shown the dependence of the laser output vs. this pinhole position across the cavity. One can see good stability of laser output, as predicted by above numerical simulation results.

4. Summary

1. We have elaborated the laser cavity, providing beam scanning across the field of vision of several hundred scanning elements. In fact, small reduce of LC SLM cell transverse size (which, in fact, can be done less than 100 mm) and some increase of the active element diameter promise the realization of scanning laser, meeting the standard TV scanning parameters.

2. We have succeeded in the reduce of the specifically cavity problem down to the effective optical problem, providing the possibility of application of standard optical design methods to the optical resonator problems.

3. This work was done during the course of an investigation carried out under the partial sponsorship of DRA of the UK. Permission to publish is gratefully acknowledged.

5. References

1. Mak, A.A., Kornev, A.F., Pokrovsky, V.P., Soms, L.N. and Stupnikov, V.K. (1993) Precise addressing of laser beams, *Proceedings of SPIE*, **1864**, 17-30.
2. Kornev, A.F., Pokrovsky, V.P., Soms, L.N. and Stupnikov, V.K. (1994) Laser systems with internal scanning, *Journal of Optical Technologies*, **61**, #1, 9-19.
3. Warde, C. and Fisher, A.D. (1987) Spatial light modulators: applications and functional capabilities, in J.L.Homer (ed) *Optical Signal Processing*, Academic Press, NY, 1987, pp.477-523.
4. Gan, M.A. et al (1992) *Optical Engineering*, **31**, p.639-700.

PART III: OPTICS

BEAM QUALITY AND EFFICIENCY OF ANNULAR GAIN LASERS

NORMAN HODGSON

Universität Potsdam

Institut für Physik

Am Neuen Palais 10

14469 Potsdam, Germany

Abstract

In high power lasers the maximum output power is limited by the efficiency of heat removal. In general, the cooling becomes more efficient if a geometry of the active medium is chosen that provides a high surface to volume ratio. If the gain medium is shaped as an annulus, a much larger cooling surface can be obtained than for a cylindrical medium of equal volume. Therefore, the maximum output power per length can be increased by one order of magnitude. Although the annular geometry is very well suited to provide high output powers and high efficiencies, this concept has not yet found commercial application. The main problem is the realization of a good beam quality without decreasing the efficiency too much. In this paper an overview of the properties of annular laser resonators applicable to commercial systems is given.

1. Introduction

In high power lasers the maximum output power is limited by the efficiency of heat removal. For sealed-off CO₂ lasers in cylindrical geometry, the temperature rise reduces the maximum output power per length to about 80W/m, independent of the tube diameter. In solid state laser materials, the pump induced stress causes irreversible damage to the medium if the pump power is increased beyond the fracture limit. For flashlamp pumped Nd:YAG rods, the fracture limit corresponds to maximum output powers between 40 and 45W per cm of rod length, depending on the crystal quality and the pumping conditions.

Lower temperatures and higher fracture limits can be attained by choosing a geometry of the gain medium that exhibits a larger surface to volume ratio than the cylindrical geometry. It is clear that annular active medium provides a much larger cooling

surface than a rod of equal volume. If a and b denote the inner and outer radii of the annulus, respectively, and the wall thickness is much larger than the inner radius, the maximum output power P_A that can be extracted from an annular gain medium reads:

$$P_A = P_R k \frac{b+a}{b-a} \quad (1)$$

where P_R is the maximum output power attainable for a rod (or gas tube) of equal length, and $k=1.5$ for solid state lasers and $k=2$ for gas lasers. For an inner radius of 30mm and a wall thickness of 5mm, an annular gas medium provides a 26 times higher output power per length compared to a conventional tube. Annular gain media have been realized in dye lasers and He-Xe lasers [6,12], HF lasers [9], CO₂ lasers [8,10,16,27,39,46], Nd:glass lasers [5], and Nd:YAG lasers [33,34,37,38,47] (Fig.1).

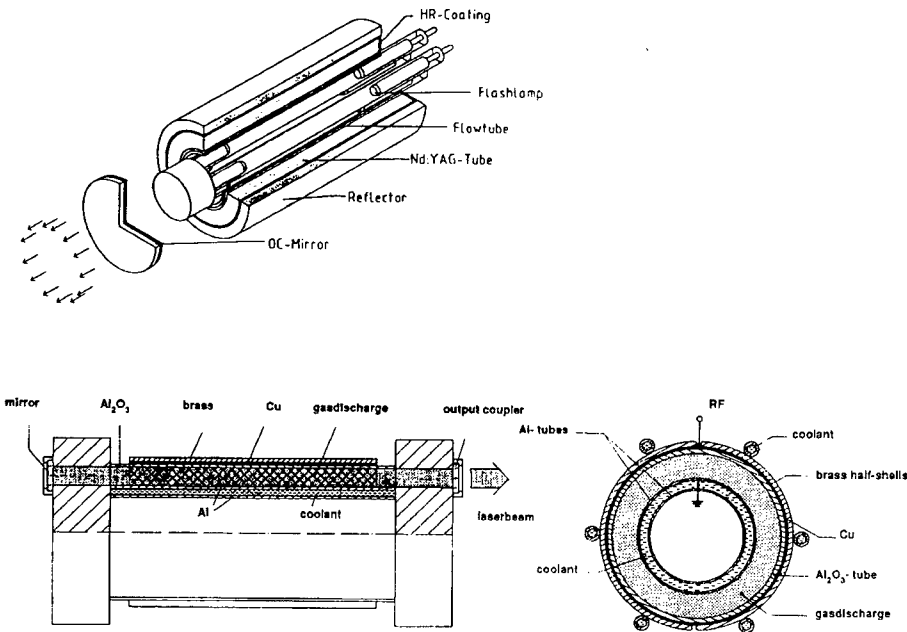


Figure 1. a) Nd:YAG laser [33] and b) CO₂ laser in annular geometry [26].

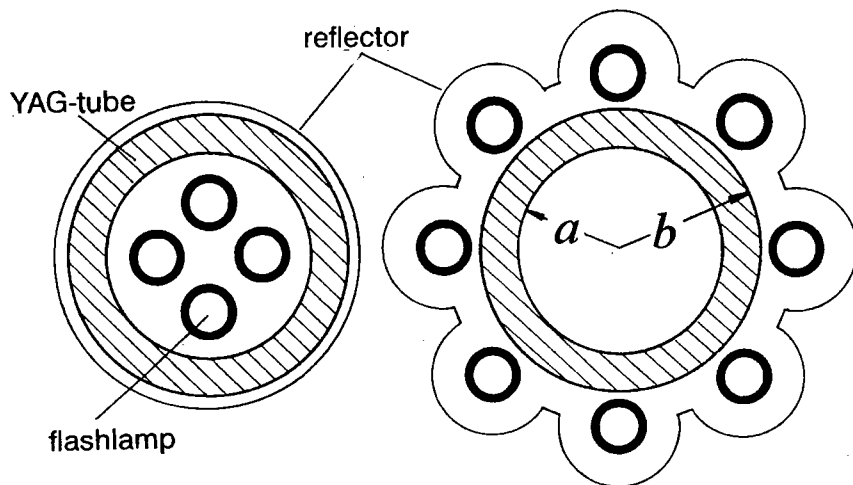


Figure 2. Pump geometries for flashlamp pumped solid state tube lasers.

For solid state lasers, another advantage of the tube geometry is the higher excitation efficiency if the flashlamps are located inside the tube (Fig.2). Since the light has to go through the active material first before being reflected by the pump cavity, a higher fraction of the flashlamp power is absorbed by the gain medium. Experiments showed that the increase in efficiency can be as high as 100%[47]. Furthermore, the large outer surface enables one to arrange many flashlamps around the tube resulting in a compact laser head that is capable of providing output powers in the multi kW range. Although the tube geometry is very well suited to provide high output powers and high efficiencies, this concept has not yet found commercial application. This is not only due to the more sophisticated, and therefore more expensive, laser head design. The main problem of the annular geometry is the realization of good beam quality without decreasing the output power too much. A variety of optical resonators suitable for annular gain media have been studied in the last two decades. Nevertheless, none of these resonator schemes are capable of providing beam properties that would justify a replacement of commercial rod or slab lasers. In weapons research, however, annular gain lasers have been used to realize high power chemical lasers with output powers in the MW range. Unfortunately, the resonator schemes used here (unstable resonator schemes) are too complex to be applicable to commercial systems [9,11-19]. In the following, an overview of the performance of annular resonator schemes that allow an incorporation into commercial lasers is given.

Considering the more sophisticated laser head, an annular gain laser must provide higher efficiencies and higher beam qualities than existing commercial products.

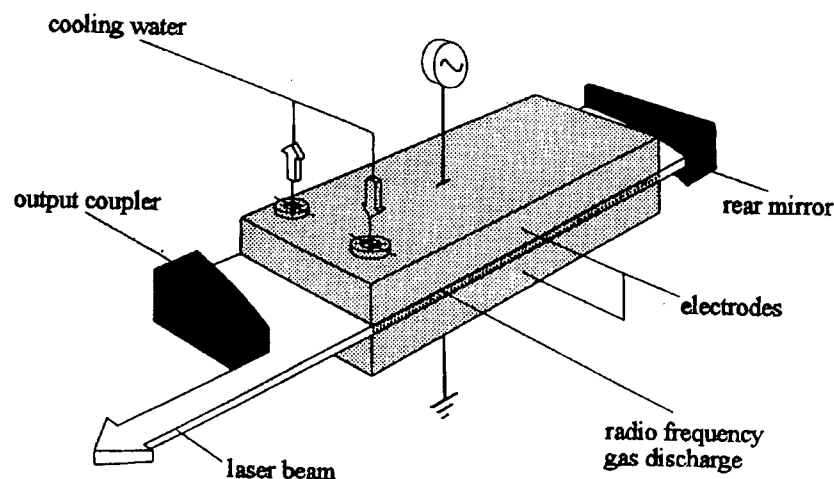


Figure 3. CO₂ waveguide slab laser with off-axis unstable resonator [49].

At present, flashlamp pumped Nd:YAG rod lasers are available that provide output powers of up to 3kW at total efficiencies of 4% and maximum beam parameter products of 25 mm mrad ($M^2=75$). In the case of CO₂, an annular version has to compete with the waveguide slab laser which exhibits maximum output powers of 2kW with an overall efficiency of 10% and beam propagation factors M^2 around 1.5 (Fig.3).

2. Stable Resonators with Toric Mirrors

Resonators with toric mirrors exhibit mode structures similar to those of conventional spherical mirror resonators. Both mirrors exhibit a radius of curvature ρ_i in the radial direction and are flat in the azimuthal direction (Fig.4). Both stable and unstable resonators can be realized [8,21]. The resonator properties are determined by the g -parameters $g_i = 1 - L/\rho_i$, the effective resonator length L , the inner radius a , and the wall thickness of the tube $d = b - a$. If the toric mirror is unwound, a one-dimensional strip resonator is obtained (Fig.3). The circumference of the annular mirrors is now represented by the height of the cylindrical mirrors. For large vertex radii r_0 , the radial modes of the unconfined stable toric resonator can therefore be approximated by one-dimensional Gauss-Hermite modes. In this so-called slab-approximation, the mode diameter and the number of oscillating radial modes can be calculated using the well-known relations for conventional spherical resonators in rectangular symmetry.

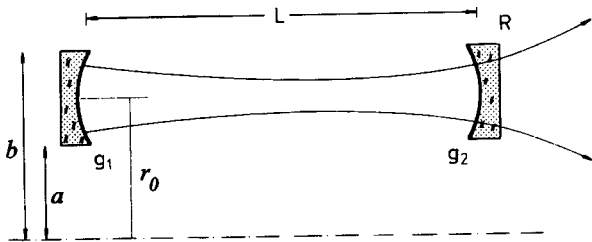


Figure 4. Stable resonator with toric mirrors (cross sectional view).

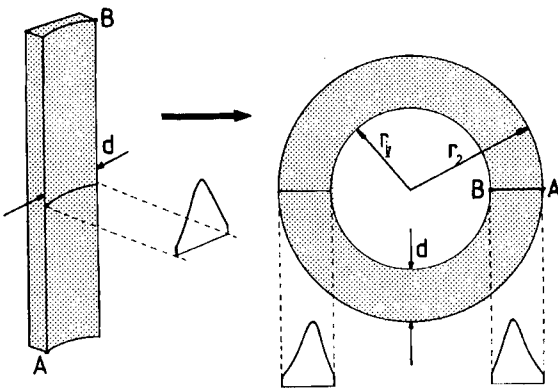


Figure 5. A toric mirror is generated by bending a cylindrical mirror. For vertex diameters $r_1 + r_2$ that are much larger than the mirror width d , the radial mode structures of toric resonators are similar to those of resonators in rectangular geometry.

However, in general the vertex radius is not large enough to neglect the influence of the bending on the mode structure. In this case, the radial intensity distributions of the modes are slightly shifted inwards (Fig.5). An analysis of the diffraction integral shows that if both mirrors are unconfined, the field distributions of the transverse eigenmodes of passive toric mirror resonators can be calculated analytically [29,36]. In polar coordinates, the field distributions read:

$$E_{p\ell}(r, \phi) \propto \frac{1}{\sqrt{r}} \exp \left[-\frac{(r-r_0)^2}{w_0^2} \right] H_p \left[\frac{\sqrt{2}(r-r_0)}{w_0} \right] \exp [\pm i\ell\phi] \quad (2)$$

where p, ℓ are the radial and the azimuthal mode index ($p, \ell \geq 0$), respectively, r_0 is the radius of the mirror vertex, w_0 is the Gaussian beam radius, and $H_p[x]$ is the Hermite polynomial of order p . Note that for large vertex radii r_0 and small beam diameter, the influence of the factor $1/\sqrt{r}$ on the mode structure becomes negligible. This is the mathematical representation of the slab approximation.

If both mirrors are unconfined, the beam radius of the transverse modes depends only on the radial mode order p . Thus, the transverse modes are highly degenerate and the simultaneous oscillation of on the order of a hundred azimuthal modes is to be expected. This also holds true if the mirrors are limited by annular apertures. The azimuthal mode discrimination remains weak, although the radial mode structure now depends on the azimuthal index [39]. The radial mode profile is shifted outward as the azimuthal mode index is increased, resulting in an increase in the diffraction losses (Fig.6). In general, the azimuthal mode discrimination increases with the mirror curvature and the mode with $\ell=0$ experiences the lowest loss if the mirror vertex is in the center of the annular gap. However, the losses are nearly degenerate for low order modes. The loss minimum can be shifted towards higher azimuthal orders if the radius r_0 of the mirror vertex is chosen smaller than the radius $(a+b)/2$ of the gap center. This will improve the azimuthal mode discrimination, but, unfortunately, will also prevent circularly symmetric modes ($\ell=0$) from oscillating. This is a major drawback because only the modes with $\ell=0$ exhibit a centered intensity profile in the far field.

The beam quality of toric stable resonators is determined by the mode with the highest radial mode order p and only slightly depends on the azimuthal structure. Similar to conventional resonators, the highest mode order can be found by adapting the beam diameter to the gap width of the annular aperture:

$$w_{00}\sqrt{p+1} \approx \frac{b-a}{2} \quad (3)$$

where w_{00} is the Gaussian beam radius at the aperture.

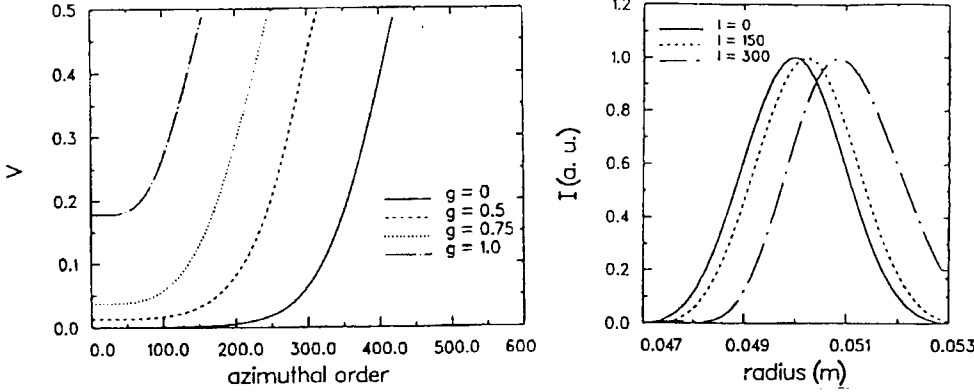


Figure 6. Calculated diffraction losses per round trip for the fundamental radial mode ($p=0$) of symmetric toric resonators as a function of the azimuthal mode order. The curve parameter is the g -parameter of the mirrors. The mirror vertex is centered with the annular gap. The right graph shows the radial intensity distribution for $g=0.5$ and different azimuthal orders. Vertex radius $r_0=50\text{mm}$, resonator length $L=1\text{m}$, wavelength $\lambda=10.6\mu\text{m}$, gap width $b-a=6\text{mm}$ [39].

The beam waist w_p of this radial mode and the corresponding half angle of divergence θ_p can then be directly calculated using the known expressions for spherical resonators. However, the waist radius w of the laser beam is given by the outer radius of the annular intensity distribution and not by the radius w_p of the mode profile in the annular gap. For a given mode order, the beam parameter product, therefore, is higher than for conventional resonators. In a geometrical approximation, the laser beam waist radius is larger than the waist radius of the radial mode in the annular gap by the factor $2b/(b-a)$, where a, b are the inner and the outer radii of the annular aperture, respectively. Thus, the beam parameter product can be approximated by:

$$w\theta = \frac{2b}{b-a} w_p \theta_p = (p+1) \frac{2b}{b-a} \frac{\lambda}{\pi} \quad (4)$$

where θ is the half angle of divergence. Figure 7 presents calculated radial intensity distributions in the near field and the far field of the fundamental mode for a toric resonator with different inner diameters of the annulus. The annular shape of the near field generates a high power content in the side lobes of the far field. An on-axis

intensity maximum in the far field is only found for modes without azimuthal structure ($\ell=0$). For higher azimuthal orders, the far field intensity distribution remains annular since all waves originating from the annular medium interfere destructively on the optical axis. Considering the lack of azimuthal mode discrimination, it is no surprise that measured far field intensity distributions of toric resonators generally contain most of the power in an annular ring (see Fig. 11).

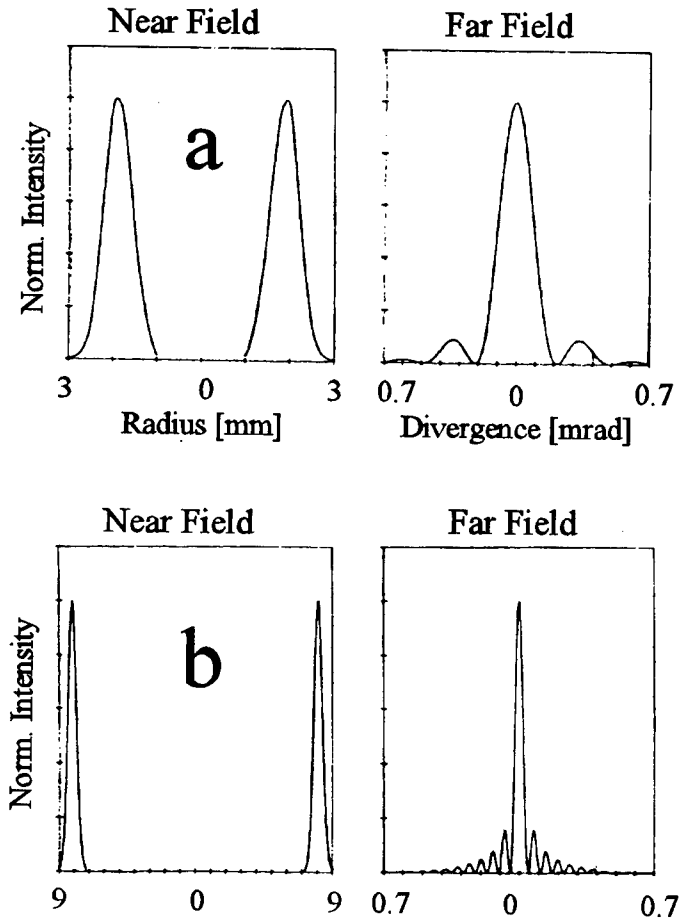


Figure 7. Calculated intensity distributions of the TEM_{00} mode for a semi-confocal toric resonator ($g_1=1$, $g_2=0.5$, $L=0.5m$, $\lambda=1.06\mu m$). The normalized intensity distributions at the flat mirror and in the far field are shown for two different tube dimensions. a) $a=1mm$, $b=3mm$, b) $a=7mm$, $b=9mm$.

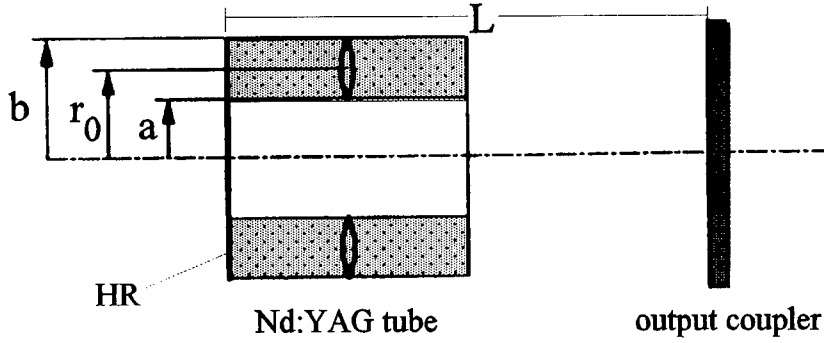


Figure 8. Schematic of pumped solid state tube laser with an internal thermal lens. The left endface of the tube is HR coated.

If an internal variable lens is induced due to the pumping process, the beam quality can be calculated using the standard lens resonator model. For the Nd:YAG tube laser depicted in Fig.1, the thermal lens in combination with the flat HR mirror can be replaced by a toric mirror with radius of curvature $1/D$ where D is the dioptric power (Fig. 8). The Gaussian beam radius at the HR mirror is given by:

$$w_0^2 = \frac{\lambda}{\pi} \sqrt{\frac{L}{D(1-DL)}} \quad (5)$$

where L is the geometrical resonator length. To a good approximation, the beam propagation factor can now be calculated using:

$$M^2 = \left[\frac{b-a}{2w_0} \right]^2 \frac{2b}{b-a} \quad (6)$$

For a 100mm long, flashlamp pumped Nd:YAG tube with an inner diameter of 35mm and an outer diameter of 53mm an average dioptric power of 0.08 m^{-1} per kW of pump power was measured. This laser provided a maximum output power of 1kW at a total efficiency of 6.7%. For this system, the beam parameter products calculated with Eqs. 5 and 6 for different resonator length are shown in Fig. 9 as a function of the mean electrical pump power. The calculated beam parameter products show a good agreement with the measured ones. Measured output powers and beam parameter products $M^2\lambda/\pi$ for a longer tube (130mm, $a=17.5\text{mm}$, $b=26.5\text{mm}$) are shown in Fig. 10. The last two figures clearly show that the beam quality of the Nd:YAG tube laser is several times worse as compared to that of Nd:YAG rod lasers.

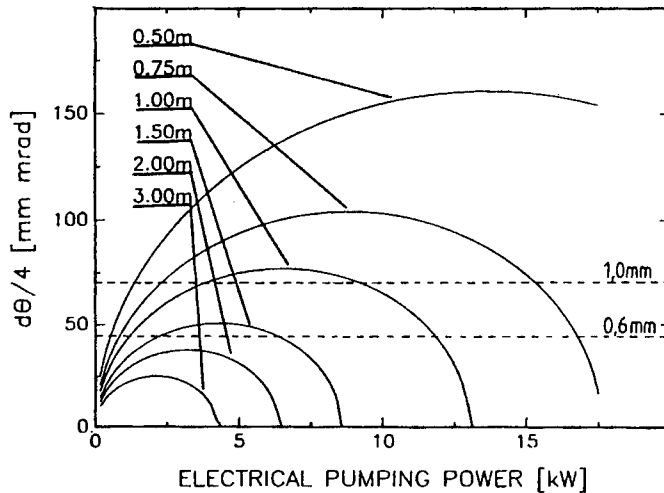


Figure 9. Calculated beam parameter products (beam radius \times half angle of divergence) for an inside pumped Nd:YAG tube laser [34]. Curve parameter is the resonator length.

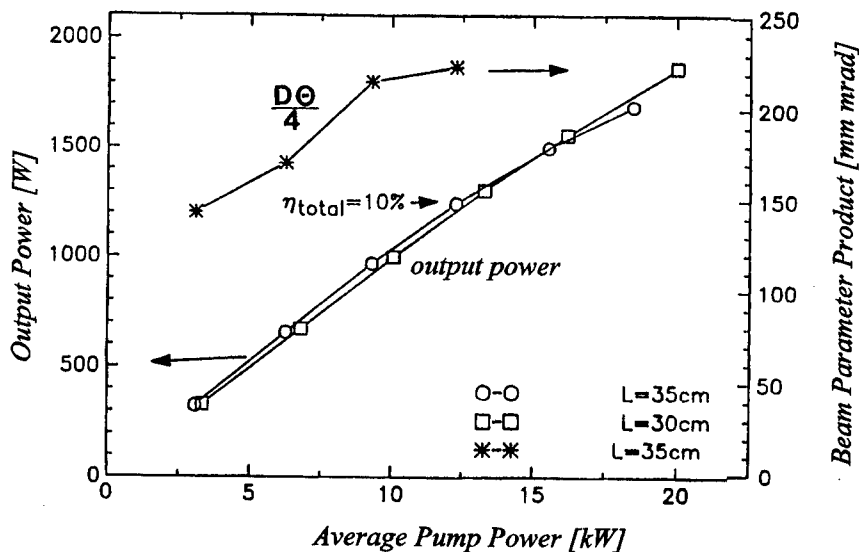


Figure 10. Measured output power and beam parameter products versus the electrical pump power for a flashlamp pumped Nd:YAG tube laser with a tube length of 130mm, an inner diameter of 35 mm and an outer diameter of 53 mm. A flat output coupler and different resonator lengths L were used [47]. Pump energy: 800 J, pump pulse duration: 2 ms.

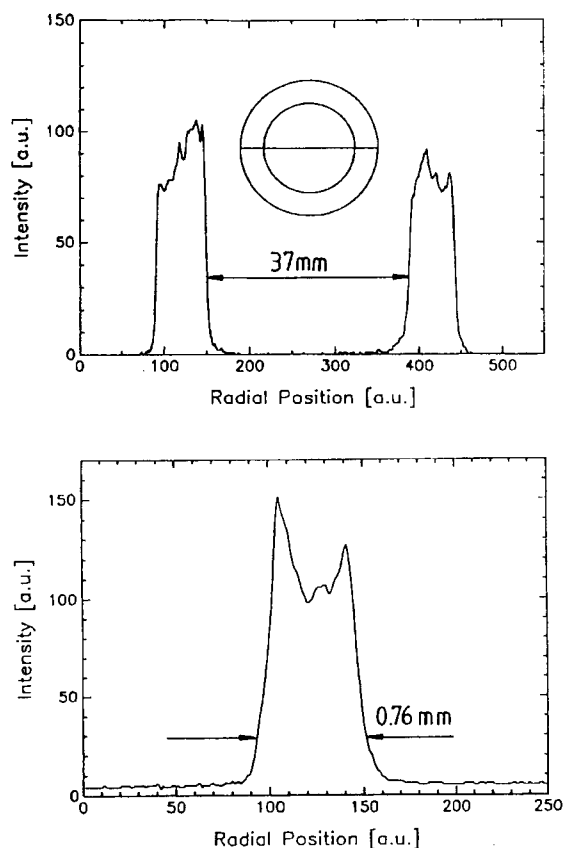


Figure 11. Recorded radial intensity profiles in the near field and the far field of a Nd:YAG tube laser with a flat-flat resonator (tube dimensions: $a=17.5\text{mm}$, $b=26.5\text{mm}$, tube length: 100mm , resonator length: 1.2m). The equivalent resonator is toric due to the thermal lensing of the tube. The far field was recorded in the focal plane of a 200mm lens. The beam parameter product is 50 mm mrad (pump power: 3kW , output power: 200W) [34].

The beam quality of annular laser beams can be improved by reducing the diameter of the central hole without increasing the beam divergence. This is not in contradiction with Liouville's Theorem because the area in phase space is not decreased. The removal of the central hole can be accomplished by an axicon telescope, as shown in Fig. 12. The beam parameter product is reduced by the same factor as the outer beam diameter. However, the axicon telescope only preserves the beam divergence if the azimuthal mode index is low. Unfortunately, in both YAG and CO_2 annular lasers, several hundred azimuthal modes may oscillate which means that this concept will not improve the beam quality. Calculated beam parameter products with and without the axicon telescope are presented in Fig. 12. This figure indicates that the beam quality will only be significantly improved if the azimuthal mode order is lower than about twice the radial mode index. Note that without the axicon telescope, the beam parameter product is almost independent of the azimuthal mode order.

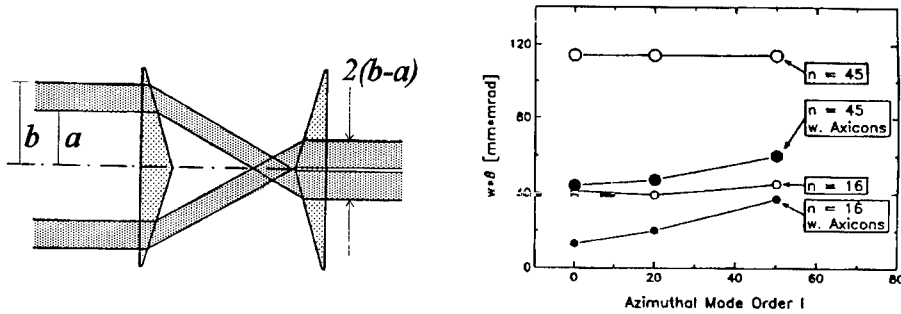


Figure 12. Calculated reduction of the beam parameter product for an annular beam of a stable toric resonator with inner radius $a=17.5\text{mm}$ and outer radius $b=26.5\text{mm}$ as a function of the azimuthal mode order l . The results for two different radial mode orders n , both with and without the axicon telescope, are shown. The beam parameter product is defined via the 86.5% power content (numerical calculation using diffraction integrals) [48].

In summary, toric resonators are not very suitable for annular gain lasers due to the low azimuthal mode discrimination. Even if fundamental mode operation in the radial direction can be attained (like in CO_2 lasers), the oscillation of higher order azimuthal modes results in an annular far field. Furthermore, due to the annular shape of the near field, the beam parameter product is an order of magnitude higher than for a conventional Gaussian beam. The goal of annular resonator design, therefore, is to break the circular symmetry of the near field by generating a compact output beam.

3. Herriott Cell Resonators

A common resonator used in annular CO_2 lasers to extract the power in a compact, low order transverse mode is the Herriott cell resonator [2,24,26,27,32]. The Herriott cell can be viewed as a folded, linear resonator that generates multiple passes through the medium (Fig. 13). The two high reflecting spherical mirrors with off-axis apertures form an optical delay line. The number of reflections and the orientation of the beams can be controlled by the mirror curvatures, the mirror distances, the location of the apertures, and the inclination of the incident beam [1,15,30]. In general, the reflected beams trace an elliptical curve on each mirror, but for special geometries the beams

lie on a surface of a hyperboloid of revolution and the intersecting points move around the mirror in a circular pattern [1,2,15,30]. The number of reflections can be increased by increasing the radius of curvature of the mirrors. There are several constraints in the design of Herriott cell resonators. The beam diameter has to be adapted to the wall thickness of the tube and with each round trip in the Herriott cell, and the beam has to be shifted in the azimuthal direction by slightly more than its diameter. Furthermore, laser oscillation between the two high reflecting folding mirrors has to be prevented by inserting a multi-segment aperture that generates losses for fields that do not propagate along the intended beam path. The output power of optimized Herriott cell resonators typically is much lower as compared to resonators with toric or spherical mirrors. This is due to diffraction losses generated at the apertures and the incomplete filling of the gain medium. Furthermore, wavefront aberrations induced by the active medium sum up due to the high number of transits, resulting in increased diffraction losses. It is for these reason, that Herriott cell resonators have not found application in commercial laser systems. As an example, Fig. 14 presents measured beam propagation factors and output powers of the Nd:YAG tube laser of Fig. 10 for a Herriott cell resonator with 14 reflections at the mirrors. Although the beam quality now is comparable to conventional rod lasers, the total efficiency is decreased to only 2%. With a second Herriott cell that provided a higher fill factor, the efficiency could be increased to 4%, but the resonator went unstable at pump powers above 4.2kW limiting the maximum output power to 160W [47].

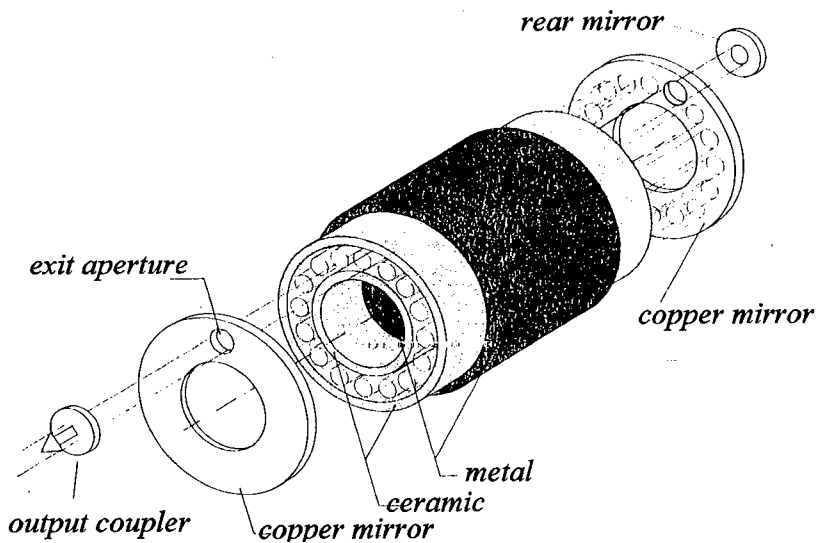


Figure 13. Herriott cell resonator for an annular CO₂ laser [26].

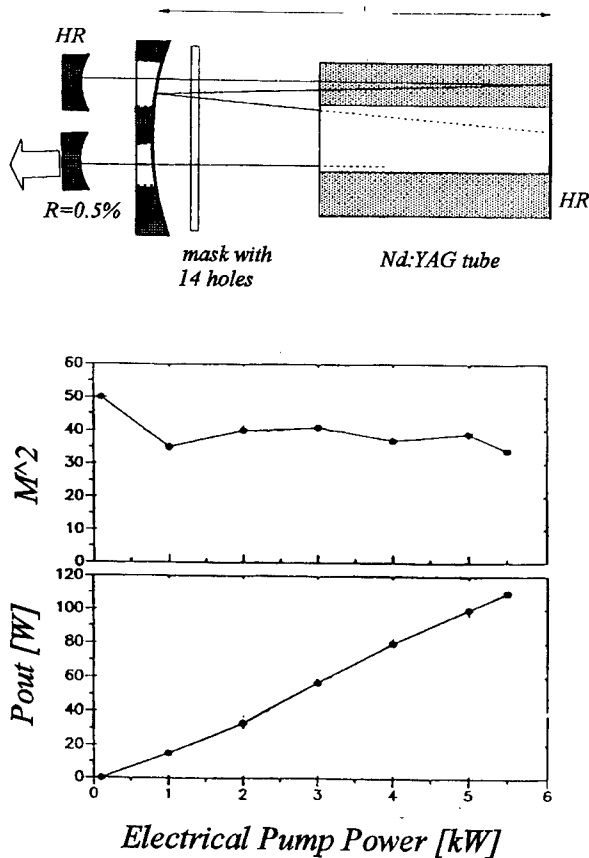


Figure 14. Measured output power and beam propagation factor as a function of the electrical pump power for the inside pumped Nd:YAG tube laser of Fig.10 using a Herriott cell resonator. The resonator length is 1m and the folding mirror has a radius of curvature of 20 m [47].

4. Azimuthally Unstable Resonators

Similar to stable resonators, toric unstable resonators provide poor azimuthal mode discrimination. This is due to the resonator working unstable in the radial direction only. Improved mode properties should thus be expected if the azimuthal direction is chosen as the unstable direction [43,46]. Such an azimuthally unstable resonator can be obtained by winding an off-axis unstable resonator around the optical axis, as shown in Fig. 15. In the radial direction either a flat-flat or a stable resonator can be chosen since the radial dimension of the annulus is usually small enough to limit the radial mode order to low values. Instead of using a parabolic mirror surface in the azimuthal direction, near diffraction limited beam quality can also be achieved with a helical output coupling mirror [43,46].

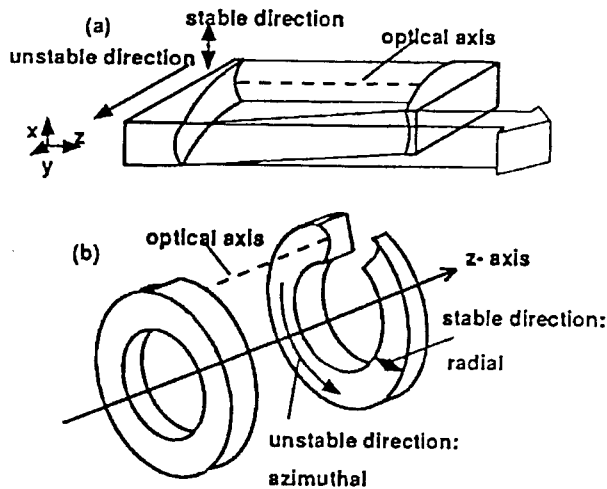


Figure 15. Azimuthally unstable resonator (b). If the resonator is unwound, a one-dimensional off-axis unstable resonator is obtained (a) [43].

The set-up of a helical resonator is similar to that shown in Fig. 15, except that the output coupling mirror has a constant slope in the azimuthal direction. In a geometrical model, the rays in the resonator are driven towards the output coupling aperture by the helical surface. However, the resonator is not unstable in the usual sense. Since the helical mirror is the annular version of a tilted flat mirror, the output coupling losses are given by the diffraction losses of a misaligned stable resonator and no geometric optics approximations for the mode structure exist like for unstable resonators. The output coupling can be increased with the slope of the helical mirror. For CO_2 lasers, typical slopes are on the order of $10\mu\text{m}/2\pi$. Measured and calculated intensity profiles in the near and the far field of a helical mirror CO_2 laser resonator are presented in Fig. 16. This resonator provided a maximum output power of 1,100W (the maximum total efficiency of 9% was attained at 450W) and beam parameter products close to the diffraction limit [41]. Note that for both resonator concepts, the output beam is highly astigmatic and beam shaping is necessary to generate round focus spots.

The application of azimuthally unstable resonators is currently limited by the fabrication of the resonator mirrors. For mid- to far-infrared lasers, the mirrors can be made of metal and flexible diamond turning techniques are available that are capable of generating nonrotationally symmetric surfaces. However, it is difficult to achieve

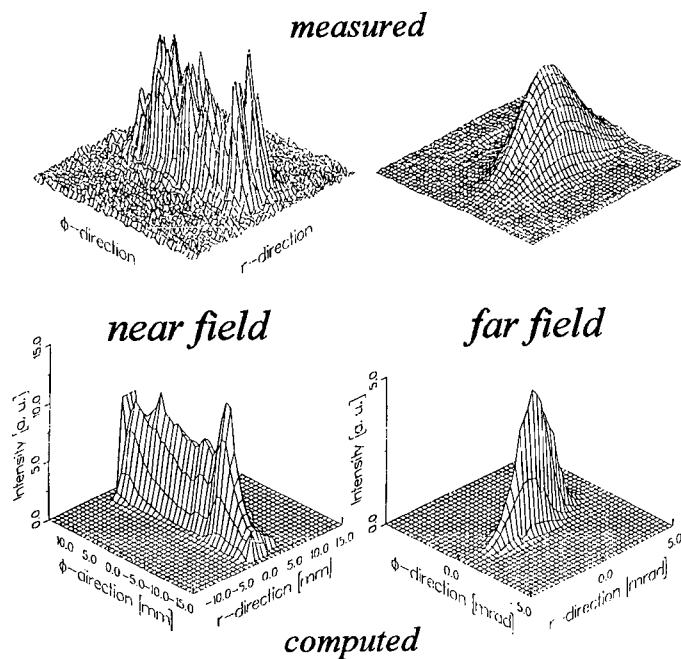


Figure 16. Measured and calculated intensity distributions in the near field and the far field of an annular resonator with a helical output coupling mirror. Resonator length: 1.36m, discharge length: 1.15m, inner radius $a=48\text{mm}$, outer radius $b=55\text{mm}$ [46].

optical surface quality and a commercial availability of these mirrors is not yet in sight. In the visible and the near-infrared spectral region, where glass is the preferred substrate material and a tighter tolerance on the surface roughness must be met, no successful manufacturing of toric or helical mirrors with optical quality has been reported yet.

An alternate annular resonator scheme that uses mirrors which are already available and that provides near diffraction limited beam quality is the tilted annular resonator as depicted in Fig. 17 [42]. Instead of a helically shaped mirror, a tilted toric or flat output coupling mirror is used. By using two flat mirrors, this resonator concept is also applicable to solid state lasers (Fig. 19). Similar to the helical resonator, the intracavity rays are guided towards the output coupling aperture. Unfortunately, no discrimination between the positive and the negative azimuthal direction is provided. Consequently, two nonparallel beams emerge from the aperture (Fig. 18). In order to achieve unidirectional operation, one of the beams can be reflected back into the resonator with an external mirror. Two times diffraction limited beam quality at a maximum output power of 700W (7% total efficiency, discharge length: 1.15m,

$a=48\text{mm}$, $b=55\text{mm}$) was reported for a diffusion-cooled CO_2 laser utilizing a tilted toric resonator [42]. By increasing the discharge length to 1.8m a similar resonator provided a maximum output power of 2kW at a total efficiency of 10% [46].

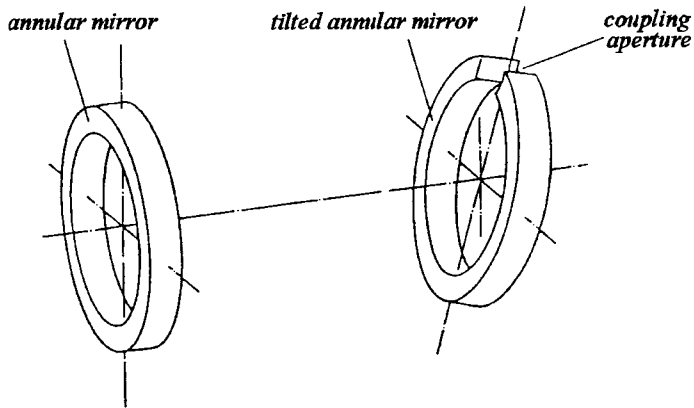


Figure 17. Annular resonator with toric mirrors and an off-axis output coupling aperture. The tilt of the output coupling mirror induces a bidirectional azimuthal energy flux towards the aperture [42].

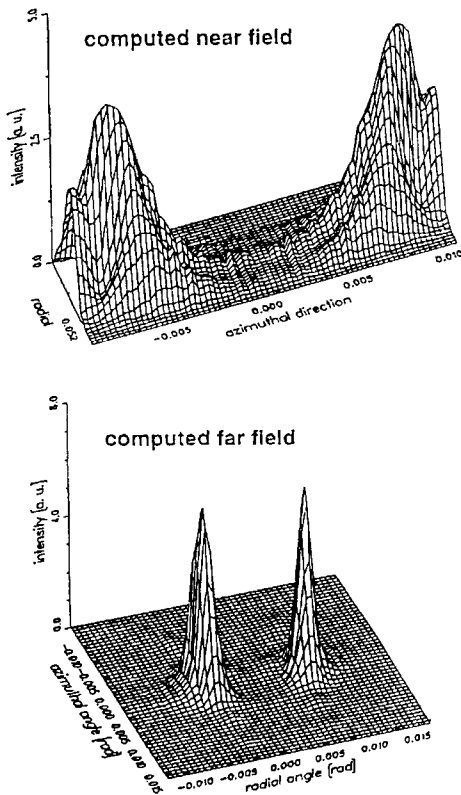


Figure 18. Calculated near and far field intensities of a tilted annular resonator. The wave vectors of the two beams are not parallel, resulting in two peaks in the far field [42].

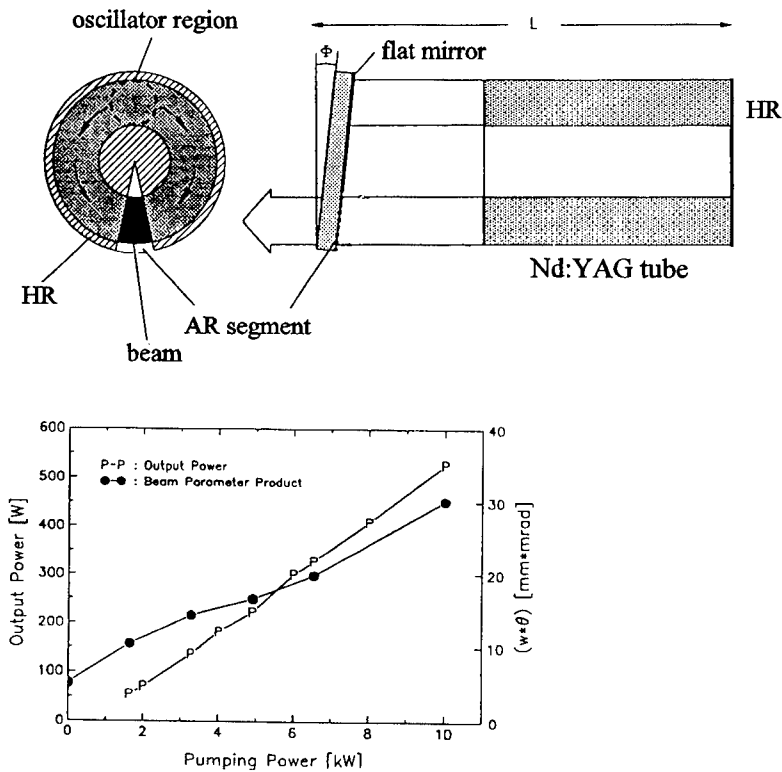


Figure 19. Measured output power and beam parameter product (beam radius \times half angle of divergence) of the Nd:YAG tube of Figs. 1 and 10 using an azimuthally unstable resonator with tilted flat mirrors [47].

5. Summary and Conclusion

The annular geometry provides output powers per gain length that are several times higher than compared to conventional rod and tube lasers. For sealed-off CO_2 lasers, the output power could be increased from 80W per meter of discharge length to 1,100 W/m. For solid state lasers, the possibility of pumping the active medium from the inside leads to an increase of the efficiency by more than a factor of 2. With a 130mm long Nd:YAG tube pumped by four Krypton flashlamps a total efficiency of 10% and an output power of 1.86kW was attained. Commercial Nd:YAG rod lasers in the kW range provide maximum efficiencies that are hardly higher than 4%. The length-scaling of the output power was increased from 40W/m (Nd:YAG rod) to 140 W/m. For both Nd:YAG and CO_2 lasers, the best trade-off between efficiency and beam

quality was obtained with tilted toric or tilted flat-flat resonators. In this resonator scheme, the laser beam is coupled out through an AR coated segment of a tilted HR mirror. By using these resonator schemes, the overall performance of annular laser systems becomes comparable to that of existing commercial multi rod Nd:YAG lasers and CO₂ waveguide slab lasers. Table 1 summarizes the results obtained with different annular lasers. Considering the more sophisticated laser head design as well as the higher misalignment sensitivity, a commercialization of lasers with an annular gain medium will only happen if a more suitable resonator design can be found.

TABLE 1. Output power, total efficiency, and beam propagation factor of inside pumped Nd:YAG and sealed-off CO₂ lasers in annular geometry. The dimensions shown are the inner radius a, the outer radius b, and the pumped length.

Laser	resonator	P_{out} [W]	η_{tot} [%]	M^2	Ref.
Nd:YAG 17.5mm, 26.5mm, 101mm	stable toric	1,000	6.7	300	[33]
Nd:YAG 17.5mm, 26.5mm, 130mm	stable toric	1,860	10	500	[38]
Nd:YAG 17.5mm, 26.5mm, 130mm	tilted flat-flat with aperture	540	5.4	90	[47]
Nd:YAG 17.5mm, 26.5mm, 130mm	Herriott cell	160	4.0	30	[47]
CO ₂ 25mm, 28.5mm, 400mm	tilted flat-flat with aperture	700	7.0	2	[42]
CO ₂ 48mm, 55mm, 1,150mm	helical, unstable	450	9.0	4	[46]
CO ₂ 48mm, 55mm, 1,150mm	tilted toric with aperture	1,100	12	2	[46]
CO ₂ 48mm, 55mm, 1,800mm	tilted toric with aperture	2,000	10	2	[46]

6. Acknowledgments

The author is gratefully indebted to Peter Loosen of the Fraunhofer Institut für Lasertechnik, Aachen, and to Horst Weber of the Technical University Berlin for helpful discussions and their support in preparing this paper.

7. References

1. J.R. Pierce, Theory and Design of Electron Beams. New York: Van Nostrand: 1954, pp. 194-197
2. D. Herriott, H. Kogelnik, R. Kompfner, Off-axis paths in spherical mirror interferometers, *Appl. Opt.* **3**, 523, 1964
3. H. Kogelnik, T. Bridges, A nonresonant multipass CO₂ laser amplifier, *IEEE J. Quantum Electron.* **QE-3**, 95, 1967
4. R.G. Greenler, Multiple reflection of light between nonparallel reflecting surfaces, *J. Opt. Soc. Am.* **557**, 1062, 1973
5. D. Milam, H. Schlossberg, Emission characteristics of a tube-shaped laser oscillator, *J. Appl. Phys.* **44**, 2297, 1973
6. P. Burlamacchi, R. Partesi, High-efficiency coaxial waveguide dyelaser with internal excitation, *Appl. Phys. Lett.* **23**, 475, 1973
7. L.W. Casperson, Cylindrical laser resonators, *J. Opt. Soc. Am.* **63**, 25, 1973
8. L.W. Casperson, M. Shabbir Shekhani, Mode properties of annular gain lasers, *Appl. Opt.* **14**, 2653, 1975
9. R.A. Chodsko, S.B. Mason, E.F. Cross, Annular converging wave cavity, *Appl. Opt.* **9**, 2137, 1976
10. R.J. Freiberg, D.W. Fradin, P.P. Chenausky, Split-mode unstable resonator, *Appl. Opt.* **16**, 1192, 1977
11. A.H. Paxton, J.H. Erkkila, Annular converging wave resonator: new insights, *Opt. Lett.* **1**, 166-168, 1977
12. P.B. Mumola, H.J. Robertson, G.N. Steinberg, J.L. Kreuzer, A.W. McCullough, Unstable resonators for annular gain volume lasers, *Appl. Opt.* **17**, 936, 1978
13. J.W. Oglund, Mirror systems for uniform beam transformation in high-power annular lasers, *Appl. Opt.* **17**, 2917, 1978
14. D. Fink, Polarization effects of axicons, *Appl. Opt.* **18**, 581, 1979
15. W.R. Trutna, R.L. Byer, Multiple-pass Raman gain cell, *Appl. Opt.* **19**, 301, 1980
16. R.A. Chodsko, S.B. Mason, E.B. Turner, W.W. Plummer, Jr., Annular (HSURIA) resonators: some experimental studies including polarization effects, *Appl. Opt.* **19**, 778, 1980
17. W.P. Latham, Jr., Polarization effects in a half-symmetric unstable resonator with a coated rear cone, *Appl. Opt.* **19**, 1222, 1980
18. J.K. Guha, J.L. Martin, R.A. Mickish, E.E. Pape, Performance of a coated cone in an annular resonator, *Appl. Opt.* **20**, 3089, 1981
19. J.K. Guha, D. Kohler, R. Mickish, J. Martin, E. Pape, P. Briggs, C. Greninger, Performance of an annular resonator with a polarizer in the annular leg, *Appl. Opt.* **20**, 4135, 1981
20. L.W. Casperson, P.M. Schienert, Multipass resonators for annular gain lasers, *Opt. Quantum Electron.* **13**, 193, 1981

21. T.R. Ferguson, M.E. Smithers, Toric unstable resonators, *Appl. Opt.* **33**, 2122, 1984
22. A.H. Paxton, Propagation of high-order azimuthal Fourier terms of the amplitude distribution of a light beam: a useful feature, *J., Opt. Soc. Am. A* **1**, 319, 1984
23. S. Marchetti, Multipass systems with mirrors of different radii, *Optics and Laser Technology* **18**(5), Oct. 1986
24. J.G. Xin, D.R. Hall, Multipass coaxial radiofrequency discharge CO₂ laser, *Opt. Commun.* **58**, 420, 1986
25. V.A. Seguin, H.J.J. Seguin, C.E. Capjack, S.K. Nikumb, H. Reshef, Multiple pass unstable resonator for an annular gain CO₂ laser, *Appl. Opt.* **25**, 3825, 1986
26. H. Schülke, Untersuchungen zur Strahlqualität von hochfrequenzangeregten CO₂-Hochleistungs-lasern, PhD thesis, Technical University Aachen, Germany 1987
27. H. Schülke, G. Herziger, R. Wester, Multipass resonators for laser systems, *Proceedings of the Society of Photo-Optical Instrumentation Engineers* vol. **801**, High Power Lasers: Sources, laser-material interactions, high excitations, and fast dynamics, 45, 1987
28. J.G. Xin, D.R. Hall, Compact, multipass, single transverse mode CO₂ laser, *Appl. Phys. Lett.* **51**, 469, 1987
29. Y. Takada, H. Saito, T. Fujioka, Eigenmode of an annular resonator, *IEEE J. Quantum Electron.* **24**, 11, 1988
30. J.G. Xin, A. Duncan, D.R. Hall, Analysis of hyperboloidal ray envelopes in Herriot cells and their use in laser resonators, *Appl. Opt.* **28**, 4576, 1989
31. J.K. Jabczyński, A diffraction-free resonator, *Opt. Commun.* **77**, 292, 1990
32. A. Duncan, J.G. Xin, D.R. Hall, Herriot cell for large-area gas discharge lasers, *Proceedings of the Society of Photo-Optical Instrumentation Engineers* vol. **1224**, 312, 1990
33. U. Wittrock, H. Weber, B., Eppich, Inside-pumped Nd:YAG tube laser, *Opt. Lett.* **16**, 1092, 1991
34. N. Hodgson, Q. Lü, S. Dong, B. Eppich, U. Wittrock, High power solid state lasers in rod-, slab-, and tube geometry, *Laser und Optoelektronik* **23**(3), 82, 1991
35. U. Habich, A. Bauer, P. Loosen, H.-D. Plum, Resonators for coaxial slow-flow CO₂ lasers, *Proceedings of the Society of Photo-Optical Instrumentation Engineers* vol. **1397**, Eighth International Symposium on Gas Flow and Chemical Lasers, 383, 1991
36. M. Morin, P.-A. Bélanger, Diffractive analysis of annular resonators, *Appl. Opt.* **31**, 1942, 1992
37. U. Wittrock, High power rod slab and tube lasers, NATO ASI, International School of Quantum Electronics, Elba, Italy, September 1992.

38. U. Wittrock, B. Eppich, O. Holst, Internally-pumped Nd:YAG tube laser with 10% efficiency and 1.8kW output power, Conference on Laser and Electro-Optics 1993, CWI 7. Washington: Optical Society of America, 1993
39. D. Ehrlichmann, U. Habich, H.-D. Plum, Azimuthal mode discrimination of annular resonators, *Appl. Opt.* **32**(33), 6582, 1993
40. D. Ehrlichmann, U. Habich, H.-D. Plum, Diffusion-cooled CO₂ laser with coaxial high frequency excitation and internal axicon, *J. Phys. D: Appl. Phys.* **26**, 183, 1993
41. U. Habich, H.-D. Plum, D. Ehrlichmann, P. Loosen, Tilted annular resonator, *Proceedings of the Society of Photo-Optical Instrumentation Engineers* vol. **2095**, 46, 1993
42. D. Ehrlichmann, U. Habich, H.-D. Plum, High-power CO₂ laser with coaxial waveguide and diffusion cooling, *IEEE J. Quantum Electron.* **29**(7), 2211, 1993
43. D. Ehrlichmann, U. Habich, H.-D. Plum, P. Loosen, Stable-unstable resonators for annular gain media, *Proceedings of the Society of Photo-Optical Instrumentation Engineers* vol. **2206**, High power gas and solid state lasers, 54, 1994
44. A. Lapucci, F. Rossetti, P. Burlamacchi, Beam properties of an R.F.-discharge annular CO₂ laser, *Opt. Commun.* **111**, 290, 1994
45. D. Ehrlichmann, U. Habich, H.-D. Plum, Ring resonator for lasers with annular gain media, *Appl. Opt.* **33**(30), 6919, 1994
46. D. Ehrlichmann, U. Habich, H.-D. Plum, P. Loosen, G. Herziger, Azimuthally unstable resonators for high-power CO₂ lasers with annular gain media, *IEEE J. Quantum Electron.* **30**(6), 1441, 1994
47. U. Wittrock, Feldstrukturen, thermooptische Effekte und Wirkungsgrade von Festkörper-Rohrlasern, PhD thesis, Optical Institute, Technical University Berlin, Germany 1994
48. B. Eppich, Resonatoren für Rohrlaser, diploma thesis, Optical Institute, Technical University Berlin, Germany 1991
49. R. Nowack, H. Opower, K. Wessel, H. Krüger, W. Haas, N. Menzel, Diffusion-cooled compact CO₂ high power lasers, *Laser und Optoelektronik* **3**, 68, 1991

UNSTABLE RESONATORS FOR SEMICONDUCTOR LASERS

GREGORY C. DENTE
GCD Associates
2100 Alvarado NE
Albuquerque, NM 87110

MICHAEL L. TILTON
Boeing
Post Office Box 5670
Kirtland Air Force Base, NM 87185

1. Introduction

Semiconductor lasers are incredibly compact and efficient. Although the vast majority of semiconductor laser applications require only a few milliwatts to a few tens of milliwatts of power, there are applications, such as free-space optical communications, for which near-diffraction-limited beams of up to several watts are required. To date, the best single, narrow-contact devices have produced approximately one hundred milliwatts of coherent output power. The problem of attaining higher output power while still maintaining spatial coherence across the output facet has proven to be very difficult. Typical good-beam-quality laser diodes are currently limited to narrow stripe widths of less than six microns. Since facet damage problems limit outputs to less than 10 to 20 mW per micron of stripe-width, good-beam-quality laser diodes are necessarily limited to lower powers.

The simplest method of obtaining higher output powers is to increase the width of the injection contact. However, because of the filamentation tendencies brought on by self-focusing in the semiconductor laser medium, these broad-area devices tend to be spatially incoherent at the output facet, producing lateral far-field divergences that are many times the diffraction limit. Various schemes have been proposed for alleviating these filamentation tendencies. Index and gain-guided arrays were tried by several groups with limited success [1-5]. In addition, more elaborate designs using external-cavity optics for lateral mode control have been tried [6,7]. A promising solution appears to be the use of unstable resonators with semiconductor lasers [8-13,19,20,22]. Unstable resonators can provide excellent mode control for large gain volume lasers [18]. It seems only natural, then, to try one-dimensional unstable resonators for lateral mode control in broad-area semiconductor lasers. Furthermore, the natural lateral divergence of the resonator should counteract the self-focusing tendencies, while allowing the device to operate in a single lateral mode.

Unstable resonators have been used extensively with gas and solid-state lasers, but only

rarely fabricated for semiconductor lasers. In 1979, Bogotov, et al. [8] achieved a half-symmetric unstable design by mechanically polishing the front facet mirror with a nylon thread coated with diamond paste; the typical curved-facet device geometry is shown in Fig. (1). Since then, various groups have used chemical etching techniques to make mirrors in single-stripe GaAs [9-12] and GaInAsP [13] lasers and in GaAs arrays, but few have shown the uniform nearfield or diffraction-limited farfield with high power that motivated the unstable resonator approach [12]. This is due in part to the chemical etching rate, which depends on the crystal plane orientation; it makes smooth, high-quality curved mirrors difficult to produce. Subsequently, researchers used a particular mirror fabrication technique that does not have this disadvantage and is suited to easily varying the mirror curvature: focused ion beam (FIB) micromachining [14,15,21,22]. The FIB system focuses a high-energy beam of gallium ions on to a small spot to sputter away material in a highly controllable fashion. This technique has the advantages of being maskless and sample orientation-independent, thereby avoiding the problems encountered with wet chemical etching. However, this method is not well suited to batch production. To circumvent this last problem, researchers developed the regrown-lens train (RLT) class of unstable resonator semiconductor laser [23,24]. These devices use closely spaced lenses that are etched and regrown into the epitaxial cladding layer. These negative power lenses create an essentially continuous unstable resonator, as illustrated in Fig. (2).

The following section, 2, presents a discussion of the geometric properties of the unstable half-symmetric resonator used in facet-mirror devices. Section 3 presents the geometrical analysis of the RLT laser. Section 4 discusses the upgrades in analysis required to move from simple geometrical theory to a relatively complete description of on-the-chip wave propagation as well as gain and carrier diffusion models. Section 5 will discuss some theoretical results obtained from both our geometrical and diffractive models. These first five sections review unstable resonator technology for semiconductor lasers. The next section, 6, presents new material relating to the mode-formation process as the laser approaches threshold. Finally, Section 7 will summarize our results and discuss the future prospects for unstable resonators applied to semiconductor lasers.

2. Geometrical Analysis: Facet Mirror Case

Unstable resonators make use of a deliberately diverging wavefront to produce transverse mode profiles that readily fill large gain volumes, while suppressing the higher-order transverse modes. In the half-symmetric unstable resonator design, the diverging wavefront is realized by creating a diverging cylindrical mirror at the outcoupling facet. We begin our geometrical analysis by calculating the round-trip lateral magnification. This quantifies the lateral mode divergence for the device, and can be related to the mirror curvature as

$$M = \frac{\sqrt{L^2 + L \cdot |R|} + L}{\sqrt{L^2 + L \cdot |R|} - L}, \quad (1)$$

in which L is the length of the device, and R is the radius of curvature of the facet mirror. The absolute value of R is used in the formula, since, by convention, a radius of curvature to the right of the surface is negative. A typical device might have a length, $L=500$ microns, with a facet mirror radius of curvature, $R= - 2200$ microns. This gives a round-trip magnification, $M=2.51$.

In one of the more straightforward experimental diagnostics, we determine the location of the virtual source point for the unstable resonator and compare it directly to the theoretical value. The virtual source point is actually a line due to the cylindrical geometry of the mirror for the one-dimensional unstable resonator. Experimentally, we reimage the virtual source line out of the diode as outlined in Fig. (3). The theoretical value for the distance (measured in air) from the curved mirror facet to the virtual source is

$$R_v = \frac{1}{n \left(\frac{1}{R_s} + \frac{1}{|R|} \right) - \frac{1}{|R|}}, \quad (2)$$

in which n is the effective index for the laser, R is the mirror radius of curvature and R_s is the distance to the virtual source point measured from just inside the curved mirror facet. This is calculated as

$$R_s = \sqrt{L^2 + L \cdot |R|} + L. \quad (3)$$

For the typical device listed above, with an effective index of refraction of $n=3.4$, we find that the virtual source line will appear at a distance $R_v = 318.8$ microns inside the front facet.

3. Geometrical Analysis: Regrown Lens Train Case

The primary drawback of the FIB micromachining process in forming curved facet mirrors on diode lasers is that it is not well suited for batch or mass production procedures. Alternatively, the wet-chemical etching and subsequent MOCVD regrowth involved in the RLT fabrication process lend themselves nicely to both batch production and reproducibility. Early attempts utilizing this technique produced high magnification unstable resonators, which, while providing strong divergence and suppression of filaments, also greatly increased threshold current densities, limiting coherent high-power operation to approximately 80 mw [23]. Later work improved upon the etch and regrowth technique as well as lens design and placement, providing for smoother lens structures, lower magnifications and higher coherent output powers (~ 1 W) [24].

The RLT unstable resonator semiconductor laser consists of a series of negative focal length lenses between two planar reflecting facets. These lenses effectively distribute the divergence along the optic axis of the device. Figure (2) illustrates the lens placement and epitaxial layout for this concept. Once again, a simple geometrical analysis of the

lens structure allows for the calculation of the virtual source location and resonator magnification. Using the ray trace schematic of Fig. (4) and the "lens maker's formula", we can relate the virtual source location, R_v , to the virtual image location, $|I|$, after refraction through the lens as

$$\frac{1}{R_v} - \frac{1}{|I|} = \frac{-1}{|f|}, \quad (4)$$

in which f is the focal length of each lens. This focal length is determined by the effective index change, $\Delta n < 0$, for the lens region, as well as the radius of each etched surface, R_E . The expression for the magnitude of this focal length is given as

$$|f| = \frac{R_E n}{2|\Delta n|}, \quad (5)$$

in which all quantities are shown in Fig. (4). Constant mode radius between elements requires that the refracted wavefront radius propagate to the virtual source radius as $|I| + P = R_v$, giving

$$\frac{1}{R_v} - \frac{1}{R_v - P} = \frac{-1}{|f|} \longrightarrow R_v = \frac{P + \sqrt{P^2 + 4P|f|}}{2} \approx \sqrt{P|f|}. \quad (6)$$

This virtual source location can be directly measured in the laboratory and gives an excellent diagnostic on the device. The magnification per lens, \bar{M} , is then defined by

$$\bar{M} = \frac{R_v}{|I|} = \frac{\sqrt{P^2 + 4P|f|} + P}{\sqrt{P^2 + 4P|f|} - P}. \quad (7)$$

The total round-trip system magnification can be determined as,

$$M = (\bar{M})^{2 \cdot N} \quad (8)$$

in which N is the number of lenses in the device.

A typical RLT device might use twenty lenses, $N=20$, spaced at intervals, $P=25$ microns. For an effective index change of $-.02$ and an etched surface radius of 500 microns, we calculate that each lens has a focal length given by $f = -4.25$ cm. The magnification per lens period is then $\bar{M} = 1.02455$. The total round-trip magnification is then $M=2.64$. Most optimized unstable resonator semiconductor lasers operate with round-trip magnifications ranging from two to four; these values prove sufficient for filament suppression.

4. On-The-Chip Wave Optical Modeling

Diffraction optics modeling for a semiconductor laser begins with the 3-dimensional paraxial wave equation shown below:

$$\left(\frac{1}{2ik} \frac{\partial}{\partial x^2} + \frac{1}{2ik} \frac{\partial}{\partial y^2} + \frac{\partial}{\partial z} \right) \vec{E} = \frac{-1}{2ik} \omega^2 \mu_0 \vec{P}_c. \quad (9)$$

We have anticipated that the electric field is essentially a travelling wave propagating in the longitudinal, \hat{z} , direction as $\vec{E}(x, y, z) \exp(ikz - i\omega t)$. The gain and carrier-induced index shifts can be associated with the imaginary and real parts of the polarizability, \vec{P}_c , respectively, such that

$$\frac{-1}{2ik} \omega^2 \mu_0 \vec{P}_c = \frac{1}{2} G(x, y, z, N) \vec{E} + ik \Delta n_c(x, y, z, N) \vec{E}. \quad (10)$$

G represents a position and carrier-dependent power-gain function. Similarly, Δn_c is a position and carrier-dependent index change. For nearly all semiconductor laser devices, the effective index approximation allows us to eliminate the transverse y -dependence. This implies that the y -variation of the TE-polarized field has a simple, single-mode behavior in the dielectric waveguide of the semiconductor laser epitaxial layers. After invoking the effective index approximation, we can reduce the wave equation to the form retaining only x and z as independent variables:

$$\left(\frac{1}{2ik} \frac{\partial}{\partial x^2} + \frac{\partial}{\partial z} \right) E = \frac{\Gamma G}{2} E + ik \Gamma \Delta n_{eff} E \equiv gE, \quad (11)$$

in which we have introduced a complex gain function, g . Γ , represents the mode confinement factor and takes into account the extent to which the optical mode overlaps the active region. Also, the gain and index changes are evaluated at the active layer.

We use standard Fourier transform propagation methods and assume that

$$E(x, z) = E(x + a_x, z), \quad (12)$$

in which a_x is a periodic window greater than the problem domain; we typically make the period window four to five times the stripe width. $E(x, z)$ can now be represented as a Fourier expansion in the following manner:

$$E(x, z) = \sum_{n=0}^{N_x-1} \phi_n(z) \exp\left(2\pi i \frac{xn}{a_x}\right). \quad (13)$$

We discretize the problem in x by defining

$$x_m = m \left(\frac{a_x}{N_x} \right). \quad (14)$$

This yields the discrete function,

$$E(x_m, z) = E(m, z) = \sum_{n=0}^{N_x-1} \phi_n(z) \exp\left(2\pi i \frac{nm}{N_x}\right). \quad (15)$$

Fast Fourier Transform (FFT) algorithms can perform the above summation quickly. From an initial field distribution, $E(x, z)$, we Fourier transform $E(x, z)$ to determine the Fourier expansion coefficients, $\phi_n(z)$. We propagate a distance, Δz , by applying the propagation law in transform space. The final result at $z + \Delta z$, including the gain/index effects, is then

$$E(x, z + \Delta z) = \sum_{n=0}^{N_x-1} \phi_n(z + \Delta z) \cdot \exp\left(2\pi i \frac{nm}{N_x}\right) \cdot \exp(\Delta z \cdot g(x, z)), \quad (16)$$

in which

$$\phi_n(z + \Delta z) = \phi_n(z) \cdot \exp\left(-\pi i \frac{\lambda n^2 \Delta z}{a_x^2}\right). \quad (17)$$

The FFT approach proves to be extremely accurate when the grid Fresnel number, given by

$$\left(\frac{\lambda \Delta z}{4\pi \Delta x^2} \right) \quad (18)$$

remains less than unity. In addition, this method can be extended to cases in which the effective index method is inappropriate, and the paraxial wave equation with two transverse dimensions must be solved directly.

4.1 GAIN/CARRIER MODEL

In modeling the diode active medium, we normally find that the simplest phenomenological approach is adequate. We assume that the diode power gain, G , and carrier-induced refractive index shift, Δn_{eff} , are linearly related to the carrier density, N , as

$$G = A(N - N_0) \quad (19)$$

$$k\Delta n_{eff} = \alpha \cdot \frac{G}{2}$$

A is the differential gain coefficient, and N_0 is the carrier density required to achieve transparency. The constant α is the antiguiding parameter that relates changes in gain to changes in index of refraction; it drives the self-focussing, or filamentation, phenomena in the semiconductor laser [16].

Finally, we must connect the carrier density, N , to the current density J [16]. An adequate steady-state rate equation for the carrier density is given by

$$0 = D_e \frac{\partial^2 N(x, z)}{\partial x^2} - \frac{N(x, z)}{\tau_s} - \frac{G\Gamma}{h\nu} [I_f(x, z) + I_b(x, z)] + \frac{\eta J(x, z)}{qW_a} \quad (20)$$

in which D_e is the effective diffusion constant, W_a is the active region thickness, τ_s is the non-stimulated recombination time, Γ is the field-filling factor, J is the injected current density, h is Planck's constant, η is the efficiency factor for current injection, and I_f and I_b are the lateral intensity distributions for both the forward and backward travelling fields inside the diode. Equation (20) can be approximated by a tridiagonal set of finite-difference equations, which we solve using a standard technique.

5. Performance Predictions

In this section, we will illustrate several results for the steady-state properties of semiconductor lasers incorporating a curved facet mirror. We must solve, in a self-consistent manner, for the forward and backward propagating fields. Also, we must ensure proper accounting of gain saturation effects in the presence of the simultaneously propagating fields. We achieve the self-consistent fields by first propagating a low intensity random field, $F(x, z=0)$, from the back facet to the front facet. On each z -step of the propagation we store the field values, while simultaneously solving for the carriers at that z -location. At the front facet, we apply the facet reflectivity including the phase shift associated with the curved mirror. This reflected value at each lateral x -location is the backward-going field, $B(x, z=L)$. We now propagate these values backward while solving for the carriers saturated by both the forward- and backward-intensity. At the back facet, we apply the facet reflectivity thereby updating the forward-field, $F(x, z=0)$. This iterative procedure continues until the intensities $|F(x, z)|^2$ and $|B(x, z)|^2$ are unchanging and determined self-consistently. For most unstable resonator calculations at two to three times threshold, we find that 20 to 50 iterations are required for intensity convergence to one part in 10^6 .

Table I describes the parameters in the present simulations. These parameters are representative of single-quantum-well AlGaAs/GaAs lasers, as described in reference [17]. In Fig. (5), we show the badly filamented near-field that can occur in a Fabry-Perot broad-area device operating at twice threshold. (We obtain this figure by grabbing one intermediate round-trip iteration after the device has reached a saturated power level.) Next, we modeled a diode with magnification 2.51. The calculated dependence of output power on injection current for this magnification is shown in Fig. (6). The device shows a threshold increase of approximately 20%- 30% relative to the same device with a Fabry-Perot resonator. Figures (7a) and (7b) illustrate the calculated near and farfield intensity profiles for a device with a magnification of 2.51 running at five times threshold. The near-field, shown here at the facet, retained its basic tophat structure with some evidence of filamentation beginning at this high drive current level. The far-field remains essentially diffraction-limited. (Note that the far-field represents the propagation of the entire near-field; no central feedback mirror obscuration is present.) The break-up of the near-field into filaments has been suppressed by the diverging action of the unstable resonator.

6. ASE Patterns In Unstable Resonators

Unstable resonators provide excellent transverse mode control for large gain-volume lasers, and, since their discovery in 1965, have been used in numerous high-power laser systems. The geometric and diffractive properties of unstable resonator modes have been

studied extensively. Numerous reviews and several books thoroughly document our current understanding. Reference [18] in particular contains complete coverage of unstable resonator theory and applications. From most practical perspectives, the field is mature, with design principles well understood. There are, however, several areas in which additional research is required. For example, the details of mode formation and mode build-up, as well as details of the laser relaxation oscillation and quantum noise limitations remain somewhat cloudy. It is well known that spontaneous emission starts the laser oscillation while fundamentally limiting the linewidth. Usually, the start-up is so fast and the laser linewidth so small that there is little practical interest in these phenomena. However, in semiconductor lasers, linewidths can range from several Mhz to several thousand Mhz, and these are of concern to many users. Furthermore, unstable resonators have begun to appear in semiconductor laser applications. This has helped rekindle interest in linewidth and mode formation properties for these devices. Much of the current research has dealt with the increase of laser linewidth beyond the Schawlow-Townes prediction, an effect attributed to an excess spontaneous emission factor, the K-factor or Petermann K-factor. References [25,26] demonstrate that an excess spontaneous emission per mode as well as noise correlations between different modes, are both a direct consequence of the non-Hermitian and biorthogonal character of the transverse eigenmodes for open or lossy optical structures; the effects are very pronounced in unstable resonators.

In this section, we will analyze some additional unusual mode formation and below threshold, amplified spontaneous emission properties of unstable resonator semiconductor lasers. The unstable resonator semiconductor laser exemplifies a 1-D unstable resonator. In the direction perpendicular to the epitaxial structure, its radiation is confined to a single transverse dielectric waveguide mode, while in the plane parallel to the epitaxy, the lateral mode is controlled by the on-the-chip unstable resonator. This unique 1-D unstable resonator feature has allowed a novel series of diagnostic tests on the unstable resonator radiation. Figure (8) shows the experimental arrangement. The output facet of an unstable resonator semiconductor laser is imaged to the input slit and then through a grating spectrometer. In the input slit of the spectrometer, ASE radiation appears as a line source that extends slightly beyond the injection stripe width. The spectrometer output aperture displays a spectrally dispersed series of facet images. Typical data are shown in Figure (9). The radiation intensity patterns are shown as $I(x, \lambda)$ [27]. It is obvious that the x -distribution of intensity is a strong function of wavelength, as well as gain level relative to threshold. Well below threshold, the patterns show a decided parabolic shape, with the wavelength that satisfies a standing-wave condition along the optic axis, or core, of the resonator concentrated near the core, while longer wavelengths are concentrated in laterally displaced regions. Nearer to threshold, the central radiation brightens and spreads out laterally while apparently sapping ASE power from the other wavelengths. Finally, at threshold the central radiation brightens still further, spreading across the entire gain region of the device. These patterns allow us to observe the spatial-spectral mode formation process of the 1-D unstable resonator. Surprisingly, the ASE distributions are not well represented in terms of modes of the unstable resonator. Note that these features will be present in all lasers using unstable resonators; the semiconductor laser with a 1-D unstable resonator allows us to see the phenomena in a particularly clear fashion.

We will elaborate on these features, as well as provide an explanation of the data based on the regenerative amplifier properties of unstable resonators. First, however, we will discuss the modes and adjoint modes of the resonator.

6.1 UNSTABLE RESONATOR MODES AND ADJOINT MODES

The normal modes of the unstable resonator are distributions of amplitude and phase that are self-replicating under a round-trip propagation through the resonator. The mode set $\{U_n(x)\}$ provides solutions to the integral equation

$$\lambda_n U_n(x) = \int K(x, x') U_n(x') dx' , \quad (21)$$

in which $K(x, x')$ is the round-trip propagator, including the total gain and phase accrual, and λ_n is the loaded eigenvalue for the n -mode. (The following section contains a detailed description of the kernel.) The kernel of this integral equation is not Hermitian, so that

$$K(x, x') \neq K^*(x', x) \quad (22)$$

and the modes are not power orthogonal. Therefore,

$$\int U_m^*(x) U_n(x) dx \neq 0 \quad \text{when } m \neq n. \quad (23)$$

However, the individual modes can always be power-normalized so that

$$\int |U_i(x)|^2 dx = 1 \quad \text{for all } i. \quad (24)$$

The adjoint mode set $\{V_n(x)\}$ is an auxiliary function set that is useful in unstable resonator analysis. These functions satisfy the integral equation,

$$\lambda_n V_n(x) = \int K^T(x, x') V_n(x') dx' , \quad (25)$$

in which

$$K^T(x, x') = K(x', x) , \quad (26)$$

and it is obvious that the spectrum of eigenvalues for K and K^T are identical. Therefore, there is a one-to-one correspondence between the modes and adjoint modes,

with the functions satisfying a biorthogonality condition as

$$\int V_m(x) U_n(x) dx = \delta_{mn} . \quad (27)$$

When the modes are power-normalized, the normalization of the adjoint modes can be picked to satisfy this last relation. References [25] and [26] provide an excellent summary of the modes, adjoint modes and excess spontaneous emission factor, K , for non-Hermitian unstable resonator systems. Significantly, when the modes are power-normalized and the adjoint modes are normalized to be biorthonormal to the modes, then the K -factor for mode U_n is

$$K_n = \int |V_n(x)|^2 dx. \quad (28)$$

The modes and adjoint modes have been used extensively in analyzing the above-threshold properties of unstable resonators. In particular, the dominant mode with the largest eigenvalue magnitude tends to diverge, filling the aperture of the unstable resonator gain and providing an excellent description of the actual operation of unstable resonators in the laboratory. However, this same mode set bears little resemblance to the ASE patterns displayed in Fig. (9). An alternative description appears to be necessary.

6.2 REGENERATIVE AMPLIFIER PROPERTIES OF UNSTABLE RESONATORS

The ASE patterns of Fig. (9) are extremely nonuniform [27]. They result from single- and multiple-pass ASE inside the resonator. An alternative perspective is offered by considering ASE as the regeneratively amplified vacuum fluctuation field that is incident on the resonator filled with gain [28]. Regenerative amplification of the vacuum field was originally used by Schawlow and Townes in their derivation of the laser linewidth formula. Recently, researchers have revived this type of analysis in order to provide a clearer picture of the origins of excess noise and the K -factor. As a first step in deriving the ASE patterns, we propose to consider the regenerative amplifier properties of unstable resonators.

Figure (10) displays the essential elements in the analysis of a regenerative amplifier. $S(x)$ represents an input field that is transmitted into the resonator. This field adds coherently onto the field $C(x)$ circulating inside the regenerative amplifier, so that the total field at the back mirror plane is

$$F(x) = S(x) + C(x) . \quad (29)$$

We complete the argument by relating the circulating field to the total field as

$$C(x) = \int K(x, x') F(x') dx' , \quad (30)$$

in which $K(x, x')$, as defined earlier, is the round-trip propagator for the unstable resonator including the total gain and phase accrual. (We emphasize that our definition of K differs from the conventional definition in that it includes the roundtrip gain and phase factor.) In this case, the round-trip begins and ends at the back mirror, but any choice of reference plane could be used. We form $K(x, x')$ by propagating from a point source at location x' at the back mirror to the feedback mirror plane. At this plane, we apply a gain/phase sheet as

$$\text{gain sheet} = \exp(g(x) \cdot L_g + i2\pi nL / \lambda), \quad (31)$$

in which $g(x)$ represents the spatial distribution of amplitude gain, n is the index, λ is the wavelength, L_g is the gain length, and L is the mirror separation at $x=0$ (optic axis). We then apply the phase contributed by the feedback mirror curvature. Finally, we propagate to the back mirror, and once again apply a gain/phase sheet to represent the gain accrual on the return pass. The result of these operations is given by a field distribution, $f_x(x)$, at the back mirror. This field represents one column of the round-trip propagation matrix for the loaded resonator as

$$f_x(x) = K(x, x'). \quad (32)$$

We then fill the matrix $K(x, x')$ by repeating this calculation for all beginning source points x' at the start/stop plane of the resonator. The matrix $K(x, x')$ gives a reasonably accurate representation of the round-trip propagator for the unstable resonator with gain. We can obtain an even more accurate representation of the distributed gain by using a larger number of gain sheets and propagators. We found that our results were not sensitively dependent on the number of these gain sheets.

We can combine these relations into a final integral equation for the field distribution of the regenerative amplifier as

$$F(x) = S(x) + \int K(x, x') F(x') dx' \equiv S + K * F. \quad (33)$$

For a given input, $S(x)$, the solution to this integral equation, $F(x)$, is the regeneratively amplified field at the back plane of the unstable resonator. This equation provides the basis for all of the following analyses.

6.3 OPTIMUM INPUT/OUTPUT FIELDS

The regenerative gain experienced by an incident field will be an extremely sensitive function of the incident wavelength, as well as the detailed field configuration in both amplitude and phase. This consideration leads to an important problem: For a given wavelength and gain setting is there an input distribution, $S(x)$, that will maximize the regenerative gain of an unstable resonator regenerative amplifier? If such solutions exist, then vacuum fluctuations in these configurations will generate the maximum ASE power, becoming the most easily observed outputs, and providing the best agreement with the observed ASE patterns.

We can phrase our optimization problem in either one of two ways:

- 1) For fixed circulating field power, find the input distribution that minimizes the required input power.
- 2) For fixed input power, find the input distribution that maximizes the circulating power.

Although these formulations lead to equivalent problems, we will develop our solution from the first form. The input field is related to the circulating field as

$$S(x) = F(x) - K^* F(x) \equiv (1 - K)^* F. \quad (34)$$

The total input power is given by

$$P_{in} = \int |S(x)|^2 dx = \int |F(x) - K^* F(x)|^2 dx, \quad (35)$$

while the total circulating power is

$$P_{circ} = \int |F(x)|^2 dx. \quad (36)$$

We now minimize the functional

$$\Omega \equiv P_{in} - a P_{circ}, \quad (37)$$

in which the Lagrange Multiplier, a , is used to incorporate the fixed circulating power constraint. The functional derivatives with respect to either F or F^* of the quantity Ω must vanish. The latter choice leads to an integral equation for F as

$$\frac{\delta \Omega}{\delta F^*} = (1 - K^+) * (1 - K)^* F - a F = 0, \quad (38)$$

in which the superscript, $+$, denotes the Hermitian conjugate of the loaded round-trip propagation matrix K . Finally, we can rearrange terms, yielding an eigenvalue equation for optimized circulating fields as

$$(1 - K^+) * (1 - K)^* F_n = a_n F_n. \quad (39)$$

The solutions to this equation represent the highest-power circulating field distributions that are possible. In addition, the spectrum of eigenvalues, a_n , for this Hermitian problem

are the reciprocal of the regenerative gains defined as the circulating powers divided by the input powers. We emphasize that since our definition of the round-trip propagator, K , depends on gain, g , as well as wavelength, λ , the eigenvalue problem and its solutions will vary with changes in gain and wavelength of the radiation. These dependencies will allow us to explain the full range of spatio-spectral phenomena occurring from well below threshold up to the laser threshold. The next section will examine details of the solutions for various settings of gain and injection wavelength.

The input field, S_n , that is associated with each circulating field, F_n , can be generated as

$$S_n = (1-K) * F_n. \quad (40)$$

Alternatively, we can derive an equation for the injected fields, S , by simply operating on both sides of the F -equation with the operator $(1-K)$. This yields

$$(1-K) * (1-K^+) * S_n = a_n S_n, \quad (41)$$

in which the spectrum of eigenvalues are identical to those generated by the F -equation. We will refer to this as the S -equation. Although the original mode equation involves the non-Hermitian operator, K , both the F -equation and the S -equation involve combinations of K leading to a Hermitian operator. For now, we note that the eigenvalues are necessarily real, while the eigenfunctions with different eigenvalues are necessarily power orthogonal.

6.4 A SAMPLING OF SOLUTIONS

We solve these equations by first storing the propagation kernel, K , as a large, but finite, matrix. Next the matrix approximation to the F - or S - equation is formed. This matrix eigenvalue/eigenvector problem is solved with the standard routine, EISPACK. The smallest eigenvalue is associated with the input field that yields the largest regenerative gain.

For our first case, we will fix the wavelength while varying the gain level. The laser parameters are listed in Table I. We pick a wavelength satisfying a standing wave or resonance condition on the optic axis of the resonator. (The optical path length of the optic axis from the back mirror vertex to the front mirror vertex is equal to an integer number of half wavelengths.) Figure (11) shows the circulating intensities for the highest gain eigenfunctions corresponding to the lowest magnitudes of the real eigenvalues, a_n . The gain settings for each case range from 80% of threshold up to 99.9% of threshold.

The near-threshold intensity, $|F_1(x)|^2$, is essentially identical to the intensity pattern of the dominant mode, $|U_1(x)|^2$, and has an eigenvalue near zero, corresponding to an enormous regenerative gain. Figure (12a) displays the intensity while Fig. (12b) shows the phase of the associated injected field, $S_1(x)$, for the 99.9% case; also on Fig (12b), we show the phase of the circulating field. Notably, as the gain approaches threshold, the

phase curvature rapidly approaches the curvature of the geometrical converging wave; this is satisfying behavior for these maximum gain solutions. More precisely, near threshold, the dominant injected field approaches the complex conjugate of the adjoint mode, $V_1^*(x)$.

For our second case, we will fix the gain to 90% of threshold, while varying the wavelength about the value that is resonant on the optic axis. Results for frequency variations are shown in Fig. (13). In particular, by tuning to lower frequencies and longer wavelengths, the distributions develop a depletion on-axis, with the lateral width of the depleted zone increasing as the wavelength is increased. We find that the peak intensity shifts off of the optic axis to a location at which a standing-wave condition is approximately satisfied for the longer wavelength; this property is in excellent agreement with the experiments [29].

Finally, in Fig. (14), we use a grey-scale plotting technique to simultaneously generate the near-field intensity as a function of x and λ . These patterns provide the closest approximation to the brightest patterns observed experimentally, as displayed in Fig. (9). The comparisons are so favorable that we must conclude that solutions for optimized regenerative gain, the solutions of the F -equation, provide an explanation for the near-field ASE patterns radiated from unstable resonators.

6.5 A VARIETY OF GAIN DEFINITIONS

We will discuss three types of gain calculation that can be made for regenerative amplifiers using an unstable or non-Hermitian resonator. First, consider the regenerative power gain realized when unit power is injected with amplitude and phase corresponding to the dominant mode, $U_1(x)$, of the resonator. On multiple round-trips, this field configuration is unchanged, except for multiplication by the round-trip loaded eigenvalue. The net regenerative mode-in/mode-out power gain is given by

$$G_M \equiv 1/|1 - \lambda_1|^2 \quad (42)$$

in which λ_1 is the feedback eigenvalue for the dominant mode in the gain-loaded resonator; near threshold, this feedback eigenvalue approaches unity.

Second, consider the maximum regenerative gain that can be obtained. This was the motivation leading to the F - and S - equations. This optimized regenerative gain is

$$G_R \equiv \int |F_1(x)|^2 dx / \int |S_1(x)|^2 dx = \frac{1}{\alpha_1}, \quad (43)$$

in which α_1 is the minimum eigenvalue of the F -equation.

Third, consider the regenerative power gain of the dominant resonator mode when the

injected field is optimized to the S -equation solution. Recall that, as the system approaches threshold, the S -equation solutions approach the complex conjugate of the adjoint modes. We can project out the dominant mode content of the circulating field and define a maximum mode gain as

$$\overline{G}_M \equiv \left| \int V_1(x) \cdot F_1(x) dx \right|^2 / \int |S_1(x)|^2 dx \quad (44)$$

in which we project using the dominant adjoint mode.

As the amplifier approaches threshold, numerical experiments yield an interesting relationship between the mode gain and the maximum mode gain. This is given by

$$\overline{G}_M = K_1 \cdot G_M \quad (45)$$

in which the Petermann K-factor of the dominant mode appears on the right-hand-side. The origin of this K-factor gain enhancement is well understood corresponding to "adjoint coupling" in which the complex conjugate of the adjoint mode allows the largest possible excitation of the dominant mode [25]. The F - and S -equations generalize this adjoint coupling to gain settings below threshold.

6.6 HERMITIAN VERSUS NON-HERMITIAN RESONATORS: SUMMARY

The Hermitian equations for the optimized circulating fields and injected fields are given as

$$(1 - K^+(g, \lambda)) * (1 - K(g, \lambda)) * F_n = a_n F_n \quad (46)$$

$$(1 - K(g, \lambda)) * (1 - K^+(g, \lambda)) * S_n = a_n S_n, \quad (47)$$

in which the eigenvalue spectrums, a_n , are identical. We have explicitly shown the gain and wavelength dependence of the round-trip operators in order to emphasize that for the non-Hermitian cases the operators on the left-hand-side, as well as all solutions, will change with gain and wavelength.

When the resonator is well represented with a Hermitian round-trip matrix, then

$K = K^+$, and it is obvious that solutions of the mode equation will solve both the F -equation and the S -equation. For laser systems with Hermitian resonators, we find that

$$U_n(x) = V_n^*(x) = F_n(x) = S_n(x) \quad (48)$$

so that an injected mode will provide the highest regenerative gain on that same mode; this is referred to as "mode-matching". Also, these eigenfunctions will not change with gain or wavelength changes. The regenerative properties of Hermitian systems are obviously far simpler than the regenerative properties of non-Hermitian systems.

7. Conclusions and Future Prospects

To date, several prototypical semiconductor lasers incorporating an unstable resonator for lateral mode control have achieved essentially diffraction-limited performance up to the one-watt cw-power level. We have concentrated our discussion on two genres of design, the curved mirror facet design, realized by focussed ion beam micromachining (FIB), and the regrown lens train (RLT) design. The primary drawback of the FIB micromachining process in forming curved mirror surfaces on diode lasers is that it is not well suited for batch or mass-production procedures. Alternatively, the wet-chemical etching and subsequent MOCVD regrowth involved in the RLT fabrication process lend themselves nicely to both batch production and reproducibility.

Despite some early successful prototype experiments, semiconductor lasers incorporating unstable resonator cavity designs are not commercially available, nor are companies planning their introduction in the near future. At least two elements contribute to this position in the commercial laser world. Firstly, the overwhelming number of users require only low to moderate powers, and companies concentrate on satisfying this traditional customer base. Secondly, the additional processing required for realizing a semiconductor laser with an unstable resonator is difficult and, typically, only research teams serving customer's special needs have made the effort. Perhaps, as semiconductor lasers gain a larger share of the laser market, more and more high-power semiconductor laser applications will be considered. These market forces coupled with improvements in processing and yield should motivate more companies to consider unstable resonators for semiconductor lasers.

The semiconductor laser with an unstable resonator exemplifies a one-dimensional unstable resonator. As such, it allows us to clearly observe the spatial and spectral evolution of the output radiation as the device gain is varied below threshold. The mode formation or ASE properties of lasers with unstable resonators prove to be considerably richer than the analogous phenomena observed in lasers using stable, nearly Hermitian, resonators. We explained the unstable resonator results by deriving Hermitian equations for the optimized circulating fields and optimized injected fields, the F -equation and S -equation. Although the original mode equation involves the non-Hermitian operator, K , both the F -equation and the S -equation involve combinations of K leading to a Hermitian operator. Therefore, the eigenvalues are real, while the eigenfunctions with different eigenvalues are power-orthogonal. We are currently exploring the potential applications of these power-orthogonal function sets.

Table I. Device Parameters

Wavelength (cm)	8.37e-05
Diode length (cm)	0.0500
Stripe width (cm)	0.0100
Magnification	2.51 (R=2200 um)
A(cm²), N₀(cm⁻³)	3.3e-16, 1.75e18
Confinement factor, W_a (Angstrom)	0.028, 100
Unsaturable loss (1/cm)	5.0
Internal quantum efficiency	0.97
Antiguinding factor	-2.7
Index	3.4
Facet amplitude reflectivities	0.565
D_e (cm²/s), t_s (ns)	25, 2.5

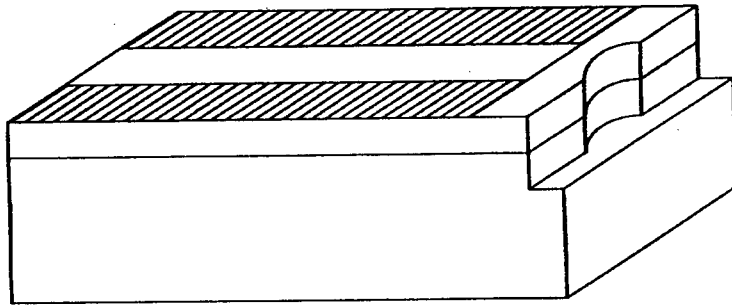


Figure 1. Half-symmetric device

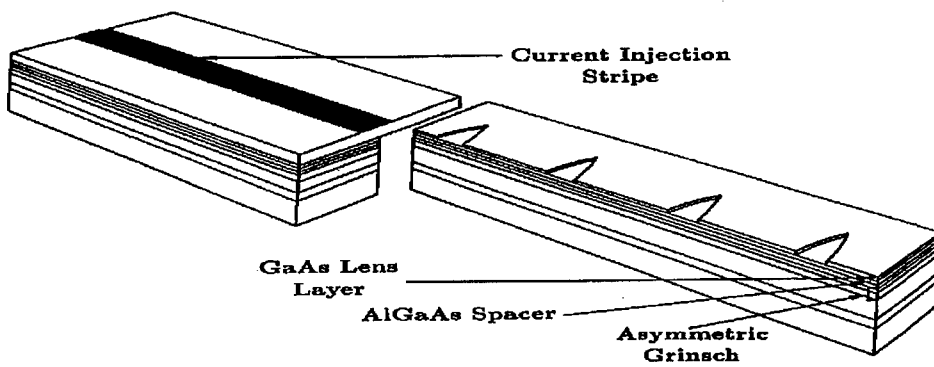


Figure 2. Regrown lens train device.

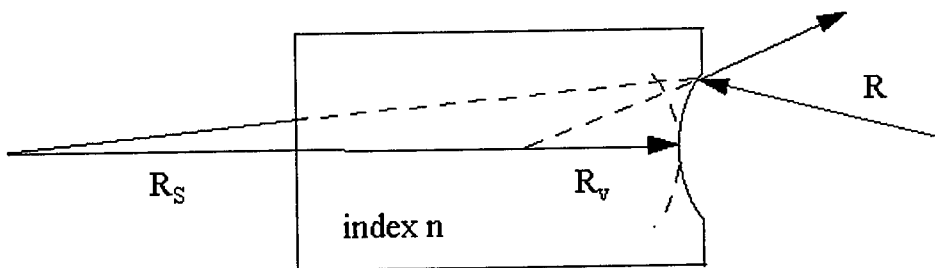


Figure 3. Ray trace for virtual source

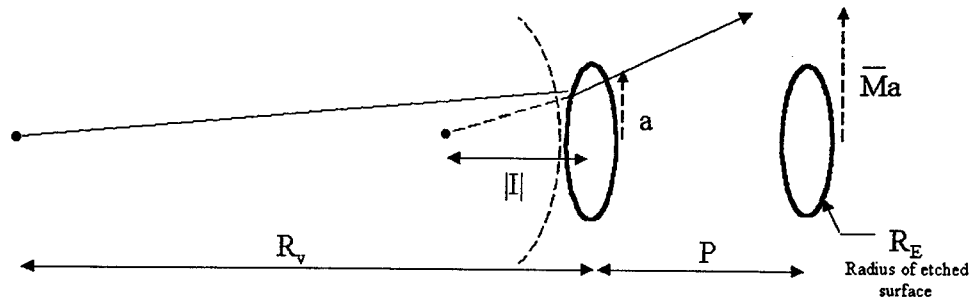


Figure 4. Constant mode radius in RLT

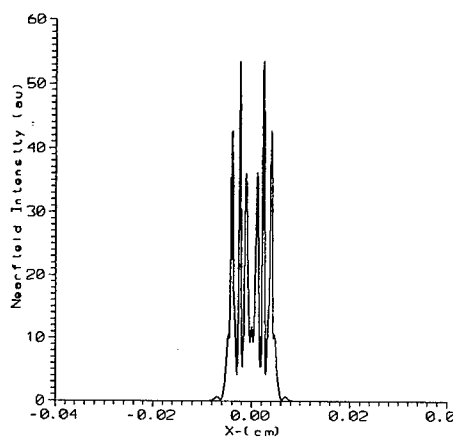


Figure 5. Nearfield (Fabry-Perot)

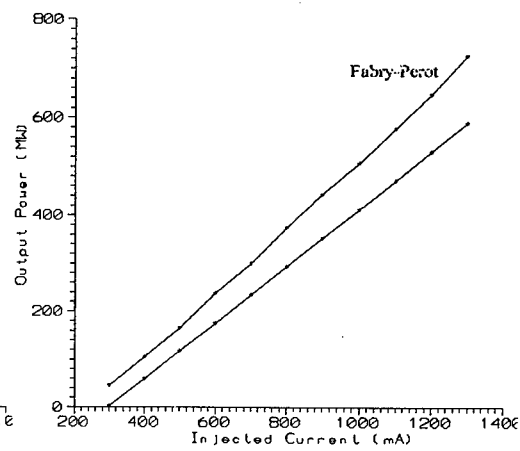


Figure 6. Power vs current

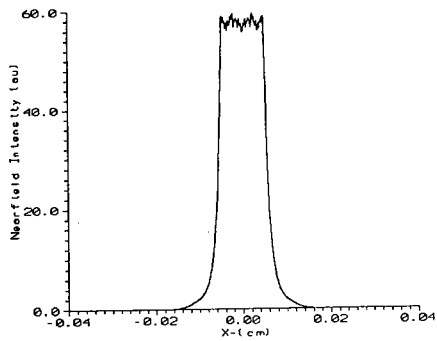


Figure 7a. Unstable resonator nearfield

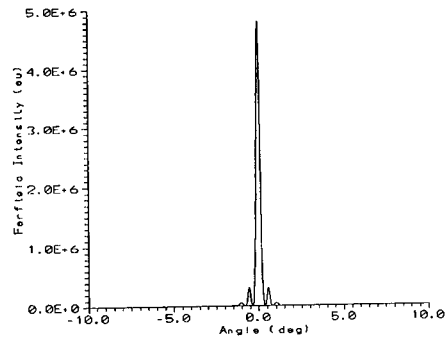


Figure 7b. Farfield.

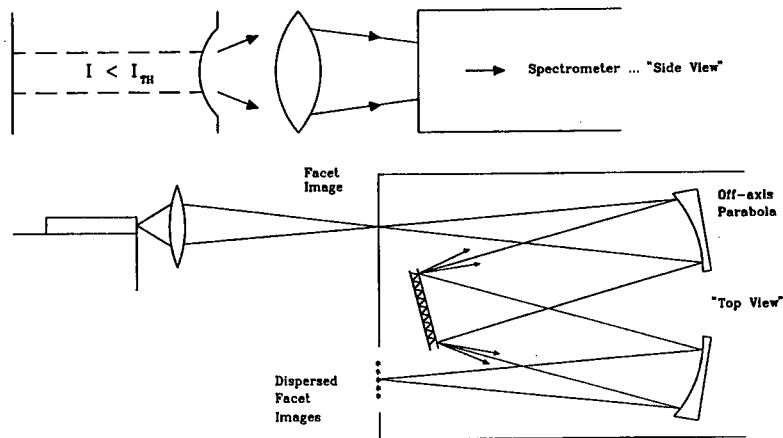


Figure 8. ASE experimental setup.

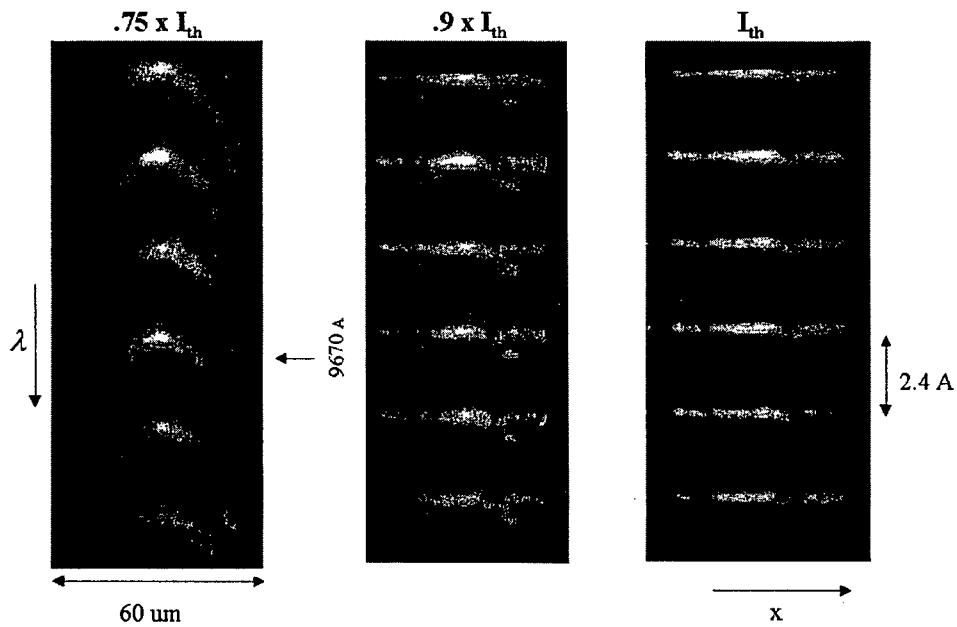


Figure 9. Dispersed ASE patterns

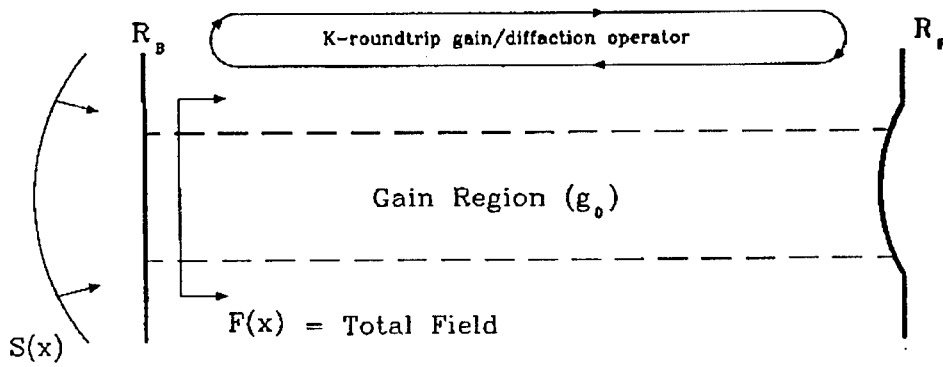


Figure 10. Regenerative amplifier definitions

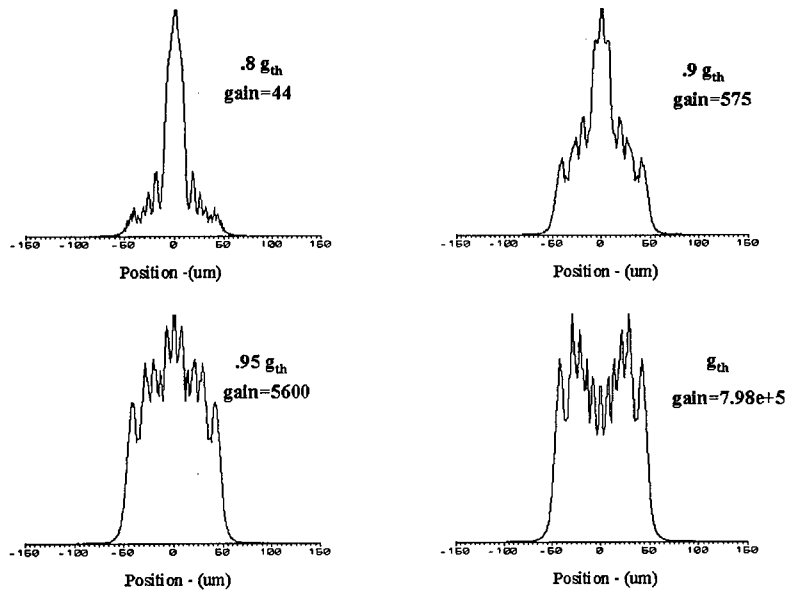


Figure 11. Circulating intensities for resonant wavelength.

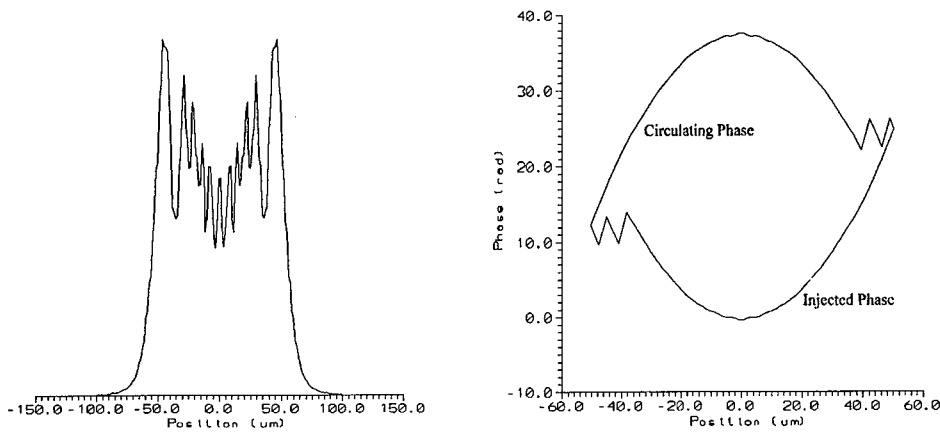


Figure 12a. Injected intensity

Figure 12b. Phase profiles.

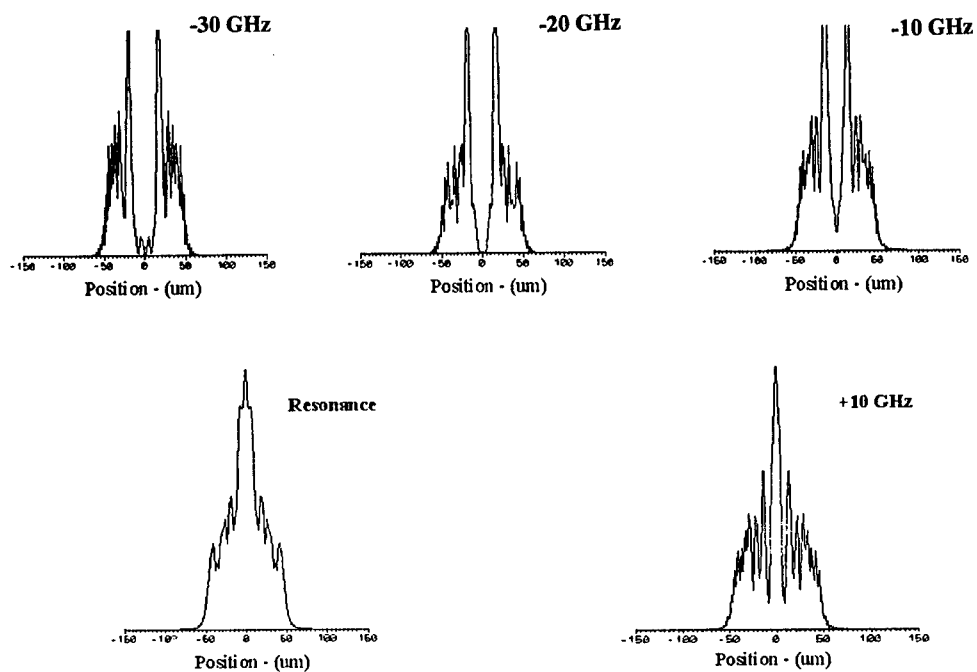


Figure 13. Varying wavelength at .9*threshold

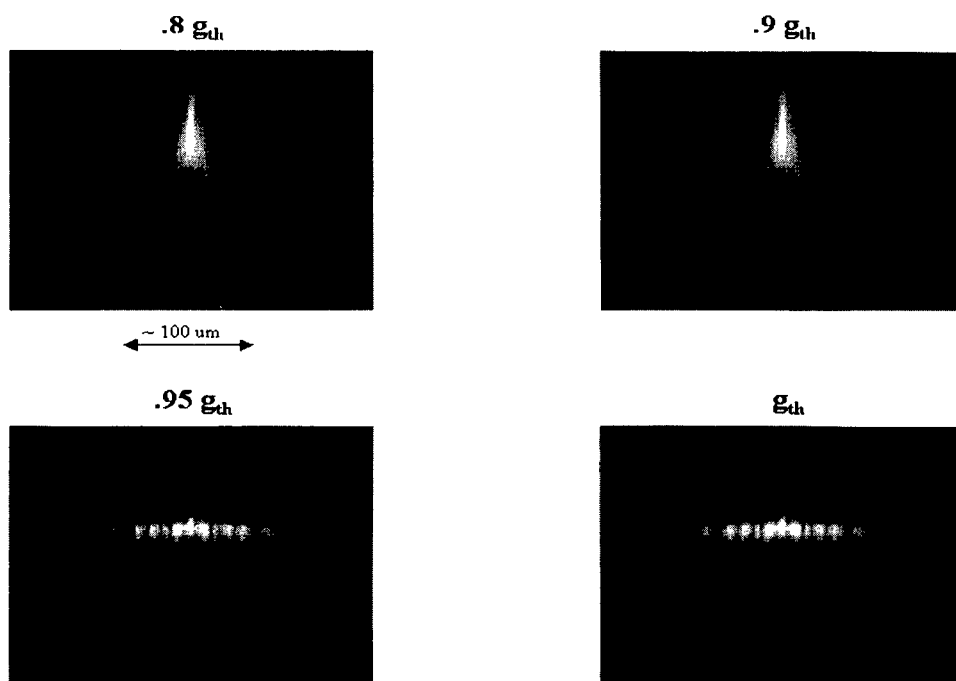


Figure 14. Grey-scale patterns

8. References

1. Ackley D. (1982) High-power multiple-stripe injection lasers with channel guides, *IEEE J. Quantum Electron.*, **11**, 1910.
2. Salzman J. and Yariv A. (1986) Phase-locked arrays of unstable resonator semiconductor lasers, *Appl. Phys. Lett.*, **49**, 440.
3. Craig R. (1985) Unstable resonator semiconductor lasers, *Ph. D. Dissertation*, UCLA, Los Angeles, CA.
4. Salzman J., Lang R., Venkatesan T., Mittelstein M. and Yariv A. (1985) Model Properties of unstable resonator semiconductor lasers with a lateral waveguide, *Appl. Phys. Lett.*, **47**, 445.
5. Salzman J., Lang R. and Yariv A. (1985) Efficiency of unstable resonator Semiconductor lasers, *Electron. Lett.*, **21**, 821.
6. Leger J. (1989) Lateral mode control of an AlGaAs laser array in a Talbot cavity, *Appl. Phys. Lett.*, **55**, 334.
7. Chang-Hasnain C., Dienes A., Whinnery J., Streifer W. and Scifres D. (1989) Characteristics of the off-centered apertured mirror external cavity laser array, *Appl. Phys. Lett.*, **54**, 484.
8. Bogatov A., Eliseev P., Man'ko M., Mikaelyan G. and Popov Yu. (1980) Injection laser with an unstable resonator, *Sov. J. Quantum Electron.*, **10**, 620.
9. Craig R., Casperson L., Stafsudd O., Yang J., Evans G. and Davidheiser R. (1985) Etched-mirror unstable-resonator semiconductor lasers, *Electron. Lett.*, **21**, 62.
10. Lang R., Mittelstein M., Yariv A. and Salzman J. (1987) Unstable resonator semiconductor lasers I – Theory, *IEEE Proc. J.*, **134**, 69.
11. Salzman J., Venkatesan T., Lang R., Mittelstein M. and Yariv A. (1987) Unstable resonator semiconductor lasers II – Experiment, *IEEE Proc. J.*, **134**, 76.
12. Biellak S., Fanning C., Sun Y., Wong S. and Siegman A. (1997) Reactive-ion-etched Unstable resonator semiconductor lasers, *IEEE J. Quantum Electron.*, **33**, 219.
13. Wang H., Liu Y., Mittelstein M., Chen T. and Yariv A. (1987) GaInAsP/InP unstable resonator lasers, *Electron. Lett.*, **23**, 949.
14. DeFreez R., Poretz J., Elliott R., Crow G., Ximen H., Bossert D., Wilson G. and Orloff J. (1989) Focused-ion-beam micro-machined diode laser mirrors, *Proc. Soc. Photo-Opt. Eng.*, **25**, 1043.
15. Bossert D., DeFreez R., Ximen H., Elliot R., Hunt J., Evans G., Carlson N., Lurie M., Hammer J., Bour D., Palfrey S. and Amantea R. (1989) Grating surface emitting lasers in a ring configuration, *Appl. Phys. Lett.*, **21**, 1190.
16. Agrawal G. and Dutta N. (1986) *Long-wavelength semiconductor lasers*, Van Nostrand Reinhold: New York.
17. Wagner D., Waters R., Tihanyi P., Hill D., Roza H., Vollmer H. and Leopold M. (1988) Operating characteristics of single quantum well AlGaAs/GaAs high power lasers, *IEEE J. Quantum Electron.*, **24**, 1258.
18. Siegman A. (1986) *Lasers*, University Science Books.
19. Tilton M., Dente G. and Paxton A. (1990) Mode control of broad-area semiconductor lasers using unstable resonators, *Proc. SPIE Laser-diode Tech. Appl. II*, **1219**, 423.

20. Salzman J., Venkatesan T., Lang R., Mittelstein M. and Yariv A. (1985) Unstable Resonator cavity semiconductor lasers, *Appl. Phys. Lett.*, **48**, 1704.
21. Harriot L., Scotti R., Cummings K. and Ambrose A. (1986) Micromachining of integrated optical structures, *Appl. Phys. Lett.*, **48**, 1704.
22. Tilton M., Dente G., Paxton A., Cser J., DeFreez R., Moeller C. and Depatie D. (1991) High power, nearly diffraction-limited output from a semiconductor laser with an unstable resonator, *IEEE J. Quantum Electron.*, **27**, 2098.
23. Nakatsuka S. and Tatsuno K. (1989) Fundamental lateral-mode operation in broad-area lasers having built-in lens-like refractive index distributions, *Japan J. Appl. Phys.*, **28**, 1003.
24. Srinivasan S., Schaus C., Sun S., Armour E., Hersee S., McInerney J., Paxton A. and Gallant D. (1992) High power spatially coherent operation of unstable resonator semiconductor lasers with regrown-lens-trains, *Appl. Phys. Lett.*, **61**, 1272.
25. Siegman A. (1989) Excess spontaneous emission in non-Hermitian optical systems. I. Laser Amplifiers, *Phys. Rev. A*, **39**, 1253.
26. Siegman A. (1989) Excess spontaneous emission in non-Hermitian optical systems. II. Laser Oscillators, *Phys. Rev. A*, **39**, 1264.
27. Bao Z., DeFreez R., Carleson P., Largent C., Moeller C. and Dente G. (1993) Spatio-spectral characteristics of a high power, high brightness cw InGaAs/AlGaAs unstable resonator semiconductor laser, *Electron. Lett.*, **29**, 1597.
28. Goldberg P., Milonni P. and Sundaram B. (1991) Theory of the fundamental laser linewidth, *Phys. Rev. A*, **44**, 1969.
29. Li H., Wang X. and Hersee S. (1997) The measurement of lateral index variations in unstable resonator semiconductor lasers from spectrally resolved near-field images, *IEEE J. Quantum Electron.*, **9**, 31.

CHEMICAL LASERS WITH ANNULAR GAIN MEDIA

RICHARD C. WADE

Science Applications International Corporation
1225 Johnson Ferry Road
Suite 100
Marietta, GA 30068

Abstract

Resonators capable of extracting highly coherent energy from DF and HF chemical laser annular gain media have been under investigation for weapon application since 1974. This survey article traces the background of interest in these devices and describes the various concepts that have been experimentally and analytically investigated. A preferred concept was selected for high power operation and is currently the subject of a high power demonstration program (Alpha). This paper also provides a summary of the Alpha Program including its history and hardware legacy.

1. Introduction

To understand the rationale for HEL community interest in annular resonators for high-power chemical lasers, let us take a hypothetical case of a space based laser weapon with a multimegawatt output power requirement. Although DF and HF nozzles operate at high efficiency, their typical power density (δ) is low. Thus configuring a linear resonator to these constraints would require, for a reasonable nozzle bank height, a cavity length in excess of 20 m. Such large cavity lengths create a variety of problems for the weapon system designer.

To ameliorate these problem areas for weapon-sized chemical laser resonators, the HEL community has since 1974 been investigating the use of gain generators configured annularly with resonators designed to efficiently extract highly coherent radiation from them. Such configurations offer efficient packaging of a large nozzle exit area while shortening the active medium length. The shorter cavity length reduces the deleterious effects of the medium refractive index inhomogeneity, diffractive losses, and misalignment sensitivity.

A considerable effort has been expended in the search for a viable resonator for use with an annular gain medium. Sponsors of these efforts from within the U.S. government have included: the Navy (PMS-405) which funded the first study contracts to investigate annular resonators, the Air Force (AFWL) which developed annular resonators principally for their Sigma/Tau Program, and DARPA which is engaged in resonator development for their space based laser (SBL) program. The DARPA effort transitioned to the Strategic Defense Initiative Organization (SDIO) space based laser program. SDIO was renamed the Ballistic Missile Defense Organization (BMDO) which currently runs the SBL Program.

In the remainder of this paper, the development of annular resonators for high-power chemical lasers is discussed. Specific concepts which have been investigated either experimentally or analytically are addressed in Section 2. Their basis of operation and major results from testing and/or analysis will be covered. Section 3 will address the two major annular chemical laser programs — Sigma/Tau and Alpha.

Section 4 concludes the article and will be a reiteration of the successes achieved and the major obstacles remaining which must be overcome in order for annular resonators to be successful in high-power chemical laser applications.

2. Annular Resonator Concepts

2.1 TORIC UNSTABLE RESONATOR

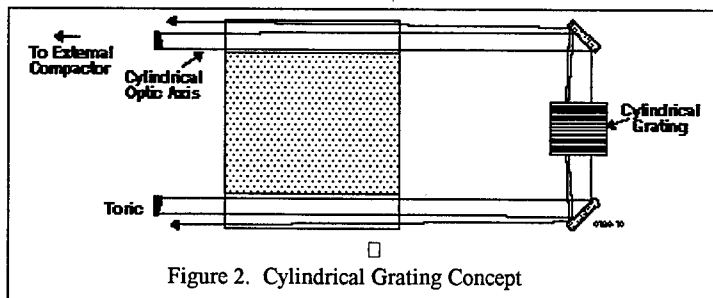
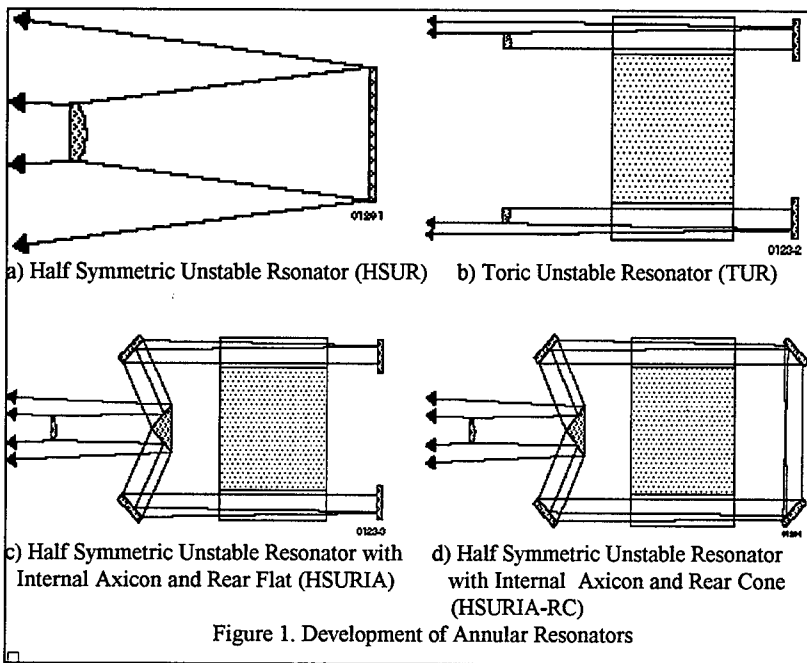
The principal requirements on an annular resonator for weapon application is to extract coherent energy from an annular gain region. To accomplish this function requires that the resonator couple its mode to the gain medium in a manner which expedites power extraction while at the same time maintaining mode control to insure good beam quality. To illustrate the methods for coupling a resonator mode to an annular gain medium, consider the linear half symmetric unstable resonator (HSUR) shown in Figure 1a. To efficiently couple it to annular gain medium this mode must at some point in its path be in an annular configuration. The most straightforward means of achieving an annular mode is to expand the resonator geometry about its optic axis (i.e., the line connecting the center of curvature of its mirrors). Doing so provides the most elementary annular resonator concept — the toric unstable resonator (TUR), as shown in Figure 1b — a purely annular resonator. The next logical step in this evolution is to combine the properties of a linear and annular resonator by providing a beam compactor within the HSUR which serves the function of expanding and recompacting the mode on each round trip through the resonator as shown in Figure 1c. As was the case with the TUR, the mode is expanded about its axis of symmetry.

The simplest of annular resonators is the toric unstable resonator (TUR). As is illustrated in Figure 1b, radial section of the resonator is equivalent to a linear strip resonator. It may be either standing wave or traveling wave resonator. It derives its name from the toric figure of the feedback mirror. The optics are surfaces of rotation, generally with a quadratic or flat figure in the radial direction. Operation of the resonator is as follows: The toric wave front reflected off the feedback mirror expands through the gain medium and is reflected back toward the feedback mirror by the rear annular flat. The wave front expands back through the gain medium to the feedback mirror where the feedback beam is regenerated by reflection from the feedback mirror and the outcoupled beam passes by it.

It was envisioned by early investigators that coherent output power would be produced in an annulus which would have to be compacted for propagation through a beam control system. Analytical results, however, indicated that single transverse mode operation was not attainable with this concept. The concept violated the commonly held opinion that unstable resonator operation was dependent on the operation of its central core — the Fresnel zone surrounding its optic axis (defined as the line connecting the center of curvature of the resonator mirrors). This central core is thought to dictate the resonator performance by providing diffractive coupling to all regions of the output mode. The toric optics form no single optic axis, thus no diffractive coupling in the

azimuthal direction takes place. Modification to enhance mode control through beam rotation were tried but were incapable of restoring mode control. Because of this major fault this concept was not considered further.

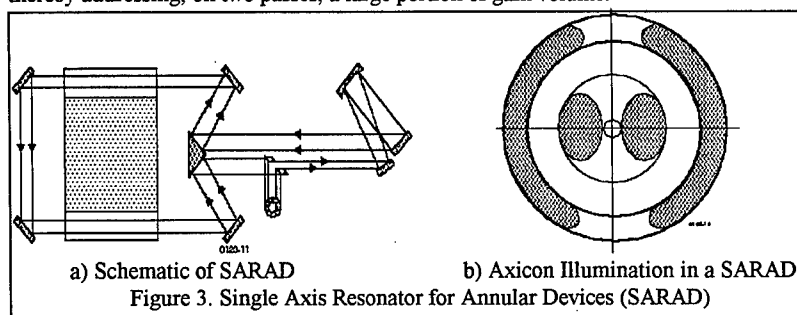
A rear element implementation which was intended to enhance mode control for the TUR is the cylindrical grating shown in Figure 2. The intent of its operation was that the radially propagating beam in the rear element would be diffracted by the grating into a variety of azimuthal directions thereby homogenizing the mode. Unfortunately experiments showed that the diffractive orders from the grating formed skewed components resulting in a different annular output beam for each diffractive order. The concept did not achieve the desired mode control.



2.2 SARAD

To alleviate the problem of mode control found in the toric resonator, the concept of the Single Axis Resonator for Annular Devices (SARAD) was created. The concept was

conceived at the AFWL and analyzed by BDM under AFWL sponsorship. As shown in Figure 3, this concept is essentially a linear resonator which employed an axicon and a rear cone or corner cube to access the annular gain medium while retaining a unique optic axis. The resonator operates as follows: The feedback beam passes through the scraper and is expanded in a telescope and coupled into one side of the annular gain medium by the axicon. After passing through the gain medium and it is reflected across the gain generator centerline by the rear element and propagates through the opposite side of the gain medium and is recompact by the axicon. The crescent shaped annular beam covers less than one half of the annulus on each pass through the gain medium, thereby addressing, on two passes, a large portion of gain volume.



The ultimate undoing of the concept was its poor extraction efficiency and highly non-uniform intensity distribution. It was difficult to form a crescent shaped beam which accessed the gain medium well. Other weaknesses include poor compatibility problems with conventional beam control systems.

2.3 HSURIA

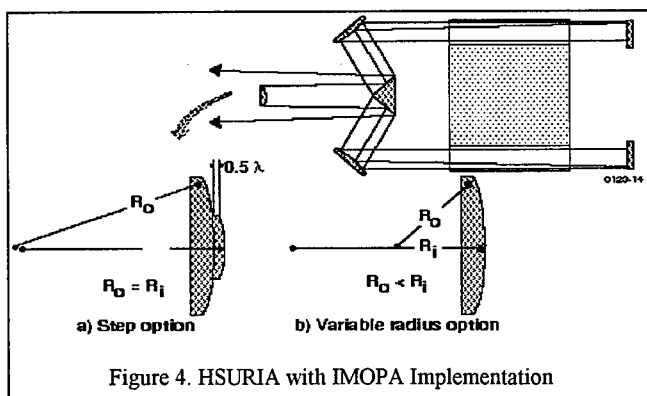
The Half-Symmetric Unstable with Internal Axicon (HSURIA) is an attempt to combine the best aspects of the toric resonator and the SARAD. As can be seen in Figure 1c, the HSURIA is a standing wave resonator which is also the annular analog of the half symmetric linear unstable resonator. It has the simplicity of the toric optics from the toric resonator and provides a single optic axis at least in the compact leg. It operates as follows: The wavefront reflected from the feedback mirror propagates through the compact leg to the beam expander inner cone where it is mapped by the beam expander into the annular region. In the annular region the wave propagates through the gain medium to the rear flat where it is reflected back toward the beam expander, again passes through the gain medium and is recompact by the beam compactor. In its compacted form the wave propagates back to the scraper mirror where the output and feedback beams are separated.

The HSURIA configuration shown in Figure 1c has been, when combined with a large number of implementation options, the subject of the largest amount of experimental and analytical investigation of any annular resonator. The following paragraphs describe the various implementation options which have been investigated.

The use of a rear flat is discussed above. It was the original implementation of the HSURIA. It has demonstrated lowest order mode operation both experimentally and analytically but was extremely sensitive to tilt of the rear element. The basic problem is the azimuthally varying optical path length induced by the rear flat tilt. Thus the wave recompact by the beam compactor contained an on-axis phase shear which degraded

mode control at very small values of tilt. Two rear element implementations intended to solve this problem were subsequently investigated. They were the corner cube and the cone (Fig. 1d). By introducing a common pass feature to the HSURIA, sensitivity to tilt of the rear element was essentially eliminated. Problems, however, remained for both designs. For the corner cube a large weight and volume allocation was needed and the relative alignment of the cube facets was critical to producing good beam quality — both problems for weapon-sized devices. For the rear cone, experiments showed operation on higher order polarization states only. The reason for this behavior was ultimately explained by Fink [1] as being a result of the polarization scrambling properties of the toric elements. Indeed the only possible modes of this concept were either radially or tangentially polarized. The solution to the polarization problem was the development of special phase shift coatings, which, when placed on the toric elements of the resonator produced no net polarization shift in a round trip through the resonator. The combination of a rear cone and polarization control coatings has been demonstrated both experimentally and analytically to produce a zero-order azimuthal mode.

Several compact leg implementation options have been developed for the HSURIA to enhance the mode control properties of the resonator. The first of these, the Integral Master Oscillator/Power Amplifier (IMOPA), is illustrated in Figure 4. It was developed by TRW for the DARPA Novel Resonator Program. The intent of its operation was to form a separate oscillator region within the HSURIA with a low equivalent Fresnel number to enhance diffractive cross coupling. The oscillator is formed by a break in the properties of the feedback mirror. The interior region of the feedback may be thought of as a separate oscillator driving an external amplifier. Energy diffracting from that central oscillator into the higher magnification region of the feedback mirror would then rapidly walk out of the feedback volume and be outcoupled. Theory indicated that the normal interleaving of modes found in unstable resonators was not present. The lowest order mode remained the lowest loss mode over a very wide range of equivalent Fresnel number. Unfortunately experiments with this configuration demonstrated very poor beam quality and analysis indicated that peak intensities on the compact leg mirrors would be greater than those in the HSURIA.



The second compact leg implementation could be construed to be a variant of the IMOPA but, in fact, has a quite different intent. This option, called the Unstable Resonator With Canceling Edge Wave (URCEW), was developed at the Air Force Weapons Laboratory and is intended to diminish edge wave effects in axisymmetric resonators. The effect is achieved by forming a small step near the periphery of the feedback mirror (Figure 5) which causes a destructive interference of the edge wave

within the resonator. This technique is in fact a more practical method of reducing the edge effects than the previously suggested methods of variable radius of curvature mirrors and serrated-edged scraper mirrors. To date no experimental results have been obtained. Analytical results indicate that a more benign output intensity distribution is possible with this concept.

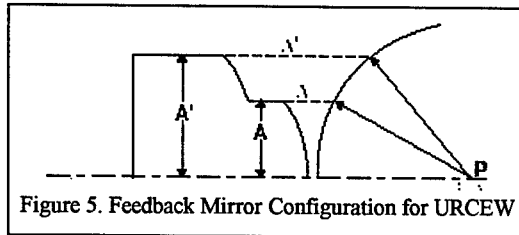


Figure 5. Feedback Mirror Configuration for URCEW

The third entry in this category is the High-order Azimuthal Mode Annular Resonator (HAMUR) or Single High Order Transverse Mode (SHOT) concepts developed by Rocketdyne for the Alpha Program and Perkin-Elmer for the Novel Resonator Program, respectively.

These options are actually combinations of compact and annular leg treatment, however, the compact leg modifications are the most important. In both these concepts the HSURIA is driven to operate on a high order azimuthal mode by increasing the losses for the fundamental mode. Normally the selected mode is a subset of a physical attribute of the device — typically the gain generator support struts. To induce the higher order mode, the strut width was increased (Figure 6) and the inner cone tip was truncated. The mode produced for a typical HAMUR case contains six segments each one half wave different in phase from its adjacent segments. This phase error was to be corrected with an external phase plate also shown in Figure 6. Experimental and analytical results for these concepts indicated that the mode control required for high power application was not attainable.

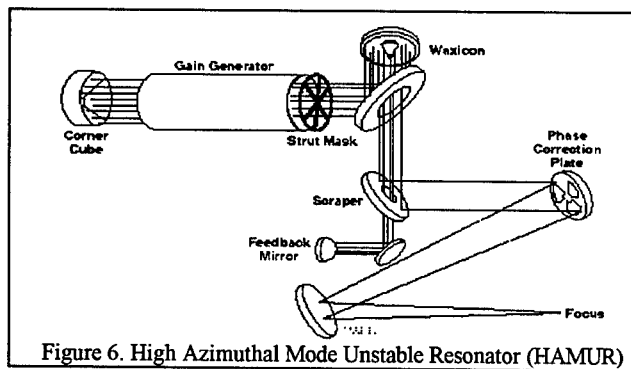


Figure 6. High Azimuthal Mode Unstable Resonator (HAMUR)

2.4 Converging Wave

Along with the HSURIA the converging wave annular resonator was the first use of a compact leg to enhance mode control. As shown in Figure 7, the converging wave resonator is essentially made up of two coupled resonators. The first is a linear, mode control resonator whose output beam is coupled out in two separate annuli. The outer annulus is the output beam and the inner annulus is coupled into an annular region with an axicon where it passes through the gain medium twice and is then injected back into

the mode control resonator. The retroreflected wave walks back through the mode control resonator being reduced in size on each round trip by a factor of the magnification until it is small enough that diffraction becomes a dominant factor. At this point the wave expands and is eventually coupled out of the resonator. The process may be thought of as self-injection locking. Because of the retro-reflection of part of the output, the resonator has a distinctly stable nature. The result, both experimentally and analytically, is a mode with exceedingly high on-axis intensities. This concept is not a good candidate for high power applications because of the potential for mirror damage in the compact leg.

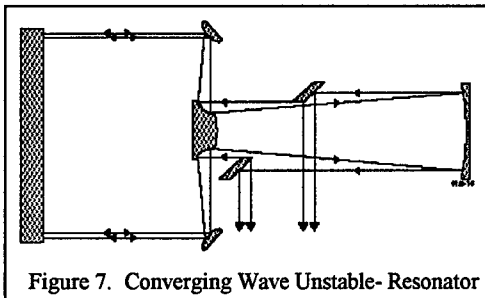


Figure 7. Converging Wave Unstable- Resonator

2.5 Annular Ring Resonators

Annular ring resonators are the annular analog of linear ring resonators. A schematic of a typical ARR is shown in Figure 8.

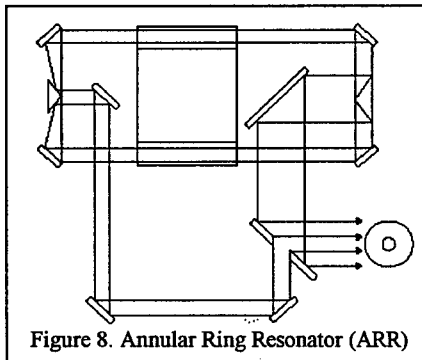


Figure 8. Annular Ring Resonator (ARR)

The basic difference in this resonator and the HSURIA type resonators are that there is only a single pass of the beam through the lasing cavity and the rear element has been replaced by a second axicon. Whereas the standing wave resonator does not have a great deal of flexibility in layout due to the need for both right and left running waves to use the same optical path, the ARR does have increased flexibility. As a result the implementation options which are applicable to it are increased. Note that the implementation options discussed in Section 2.3 — IMOPA, URCEW, and HAMUR/SHOT — are all applicable to the ring.

The basic fault of the ARR is its sensitivity to the relative alignment of the two axicons. This sensitivity is equivalent to that of the HSURIA with a rear flat and is caused by the azimuthal variation in the optical path length in the annulus due to the tilt. The strength

of the ARR relative to the HSURIA is its use of an even number of conic elements which eliminates the polarization scrambling problems.

In order to reduce the sensitivity to axicon alignment two implementation options have been investigated. The first concept is the Internal Focal Line Aperture (IFLA) concept of UTRC. This concept used a spatial filter configured as two orthogonal line filters to reduce the higher order mode content in the resonator (Figure 9). Line filters were used instead of a point filter in order to better manage the clipped energy without damaging the filter material. The concept has been extensively tested and analyzed at UTRC. The basic weaknesses of the design are that output power is decreased as a result of severe reductions in feedback power in the filtering process and the required clipping at the filters to maintain a highly focusable beam is excessive. The alignment of the line filters is also critical.

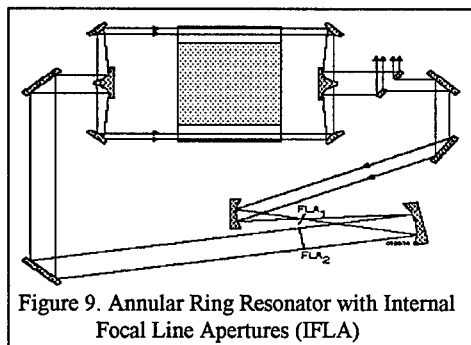


Figure 9. Annular Ring Resonator with Internal Focal Line Apertures (IFLA)

The second option considered was called the Beam Rotator with Internal Axicon (BRIA) and its schematic is shown in Figure 10. Its rationale for operation is as follows: as the beam passes through the resonator any misalignment of the axicons would result in, an on-axis phase shear which would continue in the feedback beam back through the resonator accumulating additional phase shear on each pass. The BRIA sought to reduce this sensitivity by rotating the compact beam. Thus for a rotation of 180° the phase shear introduced on the first round trip would be corrected on the second round trip. In this manner the resultant mode contains a shear of approximately one half that introduced by a single trip through the resonator. The major weaknesses of the concept were its poor extraction efficiency due to the single pass through the lasing medium, misalignment sensitivity which, although improved, was still not adequate for high power operation, and high flux loadings on the axicon inner cones.

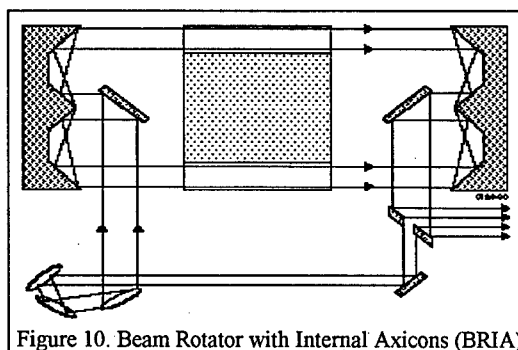


Figure 10. Beam Rotator with Internal Axicons (BRIA)

The operation of a linear resonator may be interpreted as a stable resonator core with a Fresnel number of approximately one surrounding the optic axis from which energy diffracts and is outcoupled rapidly by the resonator in a MOPA-like fashion (Figure 11). Since this central core dictates the lower limit of beam divergence of the output beam by virtue of the stimulated emission process — and thus coherence — in the IMOPA section of the resonator, the placement of the core in a relatively clean portion of the lasing flow field has generally been necessary to achieve good beam quality. That is, when the diffractive core is allowed to oscillate free and clear of perturbing effects, it emits a highly coherent diffractive output in all transverse directions which is amplified on subsequent passes through the resonator to ultimately form the output beam.

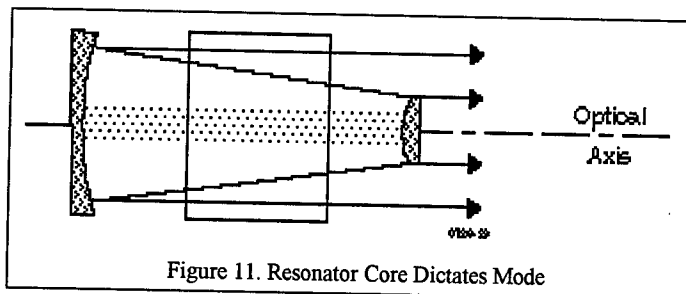


Figure 11. Resonator Core Dictates Mode

The annular resonators discussed thus far are, except for the SARAD, axisymmetric in design and therefore violate this philosophy of resonator design. In fact, the previously discussed concepts require the mapping of the diffractive core in the compact region into a thin annulus in the annular region. Diffractive cross-coupling of the beam in the annular region is negligible. Subsequent recompaction of the wave does not necessarily reform a coherent core, especially if azimuthally varying perturbations are present in the annular region. This is the primary reason that early investigators found that a long compact leg was necessary in axisymmetric configurations in order to filter out the high spatial frequency perturbations introduced in the annulus. Even with long compact legs, annular resonators remained both analytically and experimentally more sensitive to perturbations than their linear counterparts.

To alleviate these fundamental problems, an implementation option of the ARR was developed by simply decentering the feedback hole in the scraper mirror as shown in Figure 12. Note that by performing this simple transformation, the location of the optic axis is removed from the vicinity of the axicon tip. The modification also provides an unbroken core throughout the resonator. The core remains contiguous in the annular regions and can thus communicate diffractively throughout the resonator, not just in the compact beam. Beam rotation in the compact leg can be used to modify the location of the optic axis in both the compact and annular regions. The concept is referred to as the Decentered feedback Annular Ring Resonator (DARR). The major strengths of the DARR were its ability to maintain mode control despite large aberrations introduced by axicon tilts and the significantly reduced flux levels on the beam compactor inner cone. Its major weakness was the large beam quality degradation introduced by those tilts.

The principal faults of the ring resonators thus far discussed are their sensitivity to misalignment and low extraction efficiency. In order to improve the concepts, both TRW and Rocketdyne, under the DARPA sponsored Alpha Program, applied a common pass feature to the DARR. The concepts were the High Extraction Efficiency DARR (HEX-DARR) and the Common Pass DARR (CPDARR), respectively. In both cases the common pass feature was accomplished by having the annular beam enter and exit the

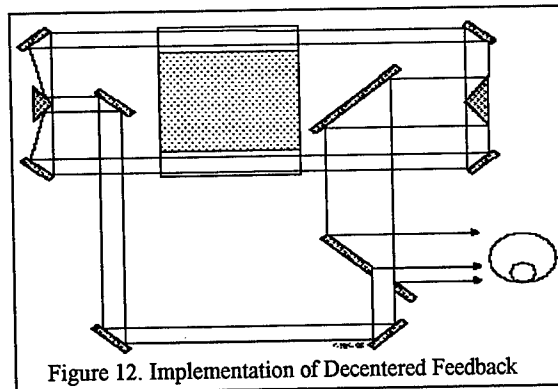


Figure 12. Implementation of Decentered Feedback

annular region on separate areas of a compound beam expander. The TRW HEX-DARR uses a combination waxicon/reflexicon as shown in Figure 13. The Rocketdyne CPDARR used a compound waxicon with separate optical zones on both inner and outer cones for the expansion and compaction regions (Figure 14a).

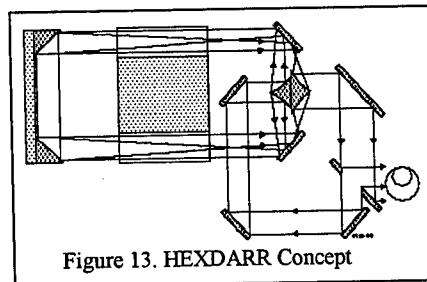


Figure 13. HEXDARR Concept

The resonators operate as follows: The plane wave leaving the feedback mirror in the preferred direction propagates to the beam expander (i.e. waxicon in Figures 13 and 14) where it is mapped into the annulus. The wave propagates through the gain medium and is reflected across the gain generator axis by the rear cone and then back to the beam compactor (reflexicon for the HEX-DARR, Figure 13 and waxicon for the CPDARR, Figure 14). The collimated output beam is then scraped off leaving the decentered feedback to proceed through the wave train

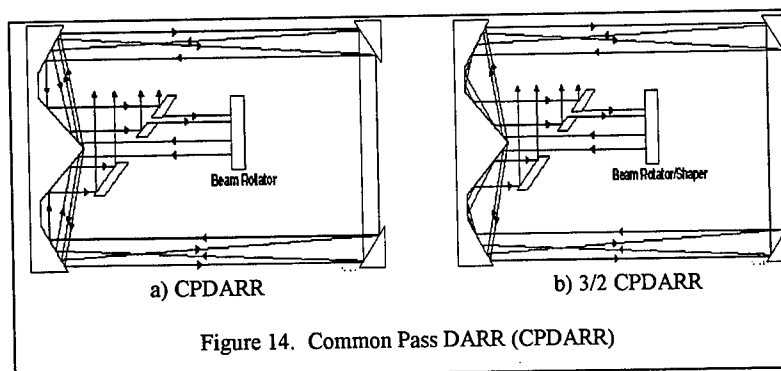


Figure 14. Common Pass DARR (CPDARR)

Analytical results for both resonators indicated excellent performance potential. The HEX-DARR shown has been the subject of extensive experimental verification in support of the Alpha program with good performance results.

Both the HEX-DARR and CPDARR have the distinct advantages of excellent mode control, low misalignment sensitivity, and significantly reduced flux levels in the compact leg relative to the axisymmetric configurations. The HEX-DARR also has the advantage of not needing polarization control coatings. The CPDARR, while still requiring special coatings, was far less sensitive than the HSURIA. Rocketdyne solved this problem with the invention of the 3/2 CPDARR (Figure 14b). The additional reflection in the beam compactor effectively descrambles the output beam polarization. An additional advantage was that a long compact leg was not required for mode control. In fact, analyses have confirmed that a zero length compact leg had it been physically possible, would have worked.

The major disadvantages of these concepts were their complexity and the possibility of supporting an undesirable reverse mode.

3. High Power Demonstration Programs

The DoD has embarked on two high power annular resonator programs — Sigma/Tau and Alpha. Both devices are intended solely to provide scaling information — Sigma/Tau, a high pressure DF device, is intended for scaling to an airborne laser weapon and Alpha, a low pressure HF device, is intended for scaling to a space-based laser weapon. The remainder of this section will discuss the resonator concepts being used on these programs.

3.1 SIGMA/TAU

The Tau Program was the annular resonator program which used the Sigma gain generator. The program was sponsored by the Air Force Weapons Laboratory (AFWL) with Rocketdyne Division of Rockwell International as the prime contractor. Testing of DF gain generator (Sigma Program) and the resonator tests (Tau Program) were completed in 1985. Tau is a megawatt class laser with near diffraction limited beam quality.

The Tau resonator is an HSURIA with a rear cone and is shown schematically in Figure 1d. The concept was selected in 1977 as a part of the competition for the program. As such the more recent advancements in resonator design in Section 2 were not available. It may therefore be considered a first generation high power annular resonator.

The major issues for the Tau resonator were the maintenance of mode control, damage-free operation of the reflexicon inner cone, and the achievement of power and beam quality goals. A key accomplishment of the Tau Program was the fabrication of annular optics at a scale consistent with weapon-sized annular resonators.

3.2 Alpha

Alpha is that ground based test bed being used to develop the technology for, and to demonstrate the feasibility of, extracting a near diffraction limited, multi-megawatt beam from a space specific cylindrical HF laser. The Alpha resonator concept is the

HEX-DARR. It is shown schematically in Figure 15. Note that uncooled optics made from single crystal silicon (Figure 16) are being incorporated throughout the design.

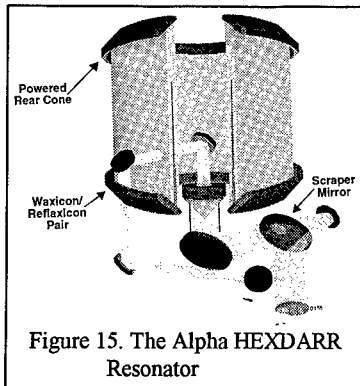


Figure 15. The Alpha HEXDARR Resonator

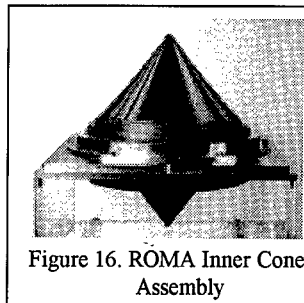


Figure 16. ROMA Inner Cone Assembly

With the HEX-DARR the achievement of mode control and tolerable mirror fluxes are far less critical issue than with any of the axisymmetric concepts. The major issues for Alpha are the achievement of the beam quality and output power goals at a scale appropriate to weapon applications. TRW has achieved those goals.

A broader view of the Alpha test environment is shown in Figure 17. Key elements include the Alpha laser (Figure 18) and the optical diagnostic Assembly (Figure 19). Figure 20 illustrates the first lasing accomplished with Alpha. Notable in this figure is the intensity uniformity and the presence of the decentered feedback hole in the outcoupled beam.

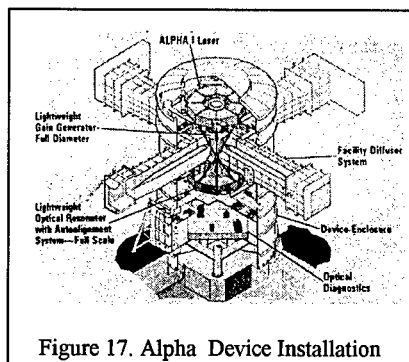


Figure 17. Alpha Device Installation

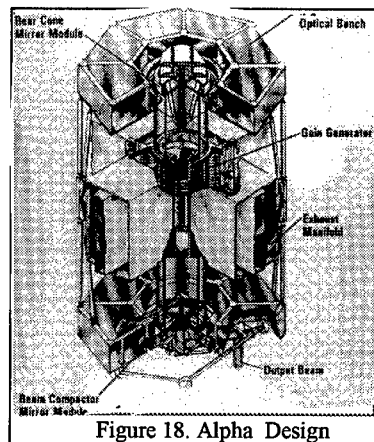


Figure 18. Alpha Design

4. Conclusions

Since 1974 a considerable effort has been expended by the HEL community to find a resonator suitable for use with annular gain media. The immensity of the available design parameter space and the difficulty in testing and analyzing the available concepts

has hampered the effort. However, it now appears that the common pass decentered annular ring resonator concepts — HEX-DARR and CPDARR — are indeed capable of being used in weapon system applications. Although these concepts have reduced significantly the impact of the deleterious effects, a considerable effort is still necessary to bring them to a maturity consistent with operational systems. The major obstacles

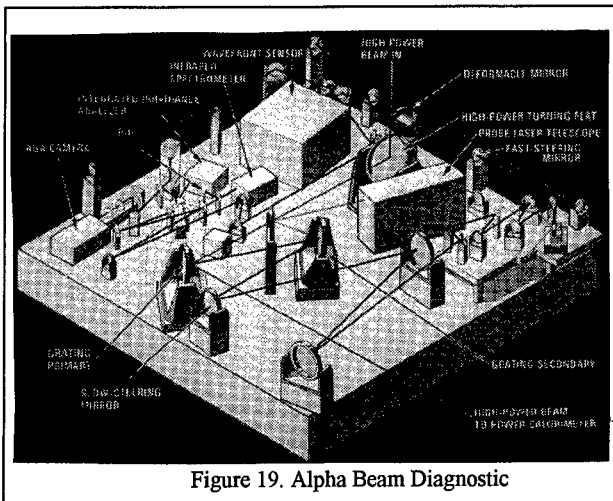


Figure 19. Alpha Beam Diagnostic

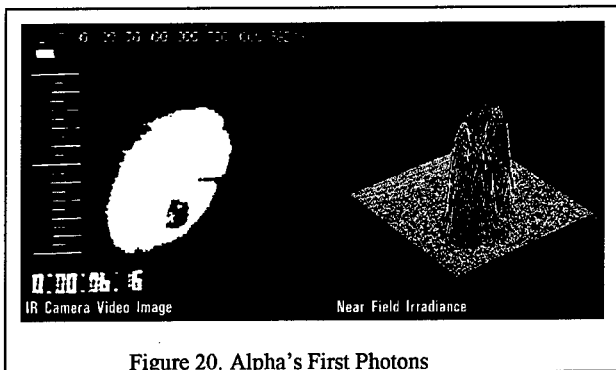


Figure 20. Alpha's First Photons

confronting their successful implementation are: 1) effective alignment concepts and controls to diminish the requirements on beam control systems, 2) control of jitter and static and thermal mirror distortion through improved mirrors and coatings, and 3) reduction in system weight through use of uncooled optics and improved nozzle performance. Current studies are providing high confidence that scaling of annular resonators to a power level consistent with current and future requirements is achievable in the near future.

5. References

1. Fink, D. (1979) Polarization Effects of Axicons, *Applied Optics* 18 5.

BEAM QUALITY CONTROL OF AN IODINE LASER WITH SBS

A.F.SHKAPA, Yu.V.DOLGOPOLOV, A.M.DUDOV,
V.A.KHRUSTALEV, G.A.KIRILLOV, G.G.KOCHEMASOV,
S.M.KULIKOV, V.M.MURUGOV, A.V.RYADOV,
A.B.SMIRNOV, S.A.SUKHAREV, AND L.I.ZYKOV
*Russian Federal Nuclear Center (VNIIEF)
Sarov, Nizhni Novgorod Region, 607190, Russia.*

Abstract

Results on creation of diffraction qualities laser installation by the 60 cm aperture with SBS with radiation energy 300 J and output radiation quality control are reported.

1. Introduction

Presently, to study the fundamental physical processes of the matter behavior in quasi stationary monochromatic super high intensity fields, the nanosecond range laser facilities are created capable focusing of radiation in a wavelength size spot [1]. What does it give us? At first, appears the capability of research of substance behavior in quasi stationary fields (comparing with typical atomic times of relaxation). At second, appears the capability of observing dynamics of process but not only results of interactions. At third, in this case we make a deal with practically monochromatic action. The main problem of such lasers is compensation of optical elements aberrations. It can be solved by using phase conjugation based on stimulated Brillouin scattering (SBS). This paper reports the experimental research results on phase conjugation of photodissociation iodine laser radiation (wavelength is $\lambda=1.315 \mu\text{m}$), various aberration type compensation and output radiation quality control.

2. Laser Setup

In powerful laser facilities the accumulation of aberrations takes place during amplification of a pulse. Due to this reason the laser spot size on a target is usually much more than radiation wavelength and makes up to 20 - 100 λ . We suggest to use a laser facility with phase conjugation for compensation of aberrations and for focusing of radiation in a wavelength size spot. Layout with explains the operation of this system is shown in fig.1. The master oscillator beam with the help of microobjective is focused in $\sim\lambda$ - size spot and propagates to the parabolic mirror with and finds its way through the laser amplifiers and with

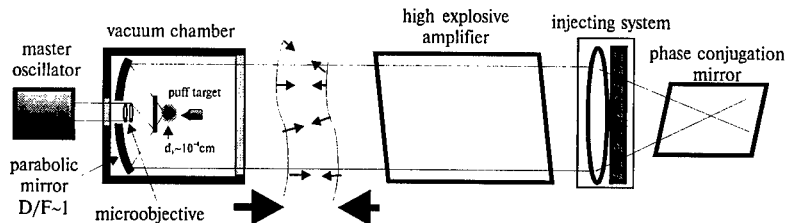


Figure 1. Principal scheme of the laser facility for obtaining superstrong light fields.

the help of special kinoform system it is injected into the phase conjugation mirror. If the phase conjugation degree is high enough, then high energy converted beam will be focused in the initial size $\sim 1\text{-}2\text{ }\mu\text{m}$.

The facility is based on a high explosive iodine laser. The master oscillator radiation passes through the modulator, forming a pulse with a duration $\tau \sim 2\text{--}20\text{ ns}$, and then enters into a vacuum chamber in which it is focused by a microobjective in a λ -size spot. 30 cm diameter parabolic mirror ($D/F \approx 1$) forms an input beam for the high explosive amplifier. After amplifying the radiation is reflected backwards in the phase conjugation device based on SBS mirror. The amplified Stokes radiation is collected by the parabolic mirror and some share of it (depending on phase conjugation fidelity) is focused in a λ -size volume.

3. Beam Quality Studies

Principle optical schematic diagram of the experimental setup for study of compensations of various aberration types and output radiation quality control of high explosive iodine laser with SBS is shown in fig.2. It includes the master oscillator of supporting radiation (MO), system forming spatial angular structure of input radiation with the optical delay line, high explosive iodine laser amplifier with the beam expanding telescope on output, device of SBS, measuring complexes of radiation parameters. MO forms a radiation of required duration for making supporting radiation with the small divergence by means of forming systems at the input of laser amplifying stages. MO consists actually of the single-frequency master oscillator and two preamplifier stages pumped by Xe flash lamps. Laser radiation parameters are: wavelength - $\lambda = 1.315\text{ }\mu\text{m}$, power - $P = 80\text{ kW}$, pulse duration - $\tau = 100\text{ }\mu\text{s}$, beam diameter - $D = 7.4\text{ cm}$, divergence (integral over pulse duration) - $\theta_{0.84E} \approx 1.10^{-4}\text{ rad}$, $\theta_{0.51} \approx 4.5.10^{-5}\text{ rad}$.

A supporting beam in experiments was realized as follows. MO radiation is applied to circular diaphragm with a diameter d_0 placed in the focal plane of the three- or five-component objective having the focal length F from 900 m to 4500 m. Objective consisted of positive lens, front focal plane of which was combined with radiating diaphragm, and one or two consecutively situated telescopic pairs, each of which consisted of negative and positive lens. Experiments were carried out at the output apertures within the range from 15 cm to 60 cm. Radiating diaphragm diameter $d_0 = 11\text{ mm}$ was chosen so that estimated divergence of supporting beam at the input of output telescope of amplifying

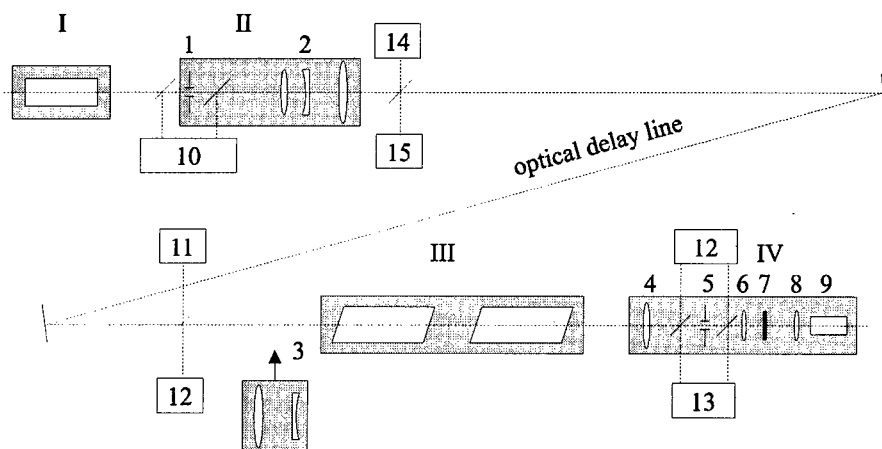


Figure 2. Optical layout of experiments on laser with phase conjugation.

I - master oscillator, II - optical forming system, III - amplifiers, IV - phase conjugation device; 1 - radiate diaphragm, 2 - three- or five-component objective, 3 - beam expanding telescope, 4, 6 - lenses of angular selector, 5 - diaphragm of angular selector, 7 - kinoform phase plate, 8 - radiation entering lens, 9 - SBS cell, 10 - measuring complexes of output radiation, 11 - measuring complex of input radiation, 12 - measuring complex of pumping radiation, 13 - measuring complex of Stokes radiation, 14, 15 - Hartmann wavefront analyzers of input and output radiation.

stages had diffraction limit. The beam passed through the air optical delay line by the length 550 m and entered into amplifying stages. Optical delay line serves for preventing an influence of powerful pulse returning from amplifying stages on working the MO. Intensity of supporting radiation at the input of amplifying stages reached 2 W/cm^2 . Amplifying stages consisted of two explosive photodissociation amplifiers with aperture 15 cm and total active length 2 m, distance between two amplifiers was 20 m. Laser mixture of gases consisted of 25 torr $\text{C}_3\text{F}_7\text{I}$ and 125 torr Xe. The amplified radiation entered into the phase conjugator. It includes the focusing system and SBS cell. Focusing system is served for entering a pumping radiation into SBS cell and making the conditions for SBS excitation.

As an active medium for SBS we used Xe - SF_6 gas mixture with the total pressure 50 atm and SF_6 partial pressure in mixture 1,5 Atm. SF_6 greatly raises laser induced breakdown threshold of mixture, allowing to work with intensities up to $\sim 10^{10} \text{ W/cm}^2$. Experiments were conducted with SBS cell having the light diameter 100 mm and length 1,5 m.

Wavefront reversal fidelity based on SBS is significantly defined by radiation intensity spatial distribution in the nonlinear medium. It ensure discrimination of nonreversed component in Stokes radiation. Usually for this in front of SBS cell are put phase plates. However even under the optimum choice of phase plate an energy of nonreversed component usually turns out to be comparable to the energy of reversed component in Stokes radiation. Using angular selection of reflected radiation it is possible at the expense of energy losses to

increase reversed component in Stokes radiation and, accordingly, to increase wavefront reversal fidelity at the whole laser system output.

In our experiments wanted radiation intensity spatial distribution in the nonlinear medium was formed by two, four and eight step-like kinoform rasters of identical Fresnel lenses with diffraction efficiency 40% and 80%. The SBS pumping radiation has been split into ~ 1000 beams which were focused into SBS cell. Directional diagram of the light beam, passed through such raster, consists of the separate maximums due to diffraction on the two-dimensional periodic structure. Directional diagram of Stokes beam, reflected from SBS cell and passed through the same raster, also consists of the separate maximums. The scheme of pump radiation input into SBS cell is build so, that, at first, angular selector for reflected radiation let a radiation of only zero diffraction order pass and, at the second, the image of raster lens focal plane is outside of SBS cell. Reversed component in Stokes radiation passing through raster recovers its wavefront and gets through the selector without the reduction. Nonreversed component in Stokes radiation suffers a partition on the ensemble of beams diffracted on the raster. They are not transmitted by the angular selector (except the zero order). Selection of reversed component is realized by the angular selector with the bandwidth $(3-4) \cdot 10^{-4}$ rad. To characterize the selection degrees of reversed component in Stokes radiation we used value equal to reduction multiplicity of nonreversed component by selector: as before [2]:

$$\eta = 1 + 2(\theta_{ph} D_{ph} / \theta_s D_{amp})^2,$$

where θ_s - a bandwidth of the angular selector for pump radiation, θ_{ph} - diagram width of scattering, D_{amp} - diameter of amplifier radiation surface, D_{ph} - diameter of raster exposure. Selected Stokes radiation on the inverse passage was amplified in amplifying stages and got to the optical scheme of supporting radiation forming. In this case scheme used as measuring objective with focal distance from 900 m up to 4500 m in different experiments. Radiation parameters - energy, divergence, pulse shape, wavefront profile, beam cross-section in the near and far zones in different points of scheme - were recorded by measuring complexes. Angular distributions of energy, intensity and axial radiant intensity of output radiation were calculated using data of energy calorimetric and photometric measurements in far zone behind calibrated diaphragms in focal plane of the measuring objective.

4. Radiation Quality Measurements

Wavefront reversal fidelity at the whole laser system output and, consequently, output radiation quality has been measured by two methods. At first, axial radiant intensity B has been determined as a result of direct energy calorimetric measurements in focal plane of the measuring objective and has been compared with axial radiant intensity B_d of similar radiator without aberration [2]. Thereby, it has been found the Strehl number $St = B/B_d$, which is a quality feature of our laser radiator [3]. At second, wavefronts of the MO supporting and output radiation have been measured and compared in one plane by the Hartmann method [4]. When the distortion of an initial wavefront is small, laser

system Strehl number does not depend on the nature of these distortions and differs from units on value, proportional root-mean-square wavefront deviation [3]:

$$St \approx 1 - \left(\frac{2\pi \cdot \Delta h}{\lambda} \right)^2 \quad (1)$$

where $(\Delta h)^2$ - root-mean-square wavefront deviation. Optical scheme of obtaining results by the Hartmann method consists of two branches of registrations, accordingly, supporting and reversed amplified laser beams. The Hartmann diaphragm is placed before measuring lens with the focal length 8 m. Diaphragm is a steel screen by diameter 280 mm with 7 mm round holes, disposed in nodes of square network. Distance between nearby holes is 14 mm.

5. Results

Conducted experiments have been directed on determination of optimum parameters of SBS pumping radiation formed by input system to achieve maximum values of Strehl number and radiance intensity. In experiments amplifier input signal, selection degree of reversed component in Stokes radiation, parameters of kinoform rasters are varied. Supporting signal intensity at the input of high explosive iodine laser have been varied in the range from 0.07 W/cm² to 2.6 W/cm². Total duration of SBS radiation pulse is 4-5 μ s with spikes duration are 0.1-0.5 μ s. Output radiation energy was about 300 J, pumping energy in SBS medium is 20-60 J, SBS reflectivity is 4-40%. Typical far radiation zones in experiments are shown in fig.3. Typical wavefront profiles of supporting beam and amplified reversed beam are presented in fig.4. As a rule Strehl number values obtained by means of the Hartmann method from formula (1) exceed in 1.5-2 times Strehl numbers obtained by direct calorimetric measurements. This disagreement can be explained by low spatial resolution of this method. It depends on diffraction blurring of beams from separated holes and assumption of wavefront smoothness. The Hartmann method does not also take into account the contrasts of spots in hand and inhomogeneity of radiation intensity in near zone. Nevertheless the Hartmann method allows to picture wavefront profile and find the places of aberration localization. Fig. 4 shows good agreement between wavefronts of supporting and amplified Stokes radiation. It confirms phase conjugation of laser system under investigation.

Dependencies of Strehl number and input radiation intensity (for 10 cm output aperture) on selection degree of reversed component in Stokes radiation (fig. 5, 6) have been investigated. It has been found that both radiant intensity at the laser system output and Strehl number rise with selection degree increase. Nonreversed Stokes component suppression at the expense of entering into SBS-cell input system both phase aberrator and angular selector have improved beam quality approximately in 15 times (Strehl number was $St \approx 0.73$) and increased radiation intensity by an order of magnitude.

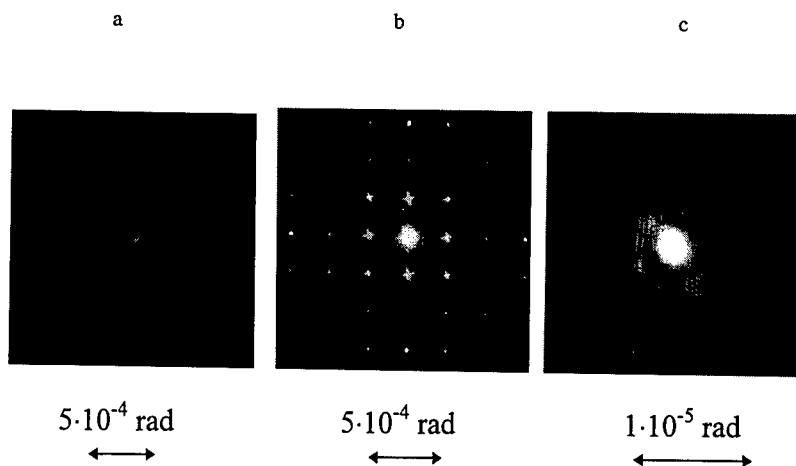


Figure 3. Typical radiation in far field.
a - pumping, b - Stokes before selection, c - output.

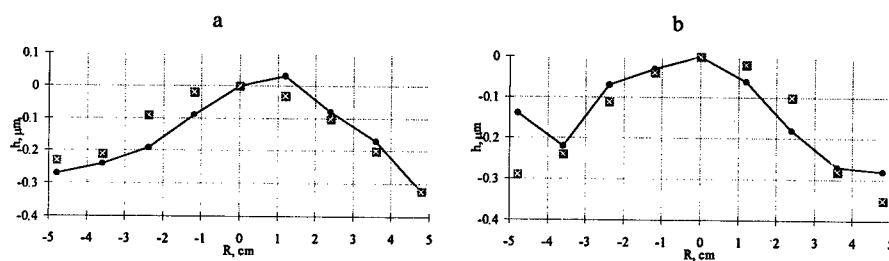


Figure 4. Wavefront pictures of amplified Stokes and master oscillator radiation.
a - vertical cross section, b - horizontal cross section.
■ - master oscillator; ● - amplified Stokes.

The dependencies of output radiation parameters versus input signal value has been investigated in two sets of experiments, when selection degree is $\eta \sim 200$ (raster $d=0.1$ cm, $f=9.2$ cm) and at $\eta \sim 460$ (raster $d=0.2$ cm, $f=12$ cm). The experiments of every set have been carried out under the same conditions: with the same kinoform raster at the same selection degree of reversed component and the same SBS threshold value. Input signal value varied in the range from 0.14 W/cm^2 to 2.6 W/cm^2 . Experimentally obtained dependencies of radiant intensity and Strehl number versus input signal have been normalized to unit and shown in fig. 7, 8. As the input signal value does not influence on spatial structure forming in the SBS cell, radiation quality, characterized by Strehl number, depends only weakly on input signal value. At the increasing input signal in 6 times the Strehl number has risen only in 1.5 times (fig. 7).

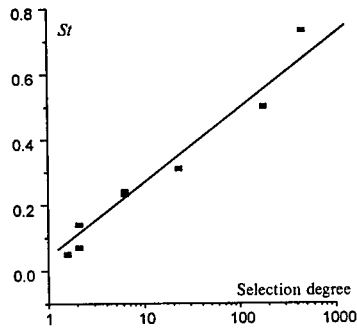


Figure 5. Laser output radiation quality versus the selection degree of the reversed component.

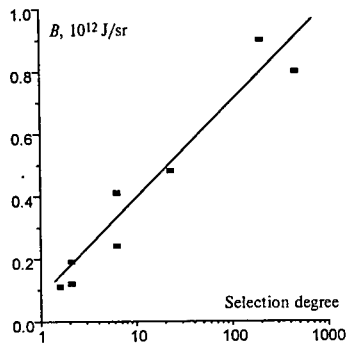


Figure 6. Radiant intensity of the laser output radiation versus the selection degree of the reversed component (output aperture is 15 cm).

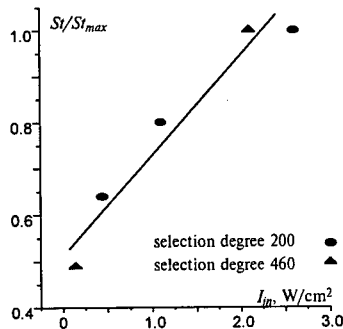


Figure 7. Laser output radiation quality versus the intensity of input radiation.

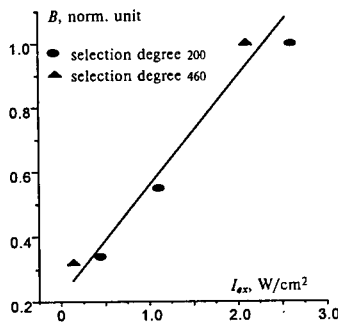


Figure 8. Radiant intensity of the laser output radiation versus the intensity of input radiation.

Radiant intensity dependence is much stronger (fig. 8). It is connected as with the rise of total power of the system (an increase of pumping energy and SBS reflectivity) as with suppression of stray generation in amplifiers. Radiation divergence in experiments with output beam aperture ~ 60 cm was at the half energy level $\theta_{0.5E} \approx (7-8) \cdot 10^{-6}$ rad (fig. 6) and at the half intensity level $\theta_{0.5I} \approx 2.5 \cdot 10^{-6}$ rad (fig. 10) that practically agree with diffraction limit for this laser. The restoration accuracy of reversed wave propagation in back direction was better than $\approx 1 \cdot 10^{-6}$ rad.

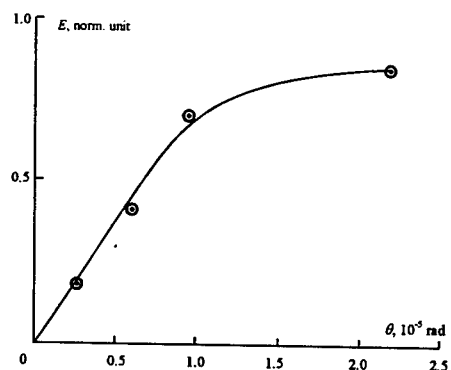


Figure 9. Angular distribution of output radiation energy with output laser aperture of 60 cm.

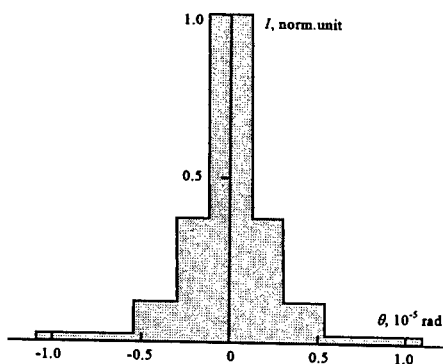


Figure 10. Angular distribution of output radiation intensity with output laser aperture of 60 cm.

6. Conclusion

Results of high energy iodine laser studies with phase conjugation ($E=300 \text{ J}$) with wavefront reversal fidelity at the whole laser system output up to the diffraction limit ($St=0.5-0.7$) are presented. The obtained experimental results confirms that the concept of creation of the laser facility with focusing of radiation in extreme small volumes can be realised.

7. Acknowledgments

The present work has been partly made under the support of ISTC within project #111.

8. References

1. Kirillov G.A., Kochemasov G.G., Kulikov S.M., Pevny S.N., Sukharev S.A., (1996) *HE-pumped iodine laser for plasma and high intensity interactions*, 12th International Conference on Laser Interaction and Related Plasma Phenomena, Osaka (Japan) 1995, AIP Conference Proceedings 369, part two, pp.866-871.
2. Dolgoplov Yu.V., Dudov A.M., Zykov L.I., Kochemasov G.G., Kulikov S.M., Murugov V.M., Sukharev S.A., Shkapa A.F. (1993) *Powerful photodissociation laser with high quality of phase conjugation*, Proceedings SPIE vol. 2095 Laser Physics, pp. 153-160.
3. Born M., Wolf E. (1970) *Principles of optics*, Moscow, Nauka.
4. L'vov L.V., Merkulov S.G., Ozerov M.A., Ryadov A.V. (1990) *Application of the Hartmann method in the investigation of the profile of wavefront of high-power pulsed lasers*, Kvantovaya elektronika, 21, no 11, pp.1055-1057 (Russia).

SBS properties of high-pressure xenon at a density of 0.3 - 1 g/cm³

L.I.ZYKOV, S.A.BUYKO, YU.V.DOLGOPOLOV,
A.M.DUDOV, V.A. EROSHENKO, G.A.KIRILLOV,
G.G.KOCHEMASOV, S.M.KULIKOV, V.N.NOVIKOV,
A.F.SHKAPA, AND S.A.SUKHAREV
*Russian Federal Nuclear Center (VNIIEF)
Sarov, Nizhni Novgorod Region, 607190, Russia*

Abstract

For xenon at the density of 0.3-1g/cm³ measurements have been made of the critical energy of thermal effect on the phase conjugation at SBS, the SBS gain coefficient, and the phonon lifetime. It has been shown that xenon is very well suited for the use in powerful gas lasers as an active SBS medium and is one of the best media for other lasers.

Presently, to study the physical processes of the matter behavior in quasi stationary superhigh intensity fields, the high-power nanosecond range laser facilities are created capable of focusing radiation to a wavelength size spot [1]. One of the difficulties faced in laser facilities of this class is compensation of optical elements aberrations and inhomogeneities of an active medium. To compensate for aberrations of the optical elements in such laser facilities and optical inhomogeneities of an active medium, one uses phase conjugation (PC) by stimulated Brillouin scattering (SBS). However, conversion of high-power laser beams in the SBS medium can be accompanied by competing processes such as SRS, optical breakdown, striction, and thermal perturbation. The present work gives the results of measuring the critical energy of thermal perturbation, SBS gain growth, and phonon lifetime in compressed xenon at densities of 0.3-1 g/cm³ [2, 3].

1. Thermal and Striction Perturbation of the SBS-medium

When a Gaussian beam is focused, depending on the pump conditions a lens is formed in the SBS medium, and the phase change in the pump radiation along the focused beam waist is:

$$\delta\varphi = \frac{2\pi^2}{\lambda^2} \left(n_2 P_L - \frac{3}{2} \frac{\beta\alpha}{TC_p} \int_0^{\tau_L} P_L dt \right) \quad (1)$$

where λ is the radiation wavelength, $n_2 = \frac{9}{2nc} \left(\frac{\beta}{v} \right)^2 \rho$ is the refractive index

non-linearity coefficient due to electrostriction, β (cm³/g) and n are the specific refraction and the refractive index of the medium, ρ (g/cm³) is the medium density, c and v are the light and sound speed in the medium, C_p (J/g.deg) is the specific heat capacity at constant pressure, P_L (W) is the pump radiation power; τ_L is the pump pulse length; T is the temperature, and α (cm⁻¹) being the laser radiation absorption coefficient in the SBS medium.

The first term of relation (1) describes the phase change connected with electrostriction appearing as a result of self-action of the pump radiation, which depends on the radiation power (intensity) in the SBS cell. Note that the SBS itself appears due to electrostriction evolution in the medium. Effect of this time-dependent component was observed for the first time in works [4, 5]. The second term is responsible for the phase change occurring with appearance of the thermal component in the SBS medium, which is determined by the pump energy absorbed in it. In this case a thermal lens is formed in the medium, which causes defocusing of the pump beam. At $\delta\phi > 2\pi$ the beam refraction distortions are becoming equal to those caused by diffraction, and as it follows from the experiment, the SBS efficiency falls down, which exhibits itself in a decrease of the reflection coefficient [5, 6, 7] and in a decrease of the phase conjugation fidelity [4, 5, 6]. For operation of the SBS mirror without a decrease in the phase conjugation fidelity, the pump radiation phase change should be $\delta\phi < 2\pi$. Then the power and energy of the laser pulse exciting SBS should be less than some critical values:

$$P_{cr} = \frac{\lambda^2}{2\pi n_2} \quad (2)$$

$$W_{cr} = \frac{\lambda^2}{2\pi} \frac{C_p \rho}{\frac{dn}{dT} \alpha} \quad (3)$$

where P_{cr} is the critical power determined by electrostriction; W_{cr} is the thermal perturbation critical energy [6].

Depending on the medium absorption coefficient (and pump conditions) the phase conjugation fidelity can be degraded by either of the factors. At small α electrostriction phenomena will dominate, at large α the thermal phenomena will be dominating. The critical energy of thermal perturbation W_{cr} is determined by the absorption coefficient α and depends mainly on purity of the applied SBS medium. However, even for an absolutely transparent medium ($\alpha = 0$) there exists some limiting value of the critical energy. It is connected with the decay of hypersonic grating in the medium, i. e., with the presence of

internal friction in it and is proportional to the Stokes frequency shift and sound speed in gas. For the gas lasers with a narrow gain line the Stokes shift should be small, and this requirement is met by xenon in the best way, from all monoatomic gases it has the lowest sound speed.

The thermal lens formation and the absorption coefficient in compressed xenon were investigated experimentally upon SBS excitation by radiation of a single-mode iodine laser ($\lambda = 1.315 \mu\text{m}$, pulse duration of 3-100 μs). The medium was probed by a beam of a He-Ne laser according to scheme [8] given in Fig.1. When a thermal lens is formed in the medium, the probe beam broadens in the plane of screen 5 and reaches photodetector 6. This signal is recorded by the oscillograph together with a SBS pump signal of the iodine laser. Typical oscillograms of the pump pulse and the probe laser signal are given in Fig.2. The oscillogram in Fig.2a shows behavior of the signal from the photodetector of the probe beam in the presence of an only thermal ("slow") component in the medium. Fig.2b illustrates joint modulation of the medium refractive index by striction ("fast") and thermal ("slow") components.

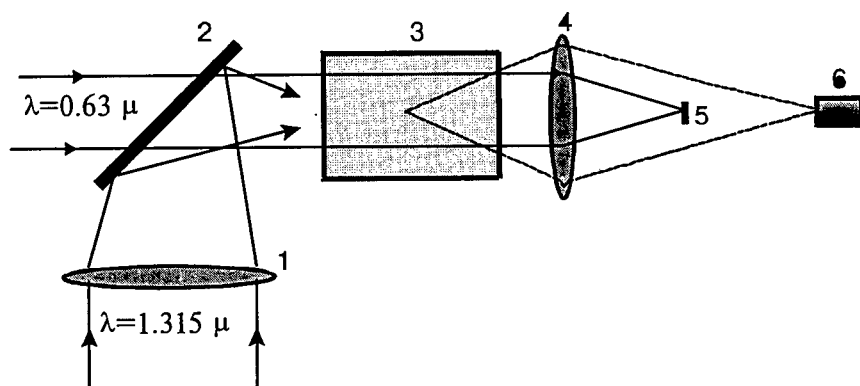


Fig. 1. Optical inhomogeneities investigation in the SBS medium (1, 4) lenses; (2) mirror; (3) cell with the SBS medium under study; (5) screen; (6) photodetector.

Experiments show that the pressure wave (and, hence, the wave of the changing refractive index) caused by striction propagates in the SBS medium with the sound speed, reflects off the walls of the cell and again (with a delay relative to the pump pulse) perturbs the medium in the probing zone. At lower pump powers traveling waves of inhomogeneities are not excited and a "slow" thermal lens with millisecond relaxation times is formed (Fig.2a). Using our experimental results and with account of our technology of SBS medium preparation, there have been obtained the following values of the absorption coefficient and critical parameters, for 46 atm Xe (density of 0.38 g/cm³) and $\lambda = 1.315 \mu\text{m}$: $\alpha \approx 5 \cdot 10^{-7} \text{ cm}^{-1}$, $P_{\text{cr}} = 3.2 \cdot 10^5 \text{ W}$, $W_{\text{cr}} = 5 \text{ J}$.

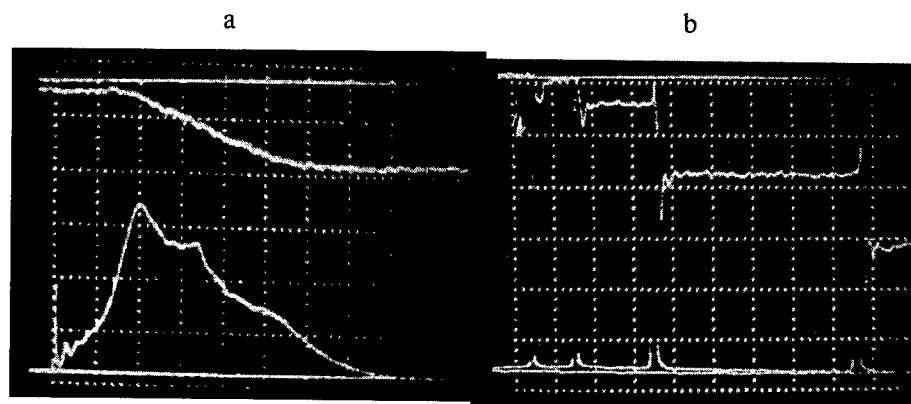


Fig. 2. Typical pulse oscillograms: probe radiation (upper beams) and SBS medium pumping (lower beams). The smallest time mark corresponds to 4 μ s.

The highest laser pulse duration at which SBS excitation in a steady-state mode occurs in the absence of thermal perturbation is: $\tau_{cr} \leq W_{cr}/P_{thr} \approx g \cdot W_{cr}/5\lambda$ [2, 9], where $P_{thr} \approx 5\lambda/g$ is the threshold power for a single-mode radiation, g is the SBS gain coefficient (cm/W). For $g = 120$ cm/GW (see below) τ_{cr} reaches the value of $\tau_{cr} \approx 1 \cdot 10^{-3}$ s. In this case during a laser pulse the striction perturbation does not affect the phase conjugation fidelity, and thermal perturbation begins to degrade it only in the end of the pulse.

2. Investigation of the SBS Gain Coefficient and Phonon Lifetime [3]

Theoretical investigations predict an increase of the SBS gain coefficient in xenon with the increase of the gas density $g \propto \rho^2$ [10]. Far from the critical point ($T_{cr} = 289.7^\circ\text{K}$, $P_{cr} = 57.6$ atm, $\rho_{cr} = 1.11$ g/cm³) the experimental results agree fairly well with this dependence, for example, $g = 1.4$ cm/GW at $P = 10$ atm ($\rho = 0.058$ g/cm³) [11], $g = 44$ cm/GW at $P = 39$ atm ($\rho = 0.30$ g/cm³) [12]. However, an attempt to obtain a high gain growth in xenon at a pressure of 220-240 atm [13] did not give results expected by the authors of this work. In work [14], as the critical point of Xe at $\rho \geq 0.7$ g/cm³ was approached, appearance of optical inhomogeneities was registered, which raised the SBS threshold. Below we give results obtained from SBS investigation in Xe at densities from 0.3 g/cm³ to 1 g/cm³ in a thermostatically controlled cell under conditions when the influence of optical inhomogeneities on the SBS threshold was small.

Scheme of experiments of SBS threshold power (P_{thr}) measurements in a steady-state excitation regime is shown in Fig. 3. Single-mode iodine laser radiation was used for SBS excitation with the following Laser radiation parameters: wavelength $\lambda = 1.315$ μ m, energy $E \approx 10$ J, pulse duration $\tau_L \approx 100$ μ s, radiation divergence $\theta_{0.84E} \approx 10^{-4}$ rad, laser beam diameter

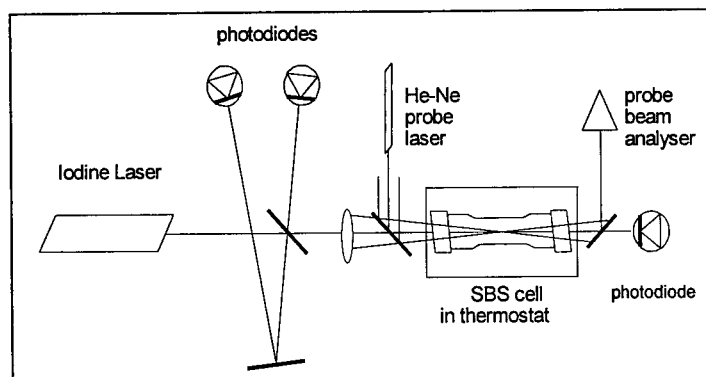


Fig. 3. Experimental setup.

$D \approx 7$ cm. Parameters of the pumping, reflected and passed through the SBS cell radiation were registered by calibrated photodiodes with the time resolution of 50 ns. The pumping power was measured in the far field of a positive lens by photo diodes with different apertures, it allowed to measure the pumping power in different angles : $1 \cdot 10^{-3}$, $1 \cdot 10^{-4}$, $5 \cdot 10^{-5}$ rad and to control the pump radiation divergence.

The laser radiation was focused into the SBS cell with a length of 25 cm and diameter of 1.5 cm by means of a lens with the focal length $F = 138$ cm. A special attention was given to Xe purity. To exclude influence of impurities, only metal (indium) linings were used in the cell construction, and it was filled through special filters. The purification efficiency from aerosol particles with a diameter more than $0.01 \mu\text{m}$ was above 99.9999 %. The thermostat maintained the cell temperature at a value of $t = 19.3^\circ\text{C}$, the temperature drift did not exceed 0.03°C per hour. The Xe pressure in the cell was measured with a relative error of 7 %, the density of Xe was determined by cell weighing. The optical quality of SBS medium was supervised with the help of a He-Ne laser which parameters were selected in such a manner that its beam simulated the pump beam in the cell. The intensity distribution in the focal plane inside the cell with Xe $I_1(\varphi)$ was compared with the distribution obtained in the absence of the cell $I_2(\varphi)$. Measurements of the intensity distribution were carried out in the focal plane with the help of diaphragm scanning across the horizontal cross section. The He-Ne radiation power passed through the diaphragm was registered by a photodiode and measured by a digital voltmeter. Comparison of both distributions ($I_1(\varphi)$ and $I_2(\varphi)$) allowed us to estimate quantitatively the deformation of a diffraction limited beam during its passage through the SBS-cell. For all investigated points these distributions coincided with on accuracy of ≈ 5 %, and only at $\rho = 1.02 \text{ g/cm}^3$ the intensity in the maximum fell down from $I_2^{\text{max}} = 1$ in the absence of the cell to $I_1^{\text{max}} = 0.62$ with it. This was taken into account in the P_{thr} calculation.

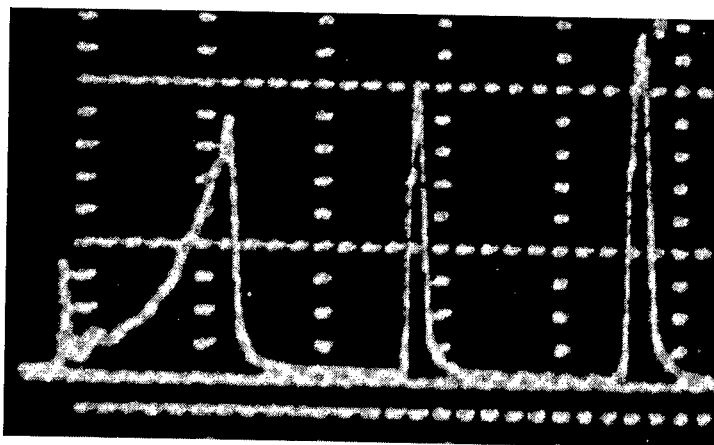


Fig. 4. Typical pumping pulse shape. Horizontal scale - 20 μ s/div.

Under the influence of Stokes radiation, as SBS excitation occurred, the mode of iodine laser generation changed and became pulse-periodic (see Fig. 4). Only the first pulse with the leading front duration of about 20 μ s, where steady-state excitation conditions were satisfied and pump energy did not exceed the critical energy of thermal defocusing W_{cr} , was used to determine the P_{thr} . The value of pumping power P_L providing the SBS reflection coefficient $R_S = 1\%$ was taken as P_{thr} :

$$P_{thr} \langle R = 1\% \rangle = P_L \langle \theta = 5 \cdot 10^{-5} \text{ rad} \rangle \cdot \frac{I_1^{max}}{I_2^{max}}.$$

The basic results of experiments are shown in Table 1, where averaged over several experiments P_{thr} values are shown. The standard deviation obtained in each series of experiments did not exceed 15 %. For the gas density we give experimentally measured values labeled by an asterisk and values, calculated using Pitser's three-parameter correlation by method of Li-Kesler [15], giving the best approximation to experiment.

Table 1 The basic results of experiments.

P , atm	39,8	43	46	47.4	50	54	56	59. 2	60.5	61	61.3	62
ρ , g/cm ³	0.30 0.30*	0.34	0.38	0.41	0.45	0.53	0.60 0.59 *	0.7 8	0.90	0.94	0.97	1.04 1.02*
P_{thr} , kW	27	24	19	14	16	11	10	11	12	11	11	12

From the obtained data we have determined the SBS gain coefficient g_i using as a reference value $g_0 = 44$ cm/GW for the Xe density of 0.3 g/cm³ given in work [12]:

$$g_i = \frac{P_{thr}^0}{P_{thr}^i} g_0,$$

where P_{thr}^0, P_{thr}^i are the corresponding threshold powers.

These results are shown in Fig. 5. The results of calculation of g for $\rho < 0.5$ g/cm³ using the available thermodynamic parameters for Xe [16] are also shown in Fig. 5. We can see that beginning with $\rho = 0.6$ g/cm³ the value

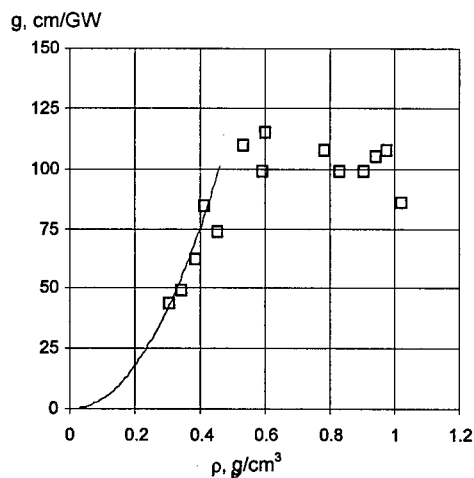


Fig. 5. SBS gain coefficient versus Xe density.
□ - experiment, — theory.

of g does not increase, which in our experiments could be only due to a decrease in the phonon lifetime. The phonon lifetime τ_{ph} has been determined using g_i values in accordance with the equality :

$$\tau_{ph} = g \left(\frac{16\pi^2 n \rho \left(\frac{\partial n}{\partial \rho} \right)^2}{\lambda^2} \right)^{-1},$$

where n is the refractive index, c is the light velocity, v - is the hypersound velocity.

The results of calculation of τ_{ph} are shown in Fig. 6. The value of $\tau_{ph} = 21.2$ ns, calculated with the use of data of hypersound absorption at

$\rho = 1.11 \text{ g/cm}^3$ and $t = 19.4^\circ \text{C}$ [17], is shown in Fig. 6 as well. A good agreement is observed between our results and those obtained in work [17].

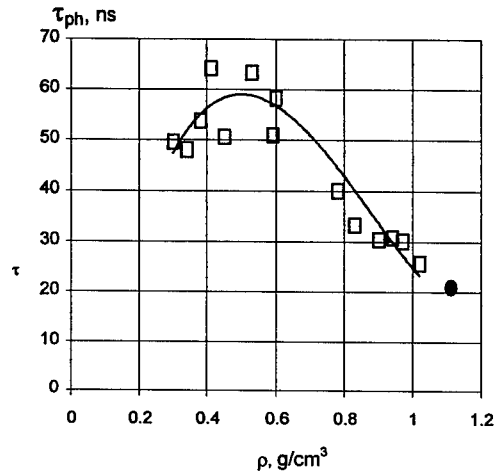


Fig. 6. Phonon lifetime versus Xe density.

□ - experiment, — - fitting curve,
• - calculated from data of work [17]

The criterion for SBS medium selection which is more resistant to the evolution of undesired thermal perturbation is that the critical energy W_{cr} should exceed the threshold energy $W_{thr} \approx P_{thr} \cdot \tau$, which is proportional to $g \cdot W_{cr} / \lambda$. The more is the value of $g \cdot W_{cr} / \lambda$ the more resistant is the SBS medium to formation of a thermal lens and the longer laser pulses it can convert. Fig. 7 shows experimental dependence of $g \cdot W_{cr} / \lambda$ for xenon in relative units. Under our conditions this value is the highest in the density range of 0.5–0.8 g/cm³.

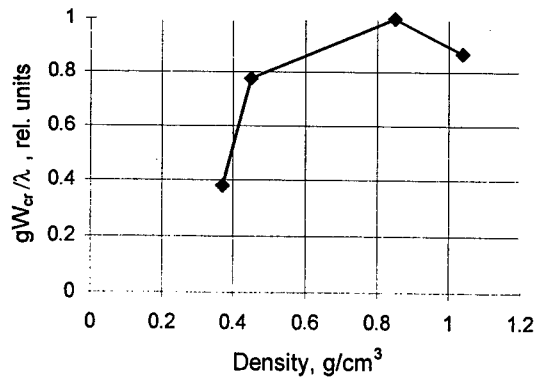


Fig. 7. $g \cdot W_{cr} / \lambda$ versus xenon density

According to the suggested criterion high-purity xenon is best suited as an active SBS medium in high-power gas lasers and is one of the best media for other lasers. (See Table 2).

Table 2

Medium	Nd-glass ГЖС-1	aceto- ne	SF ₆ 22 at	CCl ₄	SiCl ₄	TiCl ₄	SnCl ₄	Xe gas 0.6 g/cm ³ ($\lambda=1.06 \mu\text{m}$)
$g, \text{ cm/GW}$	1.2	15.8	35	4	10	20	14	120
$W_{\text{cr}}, \text{ J}$	20	$5 \cdot 10^{-4}$		11	33	28	57	4.7
$g W_{\text{cr}}/\lambda, \text{ ms}$	0.22	$7.4 \cdot 10^{-5}$		0.41	3.1	5.3	7.5	5.3
References	/18/	/18/	/12/	/9/	/9/	/9/	/9/	our data

Xenon, being a monoatomic gas, is not subjected to the evolution of competing SRS in it, and from the technological point of view is chemically inert, stable, and ecologically safe.

3. References

1. Kirillov G.A., Kochemasov G.G., Kulikov S.M., Pevny S.N., Sukharev S.A. (1996) *HE-pumped iodine laser for plasma and high intensity interactions*. 12th International Conference on Laser Interaction and Related Plasma Phenomena, Osaka (Japan) 1995, AIP Conference Proceedings 369, part two, pp.866-871
2. Dolgoplov Yu.V., Dudov A. M., Eroshenro V.A., Zykov L.I., Kochemasov G.G., Kulikov S.M., Novikov V.N., Sukharev S.A., and Shkapa A.F. (1995) *Phase-conjugate lasers in a free-running mode*. Proceedings of the 2nd International Conference "Physics of Nuclear-Excited Plasma and Problems of Nuclear-Pumped Lasers", vol.2, pp. 229-245. Arzamas-16, VNIIEF, Russia.
3. Dudov A.M., Buyko S.A., Dolgoplov Yu.V., Eroshenko V.A., Kochemasov G.G., Kulikov S.M., Novikov V.N., Scott A.M., Shkapa A.F., Sukharev S.A., Zykov L.I. (1996) *SBS properties of high-pressure xenon*. XI International Symposium on Gas Flow and Chemical Lasers and High Power Laser Conference. Edinburg, Scotland, UK, 1996. Proc. SPIE, v.3092, pp.341-344.
4. Dolgoplov Yu.V., Komarevski V.A., Kormer S.B., Kulikov S.M. et al. (1979) Experimental investigation of phase conjugation employment at SBS. ZhETF, vol.76, pp.908-923.
5. Dolgoplov Yu.V., Kir'yanov Yu.F., Kormer S.B. et al. (1979) *SBS phase conjugation investigation and its application in laser fusion facilities*. In a collection of papers "Phase conjugation of optical radiation in nonlinear media", Gorky.
6. Bubis E.L., Drobotenko V.V., Kulagin O.V., Pasmanik G.A., Stasyuk N.I., Shilov A.A.. (1988) *Thermal self-action effect on SBS excitation in absorbing media*. Kvant. Elektron., v. 15, No.1, p.147.
7. Pfeifer S.J. (1988) *Phase conjugation and aberration correction by stimulated Brillouin scattering*. SPIE, vol.1000, Laser Wavefront Control, pp.33-42.
8. Bubis E.L., Var'gin V.V., Konchalina L.R., Shilov A.A.. (1988) *Investigation of poorly absorbing media for SBS in the near-IR spectrum*. Optika and Spektroskopia, vol.65, issue 6, pp.1281-1285.
9. Andreev Nikolay, Kulagin Oleg, Palashov Oleg, Pasmanik Guerman, Rodchenkov Vladimir (1995) *SBS of repetitively pulsed radiation and possibility of increasing of the pump average power*. First Annual International Conference on Solid State Lasers for Application to Inertial Confinement Fusion. Monterey, California. SPIE, v. 2633, pp. 476-493.

10. Damzen M.J., Hutchinson M.H.R. and Schroeder W.A. (1987) *Direct measurement of the acoustic decay times of hypersonic waves generated by SBS*, IEEE J.Quant.Electron., v.QE-23, no.3, p.328.
11. Faris G.W., Jusinski L.E. and Hickman A.P., *High-resolution stimulated Brillouin gain spectroscopy in glasses and crystals*, J.Opt.Soc.Am.B, v.10, no.4, p.587 (1993)
12. Ragul'ski V.V.. (1990) *Phase conjugation at stimulated Brillouin scattering*, Moscow, Nauka.
13. Ivanov V.B., Paperny S.B., Snezhko D.A., Startsev V.R.. (1991) *SBS of microsecond pulses in gaseous xenon of the pressure above critical*. Izvestia AN SSSR, seria fiz., vol. 52, no.2, p.224.
14. Betts J.A., Pfeifer S.J., Koop C.G., and Clendening C. in *Technical Digest, CLEO'91*, paper CMG2
15. Rid R., Prausnitz J., Shervood T. (1982) *Properties of gases and liquids*, Leningrad, Chimia.
16. Vargaftik N.B. (1972) *Handbook of thermophysical properties of gases and liquids*, Moscow, Nauka.
17. Garland C.W., Eden D., and Mistura L., (1970) *Critical sound absorption in xenon*, Phys. Rev. Lett., **25**(17), 1161-1165.
18. Krainov V.V., Mak A.A., Rusov V.A., Yashin V.E.. (1991) *Phase conjugation of a high-frequency series of pulses at SBS of focused beams*. Kvant. Elektron., v. 18, no. 18, pp. 959-963.

FLATTENED GAUSSIAN BEAMS WITH RECTANGULAR SYMMETRY

S.-A. AMARANDE

Laser Department

National Institute for Laser, Plasma and Radiation Physics

P.O. Box MG-36, RO-76900 Bucharest-Măgurele, Romania.

Abstract

Characterization of flattened Gaussian beams with rectangular symmetry is extended by the analysis of two features which are generally considered important: i) on-axis intensity and ii) far-field amplitude. Their overall behaviour tends to that of functions corresponding to the case of a plane wave diffracted by a linear slit. These features, along with others already explored characteristics of flattened Gaussian beams with rectangular symmetry, such as beam propagation factor and kurtosis shape-parameter, should be useful for applications involving flat-topped laser beams.

1. Introduction

For several laser application, such as material processing and non-linear optical conversion, a beam whose cross-section has an intensity profile as uniform as possible or flat-topped is often desirable. Example of such kind of beams are highly multimode laser beams [1,2], generated by stable optical resonators, super-Gaussian beams, generated by resonators with graded-reflectivity mirrors [3] or with graded-phase mirrors [4], laser beams generated by resonators with diffractive mirrors [5] and laser beams generated by Fourier transform resonators [6]. These flat-topped beams are axially or rectangularly symmetric. When the propagation of the beams generated by stable resonators can be handled analytically, the propagation of the super-Gaussian beams can be treated only by rather complicated numerical methods [7]. A convenient way to overcome this problem is to approximate the super-Gaussian beams [8,9] by a new class of axially symmetric coherent beams, the so-called flattened Gaussian beams [10,11].

As suggested by Gori [10], we introduced flattened Gaussian beams without axial symmetry, e.g. with a waist cross section resembling a rectangle [12], by using a suitable superposition of Gauss-Hermite modes. For this new class of beams we already inferred the free-space propagation formula. We also evaluated the beam

propagation factor and the kurtosis parameter as functions of the beam order, N , by using the mode coefficients of the representation. According to the evolution of the kurtosis parameter in the free space, we classified the flattened Gaussian beams with rectangular symmetry in two types as N is greater or less than 3.

In this paper we will outline shortly the already mentioned beam propagation features. We will explore two other beam propagation features which have been considered important. These are the intensity on the optical axis as a function of the propagation distance and the far field amplitude.

2. Representation and propagation of flattened Gaussian beams in transverse Cartesian coordinates

To introduce the flattened Gaussian beams (FGBs) [10], a superposition of N suitably weighted Laguerre-Gauss beams was carried out, N representing the beam order. Many of the already existing results concerning beam characterization, are obtained by using Cartesian coordinates rather than cylindrical coordinates; moreover there are beams rather rectangularly symmetric. Therefore, we will trace back FGBs to Hermite-Gauss beams following the lines of [10]. For the sake of simplicity, we restrict ourselves to the bidimensional case (x, z) . Then by the multiplication of two distributions, flattened independently along x and y we could obtain a tridimensional FGB whose cross section is in the form of a rectangle.

We begin by writing the field distribution, $U_N(x, z)$, at $z=0$ in the form

$$U_N(x, 0) = A \cdot \exp\left(-\frac{x^2}{w_0^2}\right) \cdot \sum_{k=0}^N \frac{(x/w_0)^{2k}}{k!}, \quad N=0, 1, \dots, \quad (1)$$

where the spot-size, w_0 , facilitates comparison with the formulas of ordinary gaussian beams and A is a constant.

We then express x^{2k} , starting from a decomposition relation in Hermite-Gauss functions [13], by

$$x^{2k} = \frac{(2 \cdot k)!}{2^{3k}} \cdot \sum_{n=0}^k \frac{1}{(k-n)! \cdot (2 \cdot n)!} \cdot H_{2n}(\sqrt{2} \cdot x) \quad (2)$$

One can see that only even Hermite polynomials, H_{2n} , are involved in the combination

$$U_N(x, 0) = A \cdot \exp\left(-\frac{x^2}{w_0^2}\right) \cdot \sum_{n=0}^N c'_n \cdot H_{2n}(\sqrt{2} \cdot x/w_0), \quad N=0, 1, \dots, \quad (3)$$

where

$$c'_n = \frac{1}{(2 \cdot n)!} \cdot \sum_{k=n}^N \frac{1}{2^{3k}} \cdot \frac{(2 \cdot k)!}{k! \cdot (k-n)!}. \quad (4)$$

The Hermite-Gauss beam of order n , say $\Psi_n(x, z)$, has the following spatial distribution [14]

$$\Psi_n(x, z) = \left(\frac{2}{\pi \cdot w^2(z)} \right)^{1/4} \cdot (2^n \cdot n!)^{-1/2} \cdot H_n(\sqrt{2} \cdot x/w(z)) \times \\ \exp \left[-\frac{x^2}{w^2(z)} - i \frac{k \cdot x^2}{2 \cdot R(z)} - i \cdot k \cdot z + i \cdot \left(n + \frac{1}{2} \right) \cdot \Phi(z) \right], \quad (5)$$

where as usual

$$w(z) = w_0 \sqrt{1 + \left(\frac{z}{z_R} \right)^2}, \quad R(z) = z + \frac{z_R^2}{z}, \quad \Phi(z) = \tan^{-1} \left(\frac{z}{z_R} \right) \quad \text{and} \quad z_R = \frac{\pi \cdot w_0^2}{\lambda}.$$

One obtains for the FGB represented in Cartesian coordinates the amplitude at $z=0$

$$U_N(x, 0) = \sum_{n=0}^N c_n \cdot \Psi_{2n}(x, 0), \quad N=0, 1, \dots, \quad (6)$$

and the propagation formula

$$U_N(x, z) = \sum_{n=0}^N c_n \cdot \Psi_{2n}(x, z), \quad N=0, 1, \dots, \quad (7)$$

where

$$c_n = A \cdot \left(\frac{\pi}{2} \right)^{1/4} \cdot \frac{2^n}{[(2 \cdot n)!]^{1/2}} \cdot \sum_{k=n}^N \frac{1}{2^{3k}} \cdot \frac{(2 \cdot k)!}{k! \cdot (k-n)!}. \quad (8)$$

Drawing field distribution at $z=0$ for a few values of N we obtain the curves presented in Fig. 1.

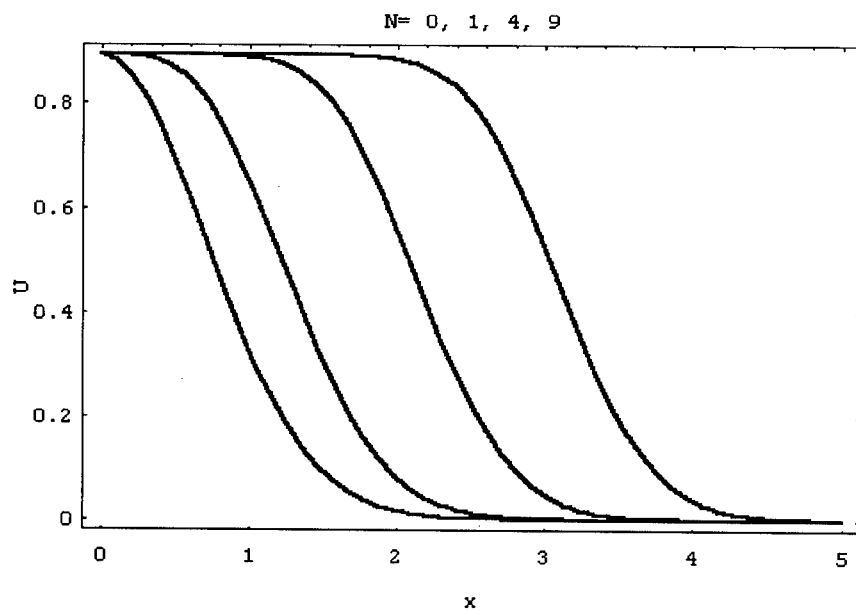


Figure 1: Transverse intensity profiles of FGBs with different beam orders versus x .

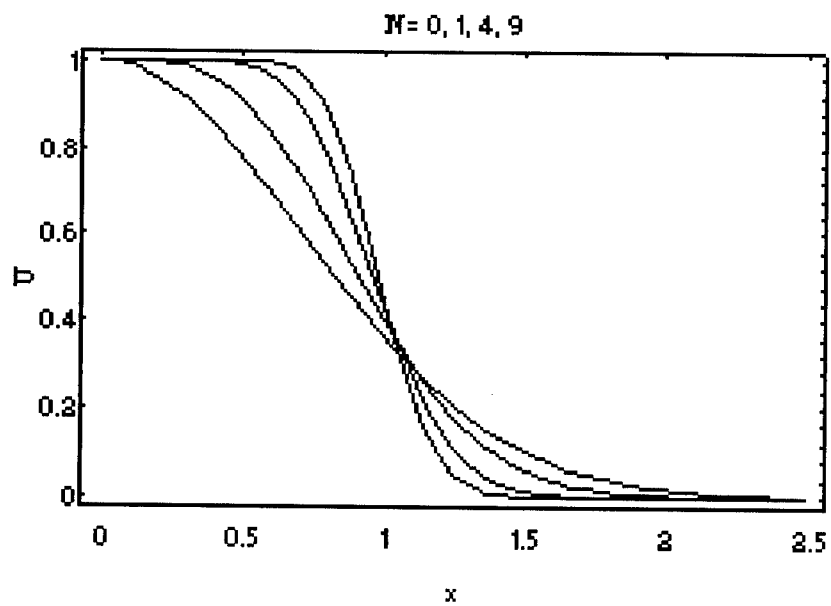


Figure 2: Transverse intensity profiles of rescaled FGBs with different beam orders versus x .

The flattened Gaussian beams can be rescaled [10,11] or normalized [12]. The rescaled FGBs are obtained by dividing in Eq. (1) the spot-size, w_0 , by $\sqrt{N+1}$

$$U_N(x) = A \cdot \exp\left[-\frac{(N+1)x^2}{w_0^2}\right] \cdot \sum_{k=0}^N \left(\frac{\sqrt{N+1} \cdot x}{w_0}\right)^{2k} \cdot \frac{1}{k!}. \quad (9)$$

So that, for the relations corresponding to rescaled FGBs, we can use the relations already inferred, replacing the spot-size, w_0 , by $w_N(0)$.

$$\frac{w_0}{\sqrt{N+1}} = w_N(0). \quad (10)$$

Their field distribution is presented in Fig. 2.

The normalized FGBs can be constructed by normalizing the mode coefficients, c_n , so that the total power $\sum |c_n|^2 = 1$, obtaining for the constant A the expression

$$A = \left(\frac{\pi}{2}\right)^{-1/4} \cdot \left\{ \sum_{n=0}^N \frac{2^{2n}}{(2 \cdot n)!} \cdot \left[\sum_{k=n}^N \frac{1}{2^{3k} \cdot k!} \cdot \frac{(2 \cdot k)!}{(k-n)!} \right]^2 \right\}^{-\frac{1}{2}}, \quad N=0,1,\dots \quad (11)$$

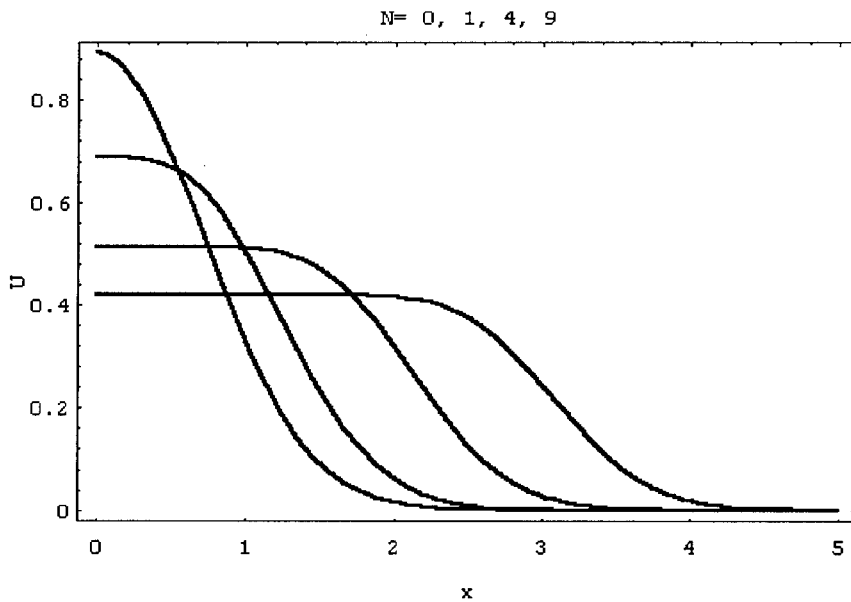


Figure 3: Transverse intensity profiles of normalized FGBs with different beam orders versus x .

The graphs of field distribution corresponding to these normalized FGBs are presented in Fig. 3.

3. Propagation of the on-axis intensity

To evaluate the on-axis intensity for rescaled FGBs we first calculated the field on the optical axis namely $U_N(0, z)$. We obtained

$$U_N(0, z) = A \cdot \left(\frac{w_N(0)}{w_N(z)} \right)^{\frac{1}{2}} \cdot \sum_{n=0}^N \left\{ [(2 \cdot n)!]^{-1} \cdot \sum_{k=0}^n \frac{1}{2^{3k} \cdot k!} \cdot \frac{(2 \cdot k)!}{(k-n)!} \right\} \times \\ \left\{ H_{2n}(0) \cdot \exp \left[-i \cdot k \cdot z + i \cdot \left(2n + \frac{1}{2} \right) \cdot \Phi(z) \right] \right\}. \quad (12)$$

Then, by using the relation [15]

$$H_n(0) = \begin{cases} (-1)^m \cdot \frac{(2m)!}{m!}, & n = 2m \\ 0, & n = 2m + 1 \end{cases}, \quad (13)$$

$$U_N(0, z) = A \cdot \left(\frac{w_N(0)}{w_N(z)} \right)^{\frac{1}{2}} \cdot \exp \left\{ -i \left[kz - \frac{1}{2} \Phi(z) \right] \right\} \times \\ \sum_{n=0}^N \left\{ \sum_{k=0}^n \frac{1}{2^{3k} \cdot k!} \cdot \frac{(2 \cdot k)!}{(k-n)!} \right\} \cdot \left\{ \frac{1 - \exp[i 2n \Phi(z)]}{2^3} \right\}^k. \quad (14)$$

Here we use the Newton's binomial expansion and

$$U_N(0, z) = A \cdot \frac{1}{w^{1/2}(z)} \cdot \exp \left\{ -i \left[kz - \frac{1}{2} \Phi(z) \right] \right\} \times \\ \sum_{k=0}^N \frac{(2k)!}{(k!)^2} \cdot \left\{ \frac{1 - \exp[2i \Phi(z)]}{2^3} \right\}^k. \quad (15)$$

On-axis intensity as a function of the propagation distance is presented in the graphics from Fig. 4.

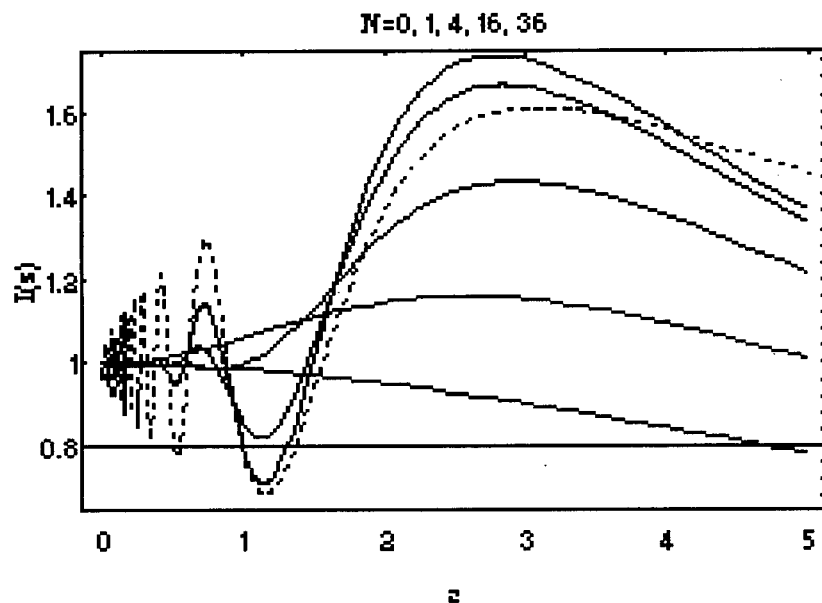


Figure 4: On-axis intensity, $I(z)$, as a function of the propagation distance z .

When N increases, the number of maxima and minima increases too, and the curves tend to the function (see Ref. [12] p. 725)

$$U(0, z) \approx 1 + i \cdot \sqrt{\frac{i}{2\pi^2 N}} \cdot \exp(-i\pi N), \quad (16)$$

corresponding to the on-axis intensity for the case of a slit aperture, which has been represented with dotted line. We suppose that the override of this curve when z is between 1 and 4, for large values of N , can be explained by the approximate form of $U(0, z)$. This point could be further clarified when the formula of the on-axis intensity will be obtained in a closed form.

4. Far-field amplitude and beam propagation factor M^2

The Fourier transform of the rescaled FGBs, namely

$$U_N(s) = \int_{-\infty}^{\infty} U_N(x) \cdot \exp[+i2\pi s x] \cdot dx, \quad (17)$$

is

$$U_N(s) = A \cdot \sum_{k=0}^N \frac{\alpha^k}{k!} \int_{-\infty}^{\infty} x^{2k} \cdot \exp[-\alpha x^2 + i2\pi s x] \cdot dx, \quad (18)$$

where

$$\alpha = \frac{N+1}{w_0^2}.$$

By using the relation [16]

$$\int_0^{\infty} x^{2n+\delta} \cdot \exp[-ax^2] \cdot \begin{cases} \sin(bx) \\ \cos(bx) \end{cases} \cdot dx = (-1)^n \cdot \sqrt{\pi} \cdot 2^{-2n-1-\delta} \cdot a^{-(2n+1+\delta)/2} \times \\ \exp\left(-\frac{b^2}{4a}\right) \cdot H_{2n+\delta}\left(\frac{b}{2\sqrt{a}}\right), \quad \text{Re } a > 0, \quad \delta = \begin{cases} 1 \\ 0 \end{cases}, \quad (19)$$

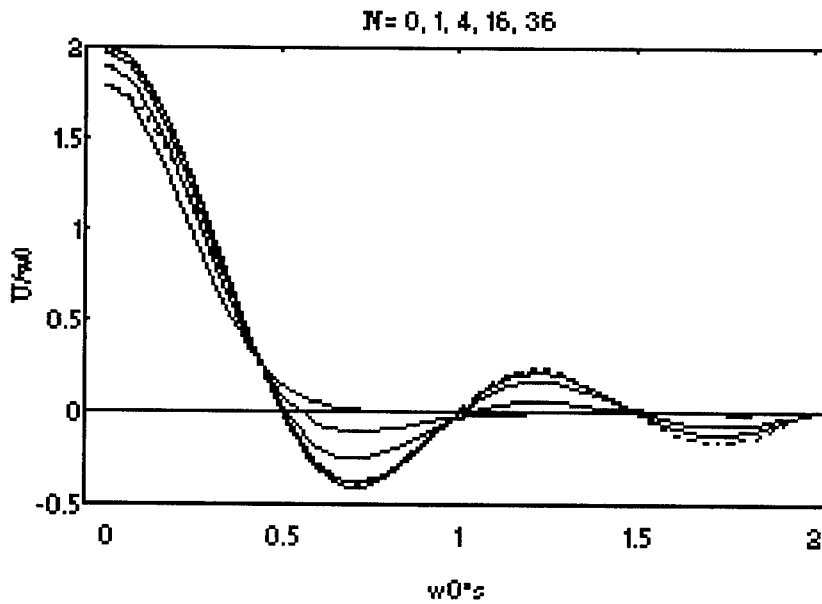


Figure 5: Fourier transform of amplitude $U_N(0, z)$ normalized to the value w_0 , for $N=0$ and 4, as a function of $w_0 s$. The dotted curve represents a Fourier transform of $\text{rect}(x/w_0)$.

we obtain a relation of the far-field amplitude

$$U_N(s) = A \cdot \sqrt{\frac{\pi}{\alpha}} \cdot \exp\left[-\frac{(\pi s)^2}{\alpha}\right] \cdot \sum_{k=0}^N (-1)^k \cdot \frac{1}{2^{2k} \cdot k!} \cdot H_{2k}\left(\frac{\pi s}{\sqrt{\alpha}}\right). \quad (20)$$

The far-field amplitude graphics is presented in Fig. 5. The limiting case (rect function), when N increases, is far-field amplitude for the case of a slit aperture (see Ref. [14] p. 720)

$$U(s) \approx (4iN)^{1/2} \cdot \text{sinc}(2\pi s) \quad (21)$$

Again, we suppose that the override of this curve, when $w_0 s$ is around 0, for large values of N , can be explained by the approximate form of $U(s)$. This point could be further clarified when the formula of the far-field amplitude will be obtained in a closed form.

The beam propagation factor, M^2 , can be evaluated [12] for every beam order N by using the relation

$$M^2 = \left(\left[\sum_{n=0}^N (2n+1) |c_n|^2 \right]^2 - 4 \cdot \left\{ \sum_{n=0}^N [(n+1)(n+2)]^{1/2} \text{Re}(c_n \cdot c_{n+2}^*) \right\}^2 \right)^{1/2}. \quad (22)$$

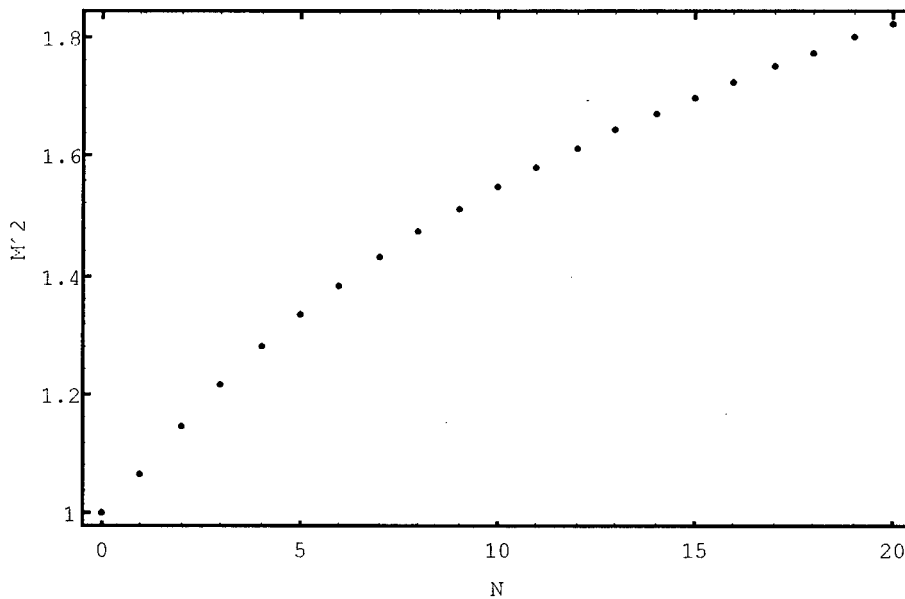


Figure 6: Beam propagation factor M^2 versus beam order N .

The results appear in Fig. 6. As expected, for $N=0$ we encounter a pure gaussian beam for which M^2 equals 1, the minimum value for this parameter.

5. Conclusions

Characterization of FGBs with rectangular symmetry is extended by the analysis of two features which are generally considered important: i) on-axis intensity and ii) far-field amplitude. Their overall behaviour tends to that of functions corresponding to the case of a plane wave diffracted by a linear slit. These features, along with others already explored characteristics of FGBs with rectangular symmetry, such as beam propagation factor and kurtosis shape-parameter, should be useful for applications involving flat-topped laser beams.

Acknowledgements

The research work leading to this paper was partially supported by the Ministry for Research and Technology of Romania, under contract with NILPRP No. A53.

References

1. Lamberton, H.M and Roper, V.G. (1978) Beam divergence of a highly multimode CO₂ laser, *J. Phys. E: Sci. Instrum.* **11**, 1102-1103.
2. Siegman, A.E., and Townsend, S.W. (1993) Output beam propagation and beam quality from a multimode stable-cavity laser, *IEEE J. Quantum Electron.* **29**, 1212-1217.
3. Piché, M. et al. (1997) Unstable resonators with variable reflectivity, *Optical Resonators-Science and Engineering NATO ARW, Smolenice Castle, Slovak Republic*, July 1-5.
4. Bélanger, P.-A. (1997) Custom laser resonators, *Optical Resonators-Science and Engineering NATO ARW, Smolenice Castle, Slovak Republic*, July 1-5.
5. Leger, J.R. et al. (1994) Diffractive optic laser resonator, *Optics and Photonics News* December, p.19.
6. Mottay, E. (1997) Optimization of beam profile in solid state lasers, *Optical Resonators-Science and Engineering NATO ARW, Smolenice Castle, Slovak Republic*, July 1-5.
7. Parent, A., Morin, M. and Lavigne, P. (1992) Propagation of super-Gaussian beams field distributions, *Opt. and Quantum Electron.* **24**, S1071-S1079.
8. Palma, C. and Bagini, V. (1994) Propagation of super-Gaussian beams, *Optics Comm.* **111**, 6-10.
9. Amarande, S.-A. (1997) Approximation of supergaussian beams by generalized flattened gaussian beams, *Proc. XI Int. Symp. on Gas Flow and Chem. Lasers and High Power Laser Conference, SPIE* **3092**.
10. Gori, F. (1994) Flattened gaussian beams, *Optics Comm.* **107**, 335-341.
11. Bagini, V. et al. (1996) Propagation of axially symmetric flattened Gaussian beams, *JOSA A* **13**, 1385-1394.
12. Amarande, S. (1996) Beam propagation factor and the kurtosis parameter of flattened Gaussian beams, *Optics Comm.* **129** 311-317.
13. Morse, P.M. and Feshbach, H. (1953) *Methods of Theoretical Physics*, McGraw- Hill, New York, vol. 1, chap. 5.
14. Siegman, A.E. (1986) *Lasers*, Univ. Sci., Mill Valley, CA, p. 646.
15. Abramowitz, M. and Stegun, I. eds. (1965) *Handbook of Mathematical Functions*, Dover, New York, p.777.
16. Prudnikov, A.P., Brychkov, Yu.A., and Marichev, O.I. (1981) *Integrals and Series*, Nauka, Moscow, p. 452.

BEAM DIVERGENCY STUDIES ON A LONG PULSE XECL EXCIMER LASER

R.M. HOFSTRA, F.A. VAN GOOR AND W.J. WITTEMAN
University of Twente
P.O. Box 217, 7500 AE Enschede, The Netherlands

Abstract.

A nearly diffraction limited output beam was obtained from a hard edge confocal positive branch unstable resonator. Improvement of the far field energy profile can be obtained by using partial reflecting hard edge out-coupling mirrors. Further improvement can be obtained by using gaussian mirrors.

1. Introduction

For the application field of our 1 kHz, 1 kW long pulse XeCl excimer laser developed by the Nederlands Centrum voor Laser Research (NCLR) [1], the divergence of the optical beam is of utmost importance. The active medium of this laser has large discharge dimensions relative to the size of the fundamental gaussian mode of a stable plano-concave resonator. The beam from such a resonator is therefore multimode with a relatively poor divergence. With our system a 1.5 m long stable resonator consisting of a concave back mirror with a radius of curvature of 10 m and a flat partial reflector (50 % reflectivity) as outcoupling mirror resulted in a homogeneous, nearly square beam of 23 mm x 22 mm having a pulse energy of approximately 500 mJ and a divergence of 7 mrad (full angle). However a diffraction limited beam of this size would have a divergence of about $30 \mu\text{rad}$. To decrease the divergence the number of oscillating modes should be decreased to, preferably, one fundamental mode with dimensions that fill the available gain volume. This can be done with an unstable resonator. For our system, having a low gain ($2 - 6 \text{ \% cm}^{-1}$) compared to the commercially available short pulse XeCl lasers and a long gain duration (approximately 250 ns), a positive branch confocal unstable resonator is found to be the best choice (compare

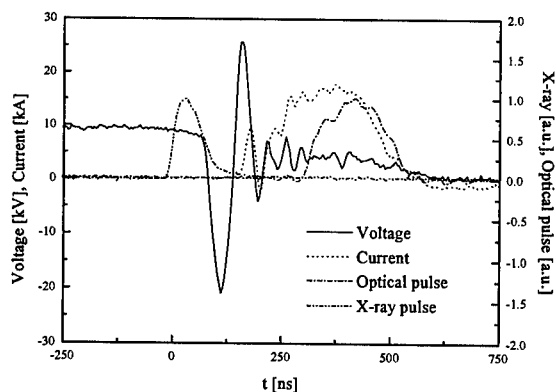


Figure 1. Typical waveforms of the discharge voltage, discharge current, x-ray preionisation pulse and optical output pulse

refs. [2, 3, 4]), with outcoupling through the convex mirror to get a collimated beam. In this paper we present a detailed experimental study of unstable resonators for a low gain, long pulse XeCl excimer laser.

2. Experimental configuration

The experiments have been performed with a XeCl laser system having a 2.5 cm x 2 cm x 60 cm (electrode distance x width x length) x-ray preionised high pressure discharge[5]. The gas mixture during the experiments consisted of approximately 1 mbar HCl, 10 mbar Xe and Ne as a buffer gas up to a pressure of 5 bar. The discharge was excited by a spiker-sustainer circuit. The laser operates in resonant overshoot mode[6]. Figure 1 shows typical waveforms for the x-ray preionisation pulse, discharge voltage and discharge current. The efficiency is maximal if the system operates under matched discharge conditions, i.e. if the voltage on the pulse forming network (PFN) equals twice the steady state voltage of the discharge. The output can be increased by increasing the PFN voltage but then the efficiency drops. If the PFN voltage is set too high the discharge becomes unstable and ends prematurely in streamers and arcs. To prevent electrode wear the system is operated under almost matched discharge conditions. The results presented in this paper are obtained under these conditions, unless stated otherwise.

The near and far field profiles are measured using a gated image intensified CCD camera. For the near field measurement the beam is transported

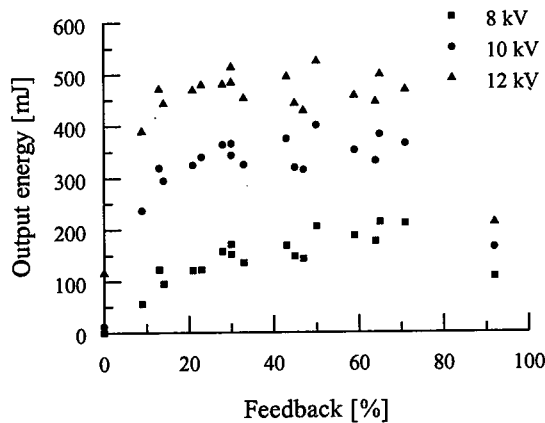


Figure 2. Output energy as a function of the geometrical feedback for different charging voltages of the sustainer

away from the laser with a relay imaging system consisting of two 50 cm focal length lenses placed 1 m apart. The focal plane of the first lens is just behind the outcoupling mirror to ensure that we have an exact image of the outcoupled field at the scintillator which is placed in the focal plane of the second lens. As a scintillator we use a thin film of a solution of sodium salicylate in water between two suprasil windows. To ensure that the response of the scintillator remains linear the beam is attenuated to about 1 % of its energy. The CCD camera we used showed some nonlinear response which was found to be related to the CCD and not to the image intensifier. Hence a correction can be made for this nonlinear response.

The focus field pattern is measured by focussing the attenuated beam (attenuation to about 0.05 %) on the scintillator using a concave mirror with a radius of curvature of 10 m. To obtain the image the CCD camera has been equipped with a microscope objective.

3. Stable resonators

The simplest type of resonator is the stable resonator. Good energy extraction from the gain medium is easily obtained if proper feedback is used. Figure 2 shows the output from a plane-plane resonator as a function of the feedback of the resonator. For a stable resonator this feedback is solely determined by the product of the reflectances of the mirrors

$$\gamma = R_1 R_2 \quad (1)$$

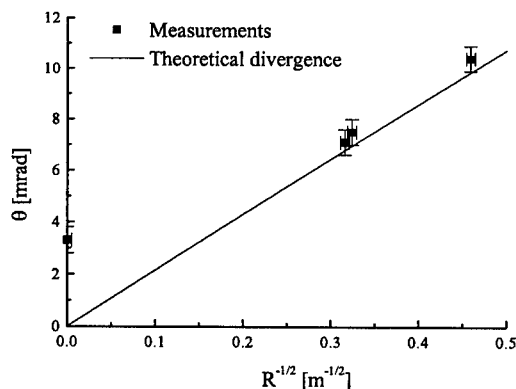


Figure 3. Divergence of the output beam from a stable resonator as a function of the radius of curvature of the rear mirror

Figure 2 shows that for a sustainer voltage higher than 10 kV the output is more or less constant for a feedback between 20 and 70 %. If the feedback is far below 20 % the outcoupling losses are larger than the gain, hence no output beam can be formed.

In our system where the discharge dimensions are much larger than the fundamental gaussian mode the output beam is multimode. This results for stable resonators, especially for stable plano-concave resonators in an output beam that is very homogeneous in the near field. From our 2.5 cm x 2.0 cm discharge (height x width) we obtained homogeneous nearly square beams with a size of about 23 mm x 22 mm.

The problem with these stable resonators is their divergence. As the output beam is multimode the divergence is rather high in comparison with the diffraction limit. Figure 3 shows the divergence of different stable plano-concave resonators as a function of the radius of curvature of the rear mirror. In approximation the divergence is given by [7]

$$\theta \approx \frac{D}{\sqrt{LR}} \quad (2)$$

where D is the dimension of one side of the beam aperture, L is the length of the cavity and R the radius of curvature of the concave rear mirror. It is seen in figure 3 that the experiments are in good agreement with the theory except for the plane-plane resonator but for this resonator the approximation is not longer valid.

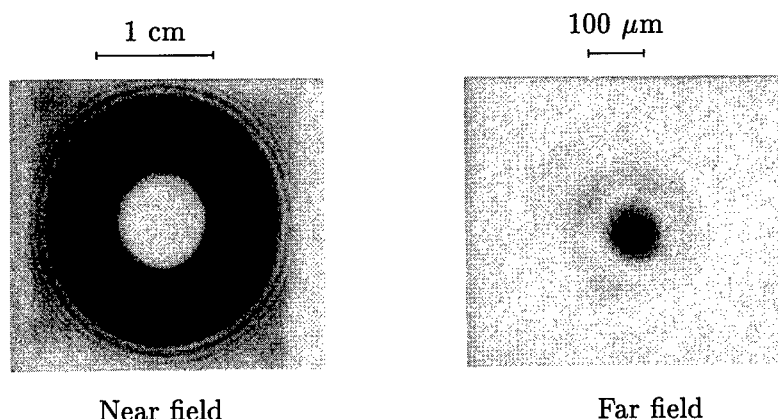


Figure 4. Near field profile (left) and focus profile (right) of the beam from a hard edge unstable resonator ($M = 2.4$) with a central HR spot of 8 mm diameter focussed by a 10 m radius concave mirror

4. Hard edge unstable resonators

To increase the size of the fundamental mode of the resonator one has to use an unstable resonator. An unstable resonator reaches this fundamental mode earlier if the magnification of the resonator is larger [8]. So the magnification ought to be chosen as large as possible within the constraints of the gain medium. In our system we found with the stable resonators a minimum feedback of 20 %. This minimum value of about 20 % for the feedback determines the choice of the magnification of the unstable resonator which is given by

$$M = -\frac{R_2}{R_1} \quad (3)$$

where R_1 is the radius of curvature of the outcoupling convex mirror and R_2 is the radius of curvature of the concave rear mirror. The feedback of an unstable resonator is given by

$$\gamma = \frac{1}{M^2} \quad (4)$$

Thus we used an unstable resonator with a magnification of 2.4 to have enough feedback (18 %).

Hard edge unstable resonators are unstable resonators where the outcoupling mirror shows a step in the reflectance profile. This results in a step in the near field intensity distribution of the outcoupled beam. For symmetry reasons we used a centered reflecting spot on the outcoupling mirror, so that the outcoupled beam shows a cylindrical symmetry as shown in figure 4. Figure 4 shows also a typical hard edge unstable resonator focus profile: not only a central peak but also a ring structure.

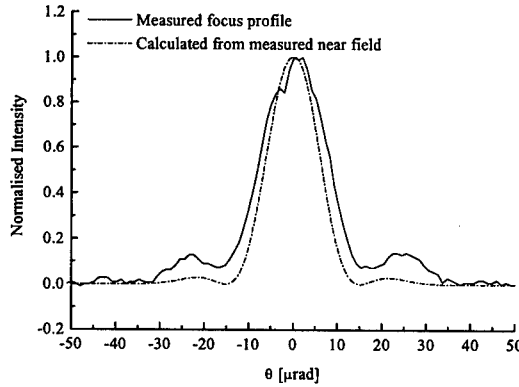


Figure 5. Comparison between far field energy distributions from theory and experiment

4.1. HIGH REFLECTIVITY HARD EDGE UNSTABLE RESONATORS

The beam profiles in figure 4 are obtained with a hard edge unstable resonator with a magnification M of 2.4 and a central high reflectivity (HR) spot of 8 mm diameter. To determine the beam quality of this beam we calculated the Times Diffraction Limited (TDL) parameter [9]. This TDL parameter is based on the comparison of the measured focus energy distribution and a calculated focus energy distribution. This calculated focus energy distribution is derived from the measured near field energy distribution using a uniform phase distribution. Figure 5 shows these two far field energy distributions for the above mentioned resonator.

The TDL-parameter can now be determined using

$$\text{TDL} = \frac{\theta_{\text{meas}}}{\theta_{\text{calc}}} \left(\frac{k_{\text{calc}}}{k_{\text{meas}}} \right)^{\frac{1}{2}} \quad (5)$$

where θ_{meas} and θ_{calc} are the measured and calculated beam divergence respectively, and k_{meas} and k_{calc} the respective energy content within that divergence angle. So the TDL parameter does not only compare focus sizes, but also contains the energy content. A beam with a value 1 for the TDL parameter is a beam that is diffraction limited, not only with respect to size but also with respect to energy.

The full divergence angle based on the first minimum is 32 μrad for the measured beam and 30 μrad for the calculated beam. The measured beam has approximately 60 % of the energy within the central peak and the calculate beam 82 % of the energy. This results in a TDL-parameter

TABLE 1. Characteristics of and experimental results obtained with the laser equipped with different hard edge unstable resonator configurations and operated under matched discharge conditions

M	R [%]	D_r [mm]	γ [%]	θ_d [μ rad]	E [mJ]	τ [ns]	k [%]
2.4	100	8	17.7	32	339	160	60
2.4	72	8	12.5	37	334	146	70
2.4	45	8	7.8	31	305	146	50
2.0	72	10	17.5	36	362	149	70
1.6	45	12	17.5	34	359	160	30

of 1.3 for our beam. Thus we reached almost the optimal result that can be obtained with this resonator. However, about 40 % of the energy is lost in side lobes. This loss of energy in side lobe(s) can be decreased by using partially reflecting hard edge outcoupling mirrors.

4.2. PARTIAL REFLECTIVITY HARD EDGE UNSTABLE RESONATORS

Table 1 shows the characteristics of different hard edge unstable resonators used in the experiments. R in table 1 is the reflectivity of the reflecting area and D_r its diameter. The *geometrical* feedback $\gamma = R/M^2$, which gives only an indication of the actual feedback, is determined by the magnification M and the reflectivity of the central area R and is independent of the size of the reflecting area. θ_d is the full divergence angle based on the first minimum in the focus energy distribution, E the output energy under matched discharge conditions, τ the pulse duration and k the percentage of energy within the central peak.

Figure 6 shows the focus energy distributions for the three resonators with the same magnification $M = 2.4$, mentioned in table 1. These resonators are identical except for the reflectivity of the outcoupler. It is seen that the 72 % spot reflectivity leads to an improved focus profile. Less energy (about 30 %) is lost in the side lobe. Further reduction to a spot reflectivity of 45 % results in a focus that has a huge side lobe. 50 % of the energy is lost in this side lobe. This is probably caused by the outcoupler: due to the coating used to obtain the reflectivity profile a phase difference between the central part of the beam and the beam edge will exist. This phase difference results in more side lobe energy. Interferometric measurements show that the 70 % mirror has a phase difference of only 0.3π and the 45 % mirror a phase difference of π .

Reduction of the reflectivity of the outcoupler results in a lower output energy as can be found in table 1. This is due to the lower feedback of the resonator, so that the output beam needs a longer build-up time, resulting

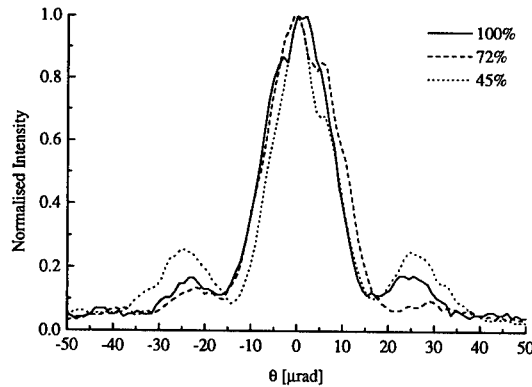


Figure 6. Focus energy distributions from resonators with different central reflectivities (100, 72 and 45 %). The magnification $M = 2.4$ for all resonators

in a shorter pulse. To keep the geometrical feedback similar for different central reflectivity values the resonator magnification has to be decreased for decreasing mirror reflectance. Experiments have been performed using resonators having equal feedback (see table 1). To ensure a proper filling of the discharge volume the size of the reflecting spot on the outcoupling mirror was also increased. This however has a negative effect on the divergence as the focus from a resonator with a larger mirror size is also somewhat larger. The obtained results were similar to those obtained with the resonators having equal magnification mentioned above. The 72 % reflectivity mirror shows an improvement and the 45 % mirror a decrease of beam quality. The output energy is even somewhat higher for these two resonators.

4.3. PHASE UNIFYING OUTCOUPLING MIRROR

The transmission phase difference of the 45 % mirror in the hard edge resonator experiments was nearly π . This phase difference can be decreased by using a special coating design: the phase unifying mirror [10, 11]. Experiments with such a mirror were performed with a resonator with magnification 1.6. Based on the coating a phase difference of only 0.16π is expected. Interferometric measurements on this phase unifying mirror show only a very small phase shift which was hardly measurable. The results obtained with this mirror were much better than those obtained with the normal 45 % mirror. Figure 7 shows the focus spots of the standard mirror res-

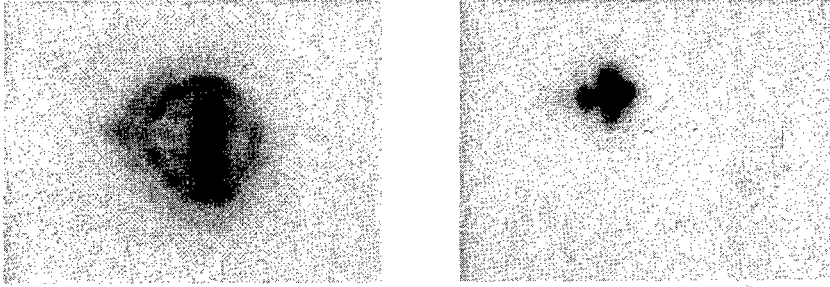


Figure 7. Focus spots from a hard edge resonator with a magnification of 1.6 and a central reflectance of 45 % fitted with a standard mirror (left) and fitted with a phase unifying mirror (right)

TABLE 2. Characteristics of and experimental results obtained with the laser equipped with different gaussian unstable resonator configurations and operated under matched discharge conditions

M	R_c [%]	D_r [mm]	γ [%]	θ_d [μ rad]	E [mJ]	τ [ns]	k [%]
2.4	65	8	11.3	25	412	144	43
2.4	45	8	7.8	28	252	120	53
2.4	17	8	3.0	27	212	115	55
2.0	65	10	16.3	27	440	137	51
2.0	45	10	11.3	37	342	129	64
2.0	25	10	6.3	35	167	100	64
1.6	45	12	17.6	50	~ 200	~ 130	-

onator and the phase unifying resonator. The improvement is clear. The diffraction angle is comparable to the diffraction angle mentioned in table 1 for the $M = 1.6$ resonator with 45 % central reflectivity: 34μ rad, however approximately 80 % of the 399 mJ output energy is found in the central peak, instead of less than 30 % for the standard mirror.

5. Gaussian unstable resonators

A hard edge outcoupler will always result in a side lobe because of the diffraction at the hard edge. A focus spot without side lobes requires a soft edge outcoupling mirror. We used nearly gaussian mirrors because they can be analysed mathematically too. In table 2 the characteristics of the used gaussian resonators are given. M is the resonator magnification, R_c the central reflectivity of the gaussian reflection profile, D_r is the $1/e^2$ diameter of this profile and γ the feedback, which is given by R_c/M^2 . θ_d is the full divergence angle based on the $1/e^2$ width of the focus profile. E , τ and

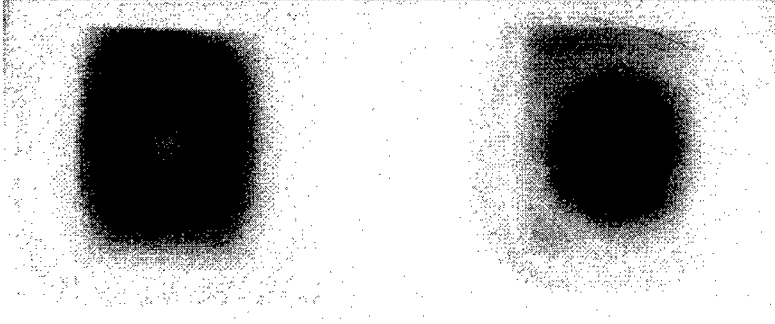


Figure 8. The near field spots of two gaussian resonators. Left: $M = 2.4$ and $R_c = 65\%$. Right: $M = 2.0$ and $R_c = 25\%$

k are the pulse energy, pulse duration and energy content within the full divergence angle respectively.

We used the same magnifications as we used for the hard edge unstable resonator. This choice was based on the good results we obtained with those resonators. We used different reflectivities to be able to see the influence on the beam. The high central reflectivity results in a beam with a smooth edged central hole in the near field as can be seen in figure 8. The energy from this resonator is quite high (412 mJ under almost matched discharge conditions) due to good filling of the discharge volume. Figure 8 also shows the near field of a low central reflectivity resonator. It was designed to have a maximally flat near field. The condition for this is [7]

$$R_c M^2 = 1 \quad (6)$$

The energy from this resonator is rather low (167 mJ) because the discharge volume is not properly filled and the optical pulse is shorter (100 ns) due to the low feedback. The beam is flat topped as expected.

It can be seen from figure 9 that the central hole in the near field of the $M = 2.4$ and $R_c = 65\%$ still leads to a small side lobe. Calculations show that this is in accordance with theory. Even from the maximally flat resonator ($M = 2.0$ and $R_c = 25\%$) still a very small side lobe is expected from theory. The experiments show a slightly wider focus with a low but wide shoulder as shown in figure 9. This shoulder results in a lower energy content within the $1/e^2$ diameter (θ_d). In table 2 the energy content within the divergence angle is given for the gaussian resonators. For the $M = 2.0$ and $R_c = 25\%$ resonator an energy content of 84 % is expected from theory and the experiments resulted in 64 %. The calculated divergence angle is $21\ \mu\text{rad}$ and the experimental value is $35\ \mu\text{rad}$, thus resulting in a value for the TDL parameter of 1.8.

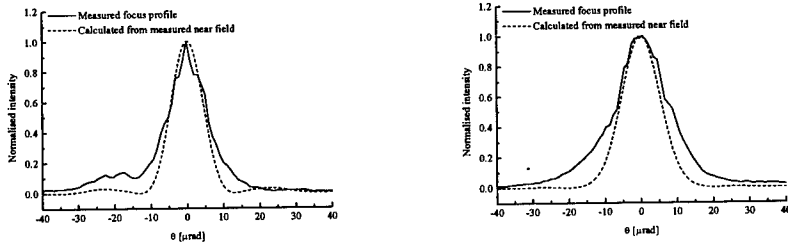


Figure 9. Measured and calculated focus energy distributions for two gaussian resonators. Left: $M = 2.4$ and $R_c = 65\%$. Right: $M = 2.0$ and $R_c = 25\%$

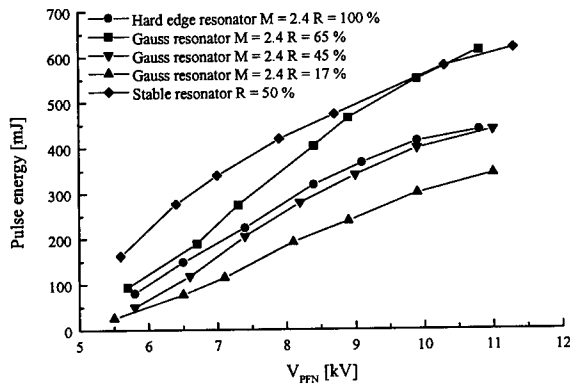


Figure 10. Output energy as a function of the sustainer voltage for different resonators

6. Performance comparison

In the previous sections we only looked at the divergence and the beam profiles. In this section a comparison will be made between the resonators with respect to output energy, pulse duration, average power and brightness.

Figure 10 shows the output energy of different resonators as a function of the sustainer voltage. It is seen that except for the highest sustainer voltage the highest output can be obtained with a stable resonator. The hard edge resonator shows an output energy reduction of about 20 % compared to the stable resonator. With the high central reflectivity gauss resonator it is possible to extract a similar amount of energy from the gain medium as with the stable resonator, especially for higher sustainer voltages. However, the

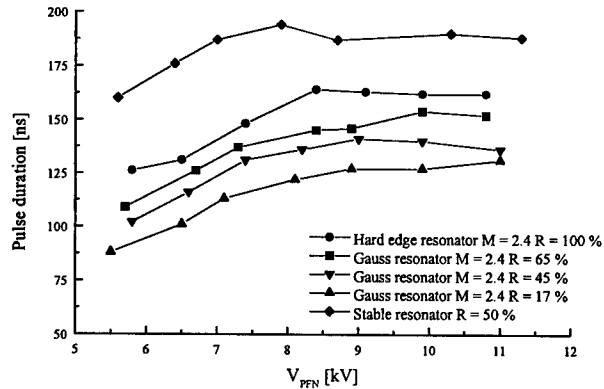


Figure 11. Pulse duration (FWHM) as a function of the sustainer voltage for different resonators

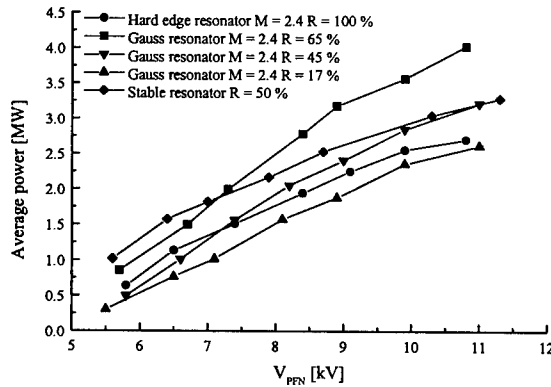


Figure 12. Average pulse power as a function of the sustainer voltage for different resonators

pulse duration is much shorter for the gaussian resonators as can be seen from figure 11. This pulse duration is even shorter than the pulse duration from the hard edge unstable resonator. This results in the highest average pulse powers, which is defined by the energy divided by the pulse duration ($= E/\tau$), for the high central reflectivity gaussian resonator as seen in figure 12.

The brightness of the beam is a convenient parameter to compare the

output from the different resonators. The brightness can be defined as

$$B = k \frac{E}{\tau} \left(\frac{1}{\pi \frac{\theta_d}{2} \frac{M D_r}{2}} \right)^2 \quad (7)$$

Under matched discharge conditions, $V_{PFN} = 8$ kV, we obtained from the HR hard edge resonator a brightness of $5.5 \cdot 10^{14}$ W/(cm²·sr). This is an enormous increase compared to the brightness from the stable plano-concave resonator: $B = 1.5 \cdot 10^{10}$ W/(cm²·sr). This could be further increased to $1.2 \cdot 10^{15}$ W/(cm²·sr) if we pushed the discharge to its limits. With the phase unifying resonator a slightly larger brightness could be obtained: $7.0 \cdot 10^{14}$ W/(cm²·sr) under matched discharge conditions and $1.4 \cdot 10^{15}$ W/(cm²·sr) maximally. The gaussian resonator with $M = 2.0$ and $R_c = 65$ % resulted in a brightness of $9.1 \cdot 10^{14}$ W/(cm²·sr) under matched discharge conditions. Hence under matched discharge conditions the best results are obtained with the gaussian resonator.

7. Conclusions

In this paper we presented results from measurements on different resonator designs for a long pulse, low gain XeCl excimer laser. A stable plano concave resonator with 50 % feedback results in a homogeneous nearly square beam with 500 mJ output energy and 7 mrad divergence under matched discharge conditions. With a high reflectivity hard edge resonator having a magnification of 2.4 a 1.3 times diffraction limited beam can be obtained. This beam has under matched discharge conditions an output energy of about 340 mJ, a divergence of 32 μ rad and a brightness of $5.5 \cdot 10^{14}$ W/(cm²·sr). The energy content of this beam within the divergence angle is about 60 %. We have shown that this can be improved by using partial reflecting hard edge outcouplers. Attention has to be paid to the phase distortion by the outcoupler. This can be diminished by using a phase unifying outcoupler. This resonator resulted in a beam with about 400 mJ output energy, 34 μ rad divergence, an energy content of about 80 % and a brightness of $7.0 \cdot 10^{14}$ W/(cm²·sr).

To reduce the side lobe energy further soft edge mirrors have to be used. We have shown that with a resonator having a magnification of 2.0 and a central reflectivity of 65 % a beam with 440 mJ energy and 27 μ rad divergence can be obtained under matched discharge conditions. The brightness of this beam is $9.1 \cdot 10^{14}$ W/(cm²·sr). Thus the best results were obtained using gaussian resonators.

Acknowledgements

The present work has been supported by the Netherlands Technology Foundation (STW). The authors would like to thank M.J. Zwegers from the Nederlands Centrum voor Laser Research (NCLR) for performing part of the measurements and J. van Hespen en T. van Drunick from the optics workshop at the Applied Physics department of Twente University for supplying us with the special mirrors used for the experiments presented in this paper.

References

1. F.A. van Goor, W.J. Witteman, J.C.M. Timmermans, J. van Spijker, and J. Couperus. High-average power xecl laser with x-ray pre-ionization and spiker-sustainer excitation. In M. Bohrer, T. Letardi, D. Schuöcker, and H. Weber, editors, *High-Power Gas and Solid State Lasers*, volume 2206 of *Proceedings Europto Series*, pages 30–40. SPIE, 1994.
2. T.J. McKee. Optical cavity design for long pulse excimer lasers. *Applied Optics*, 30(6):635–644, 1991.
3. T.J. McKee and S. Fendrykowski. Long-pulse excimer laser with a variable reflectivity mirror resonator. *Applied Optics*, 32(3):275–277, 1993.
4. S.E. Kovalenko, V. Losev, and M.R. Perrone. Super-gaussian resonators for long pulse xecl lasers. *Applied Optics*, 33(18):4082–4086, 1994.
5. J.C.M. Timmermans. *Double discharge XeCl-laser*. PhD thesis, University of Twente, Enschede, the Netherlands, 1995.
6. J.W. Gerritsen, A.L. Keet, G.J. Ernst, and W.J. Witteman. High-efficiency operation of a gas discharge xecl laser using a magnetically induced resonant voltage overshoot circuit. *Journal of Applied Physics*, 67(7):3517–3519, 1990.
7. A.E. Siegman. *Lasers*. University Science Books, 20 Edgehill Road, Mill Valley, CA 94941, USA, 1986.
8. P.E. Dyer. Unstable resonators. In D.R. Hall and P.E. Jackson, editors, *The physics and technology of laser resonators*, chapter 2, pages 21–39. Institute of Physics Publishing, Techno House, Redcliffe Way, Bristol BS1 6NX, England, 1992.
9. S. Bollanti, P. di Lazzaro, and D. Murra. How many times is a beam diffraction limited? *Optics Communications*, 134(1-6):503–513, 1997.
10. V.B. Kaul', S.V. Mel'chenko, M.R. Perrone, A. Piegari, and V.F. Tarasenko. Near diffraction limited output from a 100 ns xecl laser fitted with a phase unifying cavity. *Journal of Modern Optics*, 42(11):2229–2238, 1995.
11. M.R. Perrone. On the performance of a phase-unifying unstable resonator for excimer lasers. *Optics Communications*, 116(1-3):101–108, 1995.

OPTICAL RESONATORS FOR SLAB-WAVEGUIDE LASERS

E.F. PLINSKI, K.M. ABRAMSKI, J.S. WITKOWSKI

Laser Electronics Group

Institute of Telecommunications and Acoustics

Wroclaw University of Technology

Pl. 50-370 Wroclaw, Poland,

tel. (+48) (71) 320 25 05, fax: (+48) (71) 320 31 89,

email: eda@zr.ita.pwr.wroc.pl, kma@zr.ita.pwr.wroc.pl, jsw@zr.ita.pwr.wroc.pl

1. Introduction

A slab-waveguide configuration is the one of the most promising for the high power laser technology. The common feature of the slab configurations is a large Fresnel number $N_x = a^2/L\lambda$ for the horizontal x axis which usually is contained between a few and a few hundred, and the small Fresnel number, less than 1, for the vertical y axis $N_y = b^2/L\lambda$ (where a , b are lateral and transverse dimensions of the slab respectively, L is the length of the resonator and λ is the wavelength of the laser radiation). A large Fresnel number ($N \gg 1$) corresponding to the lateral dimension of the gain medium allows to extract high output power from the slab-waveguide laser. That specific geometrical configuration of the lasing medium requires specific optical resonators as well. They should extract the maximum output power formed into the high quality laser beam. Concerning the gain medium of the slab-waveguide lasers it can be divided into two classes: slab-waveguide geometry with and without side-walls. Considering the optical resonators, three main groups can be distinguished: resonators with spherical optics (stable and confocal unstable resonators), resonators with flat optics (with and without waveguide mode filtering), resonators with DOE mirrors (Diffractive Optical Elements). The paper includes elementary review of slab laser resonators and presents some experiments and results obtained.

2. RF excited CO₂ slab laser

In the case of the RF excited CO₂ lasers the slab configuration is particularly useful because of diffusive cooling of gas laser mixture between the electrodes (Fig.1). The electrodes form guiding walls for propagating radiation. The Fig.1 gives detail description of geometry and a way of RF excitation of the slab laser. The frequency of excitation f , the distance d between electrodes and the pressure p are the three basic parameters of the RF excited laser [1]. The investigation shows that optimal condition require fulfilling of two

basic scaling conditions:

$$df \approx 2-3 \text{ [MHz mm]} \quad \text{and} \quad pd \approx 1.7-2.0 \text{ [Torr mm]} \quad (1)$$

When the homogeneous RF discharge is obtained (the coils seen in Fig.1 ensure it) at the optimum frequency of 100-140 MHz in a typical laser medium He:Ne:CO₂ = 3:1:1+5%Xe at a pressure of 80-150 Torr between aluminium electrode spaced 1.5-2.5 mm, the

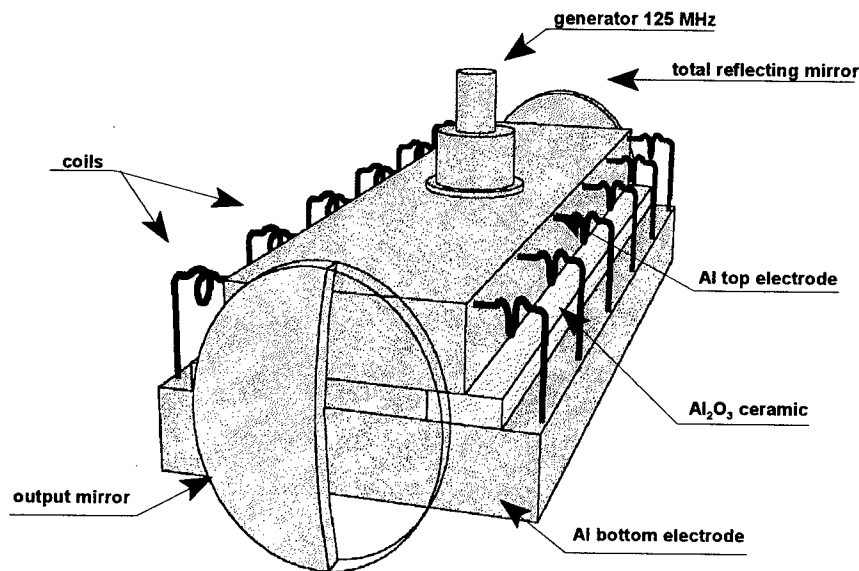


Figure 1. Construction of the RF excited slab-waveguide laser

extraction of the output power from the unit area of the slab laser at the optimum transmission of the output mirror is about 2-3 Watt/cm². Hence, the simple laser with dimensions of 1.7x20x400 mm (with alumina side-walls) filled with a homogeneous RF plasma gives the output power of 180-240 Watts with efficiency of 10-14% [2]. Typical plane-plane mirror resonator with fully reflecting and 92% reflectivity output mirrors gives the laser beam which is a mixture of a few or even a few tens of waveguide modes $EH_{m,n}$ where m is the lateral waveguide number and can reach even 50-60 and n is the transverse waveguide number and is usually equal to 1 (a basic waveguide mode). The mode structure and the line content of the output power depend on the resonator dimensions and the pressure of a lasing mixture. The main disadvantage of this construction is the bad quality of the output beam. Hence, there is necessity of searching for new resonators ensuring high beam quality of slab lasers.

3. Slab laser resonators - review

A large area discharge lasers requires designing of specific optical resonators to get high quality laser beam output. In practice, the M^2 parameter [3] applied for technological lasers should be close to 1. Considering RF discharge slab lasers, two basic groups of the

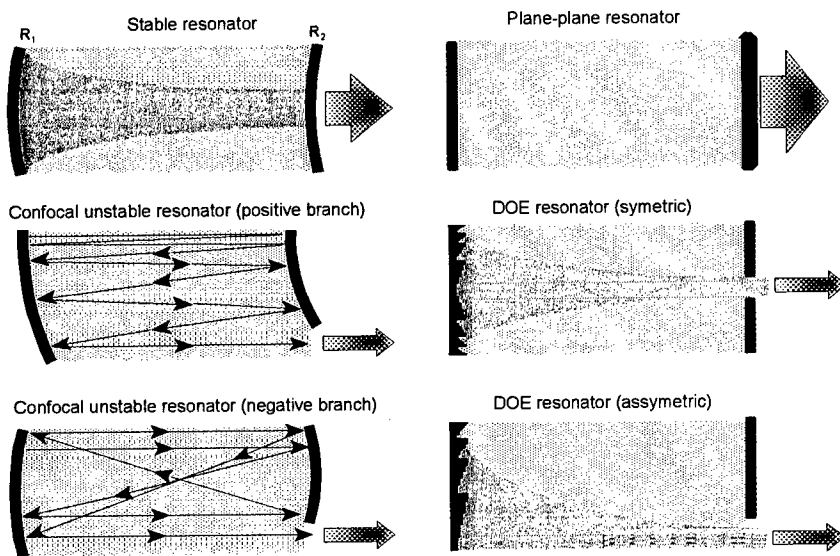


Fig. 2. Resonator configurations for the slab structure without side-walls

resonators can be distinguished: the resonators without and with side-walls. Apart of the laser mirrors, the side-walls have quite important influence in creating of an inside resonator mode structure.

The Fig.2 gives the family of the optical resonators for the slab lasers without side-walls. This resonators are characterised by waveguiding in transverse direction and free space propagation in lateral direction. They include stable, unstable and DOE configurations.

The confocal unstable resonators are commonly applied in industrial lasers. Both configurations, positive and negative branches, have different advantages and disadvantages. The positive branch forms more homogeneous distribution of the radiation inside of the resonator but it is much more sensitive to the misalignment. The negative branch does not ensure good radiation homogeneity. Nevertheless, it is very resistive to the mirror tilting. The slab laser with the positive branch of the unstable resonator gives approximately 30-40% more output power then the same laser with the negative branch configuration.

The simplest plane-plane configuration is not practical because of its huge sensitivity to: the mirror tilting, gradient of refractive index caused by plasma temperature

distribution and unflatness of the mirror applied. However, when well aligned, it forms the low order free space "Fox and Lee" mode. This mode is easily transformable by

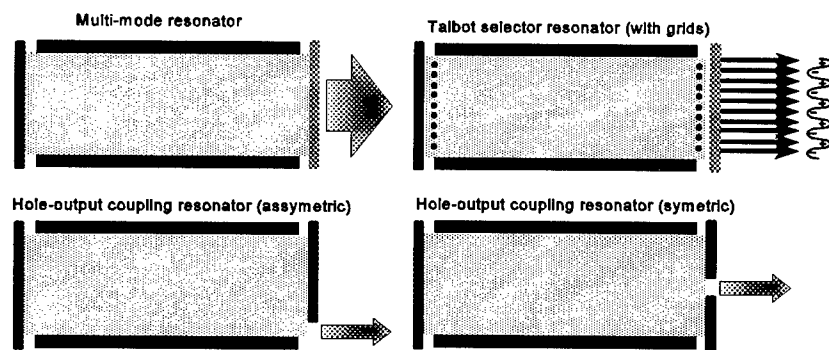


Fig. 3. Resonator configurations for the slab structure with side-walls

diffractive optics into a quasi-Gaussian beam (DOE resonators in symmetric and asymmetric configurations - see Fig.2). The slab configuration seems to be very promising for developing DOE resonators [4].

As it was mentioned above the alternative approach to the slab resonators is to use side-walls to ensure waveguiding in both lateral and transverse directions - see Fig. 3. The simplest multi-mode plane-plane resonator has been described in chapter 2. Its applicability is limited because of a high value of the M^2 parameter in lateral direction ($M_x^2 \approx 20$).

The hole-output coupling resonators, in asymmetric and symmetric versions, are rather not practical because of a very unstable output mode pattern and bad beam quality ($M_x^2 > 5$).

The most promising configuration for the slab laser with side-walls seems to be the resonator with Talbot selection, which is described below.

4. Slab lasers with Talbot selection

Our main attention is put to the resonators with so called Talbot mode filtration [5]. The idea is based on putting an in-cavity grid which matches the periodicity of the desired mode together with slab waveguide dimensions which create coherent self-imaging by Talbot effect [6].

4.1. Four-wave model

To explain the wave propagation in the slab laser with the side-walls we can use simple illustration of the two plane waves interference as is shown in Fig. 4. When two plane

waves are crossed at small angle Θ , the interference pattern is created. When the interference pattern is build up in the frame of rectangular figure (we consider 2-

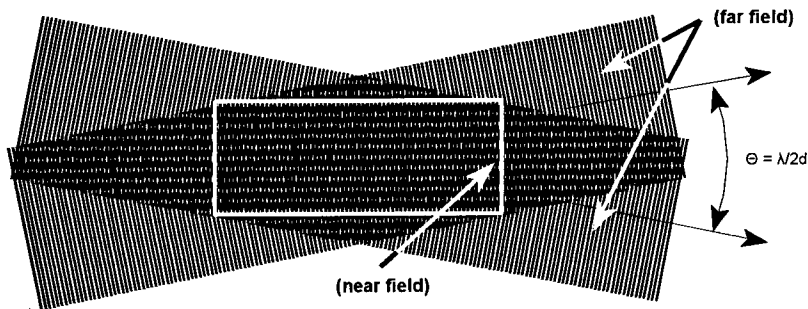


Fig. 4. Four-wave model of waveguide mode creation in the slab laser

dimensional case) according to the rule that the nodal planes overlap the side-walls, the internal radiation is exactly the same as a waveguide mode $EH_{m,n}$. Subscripts m and n denote numbers of interference fringes along x and y axes and they are the waveguide mode numbers. The slab is usually designed to be so thin in the transverse direction in order to keep $n=1$ (one fringe, one dot). In the lateral direction (large Fresnel number) the number of fringes (number of dots) is usually much larger than 1. In the CO_2 slab laser a few or a few tens of lateral modes can oscillate simultaneously. The mode structure of the output power and the number of the emission lines (of the CO_2 molecule) depend on slab-waveguide dimensions of the resonator and the pressure of the lasing mixture (the spectral width of the pressure broadened spectral line of carbon dioxide depends linearly on a pressure and is given by an approximate formula $\Delta\nu=5p$ [MHz], where p is the pressure of the mixture in Torr). The modes oscillate on the frequency ν_{qmn}

$$\nu_{qmn} = \frac{qc}{2L} + \frac{1}{32} c\lambda \left(\frac{m^2}{a^2} + \frac{n^2}{b^2} \right) \quad (2)$$

where q a large integer number corresponding to the longitudinal mode, L is the resonator length, a, b are the lateral and transverse dimensions of the slab, m, n are the longitudinal and transverse mode numbers respectively, c is the light speed.

The above mechanism of mode structure creation can be quite easily verified by diagnostic system enabling to observe the spatial Fourier transform of the laser radiation (the far field image in the focus of the lens or concave mirror) and line structure analysis (external grating). When to add the extra condition for the resonator length L , guarantying the Talbot self-imaging of the mode structure (it means when a spatial internal filter selecting well defined mode structure is inserted inside a slab resonator), the slab-

waveguide laser can operate as a single-frequency laser. A periodic wire grid can be used as the filter. The grid period d should satisfy so called Talbot condition:

$$d = \sqrt{\frac{2\lambda L_T}{k}} \quad (3)$$

where L_T is the Talbot length of the resonator, λ is a laser wavelength, k is an integer [5].

5. Experiments

We investigated the slab laser with the Talbot grid filter inserted near the slab as is shown in Fig. 5. The grids were made of gold wires 50 μm in diameters. For the construction of

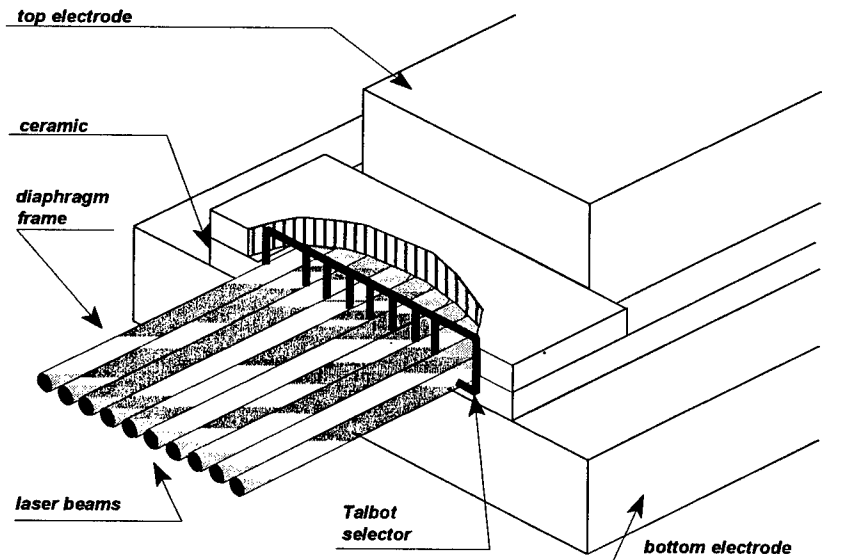


Fig. 5. Construction of the slab laser with Talbot selection

the slab 400 mm long we used the grid period $d = 2.07\text{mm}$ fulfilling Talbot condition (3). The width of the slab was 20.7 mm ($m = 10$) to select mode $EH_{10,1}$. The mirror mounts of the resonator were clamped on the thick invar rod, ensuring small thermal extension. The total reflecting mirror was equipped with three piezoelectric transducers to ensure precise tilting and tuning. The output obtained for this construction was 120 Watts at the pressure of 90 Torr and the frequency of excitation $f = 125\text{ MHz}$.

5.1 Laser beam analysis

The profiles of the laser beams formed in the resonator with the Talbot selector in the near and far fields are shown in Fig. 6. In some cases the laser can operate also in $EH_{20,1}$ mode

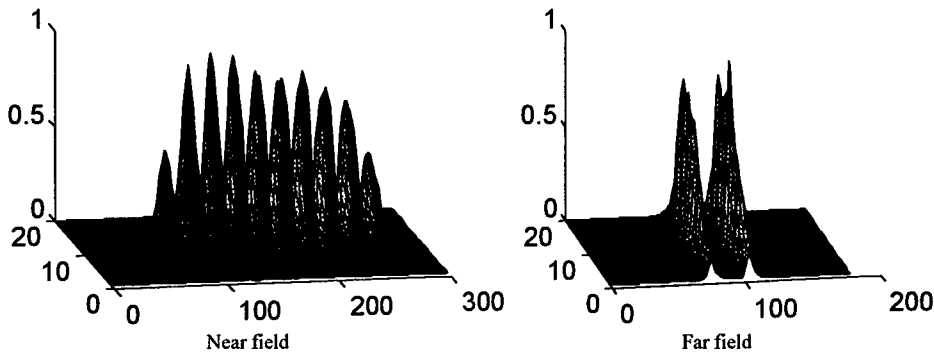


Fig. 6. Profiles of the laser beams in near and far fields

(see Fig. 7). It is specific for the slab-waveguide laser mode that its far field pattern (in practice taken in the focal plane of the lens or concave mirror) is localised in two main lobes.

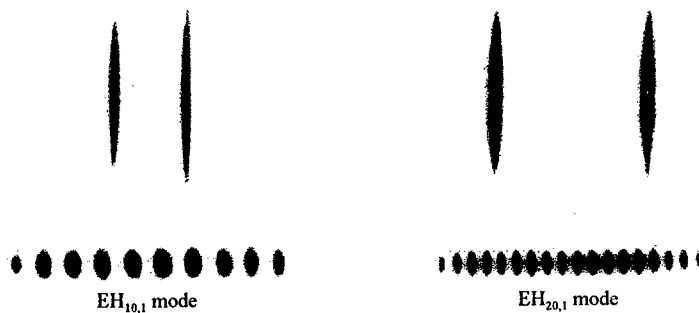


Fig. 7. Far (higher pictures) and near (lower pictures) fields patterns of $EH_{10,1}$ and $EH_{20,1}$ modes

In order to check the laser mode spectrum we built the diagnostic set-up for the mode and spectral line analyses as is shown in Fig. 8a and 8b. The evolution of the mode pattern (see Fig. 8a) shows that the laser oscillates usually on more than one spectral emission line. For the Talbot filtering it can operate on the three selected modes: $EH_{10,1}$, $EH_{20,1}$, $EH_{30,1}$. The odd modes $EH_{10,1}$ and $EH_{30,1}$ are phase-locked (it is obvious consequence of the Talbot effect). Hence, they oscillate on the same frequency (see eq. (2)) and the same spectral line (see the first pattern in Fig. 8a). The even $EH_{20,1}$ mode is never in synchronism with the basic Talbot $EH_{10,1}$ mode and it always oscillates on different spectral line.

It was also useful to find out the sensitivity of the settled mode pattern to the

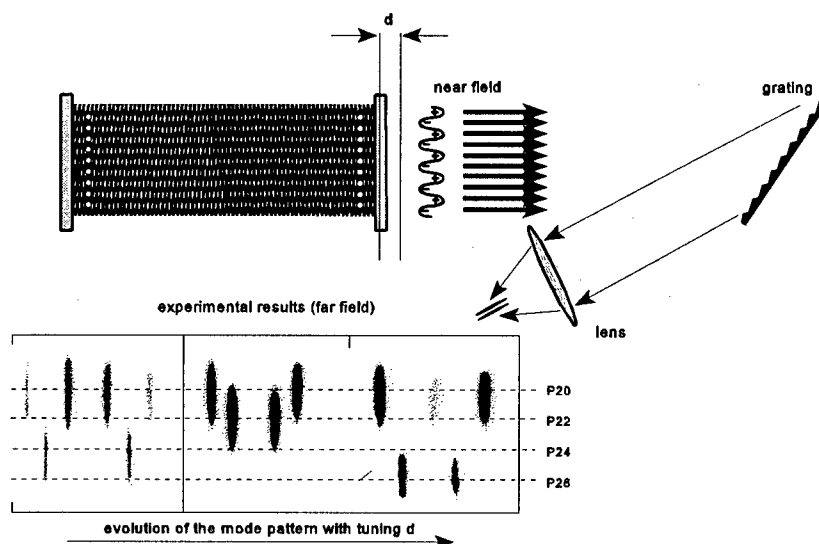


Fig. 8a. Mode and line analysis of the slab laser beams for longitudinal tuning of the output mirror

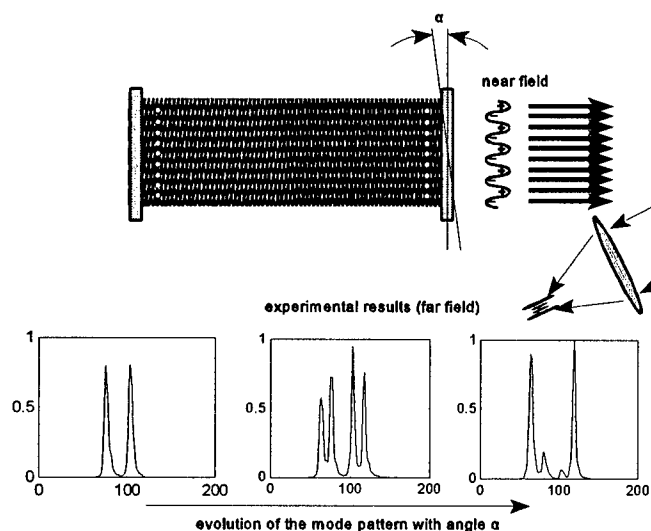


Fig. 8b. Mode analysis of the slab laser beams for the pure (no tuning) tilting of the output mirror

mirror misalignment. To check it we observed the mode patterns with mode and line selection introducing pure tilt of the output mirror. The experimental set up and some far field beam profiles are presented in the Fig. 8b. We introduce the measure of this sensitivity as a tilt angle α_i in the frame of which the considered mode still oscillates. We call it "mode keeping angle". Its value depends on the spectral emission line and the state of tuning. The measured mode keeping angles for $EH_{10,1}$ and $EH_{20,1}$ modes were included in the range of 35 to 55 μrad . To increase the mode keeping angle we introduced the second Talbot grid near the second mirror [7]. We found, that using two Talbot grids, the selected mode of the laser output is more stable and less sensitive to tilt (keeping angle increased to about 70 μrad).

5.2. Transformation of the Talbot selected beam on the external phase plate

The disadvantage of the Talbot filtration is the fact the output power in far field has two lobes. There is possibility to combine both lobes into one strong lobe by phase shifting by

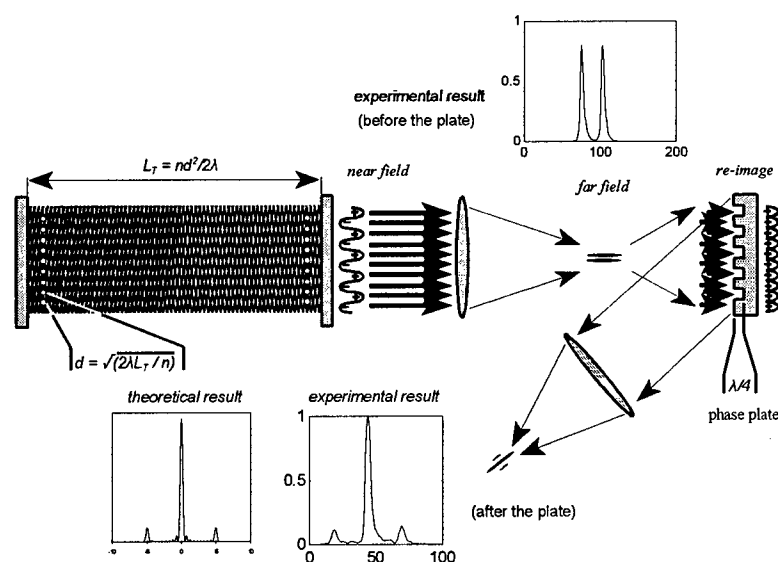


Fig. 9. Transformation of the Talbot selected beam on the external phase plate

π in each second dot of the near field pattern [7]. We have done it by application of a binary mirror with the Talbot period in the re-image plane (Fig. 9). In this figure we present both theoretical and experimental results of the beam profiles transformed via the binary plate.

5.3. M^2 measurements

The beam profile of the slab-waveguide laser in the transverse direction is usually very well defined and very near to the basic Gaussian TEM_{00} mode (its M^2 parameter is close to 1). There is different situation in the lateral direction. However, as we observed, each lobe in the double far field pattern seems to be very close to the basic Gaussian mode as

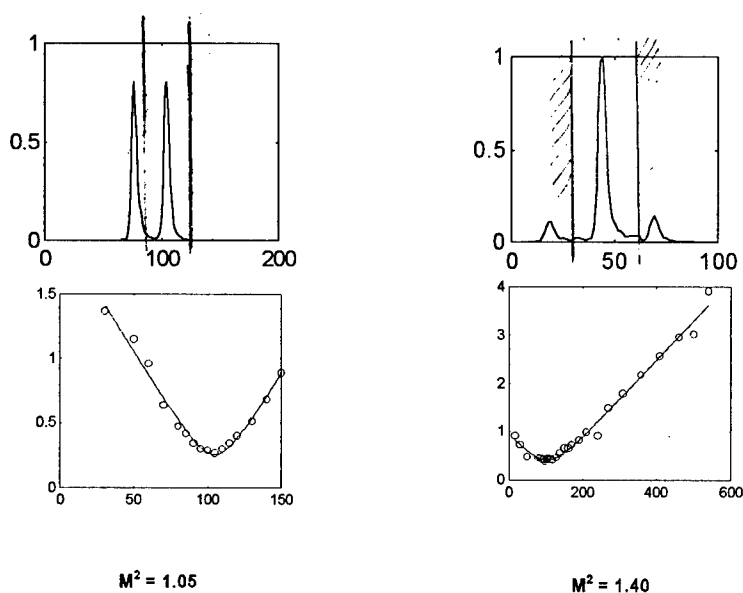


Fig. 10. M^2 measurements for one lobe of the Talbot laser beam (left pictures) and for the central lobe of the phase plate transformed Talbot laser beam (right picture)

well. So, we measured the beam quality of one spatial selected lobe in the far field pattern of the Talbot laser (see Fig. 10). The quality of the single lobe is extremely good ($M^2=1.05$). We performed the same measurements for the central lobe of the phase plate transformed laser beam. The result obtained was worse ($M^2=1.40$), but we expect a bit better result with improvement of the beam alignment on the phase plate (in our experiment we used the optical system with the concave mirrors that caused deformation of the laser beam).

Comparing the two mentioned above Talbot structures, with and without phase plate, it is obvious that in the double lobe case each lobe contains approximately half of the overall output power. The central lobe of the transformed beam contains approximately 75% of the total output power. We think that both cases are applicable. Particularly the double lobe Talbot slab laser gives two easily separable very high quality laser beams and their only disadvantage is that they are split in the power.

The system with an external reflecting phase plate for transforming two lobes into

one is not very practical. However, it may be modified into a much simpler construction where the output laser mirror plays a role of the phase plate as Fig. 11 demonstrates.

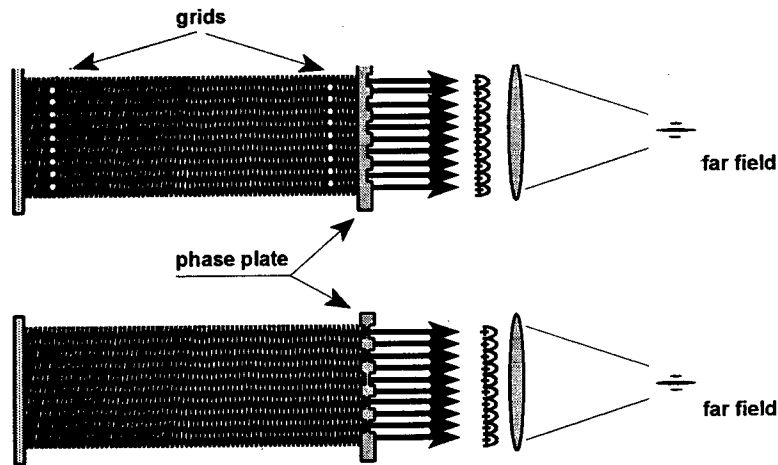


Fig. 11. Possible configurations of the slab-waveguide laser with transparent phase-plate for double lobe transformations

5.4. Slab laser as a ring laser

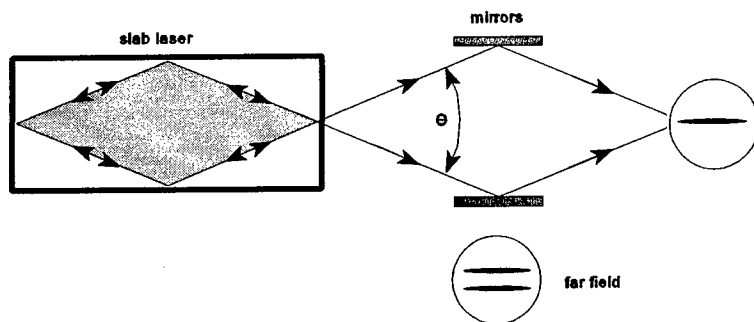


Fig. 12. Simplified model of a slab laser as a ring laser and setup for combining two lobes into one

The four wave model of waveguide mode creation in the slab-laser (see Fig. 4) shows that

each lobe of the individual $EH_{m,1}$ mode can be treated as a running wave in clock wise or anti-clock wise directions around the slab structure. This idea is shown roughly in Fig. 12. Using above model we arranged the experiment of combining two lobes of the one selected



Fig. 13. The interference pattern of overlapped lobes. Number of fringes can be controlled by the angle between crossing waves

$EH_{10,1}$ mode into single lobe. We overlapped both lobes using two adjustable flat mirrors. Overlapped lobes gave the nice stable interference pattern (Fig. 13). This simple experiment proves that it is possible to combine both lobes into one interference fringe (one intensive lobe) by proper adjustment.

6. Conclusions

In the paper we presented the short review of resonators for slab-waveguide lasers. The main attempt has been put to our research on mode selected resonators. We gave the four-wave picture of the wave propagation in the slab-waveguide structure. The mode keeping angle α_1 of the slab-waveguide individual mode has been introduced and measured. The series of measurements of M^2 parameters have been performed for basic selected constructions. We showed that the spatially selected single lobe from the slab-waveguide mode has very good quality parameter $M^2 \sim 1.05$. That is the main conclusion of our work. We also showed the original and promising concept of two lobes combining into single one without using any external binary optics.

Acknowledgements

The authors gratefully acknowledge financial support of the Polish Research Committee, Project No. KBN - 8 T11B 058 09. We also would like to thank Mr. T. Michalak, Mr. P. Duda and Mr. J. Wendland for their helpful discussions and assistance.

7. References

- [1]. Vitruk, P.P., Baker, H.J., Hall, D.R. (1994) Similarity and scaling in diffusion-cooled RF-excited carbon dioxide lasers, *IEEE Journal of Quantum Electronics*, **30**, 1623 - 1634
- [2]. Shackelton, C.J., Abramski, K.M., Baker, H.J., Hall, D.R. (1992) Lateral and transverse mode properties of CO₂ slab-waveguide lasers, *Optics Communications*, **89**, 423 - 428
- [3]. Sasnet, M.W., Johnson, T.F. (1991) Beam characterization of and measurements of propagation attributes, *SPIE* **1414**, 21-32
- [4]. Yelden, E.F., Morley, R.J., Horn, H.K., Abramski, K.M., Baker, H.J., Hall, D.R., Taghizadeh, M.R. (1994) Slab-CO₂ laser employing a hole-coupled waveguide resonators, *CLEO/EUROPE '94 CFF6*, 402
- [5]. Abramski, K.M., Baker, H.J., Colley, A.D., Hall, D.R. (1992) Single-mode selection using coherent imaging within a slab waveguide CO₂ laser, *Appl.Phys.Lett.* **60**, 2469-2471
- [6]. Talbot, H.F. (1836) *Philos. Mag. J.Sci.* **9**, 401
- [7]. Abramski, K.M., Plinski, E.F., Duda, P.A., Witkowski, J.S., Borkowicz, Z. (1996) Slab waveguide CO₂ laser with double Talbot filtration, *CLEO/Europe '96 CThC6*, 235

INVESTIGATIONS OF OPEN RESONATORS WITH DIFFRACTION COUPLING.

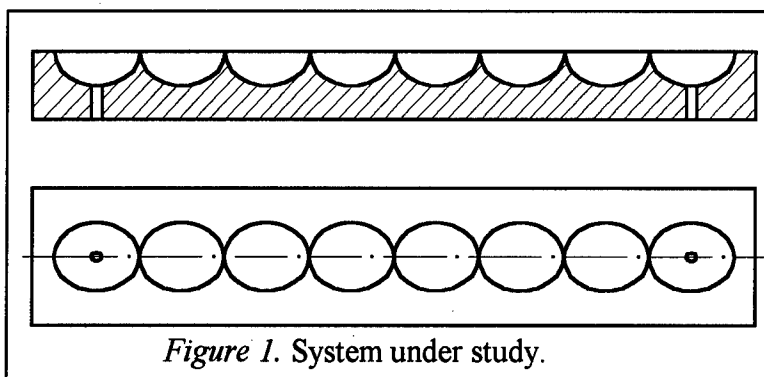
D.G. AFONIN, A.V. KAZAKOV, A.K. MALYSHKIN
*Physics Department of Moscow State University, Vorob'evy
Gory, Moscow, 119899, Russia*

Abstract

The electrodynamic system of diffraction coupled open resonators (OR) with two spherical mirrors was experimentally investigated. The system is constructed as two metal blocks, on which mechanically made spherical mirrors with small holes of coupling in centers are put one next to another. In millimeter region the frequency dependence and spatial spectra of such systems were obtained, distributions of fields of different oscillation types were investigated, merit value was estimated. The system of three diffraction coupled OR was excited at 3-4 modes of oscillations; the merit value was 300-1000. It was experimentally established, that in such systems topmost and asymmetrical oscillation modes are excited mostly effective and the major part of field energy is concentrated near rims of mirrors. It allows to produce good diffraction coupling of the neighbor OR. Real coupling coefficient was 0.2-0.7. Carried out investigations demonstrated that in the systems with the coupled resonators using unstable OR with large diffraction losses is very promising.

1. Experimental Studies

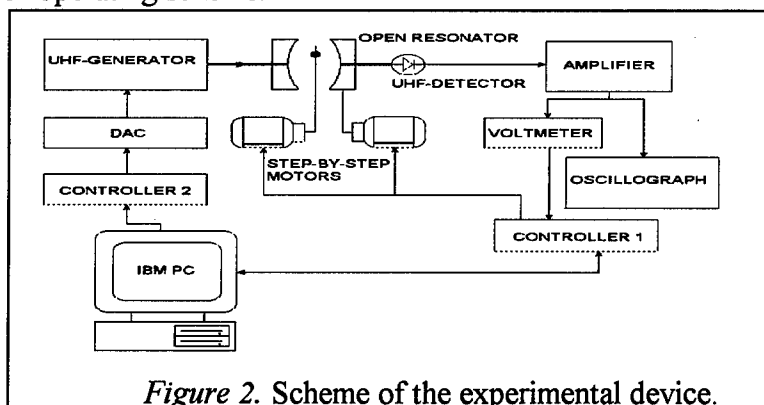
This paper is devoted to the investigations of diffraction coupled two-mirror open resonators (ORs) with spherical mirrors.



The system under investigation is presented at fig.1, it is made in a form of two metallic blocks, on which mechanically made spherical mirrors with small coupling holes in the center of them are put close to each other. Mirror curvature radius was 7.7 mm, mirror aperture - 14.4 mm, coupling hole radius - 1 mm.

Experimental investigations of ORs with diffraction coupling were carried out on automatic device [1,2] in millimeter region of wavelength; spectrum of this system was obtained both at fixed distance between mirror blocks and in change of this distance. Also the factor Q and field distribution of different oscillation types were investigated.

Experimental device (fig.2) consists of electromagnetic wave generator in millimeter region, UHF-detector, amplifier, oscillograph, digital voltmeter and elements of automation, which include IBM PC, input-output controllers, digital-to-analog converter (DAC), step-by-step motors and generator operating scheme.



The system under study is placed on the optical bench with micrometer tables and is excited through the coupling holes in one of the mirrors by means of supplying electromagnetic energy waveguide. Through the analogous hole in the other mirror and the waveguide signal comes to the UHF-detector and then through the amplifier at the same time to the oscillograph and digital voltmeter, coupled with IBM PC by means of the controller. The frequency sweep and change of distance between mirror blocks is carried out also with the help of IBM PC.

While studying a spectrum of the system in condition of changing distance between mirror blocks at fixed excitation frequency, as a rule, equidistance of excited oscillation types was found (fig.3). Changing distance between mirrors excitation of a four-five cell system with exciting area near concentric geometry of resonators was successful.

Spectrum of investigated system at excitation of three coupled OR at fixed distance between mirror edges ($L = 1$ mm) is presented at fig.4 (the signal was taken from the 3rd resonator).

Such system showed rather rare spectrum. Factor Q of individual oscillation types reached a value of $5 \cdot 10^2$. It was obtained according to the formula $Q = f / \Delta f$ (where f - oscillation frequency, Δf - resonance curve

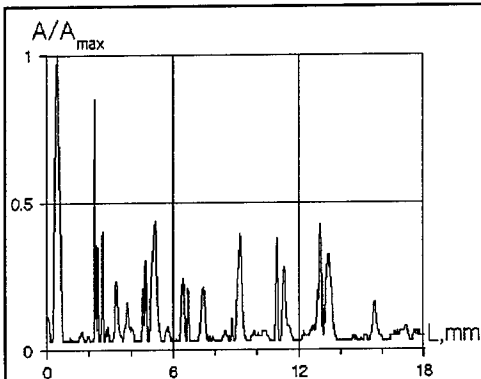


Figure 3. Dependence of transmission coefficient on distance between mirrors

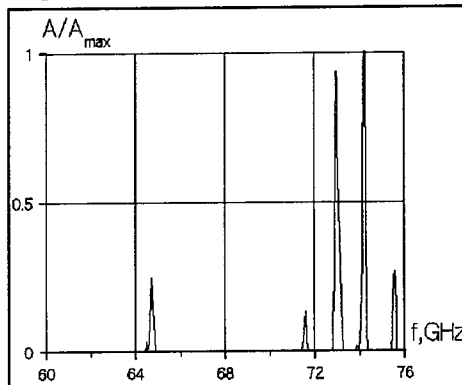


Figure 4. Dependence of transmission coefficient on frequency

width of excited oscillation type at half amplitude). Hole size did not allow the system to excite at frequencies less than 63 GHz.

Elaboration on field distribution of different oscillation types, excited in the coupled ORs system showed that in such system effectively excite only that oscillations, which field amplitude is considerably larger near mirror edges, than in the center. The example of such field distribution is presented at fig.5 (center of OR mirror is marked with dotted line). Asymmetry in field distribution was a characteristic of practically all studied oscillation types.

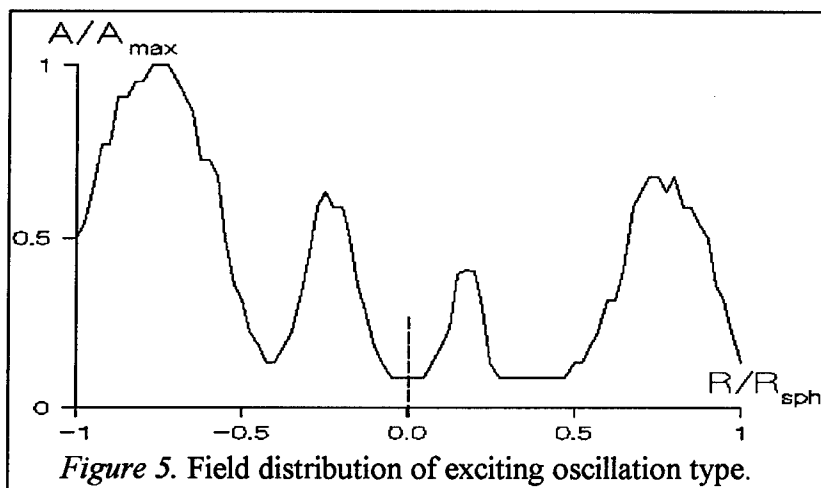


Figure 5. Field distribution of exciting oscillation type.

2. The Numerical Model

Using solutions of parabolic equation for several oscillation types let us estimate possible values of transmission coefficient and factor Q for two diffraction coupled ORs with spherical mirrors at fixed mirror aperture and different beam width.

Consider the simplest model of interaction between two identical symmetric ORs with parallel optical axes and which mirrors touch each other by edges. Suppose we know for corresponding oscillation type field distribution on the first OR mirror and out of its limits. For this purpose let's use well known analytical solutions of a problem of self oscillations of OR with spherical mirrors, expressed in terms of Gauss-Laguerre polynomials [3]:

$$\Psi_{mn}(r, \varphi) = \frac{2}{w\sqrt{1+\delta_{0m}}} \sqrt{\frac{n!}{\pi(m+n)!}} \left(\frac{r}{w}\sqrt{2}\right)^m \cdot L_m^n\left(2\frac{r^2}{w^2}\right) \cdot \exp\left[-\frac{r^2}{w^2} - i\frac{kr^2}{2R(z)}\right] \cdot \begin{Bmatrix} \cos m\varphi \\ \sin m\varphi \end{Bmatrix}, \quad (1)$$

where L_m^n - generalized Laguerre polynomial, δ_{0m} - Kronecker symbol, $w(z)$ - beam width, on which its amplitude decreases in e times, $R(z)$ - wavefront radius of curvature (z axis is fair with optical axis OR). Suppose plane $z=0$ is a system symmetry plane ($R(z)=0$), then

$$w^2(z) = w_0^2 \left[1 + \left(\frac{\lambda z}{\pi w_0^2} \right)^2 \right] \quad (2)$$

$$R(z) = z \left[1 + \left(\frac{\pi w_0^2}{\lambda z} \right)^2 \right] \quad (3)$$

$$w_0^2(z) = \frac{\lambda}{2\pi} \sqrt{L(2R - L)}, \quad (4)$$

and resonance condition is

$$kL = \pi \left[(q+1) + \frac{1}{2}(m+2n+1) \arccos \frac{R-L}{R} \right], \quad (5)$$

where m, n, q - indexes of oscillation types, L - distance between mirrors, λ - wavelength, k - wave number.

With the help of integration of field amplitude square of known field distribution of corresponding areas it is possible to estimate the energy stored in the first resonator, diffraction loss and part of them, responsible for the oscillations excitation in the second OR. Obtained results allow us to estimate value of factor Q in first OR and transmission coefficient in second OR.

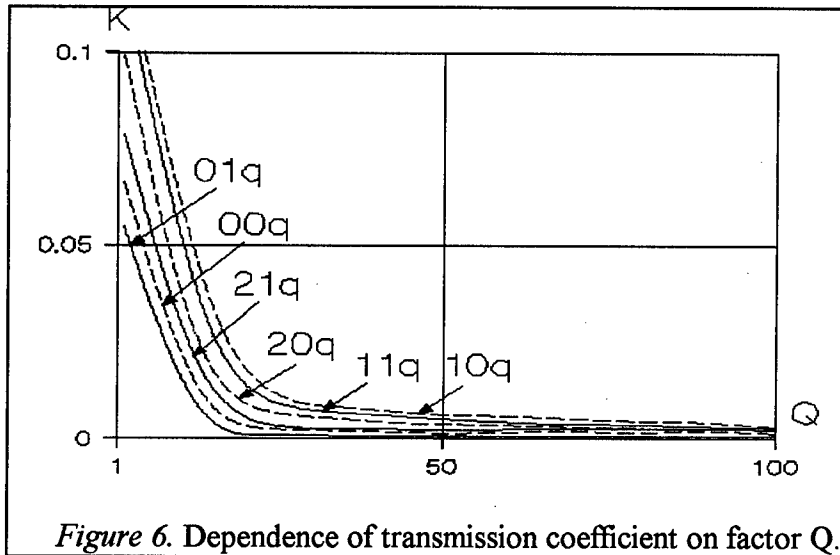


Figure 6. Dependence of transmission coefficient on factor Q .

The results, obtained for some lowest oscillation types are presented at fig.6 (an factor Q - transmission coefficient plot). From the fig.6 it is clearly seen, that increase of transmission coefficient is accompanied by fast decrease of factor Q , and asymmetric oscillations excitation (particularly for 10q oscillation type) is traded off for effective energy flow from one OR to another.

Let us note the limits for such estimation. At first, as a base of this model a solution of problem of OR with "infinite mirrors" self oscillations is taken; this solution in principal don't take into account the influence of mirror edges on field forming on OR mirror and out of it. For this reason the value of transmission coefficient from one OR to another is small while the values of factor Q is real. Secondly, it must be noted that while estimating the transmission coefficient we don't take into account efficiency of transformation of first resonator oscillation energy, transmitted into the second resonator, into the exciting resonant oscillation of this resonator.

3. Conclusions

The numerical model confirmed the supposition about the predominant exciting of highest and asymmetric oscillation types in such system, as was

showed in the experiment. The experimental investigations showed effectiveness of functioning of diffraction coupled two-mirror ORs with spherical mirrors systems near concentric geometry.

4. References

1. Afonin, D.G., Dubrovskii, V.V., Malyshkin, A.K. (1993) Avtomatizirovannaiia ustanovka dla issledovaniia electrodinamicheskikh sistem na base IBM PC XT (in Russian), *Pribory i Tekhnika Eksperimenta* N5, 75-78.
2. Afonin, D.G., Kanunov, E.R., Malyshkin, A.K. (1996) Ustanovka dla avtomatizatsii izmerenii charakteristik electrodinamicheskikh sistem v millimetrovom diapasone (in Russian), *Izmeritelnaia Tekhnika*, N11, 42-44.
3. Vainshtein, L.A. (1966) *Otkritie resonatori i otkritie volnovodi* (in Russian), izd. "Sov. Radio", Moscow.

ENHANCEMENT OF SMALL-SCALE OPTICAL NONUNIFORMITIES IN ACTIVE MEDIUM OF HIGH-POWER CW FAF CO₂ LASER

M.G.Galushkin, V.S.Golubev, Yu.N.Zavalov, V.Ye.Zavalova,
V.Ya.Panchenko
Russian Academy of Sciences, NICTL-Laser Research Center,
Svyatoozerskaya St.,1, Shatura, 140700, Moscow Region, RUSSIA

Abstract

It has been shown that high-intensity laser radiation reduces the threshold of gas discharge thermal instability in the fast-axial flow (FAF) laser. The turbulent characteristics of gas flow in the active medium of the gas-discharge laser have been measured experimentally and the estimation of their influence on the wavefront distortion of the laser beam have been made.

1. Introduction

The optical nonuniformities of the active medium are the important physical factors, influencing the high-power industrial laser beam quality. They cause linear and nonlinear aberrations of the laser beam wavefront. The small-scale (as compared with the laser beam transverse size) optical nonuniformities arise alongside with the large-scale spatial nonuniformities of the refraction index of self-sustained dc-discharge cw CO₂ lasers amplifying medium [1,2]. They are initiated by fluctuations of gas density and have a stochastic character. The investigation of the influence of the refraction index stochastic fluctuations in the space upon the spatial characteristics of the laser beam is important to determine the upper limit of the industrial CO₂ laser beam quality, because the optical nonuniformities of this kind can be compensated only by the phase conjugation method.

This work presents some results of the investigation concerning the small-scale optical nonuniformities of self-sustained dc-discharge FAF high-power cw CO₂- lasers active medium. The fluctuations of the laser mixture refraction index can be caused by ionisation-thermal instability of the discharge in a turbulent gas flow.

2. Enhancement of active medium small-scale optical nonuniformities in the field of laser radiation under self-sustained discharge thermal instability.

In the high-power fast-flow CO₂ lasers the laser radiation field has an essential effect on heat release rates at VT-relaxation [1]. It may be the cause of various

nonlinear processes. In particular, the kinetic heat release (the rise of the laser mixture temperature in the field of laser radiation) can increase the increment of the gas medium density disturbance exponential growth under thermal instability of the discharge. And thus, it can enhance the small-scale stochastic optical gas nonuniformities. This effect deteriorates the optical quality of the active medium [3]. The paper [3] considers the transverse-flow cw CO₂ laser. In the present paper we consider the FAF laser.

The temporal evolution of the temperature fluctuation δT and, respectively, of the gas mixture density $\delta \rho$, in the field of laser radiation is described by the equations of heat balance and kinetics of the CO₂ laser. In the mode approximation it have the form:

$$\frac{\partial e_3}{\partial t} = \frac{R}{N(\gamma_c + \gamma_n)} - \frac{\gamma_c}{\gamma_c + \gamma_n} \frac{e_3}{\tau_2} - \frac{\gamma_c}{\gamma_c + \gamma_n} \frac{\alpha J}{\hbar \omega_0 N_c} - v \frac{\partial e_3}{\partial x} + D_t \Delta_r e_3 \quad (1)$$

$$c_p \rho \frac{\partial T}{\partial t} = \hbar \omega_3 \gamma_c N \frac{e_3}{\tau_2} + \frac{\omega_1}{\omega_0} \alpha J + (1 - \eta) W - c_p \rho v \frac{\partial T}{\partial x} + c_p \rho \chi_t \Delta_r T. \quad (2)$$

Here e_3 is the average number of vibrational quanta of the CO₂(001⁰) molecule antisymmetric mode; N is the concentration of the CO₂:N₂:He mixture particles; γ_c, γ_n are the mole fractions of CO₂ and N₂, respectively; $N_c = \gamma_c N$ is the concentration of CO₂ molecules; $R = \eta W / (\hbar \omega_3)$, η is the efficiency of vibrational excitation (80-85%); τ_2 is the effective time of collisional nonradiative VT-relaxation of the 001⁰ mode; $\hbar \omega_0$ is the energy of a laser quantum; $\hbar \omega_1 \approx 2\hbar \omega_2$ is the energy of a vibrational quantum in the symmetrical mode; v is the gas flow velocity; α is the gain; D_t is the coefficient of turbulent diffusion; χ_t is the coefficient of turbulent heat conductivity;

$\Delta_r = \frac{1}{r} \frac{\partial}{\partial r} + \frac{\partial^2}{\partial r^2}$; $W = jE$ is the specific power input into the discharge; $\hbar \omega_3$ is the energy of a nitrogen vibrational quantum. The equations (1) and (2) are written in an

approximation of the fast VT-relaxation of the lower laser level, i.e. $\frac{\partial e_2}{\partial t} \cong 0$. As seen from the equations (1) and (2), the heat release in the laser mixture depends on radiation intensity, therefore it is nonlinear.

Further, we use the approximation $\alpha = \sigma N_c e_3$, which means the small population of the lower laser level in comparison with the upper one, i.e. $e_2 < e_3$. Then the equations (1) and (2) are simplified:

$$\frac{\partial e_3}{\partial t} = \frac{\eta}{\hbar \omega_3 (\gamma_c + \gamma_n)} \frac{W}{N} - \frac{\gamma_c}{\gamma_c + \gamma_n} \frac{e_3}{\tau_2} - \frac{\gamma_c}{\gamma_c + \gamma_n} \frac{\sigma J}{\hbar \omega_0} e_3 - v \frac{\partial e_3}{\partial x} + D_t \Delta_r e_3 \quad (3)$$

$$\frac{\partial T}{\partial t} = \hbar\omega_3 \frac{N_c}{c_p \rho \tau_2} e_3 + \frac{\omega_1}{\omega_0} \frac{N_c \sigma J}{c_p \rho} e_3 + (1-\eta) \frac{W}{c_p \rho} - v \frac{\partial T}{\partial x} + \chi_t \Delta_r T \quad (4)$$

The stability of solution of the equations set (1) and (2) will be investigated by the usual method, i.e. through linearizing the functions e_3 and T in the vicinity of the stationary solution. For this purpose, we shall write the equations for variations of δe_3 and δT :

$$\begin{aligned} \frac{\partial \delta e_3}{\partial t} = & \frac{\eta}{\hbar\omega_3(\gamma_c + \gamma_n)} \delta \left(\frac{W}{N} \right) - \frac{\gamma_c}{(\gamma_c + \gamma_n)\tau_2} \delta e_3 - \frac{\gamma_c}{\gamma_c + \gamma_n} \frac{\sigma J}{\hbar\omega_0} \delta e_3 - \\ & - \delta v \frac{\partial e_3}{\partial x} - v \frac{\partial \delta e_3}{\partial x} + \delta D_t \Delta_r e_3 + D_t \Delta_r \delta e_3; \quad (5) \end{aligned}$$

$$\begin{aligned} \frac{\partial \delta T}{\partial t} = & \frac{\hbar\omega_3}{c_p \tau_2} \left(\frac{N_c}{\rho} \right) \delta e_3 + \frac{\omega_1}{\omega_0} \frac{\sigma J}{c_p} \left(\frac{N_c}{\rho} \right) \delta e_3 + (1-\eta) \frac{1}{c_p} \delta \left(\frac{W}{\rho} \right) - \frac{\partial T}{\partial x} \delta v - \\ & - \frac{\partial \delta T}{\partial x} v + \delta \chi_t \Delta_r T + \chi_t \Delta_r \delta T. \quad (6) \end{aligned}$$

To avoid the complicated expressions, it is assumed here that τ_2 and σ do not depend on the gas temperature and density. The corresponding error related to this assumption can be easily calculated. Moreover, we neglect direct heating, because $(1-\eta) \leq 0.2$. To find an approximate solution of (5) and (6), we use the following approximations of functions e_3 and T :

$$e_3(x, r) \cong \frac{e_3(l, r)}{l} x; \quad T(x, r) \cong \frac{T_1(r) - T_0}{l} x + T_0; \quad (7)$$

$$e_3 = \int_0^l e_3(x, r) dx \cong e_3(0) \left(1 - r^2/a^2 \right); \quad T = \int_0^l T(x, r) dx \cong T(0) \left(1 - r^2/a^2 \right),$$

where $T(0) = \frac{T_1(0) + T_0}{2}$, $e_3(0) = \frac{1}{2} e_3(l, 0)$, a , l are the radius and length of the gas discharge tube (GDT); T_0 , $T(l, 0)$ are the gas temperatures at the entrance and at the exit GDT. Allowing for (7) and taking into consideration the dependence $\nu \rho = \nu_0 \rho_0$, D , $\chi \sim \nu$ from (5), (6), we obtain

$$\frac{\partial \delta e_3}{\partial t} = \frac{\eta}{\hbar\omega_3(\gamma_c + \gamma_n)} \frac{W}{N} \left(1 + \frac{T}{W} \frac{\partial W}{\partial T} \right) \frac{\delta T}{T} - \frac{\delta T}{T} -$$

$$-\frac{\gamma_c}{(\gamma_c + \gamma_n)} \left(\frac{1}{\tau_2} + \frac{\sigma J}{\hbar \omega_0} \right) \delta e_3 - \frac{e_3(l, r)}{l} v - \frac{v}{l} \delta e_3(l, r) + (\Delta_r e_3) D_t \frac{\delta T}{T} + D_t \Delta_r \delta e_3 \quad (8)$$

$$\begin{aligned} \frac{\partial \delta T}{\partial t} = & \left(\frac{\hbar \omega_3}{c_p \tau_2} \left(\frac{N_c}{\rho} \right) + \frac{\omega_1}{\omega_0} \frac{\sigma J}{c_p} \left(\frac{N_c}{\rho} \right) \right) \delta e_3 - \\ & - \frac{T_1(r) - T_0}{l} v \frac{\delta T}{T} + (\Delta_r T) \chi_t \frac{\delta T}{T} + \chi_t \Delta_r T + \frac{v}{l} \delta T_1(r). \end{aligned} \quad (9)$$

After averaging along the longitudinal coordinate we find from (8) and (9)

$$\begin{aligned} \frac{\partial \delta \bar{e}_3}{\partial t} = & \frac{\eta W(1+Y)}{\hbar \omega_3(\gamma_c + \gamma_n) NT} \frac{\delta T}{T} - \frac{\gamma_c}{(\gamma_c + \gamma_n) \tau_2} \left(1 + \frac{J}{J_s} \right) \delta \bar{e}_3 - \frac{\bar{e}_3(l, r)}{l} v \frac{\delta T}{T} - \\ & - \frac{v}{l} \delta \bar{e}_3(l, r) + (\Delta_r \bar{e}_3) \bar{D}_t \frac{\delta T}{T} + \bar{D}_t \Delta_r \delta \bar{e}_3; \end{aligned} \quad (10)$$

$$\begin{aligned} \frac{\partial \delta T}{\partial t} = & \left(\frac{\hbar \omega_3}{c_p \tau_2} \frac{N_c}{\rho} \left(1 + \frac{\omega_1}{\omega_0} \frac{J}{J_s} \right) \right) \delta \bar{e}_3 - (T_1(r) - T_0) \frac{v}{l} \frac{\delta T}{T} + \\ & + (\Delta_r T) \bar{\chi}_t \frac{\delta T}{T} + \bar{\chi}_t \Delta_r T + \frac{v}{l} \delta T_1(r), \end{aligned} \quad (11)$$

$$\text{here } \hat{Y} = \frac{T}{W} \frac{\partial W}{\partial T} = \frac{\partial \ln W}{\partial \ln T}.$$

Using (7) from (10) and (11) we obtain

$$\begin{aligned} \frac{\partial \delta \bar{e}_3}{\partial t} = & \frac{\eta W(1+\hat{Y})}{\hbar \omega_3(\gamma_c + \gamma_n) NT} \frac{\delta T}{T} - \frac{\gamma_c}{(\gamma_c + \gamma_n) \tau_2} \left(1 + \frac{J}{J_s} \right) \delta \bar{e}_3 - 2 \frac{\bar{e}_3(0)}{l} v \frac{\delta T}{T} - \\ & - 2 \frac{v}{l} \delta \bar{e}_3 - \frac{4}{a^2} \bar{e}_3(0) \bar{D}_t \frac{\delta T}{T} - \frac{4}{a^2} \bar{D}_t \Delta_r \delta \bar{e}_3(0); \end{aligned} \quad (12)$$

$$\begin{aligned} \frac{\partial \delta T}{\partial t} = & \left(\frac{\hbar \omega_3}{c_p \tau_2} \frac{N_c}{\rho} \left(1 + \frac{\omega_1}{\omega_0} \frac{J}{J_s} \right) \right) \delta \bar{e}_3 - 2(T_1 - T_0) \frac{v}{l} \frac{\delta T}{T} - \\ & - \frac{4}{a^2} \frac{T(0)}{T} \bar{\chi}_t \delta T - \frac{4}{a^2} \bar{\chi}_t \delta T(0) - \frac{2v}{l} \delta T, \end{aligned} \quad (13)$$

Here $\delta z_3 = \delta z_3(0) \left(1 - \frac{r^2}{a^2}\right)$; $\delta T = \delta T(0) \left(1 - \frac{r^2}{a^2}\right)$, and the line designates the average values along the GDT length (axis x).

The condition of solution of the linear equations set (12) and (13) is found by the well known method

$$\delta z_3 = C_1 e^{\gamma t}, \delta T = C_2 e^{\gamma t}. \quad (14)$$

After (14) substitution in (12) and (13) we have for $r=0$

$$\begin{aligned} \gamma C_1 &= b_1 C_2 + a_1 C_1, \\ \gamma C_2 &= a_1 C_1 + b_2 C_2 \end{aligned} \quad (15)$$

$$\text{where } a_1 = -\frac{\gamma_c}{(\gamma_c + \gamma_n)\tau_2} \left(1 + \frac{J}{J_s}\right) - \frac{2v}{l} - \frac{4}{a^2} D_t;$$

$$b_1 = \frac{\eta W(1 + \hat{Y})}{\hbar \omega_3 (\gamma_c + \gamma_n) T N} - \frac{2v}{l} \frac{z_3(0)}{T} - \frac{4}{a^2} \frac{D_t}{T} z_3(0);$$

$$a_2 = \frac{N_c \hbar \omega_3}{c_p \rho \tau_2} \left(1 + \frac{\omega_1}{\omega_3} \frac{J}{J_s}\right); \quad z_3(0) = \frac{\alpha_0}{1 + J/J_s} \frac{J_s}{\gamma_c N} \tau_2;$$

$$b_2 = -\frac{2v}{l} - \frac{8}{a^2} \bar{\kappa}_t - \frac{2(T(0) - T_0)}{T(0)} \frac{v}{l}. \quad (16)$$

The existence of a solution to the linear equations set (15) requires the determinant coefficients matrix to be equal to zero:

$$\begin{vmatrix} \gamma - a_1 & -b_1 \\ -a_2 & \gamma - b_2 \end{vmatrix} = 0, \quad \text{i.e. } (\gamma - a_1)(\gamma - b_2) - a_2 b_1 = 0.$$

As the result, we obtain

$$\gamma_{1,2} = \frac{1}{2}(a_1 + b_2) \pm \sqrt{\frac{1}{4}(a_1 + b_2)^2 + (a_2 b_1 - a_1 b_2)}.$$

As $a_1 < 0$ and $b_1 < 0$, then

$$\gamma = \frac{1}{2}(a_1 + b_2) + \sqrt{\frac{1}{4}(a_1 + b_2)^2 + (a_2 b_1 - a_1 b_2)}. \quad (17)$$

The thermal instability becomes possible at $a_2 b_1 \geq a_1 b_2$, where

$$a_2 b_1 = \left[\frac{\gamma_c \eta W(1 + \hat{Y})}{(\gamma_c + \gamma_n) c_p \rho T \tau_2} - \frac{\omega_3}{\omega_0} \left(\frac{2v}{l} + \frac{4D_t}{a^2} \right) \frac{\bar{\alpha}(0) J_s}{c_p \rho T} \right] \left(1 + \frac{\omega_1}{\omega_3} \frac{J}{J_s} \right), \quad (18)$$

$$a_1 b_2 = \left[\frac{\gamma_c}{(\gamma_c + \gamma_n) \tau_2} \left(1 + \frac{J}{J_s} \right) + \frac{2\sigma}{l} + \frac{4}{a^2} D_t \right] \left[\frac{2\sigma}{l} + \frac{8}{a^2} \bar{\chi}_t + \frac{2(T(0) - T_0) \sigma}{T(0) l} \right]. \quad (19)$$

The reasons for improvement of the discharge stability are clearly seen from expressions (16) and (18), (19). To them belong the convective removal and turbulent diffusion of the excited CO₂ molecules, the dependence of the flow velocity on temperature, as well as the nonuniformities of the vibrationally excited molecules and temperature along the tube GRT length, reducing the velocity of temperature perturbations growth.

On the other hand, the sluggishness of heat release in the active medium becomes an important factor stabilizing the discharge. The threshold value of the specific power input W , from which the ionisation/thermal instability begins to develop and, respectively, the small-scale casual nonuniformities of the gas refraction index are enhanced, is directly dependent on its basic parameters. The dependence of the thermal instability threshold and the time of its development on laser radiation intensities is essential.

Taken alone, the threshold condition of thermal instability emergence follows from (17) $a_2 b_1 \geq a_1 b_2$. Hence we have

$$W^* \geq \frac{c_p \rho T}{\eta(1+Y)} \frac{(\gamma_c + \gamma_n)}{\gamma_c} \left\{ \left(\frac{2\sigma}{l} + \frac{4}{a^2} D_t \right) \tau_2 \frac{\alpha J_s}{c_p \rho T} \frac{\omega_3}{\omega_0} + \frac{1}{\left(1 + \frac{\omega_1}{\omega_3} J / J_s \right)} \cdot \left[\frac{\gamma_c}{(\gamma_c + \gamma_n)} \left(1 + \frac{J}{J_s} \right) + \left(\frac{2\sigma}{l} + \frac{4}{a^2} D_t \right) \tau_2 \right] \cdot \left[\frac{2\sigma}{l} + \frac{8}{a^2} \bar{\chi}_t + \frac{2(T(0) - T_0) \sigma}{T(0) l} \right] \right\} \quad (20)$$

For example, at $\sigma = 154 \text{ m/s}$, $l = 18.5 \text{ cm}$, $T = 500^\circ \text{K}$, CO₂:N₂:He=1:6:10, $D_t \approx \chi_t = 60 \text{ cm}^2/\text{s}$, $\rho = 3 \cdot 10^{-5} \text{ g/cm}^3$, $J_s = 300 \text{ W/cm}^2$, $a = 0.8 \text{ cm}$, $\alpha = \alpha_0 / (1 + J / J_s)$, $\alpha_0 = 1 \text{ m}^{-1}$, $T_0 = 320^\circ \text{K}$, $\eta = 0.85$, $Y \approx 10$, $\tau_2 = 2 \cdot 10^{-4} \text{ s}^{-1}$ and $J = 0$, the relation (20) is fulfilled at $\eta W^* \approx 39 \text{ W/cm}^3$, and in the field of intense laser radiation, when, for example $J = 3J_s$, the threshold of thermal instability decreases and becomes $\eta W^* \approx 25 \text{ W/cm}^3$.

The heat release velocity depends on the intensity of laser radiation. Thus, the laser radiation in the vibrationally excited laser mixture has a decreasing effect upon the threshold value of the power input in the discharge with thermal instability.

Though the obtained formula (17) is approximate, it gives a full enough idea of the character and the degree of dependence of thermal instability emergence condition and development velocity and, respectively, density perturbations on the basic parameters of the laser medium and the laser radiation. In this connection, we should note that on studying the thermal instability of glow discharge in the laser mixture the final time of

VT-relaxation of vibrationally excited CO_2 molecules of the laser mixture must be taken into account. A deviation from this requirement, as it was done in [4], where the pulsed impulse laser with e-beam controlled discharge in approximation of fast VT-relaxation was considered, leads to large quantitative errors.

In discharge instability the initial density perturbations amplify in laser mixture flow through discharge area $\langle \delta \rho \rangle = \langle \delta \rho_0 \rangle \exp(\gamma \bar{x} / x)$, and initial fluctuations $\langle \delta \rho_0 \rangle$ are often caused by gas flow turbulence at the entrance of the discharge tube.

3. Small-scale optical nonuniformities, related to turbulence of active medium gas flow.

The pulsings of the turbulent gas flow density in the high-power CO_2 laser can be considered as the initial perturbations under the gas discharge thermal instability. With the steady-state discharge the turbulence determines the small-scale optical nonuniformities of the laser medium and governs the effectiveness of turbulent diffusion and thermal diffusivity, which, in their turn, influence the threshold values of the specific power input into the discharge. For these reasons, the following turbulent characteristics of the flow of the thermodynamically non-equilibrium gas become important: the root-mean-square values of density pulsations

$$\delta \rho = \left(\langle \Delta \rho^2 \rangle \right)^{1/2} \text{ and their spatial scale } l. \text{ To measure these parameters, we used}$$

the luminescence method allowing to fix the spatial distribution of electrons density and the related gas density [5]. The experiments were performed on the FAI CO_2 laser with 600 W output power [6].

As a registering device, we used an optron with an open optical path. The optron contains two silicon photodiodes, each of them having the working area of 1.25×1.25 mm size; they are placed at a distance of 3.5 mm (center to center) apart. Between them an AsGa light-emitting diode is placed, which is used only for the measurement system adjustment. The spectral sensitivity of photodiodes lies in the range of the registered light wavelengths from 430 to 960 nm with a sharp collapse at the edges of the spectral range. The sensitivity at the wavelength 800 nm is 350-400 $\mu\text{A/mW}$. No spectroscopic measurements of the discharge luminescence were carried out. It is known, that in this spectral range the lines of luminescence of the CO_2 laser gas discharge are the most intensive [7], they correspond to the electron transitions of N_2 molecules (2 positive bands), CO molecules (3 positive bands) and the bands of a γ -system of NO. The scheme of the experimental setup is presented in Fig. 1. The flux of light, emitted by a local area of the positive column of the discharge, was measured in the direction perpendicular to the flux direction. For this purpose, an optical lens was set between the transmitter and the GDT. The GDT was made from molybdenum glass.

The electrical current from each of the photodiodes was amplified by an individual amplifier operated by the scheme "current-controlled voltage supply", then the signals were sent through the block of normalizing amplifiers and the filtration block to one of

the channels of the data acquisition and processing system (DAS). The special attention was given to joining the common, ground and shield wires.

The laser was operating in the pulse-periodic pump mode. The pump pulse duration was 1,66 ms with pulse repetition rate 2,1 ms at the specific power input 14 W/cm³. The velocity of gas flow was 140 m/s (the flow rate 36 l/s).

The analog filtration of the signals with the help of low-frequency 4th order Bessel filters was performed during measurements of gas density fluctuations and their spatial scales in the gas flow. The frequency of the filter section was tuned to the value 80 kHz on the level -6 dB. The discreteness of signal sampling in each of the channels was 8 μ s. The time of sampling was from 1.3 to 3 μ s for 12-digit reading. The total number of readings reached 2¹⁴ per channel. In the some measurements the signals, proportional to the GDT current and laser power moved to the DAS in addition to the signals from the photodetector (in the case, when the optical resonator was alignment). In this case the frequency of sampling and the total volume of references were reduced by half.

The equipment employed performs the signal measurements in the frequency band up to $f_a = 1/(2 \cdot 8 \mu s) = 62.5$ kHz, i.e. the frequency band is limited from above by the time of signal sampling. This allows to identify a space scale of the fluctuations $v/f_a = 1.4 \cdot 10^4$ cm/s/62.5 kHz = 2.3 mm. At the specified magnification of the optical system ~ 1 the size of the area that gives the converged light to the photodetector is close to the size of the photodiode. Our estimations show that this space resolution is quite sufficient to define the gas density turbulent pulsations spectrum, as its spatial scale can be evaluated as $l_0 = d \cdot Re^*$, $Re \approx 7$ mm, and the lifetime of turbulent space fluctuations exceeds the observation time to the extent that the ergodicity condition of the observable casual processes is satisfied. Here d is the GDT diameter, Re^* and Re are the critical and actual values of the Reynolds number. Only two channels connected to the photodiodes were used to extend the frequency band. In this case at the continuous entry $2^{14} \cdot 8$ ms = 131072 ms the resolution of the frequency spectrum of the digital spectrum analyzer was about 8 Hz.

As the result, the spectral analysis of the registered signals was used to determine the distribution of the root-mean-square deviations of the gas density $\delta\rho$ and, respectively, the root-mean-square pulsings of the flow velocity δV depending on the spatial scale of perturbation l . The measured values of $\delta\rho$ as the functions of l for different values of the specific power of energy input in the presence of radiation are given in Fig. 2. Fig. 3 illustrates the same values in the absence of radiation.

The recalculation of the frequency scale to the spatial one was carried out in the terms of the gas velocity growth with the specific energy input and, respectively, the radiation intensity. It is clear that the distribution adheres to the law "2/3" of Obukhov-Kholmogorov [8] at $l > l_0$. The natural growth of the gas density pulsings is observed (Figs. 2,3) with the increase of the specific energy input power and the laser radiation intensity. It is explained by the increase of pulse-periodic heat release rate being the primary source of gas density perturbations.

The obtained data on the fluctuation performances of the active medium of the pulse-periodic fast-axial-flow 600 W CO₂ laser medium with self-sustained dc discharge permit to evaluate the stochastic optical path difference for a single pass through the amplifying medium. It is about 0.02λ ($\lambda = 10.6$ μ m) at the spatial scale of

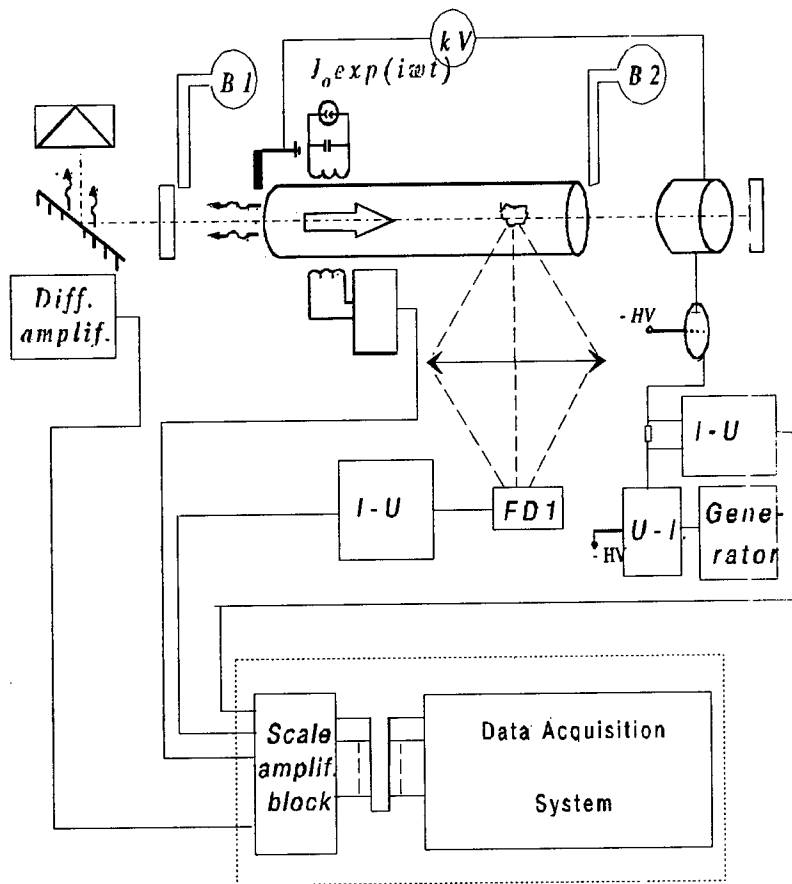


Figure 1. The experimental setup for investigation of the small-scale optical nonuniformities by the luminescence method.

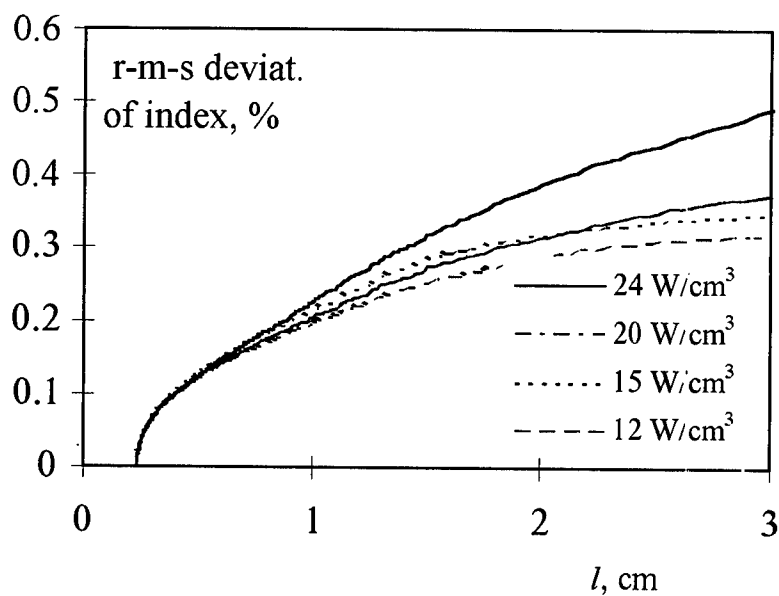


Figure 2. The root-mean-square deviations dependence the on spatial scale of turbulence nonuniformities at various power input without radiation.

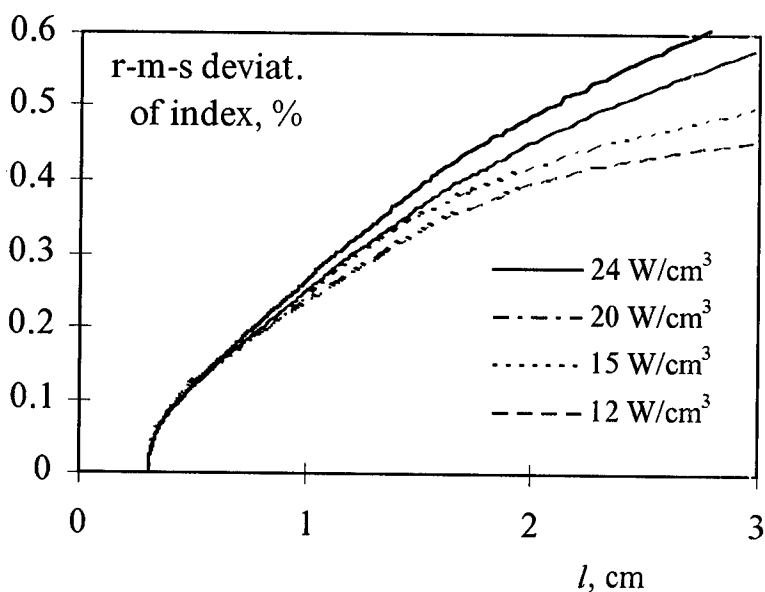


Figure 3. The root-mean-square deviations dependence on the spatial scale of turbulence nonuniformities l at various power input with radiation.

the refraction index pulsation about 1 cm for the case of $L=1.5$ m active medium optical path and power input 20 W/cm^2 .

Thus, the small-scale optical nonuniformities related to the pulsations of gas density in the high-power pulse-periodic low-pressure CO_2 lasers can influence the generated beam quality and thereby determine the limiting values of radiation brightness in the gas lasers which do not use the optical systems of phase distortion compensation on the basis of wavefront conjugation.

4. Conclusion

In the gas discharge of the high-power fast-axial-flow CO_2 laser the initial turbulent perturbations of the gas density are enhanced under the developed thermal instability conditions at the case of glow discharge energy. The intense laser radiation therewith causes the reduction of the ionization/thermal instability emergence threshold and promotes to the growth of the evolution rate of the gas density initial pulsations at the GDT entrance in time. Under the condition of the stable discharge in the pulse-periodic CO_2 laser, the small-scale optical nonuniformities originating due to the turbulent pulsation of gas density may deteriorate the beam quality at the average radiation power of several hundreds watts and more.

5. Acknowledgements

The authors wish to thank the Russian Foundation for Basic Research for financial support of this work.

6. References

1. Galushkin, M.G., Golubev, V.S., Zabelin, A.M., Panchenko, V.Ya. (1989) *Izv. Akad. Nauk USSR Ser. Fiz.* **53**, 1136-1139.
2. Rayzer, Yu.P. (1987) *Fizika gazovogo razryada*, Moscow: Nauka.
3. Galushkin, M.G., Golubev, V.S., Zabelin, A.M., Panchenko, V.Ya. (1992) *Izv. Akad. Nauk USSR Ser. Fiz.* **56**, 199-202.
4. Blinov, N.A., Boyko, V.V., Irodin, Ye.I., et al. (1985) *Kvantovaya Electr. (Moscow)* **23**, 1977-1981.
5. Garosi, G.A., Bekefi, G., Schulz, M. (1970) *Phys. Fluids* **13**, 2795-2800.
6. Dembovetsky, V.V., Zavalov, Yu.N. (1996) *Proceedings of NATO ASI "High Power Laser: Science and Engineering" Karlovy Vary, Czech Republic, 1995*, Eds R Kossowsky et al., NATO Sci. Com. ASI-3, High Technology, 7, 603-618, (Dordrecht, Netherlands: Kluwer Academic Publ.)
7. Witteman, W.J. (1988) *The CO_2 Laser*, Berlin: Springer-Verlag.
8. Landau, L. and Lifchitz, E. (1971) *Mecanique des fluides*, Editions MIR, Moscou. (franc.)

SYNTHESIS OF INTERFEROGRAMS BY LATERAL SHEAR TO MEASURE WAVE FRONT OF A LIGHT BEAM.

V.N. SHEKHTMAN

*Engineering-Physics Laboratory
St.Petersburg, Russia*

Abstracts

Interferometric analyzer of the wave front based only on lateral shear operations has maximum vibration resistance. However synthesis of a fringe patterns by only lateral shear leads, of course, to some loss of information about wavefront form. But this loss may cause only linear transformation of real form acting as an "optical wedge". In many practical cases it is essential to reconstruct only wavefront figure and its total tilt is of little practical interest.

Nomenclature

IF, $h(x)$	-interferometric function
$\varphi(x)$	-function of spatial distribution of a wavefront phase
S	-size of lateral shear of identical wavefronts
$\varphi_1(x)$	-function of spatial distribution of a wavefront phase moved from $\varphi(x)$ at a distance S
AWF	-analyzer of wave front
αx	-linear component $\varphi(x)$
$\tilde{\varphi}(x)$	-variable component $\varphi(x)$
Δh_D	-break IF in a point D
αD	-general inclination of measured wavefront
S_1	-shear on a (OD) part of the interferogram in a case optical synthesizing IF or shear on first interferogram in the case of numerical synthesizing IF
S_2	-shear on a (D, (D+S)) part of the interferogram in the case of optical synthesizing IF or shear on second interferogram at numerical synthesizing

1. Introduction.

In the report [1] the analysis of loss of the information about the form of a light beam front measured by various shear interferometers has been submitted, there is offered the method of compensation for these losses and thereby the method of complete reconstruction of wavefront by using of "synthesized" shear interferogram. This method is one of many possible variants of such synthesizing for complete or sufficient reconstruction of wave front. Synthesizing interferometric function (IF) is more correct and universal name for all these methods of wavefront reconstruction. IF describes a path difference of two interfering light beams depending on spatial coordinates at the plane of interference. For obtaining IF of the wavefront being reconstructed, can be various shear interferograms (interferograms of lateral, radial, rotary, reversal shear and etc.) used, several shear interferograms altogether and their separate sites. Submitted in [1] a fringe pattern is an example of optical synthesizing. In this case one interferogram is obtained, the various sites of which are interferograms of lateral or reversal shear of different parts of the aperture. Using such a interferogram it is possible to define IF on the entire image of a subject coinciding to the plane of interference, and completeness of reconstruction of wavefronts will be limited only by the resolution of optical system. Instead of this interferogram may be obtained three corresponding to it fringe patterns (two of a reversal and one of a lateral shifts) and carried out reconstruction of the wavefront by computer synthesizing of IF, i.e. by numerical synthesizing.

The choice of a way of the synthesizing and of a fringe pattern view depends on necessary completeness of reconstruction of wavefront and technical opportunities of realization of interferometric systems.

In [1] the interferometric system (more correct: the analyzer of wavefront (AWF)) consists of three interferometers (cascades AWF). In fig.1 for the variant of the analyzer described in [1], the section of a wave front at the plane, determined by directions of belong lateral shear and propagation of a light beam is conditionally exhibited. (O, D) is the size of the aperture, on which the wave front is investigated. In the first cascade limited by the rectangular aperture two mutually reversal images of a subject $((O, D)$ and $(D, 2D)$ corresponded them) are shifted at one image give. For the second cascade the image plane first is the one the plane of a subject. In this plane the spatial change of a phase in the direction of shear looks like an even function relative to the border D of two reversal images. These two images after the second cascade represent one new image $(O, 2D)$. In the second cascade relative lateral shear of two new images obtained from $(O, 2D)$ on size of this image is realized. We thus have the image $(-2D, 2D)$, to which correspond two periods of "infinite" periodic function $\varphi(x)$. In the third cascade relative lateral shear S of the images, obtained from the image $(-2D, 2D)$, is realized. In result interference of wavefronts at the aperture $(-2D+S, 2D)$, we receive more than one period of the "infinite" periodic IF, $h(x)=\varphi(x)-\varphi_1(x)$.

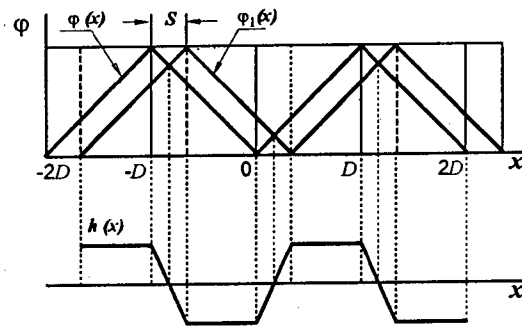


Figure 1

Practical realization of the method, described in [1], includes the cascade AWF carrying out reversing operation of the image of a subject. The result of use of this cascade is partial loss of vibration resistance of the whole device, and in the case of realization of measurements outside of laboratories the loss of contrast of the fringe pattern is possible on sites $(-D, -D+S)$, $(0, S)$ and $(D, D+S)$. The reduction of contrast on these sites depends on the width of interference fringe and its interference order. The probability of reduction of contrast is increased for that fringe between which and the zero order fringe is the greater number of interference fringes. Therefore for creation of AWF synthesizing the interference pattern intended for work outside of a laboratory sometimes it is useful to exclude the cascade of reversing and to keep only operations of lateral shear.

2. Information contained in IF synthesized with use only interferograms of lateral shear.

Interferometric AWF based only on lateral shear operations has maximum vibration resistance. However, such a way of synthesizing of IF results in some loss of the information about wavefront. We shall further show that in the case of reconstruction of wavefront with the use of synthesizing of IF only by lateral shear interferograms the loss of the information represents linear function, i.e. optical wedge.

The operations, carried out with the use of lateral shear AWF are shown on fig.2. Optical synthesizing for presentation we execute with the help of two lateral shear cascades. The size of the aperture of the investigated wavefront in a direction of shear of the images is (OD) . In the first cascade the shear is equal to the aperture. At the plane of the image of the second cascade the size of shear is usually less than half of

researched aperture, and the "infinite" periodic IF function can have breaks in coordinate points nD and $nD+S$, where $n = \dots -1; 0; 1, \dots$. These breaks are determined by a corner between the optical axis of the device and direction of a light beam. For definition of information losses created by breaks of function $h(x)$ we shall present $\varphi(x)$ by a sum of linear function αx and variable component $\tilde{\varphi}(x)$.

$$\varphi(x) = \tilde{\varphi}(x) + \alpha x \quad (1)$$

For reconstruction of a wave front the function $h(x)$ should be determined on a segment $[S, (D+S)]$. Using (1) we shall present $h(x)$ for each of two segments $[S, D]$ and $[D, (D+S)]$ of a segment $[S, (D+S)]$. Taking into account that similarly to $\varphi_1(x) = \varphi(x-S)$, $\varphi_1 \sim(x) = \tilde{\varphi}(x-S)$, we shall have for a segment $[S, D]$:

$$\begin{aligned} h_{(D-0)}(x) &= \tilde{\varphi}(x) + \alpha x - \tilde{\varphi}(x-S) - \alpha(x-S) \text{ or:} \\ h_{(D-0)}(x) &= \tilde{\varphi}(x) - \tilde{\varphi}(x-S) + \alpha S \end{aligned} \quad (2),$$

where αS is unknown constant appropriate to displacement the fringe pattern in interferogram in a point S .

Respectively, for a piece $[D, (D+S)]$ we have

$$\begin{aligned} h_{(D+0)}(x) &= \tilde{\varphi}(x-D) + \alpha(x-D) - \tilde{\varphi}(x-S) - \alpha(x-S), \text{ or:} \\ h_{(D+0)}(x) &= \tilde{\varphi}(x-D) - \tilde{\varphi}(x-S) + \alpha(-D+S) \end{aligned} \quad (3)$$

Subtracting (3) from (2) we receive expression (4) from which can be seen that the break $h(x)$ in a point D depends only on a general inclination of the wavefront:

$$h_{(D-0)}(x) - h_{(D+0)}(x) = \Delta h_D = \alpha D \quad (4).$$

For compensation for the information loss about an inclination of the wavefront it is possible to offer several ways of its measurement simultaneously with use synthesizing of IF with the use only of operations of lateral shear. For example the interferometric gauge based on properties of the variable shear interferometer described in [2] or reversal interferometer and etc.

3. Numerical synthesizing IF.

In the present paragraph we shall note one important difference between a method of numerical and optical synthesizing IF with the use of a lateral shear fringe pattern.

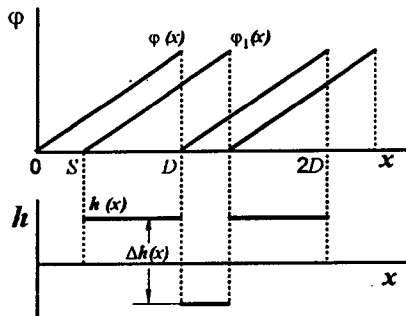


Figure 2

In fig.2 is seen that it is enough for optical synthesizing of the "infinite" IF to use two parts of the interferogram. In spite of the fact that the last ones are carried out by one installation of shear S fringe pattern consisting of two periods can be presented as two lateral shear interferograms. The ratio S_1/S_2 according to [1] should not be multiple. In fig.2 is easily seen the value of sum S_1 and S_2 . As $S_1=S$, $-S_2=-D+S$. (sign (-) before S_2 means that the vectors S_1 and S_2 are oppositely directed:

$$S_1 + S_2 = \text{size of the aperture} = (OD) \quad (5)$$

In the case of numerical synthesizing IF with the use of two separate lateral shear interferograms, fulfilment of a condition (5) results in the greatest accuracy and least complexity of reconstruction of wavefront. It is clear that at $S_1 + S_2 > (OD)$ the loss of the information takes place the reason of which is discrepancy of a range of definition $\varphi(x)$ and $h(x)$. If $S_1 + S_2 < (OD)$, the reconstruction of a wave front is possible. For this purpose it is necessary to choose a site of interferogram equal to a sum $S_1 + S_2$. It is uneasy to see that on this site the condition (5) is carried out. We shall show that after fulfilment of reconstruction of a wavefront on a chosen site it is probable to carry out the reconstruction of a wave front completely.

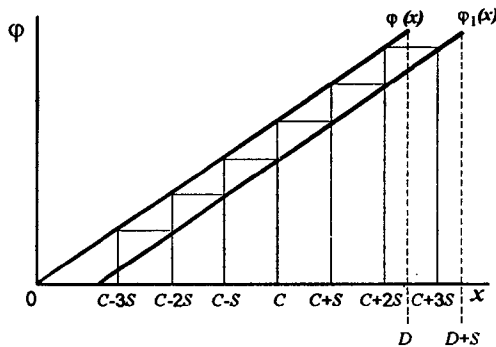


Figure 3

In fig.3 the section of moved wavefronts is conditionally shown. We shall assume that reconstruction of a wavefront is carried on a site $(C, (C+nS))$, where C is coordinate x , $n = \dots -1; 0; 1; \dots$, and S is equal to the smallest of two S_1 or S_2 . Using the theorem of shift for Fourier transform and expression $h(x) = \varphi(x) - \varphi(x-S)$ we shall write down connection between spatial spectra $\varphi(x)$ of any two near by sites and the spatial spectrum $h(x)$ one of them:

$$\int_{c-(n-1)S}^{c-(n-2)S} \varphi(x) e^{-i2\pi vx} dx = e^{-i2\pi vS} \int_{c-nS}^{c-(n-1)S} \varphi(x) e^{-i2\pi vx} dx + \int_{c-(n-1)S}^{c-(n-2)S} h(x) e^{-i2\pi vx} dx \quad (6)$$

where $n = \dots -1; 0; 1; \dots$

With the help of consecutive substitution of expressions (6) in (6), written down for a site, for example, $(C, (C+S))$, $n=1$, we obtain expression (7).

$$\int_c^{c+S} \varphi(x) e^{-i2\pi vx} dx = e^{-i2\pi vSn} \int_{c-nS}^{c-(n-2)S} \varphi(x) e^{-i2\pi vx} dx + \sum_{j=0}^{n-1} e^{-i2\pi vSj} \int_{c-jS}^{c-(j-1)S} h(x) e^{-i2\pi vx} dx \quad (7)$$

where $n = \dots -1; 0; 1; \dots$ $j = -(n-1); \dots -1; 0; 1; \dots (n+1)$.

Expression (7) demonstrates that on a site $(C, (C+S))$ it is possible to reconstruct wavefront, if the last is known on any other site of the aperture, equal to S . In the present case C is current coordinate, hence it is possible to carry out reconstruction of the wavefront form on the whole aperture.

4. The conclusion.

The offered method of reconstruction of the wavefront form by the use of synthesizing interferometric function obtained from lateral shear fringe pattern allows one to realize simple and the most vibration proof interferometric analyzer of a wavefront of a light beam. The loss of the information about a general inclination of the wavefront is not important for many practical problems. In the case of realization of the offered method this loss is easily compensated by simultaneous use of the mentioned above gauges of general wavefront inclination.

5. Refereces.

1. Shekhtman V.N., Rodionov A.Yu. and Pel'menev A.G., High Power Lasers - Science and Engineering, ed. R.Kossowsky et al., Series 3: High Technology-Vol.7, (1996), Kluwer Ac Publishers, Dordrecht/Boston/London.
2. Kolyshkina L.L., Kromin S.I. and Shekhtman V.N. (1986) Opt.-Mekh. Prom-st, #10, 51-54.

PART IV: OPTIMIZATION OF DESIGN

RESONATORS FOR LASERS USED IN PRECISION TECHNOLOGICAL OPERATIONS

S.A. DIMAKOV
Research Institute for Laser Physics
12 Birzhevaya line, St. Petersburg,
199034, Russia

1. Introduction

Currently, lasers are gaining wide use in technological processing of materials. The laser beam proved to be helpful for such technological operations as cutting, welding, scribing, hardening, marking and so on. Here are two examples of successful use of the laser beam's unique features. Materials, that cannot be welded by any other method, appear to be easily joined by laser welding. The laser-produced juncture is much stronger than the material itself. When using a laser source for technological purposes, the beam, in most cases, needs to be focused. For this reason, important parameters of the laser output emission are the beam divergence and jitter, which are determined by architecture and parameters of the laser optical scheme, by optical distortions arising in the optical beam path, and by vibrations of elements of the optical scheme.

This paper is devoted to some resonators which can be promising for using in technological lasers. Each of these resonators allows one to significantly improve laser's performance. This implies reduction of either beam divergence, or jitter, and improvement output power stability. This can, in turn, to lower the prices of the relevant laser technologies.

We will consider multi-element resonators for high-precision technological lasers. Special attention will be paid to a resonator with the so-called "cat-eye" reflector, to a resonator designed for high-power solid-state technological laser and characterized by strong thermal lens-wise distortion of its active medium, and to a resonator for the multi-chamber laser.

The first and the second types of the resonators have been studied experimentally and showed the unique features predicted theoretically. The resonator with the "cat-eye"-type reflector exhibited, as expected, a very low sensitivity to the wedge-like optical distortions. The laser with such a resonator showed a high stability both of the output power and of the direction of the beam characterized, in addition, by the divergence close to the diffraction limit. The second of the above resonators allowed us to obtain, without using phase conjugation technique, a high brightness of

technological solid-state laser emission in the presence of strong thermal lenses induced in the active rods.

We also discuss in this paper an optical scheme of the laser robot, whose movable "arm" emits radiation of a fixed angular direction with respect to the robot's "arm" end, while its position in space is changing.

2. Resonator with the "cat-eye"-type reflector.

2.1. THE "CAT-EYE"-TYPE REFLECTOR

The "cat-eye"-type (CE) reflector is successfully used by physicists in their experiments since fairly long ago. Suffice it to recall the first classical experiments of the French physicist Armand Hippolyte Louis Fizeau made in 1849 aimed at measurements of velocity of light, where the simplest version of the CE-reflector comprised a lens and a flat mirror was positioned at a distance of about 8 km from the laboratory and was used for accurate retro-reflection of the light beam [1]. Schematic of such a reflector and its principal properties can be found in [2]. The wavefront aberrations of a beam caused by its reflection from the CE-reflector are now studied fairly well (see, e.g., the discussion in [3-6]).

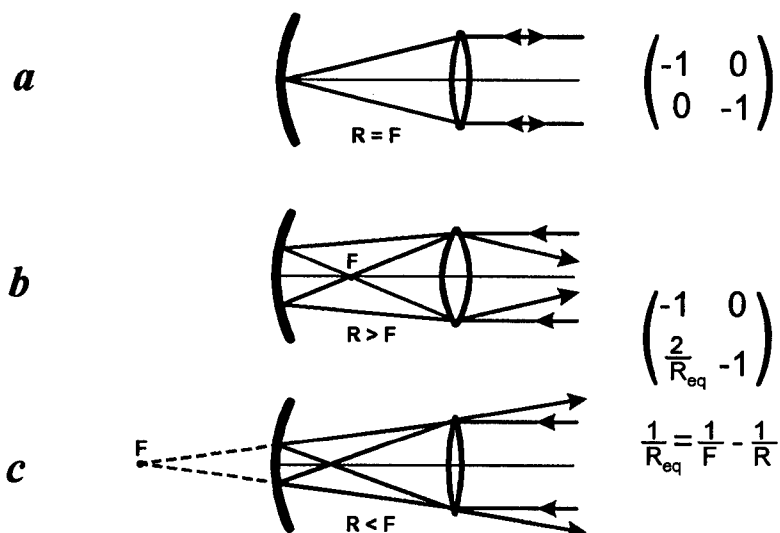


Figure 1. Schematic of a «cat-eye» type reflector.

Unlike Burch [2], we will consider a modified version of the CE-reflector comprising a focusing lens and a concave spherical mirror (Fig. 1). In the simplest version of this configuration, the spherical mirror is chosen so that its center of curvature coincides with the center of the lens, i.e., $R = l$, where R is the radius of the spherical mirror and l is the base length of the reflector. In this case, the entrance plane of the reflector, where the lens with the focal length F is positioned, is imaged onto itself reversed with respect to the center of the lens. The light beam passing through the lens is focused near the end spherical mirror. After being reflected from the end mirror, the beam is again focused by the lens and leaves the CE-reflector. The main feature of the CE-reflector is that the light beam is reflected exactly backward. The CE-reflector behaves as a phase-conjugation mirror for the first-order aberrations, and the optical matrix of such a reflector is given (at $R = l = F$) by

$$\begin{pmatrix} -1 & 0 \\ 0 & -1 \end{pmatrix} \quad (1)$$

Depending on the ratio of the curvature of the spherical mirror R and the focal length F of the lens, the CE-reflector is equivalent to a flat mirror (Fig. 1a), to a concave spherical mirror (Fig. 1b), or to a convex spherical mirror. The curvature R_{eq} of the equivalent mirror can be found from the equation

$$\frac{1}{R_{eq}} = \frac{1}{F} - \frac{1}{R} \quad (2)$$

The optical matrix of the reflector, in this case, will acquire the form

$$\begin{pmatrix} -1 & 0 \\ \frac{2}{R_{eq}} & -1 \end{pmatrix} \quad (3)$$

It is noteworthy that the term "equivalent mirror" is referred to the mirror which can be placed in the entrance plane of the CE-reflector and whose sign and magnitude of the radius of curvature are equal to R_{eq} specified by expression (2). For total equivalence of such a mirror to the CE-reflector, it should have possessed the property to reflect the light beam exactly backward, rather than in specular direction, and to reverse the pattern of the beam intensity distribution with respect to the mirror's center. By using the CE-type reflector, one can evidently realize a resonator of any configuration (flat, stable, or unstable). This resonator is likely to be insensitive with respect to arbitrary wedge-type aberrations in the laser's active medium and to misalignment or vibrations of intermediate deflecting mirrors in the resonator.

2.2. STABLE RESONATOR WITH THE "CAT-EYE"-TYPE REFLECTOR

We will consider, for brevity, only a stable resonator with the CE-reflector, although its main properties can refer to a resonator of unstable configuration. (In paper by I.B.Orlova [7], a few words is said about the unstable resonator with the CE-reflector.)

Figure 2 shows the optical schematic of the proposed resonator. It comprises a flat output mirror, a lens, and an end concave spherical mirror, the two latter constituting the CE-reflector. The aperture diaphragm of the resonator is placed in the entrance plane of the CE-reflector, i.e., immediately adjacent to the lens. It is clear that the size D of the diaphragm and the length L of the main part of the resonator allow one to choose either single-mode or multi-mode regime of operation of the laser with such a resonator. As was mentioned above, we consider for simplicity the case of self-imaging of the CE-reflector entrance plane. For this reason, when there is no aperture restrictions inside the CE-reflector, its length l is of no importance in the choice of the single- or multi-mode regime of operation.

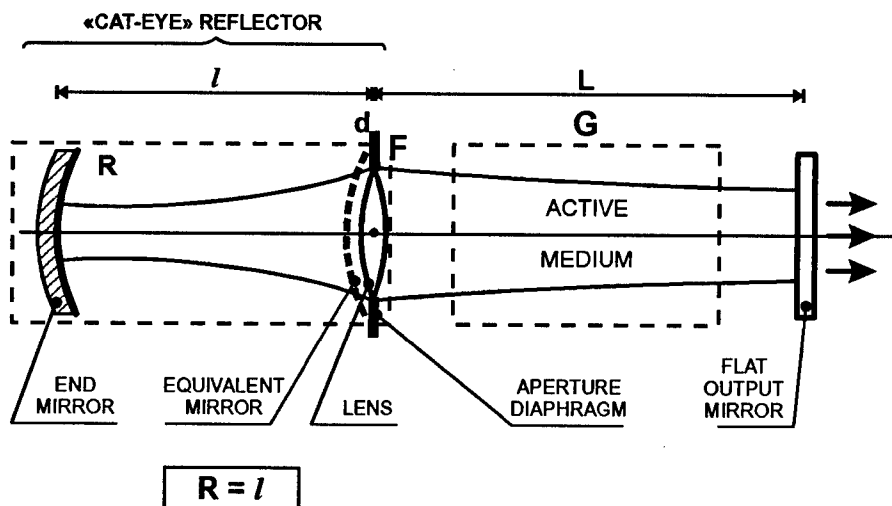


Figure 2. A resonator with a «cat-eye» type reflector.

The output beam axis of the laser with such a resonator passes through the center of curvature of the end spherical mirror (i.e., through the center of the lens) and is normal to the surface of the flat output mirror.

The unique features of the developed resonator are:

- compact form of the output beam's cross section;
- simplicity of operation in its fundamental mode;
- diffraction-limited divergence (if required);
- high stability of the output power against vibrations;
- extremely high stability of the output beam angular position;
- controllable polarization of the output beam.

Consider briefly the main properties mentioned above.

2.3. COMPARISON OF SENSITIVITY TO THE WEDGE-LIKE ABERRATIONS AND END-MIRROR VIBRATIONS OF AN ORDINARY STABLE RESONATOR AND RESONATOR WITH THE "CAT-EYE" REFLECTOR

The main feature of the resonator with the CE-reflector is its low sensitivity to the optical wedge arising in active medium of the laser. In the absence of optical distortions, the beam axis passes through the center of the lens and is directed along the normal to the output mirror (see in Fig.2 solid line, or in Fig.3a dotted line).

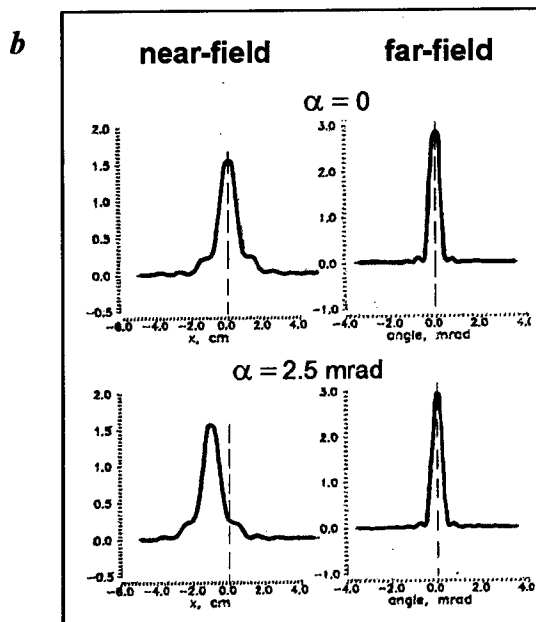
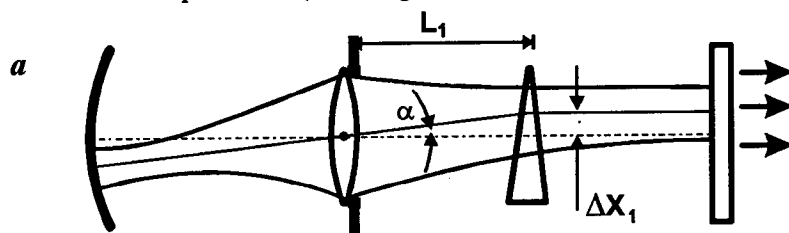


Figure 3. Illustration of displacement of the «cat-eye» resonator optical axis in the presence of an optical wedge in the laser active medium.

Imagine that the optical wedge has arisen in the active medium, being localized at the distance L_1 from the lens (Fig. 3a). In this case, the axis of the resonator will appear to be displaced from its initial position but, as before, will pass through the center of the lens and will be directed along the normal to the output coupling mirror. The displacement of the axis ΔX_1 is equal to α times L_1 . It should be noted that the direction of the laser output beam is the same in both cases (Fig. 2 and Fig. 3a) and coincides with the normal to the output mirror.

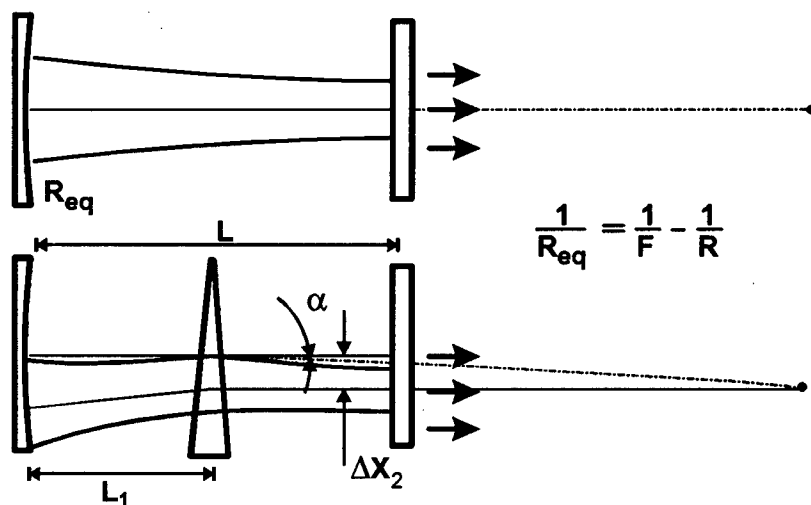


Figure 4. Illustration of displacement of the optical axis in the conventional stable resonator with an intra-cavity optical wedge.

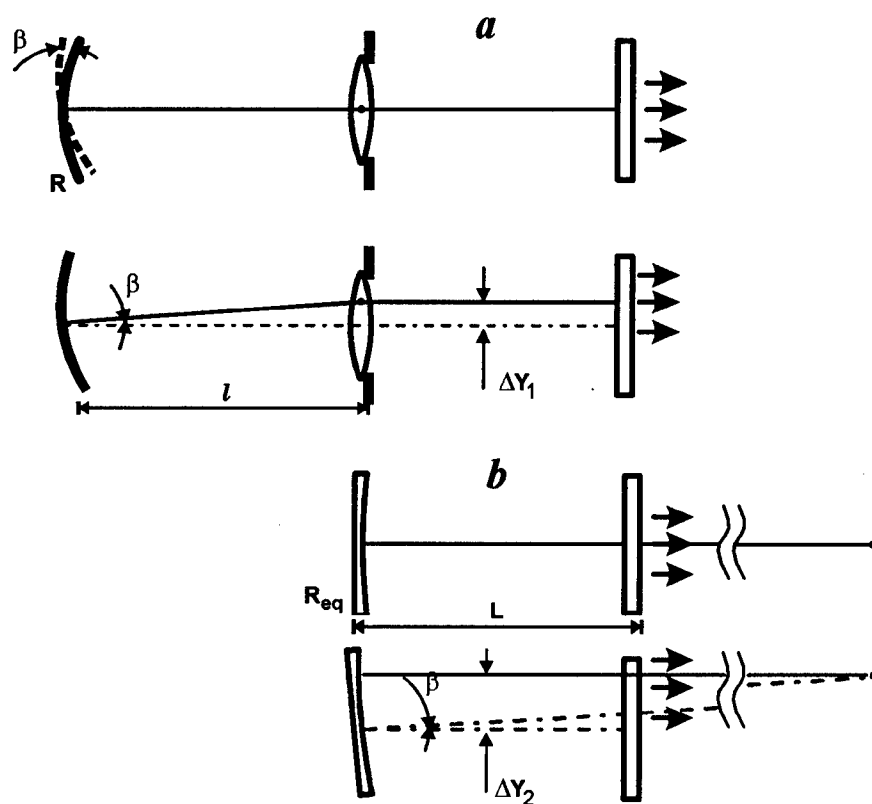


Figure 5. Change of the optical axis in the «cat-eye» resonator (a) and in the equivalent conventional stable resonator (b) at angular position errors of the end mirror.

Computer simulation has confirmed this situation. Figure 3b illustrates two cases of laser operation: without the wedge in the active medium and with the wedge of 2.5 mrad. In the presence of the optical wedge, we can see displacement of the beam in the near field, while the light intensity far-field distribution is the same in both cases.

One can notice that sensitivity to the same optical wedge of the conventional stable resonator with the equivalent end mirror is higher than that of the resonator with the CE-reflector.

In the presence of the wedge, the displacement of the axis for the conventional stable resonator ΔX_2 equals α times $(R_{eq}-L_1)$. When R_{eq} is greater than $2L_1$, the displacement of the axis in the conventional resonator appears to be larger.

$$\Delta X_2 > \Delta X_1 \quad (4)$$

In addition, it follows from these results that when the wedge is located near the diaphragm, the displacement of the axis in the equivalent resonator is the greatest, whereas the resonator with the CE-reflector shows no displacement of the axis at all.

The similar situation arises if we consider the effect of misalignment or vibrations of the end spherical mirror (Fig.5). At the tilt of each end mirror by the angle β , the displacement of the axis ΔY_1 in the CE-resonator is β times R , while in the conventional one ΔY_2 is β times R_{eq} . Since R_{eq} is greater than R , we obtain that the resonator under consideration is less sensitive to misalignments of the end mirror.

$$\Delta Y_2 > \Delta Y_1 \quad (5)$$

All said above means as follows:

- the resonator with the CE-reflector has low sensitivity to any optical wedge in its active medium or to vibrations of intermediate mirrors (if any);
- the resonator with the CE-reflector is less sensitive to vibrations of the end spherical mirror;
- it is easier to realize the single-mode regime of lasing in stable resonator with the CE-reflector.

2.4. EXPERIMENTAL RESULTS

Before proceeding to experimental confirmation of performance of the CE-reflector resonator, I will make a remark based on expertise of lasers with high-quality output beams. Several years ago, we studied the phase conjugation effect for output emission of the repetitively-pulsed CO₂-laser [8]. In that case, we used the four-wave mixing process. As is known, a very good master oscillator, as a source of the pump beams, is needed for this method [9]. We tested a large number of resonators' configurations for the master oscillator suitable for these experiments, and the resonator with the CE-reflector appeared to be the best one.

Figure 6 shows the far-field intensity distribution for lasers with a conventional resonator and with that of the CE-reflector type. Vibrations of optical elements, in case of conventional resonator, can sometimes produce oscillation of the beam's axis direction or disrupt the lasing (by reason of beam vignetting). On the contrary, the

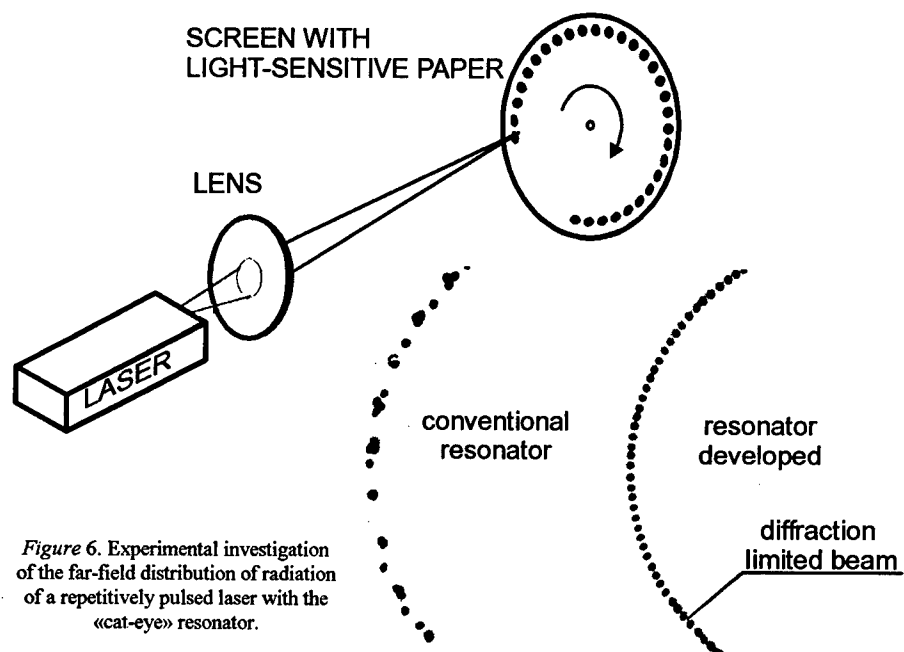


Figure 6. Experimental investigation of the far-field distribution of radiation of a repetitively pulsed laser with the «cat-eye» resonator.

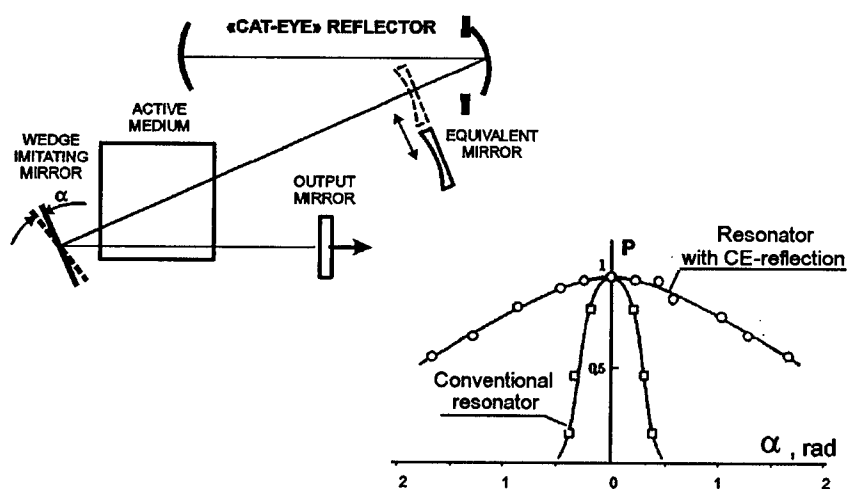


Figure 7. Experimental comparison of output power stability of CW laser with either the «cat-eye» resonator or the equivalent stable resonator, depending on misalignment angle of the intermediate flat mirror.

laser with the CE-reflector can perfectly operate in the same conditions with the diffraction-limited divergence of the beam.

Within the framework of a special test with a CW CO₂-laser [10], we have carried out experimental comparison of two resonators (conventional and CE resonators) operating in a single-mode regime (see Fig. 7). Misalignments of the deflecting mirror imitated optical wedge in the active medium. During the experiments, we measured the output power of the laser. It turned out that, in the presence of the wedge in the active medium, when there is no lasing in conventional resonator, the output power of the laser with the CE-resonator decreases only by 10 %.

Thus, even in conditions of vibrations or wedge-like aberrations in the active medium, the laser with the CE-resonator is characterized by sub-diffraction stability of the lasing axis position and high stability of the output power.

The main problem of operation of the developed resonator in lasers with high average power is related to concentration of the light energy in close vicinity of the end mirror of the CE-reflector. At present, there are several solutions of this problem. For example, it is possible to use conic optics for the CE-reflector (Fig. 8). In this case, the beam is focused into a circular line of large area, and the radiative load drastically decreases [11].

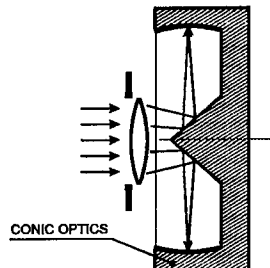


Figure 8. Schematic of the «cat-eye» reflector with the use of an axicon.

Unfortunately, the conic optics is to be manufactured with extremely high accuracy, and for this reason such elements appear to be very expensive. In addition, the angle of view of such a CE-reflector is not large, which imposes severe restrictions upon the values of the tilts of the input beam. But it looks like there is no fundamental limitations for the use of the CE-resonator in lasers with high average power and this technical problem will be eventually solved.

2.5. OPTICAL SCHEME OF THE LASER ROBOT

The resonator with the CE-reflector makes it possible not only to improve performance of laser heads, but also to change the appearance of existing laser technological complexes. In the development of these complexes, there is a trend to manufacture separately the main elements of the laser technological system. One company produces lasers, the other produces beam delivery channels or mechanics for a workpiece under processing. In this case, the quality and accuracy of the workpiece processing are

determined by perfection of each part of the laser technological system and is, therefore, very expensive.

In Fig. 9, one can see the suggested optical scheme of the laser robot. The delivery channel is included into the resonator. The output mirror of the resonator is placed at the end of the delivery channel. The delivery channel itself is designed as a mobile, flexible arm of the laser robot. In the picture, a possible design of optical articulations is shown. Its operation can be explained as follows. The beam is reflected by a deflecting plane mirror, for example, at right angle, toward the next articulation and so on. Besides, each articulation can be rotated. Hence, the laser-robot arm can take any required position in space.

Inaccuracy in angular position of the delivery channel's deflecting mirrors are automatically compensated by the CE-reflector. Radiation is always propagating along the normal to the resonator's output mirror. To reduce the effect of vibrations, it is necessary to place the focusing system close to the output mirror of the resonator or to fabricate these two elements as a single unit. So, the point of focusing of the radiation for such a design of the laser robot will always remain in one and the same place with respect to the end of the laser-robot's arm.

I believe that from the standpoint of laser users such systems deserve to be studied and manufactured.

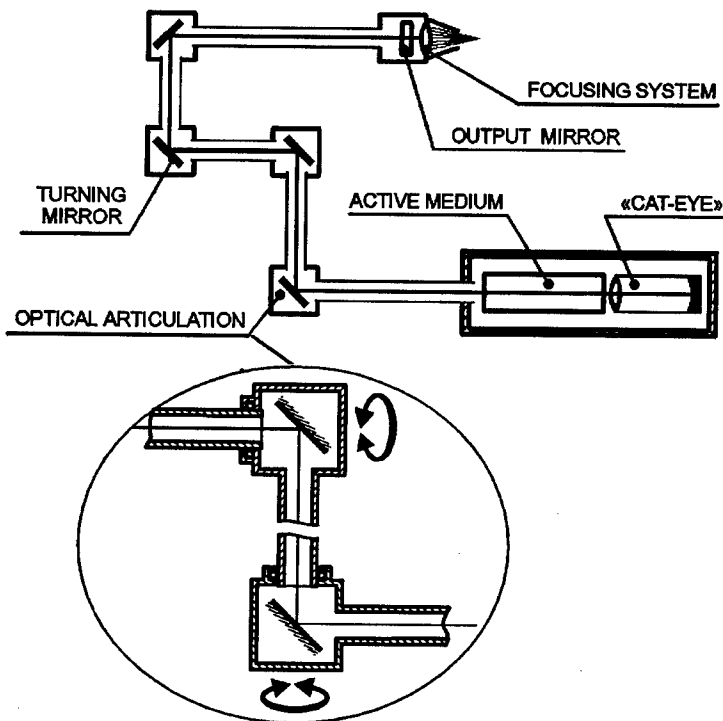


Figure 9. Optical scheme of a laser-robot.

3. Resonator for the solid-state technological laser

In most cases, as the pump level increases, unwanted thermal effects, such as thermal lenses in active media of solid-state lasers with lamp pumping, arise. For such situation, a resonator has been developed, where the just mentioned thermal lenses were used to form a self-imaging optical subsystem inside the unstable negative-branch resonator (see Fig. 10).

A detailed study of characteristics of the laser with such a resonator can be found in [12, 13]. Note that we have studied experimentally two lasers with the resonator of this type. The lasers contained, respectively, two and four active rods with induced positive thermal lenses. In our experiments, we employed standard (without any preliminary selection) YAG:Nd³⁺ rods 6.3 mm in diameter and 100 mm in length. For the maximum pump level, the equivalent focal length of the thermal lenses was about 20 cm. The average output power of the first laser was 160 W and of the second one 306 W.

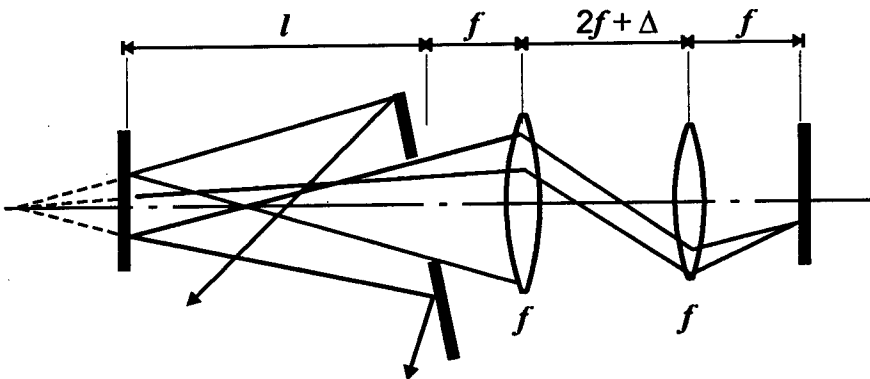


Figure 10. An unstable resonator for a laser with strong lens-like distortions in the active medium.

Nowadays, commercial lasers with the average power lying in the range between 150 and 300 W show the divergence of about 10 - 25 diffraction limits. With the developed resonator, we obtained the output beam divergence within 3 - 5 diffraction limits. This is considered to be one of the best result achieved with the solid-state technological lasers.

At present, the selective diode pumping is widely used, which allows one to significantly reduce the thermal effect. However, for the average output power of laser emission higher than 1 kW, the thermal lenses arise again in the active rods. This means that the developed resonator can be useful for these lasers as well.

4. Multi-chamber laser with repetitively-pulsed mode

In this part of the paper, one can see an example of how the use of novel resonators can change the laser design and, at the same time, improve characteristics of the output beam.

Increase in the laser output power, including lasers operating in the repetitively-pulsed mode, is practically always accompanied by change of its most important parameters: beam divergence and jitter. These parameters are not fixed for a specified laser device and, as a rule, the beam divergence and jitter increase simultaneously with increasing average output power.

Let the laser comprises, for example, three separate laser chambers (see Fig. 11). The laser chambers generate one after another: the first chamber, the second one, then the third one, and then the process is repeated. A flat mirror of the beam-integrating unit is directed to one or another laser chamber. Such laser design allows one to use a large number of laser chambers. It is evident that the laser output average power will increase as many times, as many laser chambers we use, while the beam divergence of this multi-chamber laser will be virtually the same as that of the low-power laser.

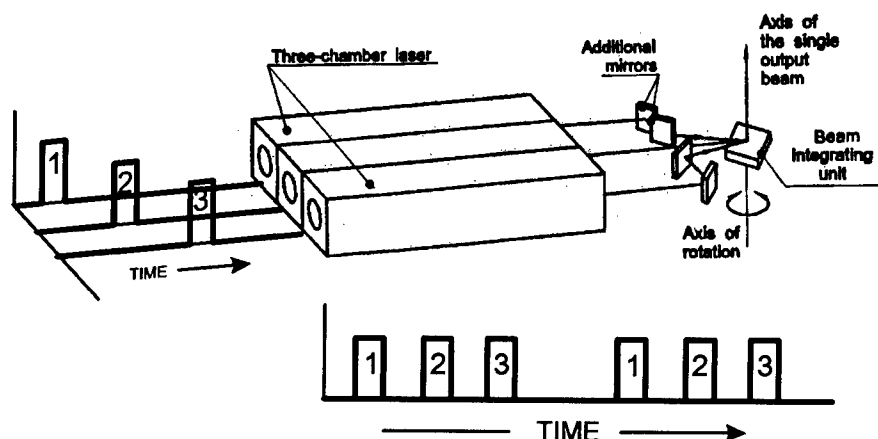


Figure 11. Basic concept of a multi-chamber version with the single radiation output.

However, a new serious problem arises associated with increase of the beam jitter in the integration unit. The problem of bringing into coincidence of the beam axes of three laser resonators is most easily solved by using the external beam-integrating scheme, whose possible configuration is shown in Fig. 11. The scheme comprises at least five mirrors, including a rotating one, whereby the beams are coupled out successively from each of three laser modules in the same direction at different moments of its rotation. In this scheme, the presence of angular errors $\Delta\varphi$ in

positions of the intermediate guiding mirrors and rotating mirror, caused by the play in the rotation drive and by vibrations of the support structure, will result in additional angular beam instability $\Delta\Theta = 2\Delta\varphi$. The use of the automatic mirror-stabilization systems is possible but this will require no less than five fine-adjustment loops. However, there is one more approach to the problem (Fig. 12).

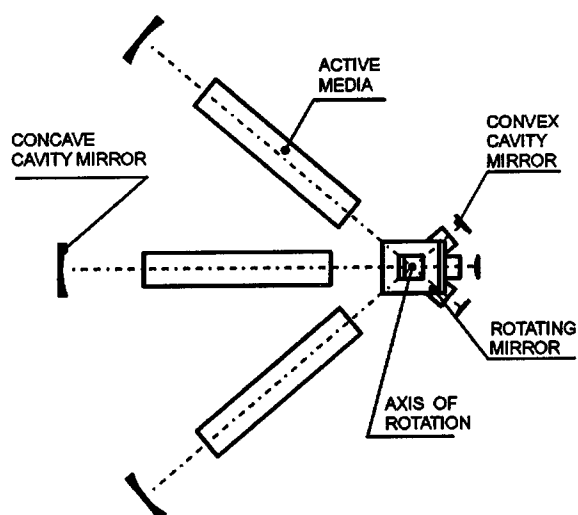


Figure 12. Principal configuration of the optical scheme with the common rotating mirror in three resonators.

Figure 12 shows the optical scheme based on the confocal unstable resonator (UR) of positive branch. The principal idea underlying the proposed arrangement is that each resonator of the three laser chambers incorporates a common rotating coupler whose rotation and position inaccuracy does not cause any angular deflection of the output beam axis. This mirror operates so that in certain moments of rotation it successively couples out radiation from the laser modules into the external optical path.

To stabilize direction of the output beam axis within fractions of the diffraction limit, the positions of the stationary resonator mirrors should be fixed to an accuracy of about 10^{-5} rad (in a beam CO_2 laser with aperture of tens cm), whereas a much lower accuracy

of $(1-5) \times 10^{-4}$ rad is necessary for spatial stabilization of the rotating coupler. Besides the UR optical scheme is designed so that the error in spatial position of the rotating coupler is almost totally corrected by the tunable lasing direction if magnification of the UR is chosen properly.

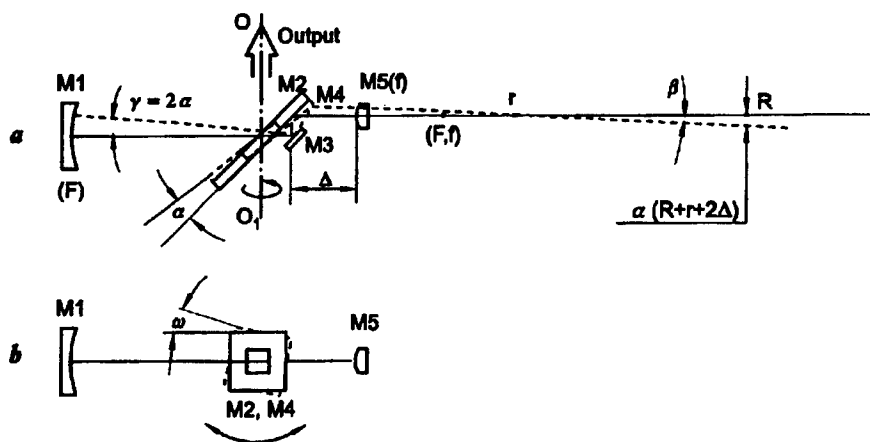


Figure 13. Illustration of the idea of compensating positioning inaccuracies of the common rotating mirror.

Figure 13 shows the optical scheme of one of the three UR-based laser modules in two mutually perpendicular planes. Here, M_1 and M_5 are the concave and convex resonator's mirrors, respectively. Flat mirrors M_2 and M_4 are placed on opposite sides of a single rotating unit. The bilateral mirror (M_2, M_4), rotated around the OO_1 axis by a step motor, is a common component of all three resonators (beam-integrating unit (BIU)). Flat mirror M_2 , placed at an angle of 45° with respect to the resonator's axis, couples radiation out of the laser. A rectangular hole in mirror M_2 is the aperture diaphragm of the resonator.

Let us consider the idea of compensation for the tilts and rotation errors in the beam-integrating unit in one of the planes, e. g., in the plane containing the OO_1 axis. Let the beam-integrating unit (mirrors M_2 and M_4) be inclined by an angle α with respect to its designed position as a result of a play in the bearing (Fig. 13a). To retain the output beam direction intact after reflection from mirror M_2 , the lasing axis inside the resonator should be tilted by the angle α with respect to its initial position. Note that along with the inclination of mirror M_2 , the position of mirror M_4 will change as well, and the center of curvature of mirror M_1 imaged by mirrors M_3 and M_4 will be displaced from its initial position at a distance of $\alpha(r+R+2\Delta)$, where r is the radius of curvature of mirror M_5 , R is the radius of curvature of mirror M_1 , and d is the distance between mirrors M_4 and M_5 (see Fig. 12 a). In this case, the lasing axis, which passes through the centers of curvature of the convex and concave mirrors in the UR, will turn by the angle

$$\beta = 2\alpha(r+R+2\Delta)/(R-r). \quad (6)$$

The beam propagating along the new axis will be titled by the angle $\gamma = \beta - 2\alpha$ with respect to the initial axis after reflection from mirrors M_4 and M_3 . Equating the obtained angle of inclination of the lasing axis γ to the required value 2α , yields the equality

$$2(r+\Delta) = R - r. \quad (7)$$

This means that the confocal UR under consideration should have the magnification in this plane

$$M = 3(1 + t), \quad (8)$$

where $t = 2\Delta/3r$.

To compensate for the error in rotation of mirror M_2 around the OO_1 axis by the angle ω in the orthogonal plane (Fig. 13 b), the resonator's axis should turn by the same angle ω , the magnification also being equal to $M = 3(1 + t)$. Thus, the errors in rotation of the mirror in the integrating unit do not cause any jitter of the output beam axis, although are accompanied by insignificant lateral shifts of the output beam. These shifts do not cause any noticeable jitter of the output beam axis.

So, this is an example of the scheme of the resonator which can serve as a multi-chamber laser, where, as was already said above, the beam divergence and jitter will be the same as in the low-power laser.

5. Conclusion

We have considered a few examples of resonators, suitable for lasers used in precision technological processes. It should be pointed out that all the resonators considered above are multi-element and, despite this fact, allow one to achieve high performance of technological lasers.

In conclusion, I fully endorse the opinion of Yu.A. Anan'ev [14] that in creation of the laser it is necessary to enlist specialists on resonators at the earliest stages of laser design.

6. References

1. Hoffman, B. (1983) *Relativity and its roots*, Scientific American Books, New York.
2. Gerrard, A. and Burch, J.M. (1975) *Introduction to matrix methods in optics*, A Wiley-Interscience Publication, John Wiley and Sons, London - New York - Sydney - Toronto.
3. Beer, R. and D. Marjaniemi, R. (1966) Wavefronts and Construction Tolerances for a Cat-Eye Retroreflector, *Appl. Opt.* **5**, 1191-1197.
4. Snyder, J.J. (1975) Paraxial ray analysis of a cat-eye retroreflector, *Appl. Opt.* **14**, 1825-1828.
5. Beer, R. (1976) Paraxial analysis of a cat-eye retroreflector: comments, *Appl. Opt.* **15**, 856-857.
6. Snyder, J.J. (1976) Paraxial ray analysis of a cat-eye retroreflector: author's reply to comments, *Appl. Opt.* **15**, 1691-1691.
7. Orlova, I.B. Influence of intra-cavity distortions on output of unstable resonators (see the paper in this book).
8. Sherstobitov, V.E., Ageichik, A.A., Bulaev, V.D., Dimakov, S.A., Gerke, M.N., Goryachkin, D.A., Kalinin, V.P., Koval', I., Paryshev, E.N., Rezunkov, Yu.A., Romanov, N.A., Rodionov, A.Yu., Stepanov, V.V. and Zemlyanykh, V.V. (1991) Phase conjugation in a high-power E-beam-sustained CO₂ laser, *Proc. of SPIE, Nonlinear Optical Processes in Solids* **1841**, 135-143.
9. Sherstobitov, V.E. Phase conjugation of CO₂ laser radiation and its applications (see the paper in this book)
10. Dimakov, S.A., Kliment'ev, S.I., Kuprenyuk, V.I., Orlova, I.B., Sergeev, V.V., Sherstobitov, V.E. (1994) Low-sensitive to misalignments resonator, *Proc. SPIE* **2257**, 187-192.
11. Dimakov, S.A., Kliment'ev, S.I., Khloponina, I.V. (1995) Cavity with "cat eye" reflector based on elements of axicon optics, in *Proc. 8-th Laser Optics Conference in St. Petersburg*, **1**, p.98.

12. Dimakov, S.A., Gorlanov, A.V., Kliment'ev, S.I., Orlova, I.B. and Svetsitskaya, N.A. (1994) Cavity for a high-power technological Nd:YAG laser with two active elements, *Opt. Spectrosc.* **76**, 599-601, Translated from *Optika i Spectroscopiya* **76**, 667-670 (In Russian).
13. Bogdanov, M.P., Dimakov, S.A., Gorlanov, A.V., Kalinin, V.P., Kliment'ev, S.I., Koval'chuk, L.V., Orlova, I.B. and Svetsitskaya, N.A. (1995) Laser with unstable resonator for technical applications, *Opt. Spectrosc.*, **79**, 622-624, Translated from *Optika i Spectroscopiya* **79**, 675-677 (In Russian).
14. Anan'ev, Yu.A. Theory of laser resonators and beam divergence (review). (see the paper in this book).

RESONATOR DESIGN CONSIDERATIONS FOR EFFICIENT OPERATION OF SOLID-STATE LASERS END-PUMPED BY HIGH-POWER DIODE-BARS

W. A. CLARKSON AND D. C. HANNA

*Optoelectronics Research Centre
University of Southampton
Southampton, SO17 1BJ
United Kingdom*

Abstract

A novel resonator design strategy for high-power diode-end-pumped solid-state lasers is described, which reduces the beam distortion and depolarisation loss due to thermally-induced lens aberrations and stress-birefringence. The approach is based on a resonator design satisfying two criteria: firstly, the laser mode radius must be appreciably smaller than the pump beam radius, and secondly, the laser mode size must decrease with decreasing power (increasing focal length) of the thermal lens. Experimental results are presented for diode-bar-pumped Nd:YAG lasers operating at various wavelengths confirming the validity of this approach. Results are also presented of a detailed investigation of thermal effects in end-pumped Nd:YAG lasers, which indicate how the various factors such as end-face curvature and the temperature and stress dependence of refractive index influence the thermal lensing behaviour. The merits of Nd:YLF for use in high-power end-pumped lasers, based on its weaker thermal lensing on the σ polarisation at $1.053\mu\text{m}$ compared to Nd:YAG, will also be considered.

1. Introduction

Advances in semiconductor laser technology over the last decade have been dramatic, leading to a very significant increase in the available output power from diode-bar sources. In parallel with these developments there has been growing interest in using high-power diode-bars as pump sources for power-scaling of solid-state lasers. At relatively low pump powers ($< \text{few watt}$), the employment of end-pumped rather than side-pumped configurations has been the preferred route owing to the much higher efficiencies achievable, the relative ease with which fundamental transverse mode operation can be selected and the enormous flexibility in cavity design and wavelength of operation. This has enabled the development of numerous novel solid-state laser devices (e.g. [1],[2]). Many of these attractive features result directly from the relative

ease with which low power diodes can be focused to small beam sizes, and their relatively narrow emission linewidths allowing short absorption lengths, \sim few mm, in the laser material.

Progress in scaling diode-end-pumped solid-state lasers to high powers, whilst retaining these attractive features, has been hindered by two main problems. The first of these has been the unfriendly and highly elliptical nature of the output beams from high-power diode-bars. Typically, these devices are constructed from a wide array of emitters, with typical overall dimensions $\sim 1\mu\text{m} \times 10\text{mm}$ and, as a consequence, produce an output beam which is nearly diffraction-limited in the plane perpendicular to the array, but is typically ~ 2000 times diffraction-limited in the array plane. This large mismatch in the M^2 beam quality factors for orthogonal planes makes it difficult to focus to the small diameter beams required for efficient end-pumping of solid-state lasers.

To permit focusing to small beam diameters it is necessary to use an optical beam delivery system which equalises the beam quality factors in orthogonal planes without significantly decreasing the brightness. To date, a number beam delivery schemes which attempt to solve this problem have been reported (e.g. coupling into optical fibre bundles [3],[4],[5], using diffractive optical components [6] or using arrays of micro-optical components [7]). However, in most cases the equalisation in the beam quality factors is also accompanied by a large decrease in brightness. More recently, an alternative beam shaping technique [8] which allows equalisation of the beam quality factors in orthogonal planes with only a relatively small reduction in brightness has been demonstrated. This approach which utilises two high reflectivity mirrors in combination with standard collimating and focusing lenses can be used to focus the output from a diode bar to a nearly circular spot of much smaller diameter than is currently possible via other reported techniques, and hence offers the attractive prospect of efficient high-power operation even on relatively low gain or quasi-three-level transitions [9].

However, the availability of high power and high intensity pump sources has further exacerbated thermal effects such as thermal lensing and thermally-induced stress-birefringence, which are particularly pronounced in end-pumped lasers owing to the high thermal loading density. One of the main problems encountered in end-pumped lasers is beam distortion due to the highly aberrated thermal lens, making it extremely difficult to simultaneously achieve high efficiency and good beam quality. To overcome this problem a number of approaches have been reported including the use of apertures to select the TEM_{00} beam [1], and aspheric lenses as compensators [2]. More recently, an alternative approach has been reported [10], which uses face-cooling to achieve axial heat flow in a laser disc and hence a significant decrease in the strength of the thermal lensing. Unfortunately, the latter approach has the disadvantage that it is only applicable to laser materials with a short absorption length for the pump light and/or laser transitions with a high gain cross-section. This is necessary to ensure that the pumped region has a high aspect ratio of pump beam size to disc thickness to minimise radial heat flow.

In this paper we describe an alternative resonator design strategy to reduce the beam distortion resulting from strong thermally-induced aberrations without using

compensating components. The underlying basis of this approach is that the aberrations which result from the Gaussian-like pump beam are most pronounced in the wings of the inversion distribution. Hence by using a resonator with a TEM_{∞} mode which is smaller than the pump beam it is possible to achieve a near-diffraction-limited output beam. However, a consequence of the smaller mode size is that it is more difficult to achieve efficient extraction of the gain stored in the wings of the inversion distribution. In addition, appropriate measures must be taken to prevent this unused inversion from providing sufficient gain for simultaneous oscillation on higher-order transverse modes. Our results indicate that this suppression of higher-order transverse modes can be achieved by applying a second condition to the resonator design, namely that the TEM_{∞} beam size in the laser rod should decrease with increasing focal length of the thermal lens. The rationale for this design is presented below. Experimental results for diode-bar-pumped Nd:YAG lasers operating at various wavelengths which confirm the benefits of this approach are described together with a results of a detailed investigation of thermal effects in Nd:YAG which indicate how various factors, such as end-face curvature and the temperature and stress-dependence of the refractive index influence the thermal lensing behaviour and hence the choice of resonator design. In addition, the merits of Nd:YLF with its weaker thermal lensing on the $1.053\mu\text{m}$ polarisation compared to Nd:YAG for use in high-power end-pumped lasers will be considered.

2. Resonator Design Considerations For Low-power Lasers

We begin our discussion with a brief review of the resonator design criteria for efficient TEM_{∞} operation of diode-pumped solid-state lasers at low powers [11],[12]. Using a simplified rate equation approach [13], and assuming Gaussian transverse intensity distributions for the pump beam and lasing mode, the following approximate expressions for threshold pump power P_{pth} and slope efficiency η_s of an end-pumped laser (fig.1) can be derived [14]:

$$P_{\text{pth}} = \frac{\pi h \nu_p (L+T) (w_p^2 + w_L^2)}{4 \sigma \tau_f \eta_q \eta_{\text{abs}}} \quad (1)$$

and

$$\eta_s = \left(\frac{T}{L+T} \right) \left(\frac{\nu_p}{\nu_L} \right) \eta_{\text{abs}} \eta_q \eta_{\text{PL}} \quad (2)$$

where ν_p and ν_L are the pump and lasing frequencies respectively, τ_f is the fluorescence lifetime, σ is the laser transition cross-section, η_q is the pumping quantum efficiency

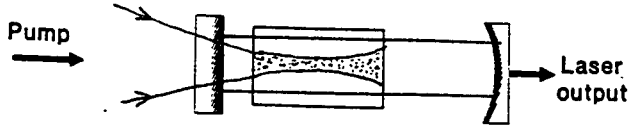


Figure 1 End-pumped solid-state laser.

(i.e. the fraction of absorbed pump photons which lead to subsequent excitation in the upper laser level), T is the transmission of the output coupler, L is the residual round-trip cavity loss, $\eta_{abs} \approx [1 - \exp(-\alpha_p L)]$ is the fraction of incident pump radiation absorbed over the length of the laser rod and w_L and w_p are the effective TEM_{00} beam radii for laser and pump respectively, which are assumed to be approximately constant over the length of the laser rod. The above expressions for threshold and slope efficiency also assume that the total cavity loss $(L+T) \ll 1$, which is usually a reasonable approximation for most low power diode-pumped lasers. The factor η_{PL} depends on the spatial overlap of the pumped region and lasing mode and on the ratio of the intracavity intensity, I to the saturation intensity, $I_s \approx h\nu_L / \sigma \tau_f$. In the low power limit where $I/I_s \ll 1$, then η_{PL} can be approximated to

$$\eta_{PL} \approx \frac{w_L^2 (w_L^2 + 2w_p^2)}{(w_L^2 + w_p^2)^2} \quad (3)$$

and at higher powers where $I/I_s \gg 1$, $\eta_{PL} \rightarrow 1$. Thus η_{PL} accounts for the variation in the slope efficiency with pump power. Physically, this can be interpreted as being due to a competition between stimulated emission and spontaneous emission in the wings of the pumped region. At high intracavity intensities there is an increased probability that inverted ions will be depleted by stimulated emission and hence an increase in the slope efficiency. The fact that the slope efficiency is power dependent makes it difficult to calculate the optimum output coupling for maximum output power from the laser (i.e. for maximum output power). However, if it is assumed that $\eta_{PL} \approx 1$, which is usually a good approximation for an optimally designed laser at low pump powers, then the optimum value for the output coupler transmission can be chosen according to the following equation:

$$T = -L + 2 \sqrt{\frac{P_p \sigma \tau_f \eta_{abs} \eta_q L}{\pi (w_L^2 + w_p^2) h \nu_p}} \quad (4)$$

where P_p is the maximum pump power available and it has been assumed that

$(L+T) \ll 1$. Thus equations (1) to (4) provide a good guide to the optimum laser design. For a given laser transition the key requirement for efficient operation is a low threshold compared to the available pump power, which can generally be achieved by keeping the net cavity losses low and using small pump beam and laser mode sizes. The laser mode size is determined by the resonator design and can in general be made very small. To ensure diffraction-limited operation it is necessary to use a resonator design in which the TEM_{00} radius is either equal to or, more ideally, larger than the pump beam radius. This prevents undepleted inversion from building up in the wings of the pumped region which may result in lasing on higher-order transverse modes. Thus the minimum laser mode size, and hence the minimum threshold pump power is determined mainly by the minimum effective pump beam size, which is in turn governed by the M^2 beam quality factor for the diode laser, the performance of the pump collimating and focusing optics and the absorption length α_p for the pump light. If we make the simplifying assumption that the pump light is absorbed linearly with distance z and is completely absorbed over two absorption lengths, then minimum effective pump beam radius w_{pmin} , defined as r.m.s beam radius which results in the minimum pumped volume, is given by

$$w_{pmin}^2 = \frac{2\lambda M^2}{\alpha_p \pi n \sqrt{3}} \quad (5)$$

For most diode laser pump sources the beam quality factors differ considerably for orthogonal planes. In the plane perpendicular to the junction the beam quality factor M_y^2 is ~ 1 . In the orthogonal plane parallel to the array the beam quality factor M_x^2 is much larger and depends on the length of the array. For a typical 1W diode laser at 809nm the emitting region has a length $\sim 200\mu m$ and produces a beam with $M_x^2 \sim 40$, suggesting a minimum effective pump beam radius of approximately $130\mu m$ for a Nd:YAG rod with a typical absorption length for the pump of $\approx 2.5mm$. This pump beam size can be achieved rather easily with a standard arrangement of lenses. Obviously, a much smaller effective pump beam size is possible in the orthogonal plane. However, since it is generally much easier to design a resonator with a nearly circular TEM_{00} mode, then clearly it is the larger of the pump beam's M^2 values which determines the laser mode radius and hence the minimum threshold pump power. Assuming a residual round-trip cavity loss L of 2% (due to imperfect antireflection coatings and leakage through the high reflector) we can estimate from equation (4) that the optimum output coupler transmission for operation at $1.064\mu m$ will be $\sim 13\%$, which would result in a threshold pump power of $\sim 125mW$ and a maximum output power of around 400mW to 500mW in a diffraction-limited beam. These operating characteristics are fairly typical of low-power diode-pumped Nd:YAG lasers. For quasi-three-level lasers the above analysis must be modified to account for the finite lower laser level population [15],[16]. However, the design strategy is essentially the same with the laser performance on a given transition being determined mainly by how

tightly the diode pump beam can be focused in the laser material. In fact it is a consequence of ability to focus the pump beam to a diameter which is much smaller than the absorption length which enables end-pumped solid-state lasers to be significantly more efficient than side-pumped lasers. The relatively weak thermal effects in low-power diode-pumped lasers in combination with the relative ease with which the requirement of $w_L \geq w_p$ for TEM₀₀ operation can be achieved, has allowed for considerable flexibility in the resonator design, of which there are numerous examples reported in the literature.

3. Focusing of High-power Diode Lasers

Due to thermal considerations scaling of diode laser pump sources to higher powers has been achieved via the construction of longer linear arrays of lower power diodes, and hence has been accompanied by a degradation in beam quality and a decrease in brightness. A typical commercially available 20W cw diode-bar at 809nm has a linear array of dimensions $\sim 1\mu\text{m} \times 10\text{mm}$ and very different beam quality factors in orthogonal planes; $M_y^2 \sim 1$ and $M_x^2 \sim 2000$. By comparison with a typical 1W diode laser, a typical 20W diode-bar has a brightness at least 2.5 times smaller. Whilst this reduction in brightness is of some significance, by far the most serious problem for end pumping is the large difference in the M^2 values for orthogonal planes. This makes it extremely difficult to focus to the small diameter beam required for efficient end-pumping. A number of beam delivery schemes which attempt to solve this problem have been reported (e.g. [5],[6],[7]). However, equalisation of the M^2 values in orthogonal planes is often accompanied by a significant decrease in brightness thus precluding the small focussed beam sizes required for efficient end-pumping of low gain or quasi-three-level lasers.

In the experimental investigations described in this work we have made use of an alternative technique which utilises only two high reflectivity mirrors to equalise the M^2 values in orthogonal planes without a significant decrease in brightness. The principle of operation of this 'two-mirror' beam shaping technique is described in detail in ref.[8]. Here we merely summarise its main features:

The construction of the two-mirror beam shaper (shown in the Figs. 2(a) and (b)) is very simple, with the two high reflectivity plane mirrors aligned approximately parallel and separated by a small distance d (typically $< 1\text{mm}$). The mirrors are transversely offset from each other, in both the x' and y' directions, so that small sections of each mirror are not obscured by the other. These unobscured sections form the input and output apertures of the beam shaper.

The principle of operation of the beam shaper can be explained with reference to Figs. 2(a) and (b), which show, respectively, plan and side views of the beam shaper, in each case the mirror surfaces being orthogonal to the plane of the figure. Light from a non-diffraction-limited laser (in this case a diode-bar) with beam quality factors M_x^2 and M_y^2 in orthogonal planes of propagation x - z and y - z , is incident obliquely at angles θ_x and θ_y in the orthogonal planes; x' - z' and y' - z' , on the unobscured section of mirror

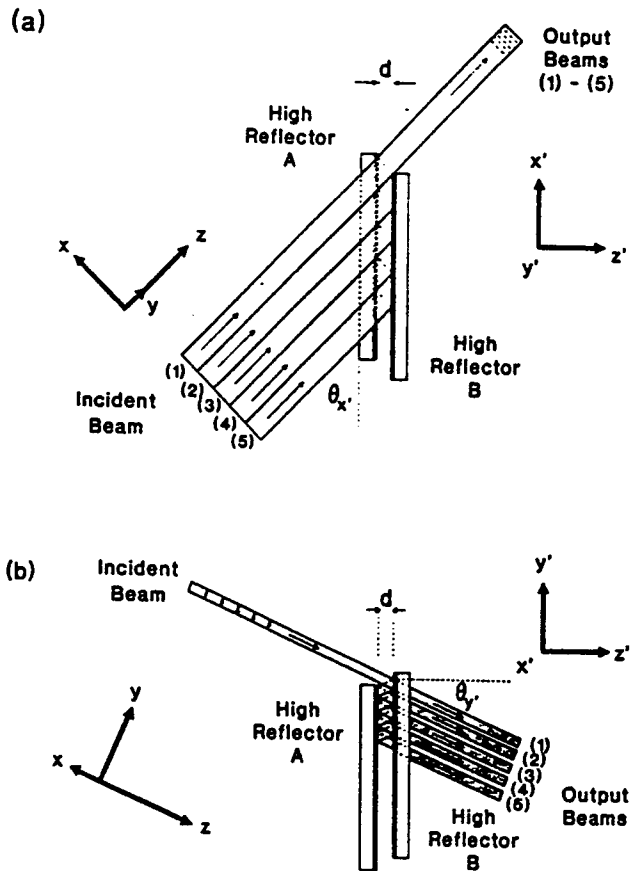


Figure 2 Two-mirror beam shaper, (a) plan view, (b) side view.

B of the beam shaper as shown. The incident beam can be considered to be composed of a number of adjacent beams. For the purpose of illustration, the incident beam has been arbitrarily chosen to consist of five parallel beams (1)-(5). Beam (1) is not incident on either mirror A or B, since it passes above mirror A (see Fig. 2(b)) and passes by the side of mirror B (see Fig. 2(a)), and so emerges with no change to its original direction (assuming any diffraction effects at the edge of mirror B are negligible). Beam (2) however, passes above mirror A but is incident on mirror B and is reflected so that it strikes mirror A immediately below beam (1). Beam (2) is then reflected at mirror A and emerges from the beam shaper in the direction of beam (1), but displaced beneath beam (1). Beam (3), after incidence on mirror B, is reflected so that it strikes mirror A underneath beam (2), is then reflected back to mirror B, where

it is reflected onto mirror A, subsequently emerging parallel to beams (1) and (2) but displaced underneath beam (2). Beams (4) and (5) undergo similar multiple reflections at mirrors A and B and finally emerge propagating beneath beams (1), (2) and (3), as shown in Fig. 2(b). Thus the action of the beam shaper is to effectively chop the incident laser beam into a specific number of beams and then to re-direct and re-position these beams so that they emerge from the beam shaper stacked on top of one another. Since the incident beam is initially many times diffraction-limited in the x-z plane (i.e. $M_x^2 \gg 2000$ for a typical diode bar), then the effect of the beam shaper is to decrease the width of the beam in the x direction, but without significantly increasing its divergence. Thus the overall result is that the composite beam which emerges from the beam shaper has a smaller value for M_x^2 . For a given incident laser beam, the number of stacked beams and their widths (in the x-z plane) can be specified by the choice of angles θ_x and θ_y , the mirror separation d and by the appropriate positioning of the beam shaper relative to the incident laser beam. Hence the factor by which M_x^2 is reduced can be controlled by the adjustment of these parameters. It should be noted however, that a reduction in M_x^2 is only possible if M_x^2 for the incident beam is much greater than unity so that chopping the beam into smaller individual beams does not result in an increased spread of these beams due to diffraction at the edge of mirror B.

In the y direction the beam size is increased, but the divergence remains approximately constant (providing that mirrors A and B are sufficiently parallel), hence the emerging beam has its M_y^2 value increased. The factor by which M_y^2 is increased depends on the total height of the composite stacked beam (in the y-z plane) and its far-field divergence. If the incident beam is reasonably well collimated in the y-z plane then M_y^2 is increased by a factor approximately equal to the total height of the emerging beam divided by the height of an individual beam. For many applications, it is desirable to minimise the increase in M_y^2 by choosing values for the mirror spacing d , and the inclination angle θ_y , so that the gap between adjacent stacked beams is minimised without significantly degrading the beam shaper's transmission due to clipping of the beams at the top edge of mirror A. For a clipping loss of $< 1\%$, the beam separation should be ~ 1.3 times greater than the $1/e^2$ incident beam height. This implies that M_y^2 would be increased by a factor of $\sim 1.3N$, where N is the number of stacked beams.

The factor by which M_x^2 is decreased depends on the width of the output beam (in the x-z plane) and its far-field divergence. As a rough guide, it should be possible to decrease M_x^2 by a factor $\sim N$ (providing that the initial value for M_x^2 is much greater than N).

The transmission T of the beam shaper is approximately given by $T = (1-L)[1-N(1-R)]$ where L is the loss due to clipping and R is the mirror reflectivity. If the incident beam is chopped many times, then many reflections are needed between the mirrors, so high reflectivity is important for achieving a high transmission.

Thus, by choosing appropriate values for the mirror separation d and inclination angles; θ_x and θ_y , it is, in principle, possible to re-configure any non-diffraction-limited laser beam with $M_x^2 \gg M_y^2$ so that M_x^2 is made approximately equal to M_y^2 , with only a very small reduction in brightness. The resulting beam can then be focused with

conventional lenses to a nearly circular spot which is suitable for end-pumping.

The beam delivery scheme used in the end-pumping experiments described here is shown in fig. 3. The pump was a 20W cw diode-bar (Opto-Power-Corporation OPC-A020-mm-CS) with 24 emitters which was initially collimated by a fibre lens and then imaged with an arrangement of cylindrical and spherical lenses, which were positioned so to produce a magnified image of the array of emitters at the entrance aperture to the two-mirror beam shaper. The beam shaper itself was constructed as shown in fig. 2 with two nominally parallel high reflectivity mirrors ($>99.8\%$ at the diode wavelength, $\sim 808\text{nm}$), and was inclined at angle $\theta_x \approx 45^\circ$ with respect to the incident beam. The mirror separation d and the inclination angle θ_y were adjusted in order to chop the incident beam into 24 constituent beams, one for each emitter, and stack them vertically below each other in the y direction. In general the choice of parameters d and θ_y , and therefore the number of stacked beams, depends on the required output values of M_x^2 and M_y^2 . However, in the case of a diode bar, with its array of emitters, it is often advantageous to image the bar onto the beam shaper and configure the beam shaper to chop the beam into its constituent emitter images. In this way it is possible to effectively remove the 'dead' space between adjacent emitters on the bar and in so doing increase the brightness. The increase in brightness depends on the ratio of the emitter width to the dead space width (i.e. the fill factor), and is approximately a factor of two for the diode bar used in our experiments. The stacked output from the beam shaper was then re-collimated in the x - z plane by a cylindrical lens of focal length 200mm and finally focused with an appropriate spherical lens selected to give the required spot size. The resulting beam quality factors, M_x^2 and M_y^2 depend on the alignment of the beam shaper and on the initial values of M_x^2 and M_y^2 at the diode bar. Thus there is some variation in performance depending on the details of the actual set-up. In an optimised arrangement, final M^2 beam quality factors of ~ 40 in orthogonal planes have been achieved, although M^2 values in the range 60 to 70 are more typical. The overall transmission of the focusing scheme is typically $\sim 75\%$, resulting in $\sim 15\text{W}$ of available pump power at the focus.

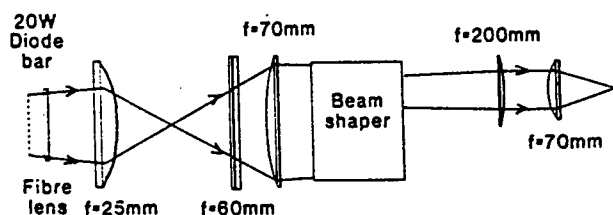


Figure 3 Focusing arrangement for a 20W diode bar

4. Prospects For Power-scaling End-pumped Lasers

Based on the focusing scheme performance described above we can estimate the threshold and output power of end-pumped solid-state lasers using this pumping arrangement from equations (1)-(4). From equation (5), the minimum effective pump beam size w_{pmin} for a pump source with $M_x^2=M_y^2=70$ is $\sim 184\mu\text{m}$. Hence for a Nd:YAG laser operating at $1.064\mu\text{m}$ with an output coupler transmission of 10% and an additional round-trip loss of 2% we predict a threshold pump power of $\sim 0.2\text{W}$ and, by making $\eta_{PL} \rightarrow 1$ using $w_L > w_p$ (say $250\mu\text{m}$), a maximum TEM₀₀ output power of $\sim 8\text{W}$ for 15W of incident pump power should in principle be achievable. In addition, since the threshold pump power is very much smaller than the maximum available pump power, it should be possible to operate at a multiwatt power levels on laser transitions with a $\sigma\tau_f$ product which is more than an order of magnitude smaller, as well as on many quasi-three-level transitions. Thus, the high brightness output from this diode-bar end-pumping scheme appears to offer an attractive route to power-scaling of numerous solid-state lasers.

5. Thermal Effects in Continuous-wave End-pumped Lasers

The predictions for laser performance described in the previous section are extremely difficult to realise in practice due to thermal effects which are particularly pronounced in end-pumped lasers owing to the high thermal loading density. The main origin of heat generation in diode-pumped lasers is usually considered to be quantum defect heating, i.e. simply due to the energy difference between pump and emitted photon [17]. In addition, for many laser transitions there are a number of other mechanisms (e.g. upconversion and excited-state absorption) which may also lead to significant extra heat loading. The heat generated results in a spatial variation in temperature, and consequently internal stresses within the laser material, and in addition, deformation of the laser rod end faces due to differential expansion. The net result is a degradation in laser beam quality due to thermal lensing, depolarisation loss due to stress-induced birefringence, and ultimately fracture of the laser rod, if the thermally-induced stress exceeds the tensile strength of the laser material. The relative extent to which these effects are detrimental to the laser performance depends on a number of factors including; the thermo-mechanical and thermo-optical properties of the laser material, the pumping geometry, the laser medium geometry and the heat-sinking arrangement. In the work described here we are restricting our consideration to end-pumped lasers with edge-cooled rods of cylindrical geometry. The attraction of edge cooling is the relative simplicity of its implementation, but due to the predominantly radial heat flow it has the disadvantage of strong thermal lensing. Face-cooling, on the other hand, offers much weaker thermal lensing, but is complicated by the need for multiple-passes of the pump beam [10] due to the short rods required for predominantly axial heat flow, and hence is only applicable to laser materials with a short absorption length for the pump and/or laser transitions with relatively high gain. The ultimate limit of power-scaling is posed

by the onset of thermally-induced stress-fracture. However, in laser materials such as Nd:YAG which has a relatively high fracture limit, it is usually thermal lensing and stress-induced birefringence which present the practical limit on diffraction-limited laser performance in end-pumped configurations. In fact, since there are numerous techniques for adequately compensating for stress-birefringence [17],[18] it is generally the case that thermal lensing is the major problem. In the case of laser materials such as Nd:YLF which have superior thermo-optical properties but inferior thermo-mechanical properties, it is thermally-induced fracture which is the most significant problem. Hence, when attempting to scale end-pumped Nd:YLF to high powers, it is necessary to take special precautions in order to avoid fracture, as will be described later.

For the present discussion we will consider the situation where thermal lensing is the major obstacle to power-scaling as is frequently the case for Nd:YAG lasers. There are two main problems which must be addressed. The first problem is that in many situations strong thermal lensing will be the major factor in determining the laser mode size, hence making it extremely difficult to design a resonator in which the laser mode size does not vary appreciably with pump power. If the mode size varies significantly so that the pump beam is no longer 'mode-matched' then higher-order transverse modes may lase, thus also leading to a degradation in beam quality. One solution to this problem is simply to design the laser to operate TEM₀₀ for only a small range of pump powers near the maximum available pump power, and then use an attenuator if it is necessary to vary the output power. The second, and certainly the most serious problem is the highly aberrated nature of the thermal lens which results from the Gaussian-like transverse intensity profile of the pump beam. This can lead to a very significant degradation in beam quality in end-pumped lasers. In many situations, it is this problem more than any other which represents the most significant obstacle to simultaneously achieving both high efficiency and a diffraction-limited TEM₀₀ output in high-power end-pumped lasers.

To enable the formulation of an appropriate resonator design strategy for achieving the optimum TEM₀₀ performance at high pump powers, it is necessary to first derive an approximate expression for the focal length of the thermal lens and determine the effect of the non-parabolic phase aberrations on beam quality. Consider an edge-cooled laser rod of radius a , length l mounted in a cooled copper heat-sink maintained a temperature $T(a)$, end-pumped by a high-power diode-laser with incident pump power P_p and intensity $I_p(r)$, as shown in fig. 4. Under steady state conditions:

$$\nabla \cdot \mathbf{h}(r,z) = Q(r,z) \quad (6)$$

where $\mathbf{h}(r,z)$ is the heat flux and $Q(r,z)$ is the power per unit volume deposited as heat in the laser medium. The heat flux gives rise to a temperature distribution $T(r,z)$ within the laser rod given by

$$h(r,z) = -K_c \nabla T(r,z) \quad (7)$$

where K_c is the thermal conductivity of the laser material. Assuming that the thermal conductivity of the heat-sink is much larger than for the laser material, which would typically be the case (e.g. using a copper heat sink), then the temperature over the whole of the rod's circumference is $T(a)$ and the heat flow is predominantly radial.

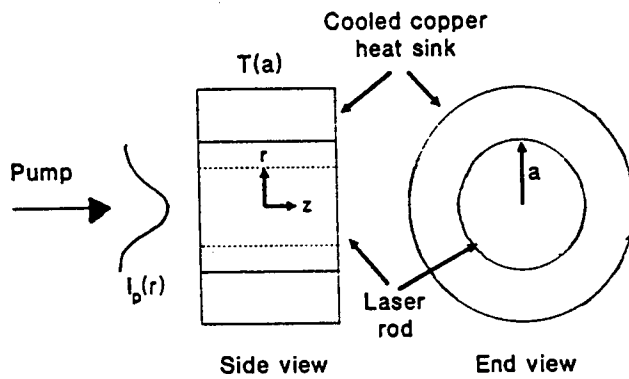


Figure 4 Heat sinking arrangement for an edge-cooled laser rod.

Hence from equation (6), the net radial heat flow from a thin disc, radius r and thickness Δz at axial position z is given by [19]

$$2\pi r \Delta z h(r,z) = \int_z^{z+\Delta z} \int_0^r 2\pi r' Q(r',z') dr' dz' \quad (8)$$

where $h(r,z)$ is now the radial heat flux. If we make the simplifying assumptions that the ground state is not significantly depleted and that the pump beam radius w_p does not vary significantly over the pumped region of the laser rod, then $Q(r,z)$ can be written:

$$Q(r,z) = \alpha_p \gamma I_p(r) \exp(-\alpha_p z) \quad (9)$$

where γ is the fraction of absorbed pump converted to heat. If the pumping quantum efficiency is unity and there are no deleterious upconversion or excited-state absorption processes, then under lasing conditions γ is approximately equal to the quantum defect (i.e. $\gamma \approx (\nu_p - \nu_L)/\nu_p$). Substituting (9) into (8) yields the following simplified expression for the radial heat flux $h(r,z)$:

$$h(r,z) = \frac{\gamma \exp(-\alpha_p z)}{r} \int_0^r I_p(r') dr' \quad (10)$$

The temperature difference $\Delta T(r,z) = T(r,z) - T(0,z)$ can be determined via substitution of (10) into (7), and the resulting phase difference $\Delta\phi(r) = \phi(0) - \phi(r)$ from

$$\Delta\phi(r) = \frac{2\pi}{\lambda} \int_0^l \Delta T(r,z) \frac{dn}{dT} dz \quad (11)$$

From equation (10) it can be seen that $\Delta T(r,z)$, $\Delta\phi(r)$, and hence the resulting beam distortion, depend on the transverse intensity distribution $I_p(r)$ of the pump beam. For high-power diode bars $I_p(r)$ has a transverse profile somewhere between Gaussian and 'top-hat' depending on the output characteristics of the diode-bar and on the particular pump beam delivery scheme used. For the pump delivery scheme used in our experiments the pump intensity profile is better approximated to a Gaussian. However, to illustrate the importance of the pump beam profile and its effects on the thermal lensing we will consider both cases of 'top-hat' and Gaussian intensity profiles.

5.1. 'TOP-HAT' PUMP INTENSITY PROFILE

In the case of a uniform pump intensity $I_p = P_p/\pi w_p^2$ for $r \leq w_p$ and $I_p = 0$ for $r > w_p$, then from equations (7), (10) and (11) it can be shown that the phase difference $\Delta\phi(r)$ is given by

$$\Delta\phi(r) = \left(\frac{P_p \gamma r^2 \eta_{\text{abs}} \frac{dn}{dT}}{2\lambda K_c w_p^2} \right) \quad (12)$$

for $r \leq w_p$, and

$$\Delta\phi(r) = \left(\frac{P_p \gamma \eta_{\text{abs}} \frac{dn}{dT}}{2\lambda K_c} \right) \cdot \left[1 + 2 \log_e \left(\frac{r}{w_p} \right) \right] \quad (13)$$

for $r > w_p$. Hence the $\Delta\phi(r)$ increases quadratically with r for $r \leq w_p$ and logarithmically with r for $r > w_p$.

5.2. GAUSSIAN PUMP INTENSITY PROFILE

In the case of a pump beam with Gaussian intensity profile; $I_p(r) = (2P_p/\pi w_p^2) \exp(-2r^2/w_p^2)$, it can be shown that the phase difference $\Delta\phi(r)$ is given by

$$\Delta\phi(r) = \left(\frac{P_p \gamma \eta_{\text{abs}} \frac{dn}{dT}}{\lambda K_c} \right) \cdot \left[- \sum_{n=1}^{\infty} \frac{1}{2n n!} \left(- \frac{2r^2}{w_p^2} \right)^n \right] \quad (14)$$

and hence $\Delta\phi(r)$ has a more complicated dependence on r which approximates to a quadratic dependence only when $r \ll w_p$.

In laser materials such as Nd:YAG the major contribution to thermal lensing arises from the temperature dependence of the refractive index, with the stress dependence of the refractive index and end-face bulging resulting in only relatively weak additional contributions to lensing, as will be seen later. Under these conditions the approximate focal length of the thermal lens f_t can be calculated by substituting the term in $\Delta\phi(r)$ which is quadratic in r into the following expression [19]:

$$f_t = \frac{\pi r^2}{\lambda \Delta \phi(r)} \quad (15)$$

This assumes that the lens is a 'thin' lens (i.e. $1/\alpha_p \ll f$), which is usually a good approximation in end-pumped lasers. However, equation (15) only gives the focal length experienced by the central portion of the laser beam, and hence is of limited value in formulating a strategy for resonator design since it does not provide any information on the aberrated nature of the lens, or any means for estimating the degradation in laser beam quality. Hence, it is more appropriate to consider an aberrated thermal lens as one whose focal length varies radially. For a thin thermal lens with a given radially varying phase difference $\Delta \phi(r)$ an approximate expression for the focal length $f_t(r)$ can be derived from simple geometrical considerations (shown in fig.(5)). The resulting expression is:

$$f_t(r) \approx \frac{2\pi r}{\lambda \frac{d\Delta \phi(r)}{dr}} \quad (16)$$

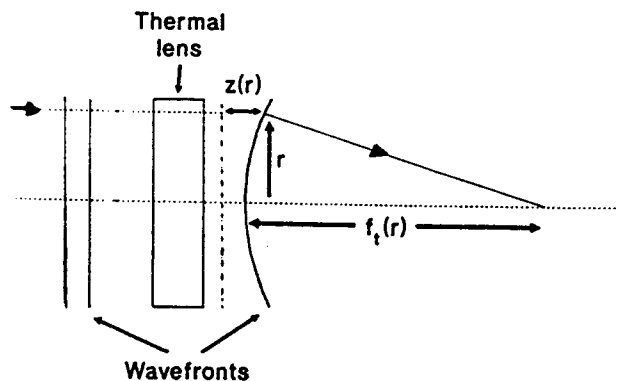


Figure 5 Radial variation in focal length for an aberrated thermal lens.

From equation (16) it can be seen that if $\Delta \phi \propto r^2$, then $f_t(r)$ is a constant and the lens has no phase aberration, and hence will not degrade the beam quality. For the 'top-hat' pump intensity profile described above, the focal length is given by

$$f_t(r) = \frac{2\pi K_c w_p^2}{P_p \gamma \eta_{abs} \frac{dn}{dT}} \quad (r \leq w_p) \quad (17)$$

$$f_t(r) = \frac{2\pi K_c r^2}{P_p \gamma \eta_{abs} \frac{dn}{dT}} \quad (r > w_p)$$

and for a Gaussian pump intensity profile the focal length is given by

$$f_t(r) = \frac{2f_t(0)}{w_p^2} \left(\frac{r^2}{1 - \exp(-2r^2/w_p^2)} \right) \quad (18)$$

where $f_t(0)$ is the focal length on axis at $r=0$, given by

$$f_t(0) = \frac{\pi K_c w_p^2}{P_p \gamma \eta_{abs} \frac{dn}{dT}} \quad (19)$$

From the expressions for focal length (17), (18) and (19) we can compare the lens powers for 'top-hat' and Gaussian pump intensity profiles for otherwise identical operating conditions. The results of this comparison are shown in fig.6, where it can be seen that the thermal lensing on axis has a lens power that is a factor-of-two stronger for the Gaussian pump and is highly aberrated with only a small region in the centre ($r \ll w_p$) having essentially constant focal length. However the 'top-hat' pump beam, in addition to producing a much weaker lens on axis, produces a lens which is essentially unaberrated over the pumped region ($r \leq w_p$). For $r > w_p$ the lens power varies in a similar fashion for both Gaussian and 'top-hat' pump beams. Thus, the transverse intensity profile of the pump beam is a very important factor in determining the thermal lens power and its phase aberration. From fig. 6 it can be seen that in order to minimise the thermal lensing and beam distortion a 'top-hat' pump beam would be preferable to a Gaussian pump beam. However, a 'top-hat' pump beam has the disadvantage that the threshold pump power can be up to a factor-of-two higher, and the slope efficiency for TEM₀₀ operation can be significantly lower as the mode profile and inversion profile are less well matched. In any case, in practice it is very difficult to achieve a pump beam with a 'top-hat' transverse intensity profile without a significant loss in pump power. Hence it is more usual to simply accept whatever the pump

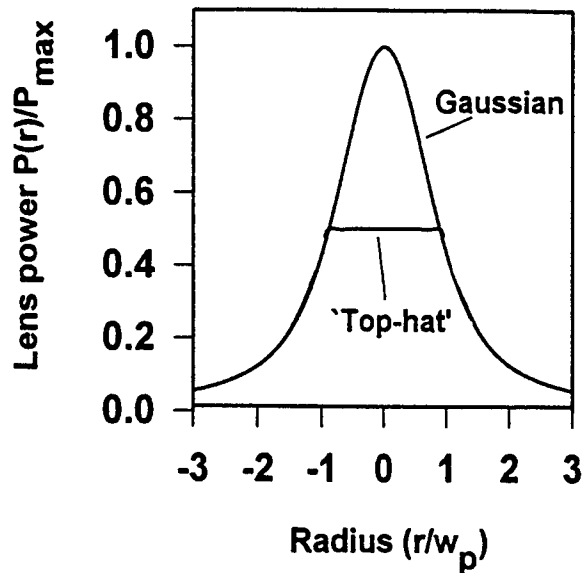


Figure 6 Predicted thermal lens power versus radius for Gaussian and 'top-hat' transverse pump intensity profiles.

delivery scheme provides and which is probably best approximated by a Gaussian transverse intensity distribution.

6. Measurement of Thermal Lensing

To test validity of this model we have determined the thermal lensing in a diode-pumped Nd:YAG rod, via a measurement of the phase difference as a function transverse position using a Mach-Zehnder interferometer. The experimental set-up (shown in fig. 7), consisted of a 10mm long Nd:YAG rod, antireflection coated at the lasing wavelength ($1.064\mu\text{m}$) and the pump wavelength ($\sim 809\text{nm}$), mounted in a water-cooled copper heat-sink, which was end-pumped by a 20W diode-bar. The diode-bar was focused, using a two-mirror beam shaping arrangement similar to that shown in fig. 3, to produce a nearly circular beam with radii; $w_{px} = 227\mu\text{m}$ and $w_{py} = 224\mu\text{m}$ and beam quality factors; $M_x^2 \approx 78$ and $M_y^2 \approx 63$ in orthogonal planes. This choice of beam size is representative of that required for efficient operation on some of the lower gain Nd:YAG transitions (e.g. at 946nm and $1.32\mu\text{m}$). The pump beam was focused through a mirror coated for high reflectivity ($>99.8\%$) at $1.064\mu\text{m}$ and high transmission ($>95\%$) at 809nm at 45° incidence, resulting in a maximum of 14.2W of pump light

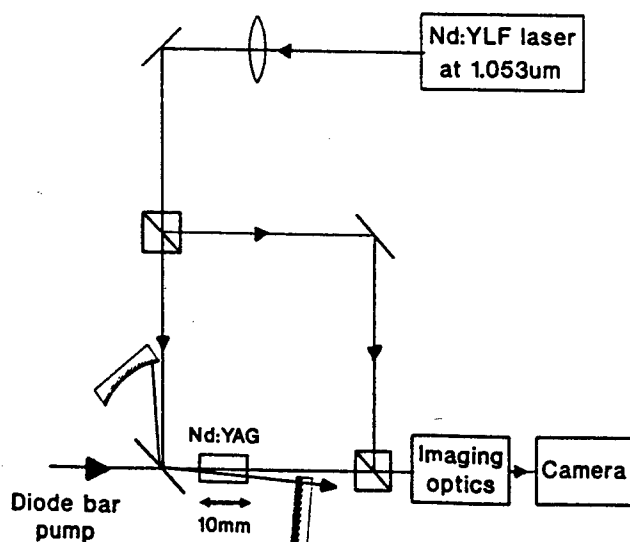


Figure 7 Mach-Zehnder interferometer for measuring the thermally-induced phase difference.

incident on the Nd:YAG rod. This mirror forms part of the Mach-Zehnder interferometer, allowing collinear propagation, along the pump beam's optical path, of the probe beam from a low-power diode-pumped single-frequency Nd:YLF ring laser operating at $1.053\mu\text{m}$. The Nd:YLF laser was chosen to provide the probe beam because its $1.053\mu\text{m}$ output experiences negligible gain in the Nd:YAG. The output from the interferometer was imaged onto a CCD camera, which was used to monitor the resulting interference pattern, from which the phase difference was calculated. Since it was anticipated that there would be a difference in thermal loading under nonlasing and lasing conditions, the phase difference was measured under both operating conditions. Laser operation at $1.064\mu\text{m}$ was achieved using the simple three-mirror resonator shown in fig. 7, which was aligned non-collinearly at the smallest possible angle to the pump beam, whilst allowing the Nd:YLF probe beam unattenuated passage through the Nd:YAG rod. At the maximum pump power the laser produced $\sim 6\text{W}$ of output in a multi-transverse-mode beam.

Under lasing conditions at the maximum available pump power, the measured phase difference as a function of radial position is shown in fig. 8(a). The solid line in fig. 8(a) is the parabolic curve which is the best fit to the phase difference data close to the centre of the pumped region. This indicates the phase difference profile that would be measured for a perfect (unaberrated) lens, and corresponds to a focal length of

$\approx 60\text{mm}$. The deviation from the ideal parabolic phase difference profile, shown in fig. 8(b), reveals the highly aberrated nature of the thermal lens with the phase aberration becoming increasingly pronounced for $r > w_p$. The resulting radial variation in focal

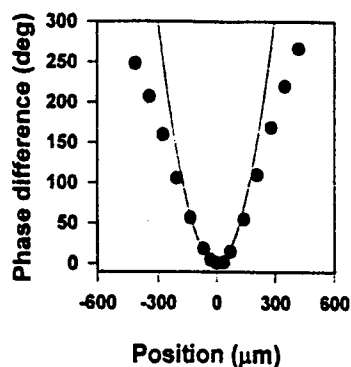


Figure 8(a) Phase difference as a function of radial position under lasing conditions.

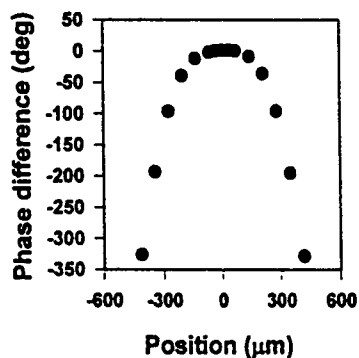


Figure 8(b) Deviation of phase difference from the ideal parabolic phase difference profile.

length can be calculated from the experimental data using equation (16), and compared with predicted variation in focal length for a Gaussian pump beam given by equation (18), where it is assumed that $K_c = 13\text{Wm}^{-1}\text{K}^{-1}$, $dn/dT = 9.86 \times 10^{-6}\text{K}^{-1}$ for YAG [20], $\gamma \approx 0.32$ [21] for $1.064\mu\text{m}$ operation, $w_p = 235\mu\text{m}$, and $\eta_{ab} = 0.94$. The result of this comparison is shown in fig. 9, where the predicted values for focal length (dashed line) correspond to a slightly weaker lens than was measured in practice. This can be easily explained since the theoretical model takes into account the contribution to lensing which

arises only from the temperature dependence of the refractive index, whereas the experimental values for focal length also include the contributions arising from end-face bulging and the radial stress dependence of the refractive index. From independent measurements of the stress-induced birefringence, using the Mach-Zehnder

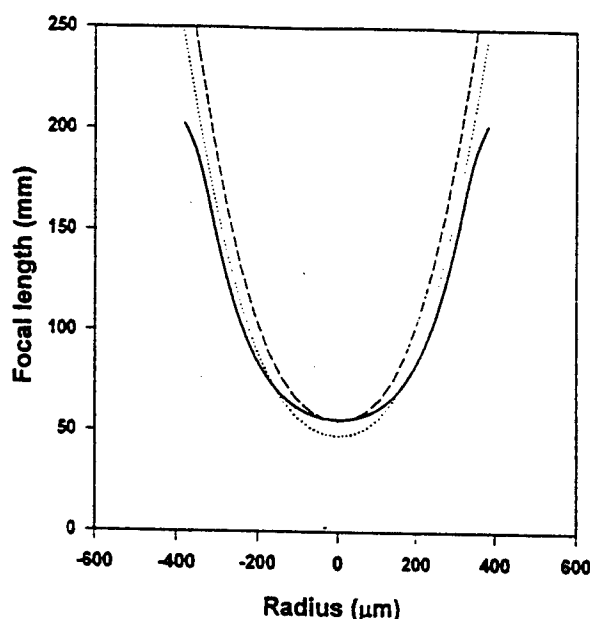


Figure 9 Radial dependence of the thermal lens focal length. (The solid line was calculated from the measured phase difference data. The dashed line represents the predicted radial dependence of focal length for a Gaussian pump beam taking into account the contribution due to the temperature dependence of refractive index only. The dotted line represents the predicted radial variation in focal length, modified to take into account the measured contributions to lensing from the stress dependence of refractive index and end-face bulging.

interferometer, and the end-face curvature, using a Michelson interferometer, we were able to show that the relative contributions to thermal lensing are approximately; 86% due to temperature dependence of refractive index, 8% due to end-face curvature and 6% due to radial stress dependence of refractive index. Taking into account these additional contributions and simply multiplying equation (19) for $f_t(0)$ by 0.86 results in a predicted focal length given by the dotted line in fig. 9, which is in good agreement with the experimental data. However, as a consequence of the Gaussian pump beam approximation the predicted values for focal length are slightly shorter than the experimental values in the centre of the pumped region.

The measured variation of lens power at $r=0$ with absorbed pump power for both

lasing and non-lasing conditions is plotted in fig. 10. In both cases there is a small departure from the linear dependence on pump power predicted by equation (18).

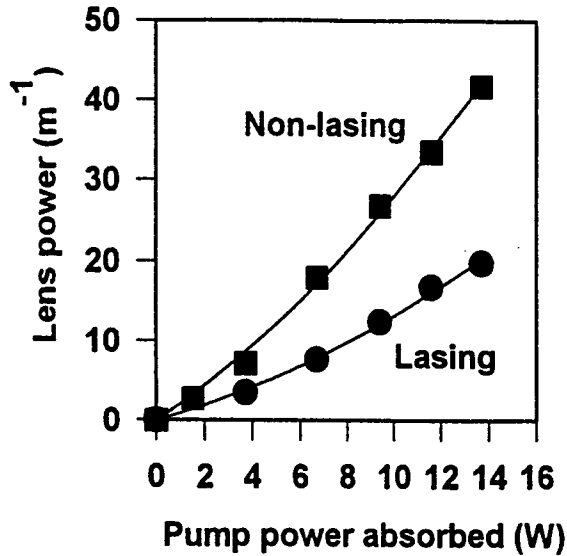


Figure 10 Thermal lens power at $r=0$ versus absorbed pump power under lasing and non-lasing conditions.

However the most striking feature is the \sim factor-of-two stronger lensing under non-lasing conditions. A full explanation for this is not yet available, but it is thought that it is at least in part due to upconversion processes [22] leading to increased thermal loading under non-lasing conditions.

7. The Effect of Thermal Lensing on Beam Quality

The highly aberrated nature of the thermal lens can lead to significant beam distortion. In order to minimise this distortion, and hopefully achieve near to diffraction-limited operation, at high pump powers it is useful to have a quantitative model which predicts the degradation in beam quality in a given situation. In ref. 23 it is shown that a laser beam with a Gaussian intensity profile and initial beam quality factor M_i^2 , after propagating through a lens of focal length f which produces a phase distortion $\Delta\phi(r)$ of the form

$$\Delta\phi(r) = \frac{2\pi}{\lambda} \left(\frac{r^2}{2f} - C_4 r^4 \right) \quad (20)$$

will suffer a degradation in beam quality with the resultant beam quality factor M_f^2 being given by

$$M_f^2 = \sqrt{(M_i^2)^2 + (M_q^2)^2} \quad (21)$$

M_q^2 is the additional contribution to the beam quality factor due to the quartic phase aberration given by

$$M_q^2 = \frac{8\pi C_4 w_L^4}{\lambda\sqrt{2}} \quad (22)$$

where C_4 is the quartic phase aberration coefficient. By comparison of equations (14) and (20) it can be seen that the phase distortion caused by thermal lensing in end-pumped lasers is generally more complicated than the example considered in ref. 23. However, if we restrict our consideration to the situation where the laser beam size is small compared to the pump beam size, so that we neglect terms higher than the quartic, then M_q^2 is given by the expression:

$$M_q^2 = \left(\frac{P_p \gamma \eta_{abs} \frac{dn}{dT}}{\lambda K_c \sqrt{2}} \right) \left(\frac{w_L^4}{w_p^4} \right) \quad (23)$$

The above expression indicates that in addition to its dependence on the power dissipated as heat and the thermo-optical and thermo-mechanical properties of the laser material, the degradation in beam quality also depends very strongly on the ratio of the laser beam radius to the pump beam radius. If $w_L \ll w_p$, then the beam quality is less strongly influenced by thermally-induced aberrations, and in the limit where $w_L/w_p \rightarrow 0$, then $M_q^2 \rightarrow 1$. However, if $w_L \geq w_p$ then even a weakly aberrated lens can result in a marked

degradation in the beam quality. The physical explanation for this is that the degradation in beam quality depends on the wavefront distortion introduced by the non-parabolic phase aberrations of the thermal lens. A laser beam with small beam radius, and hence a short Rayleigh range, will have spherical wavefronts of comparatively high curvature and hence the relative deviation in phase introduced by the aberrated thermal lens will be much smaller than would be the case for a beam with a larger radius.

One further point to note is that the presence of highly aberrated thermal lensing is not exclusive to end-pumping with high-power diodes. In fact the ability to generate strong lensing is actually determined by on the brightness of the diode pump source. Low power diodes are generally much brighter than high-power diode-bars, and hence can produce very strong and highly aberrated thermal lensing. The fact that there has been little degradation in laser beam quality observed in low power diode-pumped lasers is actually because typical pump beam sizes, and hence the laser mode sizes employed, tend to be rather small, resulting in a much shorter Rayleigh range than for the larger mode sizes required for high-power pump sources. Thus the degradation in beam quality at high pump powers is actually caused by the combination of thermally-induced aberrations and the requirement for comparatively large TEM₀₀ mode sizes which have a Rayleigh range comparable to or greater than the thermal lens focal length.

8. Beam Quality Degradation and Depolarisation Loss

The above simplified model for degradation in beam quality is strictly only valid in the regime where $w_L \ll w_p$. To confirm the validity of this model and to investigate its effectiveness outside this operating regime we have performed a simple experiment to measure the increase in M^2 for a diffraction-limited laser beam after a single-pass through a diode-pumped Nd:YAG rod. The experimental arrangement (shown in fig. 11), was very similar to that used for thermal lensing measurements shown in fig. 7. The main difference was that the second arm of the interferometer was removed and the CCD camera replaced by a Coherent Modemaster to measure the M^2 factor. The increase in M^2 value was measured under non-lasing and lasing conditions for a series of different Nd:YLF probe beam sizes in the Nd:YAG rod.

The results of this investigation (shown in fig. 12) indicate a marked increase in the M^2 value with probe beam size, due to the effect of thermally-induced lens aberrations. It is also apparent that the M^2 values measured under non-lasing conditions are significantly worse than those measured under lasing conditions. This appears to imply appreciably greater thermal loading under non-lasing conditions (by approximately a factor of ~ 2) at high pump intensities, and is consistent with the thermal lens measurements under lasing and non-lasing conditions. The calculated value for M^2 under lasing conditions is also plotted in fig. 12. From close inspection of the data it can be seen that for good beam quality (i.e. $M^2 < 1.1$), then as a rough guide we require a laser beam radius $w_0 < 140 \mu\text{m}$. The approximate analytical model is in reasonable agreement with the measured M^2 values up to larger beam size of $\approx 180 \mu\text{m}$ (i.e. $w_L/w_p \approx 0.77$), hence it can serve as a good guide as to the maximum value for the ratio

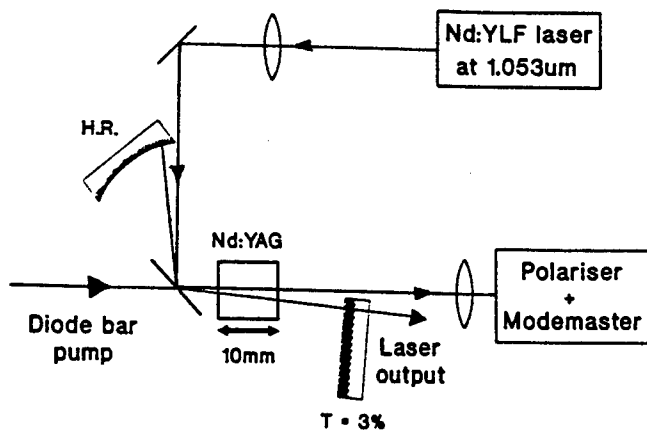


Figure 11 Experimental set-up for measuring degradation in beam quality and depolarisation loss after a single-pass through the thermal lens under lasing and non-lasing conditions.

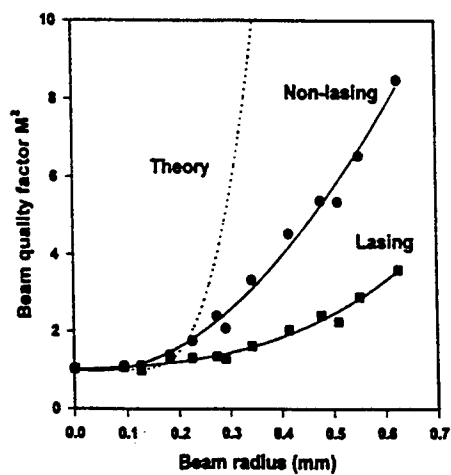


Figure 12 Single-pass degradation in beam quality versus probe beam size. The dotted line shows the beam degradation factor β for laser operation at 1.064 μm .

w_L/w_p that can be used without significantly degrading the beam quality. For larger w_L the predicted values for M^2 are higher than the experimental values because the quartic phase aberration approximation gives a much larger departure from the ideal quadratic phase difference than is the case in practice.

In addition to beam quality another important factor is the depolarisation loss due to thermally-induced stress-birefringence. This depends on a number of parameters including the pump and laser beam sizes. Unfortunately, calculating the depolarisation loss for a Gaussian pump is in general rather complicated, so instead we have simply measured it using the experimental arrangement shown in fig. 11, with the Mode-master replaced by a polariser. The single-pass depolarisation loss is plotted in fig. 13 as a function of laser beam size under both lasing and non-lasing conditions. It can be seen that there is a significant increase in depolarisation loss as the laser beam size increases. Furthermore the loss is significantly higher under non-lasing conditions, which is again consistent with a factor of ~ 2 extra heat loading.

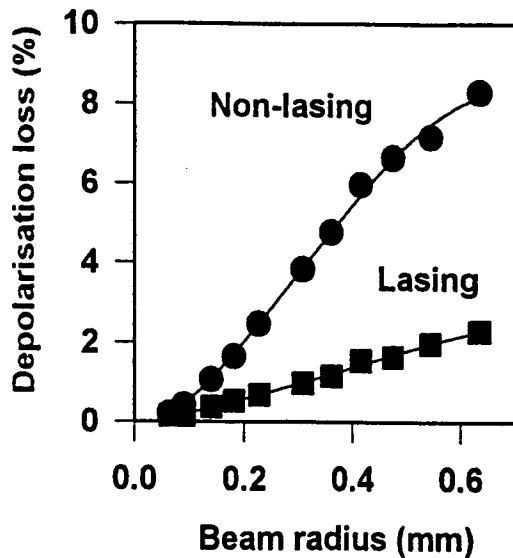


Figure 13 Single-pass depolarisation loss versus probe beam size.

9. Resonator Design Strategy

It is clear from the preceding section that in order to avoid significant degradation in beam quality and depolarisation loss for the TEM_{00} mode at high pump power, it is necessary to use a resonator with a TEM_{00} radius in the laser rod which is significantly smaller than the pump beam radius. This is in contrast to the situation at low powers

where it is generally accepted that one should use a resonator design with $w_L \geq w_p$ for efficient TEM_{∞} operation. At high pump powers, the smaller the ratio w_L/w_p the lower the depolarisation loss and the smaller the degradation in beam quality. Unfortunately one can not simply choose a resonator with an arbitrarily small laser mode size, since there will then be a significant amount of undepleted inversion in the pumped region not occupied by the laser mode, leading to multi-transverse mode oscillation and hence a non-diffraction-limited laser output. In practice therefore, it is necessary to use the largest possible laser mode size without significantly increasing the M^2 value and the depolarisation loss. The upper limit on the TEM_{∞} size that can be used for laser operation with for example, $M^2 < 1.1$, is difficult to calculate, but a rough value can be estimated from the experimental data on single-pass beam degradation and the discussion of the preceding section. One important question that now arises is which of the two requirements, that is, for good beam quality or low depolarisation loss, determines the upper limit on the laser mode size. For relatively high gain laser transitions, such as the $1.064\mu\text{m}$ line, a relatively high depolarisation loss $\sim 1\%$ per pass can be tolerated without causing a significant decrease in efficiency. Hence, from comparison of figs. 12 and 13, it can be seen that the requirement for good beam quality determines the upper limit on the laser mode size. However, for low gain laser transitions (e.g. the 946nm line) a much smaller depolarisation loss is required, indicating that the upper limit on the mode size is dictated by the requirement for low depolarisation loss. Regardless of the situation, the laser mode size must still be appreciably smaller than the pump beam size and hence there is still the problem of some undepleted inversion in the wings of the pumped region which can lead to lasing on higher-order transverse modes.

One solution to this problem is to simply use an aperture to discriminate against the unwanted higher-order modes. However, this has the disadvantage that it can significantly increase the loss for the fundamental mode and hence be detrimental to the efficiency. An alternative approach is to make use of the radially varying focal length of the thermal lens to provide the required discrimination. This is based on the principle that higher-order transverse modes, by virtue of their larger beam size than the TEM_{∞} mode, will see a thermal lens with an effective focal length which is longer than that seen by the TEM_{∞} beam. Hence, choosing a resonator design where the mode size decreases with increasing focal length of the thermal lens, will effectively decrease the ratio of beam sizes of the higher-order transverse modes to the TEM_{∞} mode. This results in a decrease in available gain for higher-order modes by virtue of their stronger spatial overlap with the fundamental mode, hence suppressing their oscillation.

10. Experiments on Power-scaling End-pumped Nd:YAG Lasers

To investigate the potential benefits of this approach we have performed a number of experiments on a Nd:YAG laser end-pumped by a high-power diode-bar. The pumping scheme used is identical to that described in earlier sections, delivering a maximum of 14.2W in a nearly circular beam of radius $w_p \approx 225\mu\text{m}$. The resonator design employed

was a simple folded cavity (fig. 14), consisting three mirrors; two plane mirrors, one having high transmission ($>96\%$) at the pump wavelength (809nm) and 5% transmission at the lasing wavelength ($1.064\mu\text{m}$) and the other with a transmission of 2% at $1.064\mu\text{m}$, and a curved high reflector of radius of curvature 100mm. The 10mm

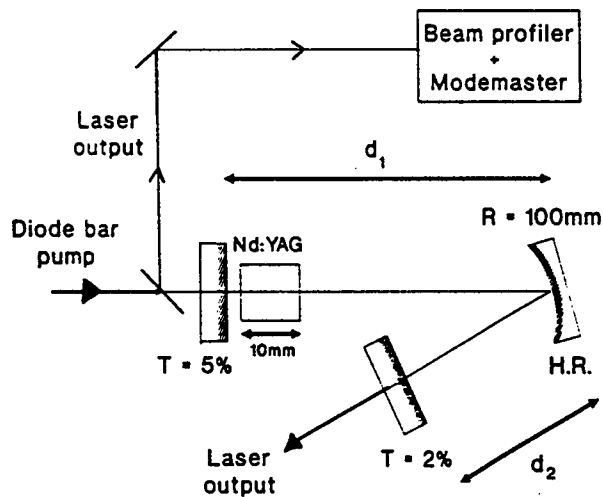


Figure 14 Resonator design for Nd:YAG laser experiments.

long Nd:YAG laser rod was mounted, as before, in a water-cooled copper heat-sink in close proximity to the pump input mirror. The use of two output couplers facilitated simultaneous monitoring of the laser output power, beam quality factor and transverse intensity profile of the output beam, whilst having the additional advantage of allowing easy determination of the laser mode size at the pump input mirror, and hence in the laser rod, without a knowledge of the resonator design and the effect of the thermal lens. This simple folded cavity, by varying the distances d_1 and d_2 between the curved mirror and the two plane mirrors, provided enough flexibility in resonator design to allow a detailed investigation of the requirements for efficient TEM_{00} operation.

Using the standard ABCD matrix formalism for resonator design [24], it can be shown that the requirement for a decrease in laser mode size in the rod with increasing focal length of the thermal lens can be realised in this simple folded cavity (fig. 14) by choosing an effective optical length for arm 1 to be just less than the sum of the focal lengths of the curved high reflector and the thermal lens focal length ($\sim 60\text{mm}$ at the maximum pump power). In our experiment the length d_1 was set to 109mm with the angle of incidence on the curved mirror made small ($<5^\circ$) to render the effects of astigmatism negligible. The avoidance of astigmatism is a particularly important aspect of the resonator design given that the requirement for a large decrease in laser mode size with increasing thermal lens focal length typically implies, as in this case, operating

close to the edge of stability. Thus in addition to using a small angle of incidence on the curved mirror, it is also important to avoid any astigmatism in the thermal lensing, due to, for example, an elliptical pump beam or a pump beam with M^2 values in orthogonal planes which differ significantly. Having set the value for d_1 to give the required resonator response to the varying thermal lens focal length, the required TEM_{∞} size in the laser rod can be obtained by simply adjusting the arm length d_2 . Calculated values for the TEM_{∞} beam radius at the laser rod are plotted as a function of thermal lens focal length for different values of d_2 in fig. 15. Without a polariser present in the

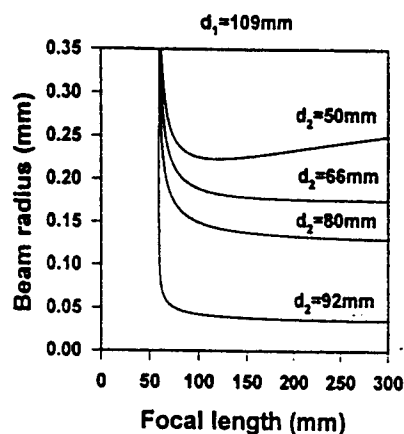


Figure 15 TEM_{∞} radius versus arm length d_2 .

cavity and at the maximum available pump power of 14.2W, it was found that TEM_{∞} operation ($M^2 \leq 1.1$) could in practice be achieved for a small range of values d_2 of approximately (70 ± 0.5) mm, resulting in a maximum output power of 6.2W (fig.16). Inserting a Brewster-angled plate into the cavity resulted in a linearly polarised, TEM_{∞} output ($M^2 < 1.1$) of slightly lower output power 5.5W, the reduction caused by an additional cavity loss of $\sim 1\%$ due to thermally-induced stress birefringence. This depolarisation loss is consistent with our expectations based on the experimental data for single-pass depolarisation loss (fig. 13) and the measured laser mode radius of $165\mu\text{m}$, which is significantly smaller than the pump beam radius. One interesting observation was that the reliability of TEM_{∞} operation was improved as a result of including a polariser in the cavity and additionally, had the benefit of extending the range of arm lengths d_2 , and hence the range of laser mode sizes, over which near diffraction-limited operation can be maintained. This can be attributed to the additional transverse mode discrimination provided by the polariser by virtue of the fact that higher-order transverse modes with larger beam sizes see, on average, a larger stress-induced birefringence and hence experience increased depolarisation loss at the polariser compared to the smaller

fundamental mode. However, as expected for both polarised and unpolarised lasers, diffraction-limited beam quality could only be maintained for a small range of pump powers (typically $< 4\text{W}$) close to the maximum power. At lower powers the laser mode size is reduced, due to the weaker thermal lens, hence the laser operates on many transverse modes. However, TEM_{00} mode operation could in principle be maintained over the full power range by careful selection and positioning of an aperture designed to strongly discriminate against higher-order transverse mode oscillation at low pump powers, while, by virtue of the change in laser modes size with increasing pump power, providing less discrimination at high powers. In this way the laser efficiency at high powers would not be affected. However, this approach would still have the disadvantage that the laser beam size and divergence would change with pump power. Thus for some applications simply operating at the maximum pump power and using an external attenuator to vary the power might prove to be a more attractive alternative.

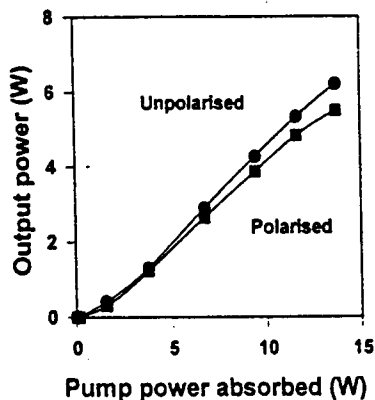


Figure 16 Nd:YAG laser output power at $1.064\mu\text{m}$ versus absorbed pump power.

To provide additional confirmation of the benefits of this resonator design approach, and in particular, to demonstrate the importance of using a resonator with a laser mode size which decreases with increasing thermal lens focal length, we have also investigated the behaviour of a similar folded cavity, but this time with arm lengths d_1 and d_2 selected to give a laser mode radius similar to that used in the previous experiment (i.e. $\sim 165\mu\text{m}$), but one which does not vary appreciably with rod focal length. At the maximum available pump power, a folded cavity with $d_1 \approx 80\text{mm}$ and $d_2 \approx 50\text{mm}$ roughly satisfies these requirements. This type of resonator might be have been considered as an attractive choice for a laser whose output characteristics (beam size and divergence) would not be strongly influenced by thermal lensing. However in practice

the minimum M^2 beam quality factor attainable for this resonator configuration was >2 . This serves to illustrate the importance of using a resonator which satisfies both of our design criteria, namely that the TEM_{∞} size should be significantly less than the pump beam size and that the laser mode size should decrease with increasing thermal lens focal length.

This design strategy has been successfully applied to other diode-bar-end-pumped Nd:YAG lasers operating on lower gain transitions at 946nm [9] and at 1.3 μ m [25], yielding diffraction-limited performance up to power levels of 2.7W and 3.2W respectively. However, due to their relatively low gain, both of these lasers when operated with Brewster plate polarisers, provided significantly lower powers due to the depolarisation loss resulting from thermally-induced birefringence. In the case of the 946nm Nd:YAG laser a maximum polarised output of 2.1W, and for 1.3 μ m operation, a maximum linearly polarised output of ~ 1.75 W were achieved. In the latter case the much higher heat loading density, which results from the larger quantum defect, makes it more difficult to achieve an efficient, linearly polarised TEM_{∞} output.

11. Power-scaling Limit

The ultimate limit to power-scaling of any laser is essentially determined by the stress-fracture limit. However, there are numerous brightness-dependent applications in areas such as non-linear optics and materials processing where scaling to high powers must be achieved without significant degradation in beam quality. In this case, given that there are numerous techniques for the compensation of thermally-induced stress-birefringence, it is in fact beam quality degradation due to the highly aberrated thermal lensing which effectively limits the maximum power that can be achieved. The strategy for resonator design described in section 9 provides a means for reducing the effects of the aberrated lens on beam quality, but it does not allow indefinite power-scaling with the maintenance of diffraction-limited beam quality. We can establish a very rough guide to the maximum power-scaling limit by requiring that $M_q^2 \leq 0.46$ (corresponding to $M^2 \leq 1.1$). The net result, obtained from equation (23), is that the maximum pump power used P_{pmax} must satisfy the following condition for good beam quality:

$$P_{pmax} \leq \frac{0.65 K_c \lambda}{\rho^4 \gamma \eta_{abs} \frac{dn}{dT}} \quad (24)$$

where $\rho = w_l/w_p$. It should be noted however that the above condition is only a rough guide, since it considers only a single-pass through the laser rod, and is only valid for $w_l \ll w_p$. It might appear from (24) that the maximum useful pump power is independent of the actual pump beam and laser mode size, and is only dependent on their ratio. At first sight this seems counter-intuitive since one might have expected a

limit dependent on pump intensity, which would have then allowed further power-scaling by simply using a larger pump beam size. However, the explanation for this is as follows: Using a larger pump beam size to reduce the pump intensity, and hence the phase aberration, would also necessitate the use of a larger laser mode size to allow efficient extraction of the gain, which would have a longer Rayleigh range. Given that beams with a longer Rayleigh range are more susceptible to beam distortion via phase aberrations, the net result of increasing the pump beam size would be to leave the value for M^2 approximately unchanged. Thus, from the point of view of optimising the laser efficiency it could be argued that it is in fact much better to use the smallest possible pump beam size, and hence laser mode size, to allow efficient utilisation of the inversion in the wings of the pumped region. Obviously, this requires a high-power diode pump source with reasonably good beam quality. The main disadvantage of intense pumping however is that, due to the very strong thermal lensing which results, TEM_{∞} operation can only be maintained over a very small power range without the use of apertures.

Fig.17 gives a rough guide to the maximum pump power that can be used for a diode-pumped Nd:YAG laser at $1.064\mu m$ with different values of ρ . This indicates that the condition $w_L \geq w_p$ for good beam quality at low pump powers becomes invalid for pump powers in excess of a few watts. Thus to avoid significant TEM_{∞} beam distortion

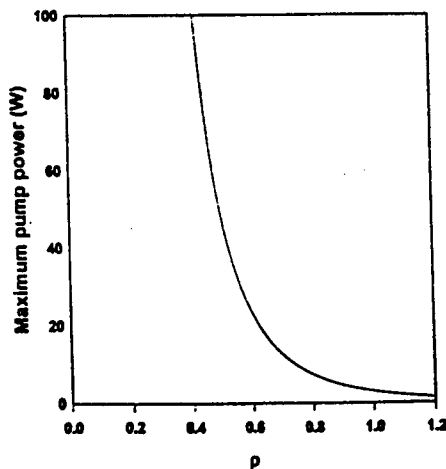


Figure 17 Rough guide to the maximum incident pump power for low TEM_{∞} beam degradation as a function of ρ .

when scaling to higher pump powers it is necessary to use progressively smaller values for ρ . However, if the ratio ρ is too small then the undepleted inversion in the wings of the pumped region leads to multi-transverse operation, even when using a resonator selected to satisfy the condition that the TEM_{∞} mode size decreases with increasing

thermal lens focal length. Under these conditions an aperture is required to provide the extra discrimination to prevent oscillation on higher-order modes. However, since the TEM_{00} intensity is very low in the wings of the pumped region it is difficult to utilise the undepleted inversion, hence the efficiency decreases. The implication of this is that there is a very definite power-scaling limit for diffraction-limited end-pumped solid-state lasers due to thermal lensing. For a Nd:YAG laser operating at $1.064\mu\text{m}$ employing an edge-cooled rod geometry and no compensation of the phase aberration, this limit is probably less than $\sim 20\text{W}$. This is well below the maximum multimode output power achievable.

12. Power-scaling with Nd:YLF

One approach to allow further power-scaling, without resorting to a change of heat-sink configuration or the use of compensating components for the phase aberration, is to use laser materials which have characteristics better suited to operation at high powers. One laser material which has recently received growing interest is Nd:YVO₄. The main attraction of Nd:YVO₄, apart from its natural birefringence, is its high $\sigma\tau_f$ product, which is \sim factor-of-two times larger than for Nd:YAG at $1.064\mu\text{m}$, and its short absorption length ($< 1\text{mm}$) for diode pump light at $\sim 809\text{nm}$. The latter allows for much tighter focusing of the pump source allowing the use of a relatively small laser mode size. Its low saturation intensity in combination with the use of a small mode size allows for better extraction of the gain in the wings of the pumped region and hence the use of resonator designs with smaller values of ρ , thus allowing scaling of TEM_{00} operation to higher powers (e.g. [1]). The main disadvantage of Nd:YVO₄ however, is that it exhibits quite strong thermal lensing, comparable to Nd:YAG, thus making it difficult to ensure TEM_{00} operation of the full range of pump power without the use of apertures.

An alternative laser material which offers some attractions for further power-scaling is Nd:YLF. In addition to its natural birefringence, Nd:YLF has the attraction that on the σ -polarisation (corresponding to $1.053\mu\text{m}$ operation) the thermal lensing is very weak. This is due to the combination of a small, negative value for dn/dT (i.e. -2×10^{-6}) and a positive contribution to thermal lensing from end-face bulging which substantially offsets the negative lensing. The net result is that, for the same thermal loading density, the thermal lensing on the $1.053\mu\text{m}$ transition in Nd:YLF is \sim six times weaker than in Nd:YAG. However Nd:YLF suffers from the problem that it has a stress-fracture limit which is \sim five times lower than Nd:YAG. This has all but limited operation of Nd:YLF lasers in cw end-pumped configurations to relatively low powers. However, with new beam shaping techniques, such as the two mirror beam shaper [8], which have led to higher brightness pump beams, a solution to the fracture problem is now presented. This involves using a longer Nd:YLF rod and distributing the absorbed pump power over a longer length by detuning the pump wavelength from the absorption peak, or using a rod with lower Nd³⁺ concentration. The pump beam with its improved beam quality, can be focused to a relatively small beam, but with a long Rayleigh

range, $z_{\text{op}} = \pi n w_p^2 / M^2 \lambda$, chosen to be comparable to or greater than the absorption length for the pump. In this way the pump beam size is kept reasonably constant over the length of the Nd:YLF crystal. Previously to adopting this strategy, the 1% Nd-doped YLF crystals employed in our experiments were found to fracture for diode pump powers in the range of 10W to 14W, when using pump beam radius of $\sim 300\mu\text{m}$. Using a 0.5% Nd-doped YLF crystal of length 15mm and a wavelength slightly detuned from the peak absorption, results in an effective absorption length for diode-bar pump radiation at $\sim 792\text{nm}$ of approximately 6mm. This allows end-pumping through opposite end-faces of the Nd:YLF crystal by two 20W diode-bars whose outputs, each using a two-mirror beam shaper, could be focussed to beam sizes of $\sim 300\mu\text{m}$, without the risk of fracture. Using this approach we have demonstrated $>11\text{W}$ of cw output at $1.053\mu\text{m}$ in a TEM_{∞} beam with $M^2 < 1.1$. The attraction of this approach is that due to the relatively weak thermal lensing, the laser mode size in a typical folded-cavity varies very little (by less than 10%) over full range of pump power. This allows for much more flexibility in resonator design, since the phase aberration is relatively small. As a demonstration of this we have also constructed a Nd:YLF ring laser end-pumped in a similar fashion by two 20W diode bars resulting in $>10\text{W}$ of single-frequency output at $1.053\mu\text{m}$, and an intracavity-frequency-doubled version (using LBO) with a single-frequency green output at 526.5nm of 6.2W, which corresponded to 8.5W of green generated internally in the Brewster-angled LBO crystal [26]. Further reduction in the Nd^{3+} concentration, improvements in pump beam quality and the use of multiple rod geometries should allow significant further scaling of TEM_{∞} power, without the risk of fracture. Thus Nd:YLF promises to be an attractive alternative to laser materials such as Nd:YAG and Nd:YVO₄ for high-power end-pumped solid-state lasers.

13. Conclusions

In end-pumped solid-state lasers employing edge-cooled rod geometries, thermal lensing, rather than stress-induced fracture, appears to present the most difficult obstacle to the scaling of diffraction-limited performance to high power levels. This is a consequence of degradation in laser beam quality due to the highly aberrated nature of the thermal lens. To reduce the effect of these non-parabolic phase aberrations we have proposed an alternative design strategy where the resonator must satisfy two conditions, which are that the TEM_{∞} mode size must be significantly smaller than the pump beam size and that the TEM_{∞} size must decrease with increasing thermal lens focal length. This resonator design approach is in stark contrast with the approach that is generally adopted for lower power lasers. We have also postulated that for this end-pumped edge-cooled geometry there is an upper power limit on a given laser transition for diffraction-limited operation. This limit depends on a number of factors including the characteristics of the laser material, and we have shown that if care is taken to avoid thermally-induced fracture, then Nd:YLF operating at $1.053\mu\text{m}$ has some advantages over Nd:YAG and Nd:YVO₄, due to its superior thermo-optical properties. However, indefinite scaling in the diffraction-limited output from end-pumped lasers can only be achieved if measures are taken to compensate for the thermally-induced aberrations [2].

14. References

1. Nighan, W. L., Dudley, D. and Keirstead, M. (1995) Diode-bar-pumped Nd:YVO₄ lasers with > 13W TEM₀₀ output at > 50% efficiency, *Conference on Lasers and Electro-Optics, Vol. 15, OSA Technical Digest Series, (Optical Society of America, Washington, D.C.)*, 17.
2. Tidwell, S. C., Seamens, J. F., Bowers, M. S. and Cousins, A. (1992) Scaling cw diode-end-pumped Nd:YAG lasers to high average powers, *IEEE J. Quantum Electron.* **28**, 997-1009.
3. Zbinden, H. and Balmer, J. E. Q-switched Nd:YLF laser end-pumped by a diode-laser-bar, *Opt. Lett.* **15**, 1014-1016.
4. Graf, Th. and Balmer, J. E. High-power Nd:YLF laser end-pumped by a diode-laser bar, *Opt. Lett.* **18**, 1317-1319.
5. Kierstead, M. S. and Baer, T. M. (1991) 10W TEM₀₀ output from a diode-pumped, solid-state laser, *Conf. Lasers and Electro-Optics, OSA Technical Digest Series, vol. 10, (Optical Society of America, Washington, D.C.)*, 490.
6. Leger, J. R. and Goltsov, W. C. (1995) Geometrical transformation of linear diode-laser arrays for longitudinal pumping of solid-state lasers, *IEEE J. Quantum Electron.* **28**, 1088-1100.
7. Yamaguchi, S., Kobayashi, T., Saito, Y. and Chiba, K. (1995) Collimation of emissions from a high-power multistripe laser-diode bar with multiprism array coupling and focusing to a small spot, *Opt. Lett.* **20**, 898-900.
8. Clarkson, W. A. and Hanna, D. C. (1996) Two-mirror beam-shaping technique for high-power diode bars, *Opt. Lett.* **21**, 375-377.
9. Clarkson, W. A., Koch, R. and Hanna, D. C. (1996) Room-temperature diode-bar-pumped Nd:YAG laser at 946nm, *Opt. Lett.* **21**, 737-739.
10. Brauch, U., Giesen, A., Karszewski, M., Stewen, C. and Voss, A. (1995) Multiwatt diode-pumped Yb:YAG thin disc laser continuously tunable between 1018 and 1053nm, *Opt. Lett.* **20**, 713-715.
11. Kubodera, K. and Otsuka, K. (1977) Diode-pumped miniature solid-state laser: design considerations, *Appl. Opt.* **16**, 2747-2752.
12. Laporta, P. and Brussard, M. (1991) Design criteria for mode size optimisation in diode-pumped solid-state lasers, *IEEE J. Quantum Electron.* **27**, 2319-2326.
13. Kubodera, K. and Otsuka, K. (1979) Single-transverse-mode LiNdP₄O₁₂ slab waveguide laser, *J. Appl. Phys.* **50**, 653-659.
14. Clarkson, W. A. and Hanna, D. C. (1989) Effects of transverse mode profile on slope efficiency and relaxation oscillations in a longitudinally-pumped laser, *J. mod. Opt.* **36**, 483-498.
15. Fan, T. Y. and Byer, R. L. (1987) Modeling and cw operation of a quasi-three-level 946nm Nd:YAG laser, *IEEE J. Quantum Electron.* **23**, 605-612.
16. Risk, W. P. (1988) Modeling of longitudinally-pumped solid-state lasers exhibiting reabsorption losses, *J. Opt. Soc. Am. B*, **5**, 1412-1423.
17. Koechner, W. (1988) *Solid-State Laser Engineering*, Springer-Verlag, New York, pp. 344.
18. Lu, G., Kugler, N., Weber, H., Dong, S., Muller, N. and Wittrock, U. (1996) A novel approach for compensation of birefringence in cylindrical Nd:YAG rods, *Optical and Quantum Electronics*, **28**, 75-69.
19. Innocenzi, M. E., Yura, H. T., Fincher, C. L. and Fields, R. A. (1990) Thermal modeling of continuous-wave end-pumped solid-state lasers, *Appl. Phys. Lett.* **56**, 1831-1833.
20. Kaminskii, A. A. (1989) *Laser crystals*, Springer-Verlag, New York, pp. 321.
21. Fan, T. Y. (1993) Heat generation in Nd:YAG and Yb:YAG, *IEEE J. Quantum Electron.* **29**, 1457-1459.
22. Guyot, Y., Manaa, H., Rivoire, J. Y., Moncorge, R., Garnier, N., Descroix, E., Bon, M. and Laporte, P. (1995) Excited-state-absorption and upconversion studies of Nd³⁺-doped single crystals Y₃Al₅O₁₂, YLiF₄ and LaMgAl₁₁O₁₉, *Phys. Rev. B*, **51**, 784-799.
23. Siegman, A. E. (1993) Analysis of laser beam quality degradation caused by quartic phase aberrations,

- Appl. Opt.* **32**, 5893-5901.
24. Kogelnik, H. and Li, T. (1966) Laser beams and resonators, *Appl. Opt.* **5**, 1550-1567.
 25. Kern, M. A., Clarkson, W. A. and Hanna, D. C. (1997) Resonator design considerations for high-power TEM₀₀ operation of a Nd:YAG laser at 1.3 μ m end-pumped by a diode-bar, *Conference on Lasers and Electro-Optics, Vol. 11, OSA Technical Digest Series, (Optical Society of America, Washington, D.C.)*, 479.
 26. Hardman, P. J., Clarkson, W. A., Martin, K. I., Butterworth, S. D. and Hanna, D. C. (1997) Mode-hop-free tuning in high-power intracavity-frequency-doubled Nd:YAG and Nd:YLF ring lasers, *Conference on Lasers and Electro-Optics, Vol. 11, OSA Technical Digest Series, (Optical Society of America, Washington, D.C.)*, 520.

HETEROGENEITY STRUCTURE OF ACTIVE MEDIUM REFRACTION FOR THREE-DIMENSIONAL PRE-MIXING AND MIXING NOZZLE BANKS OF GASDYNAMIC LASER

P.Y.Baskaev, A.V.Lavrov*, V.V.Lobachev

*Baltic State Technical University, 1-st Krasnoarmeyskaya, 1,
St.Petersburg, 198005, Russia*

**Russian Scientific Center "Applied Chemistry", 14 Dobrolubov Ave.,
St.Petersburg, 197198, Russia*

1. Introduction

As well known, the efficiency of CW high-energy laser is determined non only the ability to generate a radiation of potency energy, but optical quality of radiation as well. One will be connected with wavefront distortion and deviation of light amplitude distribution from most favorable [1].

As a rule, this problem is actual for all gas flow lasers. One of them is gasdynamic laser, where active medium is formed during extension of gas in array of small scale nozzles and during supersonic mixing donor and radiating gas.

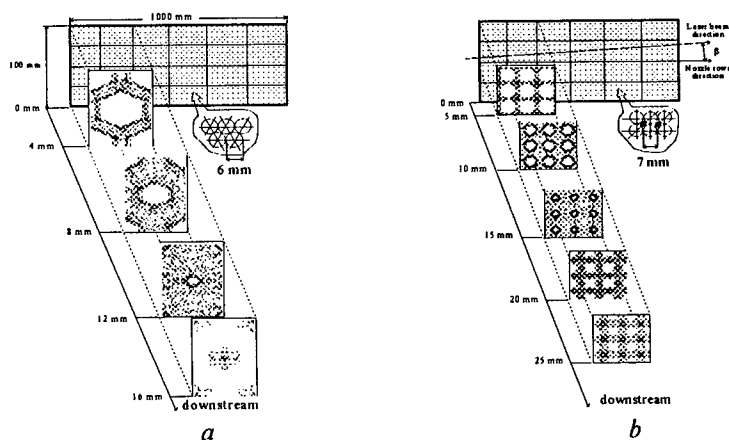


Figure 1. Schematic diagram of screen nozzle arrays and active medium density distribution in optical cavity; PGDL (a) and MGDL (b).

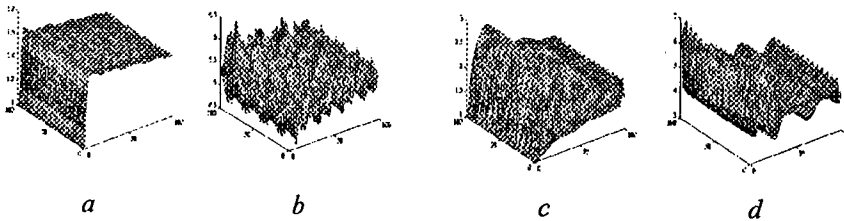


Figure 2. Amplitude (a,c) and phase (b,d) distributions of light field in laser aperture; PGDL (a,b) and MGDL (c,d).

One of the fast forming schemes of supersonic jet with the large consumption of components is scheme of three-dimensional extension in axisymmetrical nozzle array. Two active medium forming schemes are shown in Fig.1: gasdynamic laser with preliminary mixing of components (PGDL) and gasdynamic laser with supersonic mixing components in optical cavity (MGDL). Three-dimensional parabolized Navier-Stokes equations have been used for evaluation mixing of jets in gasdynamic laser [2]. The formula of Prandtl and $k-\epsilon$ turbulence model have been used for calculation of effective turbulent viscosity coefficient.

We can see the lines of constant density in optical cavity for some cuts of gas flow downstream direction in the Fig.1. As expected, structure of density distribution is rather complicated. As well, structure is determined by three-dimensional impact interaction of adjacent jets and dissipative viscosity areas of turbulent mixing. In all cases the symmetry of distribution of gasdynamical parameters and gain is determined by configuration of nozzles disposition in array.

2. Fundamentals.

For definition of radiation parameters in the output laser aperture, which was 100 x 100 mm, was carried out renovation of calculated density in all volume cavity for nozzle array of length 1000 mm. The wavefront of radiation was restored by known relation

$$\varphi(x,y) = K \int_L [n(x,y,z) - 1] dz,$$

where $n(x,y,z)$ – distribution of refraction index, L – length of nozzle array, $K = \frac{n-1}{\rho}$ –

constant of Gladstone-Dail, ρ – gas density. Intensity and amplitude distributions were restored in supposition of linear amplification in active medium by relation

$$I(x,y) = I_0 \exp \left[\int_L g(x,y,z) dz \right],$$

where $I_0=1$ – input light intensity, $g(x,y,z)$ – gain.

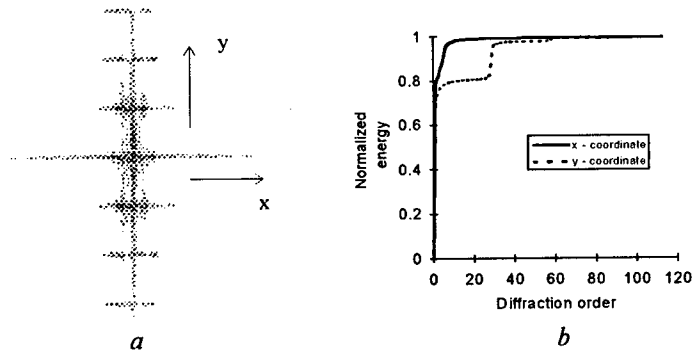


Figure 3. Fraunhofer diffraction intensity distribution (far field) (a) and normalized energy dependence on diffraction order (b).

Amplitude and phase distributions of a light field in output laser aperture for PGDL and MGDL schemes are shown in the Fig. 2. Phase and amplitude periodicity in transverse and longitudinal directions are explicitly expressed in MGDL. Period of phase modulations in transverse direction corresponds to an amount of nozzle rows in array with height 100 mm, and period of phase modulations in longitudinal direction corresponds to period of shock-wave structure. In PGDL distribution of amplitude is practically constant downstream, that is quite right.

We shall consider of a little bit integrated criterion's, which have allowed to estimate efficiency of nozzle array schemes from the point of view of a potential energy of laser amplifier and radiation optical quality. One of such criterion's is well known in optics Strehl ratio (Sh) [3]

$$Sh = \max \left\{ \frac{I(x_0, y_0)}{I_0(0,0)} \right\} = \frac{1}{S^2} \max \left| \iint_S U(x_1, y_1) \cdot \exp \left[-j \frac{k}{z} (x_0 x_1 + y_0 y_1) \right] dx_1 dy_1 \right|^2,$$

where $I(x_0, y_0)$ – distribution of intensity in zone of Fraunhofer diffraction (far field), I_0 – maximum value of intensity if $\varphi(x_1, y_1) = 0$, S – square of aperture, $k = \frac{2\pi}{\lambda}$ – wave ratio, z – a distance of radiation propagation, $U(x_1, y_1) = A(x_1, y_1) \cdot \exp[j\varphi(x_1, y_1)]$ – distribution of complex amplitude of a radiation if $A(x_1, y_1) = 1$. There is simple approximation of Sh [4], expressed per root mean scatter of phase, if $Sh > 0.3$

$$Sh \cong \exp(-D),$$

where $D = \frac{1}{S} \cdot \iint_S [\varphi(x_1, y_1) - \bar{\varphi}]^2 dS$, $\bar{\varphi} = \frac{1}{S} \cdot \iint_S \varphi(x_1, y_1) dS$ – dispersion of phase and mean phase in the laser aperture accordingly.

As well known, the classical optical integral is difficult for practical evaluations. Application of a fast Fourier transformation method has allowed to make detail parametrical research, to determine not only ratio Sh , but also angle of a laser radiation

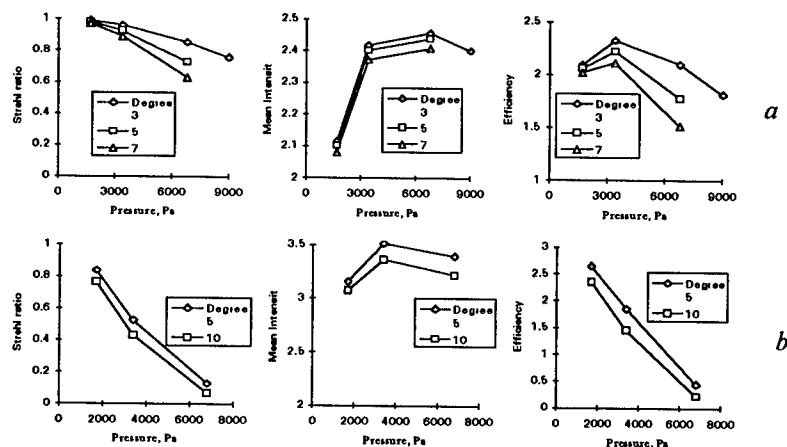


Figure 4. Strehl ratio, mean intensity and efficiency versus pressure in nozzle output for different nozzle generatrix angles; PGDL (a) and MGDL (b).

divergence by integration of light intensity diagram. For example, intensity distribution in far field and two orthogonal cuts of normalized energy angular distribution for MGDL is shown in the Fig.3.

Mean intensity I_0 in aperture was set as energy criterion of linear laser amplifier. The total efficiency of laser amplifier was determined by relation $Sh \cdot I_0$, which simultaneously takes into account tendencies of modification output energy and laser beam quality. The graphs of dependence of Strehl ratio, mean intensity and efficiency of laser on pressure are shown in the Fig.4. We can see, that Strehl ratio is reduced always with increasing any laser parameter. Also, we can see that nozzle generatrix angles strongly affect on level of active medium optical heterogeneity always. In MGDL mean intensity is a little bit higher, than would otherwise be in PGDL. This is because small relaxation losses exist in active medium. In both cases the dependence of mean intensity and laser efficiency $Sh \cdot I_0$ on pressure has explicit maximum.

Though absolute energy indexes in MGDL is higher than that one in PGDL, its optical homogeneity is somewhat below. It confirms the shift interferograms of gas flow, which specially was synthesized on computer for two cases: self-emission of laser and high quality probing emission (see Fig.5). Large amplitude of modulation of interference strips is much more for MGDL than for PGDL. By this is meant that level of wavefront distortions is high. Information about dispersion of interference light field, which is shown in the Fig.5, is tabulated in Table 1. Here, a dispersion is connected with interference contrast of light fields. Therefore, this results demonstrated the high level of spatial coherence of a radiation.

TABLE 1. Dispersion of interference fields

Shift	Dispersion			
	Self-emission interferograms		Probing emission interferograms	
	Mixing	Pre-mixing	Mixing	Pre-mixing
0	0.8823	0.5066	0.4990	0.4990
P/3	0.5490	0.5053	0.5015	0.4990
P/2	0.4521	0.4977	0.5013	0.4970

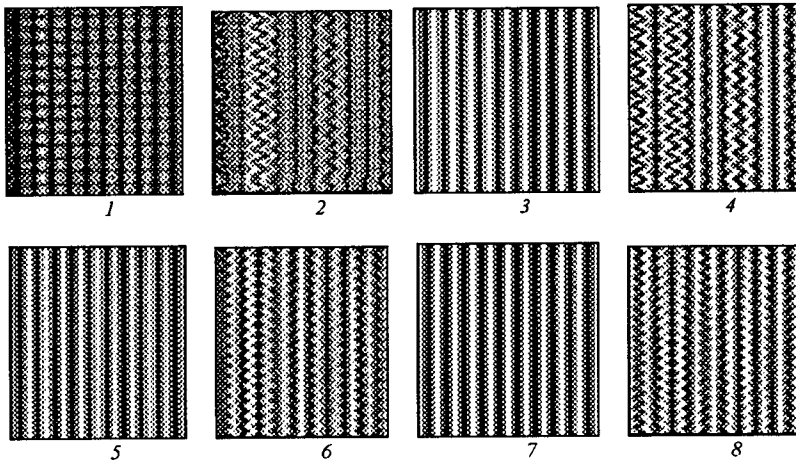


Figure 5. Computer synthesized shear interferograms of gas flow; 1-4 MGD, 5-8 PGDL; 1,3,5,7 - shift is 0, 2,4,6,8 - $P/2$ (P - period of nozzle rows), 1,2,5,6 - self-emission of gasdynamic laser, 3,4,7,8 - high quality probing emission.

It is well known that obvious way of compensating of regular wavefront distortion is orientation of nozzles rows in nozzle array in relation to direction of beam propagation. For the first time it was discussed in [5] and then it was checked experimentally and numerically in [6]. Dependence of Strehl ratio, normalized angle of laser beam divergence, mean intensity and efficiency on angle orientation of nozzle rows for MGD is shown in the Fig.6. As well as for PGDL, optimum angle of orientation is, for example, the angle between direction of beam propagation in optical cavity and direction between center of the first nozzle in first row and center of the last nozzle in second row. It is necessary to signify that some decrease of mean intensity in laser aperture at modification of orientation of nozzle rows takes place this case. It is

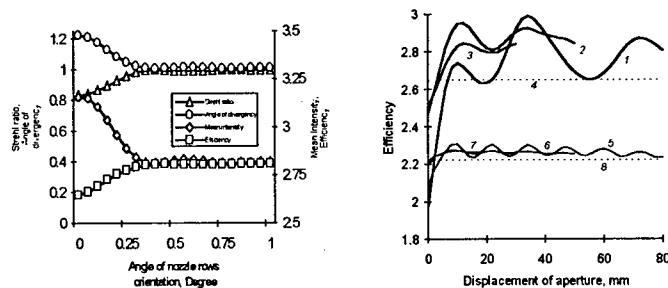


Figure 6. Strehl ratio, angle of divergence, mean intensity and efficiency dependence on angle of nozzle rows orientation (on the left); efficiency dependence on size of aperture and aperture displacement downstream (on the right), where 1,2,3,4 - MGD, 5,6,7,8 - PGDL, 1,5 - 20 x 20 mm aperture, 2,6 - 50 x 50 mm, 3,7 - 70 x 70, 4,5 - level of efficiency for 100 x 100 mm.

connected with power anisotropy of an active medium amplification in MGD.

3. Results and discussion.

Optimization of aperture size of laser amplifier is very interesting. The dependence of laser efficiency association on size of aperture and downstream displacement is shown in the Fig.6. A diminution of aperture size and its downstream displacement can some increase of efficiency for MGD especially.

Research shows, that regular periodic multiscale spatial heterogeneities take place in active medium of any gas-flow lasers [6]. It is not unexpected, since multiscale distortion is determined by physical processes and nozzle array configuration. Regular heterogeneities of a small spatial scale with size of the order of first zone of the Fresnel $d_F = \sqrt{\lambda \cdot L}$ are the most interesting. The structure and level of these heterogeneities is

determined by period of nozzle disposition in array and depth of modulation depending by conditions of supersonic jets interaction and influence of viscous effects in each nozzle and mixing zones. If the depth of periodic modulation of phase, i.e. its amplitude, does not exceed 1 radian ($Sh \approx 0,6$), then spatial frequency of this modulation $\omega \approx \frac{\sqrt{S}}{l_\omega}$

(where S – square of aperture, \sqrt{S} – equivalent size of aperture and l_ω – scale of regular phase perturbation) will not influence practically on divergence of laser radiation [7].

For regular heterogeneities it circumstance is shown in the Fig.7 (curves 1–4), where level $Sh \approx 0,6$ is critical really. Frequency ω of phase

periodicity influences on divergence of laser radiation for certain conditions. Therefore, increase of sizes of laser amplifier, i.e. its output aperture and nozzle array lengths, can reduce not only Strehl ratio, but increase a divergence of a laser radiation.

Nonregular distortions in active medium influence on divergence of a laser radiation similarly to character as regular distortions (see Fig.7 curves 5–8): If root mean scatter of amplitude of such distortions will exceed 1 radian, then the magnitude θ/θ_0 will to depend on frequency of nonregular spatial scale of phase distortions.

As well known, the most typical nonregular microscale heterogeneity in active medium is turbulent fluctuations. Though the nature of such fluctuations is very complicated, but their registration is based on violation of contrast of interference field.

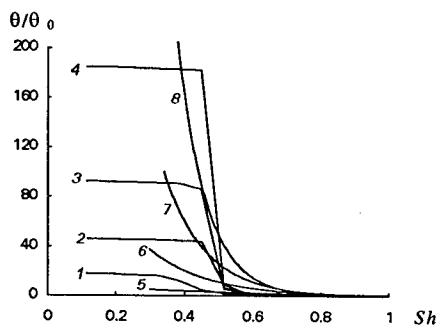


Figure 7. Dependence of normalized angle of divergence of radiation on Strehl ratio; 1-4 - regular periodic spatial frequencies of wavefront perturbations, 5-8 - nonregular spatial frequencies of wavefront perturbations, 1,5- $\omega=10$, 2 - $\omega=25$, 3 - $\omega=50$, 4,6 - $\omega=100$, 7 - $\omega=500$, 8 - $\omega=2000$.

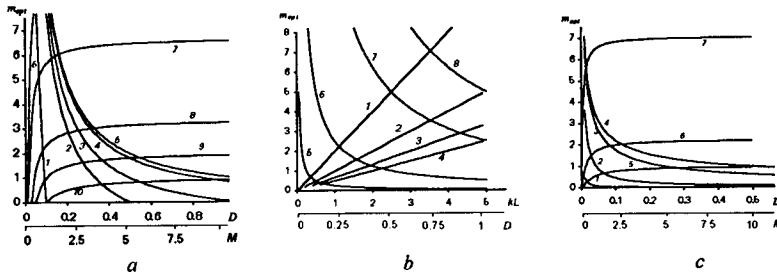


Figure 8. Dependence of magnification m_{opt} of laser amplifier length on main parameters;
 (a) - regular phase heterogeneities and linear amplification dependence on kL (1-4) and D (5-8),
 if $1-D=0.25$, $2-0.5$, $3-0.75$, $4-1$, $5-kL=0.1$, $6-1$, $7-5$, $8-10$;
 (b) - regular phase heterogeneities and saturated amplification dependence on D (1-4) and M (5-7),
 if $1-I=0.01$, $2-0.1$, $3-1$, $4-\infty$, $5-D=0.01$, $6-0.1$, $7-0.5$;
 (c) - nonregular phase heterogeneities and saturated amplification dependence on D (1-5) and
 M (6-10), if $1-I=0.1$, $2-0.5$, $3-1$, $4-5$, $5-\infty$, $6-D=0.1$, $7-0.15$, $8-0.3$, $9-0.5$, $10-1$.

Scattering of light on microscale perturbations of a refraction can reduce efficiency of transmission of radiation as well as reduce of laser output energy.

Next, we shall consider approaches of efficiency of laser amplifier. Let us assume that one of aspects of amplification of intensity is realized in active medium with expansion L [8]: linear amplification $I=I_0 \exp(kL)$ or saturated amplification $I \cong I_0 + I_S kL$, where k - gain, I_0 , I , I_S - input, output intensity and intensity of saturation, accordingly. Simultaneously, regular or nonregular heterogeneity with dispersion of phase D in active medium can arise. Further, most important parameters are shown in the Table 2.

There are following labels here: S - square of aperture of laser amplifier with a rectangular distribution of light field amplitude, $W \approx Sh$ - efficiency of radiation energy transmission, $\bar{I} = \frac{I_S}{I_0}$, $M = \bar{I}kL$, m - parameter of a proportional modification of

laser amplifier length with base L (mandatory $m > 0$), $L_m = mL$ - changed length of the laser amplifier, L - base length ($L=1$ m).

If only regular phase heterogeneities exist in active medium of high energy laser and if amplifier functions on the assumption of a linear amplification, then factor m_{opt} will be simultaneously to depend on a binary index kL and dispersion D . It is shown in Fig.8,a. The important singularity is that m_{opt} depends on dispersion D hyperbolic. By other words, at large levels of value D such situation is possible, when there is no way to compensate the drop of efficiency by increase of output energy with the help of simple magnification of length of amplifier.

If the amplifier functions at saturation then kL is replaced by M , which depends on \bar{I} . Since distortions of wavefront are regular, then m_{opt} will fall with arise in dispersion D (see Fig.8,b). Contrary to the regime of linear amplification, it is impossible to compensate the enhancement of dispersion D by enhancement of M . It is connected with the fact that limiting dependence of m_{opt} on D for $M \rightarrow \infty$ exists (see

TABLE 2. Equations for most important laser parameters

Parameters	Label	Linear amplification		Amplification of saturation	
		Regular phase field	Nonregular phase field	Regular phase field	Nonregular phase field
Output energy of laser amplifier with length L	$I\dot{I}'_0$	$SI_0 \exp(kL)$	$SI_0 \exp(kL)$	$S(I_0 + I_s kL)$	$S(I_0 + I_s kL)$
Output energy of laser amplifier with length L_m	$I\dot{I}'_{0m}$	$SI_0 \exp(mkL)$	$SI_0 \exp(mkL)$	$S(I_0 + mI_s kL)$	$S(I_0 + mI_s kL)$
Phase dispersion of wavefront of laser amplifier with length L_m	D_m	$m^2 D$	$m D$	$m^2 D$	mD
Energy of radiation in far field if length of amplifier is L	$W_L = W W_0$	$SI_0 \exp(kL - D)$	$SI_0 \exp(kL - D)$	$S(I_0 + I_s kL) \times \exp(-D)$	$S(I_0 + I_s kL) \times \exp(-D)$
Energy of radiation in far field if length of amplifier is L_m	$W_m = W W_{0m}$	$SI_0 \exp[m(kL - mD)]$	$SI_0 \exp[m(kL - D)]$	$S(I_0 + mI_s kL) \times \exp(-m^2 D)$	$S(I_0 + mI_s kL) \times \exp(-mD)$
Specific energy in far field if length of amplifier is L_m	$\overline{W} = \frac{W_m}{W_L}$	$\exp \left\{ \frac{(m-1) \times [kL - (m+1)D]}{m} \right\}$	$\exp \left\{ \frac{(m-1) \times [kL - D]}{m} \right\}$	$\frac{1 + mI_s kL}{1 + I_s kL} \times \exp[-(m-1)D]$	$\frac{1 + mI_s kL}{1 + I_s kL} \times \exp[-(m-1)D]$
Optimum magnification of laser amplifier length if $\frac{d\overline{W}}{dm} = 0$	m_{opt}	$\frac{kL}{2D}$	$\infty, \text{ if } kL > D, \\ 0, \text{ if } kL < D$	$\frac{\sqrt{D + 2M^2} - \sqrt{D}}{2M\sqrt{D}}$	$\frac{1}{D} - \frac{1}{M}$

curves 4). By this is meant that additional energy from active media, connected with increase of the length of amplifier, cannot compensate the decrease of efficiency because of fast growth of dispersion of wavefront.

The tendency of saturation is observed in the dependence of m_{opt} on M . Value m_{opt} is constant for $M > 2,5$ and any m_{opt} . Because of this, for $M > 2,5$ the next formula is true

$$m_{opt} = \frac{1}{\sqrt{2D}}.$$

If the statistical phase distortion in active media exists then the light scattering is less then in the variant with regular phase distortions. (see Fig. 8,c). It is connected with fact that dispersion of wave front increases linear with increasing of amplifier length. Three variants of relation exist between kL and D : if $kL > D$, then increase of L implies an increase in efficiency. If $kL < D$, then efficiency is a maximum for $m_{opt} \rightarrow 0$.

If $kL = D$, then efficiency is constant for any m .

Let us consider the variant when amplifier is saturated and active media is statistical inhomogeneous (see Fig. 7). This variant is look liked with the variant of regular periodic phase inhomogeneity. As a result m_{opt} decreases as the D increases. If $M \rightarrow \infty$ this condition is justified for $D \rightarrow \infty$. It is obvious that laser, which functions only for $m_{opt} \rightarrow 0$ is not optimum. Next it is necessary to decrease optical inhomogeneity in active media.

Thus, all results are confirmed main principle, whereby the optimum high-energy laser system can be created by only reasonable compromise between power indexes of laser and level of generated radiation quality. Error-free information about these parameters can be obtained during numerical simulation and/or experimental research.

4. Acknowledgments

The authors would like to acknowledge the support of Director of the NATO Advanced Research Workshop "Optical Resonators - Science and Engineering", Doctor Ram Kossowsky, without which this paper would not have been possible.

5. References

1. Anan'ev, Yu.A. (1979) *Optical cavities and the problem of divergence of laser radiation*, Nauka, Moscow.
2. Lavrov, A.V., Ikonnikov, V.K., Yegoyanc, P.A., Bersh, A.V., Bungova, T.A. (1996) Experimental and Theoretical Investigation of the Noncomplete Combustion-Driven Downstream Mixing CO₂-GDL, *Proc. 27th AIAA Plasmadynamics and Lasers Conf.*, AIAA Paper 96-2342.
3. Born, M., Wolf, E. (1964) *Principals of optics*, London - New-York.
4. Quinnell, R.D. (1981), *SPIE*, v.293, p.12-19.
5. Russell, D.A., Chu, Y.K. (1983) Aerodynamic disturbances from supersonic nozzle array, *Proc. IV Intern. Symp. on Gasdynamic and Chemical Laser*, Italy.
6. Boreisho, A.S., Duynov, S.I., Lobachev, V.V., Morozov, A.V., Popov, A.G. (1989) Optical quality of streams, formed by array of axisymmetrical nozzles, *Rus. J. of Apply Mechanics and Technical Physics*, No 4, p.94-98.
7. Bashkin, A.S., Lobachev, V.V., Fedorov, I.A. (1997) Analysis of the spatial scales of optical inhomogeneities in active media of high-power gas-flow laser amplifiers, *Rus. J. Quantum Electronics*, v.24, No 2, p.173-175.
8. Lobachev, V.V., Moshkov, V.L. (1993) Limitation at a realization of multicascade laser amplifiers, *Bel. Engineering-Physical J.*, v.63, p.83.

OPTIMIZED RESONATORS FOR HIGH ENERGY LONG-PULSE Nd:YAG LASER

T. DASCALU, N. PAVEL, M. POTERASU
*National Institute for Lasers, Plasma
and Radiation Physics
PO BOX MG 36 Bucharest, ROMANIA*

1. Introduction.

The various applications of variable long-pulse, high energy, Nd:YAG laser [1,2], (especially applications which require a constant spot size during the laser pulse), request the constant quality of the laser beam. Into a laser rod, homogeneously pumped, a parabolic temperature profile appears, and therefore the refractive index gradient is built up.

The rod behaves like a thick lens with a refractive power D , which increases with the input energy. A resonator with such a thick lens inside was investigated by several authors [3,4] for high repetition rate and high input power. The thermal equilibrium cannot be reached at low repetition rate (<5 Hz) and high energy pumping pulse and the rod's focal length increases during the pumping time. The variation of the focal length changes the divergence of the multimode laser beam during the pulse time. The optical resonator needs a special design to overcome this variation.

The purpose of this paper is to present the results on experimental investigation of thermal effects in Nd:YAG rods pumped with linear flashlamps with variable pulses from 0.5 to 10 milliseconds, pump energy up to 5000J and the design of the optical resonator to compensate the thermal effects. In order to improve the laser beam quality some optimal stable and unstable resonators with variable reflectivity mirror (VRM) were investigated.

2. Measurements of Transient Thermal Lens

Thermal effects in high energy Nd:YAG laser rod are very strong and could affect the behaviour of the laser resonator during the laser pulse when the rod is pumped for long time (millisecond). In order to measure the thermal focal length of the active media f_R we use the optical arrangement [5], presented in Fig. 1. Passing a He-Ne laser beam through the rod during flashpumping we can measure the probe beam intensity in plane P with a photodetector.

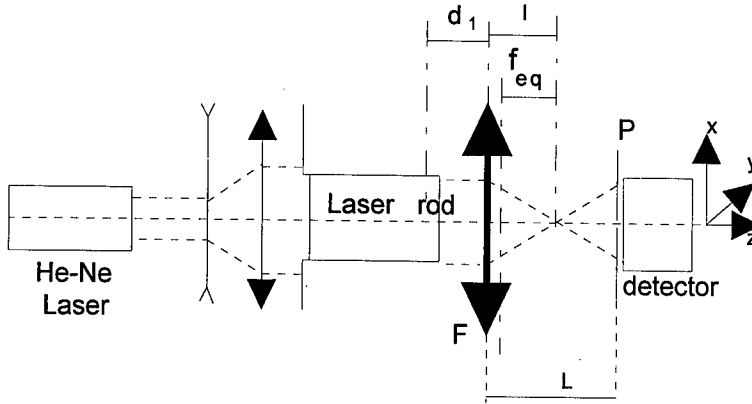


Figure 1. Experimental set-up for determination of transient refractive power in Nd:YAG rod.

The active medium is considered as a thick lens. The relation between f_{eq} (the equivalent focal length of the optical system formed by laser rod with focal length f_R and the lens F with focal length f_1) and l , the distance from F to focal plane of the optical system, is [6]:

$$l = f_{eq} \left(1 - d_1 \frac{1/f_{eq} - 1/f_1}{1 - d_1/f_1} \right) \quad (1)$$

where d_1 is the distance between the lens F and principal plane of the rod. The waist of the He-Ne laser beam after passing through the laser rod is:

$$W_0 = \frac{2\lambda}{\pi D} f_{eq} \quad (2)$$

where D is the laser rod diameter. Because it is difficult to measure W_0 at the focal plane we can measure the beam diameter W_D at the plane P and after few simple calculations described below, temporal behaviour of the waist can be obtained. At the distance z from the waist, W_D is:

$$W_D = W_0 \sqrt{1 + \left(\frac{\lambda z}{\pi W_0} \right)^2} \quad (3)$$

where $z = L - l$. Combining equations (1), (2) and (3) one can obtain:

$$af_{eq}^4 + bf_{eq}^2 + cf_{eq} + d = 0 \quad (4)$$

where:

$$\begin{aligned}
 a &= \frac{4\lambda^2}{\pi^2 D^2} & b &= D^2 \left(1 - \frac{d_1}{f_1 - d_1} \right) - W_0^2 \\
 c &= -2Db \left(L + \frac{d_1 f_1}{f_1 - d_1} \right) & d &= D^2 \left(L + \frac{d_1 f_1}{f_1 - d_1} \right)
 \end{aligned} \quad (5)$$

Knowing the value f_{eq} we can obtain the focal length for laser rod f_R by using the relation:

$$\frac{1}{f_{eq}} = \frac{1}{f_R} + \frac{1}{f_1} - \frac{d_1}{f_1 f_R} \quad (6)$$

In order to find out the temporal behaviour of W_D when the laser rod is pumped we can measure the intensities of the He-Ne beam at plane P, at the point x from the optical axis. When the laser rod is pumped, because of the thermal lens, the spot diameter of the He-Ne laser beam will vary. If the pumping system has lack of symmetry then a displacement of the probe beam Δx from the optical axis is observed. Two measurements of the beam intensities in two different points $x=0$ and $x=x_0$ are used in order to eliminate Δx . Equations (7) and (8) show the intensity at $x=0$ and $x=x_0$. The value k/W_D represents the maximum intensity I_0 in the beam's centre.

$$I_1 = \frac{k}{W_D(t)} \exp \left[- \left(\frac{\Delta x(t)}{W_D(t)} \right)^2 \right] \quad (7)$$

$$I_2 = \frac{k}{W_D(t)} \exp \left[- \left(\frac{x_0 + \Delta x(t)}{W_D(t)} \right)^2 \right] \quad (8)$$

Combining (7) and (8) we obtain:

$$\frac{k}{w_D(t)} \exp \left[- \left[\frac{w_D(t) \sqrt{\ln \left(\frac{k}{w_D(t) I_2} \right)} - x_0}{w_D(t)} \right]^2 \right] - I_1 = 0 \quad (9)$$

which provide the values for $W_D(t)$. Knowing $w_D(t)$ we can calculate $f_{eq}(t)$ and finally $f_R(t)$. In our experiments, the Nd:YAG laser rod has 84 mm length, 6.6 mm diameter, 1.1% concentration of Nd ions, and $f_1=500$ mm, $L=1330$ mm. The beam intensities were measured by using a ROL26 photodiode and the scope Tektronix466. The values of the

W_D on the plane P, without pulse pumping, is $W_D=13$ mm. The results are presented in Table 1.

The obtained data show a strong asymmetry between x and y measurement's directions. The asymmetries appear because of the pumping lamp. The plane (yz) contains the laser rod and lamp.

Table 1. Thermal transient focal length.

Pumping pulse duration (ms)	Pumping energy [J]	I_1 (mV)	I_2 (mV)	$w_D(t)$ (mm)	f_{eq} (mm)	focal length of the rod thermal lens f_R (mm)
4	315	150	125	15.99	390	1106 photodiode
7	550	145	120	17.67	371	953 displacement
9.5	950	140	110	18.75	353	749 $x=1$ mm
4	315	150	180	18.37	357	778 photodiode
7	550	140	175	18.72	353	749 displacement
9.5	950	130	160	20.29	334	628 $y=1$ mm
4	315	170	130	15.5	397	1202 photodiode
7	550	160	125	16.22	386	1056 displacement
9.5	950	150	110	18.55	355	763 $y=-1$ mm

Figure 2 shows the temporal variation of $I_1(t)$, the He-Ne laser probe beam intensity and one can observe that initial temperature of laser rod is establishes after 1.5 seconds from the end of pumping pulse.

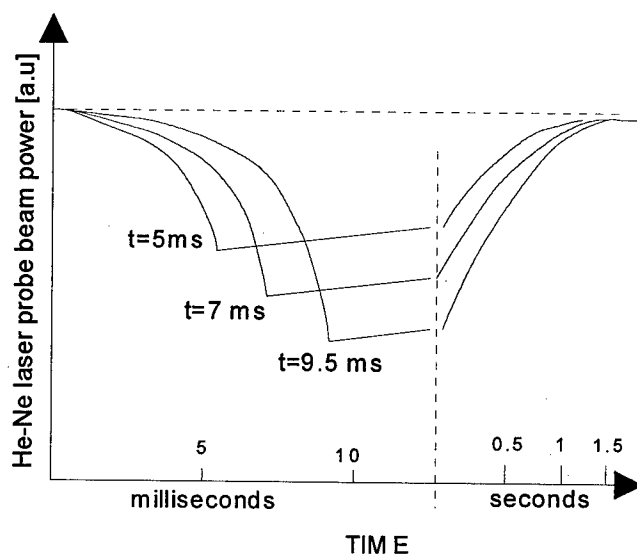


Figure 2. Temporal variation of the He-Ne laser probe beam passing through the Nd:YAG rod

Variations of the laser rod refractive powers up to 2 m^{-1} were observed when the lengths of the pumping pulse vary between 0.5 and 10 ms at different pumping energies.

3. Experiments Using Different Optical Resonators

Two kinds of resonators can be used when the constant beam quality is required: stable resonators and unstable resonators with VRM output coupler. In the case of stable resonator the laser system is designed to provide the desired beam pattern. When the laser rod is operated at a specified pumping pulse energy and duration, the behaviour of the thermal lens exhibited by the rod must be also taken into account. To find the optimal resonator parameters that maintain constant the quality of the laser beam during laser pulse, in the case of multimode laser operation with internal variable thermal lens, the matrix method was used. The best result in our case was obtained by using a plan-spherical resonator with 0.8 m length and 2 m mirror radius. In such a configuration the Nd:YAG rod (6.6x85 mm), pumped with variable pulse length, was placed nearly the output plane mirror. Figure 3 shows the numerically calculate multimode divergence and the experimental results versus optical power in the plane-spherical resonator for two different resonator lengths.

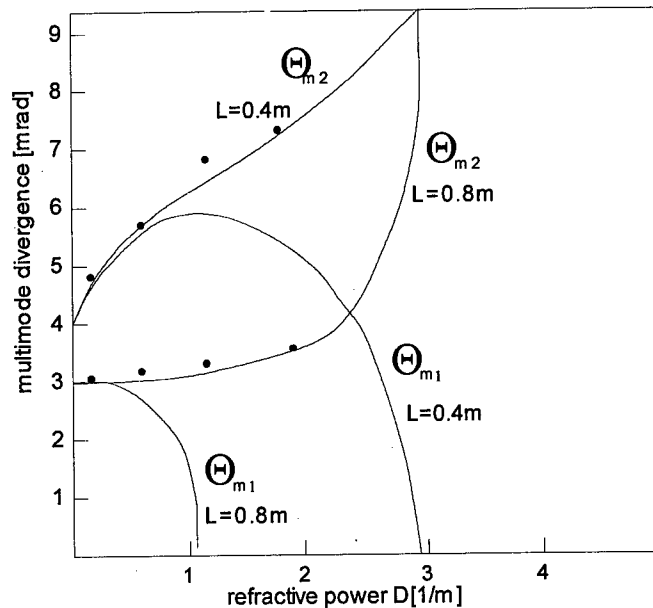


Figure 3. Multimode divergence in plan-spherical resonator (mirror radius 2 m), parameter L = resonator length.

The numerical calculus shows also that plan-spherical resonator, $L=0.8 \text{ m}$, with the laser rod very close to the flat output mirror is the most insensitive to the variations of the

refractive power. The unstable resonator with radial variable-reflectivity mirror (VRM) as output couplers were demonstrate [7,8] to be a solution for the generation of high-energy diffraction limited beams with smooth transversal profile. The reflectivity of the super-Gaussian mirror, used in our experiments as output coupler, has the analytical form:

$$R(r) = R_0 \exp \left\{ -2 \left(r / w_m \right)^n \right\} \quad (10)$$

where R_0 is the peak reflectivity, r is the radial coordinate, w_m is the spot size, and n is the order of the mirror. A 45 cm length resonator operating in the stable and unstable configurations was equipped with VRM and one 39% reflectivity ordinary mirror. The laser rod was placed 10 cm apart from the rear mirror. The comparative results about the output power and divergence of the beam are presented in Table 2. The beam divergence was measured by ASTM 43 method using a 1 m focal lens and a SCIENTECH 361 powermeter.

Table 2. Output power and divergence of the laser beam obtained from stable and unstable resonator configuration. The pulse pumping duration was 3 ms with 5 Hz of repetition rate and 150 J pump energy.

Resonator configuration	Output power (W)	Divergence (mrad)
Plane-plane stable resonator, 39% output coupler	10.5	4.0
Plane-plane stable resonator, VRM output coupler with $R_0=35\%$, $w_m=1.6$ mm, $n=4.2$	9.2	3.5
Plane-plane stable resonator, VRM output coupler with $R_0=35\%$, $w_m=1.7$ mm, $n=5$	8.8	3.2
Unstable configuration with -5m rear mirror and VRM output mirror with $R_0=35\%$, $w_m=1.6$ mm, $n=4.2$	6.5	<1
Unstable configuration with -5m rear mirror and VRM output mirror with $R_0=35\%$, $w_m=1.7$ mm, $n=5$	6.8	<1

As the table 2 shows an improved laser beam divergence was observed for VRM stable configuration as compared to usual plane-plane resonator, with only a small decrease of laser pulse energy.

4. Conclusions

The thermal transient effect induced in a Nd:YAG laser rod pumped with pulse duration up to ten milliseconds and pulse energy up to 1000J can be precisely measured by the method described above. By using the matrix method and taking into account the thermal transient effects, the optimal plane-spherical resonator which maintains constant the beam quality during the pumping pulse was determined. The beam quality, in stable configuration, was improved by using variable reflectivity mirror as output coupler.

5. References

1. Lupei, V., Dascalu, T., Florea, V., Nicolescu, V. and Mogos, M. (1991) An Automatically Controlled Nd:YAG Laser with Variable Pulse Width, *Optics&Laser Technology* **23**, 155-161.
2. Dascalu, T., Dascalu, V., Florea, V. and Lupei, V. (1992) A Simple Approach for Nd:YAG Lasers with Long Pulse Generation, *Rev.Roum.Phys.* **5**, 473-483.
3. Kortz, H.P., Ifflander, R., and Weber, H. (1981) Stability and Beam Divergence of Multimode lasers with Internal Variable Lenses, *Appl.Opt.* **20**, No.23, 4124-4136
4. Driedger, K.P., Ifflander, R. and Weber, H. (1988) Multirod Resonators for High - Power Solid State Lasers with Improved Beam Quality, *IEEE J. Quantum Electron.* **24**, 665-672.
5. Subhash, N. and Sathianadnan, K. (1984) Thermal Effects in a Nd:Glass Laser Rod Pumped in a Double Circular Close-Coupled Cavity, *IEEE J. Quantum Electron.* **20**, 111-118.
6. Born, M. and Wolf, E. (1965) *Principles of Optics*, Pergamon Press, London
7. De Silvestri, S., Laporta, P., Magni, V., Svelto, O., Arnone, C., Cali, C., Scortino, C. and Zizzo, C. (1988) Nd:YAG Laser with Multidielectric Variable Reflectivity Output Coupler, *Opt.Comm.* **67**,229-232.
8. De Silvestri, S., Magni, V., Svelto, O. and Valentini, G. (1990) Laser with Super-Gaussian Mirrors, *IEEE J. Quantum Electr.* **26**, 1500-1512.

HIGH POWER DIFFRACTION LIMITED SOLID STATE LASERS WITH STABLE RESONATORS

V. MAGNI, M. ZAVELANI-ROSSI

*Centro di Elettronica Quantistica e Strumentazione Elettronica del
Consiglio Nazionale delle Ricerche.*

Dipartimento di Fisica del Politecnico

Piazza L. da Vinci 32, 20133 Milano, Italy

1. Abstract

A review on stable resonators for high power diffraction limited solid state lasers is presented. A theoretical analysis of resonators containing a variable lens representing the rod thermal focusing, with particular attention to the problems of optical and mechanical stability (i.e. the sensitivity to misalignments), is developed. Design criteria for optimized resonators are illustrated and various examples of applications are given. Experimental results obtained with a Nd:YAG laser at 1064 nm, with Nd:YLF lasers at 1047 and 1053 nm and with an intracavity frequency doubled Nd:YLF laser working without instabilities connected to the "green problem" are discussed.

2. Introduction

The generation of diffraction limited beams of high power or energy is of great interest for many scientific and industrial applications. Stable resonators operating on the fundamental TEM_{00} mode produce high quality diffraction limited beams; however, the transverse mode dimension and, as a consequence, the extracted energy from the gain medium are generally small, unless special design procedures are applied. Multimode laser beams with an average power up to the kilowatt level can presently be generated with Nd:YAG lasers. On the contrary, the output power is reduced to a few tens of watts when a stable resonator operating on the fundamental transverse mode (TEM_{00}) is used, mainly because of the small overlapping volume of the TEM_{00} mode with the active material. Large mode volumes can be obtained with unstable resonators, but the high losses proper of unstable resonators hinder their use with low gain lasers, like continuous wave (CW) solid state lasers. To increase the output power with stable resonators a large volume TEM_{00} is required, however, if appropriate design criteria are not applied, the resonator modes and the output power become dramatically sensitive to small perturbations and to mirror misalignment. The problem is further complicated by the lens effect produced in the rod by pumping. In fact the

dioptric power can reach considerable values even at moderate lamp input power levels (e.g., about $4\text{--}5\text{ m}^{-1}$ in Nd:YAG lasers) and plays a fundamental role in determining the performances of CW or high repetition rate solid state lasers. Since, not only the gain of the active material, but also all the properties of the resonant modes depend on the pumping rate, the design of resonators for large mode volume TEM_{00} turns out to be very complicated.

Great efforts have been made to design stable resonators that can counteract or compensate for the thermal focusing of the rod. Early solutions proposed compensation of thermal lens by a convex mirror [1] or by diverging lenses ground on the end faces of the rod [2-4] that exactly eliminate the focusing effect: this compensation is, however, only effective at a given value of the pump power. Variations of the thermal focal length are allowed in concave-convex resonators [5], but only if the thermal effects are very small. An important step forward was made with the introduction of dynamically stable resonators [6,7], which allow reliable TEM_{00} mode operation with the mode volume stabilized against variations of thermal focal length (i.e. of pump power). The concept of dynamical stability has also been applied to resonators with an intracavity telescope, which give the advantage of an easy adjustment for different pump powers [8-11]. It has been demonstrated that in dynamically stable resonators the position of the laser rod has an important role and a fine optimization allows substantial improvement of the performances [12,13]. Various detailed studies on the optimization of multimode resonators with an internal variable lens have also been published [14-18].

Besides the dynamical stability, the mechanical stability of the resonator, i.e. the sensitivity to the mirror misalignment, is a key factor in designing stable resonators with large mode volume, since dynamically stable resonators might be unreliable because of the alignment difficulties [19,20]. The misalignment sensitivity has been analyzed by several authors [21-24]. For solid state lasers a comprehensive analysis of general resonators with an internal focusing rod was carried out and design procedure for optimized dynamically stable resonators with minimum misalignment sensitivity have been devised [19,25,26]. The successful application to CW Nd:YAG lasers demonstrated significant improvement of output power and of misalignment sensitivity [27,28]. The mentioned general analysis has also been extended to cover the case of crystals other than YAG with very large focusing power [29] and resonators containing arbitrary optical elements [30,31]. On the basis of the latter reference it has been demonstrated [32] that, independently of the resonator configuration, the range of input power for which the resonator is stable is inversely proportional to the mode volume and is a unique characteristic of the laser material. To obtain higher TEM_{00} output power and wider stability range than those of YAG, laser crystals with low thermal focusing are required. One of the most interesting material is Nd:YLF, which presents a very low thermal focusing. The experimental results obtained with optimized resonators demonstrate that Nd:YLF is superior than YAG for TEM_{00} mode operation [33-36]. The excellent properties of Nd:YLF for high power TEM_{00} mode operation have also been exploited in the development of high efficiency and high power CW intracavity frequency doubled lasers [37].

3. Theory of Stable Resonators with Thermal Lens for TEM₀₀ Mode Operation

In this section we present a unified analysis of resonators with an internal variable lens that represents the pumped rod. The topic is treated in the widest generality including also the possibility of an arbitrary intracavity optical systems (such as telescopes): the optical stability of the resonator, the mode volume, and the misalignment sensitivity are studied mainly as a function of the pump power i.e., of the rod focal length. The theoretical findings are supported and confirmed by experimental results. On these bases, simple and readily applicable design criteria for large mode volume, dynamically stable, minimum misalignment sensitivity resonators are described.

3.1. THERMAL LENSING

A considerable amount of heat is generated in the laser rod, mainly due to pump quantum efficiency less than unity and to the waste of energy between pump bands and laser levels. The heat removed from the rod surface generates a radial thermal gradient, which, in turn, produces the following effects that contribute to the thermal lensing of the rod: (i) temperature-induced variation of the refractive index, (ii) strain dependent variation of the refractive index, (iii) end face curvature caused by thermal expansion [38-40]. If heat generation is uniform, the bulk of the rod acts as a lens-like medium because of the quadratic variation of the refractive index as a function of the radial distance, while the term due to end face curvature introduces a small positive lens effect. For lamp pumped rods one can write for the thermally induced focal length, f , the relationship

$$\frac{1}{f} = \frac{k}{\pi a^2} P_{in}, \quad (1)$$

where P_{in} is the electric pump power entering the lamp, a is the rod radius, and k is a constant depending on the opto-mechanical properties of the laser rod and on the pumping efficiency. Since the location of the rod principal planes is almost independent of the pump power [19,41], the rod can be treated as a thin lens, provided that the distances from other optical elements are measured with reference to the rod principal planes, located at a distance $L_R/2n$ from the rod end faces (n being the refractive index and L_R the rod length). Note that, if the effect due to the end face curvature is neglected, the rod dioptric power, as expressed by Eq. (1) results to be independent of the rod length: indeed the contribution of the end face curvature to the total focal length is generally less than 6% [40], therefore, the coefficient k can be considered as independent of the rod length.

3.2. STABILITY AND MODE VOLUME

To allow a very general analysis of solid state laser resonators only two elements have to be considered: the rod and the intracavity optics. In this paper we consider only systems with rotational symmetry around the optical axis. The results of our analysis can be extended to orthogonally astigmatic systems by considering separately two orthogonal axis [42]. The resonator model is shown in Fig. 1: it is composed by two plane mirrors that enclose a lens of variable focal length, f , (representing the rod)

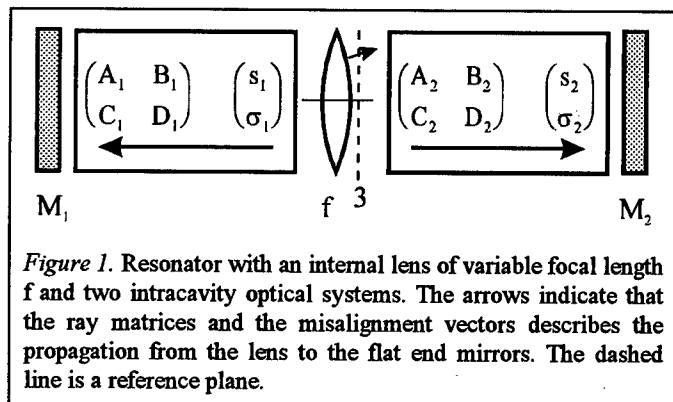


Figure 1. Resonator with an internal lens of variable focal length f and two intracavity optical systems. The arrows indicate that the ray matrices and the misalignment vectors describes the propagation from the lens to the flat end mirrors. The dashed line is a reference plane.

between two optical systems described by suitable ray transfer matrices. The ray transfer matrices shown in Fig. 1 are associated with the ray paths from the lens to the plane mirrors and also include the possible mirror curvatures and misalignments. In fact, curved mirrors

can be resolved in a plane mirror and a lens of focal length equal to the mirror radius of curvature. To make the equations that follow more readable, we define, with reference to Fig. 1, the following variables:

$$\eta = \frac{1}{f} - \frac{1}{2} \left(\frac{A_1}{B_1} + \frac{C_1}{D_1} + \frac{A_2}{B_2} + \frac{C_2}{D_2} \right) \quad (2)$$

$$u = \frac{1}{2B_1D_1} - \frac{1}{2B_2D_2} \quad (3)$$

$$v = -\frac{1}{2B_1D_1} - \frac{1}{2B_2D_2} \quad (4)$$

With this notation the transfer matrix T for propagation from mirror 1 to mirror 2 (see Fig. 1) is:

$$T = \begin{pmatrix} D_1B_2(\eta + u) & B_1B_2(\eta + v) \\ D_1D_2(\eta - v) & B_1D_2(\eta - u) \end{pmatrix} \quad (5)$$

Note that the only variable that depends on f , i.e., on the pump power, is η and that the matrix elements are linear function of $1/f$.

The condition for the optical stability of the resonator ($0 < AD < 1$) can also be expressed as [43,30]

$$ABCD < 0, \quad (6)$$

where A , B , C , and D are the elements of the matrix T . Therefore, the stability limits as a function of η are obtained by equating to zero each of the element of the matrix T : from Eq. (5) one immediately obtains $\eta = \pm u$ and $\eta = \pm v$. The corresponding expressions in terms of the rod dioptric power are listed in Table I. From Eqs. (5) and (6) we deduce that, as a function of the rod dioptric power, there are always two stability zones that are symmetrically located around the zero of the η axis and that have the same width, $\Delta\eta$, given by:

$$\Delta\eta = \Delta\frac{1}{f} = \min(|u + v|, |u - v|) = \min\left(\left|\frac{1}{B_1D_1}\right|, \left|\frac{1}{B_2D_2}\right|\right). \quad (7)$$

It is worth noting that the stability zones are crossed simply by varying the input power to the lamp. For a reason related to the misalignment sensitivity, which will be

discussed below, we denote by zone I the stability interval limited at one of the extremes by $\eta = -v$ (i.e., $B = 0$) and by zone II the interval limited by $\eta = v$ (i.e., $C = 0$). Note that v and $-v$ cannot be the boundary of the same zone. The second stability limit of each zone ($+u$ or $-u$) is immediately obtained by bearing in mind that in each zone η has a constant sign.

TABLE I. Stability limits of a resonator with a variable lens.

Stability limit	Value of η	Value of the dioptric power, $1/f$
$A = 0$	$-u$	$\frac{C_1}{D_1} + \frac{A_2}{B_2}$
$D = 0$	u	$\frac{A_1}{B_1} + \frac{C_2}{D_2}$
$B = 0$	$-v$	$\frac{A_1}{B_1} + \frac{A_2}{B_2}$
$D = 0$	v	$\frac{C_1}{D_1} + \frac{C_2}{D_2}$

The spot size ($\text{HW } 1/e^2$ of the intensity) w_3 of the TEM_{00} mode on the lens, calculated with the standard matrix method [41,42,30] by assuming that a Gaussian beam reproduces itself after one round trip, can be expressed as:

$$w_3 = \sqrt{\frac{2\lambda}{\pi}} \left[\frac{-\eta^2}{(\eta^2 - u^2)(\eta^2 - v^2)} \right]^{\frac{1}{4}}. \quad (8)$$

The plot of Eq. (8) as a function of η , i.e., of the rod dioptric power $1/f$, is shown in Fig. 2(a). The spot size w_3 goes to infinity at the stability limits and reaches a minimum in each stability zone. At this minimum, the resonator is dynamically stable [6,7,19,30] since the spot size in the rod is, at first order, insensitive to the variation of the rod focal length. Equating to zero the derivative of Eq. (8) and solving for η one obtains:

$$\eta = \pm \sqrt{uv}. \quad (9)$$

The value w_{30} of the spot size w_3 for both these values of η is

$$w_{30}^2 = \frac{2\lambda}{\pi \Delta \frac{1}{f}}, \quad (10)$$

where $\Delta \frac{1}{f}$ is given by Eq. (7). The above relationship indicates that, independently of the resonator configuration, the volume of the TEM_{00} mode in the rod at the dynamical stability is inversely proportional to the range of dioptric power for which the resonator is stable. The proportionality coefficient only depends on the laser wavelength. The

behavior of the TEM_{00} mode spot sizes reported in Fig. 2(a) shows that inside the stability zones the spot sizes have a quite smooth dependence on η ; therefore, the values of the spot sizes at the dynamical stability can be considered representative of the mode dimensions in the whole stability zone and Eq. (10) can be conveniently used for a good approximate evaluation also if the resonator is not dynamically stable.

The existence and the characteristics of the stability zones have been experimentally investigated [25] using a Nd:YAG laser with a 3 mm by 75 mm rod. The resonator was 1380 mm long and made by a convex mirror of -1200 mm radius and a plane mirror with 10% transmission. This configuration was chosen since it allows the laser to operate both in zone I and II within the current range of the power supply. The TEM_{00} was selected by using suitable apertures. Figure 3 shows the laser output power as a function of the pump power for three different distances of the rod

from the convex mirror. This figure clearly shows the existence of two well separated stability zones that are characterized by a second laser threshold at higher pump power beside the usual threshold at lower input power. All the thresholds are determined by the large diffraction losses at the stability boundaries. As predicted by the theory, at the stability edges the spot sizes rapidly diverge: this behavior explains the almost vertical drop of the output power at the stability limits. By varying the rod position inside the resonator, the input/output curves change their thresholds according to the relationship of Table I that give the rod dioptric power at the stability limits.

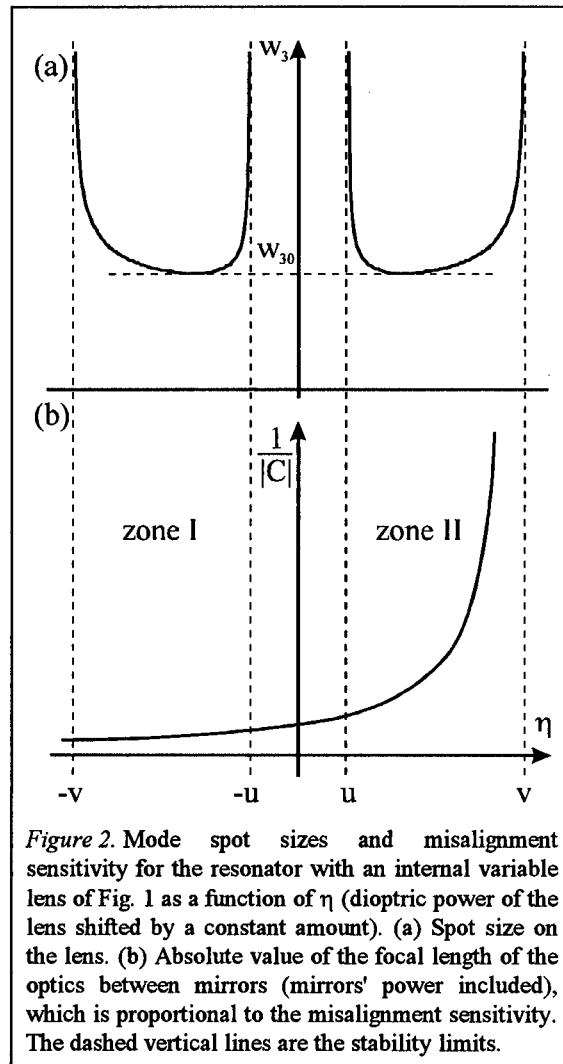


Figure 2. Mode spot sizes and misalignment sensitivity for the resonator with an internal variable lens of Fig. 1 as a function of η (dioptric power of the lens shifted by a constant amount). (a) Spot size on the lens. (b) Absolute value of the focal length of the optics between mirrors (mirrors' power included), which is proportional to the misalignment sensitivity. The dashed vertical lines are the stability limits.

3.3. PUMP POWER STABILITY RANGE

A more practical and interesting expression for the stability range is obtained by expressing the width of the stability zones in terms of the pump power [32]. The combination of Eq. (1) with Eq. (10) yields:

$$\Delta P_{in} = \frac{2\lambda}{k} \left(\frac{a}{w_{30}} \right)^2 \quad (11)$$

The quantity $(a/w_{30})^2$ is the ratio between the rod and TEM_{00} mode cross sections. For an optimized resonator, the mode cross-section in the rod must be as large as possible for a full exploitation of the active medium. Therefore, for efficient TEM_{00} mode operation the rod must be the limiting aperture. Since it has been experimentally verified that for good TEM_{00} operation the ratio between the limiting aperture radius and the mode spot size is allowed to vary between 1.2 and 2 [5,7,9,24,27,44], the ratio a/w_{30} is approximately a constant and is independent of the rod size. It is clear from Eq. (11) that, independently of the particular resonator configuration and rod dimension, the input power range for which the resonator is stable (and the laser can operate) only depends on the parameter k . This quantity is related to the opto-mechanical properties of the laser medium and on the pump power conversion rate in heat, again related to the spectroscopic properties of the material and to the pumping efficiency. In general, the pump cavity is well optimized so that the pump power conversion rate in heat is established by the given material. It follows that ΔP_{in} can be assumed as a figure of merit of the solid state laser material. As an illustrative example we have estimated the pump power stability ranges for three Nd-doped crystals, namely, YAG, GSGG and YLF, assuming $a/w_{30} = 1.7$ and using the parameter reported in

the literature for lamp pumped systems [40,45,33-36]. The results are collected in Table II. Since YLF is a birefringent crystal, for this material there are two values of the stability range related to the two emission wavelength corresponding to σ polarization ($\lambda = 1.053 \mu m$) and π polarization ($\lambda = 1.047 \mu m$). The values of ΔP_{in} of Table II have been calculated using typical data for pumping efficiency for lamp pumped lasers and can be considered representative of common situations, although

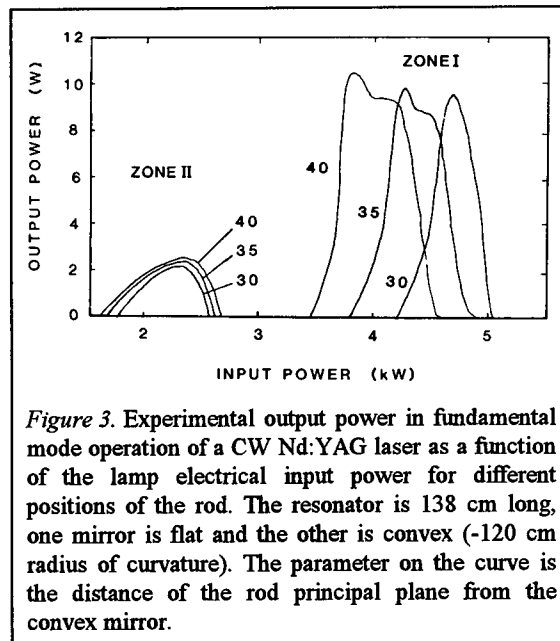


Figure 3. Experimental output power in fundamental mode operation of a CW Nd:YAG laser as a function of the lamp electrical input power for different positions of the rod. The resonator is 138 cm long, one mirror is flat and the other is convex (-120 cm radius of curvature). The parameter on the curve is the distance of the rod principal plane from the convex mirror.

slightly different results could be obtained if different relationship between thermally induced focal length and pump power are used.

TABLE II. Stability range and maximum TEM₀₀ output power for three Nd-doped crystals.

Material	Pump power stability range (W)	Maximum TEM ₀₀ output power (W) for $\Delta P_{in} / P_{in} = 15\%$
Nd:YAG	30	400
Nd:Cr:GSGG	9	70
Nd:YLF ($\lambda=1053$ nm, σ polarization)	350	8200
Nd:YLF ($\lambda=1047$ nm, π polarization)	90	1500

The relationship between pump power stability range and spot size at the dynamic stability also allows one to estimate the maximum pump power that can be extracted from a rod of a solid state laser operating on the TEM₀₀ mode. The maximum output power P_{max} is approximately proportional to the pump power P_{in} and to the mode cross section in the active material. Since the mode cross-section is inversely proportional to the pump power stability range, we conclude that

$$P_{max} \propto \frac{P_{in}}{\Delta P_{in}}, \quad (12)$$

i.e., the maximum output power is inversely proportional to the relative pump power stability range. The proportionality coefficient depends on the pumping efficiency and on the opto-mechanical properties of the material. In Table II we report the maximum TEM₀₀ output power for the three Nd doped materials considered before, calculated for a relative pump power stability range of 15%. Table II evidences the substantial advantage of nearly athermal materials, like YLF, for high power TEM₀₀ operation.

The small ΔP_{in} for Nd:YAG is certainly a significant drawback that requires a careful setting of the input power in order to obtain and maintain laser action. A more serious drawback, however, comes from the stress induced thermal birefringence, which gives rise to two different values of focal length for polarization of the beam along the radial direction, f_r , and along the tangential one, f_t . The ratio between these two values [28,40] is $f_t/f_r \approx 1.2$, while the mean dioptric power, $1/f = (1/f_r + 1/f_t)/2$, is with a good approximation proportional to the pump power entering the lamp [40]. The thermal birefringence can split the pump power stability regions for radial and tangential polarization, for large fundamental mode volumes or high input powers, to such an extent that they do not overlap. For example, if a resonator is designed to have spot size $w_{30} = 1.8$ mm, the width of the stability zone is 0.2 diopters. On the other

hand, assuming in Eq. (1) $k/\pi a^2 = 0.6 \text{ m}^{-1}\text{kW}^{-1}$ as appropriate for a 6.4 mm diameter rod [40], when the thermal lens dioptric power for tangential polarization is 3 diopters (i.e., at about 5 kW pump power) that for radial polarization is 3.6 diopters, therefore the two stability regions for different polarizations do not overlap and the laser cannot work. Therefore, for laser operation the width of the stability zone must satisfy the following condition [46]:

$$\Delta \frac{1}{f} = \frac{2\lambda}{\pi w_{30}^2} > \frac{1}{f_t} - \frac{1}{f_l} \approx 0.18 \frac{k}{\pi a^2} P_{in} \quad (13)$$

Assuming again $k/\pi a^2 = 0.6 \text{ m}^{-1}\text{kW}^{-1}$, Eq. (13) yields:

$$w_{30}^2 P_{in} < 6.3 \text{ mm}^2 \text{ kW} \quad (14)$$

This result means that the maximum achievable fundamental mode volume in a Nd:YAG rod ($\propto w_{30}^2$) at high power is limited. As an example, at an input power of 10 kW the spot size must be less than 0.8 mm. A possible solution to compensate the thermal birefringence of YAG consist in using two identical rods and a quartz 90° polarization rotator between them [47].

To overcome the problem caused by thermal lensing, two possible solutions may be envisaged: (i) reduction of the unused radiation absorbed by the rod through optimization of the pump source, (ii) use of athermal materials with low thermal focusing. Optimization of pumping and reduction of dissipated heat can be obtained with diode pumping. The second solution can be adopted in the cases where athermal materials are available (for instance, some glasses or YLF). An increment of the operating range by a factor two can also be gained designing the resonator with the two stability zones joined. It should be noted, however, that this procedure may lead to a resonator with an unacceptable high misalignment sensitivity: particular design precautions, discussed below, must be considered to avoid the divergence of the misalignment sensitivity in the middle of the operating range.

3.4. MISALIGNED OPTICAL SYSTEMS

The effects of misalignment of some components of an arbitrary optical system can be analyzed by using a 2×1 vector in addition to the usual 2×2 matrix appropriate for aligned systems [30,42,48-50]. For a generic optical system, assuming the optical axis as a reference, the position and the slope of the rays at the output plane (x_o, θ_o) are related to the corresponding quantities at the input plane, (x_i, θ_i) by an equation that, like for perfect alignment, is linear, but no longer homogeneous:

$$\begin{pmatrix} x_o \\ \theta_o \end{pmatrix} = \begin{pmatrix} A & B \\ C & D \end{pmatrix} \begin{pmatrix} x_i \\ \theta_i \end{pmatrix} + \begin{pmatrix} s \\ \sigma \end{pmatrix} \quad (15)$$

The elements of the misalignment vector (s, σ) give the position and the slope of the output ray when the input ray coincides with the reference axis of the system. The misalignment vector of a complex system is obtained by matrix multiplication on the basis of Eq. (15). Because of linearity, the superposition principle can be used to evaluate the effect of the misalignment of each simple element composing a complex system. Thus the misalignment vector is the sum of the output ray vectors obtained by assuming an input ray coincident with the reference axis and taking one misalignment

at a time. In practice, s and σ are linear combination of tilting angle and displacements of the various decentered elements.

3.5. MISALIGNMENT SENSITIVITY

The additional power losses introduced by misalignment of a component of the resonator essentially arise from the displacement of the mode axis and of the transverse field pattern on the plane of the limiting (mode-selecting) aperture, which in solid state lasers having the mode that fully utilizes the active material, is generally constituted by the rod cross-section. The position and the axis of the resonator modes coincide with the ray that retraces itself after one round trip around the resonator [30,42,48], which, for a perfectly aligned resonator, obviously coincides with the optical axis of the system. If we denote by (x_3, θ_3) the position and the slope at the reference plane marked by 3 in Fig. 1, the solution of the self-consistency equation, expressing the fact that a ray retraces itself after a round trip, gives [30]:

$$\begin{pmatrix} x_3 \\ \theta_3 \end{pmatrix} = -\frac{1}{C} \begin{pmatrix} D_2\sigma_1 + D_1\sigma_2 \\ -C_2\sigma_1 + \left(C_1 - \frac{D_1}{f}\right)\sigma_2 \end{pmatrix}, \quad (16)$$

where the symbols are defined in Fig. 1 and C is the (2,1) element of the matrix given in Eq. (5) and is the opposite of the dioptric power of the optics between the end mirrors (mirrors' power included). The detailed expression for the position and the slope of the mode axis as a function of the tilting and displacement of each decentered element can obviously be calculated only when a particular configuration is specified. However, it can be shown that the effects of mirror misalignments are given directly by Eq. (16) considering σ_1 and σ_2 as the tilting angle of the end mirrors. Eq. (16) makes clear that, whichever resonator component is misaligned, the dependence of the axis displacement on the rod focal length is always contained only in the term $1/C$. The behavior, as a function of η , of $|1/C|$ is shown in Fig. 2(b): it is apparent that one of the two stability zone, denoted by zone II, is much more sensitive to misalignment than the other, denoted by zone I. In particular, the diverging behavior in zone II might be troublesome, especially when the stability range is small.

Considering a resonator made only by the rod and the two end mirrors, we can define two misalignment sensitivity factors as [19]:

$$S_i = \frac{x_{3i}}{w_{30}} \alpha_i, \quad i = 1, 2 \quad (17)$$

where α_i is the tilting angle of end mirror i that cause the mode axis to displace by x_{3i} . Since the reduction of the output power as a consequence of misalignment is caused by the displacement of the mode away from the rod center, assuming that the decrement by a half is due to a given shifting of the mode axis, the reciprocal of the tilting angle that halves the output power can be considered proportional to the misalignment sensitivity factor given by Eq. (17). Experimental observation of the behavior of the misalignment sensitivity are reported in [20, 28].

3.6. DESIGN OF OPTIMIZED RESONATORS

On the basis of the previously discussed results we present a procedure for designing an optimized resonator [19,26]. We consider resonators made only by the focusing rod and the two end mirrors, since this approach provides for satisfactory solutions in most of the cases. Note, furthermore, that the addition of intracavity optics is not useful to increase the mode volume when the pump power stability range (i.e., the width of the stability zone) is given. The resonator has to be designed with consideration of the following requirements: (i) large mode volume in the rod, so that the active material is exploited to the greatest extent, with the rod acting as the mode selecting aperture; (ii) dynamic stability, so that the mode spot size in the rod is insensitive, to the first order, to fluctuations of pump power; (iii) minimum misalignment sensitivity, to maximize the mechanical stability of the resonator. The design procedure assumes three parameters of the laser as given, namely the rod diameter, the minimum rod focal length corresponding to the maximum pump power, and the resonator length. The rod diameter determines the maximum value of the mode spot size in the rod, which must be large enough to suppress oscillation of higher-order modes without introducing too much losses for the TEM_{00} . Our experiments indicate 1.8 as an optimum value for the ratio between the rod radius and the TEM_{00} spot size, although slightly different values can be found in the literature [5,7,9,24,44]. The minimum rod focal length depends on the pump power level at which the laser is designed to operate, and generally is determined by the maximum thermal load sustained by the rod or by the power supply limits. Lastly, the resonator length may be determined by the maximum dimensions acceptable for the laser or, in case of mode-locking operation, by the needed longitudinal-mode frequency separation. To determine the resonator configuration, which is sketched in Fig. 4, the radii of curvature of the mirrors (R_1 and R_2) and their distances from the rod principal planes (L_1 and L_2) need to be calculated, following the previous considerations. The resonator equivalent length is

$$L = L_1 + L_2.$$

Since L_1 and L_2 are the distances of the mirrors from the rod principal planes, L differs both from the physical distance between the mirrors and from the optical path length [19]. The minimization of misalignment sensitivity immediately indicates that the laser must operate in zone I, so that $B = 0$ must be one of the two stability limits. With the help of Table I, by using the matrix elements appropriate to our case, this limit can be expressed by

$$\frac{1}{L_1} + \frac{1}{L_2} = \frac{1}{f_B}, \quad (19)$$

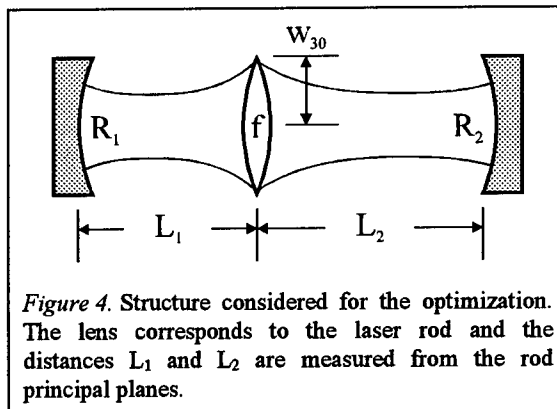


Figure 4. Structure considered for the optimization. The lens corresponds to the laser rod and the distances L_1 and L_2 are measured from the rod principal planes.

(18)

where $1/f_B$ can be set equal to $1/f_{\min}$ or to $1/f_{\min} - \Delta(1/f)$, $\Delta(1/f)$ being given by Eq. (10). The spot size w_{30} is related to the resonator configuration through Eqs. (7) and (10). Without loss of generality we can assume that for our resonator $|B_1 D_1| > |B_2 D_2|$, since the opposite case would lead to the design of a symmetric configuration. From Eqs. (7) and (10) we thus have:

$$w_{30}^2 = \frac{2\lambda}{\pi} |B_1 D_1| \quad (20)$$

that, by using the matrix element relevant to our case, can be written as:

$$w_{30}^2 = \frac{2\lambda}{\pi} L_1 \left| 1 - \frac{L_1}{R_1} \right| \quad (21)$$

Eqs. (18), (19), and (21) allow for the calculation of three of the four unknown resonator parameters, namely L_1 , L_2 , and R_1 . However, four solutions may exist, and, moreover, R_2 is still undetermined. To precisely define the resonator, the misalignment sensitivity, already controlled by the setting of the operating point in zone I, has to be optimized with the following considerations. Since the misalignment sensitivity, as given by Eq. (17), is different for the two mirrors and is a function of the rod dioptric power $1/f$, we consider for safety the worst case. We first calculate the two maximum values of the misalignment sensitivity of the two mirrors $S_1(1/f)$ and $S_2(1/f)$, reached by varying $1/f$ within the stability zone; then, we define the "worst-case" misalignment sensitivity, S_{wc} , as the higher between those two maxima. The quantity S_{wc} is a function of the distances L_1 and L_2 and of the mirror radii R_1 and R_2 , but, by definition, does not depend on the rod power $1/f$:

$$S_{wc} = S_{wc}(R_1, R_2, L_1, L_2). \quad (22)$$

By solving Eqs. (18), (19), and (21) and by minimizing S_{wc} , we obtain the following expressions that define the resonator configuration:

$$L_1 = \frac{L}{2} \left(1 + \sqrt{1 - \frac{4f_{\min}}{L}} \right), \quad (23)$$

$$L_2 = L - L_1, \quad (24)$$

$$\frac{1}{R_1} = \frac{1}{L_1} \left(1 - \frac{\pi w_{30}^2}{2\lambda L_1} \right), \quad (25)$$

$$\frac{L_1}{L_2} \frac{1}{R_1} \leq \frac{1}{R_2} \leq \frac{1}{L_2}. \quad (26)$$

Note that the greater value of the rod dioptric power in the operating zone, $1/f_{\min}$, corresponds to the stability limit $B = 0$ (i.e. $f_B = f_{\min}$). Eq. (23) shows that a real solution exists only if $L > 4f_{\min}$: this constrain is related to the fact that at the stability limit $B = 0$ the rod thermal lens images the two end mirrors onto each other and this is possible only if the distance between source and image is at least four times the focal length of the lens. Note also that the radius R_2 can be freely chosen within the interval given by Eq. (26) without affecting the stability limits, the spot size w_{30} and the value of S_{wc} . The last quantity is found to be $S_{wc} = L_2/w_{30}$ and corresponds to the misalignment sensitivity of mirror 2 at the stability limit $1/f = 1/f_{\min} - \Delta(1/f)$. Note lastly that, once the resonator has been set up, a fine optimization of the laser

performance is still experimentally possible, following [12], by moving the laser rod and leaving unchanged the total resonator length and the mirror radii.

For a given w_{30} the stability range can be doubled if the resonator is designed so that the stability zones are joined: the price paid in this case is a higher misalignment sensitivity. With the help of table I we can conclude that the two zones collapse in a wider zone if $v = 0$ or $u = 0$, in the former case, however, the stability limits $C = 0$ and $B = 0$ are reached for the same value of rod focal length and coincide with the center of the overall stability range, so that the divergence of the misalignment sensitivity occurs exactly in the middle of the stability zone, which prevents any practical utilization of such configuration. Therefore it is preferable to set $u = 0$, so that the misalignment sensitivity diverges at one of the overall stability limits. The best configuration is in this case obtained with L_1 , L_2 , and R_1 again given by Eqs. (23), (24), and (25). The radius R_2 is determined by

$$\frac{1}{R_2} = \frac{1}{L_2} \left(1 - \frac{\pi w_{30}^2}{2\lambda L_2} \right). \quad (27)$$

Note that, in this case too, the stability limit $B = 0$ corresponds to the maximum pump power level of the stability zone. Moreover note that the misalignment sensitivity diverges for a pump power corresponding to the lower limit of the overall stability zone (i.e. for $1/f = 1/f_{\min} - 2\Delta(1/f)$) and that in the center of the overall stability range mirror 1 is the more sensitive with $S_1 = L_1/w_{30}$.

The key features of the proposed design procedure that make it very simple and readily applicable can be therefore summarized as follows: the operating pump power level is essentially set only by the distances of the mirrors from the rod; the curvature of one mirror (R_1) together with its distance from the rod (L_1) determine the mode spot size in the rod; finally, the curvature of the second mirror (R_2) does not influence either the operating pump power level nor the mode volume, but only sets the misalignment sensitivity.

4. Optimized Resonator for TEM₀₀ Nd:YAG Laser

As an example of application of the procedure outlined in Sec. 3.6 we consider the design of a Nd:YAG laser using a rod of 3 mm diameter and 75 mm length. The rod focal length is $f_{\min} = 257$ mm at 5.0 kW pump power. The resonator is assumed to be 135 cm long. The appropriate spot size at the dynamically stable point for the rod diameter considered is $w_{30} = 0.83$ mm. The optimized resonator satisfying these specifications, sketched in Fig. 5(a), has $L_1 = 1006$ mm, $L_2 = 345$ mm, and $R_1 = \infty$. For the radius of curvature mirror M_2 , $R_2 = 400$ mm has been chosen, according to Eq. (26). The output is taken from the plane mirror that has a reflectivity of 80%. The output power as a function of the input power is shown as curve (a) in Fig. 5. The maximum of the curve reaches about 18 W. This laser, when mode-locked [27] with an acousto-optic modulator, gives an average output power of 14 W with pulses of 90 ps (FWHM). The short pulse duration confirms the single transverse mode operation. The optimization of the misalignment sensitivity leads to a considerable mechanical

stability: in fact, the tilting angle to reduce by 50% the output power at the peak of the curve is 1.1 mrad for the concave mirror and 10 mrad for the plane mirror.

For the same laser at the same conditions, a resonator with the joined zones has

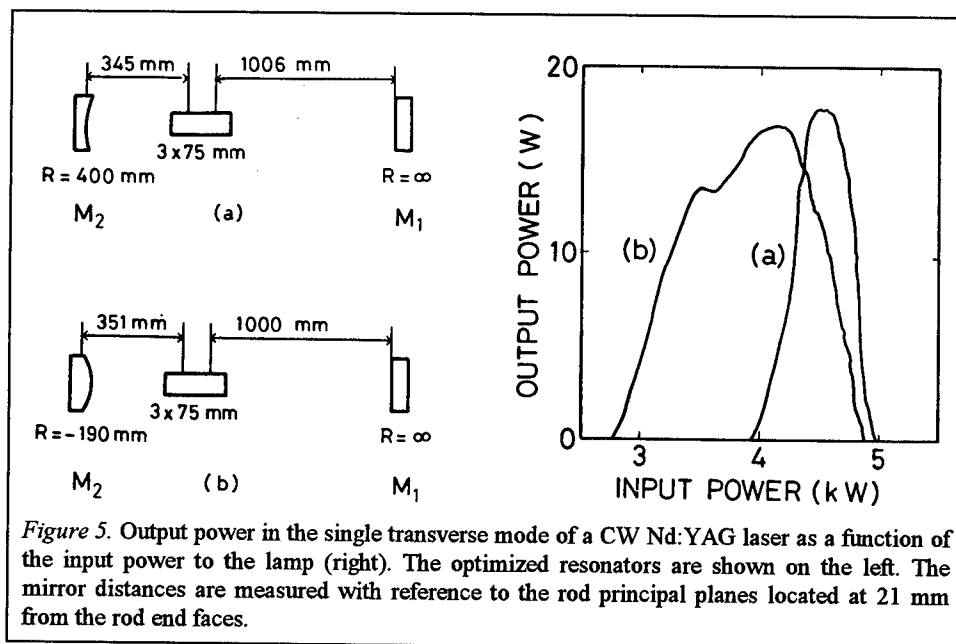


Figure 5. Output power in the single transverse mode of a CW Nd:YAG laser as a function of the input power to the lamp (right). The optimized resonators are shown on the left. The mirror distances are measured with reference to the rod principal planes located at 21 mm from the rod end faces.

also been tested. The obtained configuration is shown in Fig. 5(b): the concave mirror is replaced by a convex mirror of -190 mm radius of curvature, whereas the distances L_1 and L_2 are slightly different from those of the previous resonator to allow the utilization of the available radii of curvature for mirror M_2 . The output power curve is shown in Fig. 5 as line (b). It can be seen that also in this case the maximum power is about 18 W. The operation in mode-locking regime gives the same results as in the previous case. Although the misalignment sensitivity is higher than before, it is still satisfactory: at the peak of the output power curve the half power angle for the convex mirror is 2.2 mrad and 0.71 mrad for the plane mirror. A comparison of this results with data available from the literature and from technical data sheets, indicates that the reported value of output power (18 W) is close to the maximum obtainable from a Nd:YAG rod of the given size.

5. Optimized Resonator for TEM₀₀ Nd:YLF Laser

As shown in Fig. 5, in practice, TEM₀₀ Nd:YAG lasers of high power can only work at the value of input power corresponding to the peak of the output power curve. To overcome the limitation caused by the very small stability range of Nd:YAG, materials with lower thermal lensing (such as Nd:YLF) must be used. In the recent years high-quality Nd:YLF rods of large size have become available and CW output power as high

as 40 W [33-36] in pure TEM_{00} beams have been demonstrated. As an alternative to Nd:YAG, Nd:YLF presents the following important advantages: (i) the change of refractive index with temperature is nearly zero, so that thermal lens effects, although present, are greatly reduced; (ii) it is a uniaxial crystal, so that its natural birefringence greatly exceeds and masks the thermally induced one.

In this section we present the results we obtained by using a Nd:YLF rod of large cross-section (6.35 mm diameter) in a CW high power TEM_{00} laser. The problems connected with a large TEM_{00} mode spot size have been solved by using an appropriate resonator design both for the 1053 nm and 1047 nm transition. A careful resonator design allows us to take advantage of the higher gain of the 1047 line in terms of output power and efficiency, despite the stronger thermal lensing effects.

The Nd:YLF rod with 1% atomic Nd doping was 104 mm in length and 6.35 mm in diameter and was cut with the crystallographic axis c orthogonal to the rod axis. The rod was pumped by a 6×100 mm krypton arc lamp in a gold plated elliptic pot. By using a resonator 430 mm long with a high reflectivity concave mirror of 1 m radius of curvature, an 80% transmitting concave mirror of 1.5 m radius of curvature, and with the rod placed in the center, an output power of 80 W in multimode regime at $\lambda = 1047$ nm was achieved at 7 kW input power.

5.1. THERMAL LENS OF Nd:YLF

To appropriately design the TEM_{00} resonator a careful measurement of the thermal focal length is required. To this

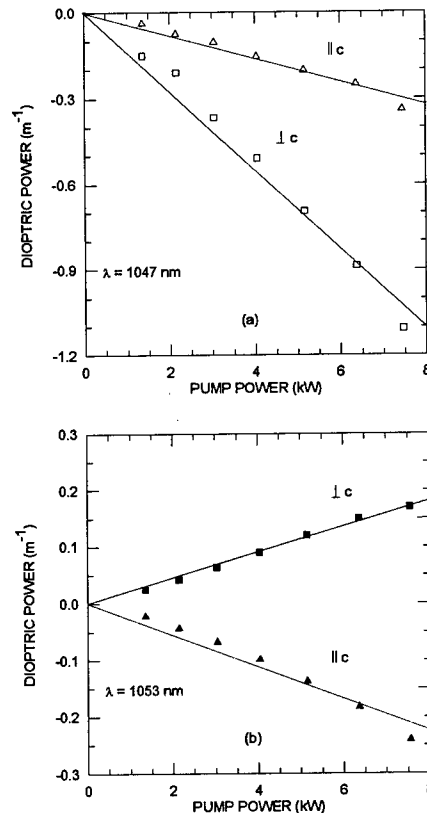


Figure 6. Dioptric power of a Nd:YLF rod (6.35 mm diameter, 104 mm length) as a function of the electrical pump power entering the lamp for two polarization of the beam. For each polarization the triangles represent the dioptric power measured in the plane parallel to c axis and the squares that in the perpendicular plane. (a) Electric field parallel to c axis; the coefficient of the interpolating straight line [Eq. (28)] are $k_x = -1.3$ m/kW and $k_y = -4.4$ m/kW. (b) Electric field perpendicular to c axis; the coefficient of the interpolating straight line are $k_x = -0.89$ m/kW and $k_y = 0.72$ m/kW.

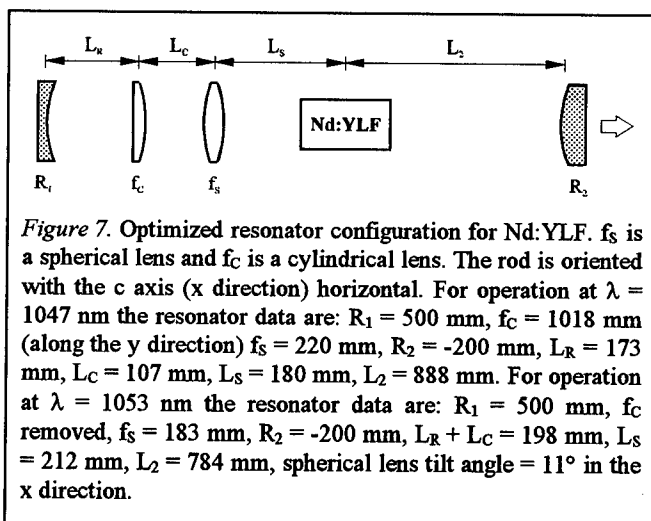
purpose, the spot size of a TEM₀₀ He-Ne passed through the pumped rod at various pump power levels has been measured at several distances from the rod. The values of the thermal focal length have been obtained by fitting the data. The Nd:YLF being anisotropic, different values of dioptric power are measured for the two different beam polarizations corresponding to the 1047 transition (electric field parallel to the c axis) and 1053 transition (electric field orthogonal to the c axis). Due to astigmatism two values of dioptric power are measured for each polarization in two orthogonal planes. The plots of the measured values of dioptric power as a function of the pump power are shown in Fig. 6. The data have been fitted, using the least mean squares procedure, by the linear relationship

$$D_{x,y} = k_{x,y} P_{in} / (\pi a^2), \quad (28)$$

D_x being the dioptric power for polarization parallel to the rod optic axis c, D_y the dioptric power along the perpendicular direction, and a the rod radius ($a = 3.18$ mm). The values of the coefficients k_x and k_y are given in the caption of Fig. 6 and substantially agree with the data reported in [34,35], except for some discrepancies which might be explained with differences in the pumping configuration. These measurements show that, although smaller than in Nd:YAG, thermal lensing effects are not negligible; furthermore, for both lines Nd:YLF presents a strong astigmatism.

5.2. RESONATOR DESIGN

Figure 7 shows the resonator structure used in the experiments: it includes a spherical lens and a cylindrical lens. The spherical lens allows operation of the resonator in a stability region of low misalignment sensitivity [36]. The cylindrical lens compensates the rod thermal lens astigmatism. The value of input power at which the astigmatism is perfectly compensated must be the highest power available from the supply. On the basis of the thermal lens data we designed and set up optimized resonators, at both 1047 nm and 1053 nm, with fundamental mode spot size w_3 inside the laser rod ranging from 1 to 2 mm. On account of the difference in the thermal lens for the polarization directions corresponding to the 1047 nm line and to the 1053 nm line, the optimized resonators are optically stable only for a specific wavelength. Therefore no tuning nor polarizing elements are required to select the operating wavelength



and polarization. To characterize the resonator, the output power, the beam profile, and the misalignment sensitivity have been measured. The beam profile has been recorded using a CCD camera. The beam was characterized by measuring its M^2 factor [51] with the following method: a waist was created, with the help of a converging lens, and its spot size w_1 is measured. A lens of focal length f was then placed after the waist and the beam spot size w_2 in its focus was recorded. The beam quality is given by $M^2 = \pi w_1 w_2 / (\lambda f)$.

5.3. EXPERIMENTAL RESULTS

The first set of experiments was carried out at 1047 nm. For values of spot size in the rod (w_3) greater than 1.65 mm, without pinholes in the cavity, a beam with a clean gaussian profile was measured. Different combinations of cylindrical and spherical lenses have been used in order to achieve astigmatism compensation at the highest lamp power. Figure 8 shows a typical input-output curve for $w_3 = 1.8$ mm, which was found to be the optimum value. With the resonator described in Fig. 7 an output power of 40 W was obtained with 7 kW pump power, with a reflectivity of the output mirror (mirror R_2 in Fig. 7) of 80%, which was the optimum value. The output power long term stability was measured to be better than 2%. Note that the threshold is determined by the optical stability of the resonator, which changes with the pump power level, and that a reasonably large input power stability range of 2 kW has been achieved. At an input power of 7 kW, corresponding to 40 W output power, the thermal astigmatism of the rod was adequately compensated and the output beam had a circular cross-section. The measured profile of the output beam at the maximum pump power is shown in Fig. 9(a) along with the gaussian fitting curve. Since a complete astigmatism compensation is obtained only at a given pumping, at an input power of 6 kW (corresponding to 20 W output power) the beam cross section was elliptical: on the output mirror the spot size along the x direction was 1.2 times larger than in the y direction. The shape of the output beam profile and the M^2 measurement, which yielded at the maximum output power the value 1.12, confirmed that the beam is essentially diffraction limited.

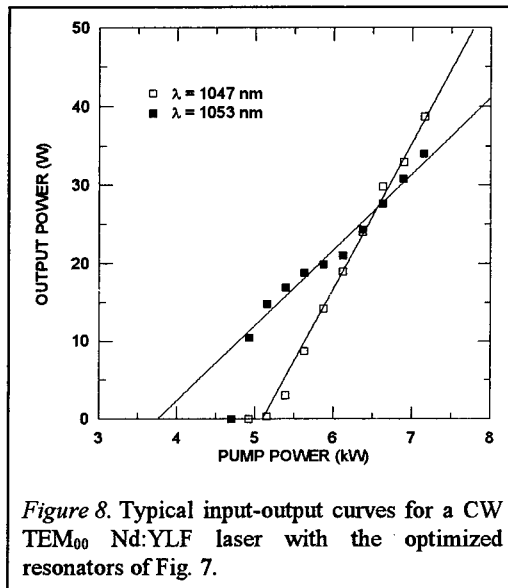


Figure 8. Typical input-output curves for a CW TEM₀₀ Nd:YLF laser with the optimized resonators of Fig. 7.

The second set of experiments was carried out at 1053 nm. Due to the higher sensitivity to intracavity losses caused by the lower gain of the transition, the cylindrical lens was removed and the astigmatism compensation was achieved by tilting the spherical lens [40], obtaining in this way two different effective focal lengths in the tangential and sagittal planes. With the resonator described in Fig. 7, which gives a spot size in the rod $w_3=1.75$ mm, using an output coupler reflectivity of 90% a maximum TEM₀₀ output power of 35 W was obtained. As the input-output curve reported in Fig. 8 shows, however, the output power drops abruptly to zero below 5 kW and the input power stability range is not as wide as would be predicted by the theory. On account of the lower astigmatism at this wavelength with respect to the 1047 nm line, the output beam cross-section remained nearly circular within a pump power range from 5 to 7 kW. The measured profile of the output beam at the maximum pump power is shown in Fig. 9(b) along with the gaussian fitting curve. At the highest output power the M^2 factor has been measured to be 1.15. The shape

of the output beam profile and the value of the M^2 factor indicate that the laser oscillates on the TEM₀₀ mode. It should be noted that with this resonator design the overall efficiency at $\lambda = 1047$ nm was 0.54% and at $\lambda = 1053$ nm was 0.46%: both these values are remarkable high for a lamp pumped TEM₀₀ laser.

Finally we evaluated the resonator sensitivity to misalignment by measuring output power as a function of the tilting angle of mirror R_1 which was the most sensitive one. The tilting angle needed to reduce the output power by 20% was about 1 mrad, which demonstrates the low sensitivity of the resonator structure to external perturbations.

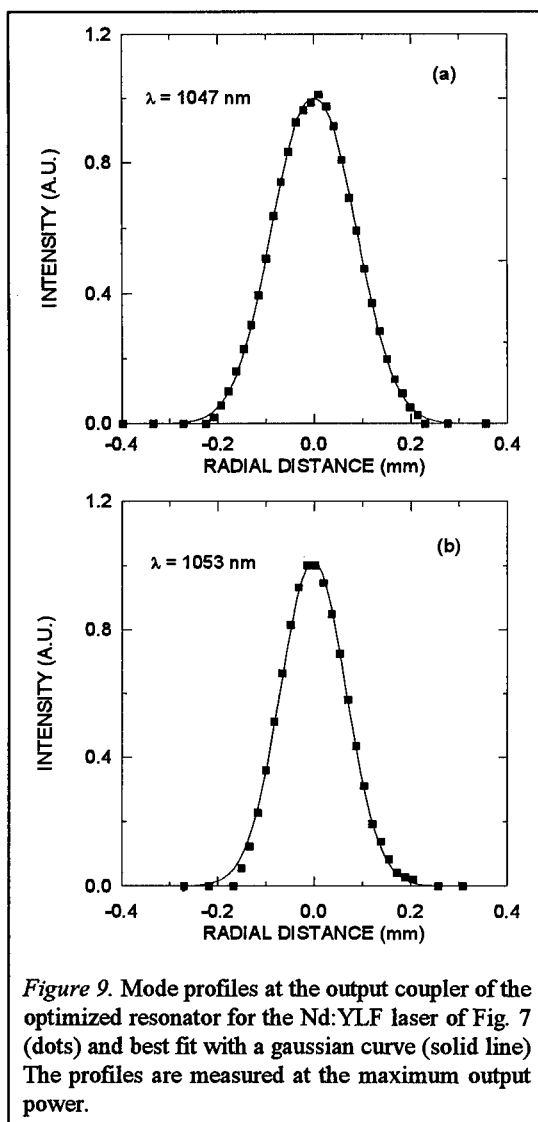


Figure 9. Mode profiles at the output coupler of the optimized resonator for the Nd:YLF laser of Fig. 7 (dots) and best fit with a gaussian curve (solid line). The profiles are measured at the maximum output power.

In conclusion, nearly perfect TEM₀₀ gaussian beams with power as high as 40 W can be generated using Nd:YLF and an optimized resonator. The experimental results indicate that the most satisfactory trade-off between thermal lensing and gain of the transition can be obtained at the wavelength of 1047 nm.

6. A High Power CW Intracavity Frequency Doubled TEM₀₀ Nd:YLF Laser

Intracavity and external resonant cavity frequency doubling of CW Neodymium lasers have been deeply studied for various applications. By using an external cavity TEM₀₀ single longitudinal mode outputs with power up to 6.5W at 532 nm have been obtained starting from an injection locked lamp pumped Nd:YAG laser [52]. If single longitudinal mode is not a requirement, intracavity frequency doubling represents a much simpler technique to achieve high output power from CW lasers. In particular, a CW lamp pumped Nd:YAG laser generating a multi-transverse mode output beam with power up to 9 W at 532 nm has been reported [53]. However, the development of CW high power intracavity doubled systems has strongly been hindered by severe power instabilities due to the nonlinear interaction of the longitudinal modes, which have been referred to as "the green problem" [54]. Recently it has been experimentally demonstrated that this problem can be effectively solved using a particular resonator design: with a long resonator operating in multi-axial-mode regime stable output beams with power as high as 14 W have been generated [55,37,56]. An alternative solution based on a ring resonator operating in single longitudinal mode has also been demonstrated [57].

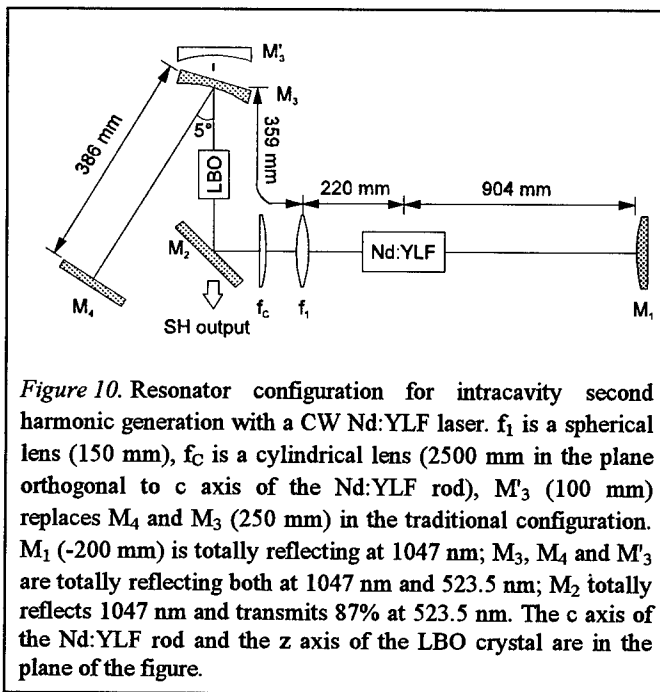
In this section we report on the development of a CW lamp pumped Nd:YLF laser intracavity frequency doubled for the generation of high power TEM₀₀ green beams ($\lambda = 523.5$ nm) and on an effective solution of the green problem that allows to obtain highly stable output power [37,55]. The key points of the developed laser mainly consist in the use of Nd:YLF as the active material, LBO as the frequency doubling crystal, and in a special resonator configuration optimized for high power TEM₀₀ operation and low sensitivity to resonator misalignment. The advantages of LBO as frequency doubler are mainly related to the possibility of type I temperature tuned noncritical phase matching (NCPM) [58]. In fact, the infrared beam remains linearly polarized as it propagates through the crystal, so that the polarization of the oscillating modes is not modified by the crystal. This property is crucial in connection to Nd:YLF that emits polarized light. The NCPM in LBO also provides a large angular acceptance and does not present the walk-off effect, so that long crystals can be used to achieve high efficiency. Finally, the resonator must be designed to provide a large TEM₀₀ mode volume in the rod, a tight focus inside the LBO crystal, and low misalignment sensitivity for stable and reliable operation.

6.1. RESONATOR DESIGN

For the experiments we used a CW lamp pumped Nd:YLF rod with 1% atomic Nd doping, 104 mm in length and 6.35 mm in diameter, cut with the crystallographic c axis orthogonal to the rod axis. The end faces of the rod were polished with opposite

tilting of 12 minutes. The LBO crystal was 15 mm long with both faces antireflection coated at 1047 nm and 523.5 nm and was mounted in an oven for temperature tuned NCPM. In these conditions the IR and SH beams propagate along the x axis of the crystal, the IR being polarized along the z axis and the SH along the y axis.

The resonator used for the experiments is shown in Fig. 10 and is basically derived from the optimized configuration described in Sect. 5. The spherical lens f_1 is designed to provide for a large mode volume in the Nd:YLF rod and to make the laser work in the low misalignment sensitivity zone. The cylindrical lens f_c compensates for the



thermal lens astigmatism of the Nd:YLF rod. Mirror M_2 is used to extract the second harmonic (SH) generated in both directions inside the nonlinear crystal. To create a focal point in the middle of the doubling crystal, a concave mirror (M_3' in Fig. 10) of radius R_3 placed at a distance $\approx R_3$ from the middle of crystal can be used. This arrangement, traditionally adopted in most of intracavity frequency doubled lasers [40], results, however, in high misalignment sensitivity. To reduce the resonator misalignment sensitivity we used a different solution: mirror M_3' was replaced by a plane mirror (M_4) and a spherical mirror M_3 that images with a suitable magnification the central plane of the crystal on the end mirror (M_4). The spot size in the Nd:YLF rod and that in the LBO crystal are the same in the two cases, but, according to theory presented in Sec. 3, this configuration presents a much lower misalignment sensitivity because the end mirror lie nearly in optically conjugated planes [30]. The resonator arm to the right of the Nd:YLF rod in Fig. 10 sets the TEM_{00} mode spot size in the rod to 1.8 mm, which is the value needed for optimum filling of the rod. In this way the laser operates on the TEM_{00} mode at 1047 nm without requiring an intracavity aperture and a wavelength selecting element, since the resonator is unstable for the second transition of Nd:YLF ($\lambda = 1053$ nm) due to the different thermal focusing. The TEM_{00} mode spot size at the beam waist inside the LBO crystal is $\approx 25 \mu\text{m}$. Mirror M_3

thermal lens astigmatism of the Nd:YLF rod. Mirror M_2 is used to extract the second harmonic (SH) generated in both directions inside the nonlinear crystal. To create a focal point in the middle of the doubling crystal, a concave mirror (M_3' in Fig. 10) of radius R_3 placed at a distance $\approx R_3$ from the middle of crystal can be used. This arrangement, traditionally adopted in most of intracavity frequency doubled lasers [40], results, however, in high misalignment sensitivity. To reduce the resonator

was used instead of a lens to avoid chromatic aberration effects and its tilting angle was kept small enough to make its astigmatism effects negligible.

6.2. EXPERIMENTAL RESULTS

The measured SH output power as a function of the intracavity IR power showed the expected parabolic behavior. Typically SH powers of 10 W could be easily obtained. At a pumping level of 7 kW the maximum measured SH power was 13.5 W in correspondence to a 155 W intracavity IR power. In this test a lens with focal length 153 mm was used instead of the concave mirror M_3 . Taking into account the residual reflectivity of mirror M_2 and the losses of the lens, the total generated power at 523.5 nm can be estimated to be 16.8 W. When mirror M_1 was replaced by one with 90% reflectivity for the IR (optimum output coupling) and the LBO temperature was detuned from the phase matching, an infrared output power of 18.5 W was obtained in correspondence to a pump power of 7 kW. This configuration, therefore, achieves about 90% conversion of the available IR power. The durability of the second harmonic crystal at these power levels is one of the major concerns of this type of systems. Bulk damage has never been observed in the various crystals tested. However, anisotropic expansion of the LBO requires particular coating to avoid damaging.

The measured degree of linear polarization of the output green beam exceeded 100:1. The measurement of the spatial quality of the green beam by the M^2 factor yielded the value 1.2 and confirmed that the green beam is essentially diffraction limited, as the infrared beam is. The ellipticity of the green beam was negligible. The LBO temperature tuning curve obtained by measuring the SH power as a function of the temperature set on the electronic oven controller changed deeply with respect to the extracavity behavior. The curve broadened from 2.8 °C to 9.5 °C (FW at half second harmonic efficiency), became asymmetric showing an abrupt drop at 162 °C, and the peak shifted by 12 °C to lower temperature. Also, a marked hysteresis was observed. All these observations can be explained, according to theoretical predictions [59], considering the crystal heating due to IR absorption.

The stability of the resonator against misalignment was characterized by measuring the reduction of the IR output power as a function of the steering angle of mirror M_3 , after detuning the LBO temperature from phase matching and replacing mirror

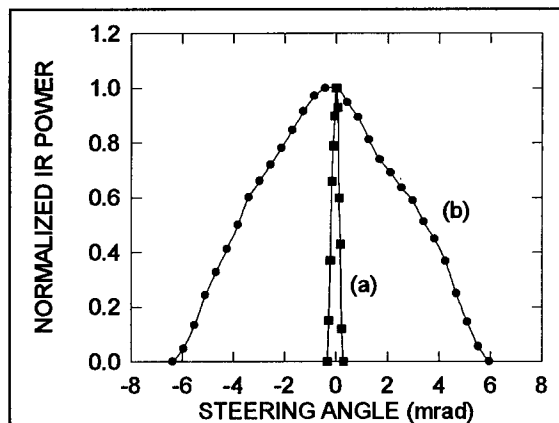


Figure 11. Normalized output power at 1047 nm as a function of the steering angle of mirror M_3 (a) or mirror M_4 (b) for the two alternative configurations shown in Fig. 10.

M_1 with a 90% reflectivity output coupler for the IR. For the purpose of comparison the measurements have been also performed on the more traditional configuration previously discussed by tilting mirror M'_3 (see Fig. 10). The data shown in Fig. 11 indicate that our configuration is about 20 times less sensitive to misalignment than the traditional one. For both resonators, the misalignment sensitivity of mirror M_1 was about one order of magnitude lower.

6.3. A SOLUTION TO THE "GREEN PROBLEM"

The temporal stability of the output power was found to be strongly dependent on the LBO alignment. With the crystal faces aligned perpendicular to the laser beam, a strongly spiking behavior was observed on a 10 ms time scale as shown in Fig. 12. When the crystal was tilted from normal incidence by 1.3° around the y axis, however, the stability improved dramatically and the peak to peak fluctuations dropped to less than $\pm 1\%$. Note that this tilting did not result in a significant change of the output power, owing to the large acceptance angle of LBO under NCPM. In this condition no significant changes in the output power were detected during hours of observation. To understand the origin of this stabilization effect upon tilting, we recorded the IR optical spectrum for the two regimes using a plane Fabry-Perot interferometer. When the crystal was tilted and the output stable, the spectrum was smooth with a bandwidth (FWHM) of ≈ 18 GHz. Taking into account the resonator length (1.92 m), this width

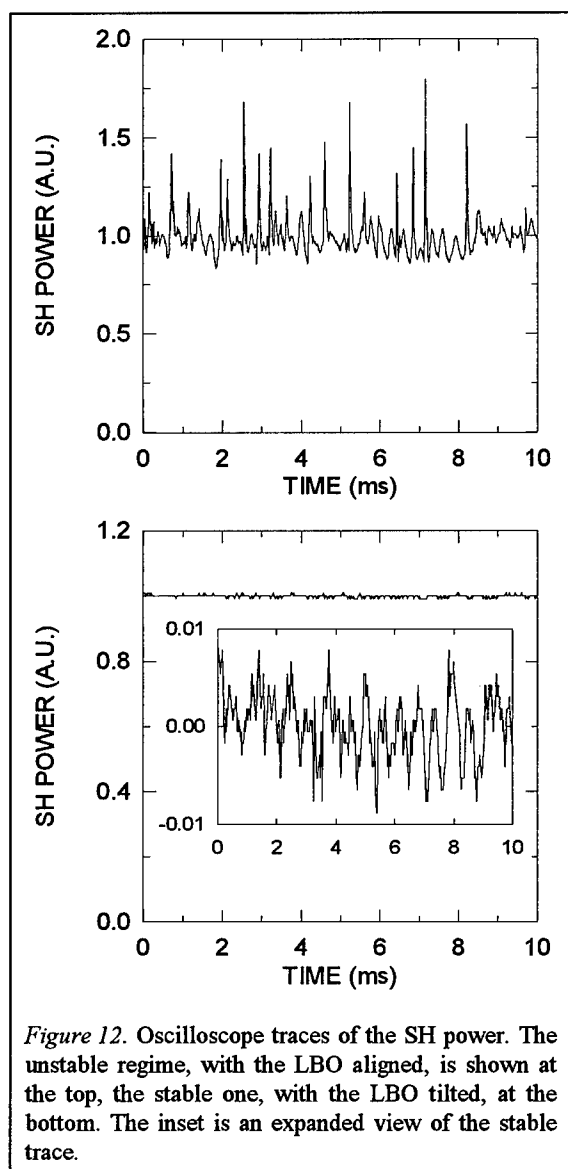


Figure 12. Oscilloscope traces of the SH power. The unstable regime, with the LBO aligned, is shown at the top, the stable one, with the LBO tilted, at the bottom. The inset is an expanded view of the stable trace.

corresponds to about 250 oscillating longitudinal modes. In the unstable regime the spectrum split up into 4-5 sub-bands separated by about 8 GHz and each containing less than 50 modes. The spectrum itself in this case was not stable because the power in the sub-bands was found to be strongly oscillating on a ms time scale.

To understand these results we recall that the dynamics of intracavity doubled lasers can be modeled by a set of rate equations, one for each longitudinal mode and one for the gain of each mode [54]. Solutions of these nonlinear equations with traditional laser parameters show instability and chaotic behavior [54,60]. The condition for the stability of the steady state solution derived in [60] predicts that the stability of the lasers increases by increasing the round trip time and the number of the oscillating modes. On the other hand it can be shown that a large ratio of the mode cross-section in the active material to that in the SH crystal tends to drive the laser unstable. On this basis we can explain the stabilization effect as being essentially due to the long resonator length and to the large number of oscillating modes. Indeed, by comparing our laser to short cavity diode pumped lasers where the green problem is usually observed we notice that the stabilization effect takes advantage by a factor $\approx 10^2$ in the number of oscillating modes (i.e., 250 instead of a few) and by a factor $\approx 10^2$ in the round trip time. On the other hand, the spot size in the active material is in our case much larger than that in the SH crystal, instead of being nearly equal, and a factor $\approx 10^3$ in the cross section ratio is therefore lost, which is however not enough to overcome the stabilization effect arising from the long cavity length. According to this interpretation, the instability observed with the LBO aligned could be explained by the reduction of the number of modes which are simultaneously oscillating, caused by some etalon effect arising from the residual reflectivity of the crystal faces. In fact, the spectral separation between two consecutive sub-bands was found to correspond to the free spectral range of such etalon. As a further proof of our interpretation we note that the insertion of a 3 mm thick glass etalon did produce a similar unstable behavior. In conclusion, the results demonstrated that the "green problem" can effectively be solved by using suitable resonators and high power CW beams in the green can be obtained with solid state lasers.

7. Conclusions

We presented a theoretical study of various problems related to stable resonators for high power diffraction limited solid state lasers, with a particular emphasis on the dynamic and mechanical stability. It has been shown that the active material thermal lens, arising from pump power dissipation in the laser rod, is a crucial element that can be usefully exploited in order to optimize the laser performance in terms of mode volume, power extraction efficiency and dynamic stability. It has also been shown that in any resonator the detrimental effects due to unavoidable mechanical instabilities can be minimized whenever a careful design is used. Finally, practical design criteria for optimized stable resonators have been derived. We proved these criteria to be successful in a few interesting cases, including high power Nd:YAG and Nd:YLF lasers. Particularly noteworthy are the performances of the CW Nd:YLF laser emitting a TEM₀₀ beam at 1047 nm of 40 W and of the CW intracavity frequency doubled

TEM₀₀ Nd:YLF laser emitting 13.5 W at 523.5 nm without the instability related to the "green problem".

8. References

1. Stickley, C. M. (1966), IEEE J. Quantum Electron. **QE-2**, 511.
2. Osterink, L. M. and Foster, J. D. (1968), Appl. Phys. Lett. **12**, 128.
3. Levine, F. A. (1971), IEEE J. Quantum Electron. **QE-7**, 170.
4. Peterson, L. M. and Carmer, D. C. (1980), IEEE J. Quantum Electron. **QE-16**, 650.
5. Chesler, R. B. and Maydan, D. (1972), J. Appl. Phys. **43**, 2254.
6. Steffen, J., Lörtscher, J. P., and Herziger, G. (1972), IEEE J. Quantum Electron. **QE-8**, 239.
7. Lörtscher, J. P., Steffen, J., and Herziger, G. (1975), Opt. Quantum Electron. **7**, 505.
8. Sarkies, P. H. (1979), Opt. Commun. **31**, 189.
9. Hanna, D. C., Sawyers, C. G., and Yuratich, M. A. (1981), Opt. Commun. **37** 359.
10. Berry, A. J., Hanna, D. C., and Sawyers, G. C. (1981), Opt. Commun. **40**, 54.
11. Hanna, D. C., Sawyers, C. G., and Yuratich, M. A. (1981), Opt. Quantum Electron. **13** 493.
12. De Silvestri, S., Laporta, P., and Magni, V. (1986), Opt. Commun. **57**, 339.
13. De Fonzo, A. P., Gitkind, N. C., Lutz, R., and Kuchta, T. A. (1988), Appl. Opt. **27**, 3604.
14. Iffländer, R., Kortz, H. P., and Weber, H. (1979), Opt. Commun. **29**, 223.
15. Kortz, H. P., Iffländer, R., and Weber, H. (1981), Appl. Opt. **20** 4124.
16. Weber, H., Iffländer, R. M., and Seiler, P. (1986), SPIE Proc. **650** 92.
17. Driedger, K. P., Iffländer, R. M., and Weber, H. (1988), IEEE J. Quantum Electron. **QE-24** 665.
18. Eggleston, J. M. (1988), IEEE J. Quantum Electron. **QE-24** 1821.
19. Magni, V. (1986), Appl. Opt. **25** 107, and Appl. Opt. **25**, 2039.
20. De Silvestri, S., Laporta, P., and Magni, V. (1986), Opt. Commun. **59** 43.
21. Fox, A. G. and Li, T. (1963), Proc. IEEE **51** 80.
22. Sanderson, R. L. and Streifer, W. (1969), Appl. Opt. **8** 2241.
23. Arnaud, J. A. (1969), Appl. Opt. **8** 1909.
24. Hauck, R., Kortz, H. P., and Weber, H. (1980), Appl. Opt. **19** 598.
25. De Silvestri, S., Laporta, P., and Magni, V., (1986), Opt. Lett. **11** 513.
26. Magni, V., Valentini, G., and De Silvestri, S. (1991), Opt. Quantum Electron. **23**, 1105.
27. De Silvestri, S., Laporta, P., and Magni, V. (1986), Opt. Lett. **11** 785.
28. De Silvestri, S., Laporta, P., Magni, V., and Svelto, O. (1987), SPIE Proc. **701** 118.
29. Metcalf, D., De Giovanni, P., Zachorowski, J., and Leduc, M. (1987), Appl. Opt. **26** 4508.
30. Magni, V., J. Opt. (1987), Soc. Am. **A 4** 1962.
31. De Silvestri, S., Laporta, P., and Magni (1988), V., Opt. Commun. **65** 373.
32. De Silvestri, S., Laporta, P., and Magni, V. (1987), IEEE J. Quantum Electron. **QE-23** 1999.
33. Vanherzeele, H. (1988), Appl. Opt. **27** 3608.
34. Vanherzeele, H. (1988), Opt. Lett. **13** 369.
35. Reed, E. and Frangineas, G. (1990), SPIE Proc. **1223** 247.
36. Cerullo, G., De Silvestri, S., Magni, V. (1992), Opt. Commun., **93**, 77-81.
37. Magni, V., Cerullo, G., De Silvestri, S., Svelto, O., Qian, L.J., and Danailov, M.B (1993), Opt. Lett. **18**, 2111.
38. Foster, J. D. and Osterink, L. M. (1970), J. Appl. Phys. **41** 3656.
39. Koechner, W. (1970), Appl. Opt. **9** 1429.

40. Koechner, W. (1996), *Solid State Laser Engineering*, 4th edition, Springer-Verlag, Berlin.
41. Kogelnik, H. (1965), *Bell Syst. Tech. J.* **44**, 455.
42. Siegman, A. E. (1986), *Lasers*, University Science Books, Mill Valley, CA.
43. Baues, P. (1969), *Opto-Electronics* **1**, 37.
44. Dembowski, J. and Weber, H. (1982), *Opt. Commun.* **42** 133.
45. Reed, E. (1985), *IEEE J. Quantum Electron.* **QE-21**, 1625.
46. Cerullo, G., De Silvestri, S., Magni, V., and Svelto, O. (1993), *Opt. Quantum Electron.* **25**, 489.
47. Scott, W. C., de Witt, M. (1971), *Appl. Phys. Lett.* **18**, 3.
48. Gerrard, A. and Burch, J. M. (1975), *Introduction to Matrix Methods in Optics*, Wiley, London.
49. Arnaud, J. A. (1976), *Beam and Fiber Optics* Academic Press, New York.
50. Nazarathy, M., Hardy, A., and Shamir, J. (1986), *J. Opt. Soc. Am. A* **3** 1360.
51. Sasnett, M. W. (1989), in *The physics and technology of laser resonators*, Adam Hilger, Bristol, p. 132.
52. Yang, S. T., Pohalski, C. C., Gustafson, E. K., Byer, R. L., Feigelson, R. S., Raymakers, R. J., and Route R. K. (1991), *Opt. Lett.*, **19**, 1493.
53. Perkins, P. E. and Fahlen, T. S. (1987), *J. Opt. Soc. Am. B* **4**, 1066.
54. Baer, J. (1986), *Opt. Soc. Am. B* **3**, 1175.
55. Cerullo, G., De Silvestri, S., Magni, V., Svelto, O., and Qian, L. J. (1993), in *Digest of Conference on Laser and Electro-Optics 1993*, Optical Society of America, Washington, DC, paper CWD7.
56. Nighan Jr., W. L., Craig, B. (1996), *Laser Focus* **32** (April), 63.
57. Selker M. D., Johnstaon, T. J., Frangineas, G., Nightingale, J. L., Negus, D. K. (1996), in *Digest of Conference on Laser and Electro-Optics 1996*, Optical Society of America, Washington, DC, paper CPD21.
58. Chen, C., Wu Y., Jiang, A., Wu, B., You, G., Li R., and Lin, S. (1989), *J. Opt. Soc. Am. B* **6**, 616.
59. Rice, R. R., Teague, J. R., and Jackson, J. E. (1978), *J. Appl. Phys.* **48**, 5750.
60. James, G. E., Harrell II, E. M., Bracikowski, C., Wiesenfeld, K., and Roy, R. (1990), *Opt. Lett.* **15**, 1141.

HIGHLY EFFICIENT HIGH-AVERAGE POWER Nd:YAG LASER WITH A PASSIVE Q-SWITCH

A. LUCIANETTI, N. G. MULLER, R. WEBER and H. P. WEBER

*Institut für Angewandte Physik
3012 Bern - Switzerland -*

A. PAPASHVILI*, V. A. KONYUSHKIN*, T. T. BASIEV*

**General Physics Institute, Russian Academy of Sciences, Moscow.*

email: lucian@iap.unibe.ch

Abstract. The performance of passively Q-switched high-average power longitudinally diode laser-pumped Nd:YAG lasers was analyzed. F_2^+ : LiF color center saturable absorbers were used as passive Q-switch. The influence of the unsaturated initial transmission, T_0 , and the pump power on the laser parameters was investigated. For T_0 between 54 % and 80 % and pump powers up to 57 W, a wide range of repetition rates, energies, durations and peak powers were obtained. A stable plane/plane resonator was chosen to have a compact and easy-to-align laser system. With $T_0 = 80$ % initial transmission, a maximum average output power of 5.8 W was achieved with 13 % slope efficiency and 50 ns pulse duration. Other parameters led to pulses as short as 10 ns.

1. Introduction

Q-switched Nd:YAG lasers are attractive coherent light sources for a large number of applications in material processing such as laser drilling [1] and laser micromachining [2]. Compact, reliable and cheap lasers are demanded for this kind of applications. Actively Q-switched lasers have been widely used to set up compact systems [3]. They are the system of choice, if specific repetition rates or pulse synchronization are needed. The disadvantage of this technique is that the laser requires an external driving circuitry and often additional optical devices like polarizers or lenses. Moreover the maximum repetition rate is usually limited to a few kilohertz. A variety of devices are suited for passive Q-switching with the effect of saturable absorption, often called "bleaching". Solid-state saturable absorbers are preferably used for passive Q-switching, because the well known dye systems acting as saturable absorbers suffer from handling and reliability issues. Using an antiresonant Fabry-Perot saturable absorber (A-FPSA) [4], passive Q-switching of microchip lasers was demonstrated [5].

Low-temperature MBE growth allows a large design freedom to adjust physical parameters of such passively Q-switched lasers, for example saturation intensity, insertion loss and modulation depth. Unfortunately, low damage thresholds, typical of semiconductors, make it difficult to scale these lasers to average power levels of several watts, as required in the micromachining applications. The passive Q-switching of cw pumped Nd:YAG laser was also demonstrated by using Cr^{4+} -doped crystals [6-9]. Stable laser operation with repetition rates of kilohertz was obtained over a large range of average output powers from hundreds of milliwatts to tens of watts. Simplicity and high damage threshold (over 40 GW/cm^2) are the characteristics of another class of saturable absorbers: Lithium Fluoride color-center crystals, $\text{F}_2^-:\text{LiF}$, ideally suited for use in compact laser-diode-pumped lasers at medium to high average output powers [10-12]. In ref. [10] a very efficient (optical slope efficiency of 40 %) laser passively Q-switched by $\text{F}_2^-:\text{LiF}$ crystals was presented, but its average output power was limited to 260 mW. In ref. [11] and ref. [12] the laser output power was 5.9 W and 24 W, respectively, but the optical slope efficiency was less than 1 % in both cases because of the flash lamp pumping.

In the present paper we describe the characterization of an all-solid-state cw diode-pumped Nd:YAG laser, operating at the wavelength of 1064 nm, passively Q-switched by $\text{F}_2^-:\text{LiF}$ crystals. A high-power end-pumped sapphire-plate cooled rod laser configuration [13] was investigated experimentally, in order to obtain both, high optical slope efficiency and high average output power. The influence of single-pass unsaturated transmissions of $\text{F}_2^-:\text{LiF}$ crystals on the laser parameter was investigated as a function of the pump power in order to achieve a large flexibility in the Q-switched pulse characteristics.

2. Experimental setup

Laser parameters of the passively Q-switched Nd:YAG laser were investigated with four different saturable absorber crystals made of $\text{F}_2^-:\text{LiF}$. The F_2^- color centers in LiF crystal are characterized by a broad absorption band centered around 960 nm, by a rather high absorption cross section ($\sigma_a = 17 \times 10^{-18} \text{ cm}^2$ at $\lambda = 1064 \text{ nm}$) and by a low saturation intensity in the range of 0.12 - 0.16 MW/cm².

The crystals used for our experiments were manufactured by the Institute of General Physics, Academy of Sciences of the USSR, Moscow. The densities of F_2^- - anions were chosen in order to provide single-pass unsaturated transmissions of $T_0 = 54 \%$, 60 %, 70 % and 80 %. The crystal lengths were 25 mm, 60 mm, 40 mm and 8 mm respectively. Due to the absorption, a fraction of the intracavity power is converted to heat inside the $\text{F}_2^-:\text{LiF}$ crystal. Controlling the temperature of the crystal is crucial in order to avoid the recombination of the color centers. Therefore the $\text{F}_2^-:\text{LiF}$ crystal was

mounted in a water-cooled copper cooling mount. Efficient thermal contact was provided by an indium foil placed between the crystal side faces and the copper mount. Fig. 1 shows the experimental setup. Compact diode laser modules (FISBA DL 50), emitting a maximum cw power of about 55 W at a wavelength of 808 nm, were used to pump the laser rod. Their radiation was focused into the Nd:YAG rod by a $f/2.5$ lens.

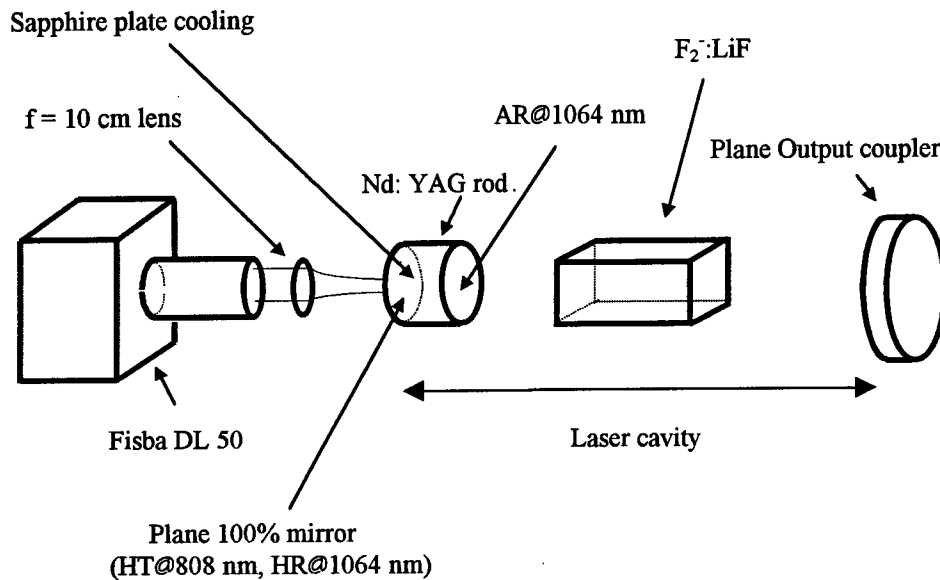


Figure 1. Experimental set-up of the longitudinally diode-pumped Nd:YAG laser with the F_2 :LiF crystal.

The pump spot diameter was measured with the knife-edge technique [14]. It had an almost rectangular shape of $1200 \mu\text{m} \times 600 \mu\text{m}$ and corresponding beam propagation factors of $M_x^2 = 450$ and $M_y^2 = 146$, respectively. During the experiments, the distance between the focusing lens and the pumped surface of the rod was adjusted in order to obtain maximum average output power. A $9.5 \times 20 \text{ mm}$ Nd:YAG rod was used as laser

crystal. The pumped face of the rod was coated for high reflectivity at 1064 nm and high transmission at 808 nm. The unpumped face was AR-coated at 1064 nm. In order to provide efficient cooling of the pumped surface, a sapphire plate was pressed directly onto the pumped rod surface [15]. Both, the cylindrical surface of the rod and parts of the sapphire plate were in contact with the cooling water. Like this, the sapphire plate provided efficient heat removal through the pumped surface. Due to the high surface quality of the rod and the sapphire plate, no water was penetrated the area between the two materials. The HR-coated surface of the rod and a plane output coupler formed a simple plane/plane resonator. Its length was set to 97 mm. This allowed to place $F_2:LiF$ crystal lengths up to 60 mm inside the resonator. The resonator was stable due to the strong positive thermal lens in the Nd:YAG rod, caused by the portion of the pump power converted to heat [16]. The lens was compensated partly by the insertion of the $F_2:LiF$ crystal giving additional stability region space inside the cavity due to its negative change of refraction index ($dn/dT = -1.2 \times 10^{-5}$). The reflectivity of the output mirror of the passively Q-switched laser was optimized for maximum average output power, depending on the single-pass unsaturated transmissions T_0 of the $F_2:LiF$ crystals.

3. Experimental results

3.A THERMAL LENS MEASUREMENT

The thermally-induced positive lens of the Nd:YAG rod and the negative lens of $F_2:LiF$ crystal influence the stability regions of the laser resonator and hence its output characteristics. Therefore the thermal lens of the rod was measured at the maximum pump power of 57 W under non-lasing conditions. A collimated He-Ne laser beam was split into a pair of parallel beams separated by a distance a with a mask with two 0.5 mm holes. The mask was aligned in such a way to have the two beams symmetric with respect to the optical axis. Then they were propagated through the Nd:YAG rod lens and a negative lens with focal length of 30 mm. The negative lens was placed at a distance $L_{lens} = 230$ mm from the rod. Finally a screen was placed at distance $L_{screen} = 650$ mm from the negative lens. On the screen the two beams were separated by a distance d . For a distance $a = 2$ mm, corresponding to about 2 times the pump diameter, a distance $d = 29$ mm was measured. From this a thermal lens of $f \cong 14$ cm was inferred. As the cavity length was shorter than the minimum value of the thermally-induced focal length, the resonator was stable up to the maximum pump power.

3.B Q-SWITCH RESULTS

During the experiments, the average output powers, repetition rates, energies per pulse, pulse durations and peak powers were measured depending on the initial transmission

of the Q-switch. The characteristics of the Q-switched diode-pumped oscillator are reported in Fig.2-6.

3.B.a Average output power

Fig. 2 shows the average Q-switched output power obtained with the different unsaturated transmissions of the $F_2:LiF$ crystals and optimized output mirror transmissions.

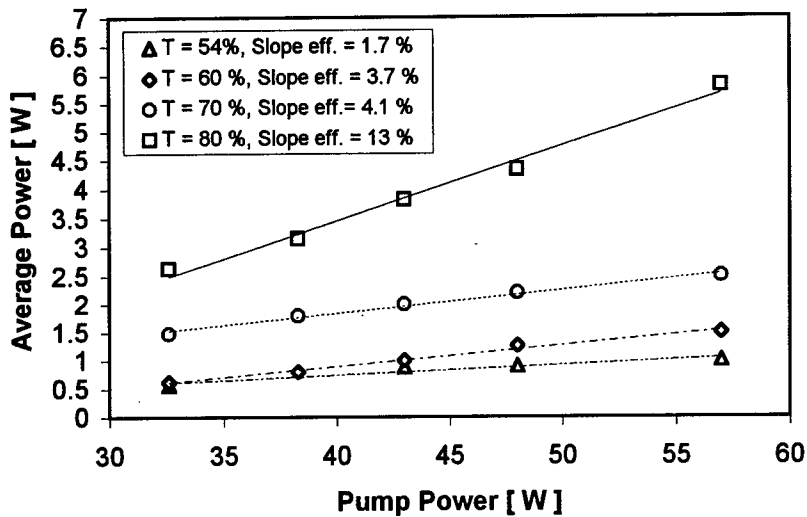


Figure 2. Average output power and slope efficiencies of the Q-switched lasers as a function of the pump power.

Optical-to-optical slope efficiencies were deduced from a linear fit to the data for every crystal length. The highest output power of 5.8 W and the highest slope efficiency achieved was 13 % with the $T_0 = 80\%$ crystal. In the cases of $T_0 < 80\%$, the slope efficiencies were decreasing with decreasing T_0 down to the minimum value of 1.7% with the $T_0 = 54\%$ crystal. An optimum reflectivity of 57% was found for $T_0 = 54\%$ and $T_0 = 60\%$. For $T_0 = 70\%$ and $T_0 = 80\%$ the optimum reflectivity of the extraction mirror was 78% and 70%, respectively.

3.B.b Repetition rate

Fig. 3 shows the dependence of the repetition rate on the pump power for different $F_2:LiF$ crystal initial transmissions. It is noted that a logarithmic scale was chosen due to the wide range of repetition rates achieved.

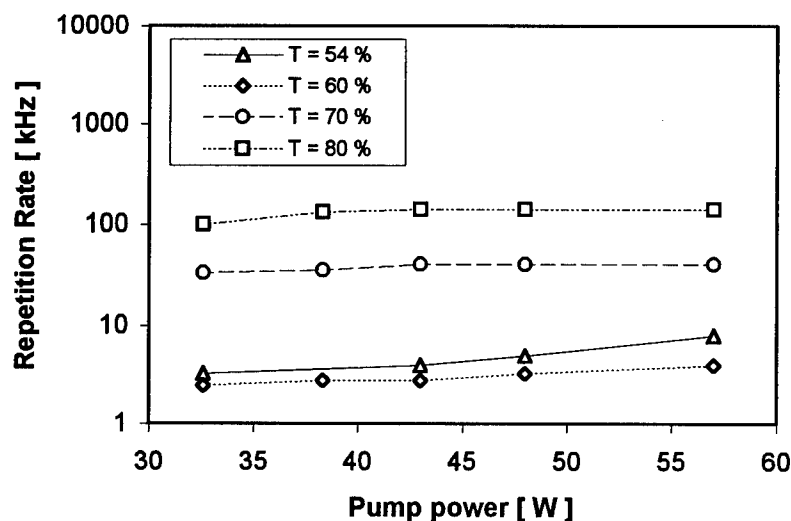


Figure 3. Repetition rate of the Q-switched laser as a function of the pump power.

A linear increase of the pulse repetition rate with pump power was observed for $T_0 < 80\%$ crystals in agreement with ref. [6]. For $T_0 = 80\%$, the repetition rate increased slightly for increasing pump powers. For pump powers beyond about 42 W the repetition rate remained at a constant value of 142 kHz. The pulse Q-switch frequency could be varied between 2.5 kHz and 142 kHz, with main steps given by the different initial transmission T_0 . Opposite to the expectations the repetition rates with $T_0 = 60\%$ were smaller than the repetition rates with $T_0 = 54\%$ for all pump powers, as cited in [17]. This is attributed partly to the high frequency fluctuations observed with low initial transmission T_0 . Thus, considering the error bar of about 25 % the repetition rates were about the same for both $T_0 = 54\%$ and $T_0 = 60\%$ color center crystals.

3.B.c Pulse energy

Fig. 4 shows the dependence of the pulse energy of the Q-switched laser on pump power. The energy was obtained by dividing the average output power with the repetition rate as shown in Fig.2 and Fig.3.

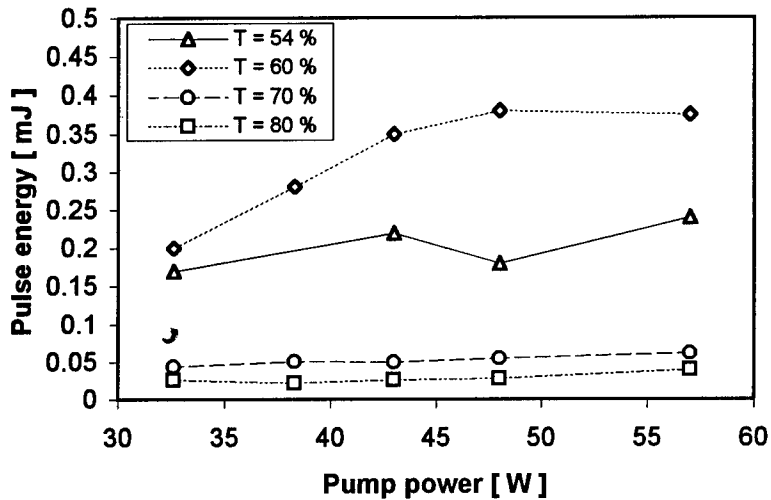


Figure 4. Energy of the Q-switched pulses as a function of the pump power.

The behavior found in Fig.4 indicates that the pulse energy from this laser system could be varied over a wide range from 22 μ J up to 0.38 mJ by varying both the initial transmission of the Q-switch and the pump power.

The pulse energy was found to increase with decreasing initial transmission. For $T_0 = 54\%$ the energies per pulse were slightly smaller than for $T_0 = 60\%$. The reason is the same, as already mentioned in Fig.3. It is also to point out that with $T_0 = 54\%$ and 48 W of pump power, the energy decreased compared to 43 W. This was due to the relatively high repetition rate ($f = 5$ kHz) at which laser was running at 48 W pump power.

3.B.d Pulse duration

Fig.5 shows the dependence of the pulse duration (full-width at half-maximum, FWHM) on the pump power.

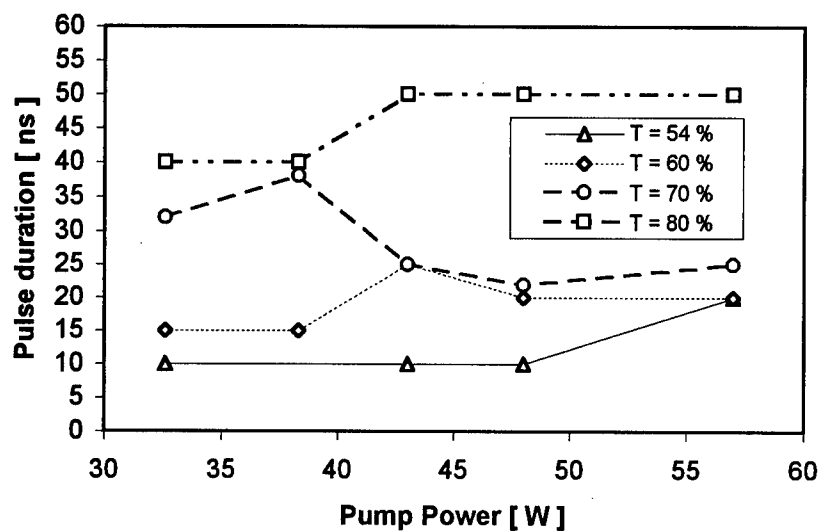


Figure 5. Pulse duration as a function of the pump power in the Q-switched laser.

The shortest pulses (10 ns) were obtained with the $T_0 = 54\%$ crystal and increased steadily with increasing initial transmission T_0 of the crystals. With $T_0 = 80\%$ the pulse width was 50 ns.

3.B.e Peak Power

Fig.6 finally shows the peak powers achieved with the passively Q-switched laser. Due to the wide range of peak powers, again, a logarithmic scale was chosen.

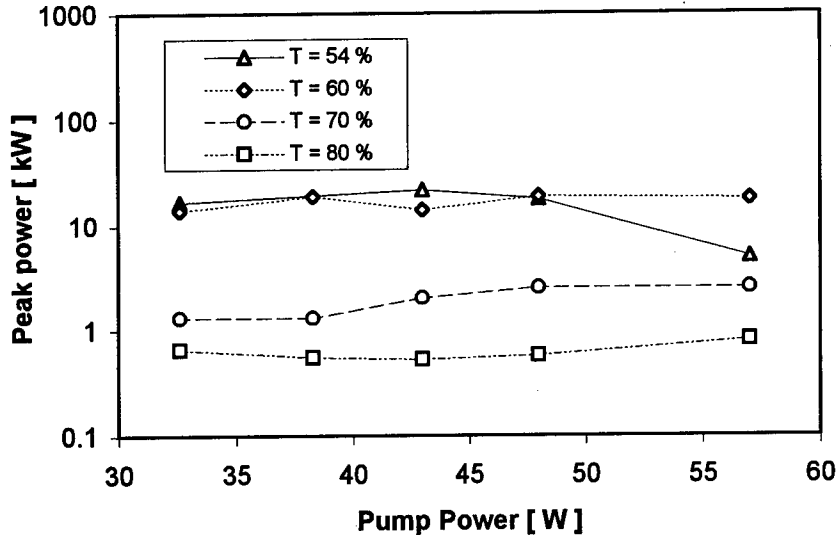


Figure 6. Peak power vs. pump power in the Q-switched laser.

The highest peak power of 22 kW was achieved with $T_0 = 54\%$ and a pump power of 43 W. This results from the small values of both pulse width and repetition rate (see Fig. 5 and Fig. 3 with $T_0 = 54\%$). The peak power, as shown in Fig. 6, decreased with increasing initial transmission T_0 of the F_2^- : LiF crystals.

There is only a small difference observed for $T_0 = 54\%$ and $T_0 = 60\%$ being less than the measurement uncertainty.

4. Conclusion

We have described the operation of a cw diode laser end-pumped Nd:YAG laser passively Q-switched by different F_2^- : LiF crystals. With a variation of the pump power and of the initial transmission of the F_2^- : LiF crystals pulse energy, repetition rate, pulse length and peak power could be varied over a wide range. This allows to easily adapt these passively Q-switched lasers to the specific requirements of applications, i.e. laser ablation or laser welding.

In conclusion, the maximum average power of 5.8 W and the maximum repetition rate of 142 kHz at a pulse duration of 50 ns was achieved with a $T_0 = 80\%$ crystal and

R = 70% output mirror. The maximum pulse energy of 0.38 mJ at a pulse duration of 20 ns was obtained with $T_0 = 60\%$ and the maximum peak power of 22 kW at a pulse duration of 10 ns with $T_0 = 54\%$. Maximum average power of 5.8 W with 13% slope efficiency is, as far as the authors are aware, the highest reported for longitudinally pumped Nd:YAG lasers Q-switched by F_2^- :LiF crystals. This is a result of the advantages of both high pump power and high slope efficiencies typical of cw longitudinal pumping.

References

1. G. Bostanjoglo, I. Sarady, Th. Beck, G. Phillips, H. Weber, Drilling of superalloys with a Q-switched Nd:YAG Laser, *Laser und Optoelektronik* **27** (6), 47-51 (1995).
2. S.V. Garnov, S.M. Klimentov, T.V. Kononenko, V.I. Konov, E.N. Lubnin, F. Dausinger, A. Raiber, Laser Processing of ceramics and metals by high intense picosecond and nanosecond laser pulses in UV, visible and IR range of spectrum, *SPIE Proceedings* **2703** (1996), 442-456.
3. W. Koechner, *Solid - State Laser Engineering*, Springer Verlag 1996, pp. 462-499.
4. L.R. Brovelli, U. Keller and T.H. Chiu, Design and Operation of Antiresonant Fabry-Perot Saturable Semiconductor Absorbers for Mode-Locked Solid-State Lasers, *JOSA B* **12** (1995), 311-322.
5. B. Braun, F.X. Kärtner, U. Keller, J. P. Meyn, G. Huber, Passively Q-switched 180-ps Nd:LaSc₃(BO₃)₄ microchip laser, *Opt. Lett.* **21** (1996), 405-407.
6. J.J. Zayhowski, and C. Dill III, Diode-Pumped Passively Q-Switched Picosecond Microchip Lasers, *Opt. Lett.* **19** (1994), 1427-1429.
7. H.J. Eichler, A. Haase, M.R. Kokta, R. Menzel, Cr⁴⁺: YAG as passive Q-switch for a Nd:YALO Oscillator with an Average Repetition Rate of 2.7 kHz, TEM₀₀ Mode and 13 W Output Power, *Appl. Phys. B* **58** (1994), 409-411.
8. Y. Shimony, Z. Burshtein, and Y. Kahlisky, Cr⁴⁺: YAG as passive Q-switch and brewster plate in a Nd:YAG laser, *IEEE J. Quantum Electron.* **31** (1995), 1738-1741.
9. Y. K. Kuo, M.F. Huang, and M. Birnbaum, Tunable Cr⁴⁺: YSO Q-switched Cr:LiCAF laser, *IEEE J. Quantum Electron.* **31** (1994), 657-663.
10. J. A. Morris, C. R. Pollock, Passive Q - Switching of a diode-pumped Nd:YAG laser with a saturable absorber, *Optics Letters* **15**(8), pp. 440-442, April 15 1990.
11. V. P. Chebotayev, S.I. Marennikov, and V. A. Smirnov, Application of LiF Crystals with F_2^- Color Centers, *Appl. Phys. B* **31** (1983), 193-199.
12. T.T. Basiev, A.N. Kravets, S.B. Mirov, A.V. Fedin, and V.A. Konyuskin, Switching of the Q factor of an industrial Nd:YAG laser using F_2^- : LiF crystals, *Sov. J. Quantum Electron.* **21**(2), 197-199, Feb. 1991.
13. S.C. Tidwell, J.F. Seamans, M.S. Bowers and A.K. Cousins, Scaling CW Diode-End-Pumped Nd:YAG Lasers to high Average Powers, *IEEE J. Quant. Electron.* **28**(4), 997-1009, April 1992.
14. A. E. Siegman, M. W. Sasnett and T.F. Johnston, Choice of Clip Levels for Beam Width Measurements Using Knife - Edge Techniques, *IEEE J. Quant. Electron.* **27**(4), 1098-1104, April 1991.

15. B. Neuenschwander, R. Weber, M. Mac Donald, M. B. Roos, and H. P. Weber, Cooling schemes for longitudinally diode laser-pumped Nd:YAG rods " submitted to IEEE J. Quant. Electron..
16. B. Neuenschwander, Investigations on Thermal Effects in Diode Laser-Pumped Solid-State Lasers, Ph.D. Dissertation, University of Bern, 1996.
17. I. Freitag and A. Tünnermann, " Passively Q-Switched, Miniature Nd:YAG Ring Lasers with Single-Frequency Output Power at 1064 nm ", in Advanced Solid State Lasers, C.R. Pollock and W.R. Bosenberg eds., *OSA TOPS* 10, 124-128.

PLANAR WAVEGUIDE LASERS OF Ti: SAPPHIRE AND Nd:YAG (YAP) GROWN BY PLD

M.JELÍNEK¹, R.W.EASON², A.A.ANDERSON², C.GRIVAS³,
D.S.GILL³, J. ŠONSKÝ¹, J. LANČŮK¹, L.M.B. HICKEY²,
N.A.VAINOS³, P.HŘÍBEK⁴

*1. Institute of Physics, Czech Academy of Sciences, Na Slovance 2,
180 40 Prague 8, Czech Republic*

*2. Dept. Of Physics and Optoelectronics Research Centre, University of
Southampton, Southampton, SO17 1BJ, UK*

*3. F.O.R.T.H.- I.E.S.L., Vasilica Vouton, P.O.Box 1527, Heraklion
71110, Crete, Greece*

*4. Faculty of Nuclear Science and Physical Engineering, Czech
technical University, V Holešovičkách 2, Prague 8, Czech Republic*

1. Introduction

Passive and active planar waveguides belong to perspective components of integrated optics and optoelectronics for generation and processing of visible and near infrared signals and for the development of new generation of integrated optics technology in which sources, non-linear structures, detectors and electronics waveguides will be produced on a single substrate. Because of this reason planar and channel waveguide lasers are of great interest during the last several years.

Waveguide lasers have excellent properties as compared with conventional bulk lasers, such as low threshold operation due to the high pumping efficiency (particularly for transitions with large population in lower laser level [1]), output power and mode pattern stability, and easy coupling with other waveguide structure devices. The future of waveguide technology is placed in the construction of widely tunable laser operating at threshold low enough to allow the pumping by laser diodes.

Planar and channel waveguide lasers were successfully created by ion implantation, liquid phase epitaxy (LPE), diffusion, thermal bonding, proton exchange

and recently also by pulsed laser deposition (PLD). The layers exhibiting at present the lowest losses were created by LPE method.

One of the novel thin film technology, the PLD, has some advantages as stoichiometric deposition of even very complex materials, a high deposition rate, enhanced film crystallinity due to the presence of high energy particles in incoming plasma plume (highly oriented or epitaxially films are grown) and the higher density in thin films than that of bulk material can be achieved. Basic experimental apparatus for laser thin film deposition consists of interaction chamber, a substrate holder with precise temperature control, and source material-target. Laser is usually located outside of the chamber.

Till now, the lasing in the following planar waveguide lasers, created by various techniques, was reached :

Er:Ti:LiNbO₃ [2,3], Nd:YAG [4,5,6,7,8,9,10,11,12,13], Yb:YAG [14,15,9], LiNdP₄O₁₂ [16], Tm:YAG [17], Ti:sapphire [18], Nd:MgO:LiNbO₃ [19,20,21], Nd:YAP [22], Nd:GGG [23], Tm:germanate glass [24], Nd:LiTaO₃ [25], Yb:Ti:LiNbO₃ [1], Yb:Er:YAG [26], TmY₂SiO₅ [27].

Recently the laser generation was obtained also in films created by method of PLD, as Nd:GGG grown on YAG substrate [28], and Ti:sapphire grown on sapphire [29].

2. Laser generation in planar waveguide lasers

The requirement of optical pumping of PW laser presents a drawback of PW lasers in comparison with diode lasers. As concern of bulk crystal pumping, a numerous pumping arrangements including longitudinal, transversal, or a hybrid set-up [6,30] have been published. A pumping arrangements of waveguide lasers include, in principle, two possible arrangements, i.e. the longitudinal (end) and the transversal (side) one. Both of them have some advantages and disadvantages. Till the time, a longitudinal pumping arrangements has been mainly used.

The longitudinal pumping arrangements is based on the coupling of pump beam into the waveguide in the direction of lasing beam. To reach a high efficient coupling of pump beam, the opposite end-faces of the waveguide has to be parallel and polished to high optical quality [16]. In the case of side pumping (pumping is perpendicular to lasing direction), three or four faces has to be polished for single or double side pumping, respectively. Hence the occasion to polish only two faces presents technological advantage of longitudinal pumping arrangements. Nevertheless the fundamental advantage of side pumping over the longitudinal pumping consists in creation of uniform inversion over the whole length of waveguide, the longer length of guide can be pumped, what results in higher slope efficiency and output power. In the case of longitudinal pumping, the length of the waveguide has to be shorter, as compared to that of side pumping, to be exploited in whole range. Thus the output power is limited to rather low average powers due to the shorter active medium. The

quality and arrangement of used mirrors significantly influence the laser efficiency. Typically the light weight plane mirrors are pressed against the waveguide ends. To avoid the damage of crystal end faces, the mirrors are sometimes separated from the waveguide end faces by thin liquid layer [7], or a large mirrors placed close to waveguide ends are used. The laser efficiency can also be increased by the coating of mirrors directly on the waveguide end faces. As the laser threshold depends on the product of the vertical and horizontal spot sizes [23], the channel structures are much advantageous for low threshold power operation. The optimum channel width depends on the waveguide height, channel structure and boundaries quality, refractive index of waveguide and surroundings, and laser wavelength and mode structure. Roughness at waveguide boundaries can lead to the scattering losses. In narrow waveguide, an enhancement of losses due to a given fabrication-induced edge roughness (e.g. 500 Å) occurs as a waveguide dimensions are reduced [31]. The smooth side walls are therefore very important. The optimum channel width can be calculated by various methods [38]. In the case of Nd:GGG [23] and Nd:YAG [7] the experimentally found optimum channel width for given layer parameters was in the range of 16÷10 µm and 20 µm, respectively. This results confirm the observation of lower waveguide losses for the larger channel width as compared to theoretical calculations, and therefore better laser performance [23]. The channel waveguide laser Nd:YAG showed a threshold reduction of 20 times compared to a PW laser.

Active-waveguides physical parameter measurements, and the rate equation analysis of the waveguide lasers, this is a journey how to receive an informations for understanding and describing the properties of the fabricated waveguides. In our case an energy level model of Nd³⁺ (or Ti³⁺) ions, and rate equation model are used for Nd:YAG(YAP) or Ti:sapphire waveguide laser design and development.

The slope efficiency and the threshold pumping power (and their dependence on the physical parameters as a stimulated emission cross-section, waveguide losses, excited level lifetime, and as well waveguide, pumping and resonator geometry) are basic characteristics such of lasers. For the Gaussian spatial distribution of the pump beam and fundamental transverse-mode oscillations the threshold pump power and slope efficiency can be described as follows [32,33]:

threshold power

$$P_{th} = \frac{\pi h \nu_p L_c}{4 \sigma_c \tau_f \alpha_p \eta_q} \left[\int_0^L \frac{\exp(\alpha_p z)}{(w_{px}^2 + w_{Lx}^2)^{1/2} (w_{py}^2 + w_{Ly}^2)^{1/2}} dz \right]^{-1} \quad (1)$$

slope efficiency:

$$S_e = \frac{(1 - R_1) \nu_L}{L_c \nu_p} [1 - \exp(-\alpha L)] \eta_q \eta_{PL} \quad (2)$$

where

$$\eta_{PL} = \frac{w_{Lx} w_{Ly} (2w_{px}^2 + w_{Lx}^2)^{1/2} (2w_{py}^2 + w_{Ly}^2)^{1/2}}{(w_{px}^2 + w_{Lx}^2)^{1/2} (w_{py}^2 + w_{Ly}^2)^{1/2}} \quad (3)$$

and

L_c is the round-trip loss exponential factor, ν_p , ν_L are the pumping and laser light frequency, τ_f is the excited level lifetime, σ_e is the stimulated emission cross-section, L is the waveguide length, R_1 is the output mirror reflectivity, α_p is the absorption coefficient of the pump radiation, η_q is the pump quantum efficiency. w_{px} , w_{py} and w_{Lx} , w_{Ly} are spot sizes for the pump and laser in the transverse direction x, y . The waveguide physical parameters as the $\text{Nd}^{3+}(\text{Ti}^{3+})$ concentration profile, absorption and emission cross section, excited level lifetime, waveguide losses, and pumping and signal mode distribution as well as waveguide pumping configuration and resonator geometry are necessary to know for the correct quantitative analysis of the waveguide amplifiers and laser generators under various experimental conditions, and for waveguide laser design and development.

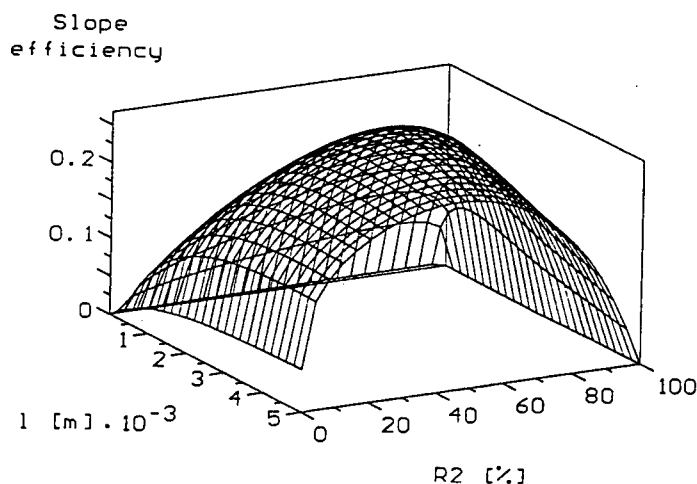


Figure 1. The evolution of the slope efficiency of longitudinally pumped Nd:YAG waveguide laser under various reflectances R_2 of the output mirror and various waveguide lengths l (the reflectance of the input endface $R_1=100\%$ at $1.064\mu\text{m}$ and summary internal waveguide laser losses 0.4 cm^{-1} where fixed)

To reach the active volume waveguide physical parameters like bulk ones is the present aim for planar active-waveguides (Nd:YAG, YAP, Ti:sapphire) fabricated by laser deposition technology and the main requirement for waveguide applications in optoelectronics. Beside the active-waveguide volume physical parameters measurement, an experimental study and theoretical analysis of waveguide amplifiers

and lasers leads to the physical properties of the fabricated planar active-waveguides characterization as well, and so to design the laser deposition conditions of active waveguides in accordance with the our demands.

The waveguide length and resonator configuration is possible to optimized and to reach efficient single mode generation by the waveguide lasers rate equation analysis. On Figure1 is shown an evolution of the slope efficiency of longitudinally pumped Nd:YAG waveguide laser under various reflectances R_2 of the output mirror and various waveguide lengths l . The reflectance of the input end-face R_1 (100% at $1.064\mu\text{m}$) and whole internal waveguide laser losses (40 m^{-1}) where fixed. The ratio of the pumping and signal mode was equal one and the Nd:YAG bulk physical parameters has been used at the calculations. For given active waveguide physical parameters the laser length l and the output reflectivity mirror R_2 an optimum values for given pump and fundamental mode spot sizes Figure1.

3. Results of PLD Ti: sapphire, Nd:YAG and Nd:YAP

We have created the active waveguide films of Ti:sapphire, Nd:YAG and Nd:YAP by laser ablation using KrF excimer laser working at wavelength of 248 nm . Sapphire of (0001) and (1102) orientations, fused silica and quartz of (0001) orientation were used for deposition of Ti:sapphire films. The Ti:sapphire films were created from crystalline Ti:sapphire targets (0.1 wt% of Ti_2O_3 , 0.12 wt% of Ti_2O_3 and 0.49 wt% of Ti_2O_3). The crystalline films of Ti:sapphire/sapphire of thickness around 10 nm exhibited waveguide losses were in the range from 1 to 4 dB/cm [34]. The films of Ti:sapphire/quartz (thickness $200\text{ nm} \div 1000\text{ nm}$) were also waveguiding. Lasing around 800 nm was observed in Ti:sapphire films grown on sapphire substrate. The waveguide layer was pumped by an argon ion laser, running on all blue green lines, with an absorbed power threshold of 0.56 W using high reflectivity ($R > 98\%$) mirrors. Using a 5% pump duty cycle and a $T = 35\%$ output coupler, a slope efficiency of 26% with respect to absorbed power is obtained, giving quasi-cw output powers in excess of 350 mW [29].

The films of Nd:YAG and Nd:YAP were ablated from monocrystalline Nd:YAG and Nd:YAP targets doped with 0.59 wt% of Nd and 0.64 wt% of Nd, respectively. The films were grown on YAP of (001) orientation and sapphire substrate of (0001) and (1102) orientations. The films were waveguiding and they supported from 6 to 30 modes dependently on the film thickness. Propagation losses as low as $0.5 \div 0.8\text{ dB/cm}$ were measured on 632.8 nm wavelength by dark mode prism coupling method. We believe that lasing will be obtained in near future.

4. Conclusion

This work demonstrates that PLD is becoming directly competitive with the other more established methods of making waveguide lasers. The laser quality films of Ti:sapphire was produced, and high quality Nd:YAG (YAP) layers were created. We believe that PLD method will be widely used for study of wide scale of materials suitable for development of planar waveguide lasers.

5. Acknowledgments

The work was supported by the grant agency of Czech Republic, Grant No. 102/96/0429

6. References

1. Jones, J.K., de Sandro, J.P., Hempstead, M., Shepherd, D.P., Large, A.C., Tropper, A.C., Wilkinson, J.S. (1995) Channel waveguide laser at 1 μm in Yb-indiffused LiNbO₃, *Optics Letters* **20**, 1477-1479.
2. Brinkmann, R., Sohler, W., Suche, H. (1991) Continuous-wave erbium-diffused LiNbO waveguide laser, *Electronics Letters* **27**, 415-417.
3. Suche, H., Wessel, R., Westenhofer, S., Sohler, W., Bosso, S., Carmannini, C., Corsini, R. (1995) Harmonically mode-locked Ti:Er:LiNbO waveguide laser, *Optics Letters* **20**, 596-598.
4. Field, S.J., Hanna, D.C., Shepherd, D.P., Tropper, A.C., Chandler, P.J., Townsend, P.D., Zhang, L. (1991) Ion Implanted Nd:YAG Waveguide Lasers, *IEEE Journal of Quantum Electronics* **27**, 428-433.
5. Hanna, D.C., Large, A.C., Shepherd, D.P., Tropper, A.C., Chartier, I. B., Ferrand, B., Pelenc, D. (1993) Low threshold quasi-three-level 946nm laser operation of an epitaxially grown Nd:YAG waveguide, *Appl. Phys. Lett.* **63**, 7-9.
6. Hanna, D.C., Large, A.C., Shepherd, D. P., Tropper, A.C., Chartier, I., Ferrand, B. (1992) A side-pumped Nd:YAG epitaxial waveguide laser, *Optics Communications* **91**, 229-235.
7. Field, S.J., Hanna, D.C., Large, A.C., Shepherd, D.P., Tropper, A.C., Chandler, P.J., Townsend, P.D., Zhang, L. (1991) Low threshold ion-implanted Nd:YAG channel waveguide laser, *Electron. Letters* **27**, 2375-2376.
8. Chandler, P.J., Field, S.J., Hanna, D.C., Shepherd, D.P., Tropper, A.C., Townsend, P.D. and Zhang, L. (1989) Ion-implanted Nd:YAG planar waveguide laser, *Electronics Letters* **25**, 985-986.
9. Sugimoto, N., Ohishi, Y., Katoh, Y., Tate, A., Shimokozono, M., Sudo, S. (1995) A ytterbium- and neodymium-co-doped YAG, *Appl. Phys. Lett.* **67**, 582-584.
10. Pelenc, D., Chambaz, B., Chartier, I., Ferrand, B., Via, J.C. (1991) Epitaxial growth of garnets for thin film lasers, *J. de Physique* **1**, 311-314.
11. Ferrand, B., Pelenc, D., Chartier, I., Wyon, Ch. (1993) Growth by LPE of Nd:YAG single crystal layers for waveguide laser applications, *Journal of Crystal Growth* **128**, 966-969.
12. Grabmaier, J.G., Grabmaier, B.C., Kersten, R.Th., Plattner, R.D., Zeidler, G.J. (1973) Epitaxially grown Nd-laser-films, *Physics Letters* **43A**, 219-220.
13. Warburton, T.J., Shepherd, D.P., Tropper, A.C., Hanna, D.C. (1996) A Thermally Bonded Nd:YAG Planar Waveguide Laser and Amplifier, *CLEO EUROPE EQEC Hamburg, Paper CFH6*, p.347.
14. Pelenc, D., Chambaz, B., Chartier, I., Ferrand, B., Wyon, C., Shepherd, D.P., Hanna, D.C., Large, A.C., Tropper, A.C. (1995) High slope efficiency and low threshold in a diode-pumped epitaxially grown Yb:YAG waveguide laser, *Optics Communications* **115**, 491-497.

15. Hanna, D.C., Jones, J.K., Large, A.C., Shepherd, D.P., Tropper, A.C., Chandler, P.J., Rodman, M.J., Townsend, P.D. and Zhang, L. (1993) Quasi-three level 1.03 μm laser operation of a planar ion-implanted Yb:YAG waveguide, *Optics Communications* **99**, 311-315.
16. Kubodera, K., Otsuka, K. (1979) Single-transverse-mode $\text{LiNdP}_4\text{O}_{12}$ slab waveguide laser, *J. Appl. Phys.* **50**, 653-659.
17. Borel, C., Remeix, A., Thony, P., Ferrand, B., Shepherd, D.P., Large, A.C., Warbuton, T.J., Tropper, A.C., Hanna, D.C. (1996) Growth by Liquid Phase Epitaxy and Laser Performance at 2.012 μm of a Tm:YAG Planar Waveguide, *Photonics West - SPIE*, San Jose, 37-41
18. Hickey, L.M.B., Anderson, A.A., Wilkinson, J.S. (1997) Ti:sapphire channel waveguide laser by thermal diffusion of titanium into sapphire, *Europ. Conf. Int. Opt. Stockholm*, Paper PD6-1.
19. Field, S.J., Hanna, D.C., Shepherd, D.P., Tropper, A.C., Chandler, P.J., Townsend, P.D., Zhang, L. (1991) Ion-implanted Nd:MgO:LiNbO₃ planar waveguide laser, *Optics Letters* **16**, 481-483.
20. Lallier, E., Pocholle, J.P., Papuchon, M., de Micheli, M., Li, M.J., He, Q., Ostrowsky, D.B., Grezes-Besset, C., Pelletier, E. (1990) Efficient Nd:MgO:LiNbO₃ waveguide laser, *Electronics Letters* **26**, 927-928.
21. Lallier, E., Pocholle, J.P., Papuchon, M., de Micheli, M., Li, M.J., He, Q., Ostrowsky, D.B., Grezes-Besset, C., Pelletier, E. (1991) Nd:MgO:LiNbO₃ channel waveguide laser devices, *IEEE Journal of Quantum Electronics* **27**, 618-625.
22. Field, S.J., Hanna, D.C., Shepherd, D.P., Tropper, A.C., Chandler, P.J., Townsend, P.D., Zhang, L. (1990) Ion-implanted Nd:YAP planar waveguide laser, *Electron. Lett.* **26**, 1826-1827.
23. Field, S.J., Hanna, D.C., Large, A.C., Shepherd, D.P., Tropper, A.C., Chandler, P.J., Townsend, P.D., Zhang, L. (1992) Ion-implanted Nd:GGG channel waveguide laser, *Optics Letters* **17**, 52-54.
24. Ezaki, M., Kumagai, H., Kobayashi, K., Toyoda, K., Obara, M. (1995) Crystal Growth of Nd:YAG Laser Films on Various Substrates by Pulsed Laser Deposition, *Jpn. J. Appl. Phys.* **34**, 6838-6841.
25. Nouh, S., Baldi, P., Hadi, K.E., de Micheli, M., Monnom, G., Ostrowsky, D.B., Lallier, E., Papuchon, M. (1995) Fabrication parameter optimization of a low-threshold high-efficiency proton-exchanged waveguide laser in Nd:LiYTaO₃, *Optics Letters* **20**, 1468-1470.
26. Shepherd, D.P., Hanna, D.C., Large, A.C., Tropper, A.C., Warbuton, T.J., Borel, C., Ferrand, B., Pelenc, D., Rameix, A., Thony, P., Auzel, F., Meichenin, D. (1994) A low threshold, room temperature 1.64 μm Yb:Er:YAG waveguide laser, *J. Appl. Phys.* **76**, 7651-7653.
27. Remeix, A., Borel, C., Ferrand, B., Wyon, C., Shepherd, D.P., Warburton, T.J., Tropper, A.C., Hanna, D.C. (1996) First laser operation of an epitaxially grown Tm:Y₂SiO₅ waveguide, *CLEO EUROPE EQEC Hamburg*, paper CFD1, p.327.
28. Gill, D.S., Anderson, A.A., Eason, R.W., Warburton, T.J., Shepherd, D.P. (1996) Laser operating of an Nd:Gd₃Ga₅O₁₂ thin-film optical waveguide fabricated by pulsed laser deposition, *Appl. Phys. Lett.* **69**, 10-15.
29. Anderson, A.A., Eason, R.W., Hickey, L.M.B., Jelinek, M., Grivas, C., Gill, D.S., Vainos, N.A. (1997) A Ti:sapphire planar waveguide laser grown by pulsed laser deposition, *Opt. Letters* -in print.
30. Baer, T.M., Head, D.F., Sakamoto, M. (1989), in *Digest of Conference on Laser and electro-optics* (Optical Society of America, Washington, D.C.), paper FJ5.
31. Tamir, T. (1988) *Guided-Wave Optoelectronics*, Springer Series in Electronics and Photonics 26, Springer Verlag.
32. Clarkson, W.A., Hanna, D.C. (1989) Effects of transverse-mode profile on slope efficiency and relaxation oscillations in a longitudinally-pumped laser, *J. of Modern Optics* **36**, 483-498.
33. Chin-Ting Lee, Lih-Gen Sheu, (1996) Analysis of Nd:MgO:Ti:LiNbO₃ waveguide lasers with non-uniform concentration distribution, *Journal of Lightwave Technology* **14**, 2268-2270.
34. Anderson, A.A., Eason, R.W., Jelinek, M., Hickey, L.M.B., Grivas, C., Fotakis, C., Rogers, K., Lane, D. (1996) Waveguiding and Crystallographic Properties of Single Ti:sapphire Layers Produced by Pulsed Laser Deposition, *CLEO/ EUROPE EQEC 96, Hamburg*, 79.

PROBLEMS OF CW CHEMICAL LASERS SCALING

A.S. Bashkin, B.I. Katargin, N.A. Pirogov
NPO Energomash,
Burdenko 1, Khimky, 141400 Moscow region, Russia

1. Introduction

NPO Energomash is a Russian leader in the field of the self-contained combustion-driven supersonic mixing HF cw chemical lasers development. Since 1972 a large number of numerical, design, technological and experimental research works have been carried out and as a result of these works HF cw chemical lasers with a flat nozzle array of different sizes providing lasing power from several kW to 400 kW were built. The purpose of the given paper is to analyze the principal physical and design problems that arise at scaling active media such lasers (both in height and in length).

One of the problems is caused by the mechanism of active medium production in the course of an exothermic chemical reaction proceeding at mixing of supersonic flows, one of which contains atomic fluorine (oxidizer flow) and other contains molecular hydrogen (fuel flow) (Fig. 1a). The fluorine atoms are generated in a combustion chamber due to thermal dissociation of excess F_2 or NF_3 at the expense of heating caused by burning of these compounds with molecular deuterium. Then the atomic fluorine flows through the supersonic nozzle thus being cooled up to a temperature not higher $300^\circ K$ and accelerated to supersonic velocity. At the exit plane of the nozzle array this flow mixes with a molecular hydrogen flow. As a result of cross diffusion and the following chemical pumping reaction $F + H_2 \rightarrow HF(v) + H$ vibration-excited molecules $HF(v)$ appear that form active medium in such lasers.

Unfortunately it was revealed that under HF molecules collisions the high-rate V-T relaxation of $HF(v)$ molecules takes place. Its negative influence can be reduced only by means of mixing process acceleration of the initial supersonic flows. There are two ways to do it: to apply nozzle arrays with a very small step and to decrease mixing flows pressures to a few torr. The slit supersonic nozzles are in common use for the oxidizer flow. The fuel supply can be performed through slit supersonic nozzles as well, but the systems of small discrete jets are of frequent use to intensify the mixing process and to provide the higher strength of nozzle array.

Furthermore, the supersonic oxidizer nozzle length must be very small to avoid the detrimental process of atomic fluorine recombination and its transformation into molecular fluorine. But in this case there arises a problem of stiffness and strength of the fine nozzle array that must withstand pressure difference from one atmosphere or above in the combustion chamber to a few torr in active medium. It restricts unlimited increasing the flat nozzle array height. Nonuniformity along the nozzle array height of the H_2 outflow through the holes in walls of special channels

(see Fig.1 a,b) with the diameter restricted by the nozzle vane thickness is also a factor limiting such increasing. So the increase of dimensions of the flat nozzle array in height is a design problem.

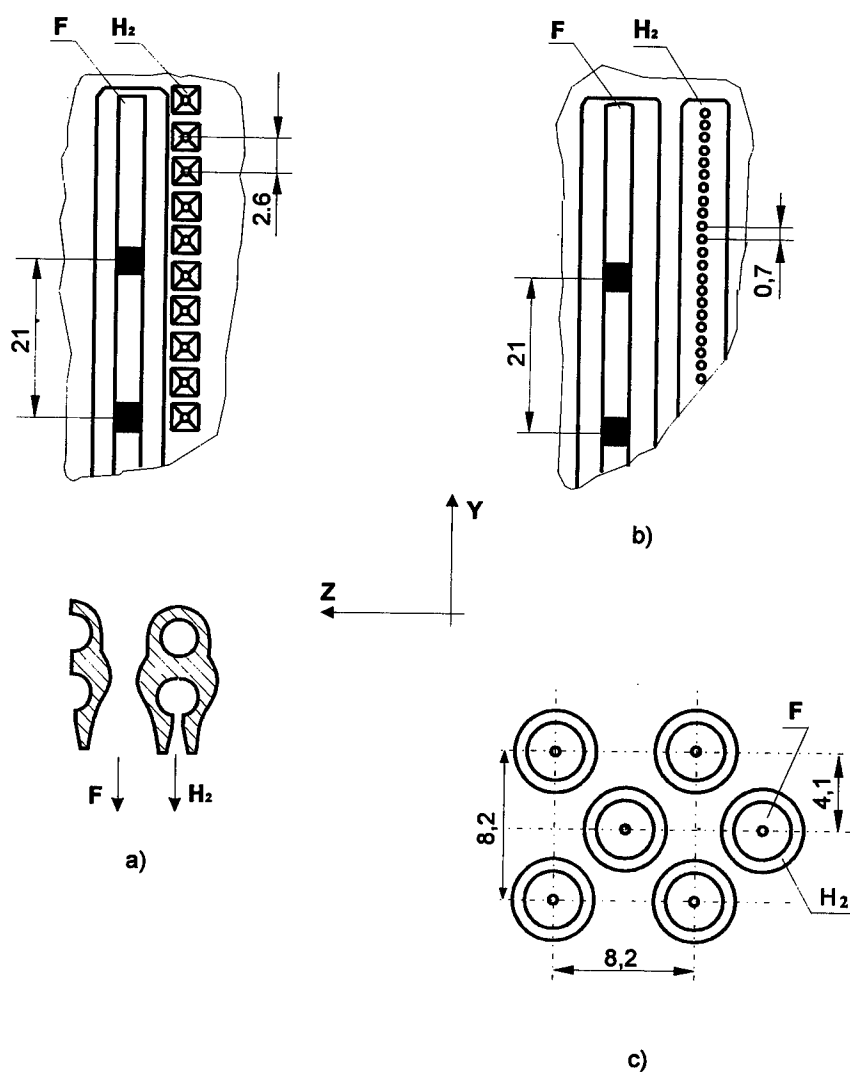


Figure 1. Configurations of the nozzle arrays of intermediate size cw chemical lasers: (a) slit oxidiser nozzles and pyramidal structure of fuel nozzles; (b) slit oxidizer and fuel nozzles; (c) axial symmetric conical nozzles for oxidizer and fuel.

It seems at first glance that the active medium can be lengthened as long as you want because there are no principal design difficulties in the last resort summing the length of the subsequent modules along the common optical axis. But a number of physical factors restricts the lengthening of active medium due to the increase of optical inhomogeneities and the restriction of the output lasing power increase because of dissipative losses and possibility of superluminescence excitation. Let us consider these factors influence and the possibility of their decrease.

2. Influence of the optical inhomogeneities

Minimal value of laser beam divergence is determined by phase distortion of the radiation wavefront arising in active medium. In case of HF cw chemical laser two main types of optical inhomogeneities can be distinguished: small-scale one caused, for example, by the necessity of spaced discrete supply of fuel flows for the better mixing and thus having as a rule periodic structure and large-scale one (comparable with the laser zone width) caused by limited velocity of reagents mixing, change of chemical composition, temperatures and active medium density, and due to the possibility of its transversal expansion via the flows movement direction. It should be noted that the compensation of wavefront phase distortion of the laser beam passing through active medium with the large-scale optical inhomogeneities does not meet any principal difficulties because it can be achieved with adaptive optics. Another situation occurs in case of small-scale periodic inhomogeneities which influence can not be avoided with adaptive optics due to small sizes of these inhomogeneities. That's why a special attention in our research was paid to measurement and searches for ways to decrease the level of such inhomogeneities in active medium of HF cw chemical lasers of two types: with an output power of 20-30 kW (these lasers were of intermediate size with the mass flow rate of 100-200 g/s and the nozzle array area of 10.8 cm × 40 cm) and with an output power of 300-400 kW (large size lasers with the mass flow rate of 1.5-1.8 kg/s and the nozzle array area of 40 cm × 150 cm). Specific power of these lasers was not less than 200 J/g.

Lateral shear interferometer was applied for the experimental measurement as the most suitable for operation under conditions of laser facility vibration. Ne-He laser radiation was used as probe beam. The phase distortion value was then recalculated for the operating wavelength about 3 μ .

We have analyzed the influence of the laser gasdynamic operational parameters and its nozzle array design features on the level of phase distortion. Some schemes of the investigated different nozzle arrays of intermediate size laser are shown in Fig. 1. Fig. 1a shows a mixing scheme with discrete hydrogen injection through a pyramidal nozzles. In this case each separate row of supersonic fuel nozzles was placed along the slit oxidizer nozzles and consisted of a set of adjoining small nozzles with a 2.6 mm step in form of quadrangular truncated pyramids. Such structure provided a fairly high amplitude of the wavefront phase distortions per 1m of active medium length equal to $0.2 \lambda \text{ m}^{-1}$. Approximately the same high level of phase distortions ($\sim 0.1 \lambda \text{ m}^{-1}$) took place for cw chemical lasers with the nozzle array shown in Fig. 1c where axial symmetric conical nozzles spaced in a

chessboard manner and intended for intensification of the mixing of oxidizer and fuel flows were used.

In order to decrease the amplitude of phase distortions the system of pyramidal nozzles for the fuel supply was replaced with a structure similar to the slit nozzle which principle of construction is shown in Fig. 1b, where fuel jet holes had a smaller step of 0.7 mm and were buried in the nozzle array body in such a way that their supersonic part downstream of the throat had the form of continuous profiled widening slit. In this case the well mixed fuel jets comes to the nozzle array exit plane in spite of the holes periodic system availability. This has provided considerable decrease of small-scale phase distortions amplitude of the wavefront to the value not more than $0.02\lambda \text{ m}^{-1}$ that corresponded to the measurement accuracy.

The method of self-compensation of small-scale periodic inhomogeneities predicted in [1] was tested on the intermediate size cw chemical laser. The essence of this phenomenon lies in the periodic structure inclination to the optical axis by an angle where the self-compensation takes place in geometrical optics approximation. This angle α can be found from the relation $\sin \alpha = j (d/L)$, where d - period of small-scale periodic inhomogeneities, L - length of active medium and j - the integer. Really for cw chemical laser with a nozzle array shown in Fig. 1a the phase distortions wavefront amplitude was decreased by about 3 times under the inclination angle increase from $\alpha=0$ to $\alpha=2d/L$.

3. Demonstration of possibility of cw chemical laser scaling (large size laser)

When we were further scaling cw chemical laser it was natural to put in its construction the best principles of the nozzle array configuration for intermediate size cw chemical laser. But it appeared to be complicated to increase simply proportionally the dimensions of the nozzle array as in that case stiffness and strength of its construction was sharply decreased and the density distribution uniformity of the fuel outflow along the nozzle array height as well. As a result in the design of one of the constructions of a flat nozzle array it was decided to divide the nozzle array into sections with 40 cm height that was essentially larger than a width of the each section (Fig. 2a). Such a division allowed to approach characteristic dimensions of each section to dimensions of the nozzle array of the intermediate size cw chemical laser but as if it was turned by 90° in the YZ plane. In this case the construction stiffness and strength were ensured by rigid ribs spaced between sections with the special collecting channels in them for fuel to provide uniform H_2 outflow at the nozzle array exit plane. The required length of such a large size cw chemical laser was assembled from the needed number of sections and in our case was equal to about 1.5m.

The design principle of the oxidizer and fuel supersonic nozzles was similar to shown in Fig. 1b. To use the self-compensation effect the nozzle vanes were inclined in sections by a small angle of $\alpha \approx 5^\circ$ to the optical axis so that the inclination angles in an adjacent sections were opposite (see Fig. 2a). The resulted measured maximum phase distortion amplitude of the wavefront corresponded to the space scale 6 mm due to the periodic structures of the flows of fuel and oxidizer in vertical direction and its value didn't exceed $\Delta\varphi \approx 0.027\lambda \text{ m}^{-1}$. Such a value of $\Delta\varphi$

provides the objective possibility to obtain the divergence of laser beam close to the diffraction limit for active media with a length not less than 6 m under the amplification regime of cw chemical laser.

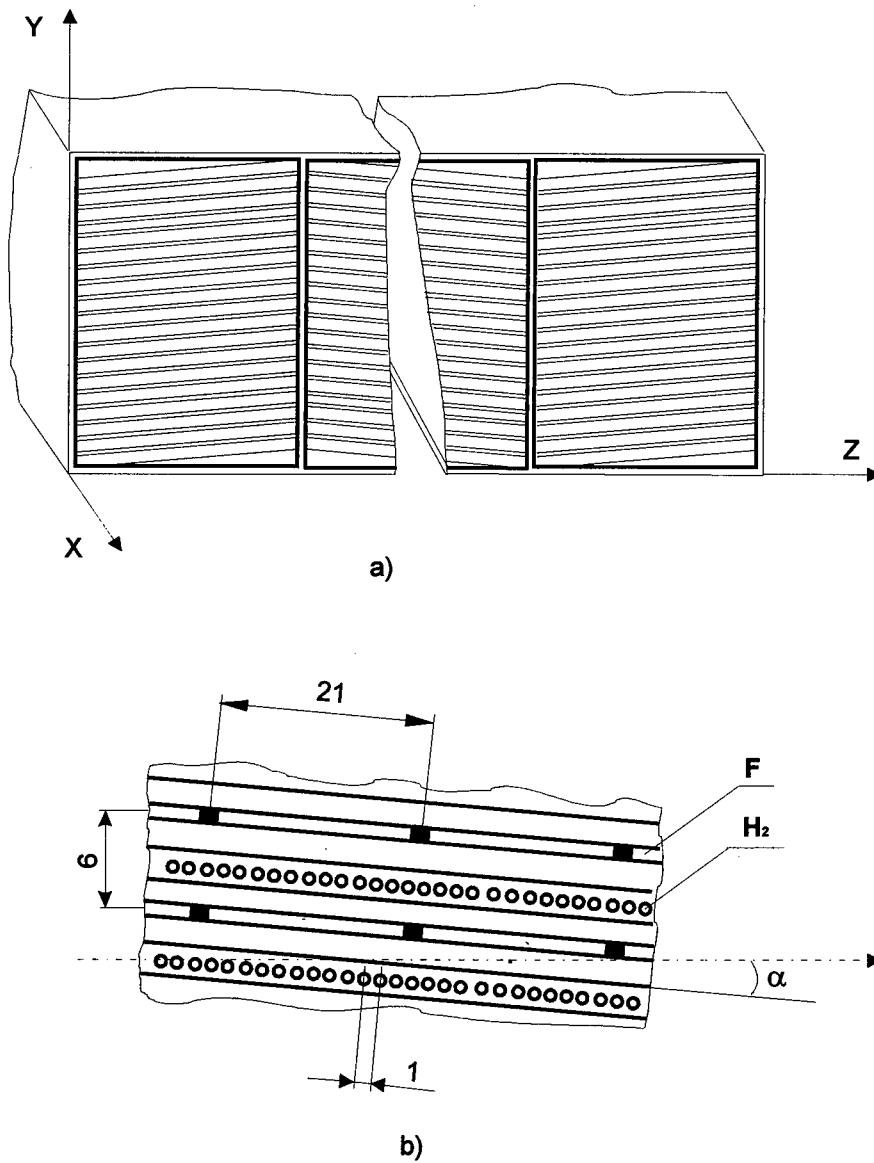


Figure 2. Configuration of the nozzle array of large size cw chemical laser.

4. Influence of the dissipative losses

As it was noted earlier with active medium length growth besides the optical inhomogeneities increase it is possible due to dissipative losses to stop the output power increase. The maximum length of active medium L_{\max} caused by this reason can be estimated if we know the coefficient of dissipative losses γ :

$$L_{\max} \approx \gamma^{-1}. \quad (1)$$

The value of γ was found using the experimental dependence of the laser output power with the nozzle array as shown in Fig. 1a on the reflection coefficient of the outcoupling mirror of the resonator. Two different approaches were used to treat the obtained curves. These approaches are distinguished by different localization of the dissipative losses: they can be concentrated in the resonator mirrors [2] or distributed along active medium [3].

In the first case the expression for a laser output power P is written in a form

$$P = P_s \frac{t}{t+a} \left[g_0 L + \frac{1}{2} \ln r \right], \quad (2)$$

where r , t , a are reflection, transmittance and dissipative losses in the outcoupling mirror, respectively, P_s is saturation power, g_0 is gain coefficient of small signal. In this case we can do formal transition to γ by formula: $a = 2\gamma L$. The processing of experimental results by means of this formula was done by application P at different values of r (not less than 3 values).

For the second case we have

$$P = P_s \ln \sqrt{1/r} \left(\frac{g_0 L}{\gamma L + \ln \sqrt{1/r}} - 1 \right). \quad (3)$$

The processing of the experimental results by means of this formula was done not for any three points of the experimental dependency as it was done in the first case but for the characteristic points of maximum power and generation threshold in the dependence of the laser output power on the output coupling coefficient ρ :

$$\rho = (1/L) \ln \sqrt{1/r}. \quad (4)$$

In this case all points of the experimental dependence are used. Using (4), we can find from (3) the following expressions for the output coupling coefficients corresponding to the maximum power (ρ_{\max}) and generation threshold (ρ_{th}):

$$\begin{aligned}\rho_{\max} &= \sqrt{g_0 \gamma} - \gamma, \\ \rho_{\text{th}} &= g_0 - \gamma.\end{aligned}\tag{5}$$

Solving the system of equations (5), we obtain

$$\begin{aligned}g_0 &= \frac{(\rho_{\text{th}} - \rho_{\max})^2}{\rho_{\text{th}} - 2\rho_{\max}}, \\ \gamma &= \frac{\rho_{\max}^2}{\rho_{\text{th}} - 2\rho_{\max}}.\end{aligned}\tag{6}$$

The calculated from (2) and (6) values of γ were in reasonably good agreement and appeared to be equal to $(1 \div 2) \cdot 10^{-4} \text{ cm}^{-1}$. But the error of the calculations was very high that led to the upper limit $\gamma \approx 8 \cdot 10^{-4} \text{ cm}^{-1}$. Thus from (1) we obtain $L_{\max} \geq 12 \text{ m}$. It is evident that this factor does not restrict the active medium length growth essentially.

5. Influence of the amplified spontaneous emission

At last one more principal physical factor that can limit the active medium length of cw chemical laser is the possibility of appearance of amplified spontaneous emission or superluminescence. We performed special experiments to determine superluminescence power of large size cw chemical laser with one total reflection mirror in the resonator when the outcoupling mirror was taken off that was equivalent to the active medium length doubling (up to 3m). The average superluminescence intensity on the output aperture of active medium was fairly high in this case $\sim 50 \text{ W/cm}^2$. Since there are several lines available in the spectrum of superluminescence (for example, about 10) the intensity of one line will be enough to reach the saturation level ($\sim 100 \text{ W/cm}^2$ for one line) at a small growth of the active medium length. It happens rather fast as the coefficient of small signal gain found from (2) and (6) and averaged by output aperture and spectral composition was equal to about $5 \cdot 10^{-2} \text{ cm}^{-1}$. This means that maximum in its distribution along the flow can reach about 10^{-1} cm^{-1} that corresponds the emission intensity growth equal to 20 at the length only 30 cm.

The given considerations was verified by calculation of the radiation amplification with the input intensity at one line 10 W/cm^2 at two passages along active medium of cw chemical large size laser. The intensity of such amplified radiation must reach $\sim 2 \text{ kW/cm}^2$ that corresponds to the high saturation of active medium. Hence, the superluminescence intensity in active media with 6 m length (for example) will reach the saturation level if there will not be taken measures for its suppression.

One of the ways of its decreasing consists in the active medium saturation of a long amplifier by radiation from the master oscillator. To decrease the requirements to the output power of the master oscillator (in order to obtain the high total gain in the amplifier) and to ensure the conditions for saturation in active medium it seems expedient to carry out a double passage of the laser beam from the master oscillator through active medium of the amplifier forward and backward. Then the total intensity of forward and backward waves in any point of active medium will be higher than the saturation threshold.

6. Conclusions

Thus, in this paper the influence of the main reasons on possibilities of cw chemical laser scaling are discussed. We have shown from the experimental results that a level of small-scale optical inhomogeneities of such lasers active medium with specific configuration of the nozzle array and optimum operational parameters could ensure divergence of the output radiation close to diffraction limit even in the case of the active medium length increase up to 6m. Influence of the estimated dissipative losses on the restriction of the output power growth gives the limit length of active medium not less than 12m. It was realized the design finding, making it possible to increase the nozzle array height up to 0.4 m. As a result the large size cw chemical laser with the length of nozzle array of 1.5 m and its height of 0.4 m was built. The experimental investigations of problem of the amplified spontaneous emission and consequently of superluminescence excitation have shown the real danger of this phenomenon in the large size cw chemical laser, though the ways are proposed to escape this danger.

7. References

1. Zelazny, S.W., Chambers, W.A., Van Tassell, W.F., et al. (1981) *SPIE*, **293**, 126.
2. Rigrod, W.W. (1965) *J. Appl. Phys.*, **36**, 2487.
3. Stepanov, B.I. (1966) *The methods of calculation of optical quantum generators*, (in Russian), Minsk.

CREATION OF CHANNELS INTO Ti:SAPPHIRE WAVEGUIDING LAYERS

J. LANČOK, M. JELÍNEK, J. BULÍŘ and P. MACHÁČ*

*Institute of Physics of the Academy of Sciences of the Czech Republic,
Na Slovance 2, 18040 Prague 8 Czech Republic, e-mail lancok@fzu.cz*

** Institute of Chemical Technology, Technická 5, 166 28 Prague 6 Czech
Republic*

Abstract

The reactive ion etching (RIE) and the laser ablation of Ti:sapphire thin waveguiding films have been investigated as a potential tool for preparation of the channel waveguide lasers.

1. Introduction

After the creation of the Ti:sapphire waveguiding layers by pulsed laser deposition (PLD) [1] the development of microchannel waveguides is next logical step. Confinement of both the pump and laser beam in a channel waveguide geometry would, assuming low propagation losses, significantly reduce the required pump power threshold in thin film waveguiding lasers [2]. The channel waveguide laser can be also more easily coupled to fiber components than the other laser sources [3]. Many techniques can be used for preparation of channel waveguides such as Ti indiffusion [4,5,6], ion implantation [7,8], proton exchange [9] and Ar⁺ etching [10] etc. The one of the suitable way to fabricate the channel waveguide from waveguiding layer is to confine the layer to stripes having width of order of several magnitude of wavelength. The roughness at waveguide boundaries, especially at channel surrounding walls, lead to the scattering losses and therefore their cannot exceed the value of $\lambda/10$. It is essential for obtaining of low waveguiding losses in channel [11]. In a narrow waveguide, an enhancement of losses due to a fabrication-induced edge roughness occurs as a waveguide dimensions are reduced [12]. The smooth side walls are therefore very important. The optimum channel width can be calculated by various methods [12]. In the case of Nd:GGG [13] and Nd:YAG [14] the experimentally found

optimum channel width for given layer parameters was in the range of $10 \div 16 \mu\text{m}$ and $20 \mu\text{m}$, respectively.

In this paper we describe the study of the preparation of rib guide with width of about $20 \mu\text{m}$ in Ti:sapphire thin films by RIE and KrF laser patterning.

2. Experimental

The RIE experiments were performed in a Chemical Vapour Deposition and RIE system of VacuTec VPS 1500/2000 with BCl_3 :He gas mixture. The dependence of the etch rate on the RIE parameters, such as rf power, reactor pressure and BCl_3 and helium flow rate, have been examined. The etch rate was determined for sapphire, platinum and SiO_2 , at different condition. The stripes of thickness of order of about 400 nm were created by using the platinum and SiO_2 masks. The substrate temperature was held in the room temperature in experiment [14].

The laser lithography have been made by KrF excimer laser (ELI-94) operating at the 248 nm wavelength with pulse duration 25 ns . A lens with focusing length of 5 cm was then used to form an image of this aperture at the target plane.

The etch rate was measured using by alpha step (Tencor Alpha Step 500).

3. Results

The following optimal etching condition were determined for sapphire patterning by using platinum and SiO_2 masks: reactor pressure 300 mTorr , flow rates of BCl_3 and He 15 and 80 sccm respectively, rf power density 0.45 W/cm^2 . At this condition the achieved etch rate of sapphire was 11.9 nm/min . and the selectivity between the sapphire and platinum was 3.87 and between the sapphire and SiO_2 was 0.55 .

At this condition the stripes of thickness of 420 nm and width of $20 \mu\text{m}$ were fabricated by using the platinum and SiO_2 masks. The etch profile of the stripe, which was carried out by using SiO_2 mask is in Figure 1.

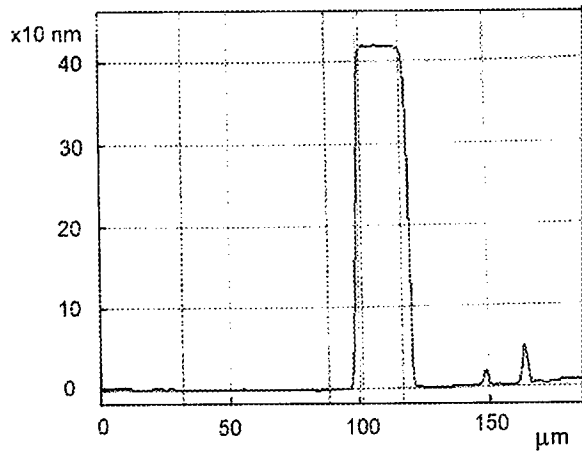


Figure 1. The etch profile of the stripe fabricated by RIE. The rf power, reactor pressure, time of etching, BCl_3 and He flow rate were 300 W, 300 mTorr, 35 minute, 15 sccm and 80 sccm, respectively. As a mask the SiO_2 of thickness 890 nm was used.

KrF ablation of Ti:sapphire material containing 0.12 wt % concentration of Ti_2O_3 was investigated to ascertain the ablation threshold, etch rate and quality of irradiated surface. From the dependence of the ablation depth on laser fluence were determined the ablation threshold 1.36 J/cm^2 with corresponding absorption coefficient $\alpha = 1.8 \times 10^5 \text{ cm}^{-1}$ by using Beers law [14]. Figures 2 and 3 show the etch profile and photo of the pit produced in Ti:sapphire by irradiation 248 nm with a fluence 3.57 J/cm^2 and 150 pulses, respectively.

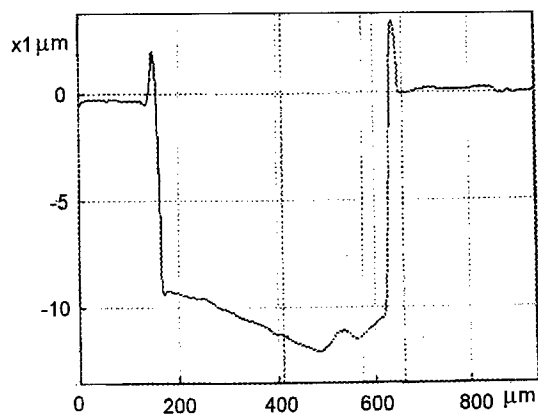


Figure 2. The etch profile of the etch pit produced in Ti:sapphire by KrF laser ablation with a fluence of 3.57 J/cm^2 .

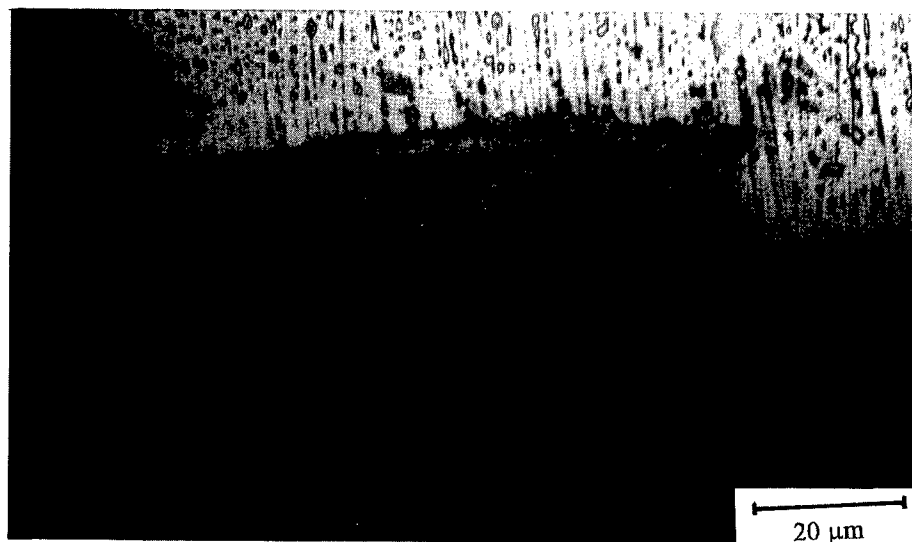


Figure 3. The photo of the etch pit produced in Ti:sapphire by KrF laser ablation with a fluence of 3.57 J/cm^2 .

4. Conclusion

The RIE etching of Ti:sapphire films in $\text{BCl}_3\text{:He}$ atmosphere was studied. The optimal etching condition for sapphire patterning by using of platinum and SiO_2 masks was found. The stripes with thickness of 420 nm and width of $20 \mu\text{m}$ was fabricated by using both platinum and SiO_2 masks. By RIE a high quality structures with smooth surface and precisely defined geometry was fabricated. The disadvantage is the small etch rate. For etching of the channel structures with thickness of 3 micrometer of more than 4 hours are needed.

The KrF laser ablation can produce etched features with high etch rate, but unfortunately the quality of the fabricated structures do not reach the quality of structures fabricated by RIE. The improvement can be found in using of ArF laser instead KrF laser [14], very good homogenization of the laser beam, and ultrasonic removing of the some large particles after etching [15].

In spite of some problems the RIE and laser patterning potentially attractive for fabrication microstructures in this active laser material for preparation channel waveguide laser.

5. Acknowledges

This work was supported by the grand agency of Czech Republic, grand No.102/96/0429

6. References

1. Anderson, A.A., Eason, R.W., Hickey, L.M.B., Jelinek, M., Grivas, C., Gill, D.S., Vainos, N.A. (1997) A Ti:sapphire planar waveguide laser grown by pulsed laser deposition, *Opt. Letters* -in print.
2. Pelec, D., Chambaz, B., Chartier, I., Ferrand, B., Wyon, C., Shepherd, D.P., Hanna, D.C., Large, A.C., Tropper, A.C. (1995) High slope efficiency and low threshold in a diode-pumped epitaxially grown Yb:YAG waveguide laser, *Optics Communications* **115**, 491-497.
3. Hanna, D.C., Large, A.C., Shepherd, D.P., Tropper, A.C., Chartier, I., Ferrand, B., and Pelec, D., (1993) Low threshold quasi-three-level 946nm laser operation of an epitaxially grown Nd:YAG waveguide, *Appl.Phys.Lett.* **63**, 7-9.
4. Brinkmann, R., Sohler, W., Suche, H. (1991) Continuous-wave erbium-diffused LiNbO waveguide laser, *Electronics Letters* **27**, 415-417.
5. Suche, H., Wessel, R., Westenhofer, S., Sohler, W., Bosso, S., Carmannini, C., Corsini, R. (1995) Harmonically mode-locked Ti:Er:LiNbO waveguide laser, *Optics Letters* **20**, 596-598.
6. Hickey, L.M.B., Anderson, A.A., Wilkinson, J.S. (1997) Ti:sapphire channel waveguide laser by thermal diffusion of titanium into sapphire, *Europ. Conf. Int. Opt. Stockholm*, Paper PD6-1.
7. Field, S.J., Hanna, D.C., Shepherd, D.P., Tropper, A.C., Chandler, P.J., Townsend, P.D., Zhang, L. (1991) Ion Implanted Nd:YAG Waveguide Lasers, *IEEE Journal of Quantum Electronics* **27**, 428-433.
8. Field, S.J., Hanna, D.C., Large, A.C., Shepherd, D.P., Tropper, A.C., Chandler, P.J., Townsend, P.D., Zhang, L., (1992) Ion-implanted Nd:YAP planar waveguide laser, *Optics Letters* **17**, 52-54.
9. Lallier, E., Pocholle, J.P., Papuchon, M., de Micheli, M., Li, M.J., He, Q., Ostrowsky, D.B., Grezes-Besset, C., Pelletier, E., (1990) Nd:MgO:LiNbO waveguide laser and amplifier, *Optics Letters* **15**, 682-684.
10. Sugimoto, N., Ohishi, Y., Katoh, Y., Tate, A., Shimokozono, M., Sudo, S. (1995) A ytterbium- and neodymium-co-doped YAG, *Appl.Phys.Lett.* **67**, 582-584.
11. Marcuse, D., (1969) *Theory of Dielectric and Optical Waveguides* 2nd edn, New York Academic.
12. Tamir, T., (1988) *Guided- Wave Optoelectronics*, Springer Series in Electronics and Photonics 26 Springer Verlag.
13. Field, S.J., Hanna, D.C., Large, A.C., Shepherd, D.P., Tropper, A.C., Chandler, P.J., Townsend, P.D., Zhang, L., (1991) Low threshold ion-implanted Nd:YAG channel waveguide laser, *Electron. Letters* **27**, 2375-2376.
14. Dyer, P.E., Jackson, S.J., Key, P.H., Metherringham, W.J., Schmidt, M.J.J., (1996) Excimer laser ablation and film deposition of Ti:sapphire, *Appl. Surface Science* **96-98**, 849-854.
15. Jackson, S.J., Metherringham, W.J., Dyer, P.E., (1995) Excimer laser ablation of Nd:YAG and Nd:glass, *Appl. Surface Science* **86**, 223-227.

PROPERTIES OF THE CAVITIES FOR COMPACT SLAB GAS LASERS

A.A. KUZNETSOV, M.Z. NOVGORODOV
*P.N.Lebedev Physical Institute, Russian Academy of Sciences,
Leninsky prosp. 53, Moscow 117924, Russia*

Abstract

The properties of positive branch unstable resonators with compact output coupling and small magnification factors typical for small-size carbon dioxide lasers are considered. The effect of reflectors misalignment on resonator losses and output beam structure has been studied.

The calculations of the resonator losses at various tilts of concave and of convex mirrors were performed. The influence of resonator magnification factor and Fresnel Number on angular dependencies of losses has been investigated.

The effect of reflecting sidewall, positioned along optical axis on the resonator losses of slab lasers has been studied.

The obtained results provide data for determination of the resonator rigidity required to achieve the necessary stability of the radiation losses as well as laser output power.

1. Introduction

Molecular gas lasers with planar discharge geometry are applied widely in the last few years [1-4]. This is due to the fact that specific output power of slab gas lasers is increased substantially as compared to conventional laser systems. At the same time many questions associated with resonators schemes selection and their properties still remain to be answered.

The one-dimensional unstable telescopic resonators are of considerable current use. This cavity configuration allows to provide effective filling of large active volume, compact output coupling, and single-resonator mode operation.

However, at the active medium dimensions typical for small-size carbon dioxide slab lasers of 10 - 100 W output power, unstable resonators must have magnification factor close to unity. The results of calculations and experiments suggest that, in this situation diffraction strongly influences an intracavity field distribution and a value of the resonator losses [5], as well as the shape of output beam [2-5]. It may also have a marked effect on the mirror tilt sensitivity of the unstable cavity.

In this paper we consider the properties of positive branch confocal unstable resonators with compact output coupling and small magnification factors. The action of reflectors misalignment on resonator losses and output beam structure has been investigated.

2. Scheme of positive branch unstable cavity

Figure 1 presents the top view of the positive branch confocal unstable resonator. The cavity consists of planar waveguide channel, concave mirror 1 of radius of curvature R_1 , and convex mirror 2 of radius of curvature R_2 . The slab waveguide channel 3 is made up of two polished metal electrodes of width D and length L_A , which are placed in parallel to each other. The interelectrode separation d is chosen with consideration for $1/d$ scaling law [6] and level of resonator losses. For carbon dioxide lasers value of interelectrode spacing conventionally lies in the range from 1 mm to 3 mm. The distance between electrodes ends and totally reflective mirrors is approximately 10 mm. This mirrors separation contributes to suppression of high order transverse modes and precludes damage of reflector surface. The optical axis 4 of the cavity is located along one of the edges of the slab, whereas the output beam 5 is located along opposite edge. The reflecting ceramics sidewall 6 positioned along the optical axis. An absence of second sidewall as well as spacing between waveguide ends and mirrors provides free circulation of gas mixture.

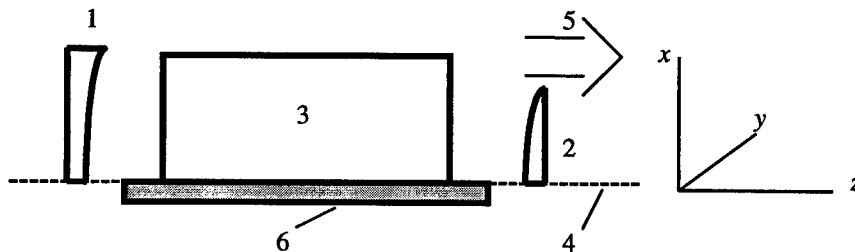


Figure 1. The scheme of a positive branch unstable cavity with compact output.
1, 2 - concave and convex mirrors, 3 - slab waveguide channel, 4 - optical axis,
5 - output beam, 6 - reflecting sidewall.

For positive branch telescopic scheme the interrelation between the curvatures of reflectors and resonator length L is given by expressions

$$R_1 = \frac{2LM}{M-1} \quad (1)$$

$$R_2 = \frac{-2L}{M-1} \quad (2)$$

where $M = -R_1/R_2$ is geometrical magnification factor of an unstable telescopic resonator. Concave reflector measures approximately D along the x direction, aperture of the convex reflector A is equal about D/M .

The values of magnification factor M and the curvatures of reflectors R_1 and R_2 are selected for optimal power coupling. The magnitude of optimal output coupling T_{opt} is determined with regard to small-signal gain k_0 of active medium by the known formula [7]

$$T_{opt} = 2bL_A \left(\sqrt{\frac{k_0}{b}} - 1 \right) \quad (3)$$

where parameter b includes the losses due to the matching of the fundamental waveguide mode to the mirrors as well as the losses associated with absorption in the waveguide channel ($\sim 10^{-3} \text{ cm}^{-1}$), and in the reflectors (< 0.01). For carbon dioxide lasers with active medium length of several tens of centimeters the optimal output coupling T_{opt} is generally no more than 0.3. Consequently, resonator magnification factor M is close to unity. As can be seen from expressions (1) and (2), it leads to the use of mirrors with large radius of curvature. Under these parameters spherical optics approximate closely to plane mirrors in the narrow dimension y and may be employed instead of cylindrical optics.

The resonator is waveguide (dual Case I configuration [8]) in the narrow dimension y , and is unstable in the other transverse dimension x . This resonator scheme provides effective use of active medium, single-mode operation, and compact coupling out of radiation.

3. Technique of calculation

A field distribution of the resonator mode is represented as the product of two functions each depending only on one transverse coordinate:

$$E(x, y) = u(x)v(y) \quad (4)$$

where $u(x)$ is lowest-losses mode of unstable resonator; the function $v(y)$, that describes the field distribution along the axis perpendicular to the slab coincides with the fundamental mode of planar waveguide channel:

$$v(y) \sim \cos(y\pi/d) \quad (5)$$

It results from high order waveguide modes discrimination both in the slab waveguide channel, and in the free space between channel edges and reflectors separated of distance approximately $5d$. The intracavity field structure along the x direction and the resonator losses were determined from the equation

$$u(x)\gamma = Ku(x) \quad (6)$$

where the function $u(x)$ describes a field structure in the reference plane inside the resonator, symbol K denotes the field transformation at the round trip through the cavity, the complex constant γ determines the amplitude damping and phase shift for the resonator mode.

The equation (6) was solved numerically by using Fox and Li algorithm. The reference plane was chosen at the convex reflector. The initial distribution of the wave amplitude was uniform. The field transformation upon passing between reflectors was determined by the known expression

$$u(x_2) = \int_{x_b}^{x_e} \frac{\exp(ikL)}{\sqrt{iL\lambda}} \exp\left[ik \frac{(x_2 - x_1)^2}{2L}\right] u(x_1) dx_1 \quad (7)$$

where $u(x_1)$ is the initial field distribution; x_b and x_e are the integration limits; λ is wavelength of radiation; $k = 2\pi/\lambda$ is wavenumber. The transformation of field distribution by reflectors was found by introducing the phase factor $\exp(ikx^2/2R_i)$, ($i=1,2$). The effect of mirrors tilt on field structure was taken into consideration by inserting the phase term $\exp(ik\alpha x)$, where α is the angle of reflector misalignment.

The output beam profiles at the different distances z from the laser head were calculated from the expression (7). As the initial distribution $u(x_1)$, field structure in the output plane was employed. The substitution of distances z for the resonator length L was used. The integration was performed within the output beam: from A to $(A+d_x)$, where d_x is the beam width along the x direction in plane of the convex reflector.

4. Results and discussion

4.1. THE LOSSES OF THE CAVITY

The intracavity field distribution and level of resonator losses were determined at different tilts of the mirrors. The investigations were performed at the parameters typical for compact carbon dioxide slab lasers of 10 - 100 W output power. The ranges of Fresnel Numbers N_F from 20 to 200 and magnification factors M from 1.1 to 1.5

have been studied more comprehensively. It corresponds to lasers with active medium of length several tens centimeters and of width several centimeters.

The geometrical optics theory supposes that the lowest-losses mode amplitude $u(x)$ is constant and intensity distribution of output beam is uniform along the x direction. In this case, at reflector misalignment the output coupling fraction T_{geom} is given by expression

$$T_{geom} = 1 - \frac{1}{(L/A)\alpha + M} \quad (8)$$

where α - angle of reflector misalignment. It can be seen from formula (8) that at angle of mirror misalignment of the order of 1 mrad a variation of T_{geom} is negligible under our conditions.

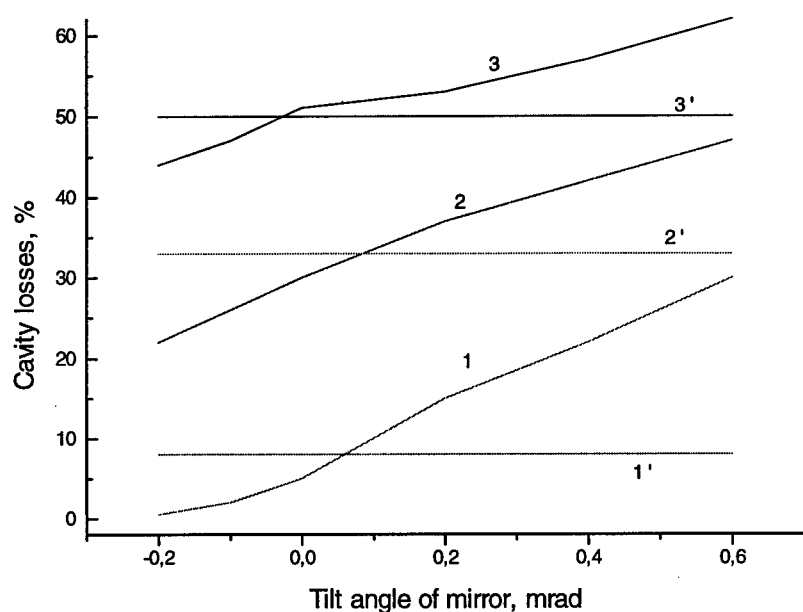


Figure 2. The angular dependencies of losses (Plots 1, 2, 3). Plots 1', 2', and 3' - geometrical approximation.

However, the computations show that under parameters studied the angular dependencies of actual losses differs significantly from results obtained by application of geometrical optics approximation. Figure 2 presents, as an illustration, calculated losses dependencies on angle of convex reflector misalignment. Fresnel Number N_F is equal 115 for all plots. Curve 1 corresponds to resonator with magnification factor $M =$

1.1, curve 2 to $M = 1.5$, curve 3 to $M = 2.0$. The plots marked 1', 2', and 3' are their respective results obtained from the geometrical consideration.

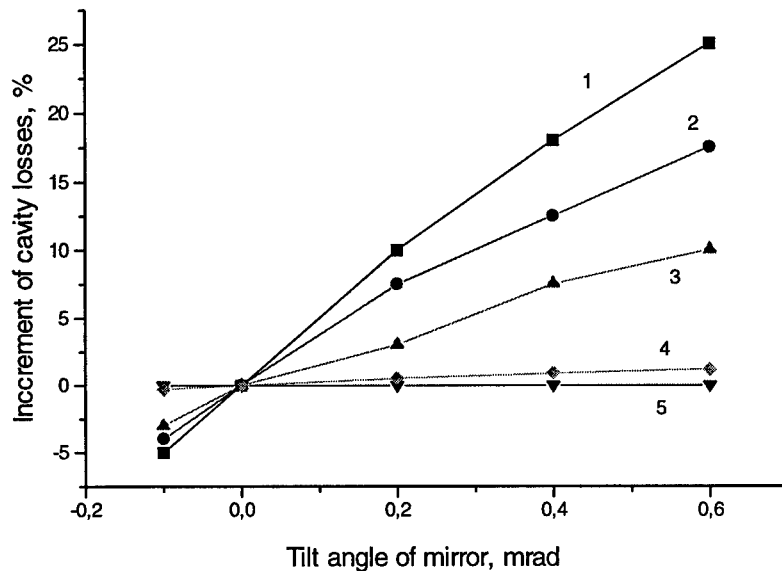


Figure 3. The increment of cavity losses at the different magnification factors.

Figure 3 shows the same data representable as losses increment relative losses of cavity with untilted mirrors. From Figure 3, it follows that for resonator with higher magnification factor the slope of angular dependence of actual losses is lower. At magnification factor $M = 5$ and Fresnel Number $N_F = 115$ the curve calculated with taken to account diffraction (Plot 4) is close to curve obtained from geometrical approximation (Plot 5).

Analogous losses dependencies on angle of convex reflector misalignment at different Fresnel Number N_F were calculated. For example, at magnification factor $M = 1.33$ the results for Fresnel Number $N_F : 40; 60; \text{ and } 170$ are close to each other. This suggests that the change of Fresnel Number N_F weakly influences angular dependencies of losses.

The resonator losses at various angles of concave reflector misalignment were determined too. The comparison of obtained data for concave mirror misalignment and for convex mirror misalignment was performed. It was established that for these cases the trend of angular dependencies of losses is similar. The slopes of the curves are of the same order of magnitude. A variation of magnification factor M and of Fresnel Number N_F has effect on a tangent of the curves in a like manner.

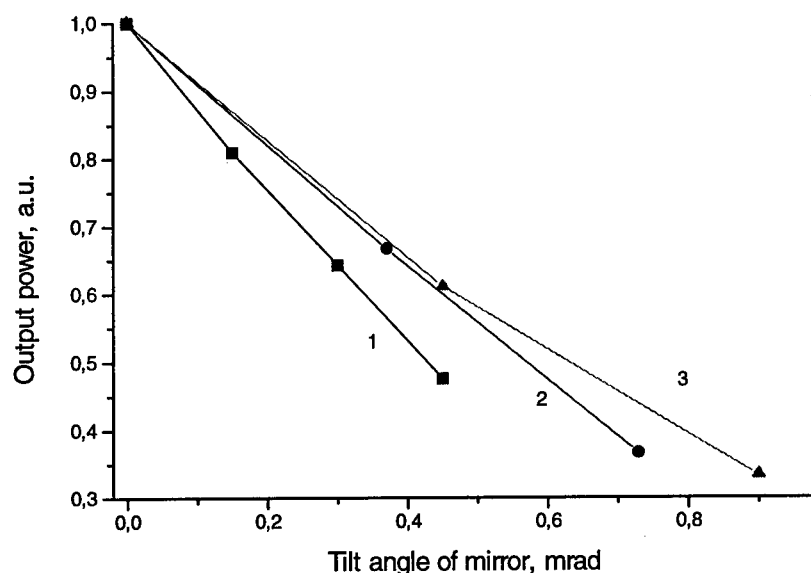


Figure 4. The angular dependencies of output power for different cavity geometry.

It is therefore concluded that for lasers of equal output power the long and narrow geometry is more proof against reflectors misalignment than short and wide geometry. To test the validity of this conclusion three carbon dioxide lasers with equal square of active medium ($\sim 100 \text{ cm}^2$) have been considered. The dimensions of discharge gaps are: laser 1 - length $L_A = 250 \text{ mm}$, width $D = 40 \text{ mm}$; 2 - $L_A = 500 \text{ mm}$, $D = 20 \text{ mm}$; and 3 - $L_A = 700 \text{ mm}$, $D = 15 \text{ mm}$. The values of resonator magnification factor M were chosen close to optimal for output power coupling and equal 1.1; 1.3; and 1.5 respectively. The apertures of convex reflector determined as $A = D/M$ are equal 36 mm, 15 mm, and 10 mm.

Using calculated losses for these lasers and known expression for power of laser generation [7] the dependencies of output power on angle of reflector misalignment were determined. Figure 4 presents obtained results. From these results it follows that for slab gas laser of equal output power the longer configuration is more resistant to reflector misalignment.

Obtained angular dependencies of losses were compared with similar data for conventional open stable resonators. At comparison we used results for CO_2 lasers (wavelength of radiation 10 μm) with open stable resonators of length 50 cm.

Magnitudes of confocal parameter g and Fresnel Number N_F are typical for molecular gas lasers with low diffraction losses and single-mode operation [9].

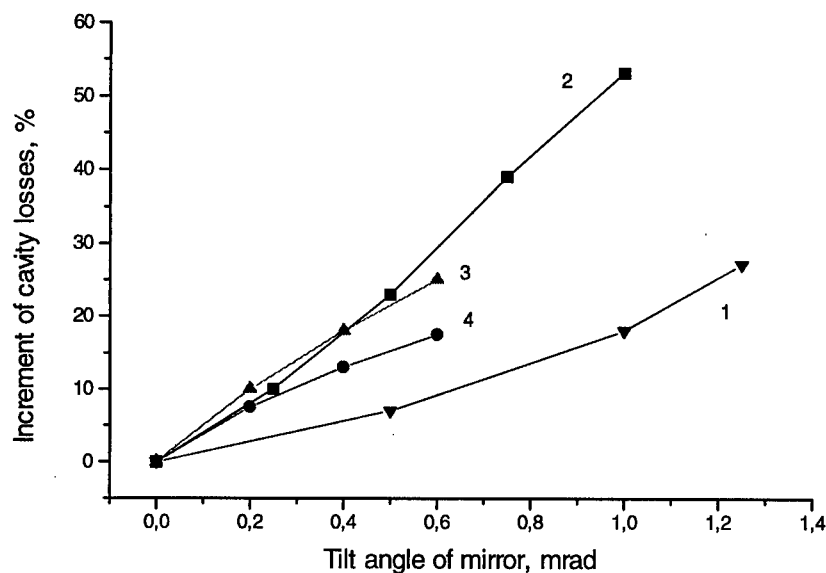


Figure 5. The angular dependencies of losses increment for stable and unstable cavities.

Figure 5 shows data for plane-concave stable resonators with $g = 0.5$, $N_F = 1.1$ (Curve 1), and $g = 0.9$, $N_F = 2.0$ (Curve 2). The data for one-dimensional unstable telescopic resonators with $N_F = 115$, magnification factors $M = 1.1$ (Curve 3), $M = 1.5$ (Curve 4) are given too. It may be seen from Figure 5 that mirror tilt sensitivities of stable and unstable resonators are comparable. From this fact transpires that the unstable resonators for slab gas lasers do not need to be substantially more rigid.

It is interesting to note that as length increased stable resonators resistance to mirrors misalignment decreased in inverse proportion to square root of L [9]. By contrast, longer unstable resonators are more resistant to reflector misalignment because of higher magnification factor.

The above presented calculations results of cavity losses and output power are appropriate for positive branch unstable resonators with reflecting sidewall positioned along optical axis (See Figure 1). Analogous computations for the similar resonators, but without sidewalls have been performed.

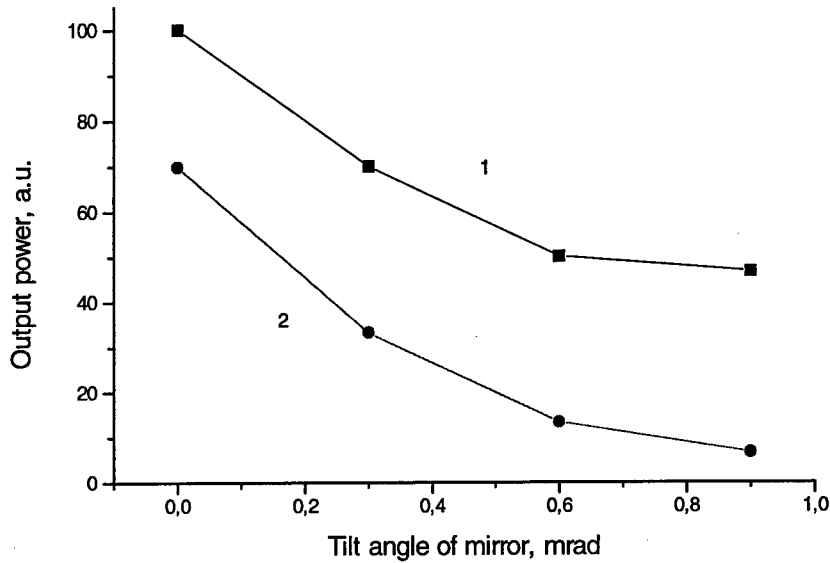


Figure 6. The angular dependencies of output power for lasers with sidewall (1) and without sidewalls (2).

Figure 6 shows dependencies of laser output power on angle of reflector misalignment for these cavity schemes. Both curves are obtained for cavities with the same Fresnel Number $N_F = 115$ and resonator magnification factor $M = 1.33$. Curve 1 corresponds to configuration with sidewall, curve 2 - without sidewalls. It may be seen from Figure 6 that absence of reflecting sidewall decreases laser power. This is because the cavity losses not associated with useful output of radiation increase in magnitude. In addition, the reflector tilt sensitivity of the scheme with reflecting side wall is somewhat below. For these reasons it is advantageous to use sidewall in such systems.

4.2. OUTPUT RADIATION STRUCTURE

The field distributions of output radiation at different distance from laser head were determined. It is shown that angle of reflector tilt markedly influences the shape of near-field pattern. Far-field pattern remains bell-shape in tilt range studied. At small angles of misalignment the divergence of radiation as well as beam quality factor M_x^2 in the x direction are changed insignificantly. Magnitude of M_x^2 was calculated according to [10]

$$M_x^2 = 4\pi\sigma_{x0}\sigma_{sx} \quad (9)$$

where σ_{x0} and σ_{sx} are minimum spatial variance and spatial frequency variance correspondingly.

The similar behaviour of near- and far-field patterns takes place in unstable cavities without mirror misalignment under changes in Fresnel Number N_F by variation in convex mirror aperture A or resonator length L [11]. The difference lies in the fact that mirror tilt causes displacement of far-field pattern. The relationship between reflector misalignment and angular shift of output beam has been investigated at variable magnification factor and Fresnel Number.

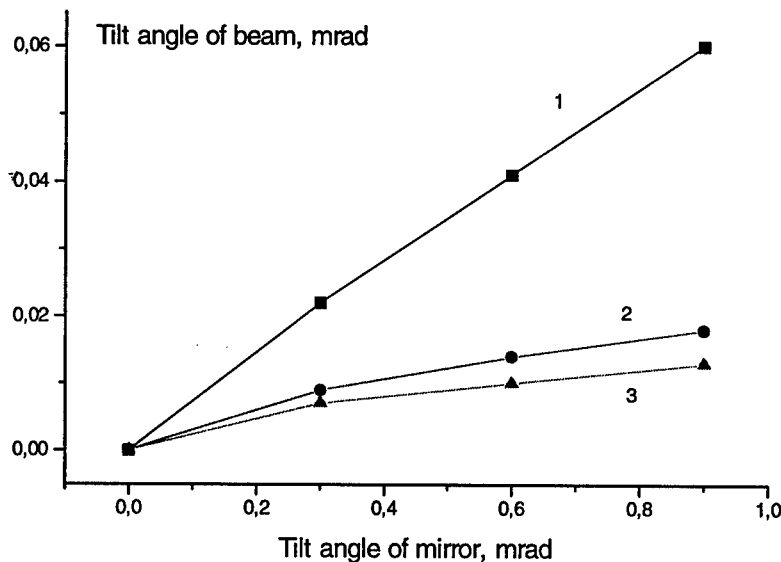


Figure 7. The tilt angle of output beam vs tilt angle of mirror at the different cavity magnifications.

Figure 7 shows tilt angle of output beam as a function of mirror misalignment angle. Fresnel Number N_F is equal 60 for all plots. Curve 1 corresponds to resonator with magnification factor $M = 1.1$, curve 2 to $M = 1.3$, curve 3 to $M = 1.5$. From Figure 7, it follows that for resonator with higher magnification factor the output beam is more resistant to reflector misalignment.

Figure 8 presents analogous dependencies for resonators with magnification factor $M = 1.3$ and different Fresnel Numbers. Curve 1 corresponds to Fresnel Number

$N_F = 40$; 2 - $N_F = 60$; and 3 - $N_F = 170$. From Figure 8 the conclusion that the change of Fresnel Number N_F weakly influences angular position of output beam.

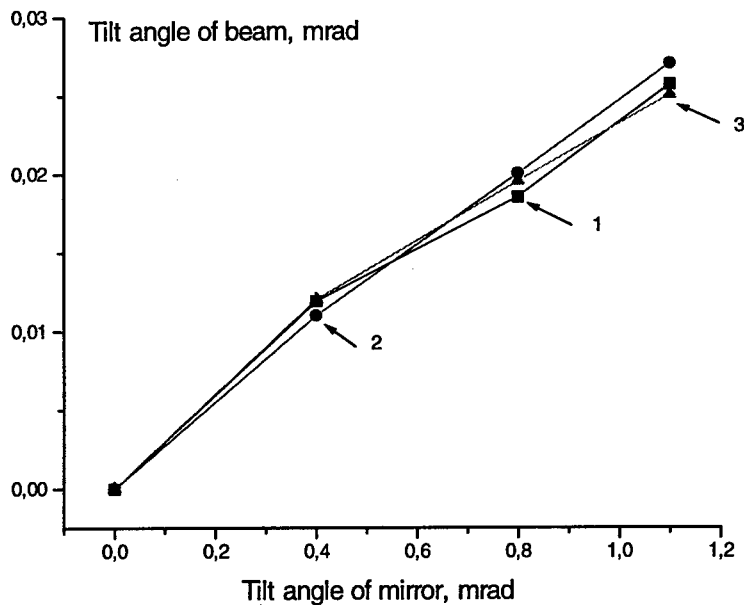


Figure 8. The tilt angle of output beam vs tilt angle of mirror at the different Fresnel Numbers.

5. Conclusion

The properties of positive branch confocal unstable resonators with compact output coupling and small magnification factors are considered. The action of mirrors misalignment on resonator losses and output beam structure has been investigated.

It was found that under parameters typical for small-size carbon dioxide slab lasers, the angular dependencies of actual losses differ significantly from results obtained from geometrical optics approximation.

From calculations it follows that the losses of resonator with higher magnification factor are more proof against reflectors misalignment. The change of Fresnel Number weakly influences angular dependencies of losses.

Open stable cavities of single-mode gas lasers and the unstable cavities have been compared. It is shown that their mirror tilt sensitivities are comparable. This suggests that unstable cavities for slab gas lasers don't need to be considerably more rigid.

The effect of reflecting sidewall, positioned along optical axis on resonator losses of slab lasers has been studied. It is shown that using of sidewall increases laser output power as well as its stability under mirrors tilts.

The effect of reflectors misalignment on field distributions of output radiation is considered. The dependencies of output beam tilt on angle of mirror misalignment are determined at the different Fresnel Numbers and magnification factors of the cavity.

The obtained results provide data for determination of the resonator rigidity required to achieve the necessary stability of the radiation losses as well as laser output power.

This work is supported by grant of Russian Interdepartmental Scientific and Technology Program "Optics. Laser Physics".

6. References

1. Colley, A.D., Villareal, F., Cameron, A.A., Vitruk, P.P., Baker, H.J., Hall, D.R. (1996) High power cw molecular gas lasers using narrow gap slab waveguides, in W.J. Witteman and V.N. Ochkin (eds.), *Gas Lasers - Recent Developments and Future Prospects*, Kluwer Academic Publisher, Dordrecht, pp. 89-103.
2. Kuznetsov, A.A., Kyun, V.V., Leont'ev, V.G., Novgorodov, M.Z., Ochkin, V.N., Shishkanov, E.F. (1996) CO₂ waveguide lasers with slab geometry, *J. of Russian Laser Research* **17**, 1-14.
3. Chernikov, S.B., Karapusikov, A.I., Stojanov, S.A. (1996) RF excited CO₂ slab waveguide laser, *Proc. SPIE* **2773**, 52-56.
4. Dutov, A.I., Ivanova, V.N., Novoselov, N.A., Semenov, V.E., Sokolov, V.N., Yur'ev, M.S., Evstratov, I.Yu., Kuuleshov, A.A., Motovilov, S.A. (1996) Experimental and computer investigations of slab waveguide RF excited CO₂ laser, *Proc. SPIE* **2773**, 23-30.
5. Kuznetsov, A.A. (1996) The output beams of slab gas lasers with waveguide-unstable cavities, *Proc. SPIE* **2788**, 95-102.
6. Abramski, K.M., Colley, A.D., Baker, H.J., and Hall, D.R. (1989) Power scaling of large-area transverse radio frequency discharge CO₂ laser, *Appl. Phys. Lett.* **54**, 1833-1835.
7. Anan'ev, Yu. (1992) *Laser resonators and beams divergence problem*, Adam Hilger, New York.
8. Degnan, J.J. (1976) The waveguide laser: a review, *Appl. Phys.* **11**, 1-33.
9. Beltyugov, V.N., Kuznetsov, A.A., Ochkin, V.N., Troitskii, Yu.V., Udalov, Yu.B. (1992) Frequency selection in cavities with diffraction grating, *Proc. P.N. Lebedev Phys. Inst.* **221**, 6-49 (in Russian).
10. Siegman, A.E. (1990) New developments in laser resonator, *Proc. SPIE* **1224**, 2-14.
11. Kuznetsov, A.A., Ochkin, V.N., Udalov, Yu.B., Witteman, W.J. (1994) The radiation divergence of planar gas lasers, *Laser Physics* **4**, 1106-1113.

Nd:YAG LASER RESONATORS USING EXTERNAL STIMULATED BRILLOUIN SCATTERING Q-SWITCHING MIRROR

A. MOCOFADESCU

Institute of Atomic Physics, National Institute for Laser, Plasma and
Radiation Physics
Bucharest 76900, P.O. Box MG-36, Romania

V. BABIN

Institute of Atomic Physics, National Institute of Optoelectronics
Bucharest 76900, P.O. Box MG-22, Romania

1. Introduction

In recent years a good beam quality of the laser light has been required for many scientific and technical applications of high power solid state lasers.

Phase conjugation via stimulated Brillouin scattering (SBS) has been demonstrated to be a simple and very efficient method for dynamically correcting the aberrations in solid state lasers [1]. Beside achieving a good beam quality another feature provided by the SBS interaction is the self Q-switching of the optical resonator.

The approach usually adopted is to include the SBS medium inside a laser cavity with a secondary mirror employed to provide feedback at the beginning of the laser action [2]. High intra-cavity intensities experienced by the SBS medium in this configuration can lead to poor spatial beam quality. This limits the repetition rate and peak power of the output.

There has been reported also an alternative cavity configuration in which SBS medium resides outside the conventional cavity [3-5]. The output beam was found to have a TEM₀₀ mode and efficient energy extraction at very high repetition rate using high purity SBS media.

We have investigated experimentally and theoretically the performance of a pulsed Nd:YAG laser system utilising external stimulated Brillouin scattering for Q-switching and phase conjugation of the cavity radiation using two configurations: linear laser resonator and ring laser resonator.

The novel feature of our linear configuration was the use of a solid state saturable absorber (LiF crystal) to onset the SBS process [7].

In comparison with the linear configurations where each round trip the laser beam travels within the cavity will generate a downshifted Stokes beam and therefore increasing the bandwidth of the laser emission, the ring configuration allows the potential of single frequency operation from the resonator. In our ring configuration the Q-switching regime was obtained in a novel oscillator two-pass amplifier system [8].

2. Linear laser resonator

2.1. EXPERIMENTAL SET-UP AND RESULTS

The experimental set-up is depicted schematically in Figure 1.

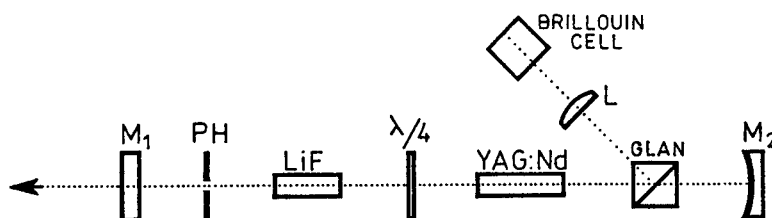


Figure 1
Schematic of the experiment for the linear configuration

The concave mirror (3m radius) with reflectivity $R > 99.5\%$ and the plane mirror with $R = 20\%$ defined a hemispherical resonator whose length was 1.1m. The Nd:YAG rod with a 6mm diameter and a 80mm length was pumped by a flash lamp in a diffuse, liquid cooled cavity. The radiation at $1.06 \mu\text{m}$ was outcoupled by a quarter-wave plate-Glan polarizer combination which provided an easy way to optimise the output energy by adjusting the coupling transmission, including the final Brillouin reflectivity. The Brillouin cell ($L = 10\text{cm}$) filled with carbon disulphide, CS_2 , was placed behind a lens (focal length = 5cm) outside the linear cavity. We choose CS_2 because of its large gain (0.06 cm/MW) for SBS. This cell acted as both a phase conjugate mirror and as a Q-switch. The pinhole selected the transverse modes by limiting the Fresnel number.

The Brillouin backscattered radiation returned to the main resonator was extracted through the mirror M_1 to be analysed. A fast vacuum photodiode (rise time 0.3ns) and a Tektronix 519 oscilloscope (bandwidth 1Gz) was used to monitor the laser pulse duration. A TRG 102 energimeter was used to measure laser beam energies. The divergence of the output radiation was estimated by putting different apertures in the focal point of a 1m focal length lens and measuring the diameter corresponding to 80% full energy.

When the quarter-wave plate is oriented in such a way that maximum of the beam energy was outcoupled by the Glan polarizer, the energy entering the Brillouin cell was about 30 mJ in the form of relaxation oscillations pulses with duration of the order of 200-300 ns. This output power proved not to be enough to onset the SBS process so we used a saturable absorber to start the Q-switching of the cavity so we put in the cavity a LiF crystal with F_2^- centres. ($T_0=10\%$)

a) An output beam with an energy of 40mJ in a pulse of 15-20 ns duration was obtained when the energy incident on the Brillouin cell was 25 mJ. The experimental recordings of the output pulse with a width (FWHM) of 40 ns and 20 ns is shown in Figure 2.

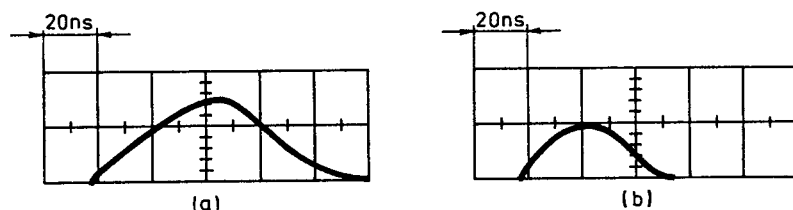


Figure 2

Pulse shape that is due to LiF crystal Q-switching (2a) and simultaneous LiF and SBS Q-switching (2b)

The Figure 2a shows the output pulse without the Brillouin cell and Figure 2b the case when the Brillouin cell is in action. The divergence was smaller than 3 mrad.

b) Introducing a pinhole (2.5mm) into the cavity the energy drooped to 5mJ but the divergence became 1.5 the diffraction limit.

2.2. THEORY

We described the passive Q-switching regime of the laser by the rate equations [6]:

$$\frac{dq}{dt} = q[Bn - \gamma_{nl}(q)]$$

$$\frac{dn}{dt} = -qBn \quad (1)$$

$$n(0) = n_{th}(1 + \zeta); q(0) = q_{sp}$$

where q is the photon density and n - the population inversion, n_{th} - is the threshold inversion, B is the Einstein coefficient and $\gamma_{nl}(q)$ represents the losses which are intensity dependent because of the SBS mirror reflectivity R . The initial population inversion $n(0)$ has been assumed above threshold by a factor $1 + \zeta$ ($\zeta \approx 2\%$).

The threshold condition for laser oscillation is:

$$IR_1 T e^{(\gamma_a - \alpha)l_r} T_G R_2 + R_G R_B I = I \quad (2)$$

where I is the laser intensity in the resonator, R_1 is the reflectivity of the output mirror, $R_2=100\%$, T is the saturable absorber transmission, T_G, R_G are the transmission and the reflectivity of the Glan polarizer, l_r -the Nd:YAG rod length, γ_a -the amplification coefficient and α the losses per unit length.

The nonlinear losses are :

$$\gamma_{nl} = \left(\frac{I_r}{I_o} \right) c\alpha + \frac{c}{I_o} \ln \frac{1 - R_G R_B}{R_1 R_2 T T_G} \quad (3)$$

I_o -the length of the resonator.

A simple steady state theory of SBS gives the analytical solution for Brillouin reflectivity of the cell, R :

$$\frac{\exp(-G)}{R} = \frac{1 - R}{\exp[(1 - R)g_B L_{eff} I] - R} \quad (4)$$

where $G \sim 25$ is related to the initial Stokes noise level, g_B is the Brillouin gain and L_{eff} is an effective interaction length which depends on the radiation focusing inside the cell.

If we introduce the normalised variables :

$$\begin{aligned} \xi &= t/\tau \\ R(\xi) &= I_s/I \\ y(\xi) &= n(\xi)/n(0) \\ x(\xi) &= (I + I_s)g_B L_{eff} \end{aligned} \quad (5)$$

where I_s is the Stokes intensity and $\tau = l_o/c$ is the round trip time of the resonator.

We obtain the following system of equations :

$$\begin{aligned} \frac{dR(\xi)}{d\xi} &= [A_0 y - G(R)]C(R) \\ \frac{dy(\xi)}{d\xi} &= -B_0 yx \\ \frac{dx(\xi)}{d\xi} &= [A_0 y - G(R)]x \end{aligned} \quad (6)$$

The initial conditions are :

$$R(0) \approx e^{-G} y(0) = 1; x(0) \approx e^{-G} \quad (7)$$

The functions and constants used in system (6) are :

$$A_0 = \frac{I_0}{c} B n(0)$$

$$B_0 = \frac{2 \frac{I_0}{c} B}{ch v g_B L_{eff}}$$

$$G(R) = \ln \frac{1 - R_G R_B}{R_1 R_2 T T_G}$$

$$C(R) = \frac{R(1 - R^2)}{2R + \frac{1 + (1 - R)e^G}{1 + (1 - 2R)e^G} \ln[R + R(1 - R)e^G]}$$

(8)

The results of the numerical simulations are presented in Figure 3.

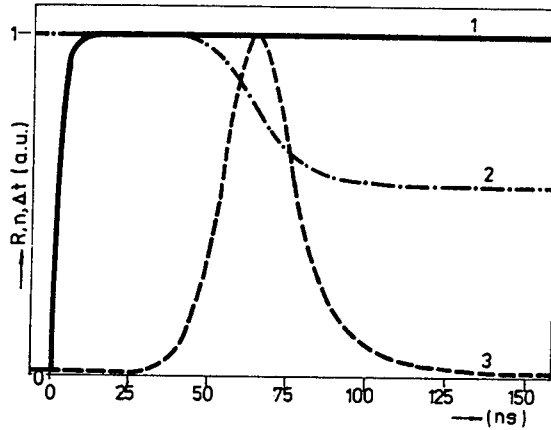


Figure 3

Plot of the SBS reflectivity R (curve 1), population inversion (curve 2), output pulse (curve 3) as a function of time

Our theoretical model which has considered the stationary approximation for the SBS interaction proved to be enough good to explain the Q-switching

regime of the linear resonator. The predicted pulse duration 25ns is close to the experimental measurements.

3. Ring laser resonator

3.1. EXPERIMENTAL SET-UP AND RESULTS

The experimental set up is depicted schematically in Figure 4.

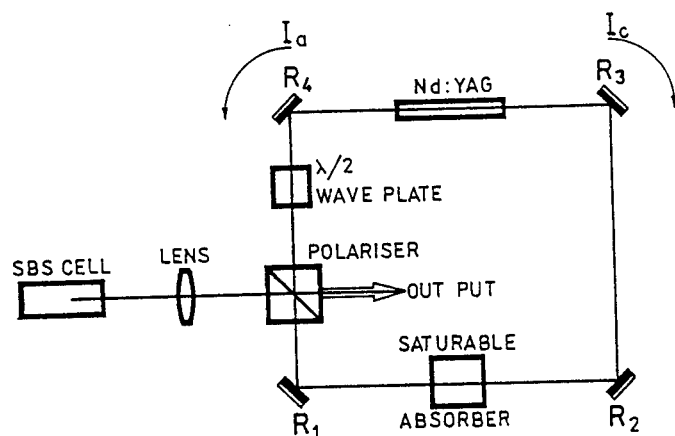


Figure 4
Schematic of the experiment for the ring configuration

The four plane mirrors with reflectivity $R \sim 100\%$ and the Nd:YAG rod with a small signal single pass gain of ~ 100 defined the ring cavity, whose length was 1m. The Nd:YAG rod with a 6 mm diameter and a 90 mm length was pumped by a flash lamp in a diffuse, liquid cooled cavity. The radiation at $1.06 \mu\text{m}$ was outcoupled by a half-wave plate-polarizer combination. The Brillouin cell ($L=10 \text{ cm}$) filled with CS_2 was placed behind a lens, which had a focal length of 10 cm, outside the ring cavity. The Brillouin backscattering radiation returned to the ring resonator has been extracted through the polarizer cube to be analysed.

A fast photodiode and a Le Croy digital oscilloscope (2GHz) have been used to monitor laser pulse duration. Mollectron detectors have been used to measure laser beam energies. The transversal structure of the output radiation was monitored by a CCD camera and a SPIRICON system.

The energy entering the Brillouin cell was about 120-130 mJ in the form of relaxation oscillations pulses with duration of the order of 200-300 ns but this output power could not reach the SBS threshold. We used a saturable absorber (Kodak liquid saturable absorber for Nd:YAG laser radiation) to initiate the SBS

process. It was mounted in the cavity and aligned such the reflection of the cuvette's windows would not cause feedback and the transmission was reduced until a single Q-switched spike was obtained. This has the additional effect of pre-Q switching the laser yielding pulses of duration ≈ 50 ns in the clockwise (I_c) and anti-clockwise (I_a) directions.

The output, I_c , was incident on the cell containing CS_2 . Reflection from the SBS cell reinjected, I_c , back into the ring where it contributed to the flux, I_a . The clockwise travelling output from the rod, via polariser, was p-polarised and after one pass through the half wave plate became s polarised component and was focused into the SBS cell. Because the SBS interaction preserves the polarisation state, the re-injected radiation was also s-polarised but having a frequency which corresponded to the first Brillouin Stokes shift $\omega_1 = \omega_0 - \omega_B$, where ω_0 is the linecentre of the Nd:YAG crystal and ω_B is the acoustic frequency. After one complete round trip $s_0(\omega_1)$ was converted to $p_1(\omega_1)$ by the half wave plate and then made a second round trip before reversion back into $s_2(\omega_1)$ and emission through polariser as the output. The cavity therefore acts as an oscillator-two pass amplifier system.

The laser visible in Figure 4 started in the free-running regime with a low Q factor determined by the losses of the cell and of the saturable absorber. The SBS reflectivity of the cell increased rapidly with the incident wave intensity and the ring resonator with the Brillouin mirror reached a high Q factor.

The output beam with an energy of 40 mJ in a pulse of 15-20 ns duration was obtained at 2Hz. At higher repetition rates Q-switching action become unreliable due to the fact that the saturable absorber was not circulated and excessive thermal loading may appear.

A typical output pulse with a width (FWHM) of 15 ns is shown in Figure 5

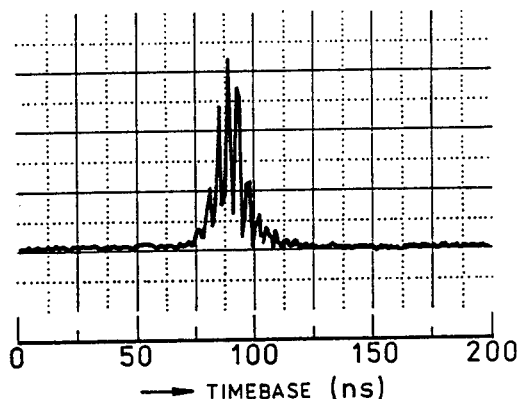


Figure 5

Pulse shape that is due to simultaneous liquid saturable absorber and SBS Q-switching

The Q-switched laser was partially mode-locked indicating that there exist many longitudinal modes oscillating during the lasing process.

Under proper alignment of laser mirrors, and with an aperture of $d=1,5$ mm the laser could operate in the TEM_{00} mode and the energy of the pulses diminished to 5 mJ.

3.2. THEORY

The system describing the Q-switching regime is the same as in the case of the linear resonator.

The threshold condition for the two intensities I_a and I_c are derived considering an imaginary plane between the polariser and mirror R_1 :

$$I_a R_1 T R_2 R_3 e^{(\gamma_a - \alpha)l_r} R_4 (1 - R_{out}) + I_c R R_{out} = I_a \quad (9a)$$

$$I_c (1 - R_{out}) R_4 e^{(\gamma_c - \alpha)l_r} R_3 R_2 T R_1 = I_c \quad (9b)$$

where R_{out} is the reflectivity of the output mirror (polariser), $R_1=R_2=R_3=R_4=100\%$, T is the transmission of the saturable absorber ($T=30\%$), l_r is the rod length and α are the losses per unit length of the laser rod.

We define :

$$\delta = \frac{I_c}{I_a} \quad (10)$$

Thus, the nonlinear losses $\gamma_{nl}(q)$ have the form :

$$\gamma_{nl} = \frac{2l_r \alpha}{\tau} + \frac{1}{\tau} \ln \left\{ \frac{1 - R\delta R_{out}}{[(1 - R_{out}) T R_1 R_2 R_3 R_4]^2} \right\} \quad (11)$$

where $\tau=l_r/c$ is the round trip time of the resonator. In the expression of the nonlinear losses we neglect the term referring to the linear losses $2l_r \alpha/\tau$, which is very small.

The steady state theory of SBS (eq. 4) have been considered again to find the analytical solution for R .

If we introduce the normalised variables :

$$\xi = t/\tau$$

$$R(\xi) = I_a/I_c \frac{1 - R_4 (1 - R_{out}) R_1 T R_2 R_3 e^{(\gamma_a - \alpha)l_r}}{R_{out}} \quad (12)$$

$$y(\xi) = n(\xi)/n(0)$$

$$x(\xi) = (I_c + I_a) g_B L_{eff}$$

we obtain the following system of equations :

$$\begin{aligned}
\frac{dR(\xi)}{d\xi} &= [A_0 y - H(R)]C(R) \\
\frac{dy(\xi)}{d\xi} &= -B_0 yx \\
\frac{dx(\xi)}{d\xi} &= [A_0 y - H(R)]x
\end{aligned} \tag{13}$$

The initial conditions are the same as in (7), A_0 , B_0 and $C(R)$ are identical as in (8) and $H(R)$ has the following expression :

$$H(R) = \ln \left[\frac{1 - R\delta R_{out}}{[(1 - R_{out})TR_1R_2R_3R_4]^2} \right] \tag{14}$$

The results of the numerical simulations are presented in Figure 6.

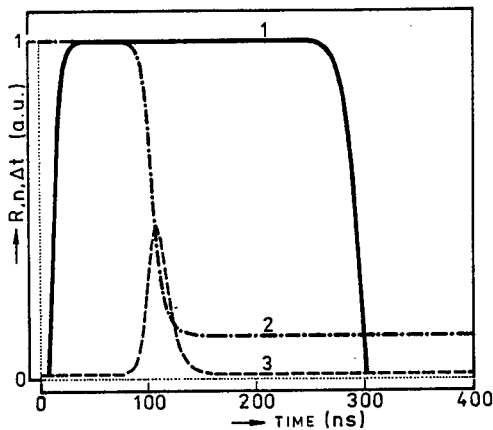


Figure 6
Plot of the SBS reflectivity R (curve 1), population inversion (curve 2), output pulse (curve 3) as a function of time for $R_{out} = 0.5$.

Despite its simplicity, this model accurately reproduces the narrowing for increased losses by stimulated Brillouin scattering in the ring resonator. The predicted pulse duration 20 ns is in good agreement with experiment.

4. Conclusions

We demonstrated a SBS Q-switching of a linear and ring resonator based on the gain material Nd:YAG. The power generated in the free-running regime proved to be not enough to reach the threshold of the SBS process in CS₂. However we succeeded to start operation of the laser in the Q-switching regime using a saturable absorber.

A theoretical description of the external SBS Q-switched resonators has been developed, using the stationary approximation for the SBS interaction and good agreement between experimental data and theory was obtained. The predicted pulse was smooth since the equations modelled take no account of propagation effects within the resonator and the subsequent frequency shift which is characteristic for SBS.

References

1. Rockwell, D.A. (1988) A review of phase-conjugate solid state lasers, *IEEE J. Quantum Electronics* **24**, 1124-1140.
2. Meng, H., Eichler, H.J. (1991) Nd:YAG laser with a phase-conjugating mirror based on stimulated Brillouin scattering in SF₆, *Optics Letters* **16**, 569-571.
3. Agnesi, A., Reali, G.C. (1992) Passive and self Q-switching of phase conjugation Nd:YAG laser oscillators, *Optics Communications* **89**, 41-46.
4. Pashinin, P.P., Shklovsky, E.I. (1991) Characteristics of a SBS self-injection locked laser, *Laser Physics* **1**, 160-165.
5. Lamb, R.A., Damzen, M.J. (1993) Q-switching of a Nd:YAG phase conjugate laser using external stimulated Brillouin scattering, *OSA Proceedings on Advanced Solid state lasers* **15**, 112-116.
6. Siegman, A.E. (1986) *Lasers*, University Science Book.
7. Mocofanescu, A., Agafitei, A., Dabu, R., Fenic, C., Stratan, A., (1996) Q-switching of a Nd:YAG laser resonator using Brillouin scattering, *Optoelectronica* **4**, 139-142.
8. Mocofanescu, A., Udaiyan, D., Damzen, M.J., Babin, V., Nd:YAG laser with a ring resonator and a phase-conjugating mirror based on external stimulated Brillouin scattering, (1996), *Proc. SPIE* **2771**, 28-33.

THE CONSTRUCTION OF LASER GYROSCOPE

V.E.ZHAROV, S.N.MARKOVA AND V.A.KRAINOV
*Sternberg State Astronomical Institute,
Moscow State University
Universitetsky Prospect 13 Moscow, 119899, Russia*

Abstract.

The passive ring laser resonator of square size with a side equal to 3.1 m is created in Sternberg State Astronomical Institute for the determination of the Earth angular rate.

This work deals with the construction of resonator and mode-watching system, estimation of the resonator parameters, influence of the temperature variations on the mode structure, control of the resonator perimeter, influence of the nonplanarity and the light polarization on the quality factor and, thus, on the accuracy of the Earth rotation measurements.

1. Introduction

Great attention is paid now to the determination of the Earth's angular rate Ω and the universal time $UT1 - UTC$, connected with it, with high precision and time resolution. Another important task is to do observations non-dependent on weather [1], the transparency and changes of the reflective index of the atmosphere. First of all it is interesting to geophysicists because the Earth rotation is connected with the processes in the oceans and atmosphere, tides in the Earth's crust and so on [2].

The processes, mentioned above, cause the variations of the Earth rotation rate about $\delta\Omega/\Omega \approx 10^{-9}$, where $\delta\Omega/\Omega = -LOD(s)/86400s$; LOD - length of day is excess of duration of the day on 86400 s. The seasonal variations of the LOD are of order $\delta\Omega/\Omega \approx 5 \cdot 10^{-8}$. Fig.1 shows the LOD variations during 3 years. The data were obtained by the International Earth Rotation Service (IERS). Diurnal variations of the universal time are shown on Fig.2 and are of order $\delta\Omega/\Omega \approx 5 \cdot 10^{-9}$.

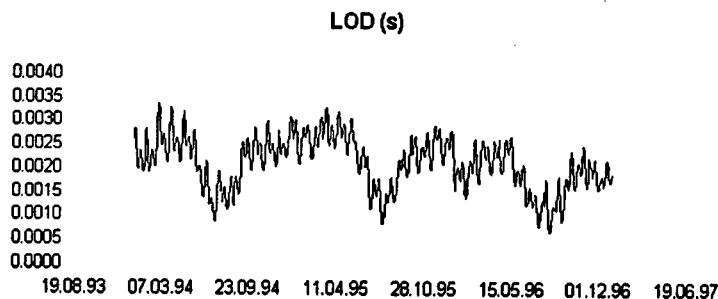


Figure 1. Length-of-day (LOD) variations determined by the IERS.

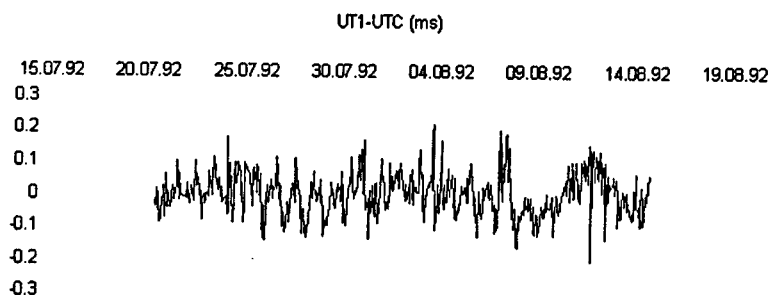


Figure 2. Variations of the universal time $UT1-UTC$ determined during *SEARCH-92* Campaign by GSFC using VLBI-observations.

Active and passive laser gyroscopes (or simply the ring resonators with large perimeter and square) are planned to use to determine high-accuracy variations of the Earth's rotation [4], [19]. The potential frequency resolution of a ring laser gyro is arguably greater than that of any other device [23]. The construction and the main characteristics of the passive laser gyro build in Sternberg State Astronomical Institute (Moscow, Russia) are discussed in this paper.

2. The construction of the ring resonator and mode-watching system

The operation of laser gyro is based on the "Sagnac" effect: in the presence of rotation with respect to inertial space perpendicular to the plane cavity, there appears the frequency difference between two beams propagating in the opposite directions in the cavity. It can be explained by the fact that the optical length of clockwise (CW) and counter-clockwise (CCW) paths round the ring are no longer equal [16].

We have chosen the passive resonator gyro [6]. The scheme is attractive because it eliminates the problems associated with the gain medium inside the interferometer itself. This kind of interferometers is free from beam locking, the variations of the light path optical length due to the variations of refraction index of the gain medium, different thermal effects in the gain medium.

Active gyros are usually used to determine high rotation rates. As it is shown by Privalov [21] using common He-Ne ring laser we are able to determine the rotation rate with accuracy $10^{-5} - 10^{-6}$ due to the processes in the gain medium only. The further increasing of the measurement accuracy is connected with serious improvement of the device parameters and measurement time increase. The measurement time determines the frequency resolution. So the detection of the subdiurnal variations of the LOD requires integration time of about one hour.

The active ring laser for geodesy is installed in Canterbury, New Zealand [19], [20]. Bilder *et al.* have built the active rectangular 3.5 m perimeter gyro and are planning to build the resonator with dimensions $4.2 \text{ m} \times 4.2 \text{ m}$. They have achieved the demanded accuracy of the determination $\delta\Omega/\Omega \sim 10^{-9}$ by increasing the measurement time to 8 days, decreasing the temperature fluctuations to ± 10 millidegrees over days by underground location (30 m underground) of the ring. To improve the achieved accuracy square ring of 16 m perimeter and 16 m^2 area, which enhances both the signal and reduces the noise, is planned to build. Cavity losses are expected to decrease by an order of magnitude, due to mirrors with lower loss. Other He-Ne I_2 -stabilized laser, placed in monolithic Zerodur bloc [22] with low loss dielectric mirrors, is installed 15-20 meter underground at Wettzell, Germany.

The beat frequency depends on the angular frequency Ω of rotation with respect to the local inertial frame, the area S and the perimeter L of the ring, and the optical wavelength λ :

$$\Delta f = \frac{4S\Omega}{\lambda L}.$$

We have built, the so-called, amplitude detector. As being excited by the internal generator the forced oscillations of the rotating ring cavity will have unequal dissipation in the detuned ring resonator. It will result in the intensity alteration of the counter-propagating waves. This effect can be used to determine the rotation rate of the platform [5].

Passive ring resonators are usually used to determine the phase degeneracy. But as it is shown in the work [16] the accuracy of the frequency difference determination is $6 \cdot 10^3$ times better than the phase degeneracy measurements.

The determination of the passive gyro shape is made by examining the parameters of the resonator eigenmode [12]. The resonator modes have to be

stable, it means that the beam divergence can be compensated by focusing with the help of spherical mirrors. The parameters of the resonator was obtained by the ray matrix method [7].

Many authors [8] prefer to work with resonators having three sides. This construction gives us only one resonator plane but the ratio L/S is less than in the case of four-side resonator. The theoretical limit of the Δf determination will be more in three-side resonator than in the case of four-side one. But at the same time four-side resonator can be done by two planes with some angle δ between them (the so-called nonplanar resonator) [9]. So we must estimate the effect of the nonplanar resonator on the accuracy of the determination of the value $\delta\Omega/\Omega$. It becomes important when we are going to achieve the accuracy of the determination $\delta\Omega/\Omega \sim 10^{-9}$.

Our passive resonator has a square form with the side equal to 3.1 m. It is mounted in the separate cellar on a massive plate to avoid the random oscillations of the soil, caused, for example, by Moscow traffic. But at the same time this construction can lead to the long-periodical changes of the mirror positions.

The resonator is formed by two flat (R_1, R_3) and two spherical (R_2, R_4) mirrors with $R_{2,4} = 10$ m, the arms length ($l = 3.1$ m) and the mirror curvature radius is chosen to form stable resonator modes (Fig.3).

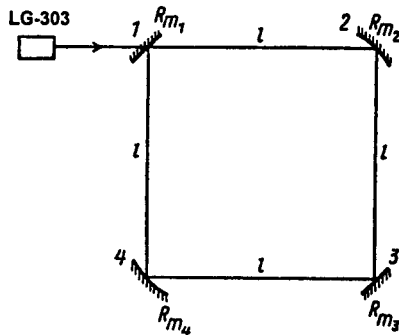


Figure 3. Schematic optical diagram of the ring resonator. The mirrors 1 and 3 are flat, and mirrors 2 and 4 are spherical.

The calculated resonator eigenmodes have the following spot size dimensions in beam waist, located on the flat mirrors: $\omega_x = 1.086$ mm, $\omega_y = 0.841$ mm. The input (R_1) and output (R_3) mirrors are flat.

The experimentally measured laser beam parameters at beam waist are $\omega_{0x} = \omega_{0y} = 0.222$ mm.

The reflection index measured at the angle of incidence 45° for flat mirrors – 96%, for spherical – 99%. The spherical mirrors are mounted on the piezoelectric rods (piezoelectric length transducers (PT)). It permits us to move them and to vary the resonator length up to $\pm 2 \mu\text{m}$. We use

specially stabilized *He - Ne* laser LG-303 with $W = 1.5$ mW working at TEM_{00} mode for our experiments.

The square form of our resonator courses the changes of the laser light polarization. In the case of the plane resonator these questions are discussed in the work [10]. The same questions for nonplanar resonators are under the consideration in the works [17] and [9]. This effect decreases the gyro quality factor and thus decreases the accuracy of our device.

We use special matching lens system [18]. The parameters of lens mode-matching system (spherical and cylindrical lenses, flat mirrors) were obtained by ray matrix method using the complex beam parameter $q(z)$:

$$\frac{1}{q(z)} = \frac{1}{R(z)} + \frac{i\lambda}{\pi} \omega(z)^2.$$

We used the simplex-method to take into account the additional limitation on the unknown parameters. The parameters of the system (the lens optical forces (F_i) and distances (l_i) between lenses) are determined by this method: the value $|q_x - Aq_{0x}|^2 + |q_y - Aq_{0y}|^2$ is minimized, where A is the matrix, depending on l_i and F_i , q_x and q_y corresponds to input resonator beam, q_{0x} and q_{0y} corresponds to output laser beam.

We have estimated matching mirror system and the mixed one (mirrors and lenses) by the same method, but the lens system seems to be more attractive [12](Fig. 4).

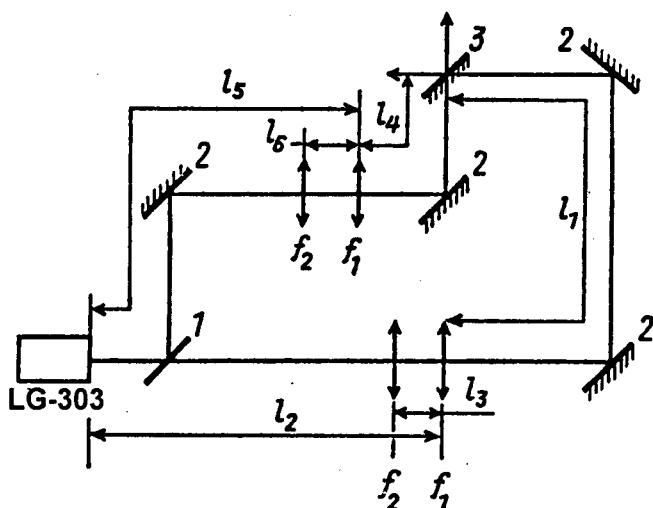


Figure 4. Mode-matching system: 1-light-dividing prism, 2-flat mirrors, 3-the input passive resonator mirror.

To avoid the problem of uncorrelated laser jitter, when two separate lasers are used, we decided to derive two independently controlled laser

frequencies from one laser. With the help of special optical glass cube we divided laser beam into two beams. Then they both penetrate through their own matching system and enter the cavity through the flat mirror.

The beam returning from the passive cavity can cause some perturbations in laser. It leads to laser unstable work. That is why we have to use non-interaction elements – acousto-optics modulators (AOM) (sound transducers), deflecting laser beam and shifting laser light frequency. The frequency shift is constant and is equal to $f_1 = 25$ MHz for the CW beam. It is obtained from the frequency standard (ST). It is variable ($f_2 = f_1 + \Delta f$) for the CCW beam. We determine the rotation rate by making frequency difference measurement. We measure

$$\Delta f = f_2 - f_1 = \frac{4S\Omega}{\lambda L} \sin \varphi \approx 295 \text{ Hz},$$

where $\lambda = 0.63 \mu\text{m}$ is the laser wavelength, φ is the latitude of the place.

The cavity is tuned to the frequency equal to $f_0 + f_1$ with the help of voltage feedback loop by moving one of the spherical mirrors. We receive signal needed for the loop work on the detector D_1 output. The perimeter of the ring is kept during the measurement time with error less than 30 \AA . In order to obtain the stable work of the loop another spherical mirror is jittering with the frequency $f_m = 2 \text{ kHz}$ and the amplitude equal to the tenth parts of λ . The differential signal of D_1 (DA) and D_2 is guiding the f_2 frequency synthesizer (FS). The schematic diagram of the passive laser gyro is given in the Fig. 5.

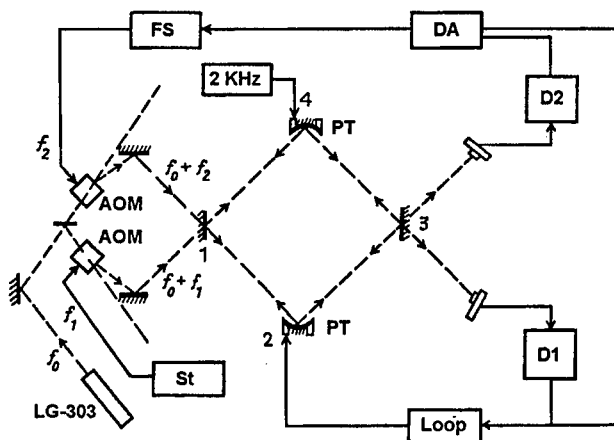


Figure 5. Schematic diagram of the passive laser gyroscope – rotation sensor.

The optical circuit is vacuumed to avoid the influence of air convection. We have done it by steel tubes and special cavities for mirrors. Using three vacuum pumps we can have pressure $p = 10^{-3} \text{ Pa}$ in the cavity.

3. The estimation of the parameters and accuracy of our device

Gyroscope parameter changes $\delta l/l$, laser frequency $\delta f/f_0$, angle of rotation axes inclination in respect to the cavity plane $\delta\varphi$ cause the changes of the expression $4Sf_0/cL$, where c is light velocity [24]. These variations cause the variations of the measured frequency Δf even if the Earth's rotation rate Ω is stable:

$$\delta(\Delta f) = \frac{lf_0\Omega}{c} \left(\frac{\delta\Omega}{\Omega} + \frac{\delta l}{l} + \frac{\delta f}{f} + \operatorname{ctg}\varphi\delta\varphi \right) \sin\varphi,$$

where l is the square cavity side length.

To determine $\delta\Omega/\Omega$ with error 10^{-9} per day the other parameters must have errors less than 10^{-9} per day.

The fluctuations $\delta(\Delta f)$ depend on the following reasons:

- Laser frequency stability have to be less than 10^{-9} . Our laser has frequency stability not more than 10^{-8} .
- The total thermal cavity length variations have to be less than $\lambda/2$, it corresponds to the temperature variations equal to $\approx 0.005^\circ$ per day.
- The $\delta\varphi$ variations are caused by
 - the polar motion ($\approx 10^{-7}$ per year),
 - the tides in the Earth crust ($\approx 10^{-7}$ per day),
 - random causes (?).
- The random mirror jitter have to be not more than $\lambda/2$.

The accuracy of determination of $\delta\Omega$ is connected with the accuracy δf of the frequency difference $f_2 - f_1$ measurements [10]:

$$\delta\Omega = \frac{\lambda L}{4S} \delta f, \quad \text{where } \delta f \text{ is equal to } \delta f \approx \frac{\sqrt{2}\Delta f_s}{\sqrt{N_{ph}\eta\tau}},$$

where N_{ph} is the mean photon quantity reaching detector with efficiency η per second, τ is integrating time. The Δf_s is spectral resonator line width. It is connected with cavity quality factor $Q = 2\pi L/(\alpha\lambda)$ by the equation $\Delta f_s = f_0/Q$, where α is cavity total loss coefficient.

In our case $N_{ph} = 1.5 \cdot 10^{14}$ photon/s in each beam, $\eta = 0.7$; $\alpha \approx 0.1$ (reflection coefficient ≈ 0.96); $f_0 = 4.8 \cdot 10^{14}$ Hz, we will obtain $Q \approx 1.2 \cdot 10^9$ and $\Delta f_s \approx 0.4$ MHz. The theoretical precision limit is

$$\frac{\delta\Omega}{\Omega} \approx 5 \cdot 10^{-6}, \quad \text{when } \tau = 1000 \text{ seconds,}$$

$$\frac{\delta\Omega}{\Omega} \approx 5 \cdot 10^{-7}, \quad \text{when } \tau = 1 \text{ day.}$$

If laser output is 50 mWt, $N_{ph} = 50 \cdot 10^{14}$ photon/s in each beam, $\eta = 0.7$; $\alpha \approx 0.04$ (reflection coefficient ≈ 0.99); $Q \approx 3.1 \cdot 10^9$ and $\Delta f_s \approx 0.15$ MHz the corresponding theoretical precision limit is

$$\frac{\delta\Omega}{\Omega} \approx 2 \cdot 10^{-7}, \quad \text{when } \tau = 1000 \text{ seconds,}$$

$$\frac{\delta\Omega}{\Omega} \approx 2 \cdot 10^{-8}, \quad \text{when } \tau = 1 \text{ day.}$$

It means that our detector sensitivity is be enough to register the tides in the Earth crust.

As we have already mentioned above the other limiting factor is that the centers of the square form resonator mirrors can determine two planes with the angle δ (differing from 180°) between them. This angle has constant value if the platform is absolutely rigid. It is shown in our previous work [14] that the constant value of this angle leads to the constant difference Λ of the measured Earth rotation frequency from the real one. This difference value can be found by the comparison of the obtained instrumental data with the results published by IERS. We have the difference ± 0.5 mm in the mirror centers position in height, so the value of the angle δ is $\sim 30''$. The corresponding difference $\Lambda \approx 3 \cdot 10^{-8}$. We must take it into account in our experiments. Random thermal deformations cause variations of angle δ , and the estimated value of error is $\delta\Omega/\Omega \approx 3 \cdot 10^{-8}$.

This case corresponds to the mirror $10''$ inclination, and it leads to tuning the resonator from TEM_{00} mode to TEM_{01} , as we have observed in the experiment (Fig. 6).

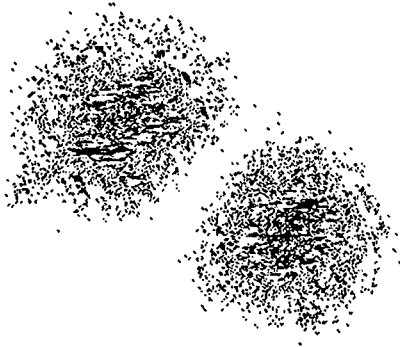


Figure 6. TEM_{01} resonator mode.

The oscillographic pictures of our resonator modes are represented in Fig.7, random perimeter changes are shown in Fig.8-9. During 10 s time interval the perimeter changes up to 0.1λ .

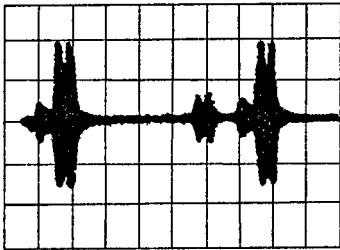


Figure 7. Oscillogram of resonator mode.

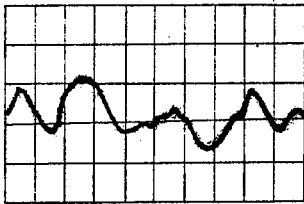


Figure 8. Thermal perimeter changes on 10 s time interval.

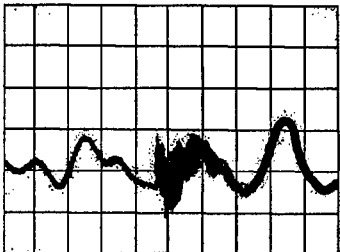


Figure 9. High-frequency perimeter changes (the strike of the gyro fundament).

The square resonator form causes the changes of light polarization from linear to elliptical. The relatively ill-studied anisotropy in birefringence always presents. Our estimations (for linear phase birefringence is equal to 30 arc minutes) lead to relative change of $\delta\Omega/\Omega \approx -2 \cdot 10^{-6}$.

The frequency difference $\Delta f'$ after the full round trip in the nonplanar circuit is given by the equation

$$\Delta f' = \gamma \Delta f,$$

where $\Delta f = f_1 - f_2$. The ratio of the measured Earth rotation frequency Ω_m in the case of the nonplanar resonator to theoretically estimated one for the ideal plane resonator Ω_e will be:

$$\Lambda = \frac{\Omega_m}{\Omega_e} = \gamma.$$

The variable part of the angle $\delta(t)$ exists due to the temperature variations of the different parts of our ring resonator: the platform, the vacuum tubes, the metallic holding constructions etc. There exist some variable values of the measured Ω_m . These variations are determined by the equation

$$\delta\Omega_m = -\Omega_e\gamma^3 \sin 2\delta \cdot \Delta\delta(t),$$

where

$$\delta(t) = \delta_0 + \varepsilon \cdot \sin\left(\frac{2\pi}{P_1}t + \psi\right),$$

here δ_0 is a constant angle, ε is amplitude variations, P_1 is the period of changes, ψ is a random phase. If the amplitude ε is less than δ_0 , the rotational rate variation will be:

$$\delta\Omega_m \approx -2\pi\varepsilon \frac{\Delta t}{P_1} \Omega_e \cos\left(\frac{2\pi}{P_1}t + \psi\right) \sin 2\delta_0,$$

where Δt is the measurement time for $\Delta f'$.

The variations of the angle $\delta(t)$ exist due to the thermal difference between different parts of the platform. The effective phase rate is changing in this case. The phase rate changes can be estimated in the following model. The height of the platform will change due to the temperature gradient $\delta h = \alpha \Delta T h$. Here α is the linear expansion coefficient of the platform material, ΔT is the temperature gradient, h is the platform height over the floor. The height h changes in

$$\delta h = 5 \cdot 10^{-6} \frac{\Delta T}{1^\circ} h$$

with the temperature changes equal to 1° C. The platform inclination is determined by the equation

$$\theta = \frac{\delta h}{L}.$$

This inclination causes variations of the optical path in the both resonator arms:

$$\delta L_{opt} = 2.5 \cdot 10^{-11} \frac{h^2}{L} \left(\frac{\Delta T}{1^\circ}\right)^2.$$

To tune the resonator from TEM_{00} mode to TEM_{01} we have to change the optical path by δL_t [15] where

$$\delta L_t \approx 0.09 \left(\frac{\lambda}{r}\right)^2 L.$$

The radius of the resonator mirrors is r . Using this estimations we can have

$$\frac{\delta L_{opt}}{\delta L_t} \approx 2.7 \cdot 10^{-10} \left(\frac{r}{\lambda}\right)^2 \left(\frac{h}{L}\right)^2 \left(\frac{\Delta T}{1^\circ}\right)^2.$$

When $r = 2$ cm, $h = 1$ m, $\Delta T = 1^\circ$ this ratio is equal to 0.04. This temperature variation causes the platform angle θ inclination approximately equal to $0.3''$. Considering the last equation we must conclude that this temperature variation cannot cause the mode changes in our resonator. But we have observed the transition from TEM_{00} mode to TEM_{01} mode with the temperature changes even less than 1° . It can be explained only by the fact that rigid metal constructions of our resonator have different deformations: the tube bend, the corresponding inclination of the mirrors etc. We can obtain from the ratio

$$\delta L_{opt}/\delta L_t = 0.04,$$

the value of the angle $\theta = 8''$. This tube bend will cause the variations of the measured Earth rotation rate of the order of 10^{-8} when $\Delta t = 3$ h. The angle θ changes due to the temperature variations with the period equal to one day. The given equations show that changes of the optical path are proportional to $(\Delta T)^2$. The temperature variations diminishing in 10 times will decrease the influence of the tube bend in 100 times.

The generation of the resonator modes of high orders is not good. We have to thermostabilize the experimental system with the accuracy 0.1° to prevent the mode transition in our resonator system.

The received accuracy estimations showed that the laser frequency variations can be regarded in finding the source of errors. We consider mainly thermal deviations and mirror quality to limit the accuracy of our detector as we can exclude any mechanical (microseismic) jitter of the optical elements.

We have measured seismic jitter of the gyro base for three days [13]. We used piezoceramic acceleration detector and induction seismodetector. Both measurements gave the same spectra. The variations are weak and we can consider the base horizontal jitter is absent. The vertical base jitter acceleration spectrum for the frequency range $0 \div 50$ Hz was analyzed. The vertical shift is equal to $5.6 \cdot 10^{-5} \text{ m} = 5600 \text{ \AA}$ at 3 Hz frequency. The platform and our device are oscillating as a whole body with this frequency. It means that seismic jitter does not influence the gyro work.

To find the real variation of the Earth's rotation rate we must determine the temperature of the base continuously. It will give us the opportunity to exclude this temperature variations of Δf from consideration. To determine the temperature distribution in the base mass we used traditional bridge circuit with thermoresistances. The experiment was performed from 6.30 a.m. to 6.00 p.m. Unfortunately we found that one of the base corners was cooling quicker than another one approximately by $0.002^\circ/h$. This temperature difference courses the optical length variations $\delta l/l \approx 10^{-8}$.

4. Conclusions

The accuracy of the resonator length control is about 30 \AA in our case. We have performed the temperature monitoring of the system for 12 hours and found that the temperature variations equal to 0.5°C lead to the changes in mode structure from TEM_{00} to TEM_{01} . For further experiments we have to thermostabilize the resonator body with accuracy 0.05°C . Due to the temperature changes our four mirror resonator becomes nonplanar and it leads to the additional quality factor changes. The chosen geometrical resonator form changes the linear polarization of the input light to elliptical one. It also changes the quality factor and the accuracy of our measurements. In this work we estimate the quality factor changes using the possible temperature variations.

For the achievement of the theoretically estimated accuracy of our instrument (10^{-8} per one hour integration) we need to thermostabilize the resonator, change the resonator mirrors by the mirrors with reflection index 0.99, change our laser by more powerful with output power not less than 50 mW.

References

1. Feissel M. and Gambis D. (1993) *Adv. in Space Research*, Pergamon Press, **13**, no 11, pp. 143-144
2. Moritz G. and Muller A. (1987) *Earth rotation: theory and observation*. Ungar Publ. Co, New York.
3. Carter W.E. and Robertson D.S. (1993) *Adv. in Space Research Pergamon Press*. **13**, no 11, pp. 197-198
4. Blinov N.S., Zharov V.E. and Sazhin M.V. (1989) *Proc. Intern. Symp. "Geodesy and Physics of the Earth"*, Potsdam, **102**, part 1, pp. 59-60
5. Bichkov S.I. et. al. (1975) *Laser Gyroscope*. Moscow (in Russian)
6. Sanders V.E., Prentiss M.G. and Ezekiel S. (1981) Passive ring resonator method for sensitive inertial rotation measurements in geophysics and relativity, *Optics letters*, **6**, no 11, pp. 569-571
7. Gerrard A. and Burch J.M. (1978) *Introduction to Matrix Methods in Optics*. Mir, Moscow (in Russian)
8. Seregin V.V. and Kukuliev R. M. (1990) *Laser Girometers and their application*. Moscow (in Russian)

9. Kravtsov N.V., Nani O.E., Rilov S.I. and Firsov V.V. (1993) *High stabil ring monolithic ring lasers*. MSU, Moscow (in Russian)
10. Ezekiel S. and Balsamo S. R. (1977) Passive ring resonator laser gyroscope, *Appl. Phys. Lett.*, **30**, no 9, pp. 478-480
11. Bilger H.R., Stedman G.E. and Wells P.V. (1990) Geometrical dependence of polarisation in near-planar ring lasers, *Optics communications*, **80**, no 2, pp. 133-137
12. Zharov V.E., Markova S.N., Sazhin M.V. and Fedoseev E.N. (1992) The determination of the optical scheme parameters of passive laser gyroscope, *Vestnik Mosk. Un-ta, ser. Physics. Astronomy*, **33**, no 1, pp. 60-63 (in Russian)
13. Zharov V.E., Markova S.N., Sazhin M.V. and Krainov V.A. (1995) The determination of the parameters of laser gyroscope for monitoring of the Earth rotation, *Vestnik Mosk. Un-ta, ser. Physics. Astronomy*, **36**, no 3, pp. 81-88 (in Russian)
14. Zharov V.E., Markova S.N. and Sazhin M.V. (1997) The influence of the gyroscope plane inclination on the accuracy of the determination of the Earth rotation parameters, *Vestnik Mosk. Un-ta, ser. Physics. Astronomy*, **38**, no 1, pp. 60-63 (in Russian)
15. Ananiev Y.A. (1979) *Optical Resonators and the Problem of Light Divergence*. Nauka, Moscow (in Russian)
16. Chow W.W., Gea-Banacliche J., Pedrotti L.M., Sanders V.E., Schleich W. and Scully M.O. (1985) The ring laser gyro, *Rev. Mod. Phys.*, **57**, no 1, pp. 61-104
17. Nilsson A.C., Gustafson E.K. and Byer R.L. (1989) Eigenpolarization theory of monolithic nonplanar ring oscillators, *IEEE Journal of Quantum Electronics*, **25**, no 4, pp. 767-790
18. Shaw G.L. et. al. (1983) Mode matching for a passive resonant ring laser gyro, *Applied Optics*, **22**, no 16, pp. 2487-2491
19. Bilder H.E., Stedman G.E., Li Z., Schreiber U. and Schneider M. (1995) Ring lasers for geodesy, *IEEE Transactions of Instrumentation and measurement*, **44**, no 2, pp. 468-470
20. Bilder H.E., Stedman G.E., Li Z., Poulton M.P., Rowe C.H., Vetharaniam I. and Wells P.V. (1993) Canterbury ring laser and tests for nonreciprocal phenomena, *Aust. J. Phys.*, **46**, pp. 87-101
21. Kozubovskii V.R. and Privalov V. E. (1995) Ring lasers for precise measurements, *Optica and Spectroscopia*, **78**, no 5, pp. 842-871 (in Russian)
22. Troy C. T. (1997) Laser gyro for monitor rotation of the Earth, *Photonics Spectra*, **2**, pp. 42
23. Anderson R., Bilder H.E. and Stedman G.E. (1994) The "Sagnac" effect: a century of earth rotated interferometers, *Am. J. Phys.*, **62**, no 11, pp. 975-985
24. Privalov V. E. (1992) *Laser interferometers for mechanical measurements*. Mech. Inst., StP. (in Russian)

PART V: LATE SUBMISSION

SBS properties of high-pressure xenon at a density of 0.3 - 1 g/cm³

L.I.ZYKOV, S.A.BUYKO, YU.V.DOLGOPOLOV, A.M.DUDOV,
V.A. EROSHENKO, G.A.KIRILLOV, G.G.KOCHEMASOV,
S.M.KULIKOV, V.N.NOVIKOV, A.F.SHKAPA, AND
S.A.SUKHAREV

*Russian Federal Nuclear Center (VNIIEF)
Sarov, Nizhni Novgorod Region, 607190, Russia*

Abstract

For xenon at the density of 0.3-1g/cm³ measurements have been made of the critical energy of thermal effect on the phase conjugation at SBS, the SBS gain coefficient, and the phonon lifetime. It has been shown that xenon is very well suited for the use in powerful gas lasers as an active SBS medium and is one of the best media for other lasers.

Presently, to study the physical processes of the matter behavior in quasi stationary superhigh intensity fields, the high-power nanosecond range laser facilities are created capable of focusing radiation to a wavelength size spot [1]. One of the difficulties faced in laser facilities of this class is compensation of optical elements aberrations and inhomogeneities of an active medium. To compensate for aberrations of the optical elements in such laser facilities and optical inhomogeneities of an active medium, one uses phase conjugation (PC) by stimulated Brillouin scattering (SBS). However, conversion of high-power laser beams in the SBS medium can be accompanied by competing processes such as SRS, optical breakdown, striction, and thermal perturbation. The present work gives the results of measuring the critical energy of thermal perturbation, SBS gain growth, and phonon lifetime in compressed xenon at densities of 0.3-1 g/cm³ [2, 3].

1. Thermal and Striction Perturbation of the SBS-medium

When a Gaussian beam is focused, depending on the pump conditions a lens is formed in the SBS medium, and the phase change in the pump radiation along the focused beam waist is:

$$\delta\varphi = \frac{2\pi^2}{\lambda^2} \left(n_2 P_L - \frac{3}{2} \frac{\beta\alpha}{TC_P} \int_0^{\tau_L} P_L dt \right) \quad (1)$$

where λ is the radiation wavelength, $n_2 = \frac{9}{2nc} \left(\frac{\beta}{v} \right)^2 \rho$ is the refractive index non-linearity coefficient due to electrostriction, β (cm^3/g) and n are the specific refraction and the refractive index of the medium, ρ (g/cm^3) is the medium density, c and v are the light and sound speed in the medium, C_p ($\text{J}/\text{g}\cdot\text{deg}$) is the specific heat capacity at constant pressure, P_L (W) is the pump radiation power; τ_L is the pump pulse length; T is the temperature, and α (cm^{-1}) being the laser radiation absorption coefficient in the SBS medium.

The first term of relation (1) describes the phase change connected with electrostriction appearing as a result of self-action of the pump radiation, which depends on the radiation power (intensity) in the SBS cell. Note that the SBS itself appears due to electrostriction evolution in the medium. Effect of this time-dependent component was observed for the first time in works [4, 5]. The second term is responsible for the phase change occurring with appearance of the thermal component in the SBS medium, which is determined by the pump energy absorbed in it. In this case a thermal lens is formed in the medium, which causes defocusing of the pump beam. At $\delta\phi > 2\pi$ the beam refraction distortions are becoming equal to those caused by diffraction, and as it follows from the experiment, the SBS efficiency falls down, which exhibits itself in a decrease of the reflection coefficient [5, 6, 7] and in a decrease of the phase conjugation fidelity [4, 5, 6]. For operation of the SBS mirror without a decrease in the phase conjugation fidelity, the pump radiation phase change should be $\delta\phi < 2\pi$. Then the power and energy of the laser pulse exciting SBS should be less than some critical values:

$$P_{cr} = \frac{\lambda^2}{2\pi n_2} \quad (2)$$

$$W_{cr} = \frac{\lambda^2}{2\pi} \frac{C_p \rho}{\frac{dn}{dT} \alpha} \quad (3)$$

where P_{cr} is the critical power determined by electrostriction; W_{cr} is the thermal perturbation critical energy [6].

Depending on the medium absorption coefficient (and pump conditions) the phase conjugation fidelity can be degraded by either of the factors. At small α electrostriction phenomena will dominate, at large α the

thermal phenomena will be dominating. The critical energy of thermal perturbation W_{cr} is determined by the absorption coefficient α and depends mainly on purity of the applied SBS medium. However, even for an absolutely transparent medium ($\alpha = 0$) there exists some limiting value of the critical energy. It is connected with the decay of hypersonic grating in the medium, i. e., with the presence of internal friction in it and is proportional to the Stokes frequency shift and sound speed in gas. For the gas lasers with a narrow gain line the Stokes shift should be small, and this requirement is met by xenon in the best way, from all monoatomic gases it has the lowest sound speed.

The thermal lens formation and the absorption coefficient in compressed xenon were investigated experimentally upon SBS excitation by radiation of a single-mode iodine laser ($\lambda = 1.315 \mu\text{m}$, pulse duration of 3-100 μs). The medium was probed by a beam of a He-Ne laser according to scheme [8] given in Fig.1. When a thermal lens is formed in the medium, the probe beam broadens in the plane of screen 5 and reaches photodetector 6. This signal is recorded by the oscillograph together with a SBS pump signal of the iodine laser. Typical oscillograms of the pump pulse and the probe laser signal are given in Fig.2. The oscillogram in Fig.2a shows behavior of the signal from the photodetector of the probe beam in the presence of an only thermal ("slow") component in the medium. Fig.2b illustrates joint modulation of the medium refractive index by striction ("fast") and thermal ("slow") components.

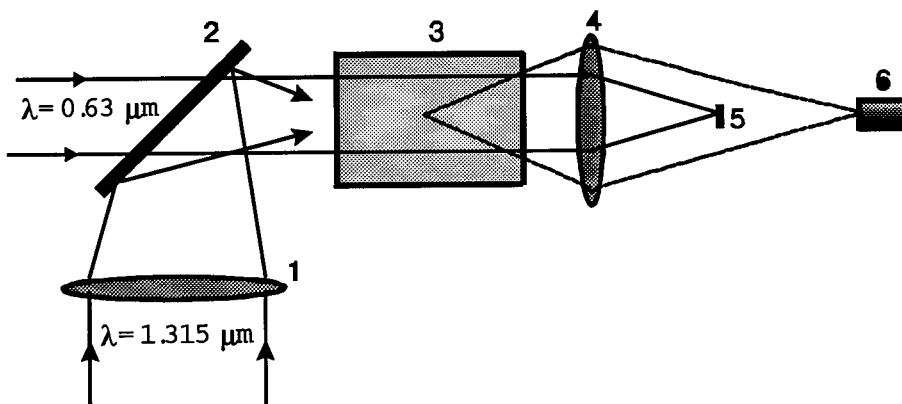


Fig. 1. Optical inhomogeneities investigation in the SBS medium (1, 4) lenses; (2) mirror; (3) cell with the SBS medium under study; (5) screen; (6) photodetector.

Experiments show that the pressure wave (and, hence, the wave of the changing refractive index) caused by striction propagates in the SBS medium with the sound speed, reflects off the walls of the cell and again (with a delay relative to the pump pulse) perturbs the medium in

the probing zone. At lower pump powers traveling waves of inhomogeneities are not excited and a "slow" thermal lens with millisecond relaxation times is formed (Fig.2a). Using our experimental results and with account of our technology of SBS medium preparation, there have been obtained the following values of the absorption coefficient and critical parameters, for 46 atm Xe (density of 0.38 g/cm³) and $\lambda = 1.315 \mu\text{m}$: $\alpha \approx 5 \cdot 10^{-7} \text{ cm}^{-1}$, $P_{\text{cr}} = 3.2 \cdot 10^5 \text{ W}$, $W_{\text{cr}} = 5 \text{ J}$.

a

b

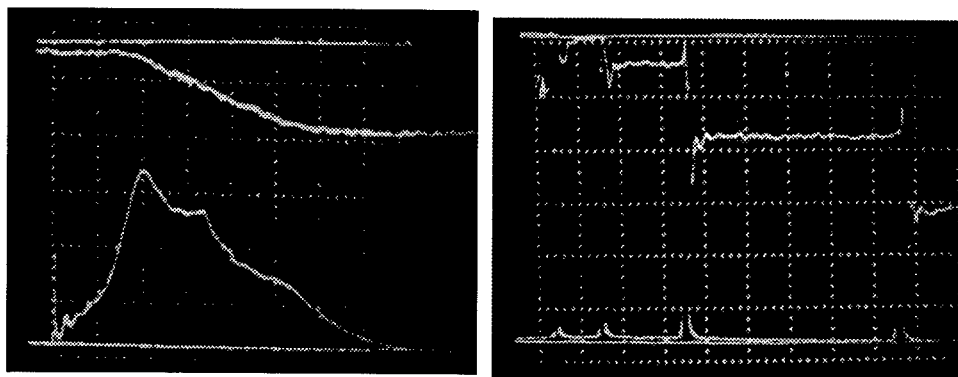


Fig. 2. Typical pulse oscillograms: probe radiation (upper beams) and SBS medium pumping (lower beams). The smallest time mark corresponds to 4 μs .

The highest laser pulse duration at which SBS excitation in a steady-state mode occurs in the absence of thermal perturbation is: $\tau_{\text{cr}} \leq W_{\text{cr}}/P_{\text{thr}} \approx g \cdot W_{\text{cr}}/5\lambda$ [2, 9], where $P_{\text{thr}} \approx 5\lambda/g$ is the threshold power for a single-mode radiation, g is the SBS gain coefficient (cm/W). For $g = 120 \text{ cm/GW}$ (see below) τ_{cr} reaches the value of $\tau_{\text{cr}} \approx 1 \cdot 10^{-3} \text{ s}$. In this case during a laser pulse the striction perturbation does not affect the phase conjugation fidelity, and thermal perturbation begins to degrade it only in the end of the pulse.

2. Investigation of the SBS Gain Coefficient and Phonon Lifetime [3]

Theoretical investigations predict an increase of the SBS gain coefficient in xenon with the increase of the gas density $g \propto \rho^2$ [10]. Far from the critical point ($T_{\text{cr}} = 289.7^\circ\text{K}$, $P_{\text{cr}} = 57.6 \text{ atm}$, $\rho_{\text{cr}} = 1.11 \text{ g/cm}^3$) the experimental results agree fairly well with this dependence, for example, $g = 1.4 \text{ cm/GW}$ at $P = 10 \text{ atm}$ ($\rho = 0.058 \text{ g/cm}^3$) [11], $g = 44 \text{ cm/GW}$ at $P = 39 \text{ atm}$ ($\rho = 0.30 \text{ g/cm}^3$) [12]. However, an attempt to obtain a high gain growth in xenon at a pressure of 220-240 atm [13] did not give results expected by the authors of this work. In work [14], as the

critical point of Xe at $\rho \geq 0.7 \text{ g/cm}^3$ was approached, appearance of optical inhomogeneities was registered, which raised the SBS threshold. Below we give results obtained from SBS investigation in Xe at densities from 0.3 g/cm^3 to 1 g/cm^3 in a thermostatically controlled cell under conditions when the influence of optical inhomogeneities on the SBS threshold was small.

Scheme of experiments of SBS threshold power (P_{thr}) measurements in a steady-state excitation regime is shown in Fig. 3. Single-mode iodine laser radiation was used for SBS excitation with the following Laser radiation parameters: wavelength $\lambda = 1.315 \text{ }\mu\text{m}$, energy $E \approx 10 \text{ J}$, pulse duration $\tau_L \approx 100 \text{ }\mu\text{s}$, radiation divergence $\theta_{0.84E} \approx 10^{-4} \text{ rad}$, laser beam diameter $D \approx 7 \text{ cm}$. Parameters of the pumping,

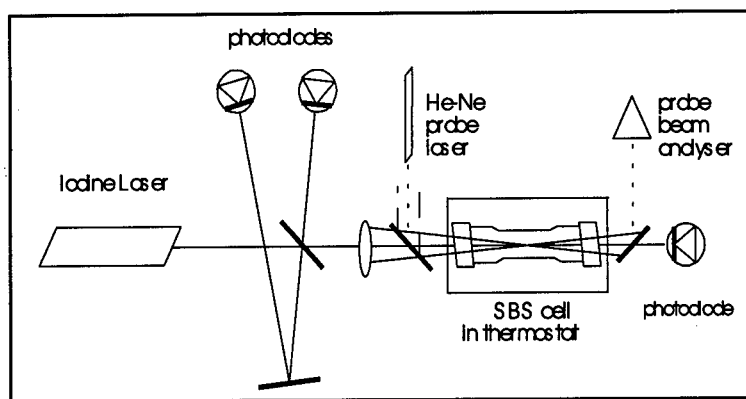


Fig. 3. Experimental setup.

reflected and passed through the SBS cell radiation were registered by calibrated photodiodes with the time resolution of 50 ns . The pumping power was measured in the far field of a positive lens by photo diodes with different apertures, it allowed to measure the pumping power in different angles : $1 \cdot 10^{-3}$, $1 \cdot 10^{-4}$, $5 \cdot 10^{-5} \text{ rad}$ and to control the pump radiation divergence.

The laser radiation was focused into the SBS cell with a length of 25 cm and diameter of 1.5 cm by means of a lens with the focal length $F = 138 \text{ cm}$. A special attention was given to Xe purity. To exclude influence of impurities, only metal (indium) linings were used in the cell construction, and it was filled through special filters. The purification efficiency from aerosol particles with a diameter more than $0.01 \text{ }\mu\text{m}$ was above 99.9999% . The thermostat maintained the cell temperature at a value of $t = 19.3 \text{ }^\circ\text{C}$, the temperature drift did not exceed $0.03 \text{ }^\circ\text{C}$ per hour. The Xe pressure in the cell was measured with a relative error of 7% , the density of Xe was determined by cell weighing. The optical quality of SBS medium was supervised with the help of a He-Ne laser which parameters were selected in such a manner that its beam simulated the pump beam in the cell. The intensity distribution in the

focal plane inside the cell with Xe $I_1(\phi)$ was compared with the distribution obtained in the absence of the cell $I_2(\phi)$. Measurements of the intensity distribution were carried out in the focal plane with the help of diaphragm scanning across the horizontal cross section. The He-Ne radiation power passed through the diaphragm was registered by a photodiode and measured by a digital voltmeter. Comparison of both distributions ($I_1(\phi)$ and $I_2(\phi)$) allowed us to estimate quantitatively the deformation of a diffraction limited beam during its passage through the SBS-cell. For all investigated points these distributions coincided with on accuracy of $\approx 5\%$, and only at $\rho = 1.02 \text{ g/cm}^3$ the intensity in the maximum fell down from $I_2^{\max} = 1$ in the absence of the cell to $I_1^{\max} = 0.62$ with it. This was taken into account in the P_{thr} calculation.

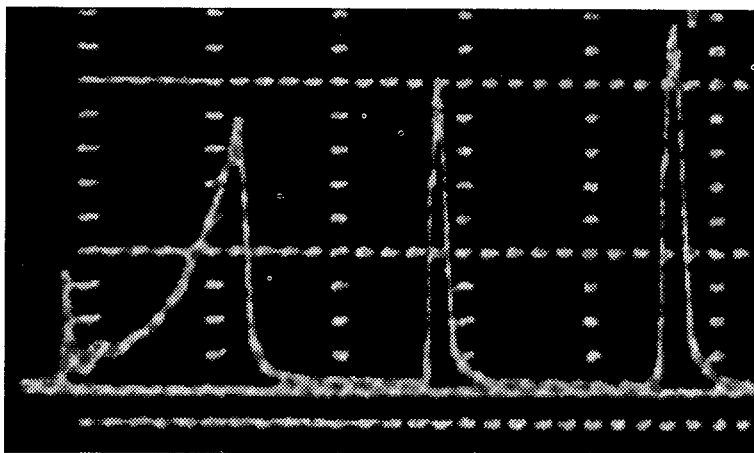


Fig. 4. Typical pumping pulse shape. Horizontal scale - $20 \mu\text{s/div}$.

Under the influence of Stokes radiation, as SBS excitation occurred, the mode of iodine laser generation changed and became pulse-periodic (see Fig. 4). Only the first pulse with the leading front duration of about $20 \mu\text{s}$, where steady-state excitation conditions were satisfied and pump energy did not exceed the critical energy of thermal defocusing W_{cr} , was used to determine the P_{thr} . The value of pumping power P_L providing the SBS reflection coefficient $R_s = 1\%$ was taken as P_{thr} :

$$P_{\text{thr}} \langle R = 1\% \rangle = P_L \langle \theta = 5 \cdot 10^{-5} \text{ rad} \rangle \cdot \frac{I_1^{\max}}{I_2^{\max}}.$$

The basic results of experiments are shown in Table 1, where averaged over several experiments P_{thr} values are shown. The standard deviation obtained in each series of experiments did not exceed 15% . For the gas density we give experimentally measured values labeled by an asterisk and values, calculated using Pitser's three-parameter

correlation by method of Li-Kesler [15], giving the best approximation to experiment.

Table 1 The basic results of experiments.

P, atm	39, 8	43	46	47. 4	50	54	56	59. 2	60. 5	61	61. 3	62
ρ , g/cm ³	0.3 0 0.3 0*	0.3 4	0.3 8	0.4 1	0.4 5	0.5 3	0.6 0 0.5 9*	0.7 8	0.9 0	0.9 4	0.9 7	1.0 4 1.0 2*
P _{thr} , kW	27	24	19	14	16	11	10	11	12	11	11	12

From the obtained data we have determined the SBS gain coefficient g_i using as a reference value $g_0 = 44$ cm/GW for the Xe density of 0.3 g/cm³ given in work [12]:

$$g_i = \frac{P_{thr}^0}{P_{thr}^i} g_0,$$

where $P_{thr}^{0,i}$ are the corresponding threshold powers.

These results are shown in Fig. 5. The results of calculation of g for $\rho < 0.5$ g/cm³ using the available thermodynamic parameters for Xe [16] are also shown in

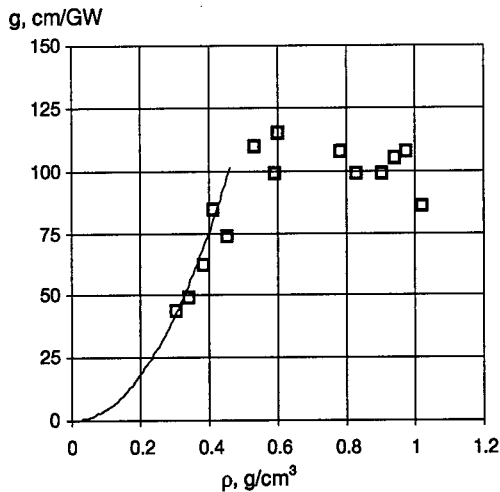


Fig. 5. SBS gain coefficient versus Xe density.
- experiment, - theory.

Fig. 5. We can see that beginning with $\rho = 0.6$ g/cm³ the value of g does not increase, which in our experiments could be only due to a decrease in the phonon lifetime. The

phonon lifetime τ_{ph} has been determined using g_i values in accordance with the equality :

$$\tau_{ph} = g \left(\frac{16\pi^2 n \rho \left(\frac{\partial n}{\partial \rho} \right)^2}{\lambda^2 c v} \right)^{-1},$$

where n is the refractive index, c is the light velocity, v - is the hypersound velocity.

The results of calculation of τ_{ph} are shown in Fig. 6. The value of $\tau_{ph} = 21.2$ ns, calculated with the use of data of hypersound absorption at $\rho = 1.11$ g/cm³ and $t = 19.4$ °C [17], is shown in Fig. 6 as well. A good agreement is observed between our results and those obtained in work [17].

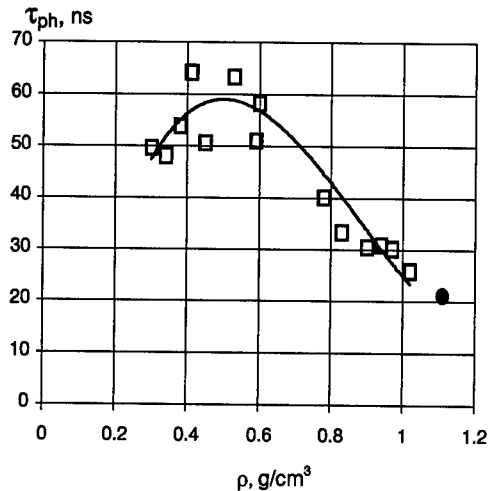


Fig. 6. Phonon lifetime versus Xe density.

- experiment, — - fitting curve,
• - calculated from data of work [17]

The criterion for SBS medium selection which is more resistant to the evolution of undesired thermal perturbation is that the critical energy W_{cr} should exceed the threshold energy $W_{thr} \approx P_{thr} \cdot \tau$, which is proportional to $g \cdot W_{cr} / \lambda$. The more is the value of $g \cdot W_{cr} / \lambda$ the more resistant is the SBS medium to formation of a thermal lens and the longer laser pulses it can convert. Fig. 7 shows experimental dependence of $g \cdot W_{cr} / \lambda$ for xenon in relative

units. Under our conditions this value is the highest in the density range of 0.5-0.8 g/cm³.

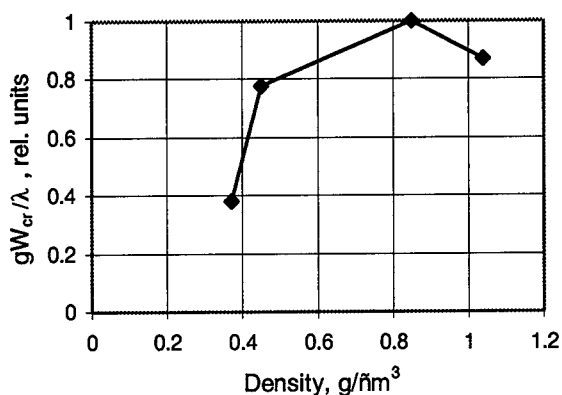


Fig. 7. gW_{cr}/λ versus xenon density

According to the suggested criterion high-purity xenon is best suited as an active SBS medium in high-power gas lasers and is one of the best media for other lasers. (See Table 2).

Table 2

Medium	Nd-glass 1	•cet o-ne	SF ₆ 22 •t	CCl ₄	SiCl ₄	TiCl ₄	SnCl ₄	•• gas 0.6 g/cm ³ (λ=1.06 μm)
g, cm/GW	1.2	15.8	35	4	10	20	14	120
W _{cr} , J	20	5·10 ⁻⁴		11	33	28	57	4.7
g W _{cr} /λ, ms	0.22	7.4·10 ⁻⁵		0.4 1	3.1	5.3	7.5	5.3
References	/18/	/18/	/12/	/9/	/9/	/9/	/9/	our data

Xenon, being a monoatomic gas, is not subjected to the evolution of competing SRS in it, and from the technological point of view is chemically inert, stable, and ecologically safe.

3. References

1. Kirillov G.A., Kochemasov G.G., Kulikov S.M., Pevny S.N., Sukharev S.A. (1996) *HE-pumped iodine laser for plasma and high intensity interactions*. 12th International Conference on Laser Interaction and Related Plasma Phenomena, Osaka (Japan) 1995, AIP Conference Proceedings 369, part two, pp.866-871

2. Dolgoplov Yu.V., Dudov A. M., Eroshenko V.A., Zykov L.I., Kochemasov G.G., Kulikov S.M., Novikov V.N., Sukharev S.A., and Shkapa A.F. (1995) *Phase-conjugate lasers in a free-running mode*. Proceedings of the 2nd International Conference "Physics of Nuclear-Excited Plasma and Problems of Nuclear-Pumped Lasers", vol.2, pp. 229-245. Arzamas-16, VNIIEF, Russia.
3. Dudov A.M., Buyko S.A., Dolgoplov Yu.V., Eroshenko V.A., Kochemasov G.G., Kulikov S.M., Novikov V.N., Scott A.M., Shkapa A.F., Sukharev S.A., Zykov L.I.. (1996) *SBS properties of high-pressure xenon*. XI International Symposium on Gas Flow and Chemical Lasers and High Power Laser Conference. Edinburg, Scotland, UK, 1996. Proc. SPIE, v.3092, pp.341-344.
4. Dolgoplov Yu.V., Komarevski V.A., Kormer S.B., Kulikov S.M. et al. (1979) Experimental investigation of phase conjugation employment at SBS. *ZhETF*, vol.76, pp.908-923.
5. Dolgoplov Yu.V., Kir'yanov Yu.F., Kormer S.B. et al. (1979) *SBS phase conjugation investigation and its application in laser fusion facilities*. In a collection of papers "Phase conjugation of optical radiation in nonlinear media", Gorky.
6. Bubis E.L., Drobotenko V.V., Kulagin O.V., Pasmanik G.A., Stasyuk N.I., Shilov A.A.. (1988) *Thermal self-action effect on SBS excitation in absorbing media*. *Kvant. Elektron.*, v. 15, No.1, p.147.
7. S.J.Pfeifer. (1988) *Phase conjugation and aberration correction by stimulated Brillouin scattering*. SPIE, vol.1000, Laser Wavefront Control, pp.33-42.
8. Bubis E.L., Var'gin V.V., Konchalina L.R., Shilov A.A.. (1988) *Investigation of poorly absorbing media for SBS in the near-IR spectrum*. *Optika and Spektroskopia*, vol.65, issue 6, pp.1281-1285.
9. Andreev Nikolay, Kulagin Oleg, Palashov Oleg, Pasmanik Guerman, Vladimir Rodchenkov. (1995) *SBS of repetitively pulsed radiation and possibility of increasing of the pump average power*. First Annual International Conference on Solid State Lasers for Application to Inertial Confinement Fusion. Monterey, California. SPIE, v. 2633, pp. 476-493.
10. Damzen M.J., Hutchinson M.H.R. and Schroeder W.A. (1987) *Direct measurement of the acoustic decay times of hypersonic waves generated by SBS*, *IEEE J.Quant.Electron.*, v.QE-23, no.3, p.328.
11. Faris G.W., Jusinski L.E. and Hickman A.P., *High-resolution stimulated Brillouin gain spectroscopy in glasses and crystals*, *J.Opt.Soc.Am.B*, v.10, no.4, p.587 (1993)
12. Ragul'ski V.V.. (1990) *Phase conjugation at stimulated Brillouin scattering*, Moscow, Nauka,.
13. Ivanov V.B., Paperny S.B., Snezhko D.A., Startsev V.R.. (1991) *SBS of microsecond pulses in gaseous xenon of the pressure above critical*. *Izvestia AN SSSR, seria fiz.*, vol. 52, no.2, p.224.
14. Betts J.A., Pfeifer S.J., Koop C.G., and Clendening C. in *Technical Digest, CLEO'91*, paper CMG2
15. Rid R., Prausnitz J., Shervood T. (1982) *Properties of gases and liquids*, Leningrad, Chimia.
16. Vargaftik N.B. (1972) *Handbook of thermophysical properties of gases and liquids*, Moscow, Nauka.
17. Garland C.W., Eden D., and Mistura L., (1970) *Critical sound absorption in xenon*, *Phys. Rev. Lett.*, 25(17), 1161-1165.
18. Krainov V.V., Mak A.A., Rusov V.A., Yashin V.E.. (1991) *Phase conjugation of a high-frequency series of pulses at SBS of focused beams*. *Kvant. Elektron.*, v. 18, no. 18, pp. 959-963.

NEW OPTICAL SCHEME OF COMPLICATED RESONATOR IN A TWO-FREQUENCY NH_3 - CO_2 LIDAR

D.L. GLEBOV*, V.A. STEPANOV*, B.I. VASILIEV**,
A.B. YASTREBKOV*

**) Ryazan State Pedagogical University*

****) Lebedev Physical Institute. Institute of Quantum Radiophysics*

1. Introduction

An ammonia laser is an effective source of the powerful IR radiation in the range from 745 to 928 cm^{-1} . Together with a pumping laser (TEA CO_2 laser) they are a very perspective laser system for the probing of atmosphere by a method of the differential absorption with scattering (DAS method), since the range from 9 to 13,5 μm is the most informative at identification of pollution and at the control of their level.

2. Optical Scheme NH_3 - CO_2 Lidar

In [1] a special optical scheme of the NH_3 - CO_2 lidar acting on the DAS method with the simultaneous synchronous ranging of atmosphere by two wavelengths

in the diapason from 9 to 13,5 μm was offered. However a characteristic demerit this optical scheme is the non-uniform spectral distribution of the energy generation in the NH_3 laser (figure 1, [2]).

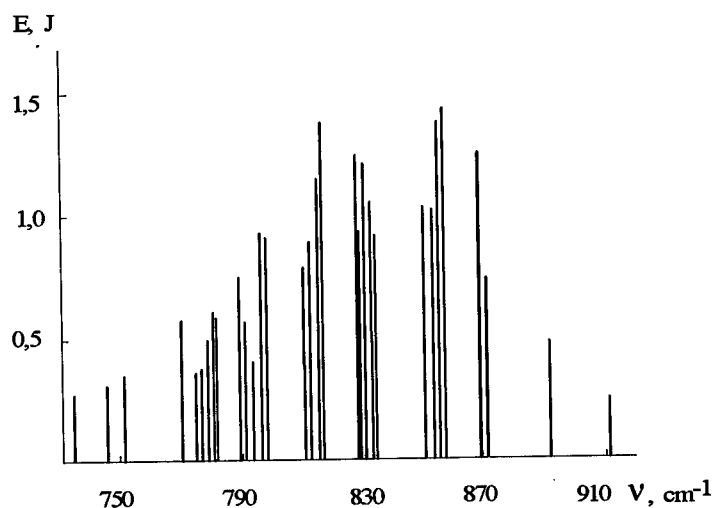


Figure 1. The spectral distribution of the NH_3 laser energy

It is visible, that the ratio of the energy of generation of the strongest lines to the energy of generation of the most weak lines reaches the magnitude of five.

This demerit it is possible partially to remove using the saturation effect in the NH_3 amplifier. The laser and amplifier beams are propagated noncoaxially in usual scheme NH_3 laser - amplifier [3], hence for the spatial combination the beams it is necessary the additional optical elements. In the present message the optical scheme of a two-frequency NH_3 - CO_2 lidar with coaxial propagation of a probing beams is offered, which has the smooth distribution of energy in a spectrum of the generation of NH_3 laser.

Figure 2 shows the optical scheme giving the opportunity to realize the coaxial two-frequency lidar with NH_3 laser acting as generator-amplifier

without the use of the additional optical elements.

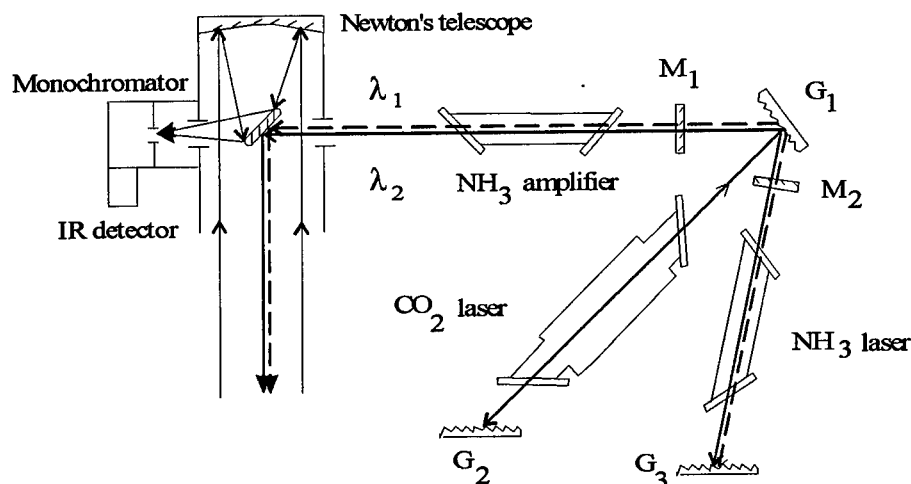


Figure 2. The optical scheme of the two - frequency NH₃ - CO₂ lidar

G₁ - grating 75 mm⁻¹, G₂ - grating 150 mm⁻¹, G₃ - grating 100 mm⁻¹, M₁, M₂ - mirrors

The CO₂ laser resonator is formed by the grating G₂ (150 mm⁻¹, the blazing angle is 41°) and two semitransparent mirrors M₁ and M₂ connected via grating G₁ (75 mm⁻¹, the blazing angle is ~0°). The pumping radiation reflecting from the grating G₁ in the first and minus first orders is dividing on the two about identical beams and then its is directed in two ammonia cells, one is used as generator and the another is used as amplifier. The resonator of the NH₃ generator is formed by the mirror M₂ and the grating G₃ (100 mm⁻¹, the blazing angle is 30°) acting at the first order autocollimation of the ammonia radiation. The tuning of the ammonia laser radiation (from 11 to 13,5 μm) is made by turn of the grating G₃. The ammonia laser radiation reflected in the zero order is directed to the NH₃ amplifier. The output ammonia radiation will be coaxial with the pumping radiation. Since the NH₃ laser levels are lied very low (energy of the lower laser levels is approximately equal kT) it is needed the

saturation active medium by the pumping radiation, at that the part pumping energy passed through the NH_3 cell and may be to used as the reper's beam of the NH_3 - CO_2 lidar. The spectral distribution of the NH_3 laser energy is smoothing at condition of the NH_3 amplifier saturation.

Really, from [3] follows, that the intensity of saturation I_s of the active medium of the ammonia amplifier is equal $70\text{-}90 \text{ kW} / \text{cm}^2$. The energy radiation density of a pumping reaches of the magnitude equal of $0,5 \text{ J} / \text{cm}^2$ in our optical scheme, that it is close to the magnitude of the energy radiation density of a pumping indicated in work [3]. Hence the factor of linear amplification will be also close to $0,05 \text{ cm}^{-1}$ at the same quantities of a partial pressure mixture of ammonia and nitrogen. In this case a weak lines of generation (the lines possessing the energy of generation bellow of the 500 mJ level in a figure 1) have the input amplifier intensity less I_s , and strongest lines have the input amplifier intensity more I_s . Accounts show, that on a output of such amplifier the weak lines are increased in 4-5 times, and strong lines are increased only in 2 times, that results in essential smoothing of a generation spectrum of an ammonia laser. Thus the ratio of energy generation strong lines to weak lines in our case does not exceed twice.

3. Potentialities of NH_3 - CO_2 Lidar

In the conclusion we shall purpose the list of the possible pollution of atmosphere detected by means of two - frequency NH_3 - CO_2 lidar. Table 1 demonstrates potentialities of such lidar.

For example it is necessary to tune the NH_3 laser on frequency of generation equal of 796 cm^{-1} (transition aP (7,3)) for detecting of the CCl_4 molecules .

TABLE 1. The list of the possible pollution of atmosphere detected by $\text{NH}_3\text{-CO}_2$ lidar

Molecule	Mode ¹⁾	Frequency of vibrations, cm^{-1}	Laser transition	Frequency of generation, cm^{-1}
CH_3I	ν_6	882,5	sP(4,k) NH_3	881,1
CH_2Br	ν_7	810	aP(6,5) NH_3	809,7
CHF_2Cl	ν_4	812	aP(6,4) NH_3	812,0
CHCl_3	ν_5	774	aP(8,5) NH_3	774,0
CF_4	$\nu_2 + \nu_4$	1076	9R(16) CO_2	1076
CF_3Cl	ν_2	781	aP(8,1) NH_3	780,4
CF_2Cl_2	$\nu_3 + \nu_5$	780	aP(8,1) NH_3	780,4
CF_2ClBr	ν_2	872	aP(3,1) NH_3	872,6
CF_2Br_2	ν_8	831	aP(5,4) NH_3	830,2
CF_2NCl	ν_4	771	aP(8,6) NH_3	770,9
CFCl_3	ν_4	847	sP(6,k) NH_3	847,4
CFCl_2Br	ν_2	796	aP(7,3) NH_3	796,0
CCl_4	ν_3	796	aP(7,3) NH_3	796,0
Cl_2CNCI	ν_3	746	aP(9,8) NH_3	745,3
NO_2	ν_2	756,8	? NH_3	?
SO_2	$\nu_3 - \nu_2$	854,07 ?	aP(4,0) NH_3	853,6
N_2O_3	ν_4	773	aP(8,5) NH_3	774,0
N_2O_5	ν_{13}	860	? NH_3	?
H_2SO_4	ν_4	834	aP(5,2) NH_3	834,0
CS_2	$\nu_1 + \nu_2$	1070,97 ?	? CO_2	?
SO_3	ν_1	1068	? CO_2	?
CCl_3Br	ν_4	775	aP(7,3) NH_3	96,0
CClBr_3	ν_1	745	aP(9,8) NH_3	745,3

¹⁾The data are taken from the reference book Krasnov K.S. (1979) Molecular constant of the inorganic compounds, Chemistry Publishers, Leningrad.

4. Conclusions

Thus the simple convenient scheme of a coaxial two - frequency $\text{NH}_3 - \text{CO}_2$ lidar for probing of atmosphere by the DAS method with output energy of generation at a level of 1 J is offered.

5. References

1. Vasiliev B.I., Yastrebkov A.B. (1994). NH₃-CO₂ lidar for ranging of the atmosphere in diapason from 9 to 13,5 μ m, Izv. RAN. Ser. fizicheskaya **58**, N 2, 202-206,
2. Vasiliev B.I., Grasiuk A.Z., Dyad'kin A.P., Sukhanov A.N., Yastrebkov A.B. (1980) An optically pumped high-power efficient NH₃ laser tunable in the range of 770-890 cm⁻¹, Sov. Kv. elektronika **7**, N 1, 116-122.
3. Achrarov M., Grasiuk A.Z., Vasiliev B.I., Yastrebkov A.B. (1983) NH₃-N₂ laser - amplifier in the diapason of 800-870 cm⁻¹, KSF(Soviet Physics - Lebedev Institute Reports), N 2, 3-9.

INDEX

- | | | | |
|--------------------------|-------------------------|------------------------|-------------------------|
| Abserrations | 341 | Eigenmodes | 31, 44 |
| Thermal | 315 | Emission, Spontaneous | 433 |
| Ablation | 438 | Erbium | 103 |
| Acousto-optics modulator | 468 | Excimer | 104, 253 |
| Aperture | 144 | | |
| Astigmatism | 5 | Field, Electromagnetic | 40 |
| | | Flashlamp pump | 165 |
| Beam | | Four-wave model | 270 |
| Analysis | 272 | Gain Coefficient | 236 |
| Angular | 9 | Gain, guided duct | 40 |
| Converging | 3 | Gaussian Beam | 5 |
| Divergence | 253 | Gyroscope | 463 |
| Gaussian | 5, 243 | | |
| Guide | 22, 23, 60 | Heat sink | 338 |
| Hermite-Gaussian | 37 | Hermitian | 15, 37, 200 |
| Intensity profiles | 173, 178 | Heterogeneity | 363 |
| Propagation factor | 163, 225 | History | 3 |
| | 249 | Hologram | 121 |
| Quality | 3, 163, 225 | Holographic | |
| | 347 | optical element (HOE) | 141 |
| Rectangular symmetry | 243 | Huygens Integral | 32 |
| Beamsplitters | 131 | Huygens-Fresnel | 4 |
| Brightness | 264 | | |
| | | Inhomogeneities | 68 |
| Cat eye reflector | 312, 318 | Optical | 235, 429 |
| Cavity, Conjugated | 153, 155 | Instabilities, Thermal | 289 |
| Chemical lasers | 427 | Intensity profiles | 340 |
| CO ₂ | 12, 22, 119 | Interferometer- | |
| | 123, 164, 174, 267, 289 | Mach-Zehnder | 346 |
| Coupling | 35, 281 | Interferometry | 301 |
| Matched | 6 | | |
| Cr:LiSAF | 92 | KrF | 438 |
| | | | |
| Design optimization | 309 | Laser | |
| Diffraction grating | 138 | Alpha technology | 221 |
| Diffraction limit | 381 | Annual gain | 163, 211 |
| Diffraction- | | Chemical | 211, 427 |
| optical element (DOE) | 133, 139 | CO ₂ | 22, 119, |
| Diode bar | 335 | | 123, 164, 174, 267, 289 |
| Dissipative losses | 432 | | |
| Distortions | | Aberrations | 126 |
| Amplitude | 63 | Amplifier | 126 |
| Intra cavity | 55 | Cr:LiSAF | 92 |
| Light Induced | 73 | Diode | 332 |
| Phase | 64 | Er | 113 |
| Divergence | 41 | Excimer | 114, 253 |
| Angular | 9 | Gasdynamics | 363 |
| Beam | 3 | Gyroscope | 463 |
| | | High Power programs | 221 |
| Eigenfunction | 4, 13, 50 | Iodine | 225 |

KrF	438	TEM	170, 331,
Low power	329		337, 383, 393, 470
Multi chamber	322	Multiple	20
Nd	107	Nonorthogonal	29
Nd:YAG	143, 163,	Optical	29
	171, 327, 344, 352, 373,	Single	20
	393, 407, 419, 453		
long pulsed	373	Nd:YAG	143, 163,
Nd:YLF	344, 358,		171, 327, 344, 352, 373,
	395		393, 407, 419, 453
Frequency doubled	399	Nd:YLF	344, 356,
Parametric equations	370		395
Power output table	181	Neodymium	107
Ring	277	Noise	48
Robot	319	Nozzle banks	363
Semiconductor	185		
Slab	166, 267,	Optical axis	315
	441	Element diffraction	133
Solid State	165, 321,	Element holographic	141
	327, 381	Modes	29
Tea	122, 138	Nonuniformities	289, 295
Ti:Sapphire	419, 435	System misalignment	389
Lateral Shear	303	Optics	161
Lens train	187	Output power Table of	181
Light Scattering	70		
		Performance	263
M ²	10, 58, 249,	Phase Conjugation	119, 125,
	262, 276, 331, 334, 349		144, 225
Measurements		Phonon life time	236
Beam quality	228	Photons	34, 325
Noise	48	Power scaling	336, 356
Thermal lense	343, 410	Pulsed laser deposition	419, 435
Wave front	301	Pumping-End	327, 352,
Medium, Active	363		330
Mirror	69, 313	Q switching	407, 453
Facet	186	Quadrature coefficients	43
Flat	314		
Outcoupling	260	Radiation	
Phase Correction	133	Distribution	232
Phase conjugate (PCM)	119, 127,	Electromagnetic	34
	130	Quality measurements	228
Primary	145	Spatial filtration	7
Q switching	453	Resonator	
Rotating	324	2D	58
Secondary	145	Active medium	18
Self Pumped	149	Amplitude	63
Toric	166	Analysis	30
Modes	56	Annular gain	217
		Configuration	269

Design optimization	327, 391	Talbot filtration	269
Design strategy	351	Tea laser	122
Hermitian	200	Technological Precision	311
Herriott cell	174	Telescope	133
Hollow	13	Thermal effects	336
Large length	23	Thermal lense	171, 410,
Linear	454		395
Open	282	Ti:Sapphire	419, 435
Ring	458, 464	Turbulence	295
Single axis	213		
Slab	22	Wave	
Stable	10, 166, 251,	Converging	15, 216
	255, 313, 315, 381	Optical modeling	189
Theory	13	Spherical aberrations	8
Unstable	55, 176, 185,	Waveguide	22, 60
	192, 257, 441	Annular	23
Gaussian	261	Channels	435
Toric	212	Planar	419
With internal axicon	214	Slab	166, 267
RF excitation	267		
		Xenon, high pressure	233
Scaling problems	429	Xe-SF ₆ gas	227
Semiconductor laser	185		
Shear Interferometry	301		
Slab	166, 267,		
	441		
Spatial filtering	7, 26		
Spherical aberrations	8		
Stimulated Brillouin			
scattering (SBS)	120, 225,		
	233, 453		

LIST OF PARTICIPANTS

Dr. Krzysztof M. Abramski
Department of Electronics
Technical University of Wroclaw
Wybrzeze Wyspianskiego 27
Wroclaw Poland
Tel: +48.71.320.3024
FAX: +48.71.223.473
E mail: kma@zr.ita.pwr.wroc.pl

Dr. Dmitry Afonin
Physics Department
Moscow State University
Vorobevy Gory
199899 Moscow Russia
Tel: +7.095.939.2094
FAX: +7.095.932.8820
E mail: afonin@radi1.phys.msu.s

Dr. Stefan Amarande
Laser Department
Institute of Atomic Physics
P.O.Box MG-36
R-76900 Bucharest Romania
Tel: +40.1.780.6925
FAX: +40.1.420.9391
E mail:

Prof. Yuri A. Anan'ev
Physics Department
State Technical University
St. Petersburg 199034, Russia
Tel:
FAX:
E mail: yuri@anan.hop.stu.neva.r

Dr. Serguei G. Anikitchev
SGA
44 Painted Rock Ave.
Richmond Hill Ont. L4S 1R6 Can
Tel: +1.905.780.6945
FAX:
E mail: sga@interlog.com

Dr. Howard J. Baker
Department of Physics
Heriot-Watt University
Riccarton
Edinburgh EH14 4AS, UK
Tel: +44.131.451.3085
FAX: +44.131.451.3088
E mail: ophthjb@optfs1.phy.hw.ac.

Dr. Anatoly Bashkin
NPO Energomash
Burdenko 1, Chimky
141400 Moscow Russia
Tel: +7.095.572.2947
FAX: +7.095.251.7504
E mail:

Prof. Pierre-Andre Belanger
Department de Physique
Universite Laval
Sainte-Foy Que G1K 7P4 Canada
Tel: +1.418.656.2234
FAX: +1.418.656.2623
E mail: mpiche@phy.ulaval.ca

Dr. Alexander Betin
Optical Physics
Hughes Research Laboratory
Loc MA Buildg. 250, M.S. RL65
Malibu CA 90265, USA
Tel: +1.310.317.5028
FAX: +1.310.317.5679
E mail: abetin@msmail4.hac.com

Prof. William A. Clarkson
Director, Optoelectronics Research
University of Southampton
Southampton SO17 1BJ, UK
Tel:
FAX:
E mail: wac@orc.soton.ac.uk

Dr. Traian Dascalu
Institute of Atomic Physics
P.O.Box MG-36
R-76900 Bucharest Romania
Tel: +40.1.420.6925
FAX: +40.1.420.9391
E mail: dascalu@roifa.ifa.ro

Dr. Gregory Dente
GCD Associates
2100 Alvarado NE
Albuquerque NM 87110 USA
Tel: +1.505.846.6136
FAX: +1.505.846.4313
E mail: tilton@plk.af.mil

Prof. Sergey Dimakov
Vavilov State Optical Institute
Birgevaya lin. 12
St. Petersburg 199034, Russia
Tel:
FAX:
E mail: dimakov@ilph.spb.su

Prof. Hans J. Eichler
Optisches Institut
Technische Universitaet Berlin
Str. des 17. Juni 135
10623 Berlin Germany
Tel: +49.30.3142.2458
FAX:
E mail: eichler@physik.tu-berlin.

Mr. Xin-min Han
Chemical Lasers
Dalian Instit. of Chemical Physics
P.O.Box 110-707
116023 Dalian China
Tel: +86.411.467.1991 x669
FAX: +86.411.467.9766
E mail: swell@gingko.dlut.edu.cn

Dr. Norman Hodgson
Chair for Photonics
University of Potsdam
AmNeuen Palais 10
14469 Potsdam Germany
Tel: +49.331.977.1026
FAX: +49.331.977.1134
E mail:

Mr. Ramon Hofstra
Dept. of Applied Physics
Twente University
P. O. Box 217
7500 AE Enschede The Netherlan
Tel: +31.53.489.3976
FAX: +31.53.489.1102
E mail: r.m.hofstra@tn.utwente.nl

Mr. Athanasios Ioannou
University of Patras
Patra Greece
Tel: +30.61.997470
FAX: +30.61.991980
E mail: aioannou@physics.upatra

Prof. Miroslav Jelinek
Institute of Physics
Czech Academy of Science
2 Na Slovance
18040 Prague 8 Czech Republic
Tel: +420.2.815.2733
FAX: +420.2.858.4569
E mail: jelinek@fzu.cz

Mr. Yu-gi Jin
Chemical Lasers
Dalian Instit. of Chemical Physics
P.O.Box 110-707
116023 Dalian China
Tel: +86.411.467.1991 x820
FAX: +86.411.467.9766
E mail: swell@gingko.dlut.edu.cn

Dr. Ram Kossowsky
Emerging Technologies, Inc.
6327 Burchfield Avenue
Pittsburgh PA 15217, USA
Tel: +1-412.421.4408
FAX: +1-412.421.4342
E mail: ramkoss@mindspring.co

Dr. Hanita Kossowsky
Emerging Technologies, Inc.
6327 Burchfield Avenue
Pittsburgh PA 15217, USA
Tel: +1-412.421.4408
FAX: +1-412.421.4342
E mail:

Dr. Aleksey A. Kuznetsov
Low Temperature Plasma Physics
Lebedev Physical Institute
Leninski Prospect 53
117924 Moscow Russia
Tel: +7.095.132.6476
FAX: +7.095.938.2251
E mail: smith@sci.lpi.msk.su

Mr. Jan Lancok
Multilayers Structure Department
Institute of Physics
Na Slovance 2
18040 Prague 8 Czech Republic
Tel: +420.2.6605.2733
FAX: +420.2.858.4569
E mail: lancok@fzu.cz

Dr. Alexander Lavrov
Laboratory 855
R.S.C. Applied Chemistry
14 Dubrolubov Ave.
197198 St. Petersburg Russia
Tel: +7.812.314.1671
FAX: +7.812.238.9270
E mail: lavrov@ban.spb.ru

Dr. Antonio Lucianetti
Institute of Applied Physics
University of Bern
Sidlerstrasse 5
CH-3012 Bern Switzerland
Tel: +41.31.631.8938
FAX: +41.31.631.7765
E mail: lucian@iap.unibe.ch

Dr. Vittorio Magni
Dopartimento di Fisica
Politenico di Milano
Piazza L. da Vinci 32
20133 Milan Italy
Tel: +39.2.2399.6150
FAX: +39.2.2399.6126
E mail: magni@axp7000.cdc.poli

Dr. Svetlana N. Markova
Shternberg Astronomical Institute
Moscow State University
Universitetsky Prospect 13
119899 Moscow Russia
Tel: +7.095.939.1049
FAX: +7.095.932.8841
E mail: snm@sai.msu.su

Ms. Manjusha Mehendale
Physics Department
University of Illinois
845 W. Taylor St. M/C 273, Rm 22
Chicago IL 60607 USA
Tel: +1.312.996.5361
FAX: +1.312.996.9016
E mail: manjusha@tiger.cc.uic.e

Ms. Anca Mocofanescu
Laser Department
Institute of Atomic Physics
P.O.Box MG-54
R-76900 Bucharest Romania
Tel: +40.1.780.6925
FAX: +40.1.420.9391
E mail: amocof@roifa.ifa.ro

Prof. Vladimir Moshkov
Vavilov State Optical Institute
Birgevaya lin. 12
St. Petersburg 199034, Russia
Tel:
FAX:
E mail:

Dr. Eric Mottay
CE 2901
B.M. Industries
91029 Evry Cedex France
Tel: +33.164.97.53.54
FAX: +33.1.64.97.52.03
E mail:

Mr. Nicholas G. Muller
Institute of Applied Physics
University of Berne
Sidlerstrasse 5
CH-3012 Berne Switzerland
Tel: +41.31.631.8948
FAX: +41.31.631.3765
E mail: muller@iap.unibe.ch

Mr. Valentin D. Nelea
Laser Department
Institute of Atomic Physics
P.O.Box MG-36
R-76900 Bucharest Romania
Tel: +40.1.780.6925
FAX: +40.1.420.9391
E mail:

Dr. Josef Novak
Institute of Electrical Engineering
Slovak Academy of Science
Dubravska cesta 9
842 39 Bratislava Slovak Republic
Tel: +421.7.375.826
FAX: +421.7.375.816
E mail: eleknova@savba.sk

Mr. Igor Novprienok
Institute of Electronics
Belarus Academy of Science
22 Logoiski Trakt
220841 Minsk-90 Belarus
Tel: +375.172.65.64.33
FAX: +375.172.65.25.41
E mail: inel@bas17.basnet.minsk.

Prof. Irena B. Orlova
Vavilov State Optical Institute
Birgevaya lin. 12
St. Petersburg 199034, Russia
Tel:
FAX:
E mail: yuri@anan.hop.stu.neva.r

Dr. Vadim A. Parfenov
S.I.Vavilov State Optical Institute
12. Birzhevaya liniya
199034 St.Petersburg Russia
Tel:
FAX: +7.812.218.3720
E mail: parfenov@soi.spb.su

Mr. John Parthenios
University of Patras
Patra Greece
Tel: +30.61.997470
FAX: +30.61.991980
E mail: iparthen@physics.upatras.

Prof. Peter Persephonis
University of Patras
Patra Greece
Tel: +30.61.997470
FAX: +30.61.991980
E mail: pet-per@physics.upatras.g

Prof. Michel Piche
 Department de Physique
 Universite Laval
 Sainte-Foy Que G1K 7P4, Canada
 Tel: +1.418.656.2753
 FAX: +1.418.656.2623
 E mail: mpiche@phy.ulaval.ca

Dr. Andrew M. Scott
 Defence Research Agency
 Malvern WR14 3PS UK
 Tel: 44.1684.895.418
 FAX: 44.1684.896.270
 E mail: amscott@dra.hmg.gb

Dr. Margarida Pires
 Physics Department
 INETI
 Est. Palo Do, Lumiar 1699
 Lisboa Portugal
 Tel: +351.1.716.5141
 FAX: +351.1.716.3048
 E mail:

Dr. Valentin Shekhtman
 Engineering Physical Lab., EFL Lt
 Box 260, Pushkin 8
 189620 St. Petersburg Russia
 Tel: +7.812.476.2059
 FAX: +7.812.311.9678
 E mail: efl@shekhtman.spb.ru

Dr. Edward W. Plinski
 Department of Electronics
 Technical University of Wroclaw
 Wybrzeze Wyspianskiego 27
 Wroclaw Poland
 Tel: +48.71.320.3024
 FAX: +48.71.223.473
 E mail: eda@zr.ita.pwr.wroc.pl

Prof. Vladimir E. Sherstobitov
 Laser Physics
 Vavilov State Optical Institute
 Birgevaya lin. 12
 St. Petersburg 199034, Russia
 Tel:
 FAX:
 E mail: sherstob@ilph.spb.su

Dr. Kirill Prokhorov
 VKIV
 General Physics Institute
 Vavilov Street 38
 Moscow 117942 Russia
 Tel: +7.095.135.3448
 FAX: +7.095.135.3448
 E mail: cyrpro@kapella.gpi.ru

Dr. Eugen F. Shishkanov
 Department of Physics
 RSPU, Radiological University
 46 Svoboda Str.
 390000 Ryazan Russia
 Tel:
 FAX:
 E mail: yastreb@ttc.ryazan.ru

Dr. Carlos B. Roundy
 President
 Spiricon, Inc.
 2600 North Main
 Logan UT 84341 USA
 Tel: +1.801.753.3729
 FAX: +1.801.753.5231
 E mail: spiricon@cache.net

Dr. A. F. Shkapa
 Inst. of Experimental Physics, Lase
 Russian Fed. Nuclear Center
 Prospect Mira, 37 (VNIIEF)
 607190 Sarov, N. Novgorod Reg.
 Tel: +7.831.30.45893
 FAX: +7.831.30.54565
 E mail: shkapa@otd13.vniief.ru

Prof. Anthoni E. Siegman
Ginzton Laboratory
Stanford University
Mail Code 4085
Stanford CA 94305, USA
Tel: +1.415.723.8669
FAX:
E mail: siegman@ee.stanford.edu

Dr. Martin Stickley
Chief, Lasers, Optics and Materials
European Office of Aerospace R&D
223/231 Old Marylbone Rd.
London NW1 5TH UK
Tel: +44.171.514.4354
FAX: +44.171.514.4960
E mail: mstickley@coard.af.mil

Dr. Vladimir Venediktov
Institute for Laser Physics
SC / Vavilov State Optical Institute
Birjevaya, 12, 199034, St.-Petersbu
St. Petersburg Russia
Tel: +7.812. 218.1093
FAX: +7.812. 218.5891
E mail: vened@ilph.spb.su

Dr. Richard C. Wade
Science Application Int'l Corp.
1225 Johnson Ferry Road
Marietta GA 30068-2767 USA
Tel: +1.770.973.8935
FAX: +1.770.973.6971
E mail: dick_wade@cpqm.saic.co

Dr. Robert Walter
W.J. Schafer Associates, Inc.
2000 Randolph Road. SE
Albuquerque NM 87106. USA
Tel: +1.505.242.9992
FAX: +1.505.242.9975
E mail: bwalter@wjasa.com

Dr. Andrei B. Yastrebkov
Department of Physics
RSPU. Radiological University
46 Svoboda Str.
390000 Ryazan Russia
Tel:
FAX:
E mail: yastreb@ttc.ryazan.ru

Dr. Valentina Ye. Zavalova
Laser Physics Division
Laser Research Center
Svyatoazerskaya St. 1
140700 Shatura, Moscow Reg. Ru
Tel: +7.09645.25995
FAX: +7.09645.22532
E mail: center@laser.nictl.su

Dr. L. I. Zykov
Inst. of Experimental Physics, Lase
Russian Fed. Nuclear Center
Prospect Mira, 37 (VNIIEF)
607190 Sarov, N. Novgorod Reg.
Tel: +7.831.30.45893
FAX: +7.831.30.54565
E mail: zykov@otd13.vniief.ru